The Hipparcos and Tycho Catalogues

SP–1200
June 1997

The Hipparcos and Tycho Catalogues

Astrometric and Photometric Star Catalogues

derived from the

ESA Hipparcos Space Astrometry Mission

A Collaboration Between

the European Space Agency

and

the FAST, NDAC, TDAC and INCA Consortia

and the Hipparcos Industrial Consortium led by

Matra Marconi Space

and

Alenia Spazio

European Space Agency
Agence spatiale européenne

Cover illustration: an impression of selected stars in their true positions around the Sun, as determined by Hipparcos, and viewed from a distant vantage point. Inset: sky map of the number of observations made by Hipparcos, in ecliptic coordinates.

Published by:	ESA Publications Division, c/o ESTEC, Noordwijk, The Netherlands
Scientific Coordination:	M.A.C. Perryman, ESA Space Science Department and the Hipparcos Science Team
Composition:	Volume 1: M.A.C. Perryman Volume 2: K.S. O'Flaherty Volume 3: F. van Leeuwen, L. Lindegren & F. Mignard Volume 4: U. Bastian & E. Høg Volumes 5–11: Hans Schrijver Volume 12: Michel Grenon Volume 13: Michel Grenon (charts) & Hans Schrijver (tables) Volumes 14–16: Roger W. Sinnott Volume 17: Hans Schrijver & W. O'Mullane Typeset using TEX (by D.E. Knuth) and dvips (by T. Rokicki) in Monotype Plantin (Adobe) and Frutiger (URW)
Film Production:	Volumes 1–4: ESA Publications Division, ESTEC, Noordwijk, The Netherlands Volumes 5–13: Imprimerie Louis-Jean, Gap, France Volumes 14–16: Sky Publishing Corporation, Cambridge, Massachusetts, USA
ASCII CD-ROMs:	Swets & Zeitlinger B.V., Lisse, The Netherlands
Publications Management:	B. Battrick & H. Wapstra
Cover Design:	C. Haakman
©1997	European Space Agency ISSN 0379–6566 ISBN 92–9092–399-7 (Volumes 1–17)
Price:	650 Dfl ($400) (17 volumes) 165 Dfl ($100) (Volumes 1 & 17 only)

Volume 2

The Hipparcos Satellite Operations

Compiled by:

M.A.C. Perryman & K.S. O'Flaherty (ESA–ESTEC)

D. Heger (ESA–ESOC) & A.J.C. McDonald (ESOC/Logica UK Ltd)

with the support of

The Hipparcos Science Team,

M. Bouffard (Matra Marconi Space),

and

B. Strim (Alenia Spazio)

Launch of the Hipparcos Satellite by Ariane 4 Flight V33, 8 August 1989 (Photo: CSG Kourou)

Volume 2: The Hipparcos Satellite Operations

Contents

Section C: Interfaces with the Scientific Consortia

Section D: Payload and Spacecraft Performances

Section E: Real-Time Attitude Control and Determination

Section F: End of Mission

Appendices

Foreword

The Hipparcos astrometry mission was accepted within the European Space Agency's scientific programme in 1980. The Hipparcos satellite was designed and constructed under ESA responsibility by a European industrial consortium led by Matra Marconi Space (France) and Alenia Spazio (Italy), and launched by Ariane 4 flight V33 on 8 August 1989. High-quality scientific data were acquired between November 1989 and March 1993, and communications with the satellite were terminated on 15 August 1993. The Hipparcos and Tycho Catalogues, representing the most accurate and comprehensive astrometric and photometric star catalogues compiled to date, were finalised within three years of the end of the satellite operations—almost exactly corresponding to the schedule anticipated by the scientific consortia before the satellite launch. All of the scientific goals motivating the mission's adoption in 1980 were surpassed.

An enormous effort—scientific, technical, and managerial—was devoted to the satellite design, construction, testing and calibration, in a commitment extending over approximately eight years; in parallel, teams of European scientists worked closely with ESA to prepare a complex chain of computer programs ready to process nearly 1000 Gbits of satellite data in what amounted to the largest single data analysis problem ever undertaken in astronomy.

Ultimate success was not easily won. After a nominal launch, the failure of the apogee boost motor left the satellite in an unplanned, highly eccentric geostationary transfer orbit. A mission which was designed to have a single ground station, operated in a geostationary orbit for 24 hours a day, turned out instead to consist of a satellite in contact with the ground station for less than 10 hours a day, repeatedly crossing the harsh radiation environment of the van Allen belts. Further ground stations were brought into the telecommunications network. ESOC, in collaboration with Matra Marconi Space, developed new operational procedures to accommodate the new orbit, the revised data to be sent to the scientific data reduction groups, and contingency procedures to maintain the flow of scientific data. The payload and spacecraft subsystems all worked within their design specifications, the satellite was eventually operated for more than the 2.5 years nominal mission duration, and scientific data of extremely high quality were acquired.

This volume is intended as a detailed description of the manner in which the scientific data were collected. In addition, it provides a summary of the satellite and payload performances, and a record of the technological investigations and resulting knowledge derived from the operation of the Hipparcos satellite. It includes details of the major spacecraft and payload subsystems, the radiation environment, understanding of the payload evolution, perturbing torques acting on the satellite, and details of the development of two- and zero-gyro operational procedures implemented as gyro failures threatened to terminate operations prematurely.

The material in this volume has been based on the pre-launch technical description, published in 1989 as ESA SP-1111 Volume I, combined with the ESOC Operations Report produced by the Operations Team at the end of the mission. Significant parts of the report are taken from the Matra Marconi Space 'In-Orbit Performance Verification Report' prepared under ESA contract. Other material was taken from technical notes compiled throughout the satellite operations phase.

Significant additional material was included as follows:

- material in Chapter 5 is based on Davies, P.E. & McDonald, A.J.C., 1991 *Results of the Hipparcos In-Orbit Payload Calibration*, Journal of the British Interplanetary Society, Vol. 44, 37;

- material in Chapter 7 is based on Crabb, R.L., 1994 *Solar cell radiation damage*, Radiat. Phys. Chem. 43, 93–103; Nieminen, P.J., 1995 *Standard radiation environment monitor detector design and simulations*, ESTEC Working Paper 1829; Section 7.4 is from Daly, E.J. et al., 1994 *Radiation-belt and transient solar-magnetospheric effects on Hipparcos radiation background*, IEEE Trans. Nucl. Sci. NS-41, 6, 2376;

- parts of Chapter 10 are from Lindegren, L. et al., 1992 *Geometrical stability and evolution of the Hipparcos telescope*, Astronomy & Astrophysics, 258, 35, and updated by L. Lindegren and F. van Leeuwen;

- material in Chapter 11 was taken from Crabb, R.L. & Robben, A.P., 1993 *In-flight Hipparcos solar array performance degradation after three and a half years*, Proc. European Space Power Conference, Graz, Austria, ESTEC/XPG-WPP-054;

- parts of Chapter 14 were taken from Batten, A.J. & McDonald, A.J.C., 1989, *Hipparcos precise attitude determination: methods and results*, Int. Symp. Space Dynamics, Toulouse, France;

- material in Chapter 15 is based on Auburn, J.H.C., Batten, A.J. & McDonald, A.J.C., 1991 *Hipparcos attitude determination with two gyros and a star mapper*, Proc. 3rd International Symp. Spacecraft Flight Dynamics, Darmstadt, Germany, ESA SP-326, 213.

The composition of the ESA-ESOC Launch and Operations Teams are given in Appendix A to this volume. The key personnel involved from Matra Marconi Space (the satellite Prime Contractor) and Alenia Spazio (responsible for the spacecraft and for the satellite integration), along with the industrial sub-contractors, are given in Volume 1. Detailed acknowledgments are also included in Volume 1.

The Bibliography covers all aspects of the Hipparcos mission published up until 1996, including scientific papers referring to the construction of the Hipparcos Input Catalogue and to the data analysis tasks, and published progress reports, in both refereed journals, conference proceedings, and the popular press.

We take this opportunity to attribute the overall success of ESA's Hipparcos space astrometry mission to the scientific and political groups who encouraged and supported the possibilities of space astrometry from the project's origins in 1967 through to the ESA advisory structure which ultimately ensured its completion; to the ESA Project Team which supervised all technical aspects; to European industry under the leadership of Matra Marconi Space and Alenia Spazio which turned concept into reality; to the ESOC Operations Team for meeting a seemingly impossible challenge of maintaining satellite operations for more than three years; and to the Hipparcos scientific teams for their relentless pursuit of milliarcsec astrometry.

M.A.C. Perryman, Hipparcos Project Scientist
D. Heger, Hipparcos Spacecraft Operations Manager

PROLOGUE

This chapter provides a general background to the Hipparcos mission leading up to launch. It summarises the requirements for improved astrometric measurements (positions, parallaxes and proper motions) of the stars, a short history of the development of astrometric measurements, and a summary of the development of the Hipparcos project itself.

Introduction and Historical Background

Introduction

The achievable accuracy of stellar positions measured from the ground is limited by numerous observational difficulties, important among them being the effects of an inhomogeneous and fluctuating atmosphere, instrumental flexure, and the inability to observe all parts of the celestial sphere simultaneously or even sequentially from any single observing location. There are, nevertheless, important astronomical and astrophysical reasons why more precise positional measurements have been urgently needed.

The observational situation promised to make a rapid and dramatic change when, at the request of the scientific community, and following an internal feasibility study supported by its member state scientists, the European Space Agency (ESA) undertook the Hipparcos space mission. This mission was dedicated to the precise positional measurement of some 120 000 stars. Launched by Ariane 4 on 8 August 1989, the final outcome of the mission is two major catalogues—the Hipparcos and Tycho Catalogues—of star positions, parallaxes, and proper motions, along with photometric and other data on the stars observed.

Historical Context

Confirmation of the Earth's spherical form, assumed by the Pythagorian School as early as the sixth century B.C., first emerged with the evidence provided by Aristotle in *De Caelo* (around 340 B.C.) and the first scientific measurements of the Earth's size by Eratosthenes in about 240 B.C. And while the principle of the measurement of

the Earth–Moon distance had already been described by Aristarchus of Samos around 250 B.C., it was about 120 B.C. when Hipparchus first calculated the distance of the Moon from the Earth, by measuring the Moon's parallax. A comparison of Hipparchus' star catalogue of 1080 stars with the work of his predecessors led to the discovery of the precession of the equinoxes and the eccentricity of the Sun's path. All this was achieved by measurements with the naked eye, the resolution power of which is limited to a few minutes of arc. These early observations were rarely accurate to better than about 30 minutes of arc, due to the primitive instruments used.

Little advance was made in astrometry, as in other branches of science, during the millenium of the 'Middle Ages', in which western civilisation remained with the concept of a universe with the Earth at its centre. However, the awakening of man's scientific curiosity at the time of the Reformation led to revised interest in astrometry. Copernicus propounded the heliocentric concept, and Tycho Brahe, using his brass azimuth quadrant and many other new instruments, carried out a long series of observations during the second half of the sixteenth century. These observations were to provide the basis for Kepler's Laws of planetary motion.

Although observations were still being made with the naked eye, this was soon to change. By 1609 Galileo, using information obtained from Holland (where the instrument was invented and first built in 1604), was making use of the optical telescope, and this landmark was to be of particular significance for astrometry. The angular error in astrometric measurements fell to about 15 seconds of arc by 1700, and to about 8 seconds of arc by 1725. This made it possible to detect stellar aberration (small positional displacements due to the vectorial composition of the velocity of light to the Earth's orbital velocity) and nutation (an 18.6 year wobble in the Earth's spin axis produced by the gravitational influence of the Sun and Moon).

Remeasurement of the rate of precession was made by Edmund Halley, who compared contemporary observations with those that Hipparchus and others had made. While most of the stars displayed a general drift amounting to a precession of about 50 seconds of arc per year, Halley announced in 1718 that three stars, Aldebaran, Sirius and Arcturus, were displaced from their expected positions by large fractions of a degree. Halley deduced that each star had its own 'proper motion'.

Eventual improvements in observational precision during the 18th century (see Figure 1), revealed the motions of many more stars, and in 1783 William Herschel found that he could partly explain these motions by assuming that the Sun itself was moving. This suggested that some stars might be relatively close to the Sun, and so astronomers intensified their efforts to detect 'trigonometric parallax', the apparent oscillation in a star's position arising from the Earth's annual motion around the Sun.

Friedrich Bessel was the first to publish a parallax value, in 1838, following his studies of the motion of 61 Cygni. Bessel's careful analysis of the measurement errors and his use of both coordinates on the sky gave credibility to his results, after many previous claims from astronomers to have measured a stellar parallax. Thomas Henderson is credited with the first measurement of stellar parallax, that of the bright star Alpha Centauri, from observations made at the Cape of Good Hope, in 1832–33, although he did not analyse the measurements for some years; the two components of this star, together with a faint companion called Proxima Centauri, form the nearest known group of stars to the Sun, at a distance of a little more than 4 light years. Wilhelm Struve measured the parallax of Vega in 1837–38.

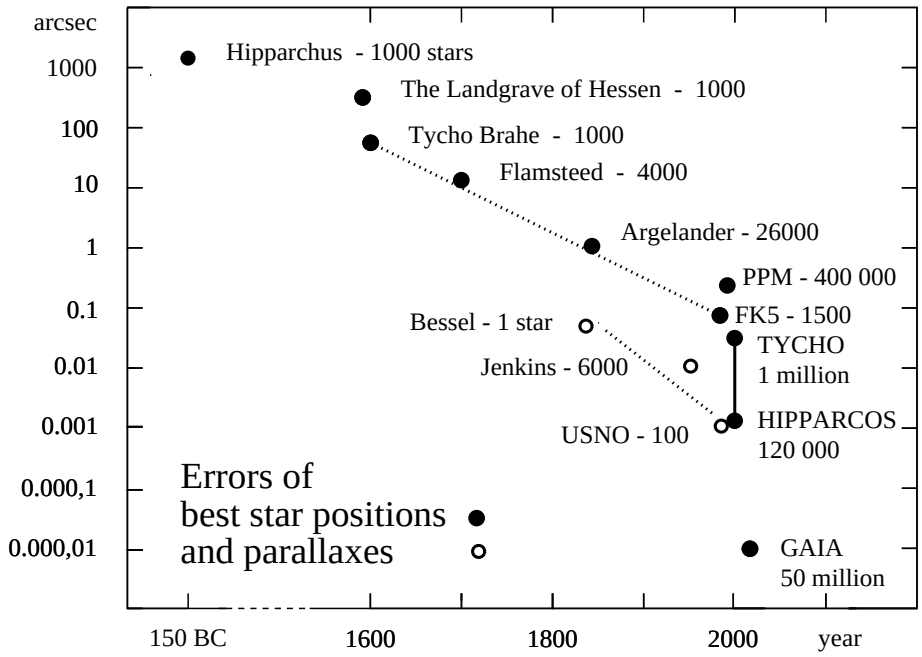

Figure 1. *Improvement in the angular precision of astrometric measurements as a function of time. All points refer to ground-based observations or catalogues, with the exception of the Hipparcos and Tycho Catalogues derived from the Hipparcos mission, and the proposed GAIA space astrometry mission (courtesy E. Høg).*

Observations improved substantially with the invention of photography, which gave astrometry yet another tool it could use. In 1887 a world-wide cooperative programme was started to make a full photographic survey of the sky. Eighteen countries were involved in this project, called the 'Carte du Ciel'. All observatories involved used the same design of astrograph, plates, and observing protocols. In the mean, a precision of around 1 arcsec was obtained by this programme for 13 million stars.

Determinations of photographic trigonometric parallaxes have been made at more than a dozen observatories since the early part of this century. The technique is to measure the shift of the selected star relative to a few stars surrounding it on some 20 or more plates taken over a number of years. Several thousand trigonometric parallaxes have now been measured from the ground; however, only a few hundred are considered to be known with an accuracy of better than about 20 per cent, while the systematic effects remain both conspicuous but uncertain.

Effort over the past one hundred years or so has resulted in observational uncertainties in astrometric measurements being reduced by an order of magnitude due to instrumental refinements. However, further rapid progress on the ground was considered unlikely, since the most significant uncertainties remaining are caused by the Earth's atmosphere. Averaging out the dominant effects of atmospheric turbulence proved to be relatively efficient, yet the comparisons between results from different observatories still showed systematic differences due to slowly varying refraction effects. The study of these effects has as yet eluded their precise description; in consequence they cannot therefore be reduced with confidence.

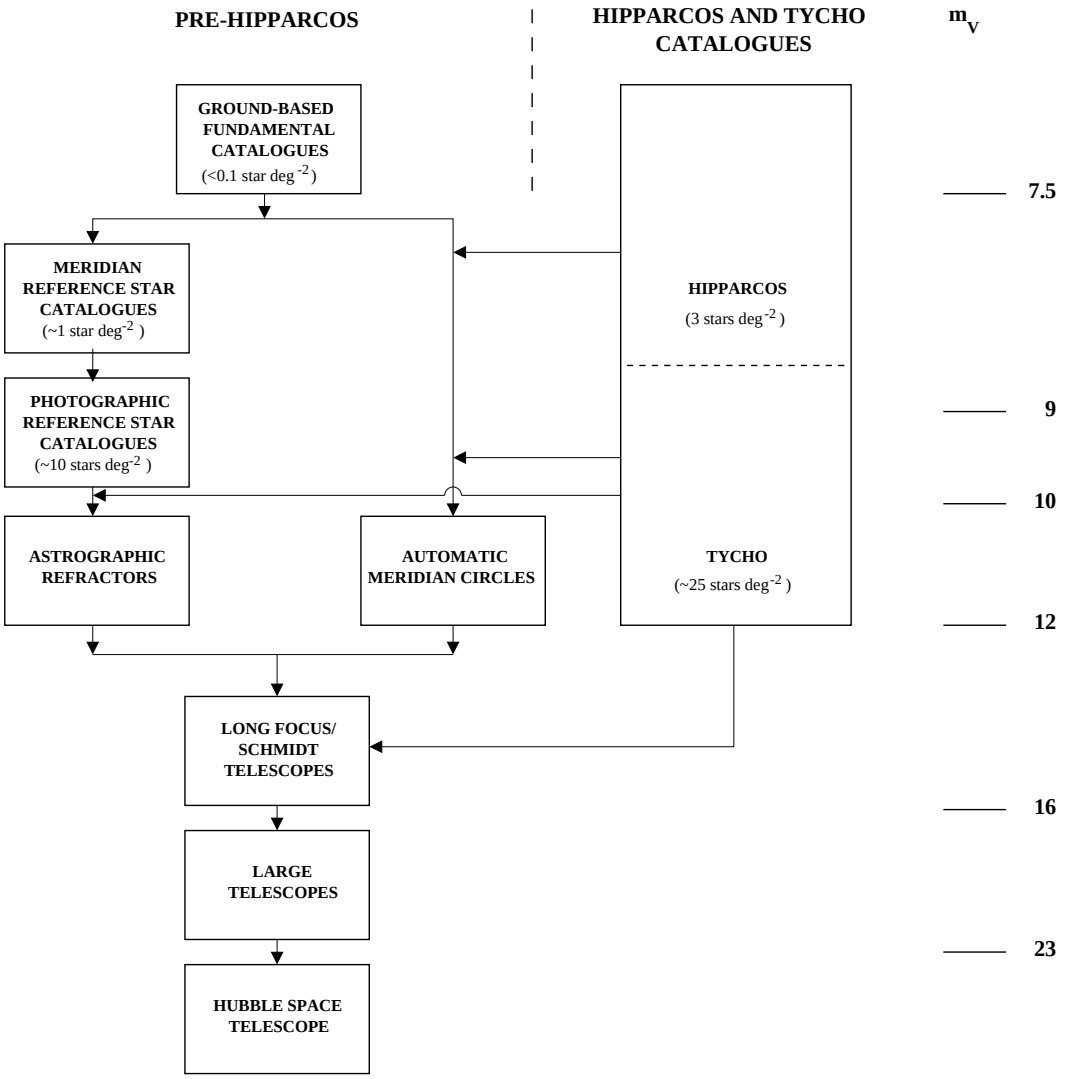

Figure 2. *The expected role of the Hipparcos and Tycho positional measurements in the determination of the position of faint objects (right), compared with the situation existing before launch (left).*

New approaches to astrometry were necessary, and in the 1960's, some astronomers considered that the best prospect for major advances in this field was to go into space. The Hipparcos mission was undertaken to revolutionise this long, difficult, and very important task. The expected role of the Hipparcos and Tycho positional measurements in the determination of the position of faint objects, compared with the previous situation, is shown in Figure 2. A summary of the key features of the intended and actual mission results is given in Table 1.

Evolution of the Hipparcos Project

Developments before Acceptance by ESA

A preliminary proposal for a space astrometry mission was submitted by P. Lacroute to the Centre National de la Recherche Scientifique (CNRS) in France in March 1966. The proposal was made to build up a reference system using about 700 stars brighter than 7 mag, with relative positions known to better than about 0.01 arcsec. Already, in his first proposal, two key features of Hipparcos were used: a beam combiner (more complex than that eventually adopted, with three surfaces resulting in a symmetric image), and the observation of the light modulated by scanning slits.

In August 1967, a new version of the project was presented in Prague at the meeting of the International Astronomical Union (IAU). A revision of this proposal was then presented to the Centre National d'Etudes Spatiales (CNES) in France, in November 1967. Not only was this version technically more elaborate than before, but also, and perhaps more importantly, the scientific significance of the prospective results was better emphasised. Amongst the ideas that were submitted to CNES in order to demonstrate the feasibility of the project, was the idea—quickly rejected—that it could be flown on a balloon. Some funds were subsequently made available by CNES for optical calculations, and for the trial manufacture of a 'beam-combining mirror' in 1969. It proved to be impossible, however, to construct such a mirror that would be able to resist the vibrations encountered during launch.

In August 1970, a paper was presented at the IAU meeting in Brighton on the subject of astrometric measurements from space. There were no major changes to the technical proposal, and it served to draw the attention of the astronomical community to the possibility of measuring absolute trigonometric parallaxes to better than 0.005 arcsec. In 1970, CNES stopped their studies of the project, not only because of technical difficulties which, at that time, seemed to be beyond the state of the art in space technology, but also as a result of the political decision taken to stop the French national space programme, and to use the funds to support European cooperation within the European Space Research Organisation (ESRO).

New ideas were introduced at the Astrometry Symposium in Perth in 1973. A description of the mission was made at a meeting of the ESRO Astronomy Working Group in Frascati in 1973 by J. Kovalevsky. The Working Group selected thirteen projects that merited further consideration. In November 1973, a report was submitted to the European Space Research Organisation pointing out—in addition to a design based on that of the earlier satellite TD1—the technical potential of a similar system that could be flown on Spacelab. Such a system could use more powerful optics and could reach fainter stars, but would not have yielded as many measurements as a scanning satellite. By that time, the prohibitive cost of the eight shuttle launches required for an astrometric Spacelab mission was not fully recognised.

This report was followed by a symposium on 'Space Astrometry' organised by ESRO, soon to become the European Space Agency, in October 1974 in Frascati. This symposium was organised in order to assess the support of these ideas amongst astronomers, and many astronomers interested in the possibilities of space astrometry attended this meeting.

Table 1. Summary of the results from the Hipparcos mission intended before launch, and the actual results contained in the Hipparcos and Tycho Catalogues.

	Intended	Actual
Hipparcos Catalogue:		
Number of stars	100 000 (in 1980)	118 218
Limiting magnitude	V = 12.4 mag	V = 12.4 mag
Completeness	7.3–9.0 mag*	7.3–9.0 mag*
Positional accuracy (B = 9 mag)	0.002 arcsec	~ 0.001 arcsec
Parallax accuracy (B = 9 mag)	0.002 arcsec	~ 0.001 arcsec
Annual proper motion accuracy (B = 9 mag)	0.002 arcsec	~ 0.001 arcsec
Systematic errors	<0.001 arcsec	~ 0.0001 arcsec
Tycho Catalogue:		
Number of stars	> 400 000 (in 1982)	1 058 332
Limiting magnitude	B = 10 – 11 mag	B ~ 12.2 mag
Positional accuracy (B = 10 mag)	0.03 arcsec	~ 0.01 arcsec
Photometric precision (B = 10 mag)	0.05 mag	~ 0.02 mag
Observations per star	~ 100	130

* Depending on galactic latitude and spectral type

A mission definition study was subsequently carried out, by a group of European astronomers with the support of ESA personnel. This study was able to define a mission with more emphasis on the astrophysical aspects of an astrometry satellite, because new technical ideas made it possible to observe a larger number of stars, and also faint ones, with a higher precision than previously, and even with a smaller telescope aperture. The following technical innovations were introduced in December 1975 by E. Høg of Copenhagen University Observatory, and were incorporated in the final Hipparcos satellite.

A grid with only one slit direction was introduced for scanning the stars in only one coordinate, namely along the great circle connecting the two fields of view. The relative advantages of chevron and parallel slits had been the subject of lengthy discussions, with the simpler one-dimensional modulating grid having been adopted following simulations which showed that, even with one-dimensional measurements, good rigidity of the sphere solution would result. The one-dimensional scanning utilises the fact that the two-beam telescope is primarily a one-dimensional device. An image dissector tube was proposed instead of the previous photomultipliers, allowing the selection of target stars, and consequently longer and cleaner integration per passage, providing an improvement in overall efficiency of about 100 times with respect to the use of photomultipliers alone. This also allowed for a pre-selection of programme stars, corresponding to the adopted 'input catalogue' concept. The passive attitude stabilisation of the TD1 satellite was replaced by an active attitude control, which in turn opened the way for a 'revolving scanning' attitude motion, giving a more efficient coverage of the sky. The preferred mission was a dedicated astrometric satellite with a measurement lifetime of three years, during which the positions, parallaxes, and annual proper motions of about 100 000 selected stars would be obtained to some ±0.002 arcsec accuracy.

The study results were presented at an international Colloquium on Space Astrometry held at Copenhagen University in June 1976. Shortly afterwards, ESA approved a feasibility study of the project.

The problem of deriving the astrometric data from one-dimensional measurements of the sky by a scanning satellite was studied at Copenhagen, where L. Lindegren was introduced to the problem in September 1976. He subsequently presented the mathematical formulation of the three-step method, and estimates of the precision and correlation coefficients of the five astrometric parameters. The three-step method was later developed by both data reduction consortia. Their implementations are based on contributions by the geodetic institutes in Copenhagen and Delft starting in 1977, thus exploiting their expertise in solving large systems of similar geodetic networks with least-squares methods.

When the Phase A study started in 1977, ESA had just decided that the Ariane launcher should be used for future missions. This opened the way for a heavier payload and a geostationary orbit. The new possibility was adopted by the science team, and the previous concept of a near-Earth spacecraft in polar sun-synchronous orbit was abandoned.

The proposed active attitude control was based on the use of reaction wheels in the spacecraft, although the small disturbances (or 'attitude jitter') from the mechanical bearings might have jeopardised the astrometric mission, aimed at angular measurements in the range of 2 milliarcsec. In fact, the studies were never able to supply reliable estimates of the attitude jitter before attitude control by cold-gas jets was introduced by the satellite prime contractor in 1982. This control provides the same very smooth attitude motion between each jet firing as the passive stabilisation would have given. The smooth motion can be used to improve the precision for bright stars by 'dynamical smoothing', an idea advocated by P. Lacroute since the TD1-concept was proposed.

The dialogue with the international scientific community was continued at special meetings: at the General Assemblies of the International Astronomical Union in Grenoble in 1976 and in Montreal in 1979, and at the Colloquium on 'European Satellite Astrometry' in Padua in 1978. Coordination with ground-based astrophysical observations of the stars to be selected for Hipparcos was emphasised at these meetings, and so was the coordination with the planned space astrometry from the Hubble Space Telescope. Technical studies by ESA and outside contractors were continued, and members of the ESA science team investigated the data reduction aspects.

From June 1978 until February 1980, a large promotional campaign was conducted throughout Europe in favour of Hipparcos. An early and informal call for stars to be included in the observing programme, in an attempt to judge the scientific interest in the project, was released independently by E. Høg and C. Turon—they were able to collect about 170 research proposals submitted by 125 astronomers from 12 countries. P.L. Bernacca generated interest in 24 scientific institutes, from 8 countries, for hardware and software aspects of the mission, and demonstrated the potential availability of about 330 man years of effort necessary for the preparation of the data analysis facilities, one of the critical requirements for mission approval. As a result, the project obtained increasing attention from the national delegates in the ESA Science Programme Committee, which approved the project in March 1980.

Many of the astronomers and other scientists involved in the early assessment studies have continued their involvement with the mission, both through the ESA advisory teams, and through the setting up, in 1982, of the consortia who took responsibility for the scientific aspects of this project. The detailed design study was completed in December 1983, and the hardware development phase began early in 1984.

Technical and Scientific Involvement in Hipparcos after 1980

With the inclusion of the Hipparcos project within its mandatory science programme in 1980, the European Space Agency assumed overall responsibility for the satellite design and hardware manufacture, including the payload. This was contracted out to a European industrial consortium, with Matra Espace (France, now Matra Marconi Space) as industrial prime contractor, and with Aeritalia (Italy, now Alenia Spazio) responsible for procurement of the spacecraft, as well as for the integration and testing of the complete satellite.

Industrial responsibility at system level covered management, engineering and assembly, as well as integration and testing of the complete satellite. This responsibility was shared by eleven European firms, with some thirty five sub-contracted European firms, and a total of about 1800 individuals, participating at all levels (see Volume 1).

Working closely with the European Space Agency since the project's approval in 1980, European scientific teams undertook the scientific tasks necessary for the successful completion of the project as a whole. This included the Hipparcos Science Team, set up to advise the Agency on the detailed scientific considerations related to the payload design and development, and operational and calibration aspects, both on ground in advance of the satellite launch, and subsequently in orbit. While the scientific advisory role has been essential for the successful design of the mission concept, and is one shared by all ESA scientific missions, the scientific participation in the Hipparcos project has been especially fundamental.

One aspect of this scientific involvement was the preparation of the Hipparcos Input Catalogue by a consortium of institutes known as the Input Catalogue Consortium (INCA). This consortium was selected by ESA on the basis of responses to an Announcement of Opportunity issued in 1981. The consortium was subsequently entrusted with the task of defining the unique list of stars that were to be observed by the satellite, on the basis of scientific merit and satellite operational requirements.

An Invitation for Proposals was issued by ESA in 1982 to the worldwide (and not only European) scientific community. This resulted in more than 200 observation proposals being submitted, together comprising more then 600 000 objects. Advice on the scientific aspects of the selection of stars from the proposals was given by the Scientific Proposals Selection Committee and the Hipparcos Science Team.

The complete reduction of data from the satellite, from some 10^{12} bits of photon counts and ancillary data, to a catalogue of astrometric parameters and magnitudes for the 120 000 programme stars, was independently undertaken by two scientific consortia, NDAC (the Northern Data Analysis Consortium) and FAST (the Fundamental Astronomy by Space Techniques) Consortium. Both consortia were also selected on the basis of responses to a parallel Announcement of Opportunity issued by ESA in 1981. The selection of two parallel data reduction teams was motivated by the size and complexity of the reductions. The two independent approaches also facilitated the overall validation of the final results. The end product was a single, agreed-upon catalogue.

A later enhancement to the project, which emerged during the detailed design study, was the addition of the two-colour star mapper channels that led to the Tycho experiment, proposed by E. Høg in March 1981, and the subsequent formation of the Tycho Data Analysis Consortium (TDAC) in 1982. The Tycho Consortium was set up to analyse

the data from the star mapper data stream, eventually resulting in the Tycho Catalogue of more than a million stars.

The close collaboration between the Agency and the scientific teams led to a satellite design which fully reflected the scientific requirements. The activities of all of the participating scientific institutes were funded by national agencies, universities, and private foundations. Altogether, some 200 scientists were involved in the work of the four scientific consortia. These activities, and the organisation of the scientific consortia, are described in detail in Volumes 3 and 4.

1. OVERVIEW OF THE HIPPARCOS SATELLITE

This chapter describes the operating principle of the Hipparcos satellite, with reference to the measurement principle, the constraints and properties of the nominal satellite orbit, and the satellite environmental conditions. An overview of the main satellite subsystems: attitude control, data handling and on-board processing, the mechanical and electrical design, and the overall operational concept—is given, along with a description of the ground segment. The scientific and operational concepts introduced in this chapter are described in greater detail in subsequent chapters.

1.1. Operating Principle

The primary goal of the Hipparcos mission was the measurement of the positions, proper motions, and trigonometric parallaxes of about 120 000 stars. To achieve this, a special optical telescope was designed to function on a spacecraft placed in geostationary orbit, above the Earth's atmosphere. The telescope had two fields of view, each of size $0\overset{\circ}{.}9 \times 0\overset{\circ}{.}9$, and separated by about 58°. The satellite was designed to spin slowly, completing a full revolution about its spin axis in just over two hours. At the same time, it could be controlled so that there was a slow change in the direction of the axis of rotation. In this way, the telescope could scan the complete celestial sphere.

Measurements of the angles between pairs of stars, inferred from the relative phases of the modulated signals created by the main grid, were built up over the three-year lifetime of the satellite in orbit. From many such measurements, made at many different orientations, and at many different epochs, a whole-sky astrometric catalogue (the Hipparcos Catalogue) was built up, containing the positions, parallaxes, and proper motions of all of the stars on the pre-defined observing list. This list, which contained about 120 000 stars, constituted the so-called 'Hipparcos Input Catalogue'. The Tycho Catalogue was constructed from the data sent to the ground from the satellite's star mapper.

The measurement principle of Hipparcos is illustrated in Figure 1.1. The payload was centred around an all-reflective Schmidt telescope with an entrance pupil of 290 mm and a focal length of 1400 mm, the light from two sections or 'fields' of the sky was conveyed through two baffles, set at a fixed angle of close to 58°. A 'beam combiner' allowed the

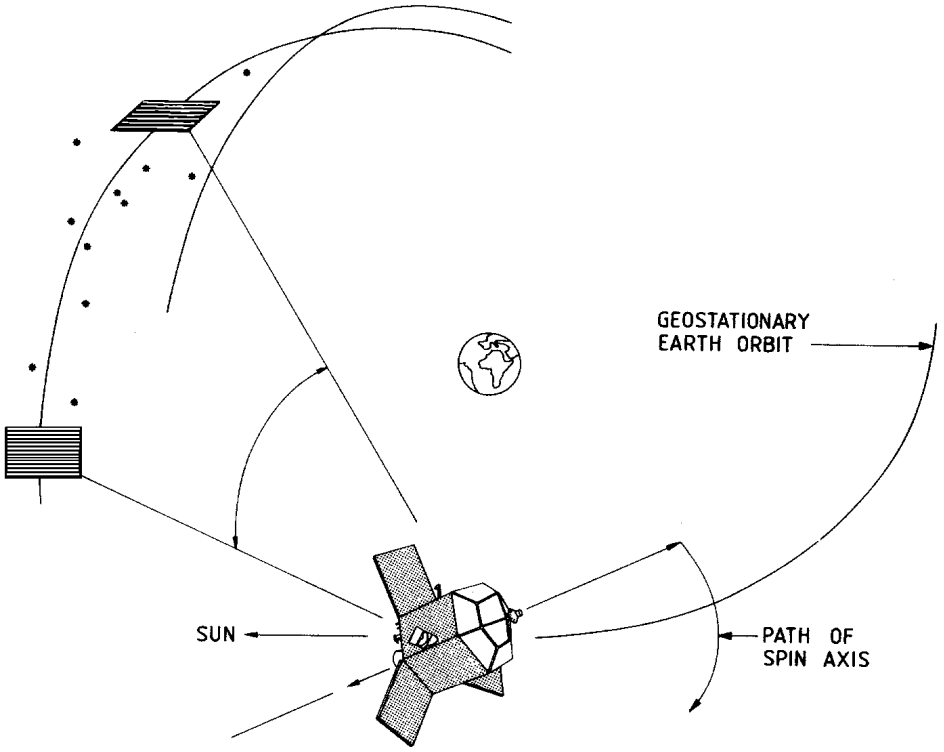

Figure 1.1. *The measurement principle of the Hipparcos satellite. The two fields of view scanned the sky continuously, and relative positions of the stars along the scanning direction were determined from the modulated signals resulting from the satellite motion. Although the nominal geostationary orbit was not achieved, the same scanning motion was implemented in the actual (transfer) orbit.*

two fields to be projected onto the same focal surface by means of the spherical primary mirror. It was then possible to determine the true angle between two stars, one in each field of view, by using the known or 'basic angle' of 58° between the two fields of view, plus the apparent separation measured on the focal surface of the telescope. This choice for the basic angle was influenced by the goal of connecting stars with very different parallax factors by measurements within the combined field of view. The precise value chosen was selected by considering the 'rigidity' of the resulting measurements made over a great circle scanned by the satellite, as illustrated in Figure 1.2.

As the satellite slowly rotated at its nominal scanning velocity of approximately 1 revolution every 2 hours 8 minutes, the images of the stars in the fields of view moved across the focal plane grids. These signals were sampled by detectors behind these grids. Two different types of detector were used in the Hipparcos payload—an image dissector tube for the main grid and photomultiplier tubes for the star mapper grids. To protect the detectors from excessive illumination due to occultations by the Earth and Moon, shutters were built into the payload so that the detector photocathodes could be shielded from the bright occulting source.

The surface on which the two fields of view were focused contained 2688 parallel slits in an area of about 2.5×2.5 cm^2, covering about $0\overset{\circ}{.}9 \times 0\overset{\circ}{.}9$ on the sky (see Figure 2.10). As the telescope slowly scanned the sky, the star light was modulated by the slit system, and the modulated light was sampled by an image dissector tube

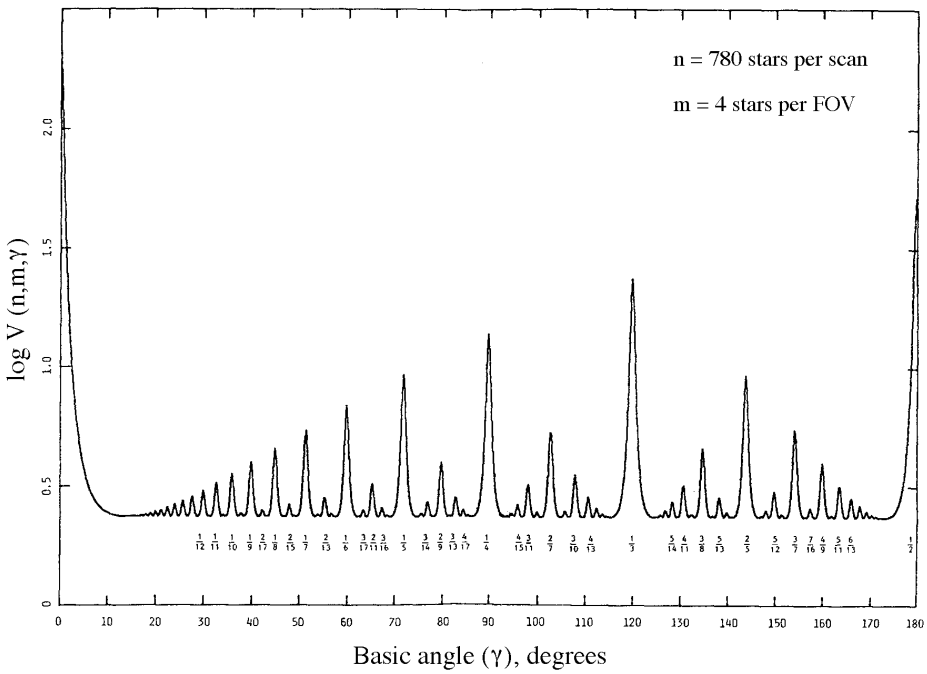

Figure 1.2. *The 'rigidity' of the solution for star abscissae on a great circle scanned by the satellite is strongly influenced by the choice of the 'basic angle' between the two fields of view. The chosen value of 58° was selected as providing good rigidity (resulting from good connectivity between the stars observed on each great circle), at the same time allowing the simultaneous measurements of stars having very different parallax factors. Peaks in the function indicate basic angles which would be unsuitable from the point of view of the rigidity of the great circle solutions. FOV refers to field of view.*

detector, at a frequency of 1200 Hz. At any one time, some four or five of the selected (or programme) stars were present in the two fields of view. The image dissector tube consisted of a photomultiplier with an electromagnetic deflection system that allowed only one small part of the photocathode to be sampled at any given time. This small sensitive area, referred to as the instantaneous field of view, covered an area of about 38 arcsec in diameter (projected on the sky). The size of the instantaneous field of view was minimised as the result of a 'piloting budget', accounting for the *a priori* errors on the star positions, the performance of the satellite real-time attitude determination, and the fact that the instantaneous field of view was stepped discretely to follow the moving star images.

The detector could only follow the path of one star at a time, but under rapid computer control it was able to track all the programme stars for short intervals of time during their passage across the field, which took about 20 s. In this way, measurements of the relative positions of the programme stars were continually being made, distributing the available observing time amongst the visible stars, the observations being made quasi-simultaneously in order to eliminate any residual attitude jitter. Due to the scanning motion of the satellite, the majority of stars in the field of view at any time appeared first in the preceding field of view, and then in the following field of view about 20 minutes later. As the scans also overlapped laterally when the satellite rotation axis changed on each sweep of the sky, the stars would appear again, but this time compared with other stars. In this way, a dense net of one-dimensional measurements of the relative separations of the stars was slowly built up.

The satellite spin axis was kept at a constant inclination of approximately 43° to the direction of the Sun, and revolved around the Sun once in approximately eight weeks, resulting in a continuous and systematic scanning of the celestial sphere. Throughout the scanning motion the satellite therefore remained in a constant thermal environment, modulated only by the satellite rotation. Any region of the sky was scanned many times during the mission by great circles which intersected at well-inclined angles as a result of the choice of the 43° sun aspect angle. A typical star was observed some 80 times in each field of view throughout the lifetime of the satellite. The number of possible connections between the observed stars was considerably enhanced due to the almost simultaneous observation of stars separated by the large basic angle. The individual measurements were combined to form the final Hipparcos Catalogue, including the displacements due to parallax and proper motion, using techniques similar to those used in triangulation in surveying the Earth's surface.

The real-time attitude determination on board, required for autonomous piloting of the detector's instantaneous field of view, was achieved by the on-board computer using the spacecraft rotation rates, as measured by three independent gyros, the biases in those gyros (the gyro drifts), knowledge of times and durations of thruster firings, and critically, the measurements of transit times of stars crossing the star mapper grid. By comparing the measured crossing times of designated stars with those expected from the theoretical motion of the spacecraft, it was possible for the on-board computer, using a Kalman filter, to estimate the amount that the spacecraft had deviated from the predefined attitude.

The image dissector tube signal, as modulated by the main grid, was assumed to be of the form (see Figure 1.3):

$$I(t) = I_{BG} + I_0[1 + M_1 \cos(2\pi\omega t + \theta_1) + M_2 \cos(4\pi\omega t + \theta_2)] \qquad [1.1]$$

where:

- $I(t)$ is the instantaneous count rate at time t
- I_{BG} is an additional signal due to background noise and detector dark current
- I_0 is the mean count rate for the observed star (dependent on magnitude and colour)
- M_1 is the first modulation coefficient for the observed star
- M_2 is the second modulation coefficient for the observed star
- t is the time relative to a reference observation (mid-frame) time (s)
- ω is the grid frequency of the image dissector tube signal in Hz, i.e. $\omega = v/s$ where v is the angular scanning velocity of the satellite (arcsec s^{-1}), and s is the grid slit spacing (arcsec)
- θ_1 is the phase of the first harmonic of the signal at $t = 0$
- θ_2 is the phase of the second harmonic of the signal at $t = 0$

In addition to the main instrument (there was a second image dissector tube detector provided for redundancy), the payload included two star mappers, the second also being provided for redundancy purposes—the non-operational detectors were usually switched off when not in use. The function of the star mapper was to provide data allowing real-time satellite attitude determination, a task performed on-board the satellite, as well as the *a posteriori* reconstruction of the attitude, a task carried out on the ground. The continuous flow of star mapper data was also used to create the Tycho Catalogue,

comprising astrometric and two-colour photometric measurements of all stars, down to about 10–11 mag.

The star mapper consisted of a star mapper grid, located at opposite sides of the primary modulating grid (see Figure 2.10), and two photomultipliers measuring the light transmitted by the whole star mapper grid in two different spectral bands, roughly corresponding to the Johnson B (blue) and V (visual) bands. The spectral separation was performed by means of a dichroic beam splitter, which directed that part of the signal with $\lambda < 465$ nm toward the 'blue' photomultiplier (referred to as the B_T channel) and that part of the signal with $\lambda > 475$ nm toward the 'visible' photomultiplier (the V_T channel)—the subscripts 'T' referring to Tycho, and drawing attention to the distinction between the Tycho and Johnson photometric systems.

Each star mapper consisted of two sets of four slits, each set at different inclinations with respect to the scanning direction, so that the satellite attitude could be derived from the photomultiplier signals as the star images moved across the grid. Both channels were sampled at 600 Hz by the on-board data handling subsystem. In total, the image dissector tube and star mapper data comprised 83 per cent of the telemetry stream.

The photomultiplier tube signal for each of the star mapper channels was assumed to be of the form (see Figure 1.4):

$$I^*(t) = I^*_{BG} + I^*_0 \sum_{k=1}^{N} S(vt - p_k) \qquad [1.2]$$

where:

$I^*(t)$ is the instantaneous count rate at time t

I^*_{BG} is an additional signal due to background noise and detector dark current

I^*_0 is the peak count rate at the centre of a slit

N is the number of slits in a slit system ($N = 4$)

$S(x)$ is the single-slit response function, i.e. the normalised signal transmission factor as a function of distance from the source to the centre of the slit, in arcsec

v is the angular scanning velocity of the satellite (arcsec s^{-1})

t is the time relative to the central observation time (s)

p_k is the position of the k-th slit in the slit system (arcsec)

The payload is described in detail in Chapters 2 and 3. The nominal scanning law and the star observing strategy are described in Chapter 8. The processing of the main grid and star mapper data, leading to the construction of the Hipparcos and Tycho Catalogues, are described in detail in Volumes 3 and 4 respectively.

The spacecraft provided the structure platform for mounting the payload main assembly via an interface structure, the external baffles to protect the detectors from stray light from the Sun and the Earth, and the appropriate mounting surfaces for all spacecraft hardware including the apogee boost motor, solar arrays and antennae. In addition, the spacecraft supported a shade structure surrounding the payload which ensured maximum thermal decoupling from the external environment.

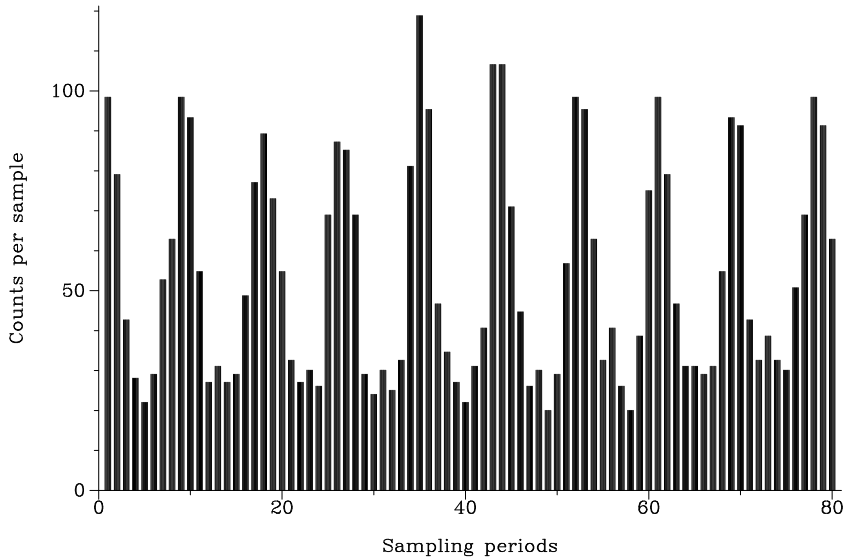

Figure 1.3. *Image dissector tube signal. The information transmitted to the ground from the main detector consisted of the photon counts per 1200 Hz sample. The main peaks correspond to the first signal harmonic, and the (marginally visible) intermediate peaks correspond to the second harmonic. The brightness of the star at the time of the measurement is given by the amplitude of the signal, while the phase of the modulated signal with respect to some reference phase provides the relative position of the star image, along the scanning direction, modulo one grid step. The data corresponds to observations of 1/15 s for HIP 114347, Hp = 5.3 mag, in April 1991.*

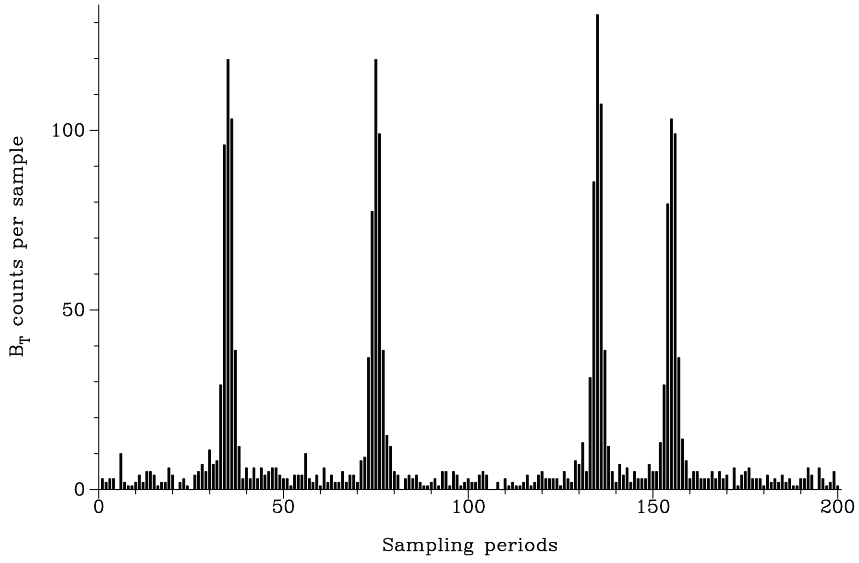

Figure 1.4. *Photomultiplier tube signal (blue channel) for the transit of one star over a single slit system. The information transmitted to the ground from the star mapper detector consisted of the photon counts per 600 Hz sample measured simultaneously in the B_T and V_T channels. The four peaks corresponding to the four aperiodically spaced star mapper slits, yield the star intensity and position after appropriate filtering. The observation is for HIP 35946, B_T = 6.62 mag, transits for the vertical slits and the following field of view.*

1.2. Constraints and Properties of the Nominal Orbit

Due to the measurement principle of Hipparcos, which needed as input a continuously updated 'programme star file' of star positions predicted to cross the instrument's field of view as a function of time, the satellite required permanent attendance by the ground segment in order to pursue the nominal mission. This requirement would have been best fulfilled by a geostationary orbit (equatorial plane, 36 000 km height, 24-hour period), which would have kept the satellite in a fixed position with respect to a single ground station. From this orbit, as opposed to low-Earth orbits, the Earth obscures only a small portion of the celestial sphere being scanned. The station 12°W was originally chosen from the geostationary orbit segments available in order to optimise the accuracy of the orbit determination from the single ground station. In practice, the target geostationary orbit was not achieved, and the mission was conducted with the satellite in a highly elliptic geostationary transfer orbit, as described more fully in subsequent chapters.

Eclipse Operations

For a period of 45 days around the two equinoxes, the orientation of the nominal Hipparcos (geostationary) orbit relative to the ecliptic was such that the Earth would have passed between the Sun and the satellite every 24 hours. Such eclipses would have lasted up to 72 minutes, during which time there would be no energy input to the solar arrays and the power subsystem would have to rely on its batteries. At the same time, the heat input would fall, changing the thermal balance of the satellite. While the satellite had been designed for these eclipse conditions, extreme eclipse durations were considerably longer for the actual geostationary transfer orbit, placing complex constraints on the power subsystem at these times.

Occultation of the Fields of View

The satellite scanned the sky with its spin axis pointed in a direction that moved only slowly, with an orbital period in its actual geostationary transfer orbit of 10.66 hours. This meant that the scanning great circle intercepted the Earth's disc about four times per day, with all or part of each field of view being exposed to this bright source in one or more consecutive scans. Since the Earth is very bright from such an orbit, shutters in front of the detectors were closed some time before the actual disc of the Earth entered the field of view, and they remained closed until after it had passed. The actual duration of the interruption was determined by the straylight protection characteristics of the payload baffles, and ranged from a few minutes to more than one hour. Similar interruptions were caused by occultation due to the Moon although, subtending a smaller angle and being less bright, the corresponding interruptions were shorter.

The impacts of such interruptions in data collection were threefold: (i) the 'dead time' had to be accounted for in estimating the mission duration needed for the required number of scientific measurements; (ii) the rigidity of solution of the great-circle equations would be degraded if measurements could not be linked between the two fields of view and between consecutive revolutions; and (iii) while the star mapper was not

operating the satellite attitude would drift with only gyroscope measurements, leading to degradation in pointing accuracy and even additional operations needed to return to the nominal scanning law after the interruption.

Simulations showed that the dead time for the nominal geostationary orbit, due to occultations, would be about 5 per cent, which was within the budget foreseen during mission definition, and that mission accuracy requirements could be achieved with up to 40 per cent of great circles interrupted, which exceeded the predicted percentage for the nominal geostationary orbit with a clear margin. The real-time attitude determination performance was also demonstrated in simulations, showing that conditions leading to the need for a full reinitialisation of the pointing would occur only once or twice in the entire mission. In practice, as a consequence of the revised orbit, dead time was significantly larger, and pointing reinitialisation was frequently required.

1.3. Satellite Environmental Conditions

The following environment conditions expected for the nominal geostationary orbit were taken into account in the overall satellite design.

Mechanical Environment

The dominant mechanical environment driving the satellite design was that encountered during the launch phase, which exposed the satellite to static and quasi-static accelerations, random vibration, and acoustic sound pressure.

Thermal Environment

There were two cases of thermal environment driving the design: (a) the transfer and near synchronous orbit, when the satellite was spinning, the solar arrays were stowed, the internal power consumption was low, and the sun aspect angle with respect to the spin axis was between 90° and 115° (the upper limit of the sun aspect angle determined by the launch window); and (b) the geosynchronous orbit, when the satellite would be three-axes controlled, the solar arrays would be deployed, the internal power consumption would be high, and the sun aspect angle would be 43°.

The sun aspect angle was given by the nominal scanning law, but could go to 0° ('sun-pointing') for emergency sun acquisition and for initialisation. The thermal design had to cope with both somewhat contradictory cases by appropriate multi-layer insulation, radiators, and electrical heaters. The compliance of the satellite with the thermal environment, in addition to comprehensive mathematical modelling and analyses, was verified by thermal-balance and the thermal-vacuum tests before launch.

Electromagnetic Environment

The electromagnetic environment was generated externally by the launch vehicle and the passenger satellite in the dual launch, and internally by the satellite electrical equipment. A margin between electromagnetic emission and electromagnetic susceptibility

was ensured by introducing a strict grounding and isolation scheme, careful shielding of units and harness, and interface circuits with common mode rejection capability.

Radiation Environment

Semiconductor lifetime: Semiconductors degrade when exposed to ionising radiation. The degradation of high-reliability component parameters as a function of radiation dose is well known, and this degradation had to be taken into account as a life-limiting factor. For each electronic unit, a radiation analysis was performed, consisting of computing the dose a component would be subjected to, taking into account the radiation shielding of the surrounding material of the unit and the satellite. Then, either the circuit design was able to accommodate the degraded parameters at the projected end of life, or additional local shielding had to be applied.

Single event upset: The 'single event upset' effect is the result of a high-density ionisation due to heavy and high-energy particles. It can cause such a high local charge deposition in a semiconductor that the logical state of a flop-flip or a memory cell is changed. Although this is generally a recoverable error, and no permanent damage results, it can upset the on-board computer systems. The satellite system was designed in such a way that no computer function was crucial for the satellite safety. However, a frequent computer upset would interrupt and degrade the mission.

The following measures were taken to protect the satellite against single event upsets: (a) the control law electronics used a processor of low radiation susceptibility, while the control law electronics memory employed an 'error detection and correction logic' which corrected any single bit error; and (b) the on-board computer used a radiation-hardened processor. The on-board computer memory was continuously checked for parity errors, which then had to be corrected from ground.

Electrostatic discharge: Electrostatic discharges have troubled many geostationary satellites. In a plasma environment, the satellite surfaces are charged up to different potentials, depending on the material properties and sun illumination. The potential differences can reach a few thousand volts, sufficient to cause sudden electrostatic discharges which interfere with the satellite electrical system. Hipparcos was designed to avoid differential charge-up, and also to provide protection against discharge effects should they occur.

To avoid differential charge-up, all surfaces exposed to space were required to be electrically conductive. This requirement had a significant impact on the thermal control design, as it ruled out the most conventional thermal control materials. The surface materials selected for the satellite were conductive black paint, aluminium and indium-tin-oxide coated optical surface reflectors. The only compromise, made for cost reasons, was the non-conductive glass cover of the solar cells. To verify that no differential charge-up could occur, mathematical models to analyse the phenomenon of electrostatic discharge were performed. The properties of the satellite surface materials, which were a sensitive input to the analyses, were measured in a special test programme performed within the development programme.

To protect against discharge effects, the whole spacecraft was shielded. This was done implicitly in the lower part of the spacecraft by aluminium panels forming a metallic box to house the spacecraft equipment. The upper part was mainly framework, supporting

the multi-layer insulation to protect the payload. A 0.1 mm thick aluminium foil surrounding the framework formed the electrostatic discharge shield.

Electrostatic discharge protection was also the driver for the electrical grounding and isolation concept. The concept chosen was a distributed single-point grounding scheme. Each box had its own secondary power supply, isolated from the main bus and grounded to the box structure, thus providing the box signal ground. Signal lines between boxes had common-mode rejection capability—signal receivers were either differential amplifiers, opto-couplers, or floating relay coils. For digital links, standardised transmitters and receivers were developed for use by all electrical subsystems, referred to as the 'standard balanced digital link'.

Darkening of optical elements: Prolonged exposure to ionising radiation can alter the transmission characteristics of optical materials. The extent of transmission loss is wavelength-dependent, being more significant for shorter wavelengths. During its operation, the satellite would be continuously exposed to trapped electrons and protons in the Earth's outer radiation belts. Although the protons would not normally be sufficiently energetic to penetrate the outer wall of the satellite, any so-called 'anomalously large solar events' could generate increased levels of high-energy protons.

In order to minimise the effects of this radiation, the transmitting optical elements were made of glass types that showed maximum resistance to irradiation darkening, subject to their general properties (spectral transmission and refractive index) being compatible with the requirements of the mission. At the same time, the relay optics and detector windows were shielded by layers of aluminium, and additional material was added to the structural elements to provide shielding in directions where this was not already provided by existing hardware.

In assessing the predicted end-of-mission performance in advance of launch, the expected degradation of optical transmission was calculated on the basis of the best-available knowledge of the radiation environment in geostationary orbit, and accounting for two anomalously large solar flares. This was considered to be consistent with previous experience at the phase of the solar cycle (around maximum) at which the Hipparcos measurements would take place.

The Cerenkov effect: A charged particle passing through a transparent dielectric medium with a velocity greater than the velocity of light in the medium, emits visible electromagnetic (Cerenkov) radiation. The Earth's outer radiation belts, through which the (nominal and actual) orbit of Hipparcos passed, contained electrons sufficiently energetic to generate light by this effect in the dioptric elements of the payload optics.

Depending on the direction of motion of the individual electron and the distance of each optical element from the detector, the part of the emitted light that falls within the spectral measurement range may make a significant contribution to the background count rate, against which the stellar signals had to be detected and measured. However, the pulse width of the Cerenkov light flash being much smaller (~ 0.1 ns) than the time resolution of the photomultiplier (~ 40 ns), one or more photons generated by each incident high-energy electron would produce just one pulse recognised above the discriminator threshold as a background count.

The measures implemented to counteract this effect included the provision of additional material to shield sensitive elements in directions where such shielding was not provided

by the satellite hardware itself, and the masking of unused areas of transmitting optics. The radiation shielding requirements were estimated by Monte-Carlo studies.

It was verified that the predicted residual count rate would not induce an unacceptable degradation of mission performance. The effect was particularly important for the star mapper, because of its large field of view, where it was expected to contribute the major part of the background count rate. For the main mission, the use of a restricted instantaneous field of view was expected to reduce drastically the proportion of the emitted light to which the detector was sensitive.

1.4. Attitude Control Concept

The attitude and orbit control subsystem provided the control, stabilisation and measurement about the three satellite axes during all phases of the mission, and performed all orbit manoeuvres. Orbit reconstitution data with an accuracy of about 1.5 km in the instantaneous satellite position and 0.2 m s^{-1} in the instantaneous velocity vector were performed at ESOC. The attitude determination used rate-integrating gyroscopes, the drifts of which were calibrated in real-time using star mapper data from star crossings occurring every 20 s on average, although later in the mission, as a result of progressive gyro failures, the gyro input had to be replaced by star mapper data and a disturbance-torque model. Cold nitrogen thrusters (with a nominal thrust of 0.02 N) were used for the attitude control.

An extremely smooth satellite motion was required because of the measurement principle. The sequential detection of the grid-modulated light from each star made the phase extraction sensitive to any jitter during this sequence. Furthermore, the interlacing of bright and well-measured stars along a great circle depended on the smoothness and predictability of the motion. This interlacing significantly improved the astrometric accuracy. Therefore, the trade-off and selection of the attitude control concept was one of the key decisions influencing the feasibility and performance of the Hipparcos mission. The decision was complicated by the difficulty of acquiring experimental data on microvibration in a 1*g* environment, and by doubts about the applicability of conventional finite-element models to this problem. The attitude control candidates considered during the early phases of the satellite design were reaction wheels, magnetic actuators and small thrusters:

(i) reaction wheels, the classical means of providing a continuous attitude control, were discarded, because of the resulting high level of attitude jitter caused by bearing noise. This problem could not be solved by considering the use of mini reaction wheels, or reaction wheels with magnetic bearings, or special suspension mounts for the wheels;

(ii) magnetic torquers, i.e. magnetic coils generating a torque within the Earth's magnetic field, were discarded, because there are uncontrollable areas depending on the angle between the coil and the Earth's magnetic field, which would still require additional reaction wheels. The control is complex, and depends on the attitude to the Earth's magnetic field, which would vary throughout the mission as a consequence of the adopted scanning law. Also, the Earth's magnetic field itself can vary significantly during magnetic storms. Furthermore, the magnetic actuators could interfere with the image dissector tube detector, which was inherently magnetically sensitive;

(iii) small thrusters, when actuated, cause an attitude discontinuity and excite an attitude jitter. This was shown to be acceptable if the actuations were not too frequent, sufficiently weak and with higher frequencies suppressed, and if the jitter could be damped out to acceptable levels in a time period small compared with the time for which a star would be observed.

The last of these attitude-control concepts was chosen, with specially designed 0.02 N 'cold gas' thrusters. The satellite was designed to operate in free drift in a ±10 arcmin band around the orientation given by the nominal scanning law. If any axis exceeded this band, the thrusters would be fired. If, at the same time, the other axes exceeded a narrower inner band, their thrusters would also be fired in a synchronised manner. This synchronised firing scheme, plus an optimisation of impulse bit and disturbance torque prediction, led to a predicted average time between thruster firings of 400 s, with the firings causing a disturbance for less than 2 s.

Other sources of jitter that had been carefully assessed before launch, in addition to that due to gas jet actuations, were gyro mechanical noise, apogee boost motor residuals, payload shutter mechanism actuations, and the impact effects of micrometeorites. In addition, the frequencies to which the measurement principle and the star observing strategy were especially sensitive were avoided by suitable control of the satellite natural frequencies.

1.5. Data Handling and Processing

The system design for the on-board data handling and data processing was determined by the following requirements:

(a) the continuous uplink of *a priori* star position and magnitude information from the Hipparcos Input Catalogue in the form of the programme star file, for a look-ahead time of several minutes;

(b) the real-time computation of the star observing strategy and the image dissector tube piloting from the programme star file and the actual satellite attitude;

(c) the real-time attitude determination from gyro and star mapper data with a high degree of accuracy (1 arcsec) as an input to the star observing strategy and image dissector tube piloting;

(d) the time tagging of the measurements with a stability of 5 μs over 5 minutes, corresponding to a satellite spin phase of about 1 milliarcsec (5 minutes roughly corresponded to the time between bright, well-measured stars to be linked on a great circle).

As a result of this architecture, the on-board processing was shared between two computers: the central on-board processor and the control-law electronics. The on-board computer performed the star observing strategy and the detector piloting. In addition, it performed the 'outer loop' of the real-time attitude determination, based on reference star data from the programme star file, and on measurements from the star mapper. It also performed the thermal control of the payload. The control-law electronics performed the 'inner loop' of the real-time attitude determination, based on gyro data, and also the control law which generated the commands for the thrusters.

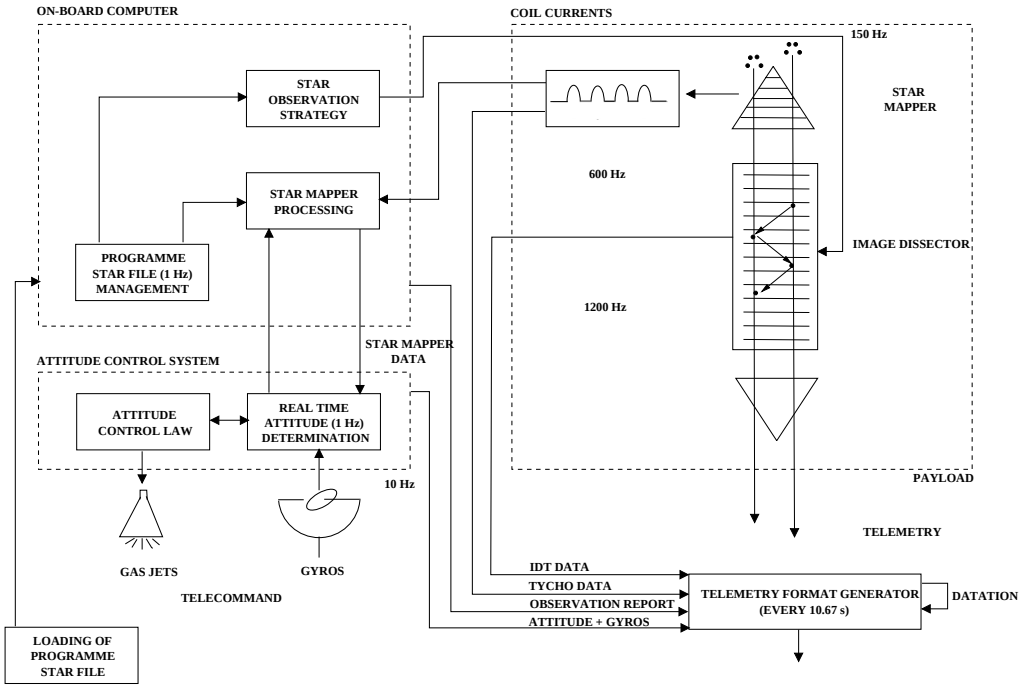

Figure 1.5. *A block diagram of the main measurement and operational functions on board the satellite. To the top left, the uplinked programme star file was used by the on-board computer to determine the details of the star observing strategy over the coming minutes. Information on the satellite attitude was provided by a combination of gyro and star mapper data (bottom left), which was also used to determine the gas jet actuations necessary to maintain the satellite in its pre-defined scanning law. Attitude information and information from the programme star file was used to point the instantaneous field of view of the image dissector tube, and to acquire relevant extracts of the star mapper data stream (top right). All relevant data were interleaved and sent to ground in real time (bottom right).*

The whole on-board system was synchronised by broadcast pulses. The piloting, the image dissector tube sampling, and the format generation was synchronised in 150 Hz cycles. Thus, the time tagging of the payload data was given implictly by the location within the telemetry format. The less time-critical on-board computer and control-law electronics data were interleaved into fixed telemetry format slots as packet telemetry. The on-board computer and control-law electronics computations were synchronised by the telemetry format pulse.

The overall concept of the acquisition of scientific data by the satellite is depicted in Figure 1.5. The programme star file was loaded from ground. It contained information on the programme stars to be observed by the image dissector tube, and reference stars used to perform the attitude determination on-board. The programme star file was managed by the central on-board software.

The central on-board software retrieved information about the reference stars from the programme star file and, by means of attitude information from the attitude and orbit control system, computed the expected transit time of the reference stars passing over the star mapper slits. In a time window around the expected transit time, star mapper samples were acquired and filtered to determine the actual transit time of the reference star. The difference between expected and measured transits was then used as an error signal for the attitude determination, which was continuously performed for the three axes by means of gyro measurements. The real-time attitude determination

outputs were used for attitude control within a band of ±10 arcmin around the nominal scanning law, and for computing the positions of programme stars in the field of view for proper piloting of the image dissector tube.

The central on-board software retrieved information about the programme stars that were to appear in the field of view for the next observation frame of $T_4 = 2.133\ldots$ s and computed the star observing strategy, i.e. the pattern of interleaved subsequent star observations, according to star criteria contained in the programme star file. These criteria were priority, target observation time, and minimum observation time (see Chapter 8 for further details of the observation programme and the star observing strategy).

By means of the real-time attitude determination, the expected star position in the field of view needed to pilot the image dissector tube was computed as a function of time. With this information, the star observation pattern was converted into a series of coil current pairs, which commanded the instantaneous field of view of the image dissector tube to the star images to be observed. The resulting image dissector tube counts per sampling period were inserted into the satellite telemetry as a continuous data stream. The corresponding observation frame characteristics were inserted into the telemetry by the central on-board software as data packets.

In addition to providing the on-board attitude reference, the star mapper performed astrometric and photometric measurements as part of the Tycho experiment. The light passing through the star mapper grid was measured with two photomultiplier tubes in two different colours, the B_T and V_T channels. The photomultiplier counts per sampling period, after data compression, were also inserted into the satellite telemetry as a continuous data stream.

1.6. Operational Concept

The complexity of on-board processing, and the intensive ground segment involvement, required that the system design was based on a clear operational concept.

Hipparcos was designed as a geostationary satellite with permanent single station ground contact, run to the maximum extent from the ground. On-board processing was intended only if ground processing was prohibitive due to excessive uplink rates (e.g. the implementation of the star observing strategy), or was not feasible due to the telemetry or telecommand turnaround time (e.g. attitude determination and control, image dissector tube piloting). On-board scientific data reduction was not accepted, in order to avoid systematic errors imposed by the associated modelling. The ground segment was designed to monitor satellite health and to initiate corrective actions in case of failure. Only if a failure required a fast reaction to avoid permanent damage to the satellite was an automatic back-up mode provided.

Normal operation was to be performed by means of on-board computers and software. Re-configuration and configuration status monitoring would be performed on a higher, independent level. Automatic back-up modes would override normal operation and configuration. Direct ground commands would override any automatic back-up mode.

During transfer and drift orbit, the satellite would be spinning, and its survival would depend on the proper function of the active nutation damping. A malfunction resulting in excessive nutation would be detected on-board by an accelerometer. It would trigger an automatic switch-over to a completely redundant control and actuation system.

In the intended geostationary phase, when the solar arrays were deployed and the satellite was three-axis controlled, the satellite would be sensitive to attitude errors. At excessively large solar aspect angles, partial shadowing could damage the solar cells and direct sunlight could blind the payload. In sunlight, an attitude error would be detected by a special attitude anomaly detector. An automatic sun acquisition would be triggered by independent back-up hardware. In eclipse, an attitude error would be detected by monitoring the thruster actuations. An anomaly would trigger an automatic spin-up to increase the gyroscopic stiffness. This would keep the satellite in a safe attitude sufficiently long for the ground segment to detect the failure and initiate recovery actions.

Permanent electrical power supply would be essential for the survival of the satellite. Anomalies would be detected through main-bus undervoltage and battery-cell under-voltage, and these would trigger an automatic shedding of non-essential loads.

1.7. Satellite Mechanical and Electrical Design

The satellite consisted of two major hardware elements, namely the spacecraft and the payload. These two hardware elements, together with the on-board software made up the satellite system. As the satellite exploded view shows (Figure 1.6), there was a spacecraft module providing: structural support for its subsystems and for the payload via the interface structure; electrical power supply by solar arrays and batteries; telecommunication and data handling; and the attitude and orbit control required to place the satellite on station and then execute the scanning law. Another spacecraft element was the apogee boost motor, which was designed to inject the satellite from transfer-orbit apogee into near-synchronous orbit. Finally, there was the shade structure needed to provide a stable thermal environment for the payload. The Hipparcos launch and on-station configurations are shown in Figure 1.7.

The electrical subsystems are listed in Table 1.1. The primary power supply was a regulated 50 V DC power bus. At subsystem level (data handling, attitude and orbit control, and payload), there were DC/AC inverters supplying the units with square wave 50 V AC power. The communication between subsystems was through the ESA-standard on-board data handling bus.

The electrical power subsystem supplied the primary electrical power, generated by the solar generator, to the payload and the spacecraft subsystems. Power distribution was through a 50 V DC mains regulated bus and AC secondary power buses. Two rechargeable nickel-cadmium batteries, each with the capacity of 10 Ah, provided continuous power supply during launch and eclipse periods.

The solar generator provided electrical power by use of solar cells arranged on three identical solar panels. The subsystem generated electrical power in transfer orbit when the solar arrays were folded against the satellite body, as well as in operational orbit when the panels were deployed. When deployed, the three panels together provided

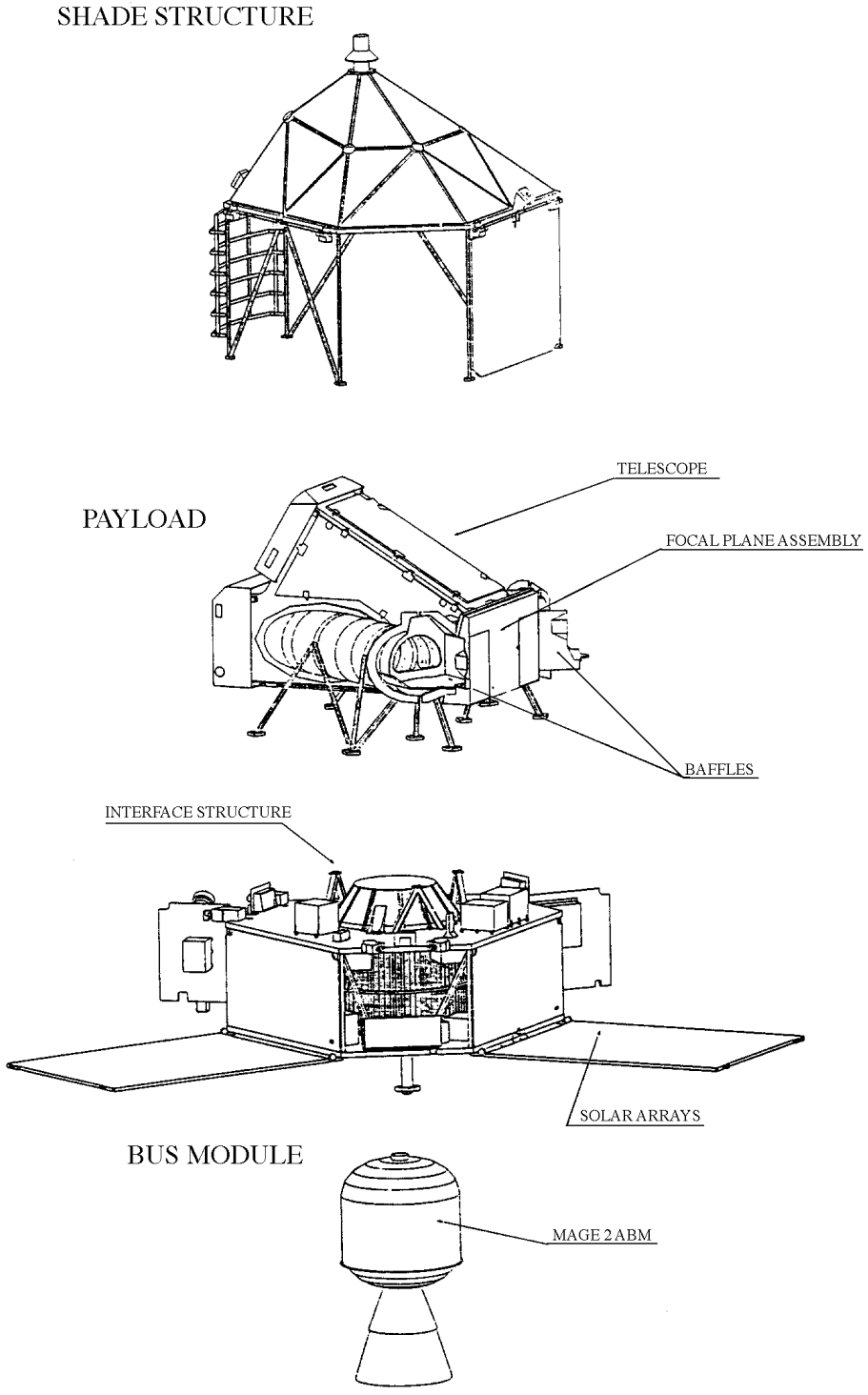

Figure 1.6. *Exploded view of the satellite, illustrating the location of the two fields of view within the payload.*

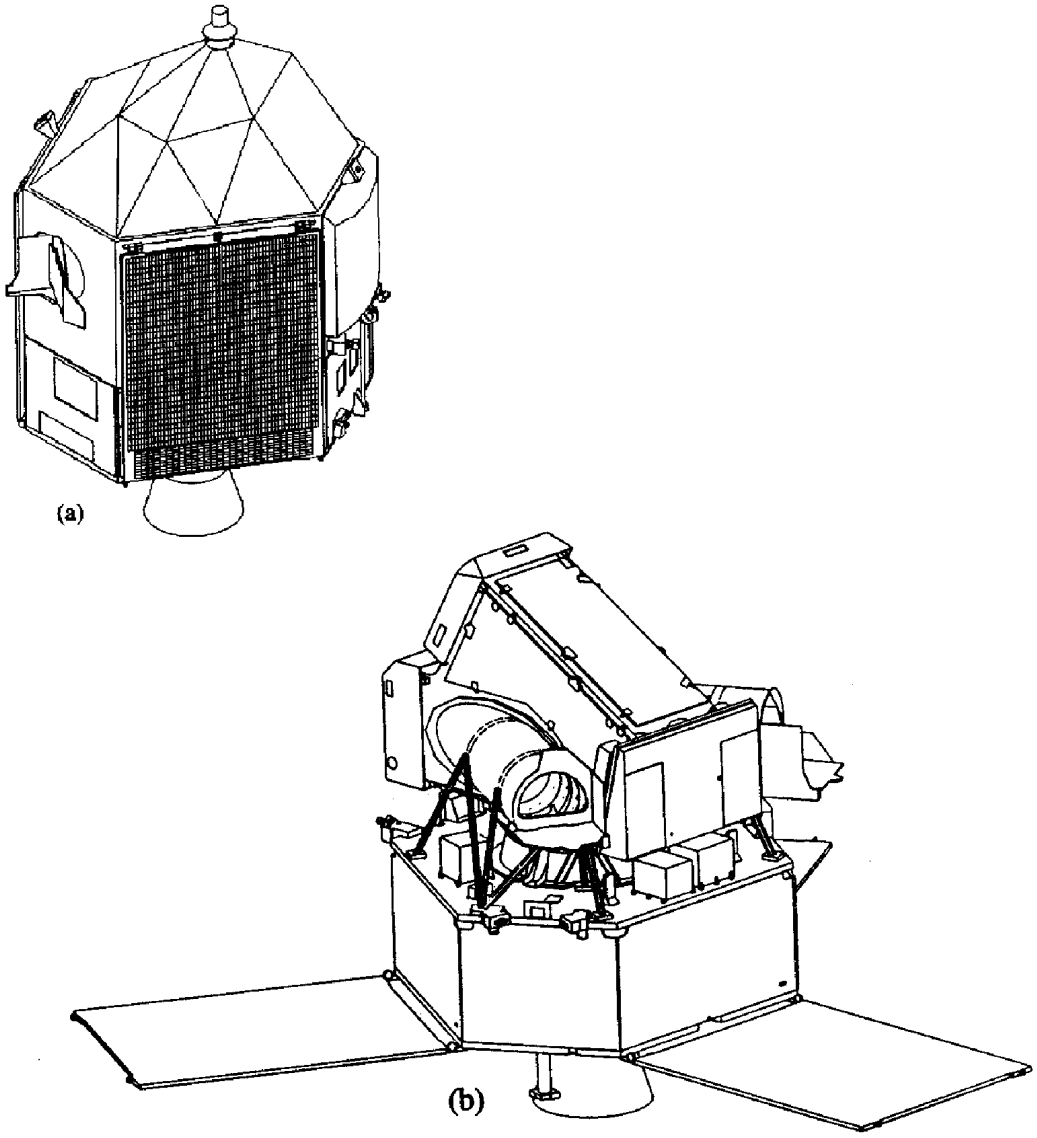

Figure 1.7. *(a) Satellite launch configuration with the solar arrays stowed, and (b) on-station configuration with the solar arrays deployed (and with the shade structure removed for illustration purposes).*

some 350 W of power to the on-board systems. The adopted scanning law meant that the solar panels were at a constant inclination to the Sun throughout routine operations.

Some of the main characteristics of the satellite and its operational environment are listed in Table 1.2. The mass budget for the satellite at launch, rounded to the nearest kilogram, is given in Table 1.3. The power budget is given in Table 1.4 for the pre-operational phase (i.e. in transfer and near synchronous orbit, when the satellite was spinning, the solar arrays were stowed and the payload and on-board computer were off), and for the operational phase (i.e. when the satellite was spinning, the solar arrays were deployed and at a sun aspect angle of 43°).

Table 1.1. Electrical subsystems and acronyms.

Subsystem Description	Acronym
Telecommunication subsystem	TCMS
Data handling subsystem	DHSS
Solar generation subsystem	SGSS
Electrical power subsystem	EPSS
Spacecraft thermal control subsystem	STCS
Attitude and orbit control subsystem	AOCS
Reaction control assembly	RCA
Detection subsystem	DTSS
Payload service electronics units	SEU

Table 1.2. Main satellite characteristics.

Launch mass	1140 kg
Power requirements	295 W (nominal)
Uplink data rate	2 kbits s^{-1}
Downlink data rate	24 kbits s^{-1}
Satellite orbit	Geostationary transfer (Geostationary planned)
Inclination to sun	43°
Spin rate	11.25 rev per day (168.75 arcsec s^{-1})

Table 1.3. Satellite mass budget.

Element	Mass (kg)
Spacecraft	400
Payload	210
Apogee boost motor propellant	463
Hydrazine (expelled after station acquisition)	32
Cold gas (nitrogen)	10
Balancing mass	25
Total launch mass	1140

Table 1.4. Satellite power budget for the pre-operational and operational periods.

System	Pre-operational Period (W)	Operational Period (W)
Electrical power subsystem	22	22
Telecommunication subsystem	31	31
Data handling subsystem	21	45
Attitude and orbit control subsystem	31	80
Spacecraft thermal control	10	3
Payload thermal control	–	64
Payload	–	25
Total	115	270
Solar generation power	155	368

1.8. Ground Segment Overview

Ground segment activities were controlled throughout the mission from the European Space Operations Centre (ESOC) whose role throughout the mission was to ensure that the maximum science data was collected with the best quality possible. This implied that not only the safety of the satellite was ensured, but also its efficiency was kept as high as possible at all times. This was achieved by setting up a mission control team several years before launch to prepare it and to operate the mission after launch. To do this, the team organised a ground segment which comprised all the facilities needed to control the satellite and collect the science data.

The operations team throughout the routine phase comprised some twenty persons. While the functions of the control team were numerous, they could be separated into the following three major areas:

(a) the first group, the spacecraft control team, dealt with the monitoring and control of the satellite, the creation of the mission plan, the command generation, the management of spacecraft parameters and commands (ground-resident satellite data base), the spacecraft performance evaluation, and the on-board software updates;

(b) the second group, the flight dynamics team, dealt mainly with the real-time attitude monitoring and correction of the spacecraft, the programme star file generation, mission plan preparation, the payload performance monitoring, the payload calibrations, and the Hipparcos Input Catalogue maintenance;

(c) the third group, the software support team, was responsible for maintaining the software which processed telemetry and telecommanding in real-time. In addition they performed the data archiving and produced the final tapes which were sent to the Hipparcos data reduction consortia for subsequent processing.

In addition to the above, ESOC infrastructure support guaranteed appropriate hardware availability, the scheduling of ground station coverage, the link configurations to the various ground stations and computers, satellite ranging support, orbit determination and other facilities common to all ESOC controlled satellites.

The Hipparcos ground segment was originally intended to comprise only a single ground station at Odenwald, combined with the operations control centre at ESOC. With the non-nominal 10.66-hour orbit, a single ground station would have provided only limited operational coverage, insufficient to allow the development of an interconnected observational network critical to the data reduction concept. Within a few months of launch, additional ground stations were brought into the network, so that the final operational network ultimately comprised three major elements: ground stations located in Odenwald (Germany), Perth (Australia), Kourou (French Guyana) and Goldstone (USA); the operations control centre at the European Space Operations Centre in Darmstadt, Germany; and a communications system interconnecting these sites.

During the mission, the spacecraft was controlled from the following control rooms based at ESOC: (i) the operations control centre had the overall responsibility for all satellite and mission control activities; (ii) the main control room was only used during

critical mission control phases or emergency operations; (iii) all routine operations were controlled from the Hipparcos dedicated control room. This room was equipped with three workstations connected to the Hipparcos dedicated computer system; (iv) the flight dynamics room was used during critical mission phases and important manoeuvres, with the routine flight dynamics attitude and payload functions transferred to the Hipparcos dedicated control room to ease the operational interface between the control teams; and (v) the ground control room established the connections between the relevant ground stations and the operations control centre as well as the data line connections between the computer systems.

The main control room was used during the launch and early orbit phase of the mission. All operations were performed using the allocated general-purpose interactive workstations which interfaced with the data processing facilities and data files of the Hipparcos dedicated control system computer. Ranging operations were initiated from the multi-satellite support system. Each workstation was equipped with three displays for alphanumeric and graphical presentation of telemetry data in real-time or retrieval mode. Hardcopy devices allowed instant record of the displays. The operations control center had a number of intercom voice loops which allowed two-way voice communications between all teams in the operations control center, the ground stations and the launch range.

During the routine phase of the mission, the dedicated control room was used for all monitoring and control functions. The room was equipped with three workstations and had in addition terminals connected to the off-line computer. Hardcopy devices were attached to each workstation. Voice loop and telephone communications facilities were provided. During critical or contingency phases additional workstations were connected on-line in the main control room.

The flight dynamics control room was equipped with terminals to both the on-line and the off-line Hipparcos computers as well as to the multi-satellite support system computers for use in the launch and early operations phase. Hardcopy facilities were available for printing information from the computer displays. Voice contact between the main control room and/or dedicated control room was possible by means of the intercom facility.

The Hipparcos operational software consisted of two separated systems: (i) the on-line software, providing support to all activities related to the near real-time satellite control operations, and (ii) the off-line software, providing support to all non real-time activities.

The on-line software was resident on a VAX 785 machine, with a VAX 785 as back-up (one of the VAX 785 computers was replaced by a more powerful VAX 8650 machine in January 1990). In addition, a VAX 4090 workstation was installed in early 1993 to deal with the large increase in software demands precipitated by the satellite's gyro failures. The off-line software (referred to as the multiple virtual system, or MVS) was run on a Comparex 8/96 mainframe computer, the two computers being interconnected by a high-speed data link. This allowed the use of both machines during some on-line activities, such as the programme star file production, and payload calibration and monitoring. Additional off-line processing was supplied on an IBM-PC PS/2 for use in performing real-time attitude determination.

The on-line software supported the following tasks: the telemetry processing chain, the telecommanding chain, real-time operator interface, maintenance of operational data bases, telemetry filing and archiving, report generation, and ranging support. In

addition it also supported on-board computer and control law electronics monitoring and updating real-time attitude monitoring, ground real-time attitude determination, payload performance monitoring, real-time payload calibration, and link control and monitoring.

In addition to the Hipparcos specific software, a number of general software facilities were implemented on the on-line software system. This general software was called the spacecraft control and operating system, or SCOS, and provided standard telemetry processing, workstation displays, reading telemetry data from history files, and data base editing facilities.

The off-line software system concentrated on the following tasks: off-line telecommand preparation, on-board software maintenance, spacecraft performance evaluation system, mission planning support, programme star file support, Hipparcos Input Catalogue maintenance, payload calibrations and monitoring, calibration support and analysis, data reduction consortia tape production, and star pattern matching.

In addition, orbit determination was performed on the multi-satellite support system.

2. THE PAYLOAD: OVERVIEW AND OPTICAL ELEMENTS

This chapter gives an overview of the Hipparcos payload with particular reference to the optical elements. Images of stars from the two fields of view were brought together by the 'beam-combining mirror', the spherical mirror, and the flat folding mirror, to a focal surface where the modulating grid was located. Manufactured on the same substrate, the 'main grid' consisted of 2688 parallel slits, with a projected spacing of 1.208 arcsec and covering a field of $0\overset{\circ}{.}9 \times 0\overset{\circ}{.}9$, and the 'star mapper grids' each consisting of two sets of four slits (vertical and chevron). Modulated signals from the main grid represented the basic primary mission data, while the modulated signals from the star mapper grid yielded information on the three-axis attitude of the satellite. Light coming through the main grid was transferred to the image dissector tube detector by the main detector relay lens assembly, and light modulated by the star mapper grid was 'picked off' by a 45° prism and transferred to the photomultiplier (star mapper) detectors by the star mapper relay lens assembly. A 'chromaticity filter' could be inserted into the parallel beam to provide in-orbit measurements of the telescope's chromatic aberration.

2.1. Introduction

The Hipparcos payload was built around an all-reflective Schmidt telescope, working in the visible part of the electromagnetic spectrum. It had an entrance pupil of 290 mm diameter and a focal length of 1400 mm. A modulating grid was located at the telescope's focal surface, consisting of 2688 parallel slits with a period of 1.208 arcsec, and covering a square field of about $0\overset{\circ}{.}9 \times 0\overset{\circ}{.}9$.

The modulating grid was re-imaged onto the photocathode of an image dissector tube by means of a set of folding mirrors and relay lenses, constituting the image dissector tube relay optics. Two image dissector tube detectors and two sets of relay optics were used in cold redundancy (i.e. the redundant detector was switched off when not in use), the selection being performed by means of a switching mirror.

The instantaneous field of view of each image dissector tube was nominally circular, with a diameter of about 38 arcsec. It could be directed to any point of the $0\overset{\circ}{.}9 \times 0\overset{\circ}{.}9$ field by varying the currents applied to the deflection coils.

Table 2.1. Payload characteristics.

Optics:	Telescope configuration	All-reflective Schmidt
	Field of view	$0\overset{\circ}{.}9 \times 0\overset{\circ}{.}9$
	Separation between fields	58°
	Diameter of primary mirror	290 mm
	Focal length	1400 mm
	Scale at focal surface	6.8μm per arcsec
	Mirror surface accuracy	$\lambda/60$ rms (at λ = 550 nm)
Primary Detection System:	Modulating grid	2688 slits
	Slit period	1.208 arcsec (8.2μm)
	Detector	Image dissector tube
	Photocathode	S20
	Scale at photocathode	3.0μm per arcsec
	Sensitive field of view	38 arcsec diameter
	Spectral range	375–750 nm
	Sampling frequency	1200 Hz
Star Mapper (Tycho) System:	Modulating grid	4 slits perpendicular to scan
		4 slits at $\pm 45^\circ$ inclination
	Detectors	Photomultiplier tubes
	Photocathode	Bi-alkali
	Spectral range (B_T)	$\lambda_{\rm eff}$ = 430 nm, $\Delta\lambda$ = 90 nm
	Spectral range (V_T)	$\lambda_{\rm eff}$ = 530 nm, $\Delta\lambda$ = 100 nm
	Sampling frequency	600 Hz

In addition to the primary detection chain (consisting of the modulating grid and the image dissector tube), the payload included two star mappers which were also used in cold redundancy. The primary function of the star mapper was to provide data allowing the on-board three-axis satellite attitude determination (a task performed by the on-board computer) and the *a posteriori* determination of the attitude (a task performed by the data analysis consortia on the ground).

Each star mapper consisted of a star mapper grid, located at one side of the main modulating grid, and two photomultipliers, measuring the light transmitted by the whole star mapper grid in two different spectral bands—B_T and V_T. The spectral separation was accomplished by means of a dichroic beam splitter, which reflected the shorter wavelength light (the B_T band) onto one photomultiplier and transmitted the longer wavelength light (the V_T band) onto the other.

Table 2.1 provides a summary of some of the key features of the payload. Tables 2.2–2.4 give a summary of the transmission of the various elements comprising the Hipparcos payload, both for the primary detection chain, and for the Tycho B_T and V_T chains, respectively. These figures are based on measurements at unit level during the on-ground calibrations.

Table 2.2. Spectral transmittance/quantum efficiency (QE) of the main detection chain, taking into account all payload elements (predicted performance at the start of the mission based on ground calibrations).

λ (nm)	Beam Combiner	Mirrors	Grid Substrate	Relay Optics	Detector	Total QE*
350	0.86	0.74	0.73	0.16	0.02	0.002
375	0.85	0.72	0.82	0.56	0.03	0.009
400	0.95	0.90	0.91	0.79	0.04	0.027
425	0.96	0.92	0.92	0.81	0.06	0.042
450	0.97	0.94	0.93	0.83	0.08	0.058
475	0.97	0.94	0.94	0.85	0.08	0.060
500	0.97	0.94	0.94	0.88	0.07	0.055
525	0.97	0.94	0.94	0.90	0.06	0.050
550	0.97	0.94	0.94	0.91	0.05	0.044
575	0.97	0.94	0.94	0.92	0.05	0.038
600	0.97	0.95	0.94	0.91	0.04	0.033
625	0.97	0.95	0.94	0.90	0.04	0.027
650	0.97	0.95	0.94	0.84	0.03	0.022
675	0.97	0.95	0.93	0.78	0.03	0.018
700	0.97	0.95	0.93	0.72	0.02	0.014
725	0.97	0.95	0.93	0.65	0.02	0.010
750	0.97	0.95	0.92	0.58	0.01	0.008
775	0.97	0.95	0.91	0.52	0.01	0.005
800	0.97	0.95	0.90	0.45	0.01	0.004
825	0.97	0.95	0.90	0.40	0.01	0.002

* In determining the average count rate from a star, the total efficiency given is further affected by the opaque parts of the modulating grid. This factor is nominally given by the ratio of the slit width to the grid period, or $3.13/8.20 \simeq 0.38$ (Table 2.5), but in reality it is further reduced by diffraction. The absolute detection efficiency, of about 10^{-2}, takes this into account.

2.2. Payload Configuration and Layout

The overall payload configuration is shown in Figure 2.1. The payload functional diagram is shown in Figure 2.2 and the payload electrical block diagram in Figure 2.3. The payload consisted of four main assemblies (see Figure 2.4):

(a) the two baffle assemblies: two external baffles protected the telescope assembly from stray light. They were mounted separately on the spacecraft upper platform, with no mechanical link with the other assemblies of the payload, except for the overlapping multi-layer insulation;

(b) the telescope assembly: this included all elements between the two optical entrance apertures and the grid unit: the three telescope mirrors and all associated structural elements necessary to maintain them at their nominal positions. All hardware associated with the thermal control (the multi-layer insulation, heaters, and thermistors) rested on separate structural elements. The telescope assembly also ensured the mechanical and thermal conductive interfaces with the spacecraft. An isostatic mounting of the payload onto the spacecraft employed three titanium bipods;

Table 2.3. Spectral transmittance/quantum efficiency (QE) of the B_T star mapper detection chain (vertical slits) taking into account all payload elements. The table gives the predicted performance at the beginning of the mission based on ground calibrations, i.e. without transmission degradation due to irradiation effects.

λ (nm)	Beam Combiner	Mirrors	Grid	Dichroic	Relay Optics	Diffraction Loss	Detector QE	Total QE
350	0.86	0.72	0.83	0.01	0.87	0.865	0.15	0.001
375	0.85	0.63	0.88	0.50	0.92	0.815	0.18	0.032
400	0.95	0.86	0.90	0.85	0.93	0.785	0.20	0.091
425	0.96	0.92	0.91	0.92	0.93	0.760	0.20	0.105
450	0.97	0.93	0.92	0.80	0.93	0.735	0.20	0.091
475	0.97	0.93	0.92	0.20	0.93	0.720	0.17	0.019
500	0.97	0.93	0.92	0.04	0.93	0.700	0.15	0.004
525	0.97	0.93	0.92	0.00	0.93	0.690	0.14	0.000
550	0.97	0.93	0.92	0.00	0.94	0.680	0.11	0.000
575	0.97	0.93	0.92	0.00	0.94	0.670	0.07	0.000
600	0.97	0.93	0.91	0.00	0.94	0.660	0.04	0.000
625	0.97	0.93	0.90	0.01	0.92	0.655	0.02	0.000
650	0.97	0.93	0.88	0.03	0.89	0.650	0.01	0.000
675	0.97	0.93	0.87	0.03	0.85	0.645	0.00	0.000
700	0.97	0.94	0.85	0.02	0.80	0.640	0.00	0.000
725	0.97	0.94	0.84	0.03	0.76	0.635	0.00	0.000
750	0.97	0.94	0.83	0.03	0.70	0.630	0.00	0.000
775	0.97	0.95	0.81	0.03	0.65	0.625	0.00	0.000

Table 2.4. Spectral transmittance/quantum efficiency (QE) of the V_T star mapper detection chain (vertical slits) taking into account all payload elements. The table gives the predicted performance at the beginning of the mission based on ground calibrations, i.e. without transmission degradation due to irradiation effects.

λ (nm)	Beam Combiner	Mirrors	Grid	Dichroic	Relay Optics	Diffraction Loss	Detector QE	Total QE
350	0.86	0.71	0.83	0.00	0.70	0.865	0.15	0.000
375	0.85	0.63	0.88	0.00	0.66	0.815	0.17	0.000
400	0.95	0.86	0.90	0.00	0.83	0.785	0.19	0.000
425	0.96	0.92	0.91	0.00	0.85	0.760	0.19	0.000
450	0.97	0.93	0.92	0.00	0.86	0.735	0.19	0.000
475	0.97	0.93	0.92	0.38	0.87	0.720	0.17	0.008
500	0.97	0.93	0.93	0.85	0.88	0.700	0.16	0.068
525	0.97	0.93	0.92	0.95	0.88	0.690	0.14	0.068
550	0.97	0.93	0.92	0.94	0.89	0.680	0.12	0.058
575	0.97	0.93	0.91	0.95	0.89	0.670	0.08	0.038
600	0.97	0.93	0.90	0.97	0.89	0.660	0.04	0.017
625	0.97	0.93	0.88	0.96	0.88	0.655	0.02	0.009
650	0.97	0.93	0.87	0.95	0.85	0.650	0.01	0.003
675	0.97	0.93	0.85	0.94	0.81	0.645	0.00	0.001
700	0.97	0.94	0.85	0.93	0.76	0.640	0.00	0.000
725	0.97	0.94	0.84	0.93	0.72	0.635	0.00	0.000
750	0.97	0.94	0.83	0.93	0.67	0.630	0.00	0.000
775	0.97	0.95	0.81	0.92	0.63	0.625	0.00	0.000

Colour figure to be inserted here

Figure 2.1. *Overview of the payload. Light entered from the two baffles (shown red and blue) and fell onto the beam-combining mirror, where it was brought to a common focus where the modulating grids were located (top). In the bottom figure, the path of the light reaching the (main) image dissector tube detector is shown as a red-dashed line, while the light reaching the star mapper detector is shown in blue. A dichroic filter split the latter into the B_T and V_T channels, which were detected separately.*

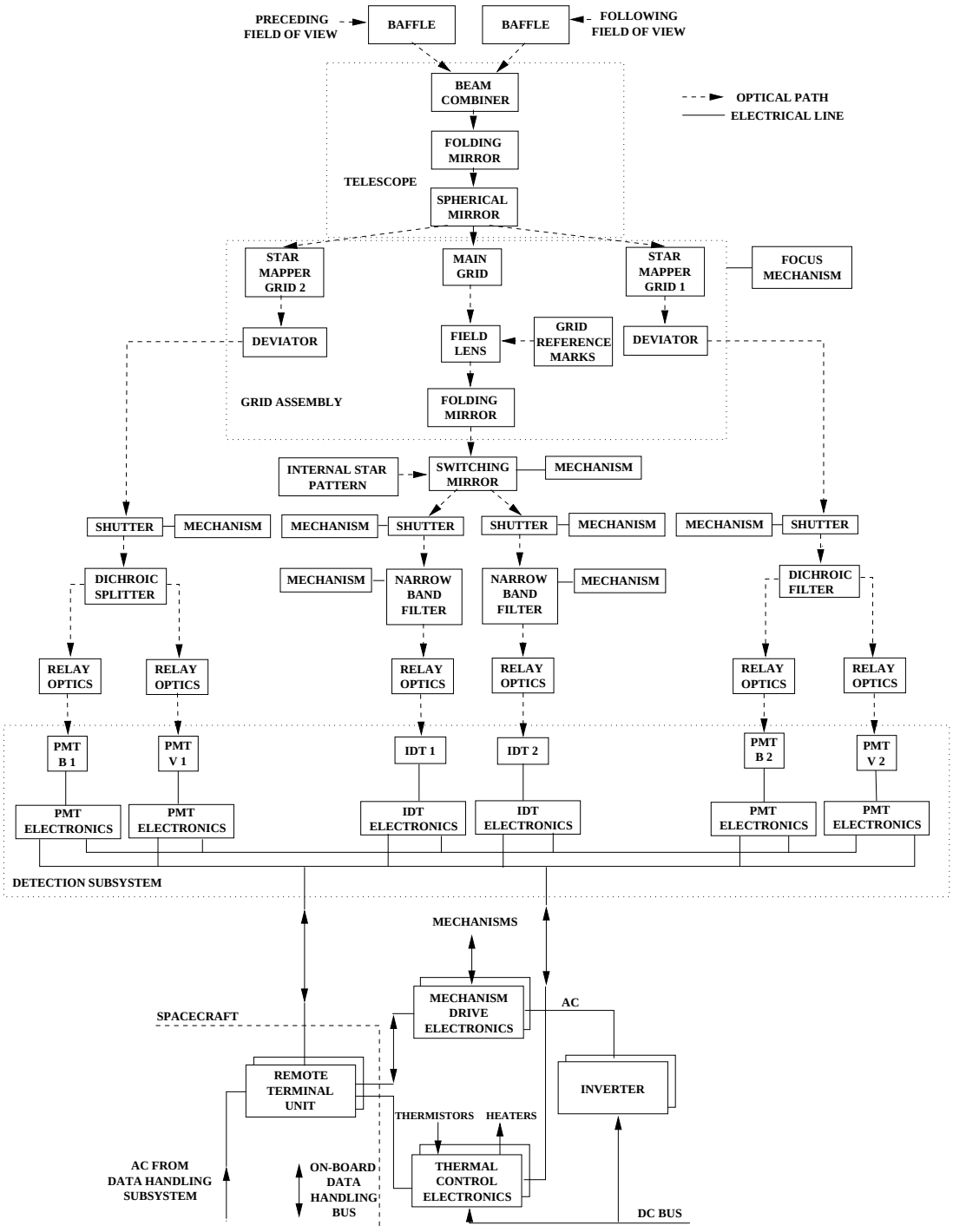

Figure 2.2. *Payload functional diagram, illustrating the path of the light through the payload, along with the corresponding shutters, mechanisms, and detectors associated with the (main) image dissector tube detectors (IDT) and the star mapper photomultiplier tubes (PMT). Redundant systems (indicated 1/2) were provided in all paths, eliminating single-point failures in the payload.*

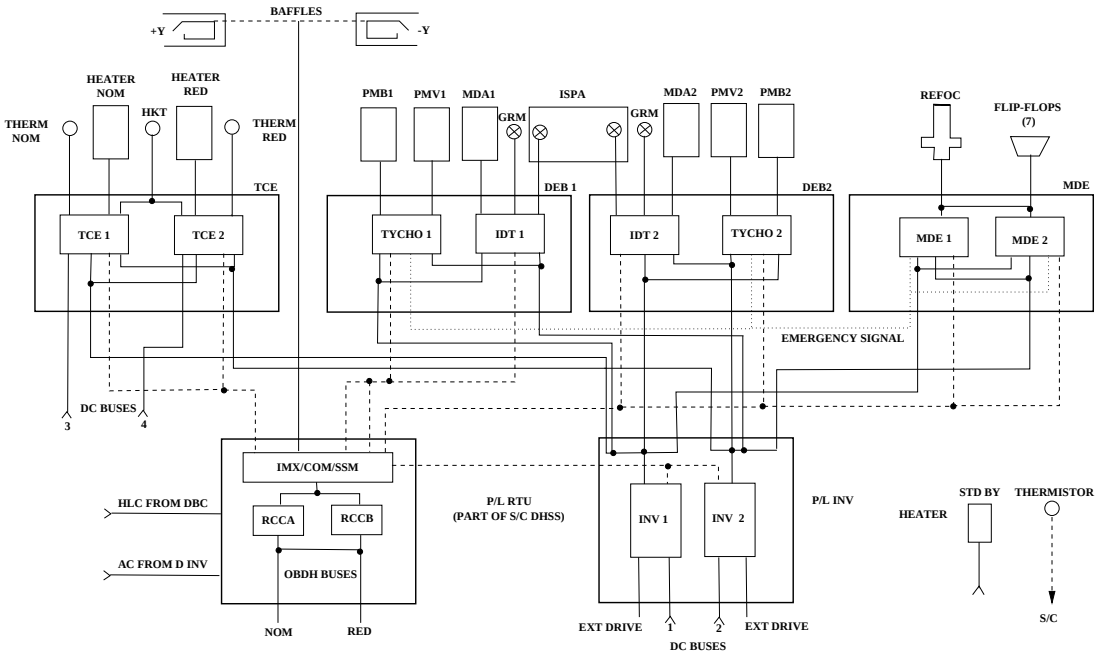

Figure 2.3. *Payload electrical block diagram. Heaters and thermistors were associated with each of the redundant thermal control electronics (TCE). DEB: detection electronics box; GRM: grid reference marks; IDT: image dissector tube; INV: invertor; MDE: mechanism drive electronics; OBDH: on-board data handling; RTU: remote terminal unit; PM: photomultiplier (star mapper).*

(c) the focal-plane assembly: this included all elements from the grid to the image dissector tube and photomultiplier detectors. The focal-plane assembly was mechanically attached to the telescope assembly. It consisted of a rectangular platform supporting all the equipment required to transform the optical signals produced by the telescope assembly into electrical digital signals. The main components of the focal-plane assembly were: the refocusing assembly comprising the main grid, the star mapper grids, and the focus mechanism; the relay optics, filters, and mirrors, required to relay the photons from the grid to the detectors; the detectors (image dissector tubes and photomultipliers); the detection electronics; the mechanisms (shutters, switching mirror, etc.); and an internal star pattern assembly used for calibration purposes;

(d) the service electronics units, consisted of the payload inverter, the thermal-control electronics, and the mechanism drive electronics. Functionally, these three units were complemented by the remote terminal unit (not strictly part of the payload items). These boxes were installed on the upper platform of the spacecraft and had no mechanical link with the rest of the payload, except for the electrical cables.

The payload main assembly was a higher-level assembly, consisting of the telescope assembly and the focal-plane assembly, as illustrated in Figure 2.5. The payload main assembly was a single physical box after integration of the focal-plane assembly onto the telescope assembly.

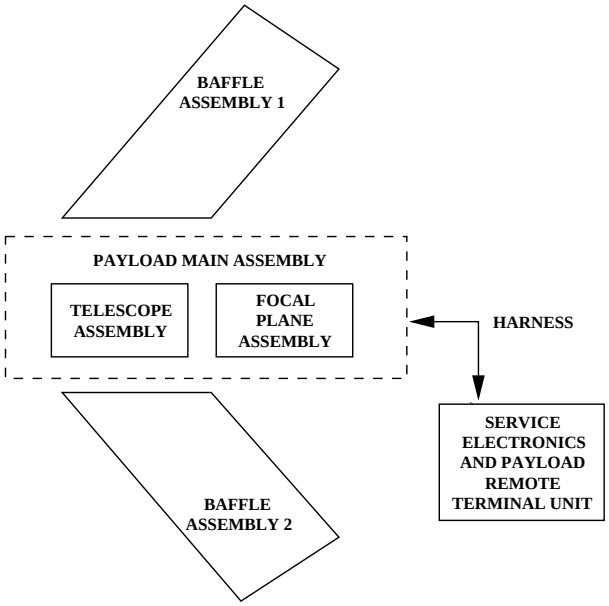

Figure 2.4. *Breakdown of the payload hardware at assembly level.*

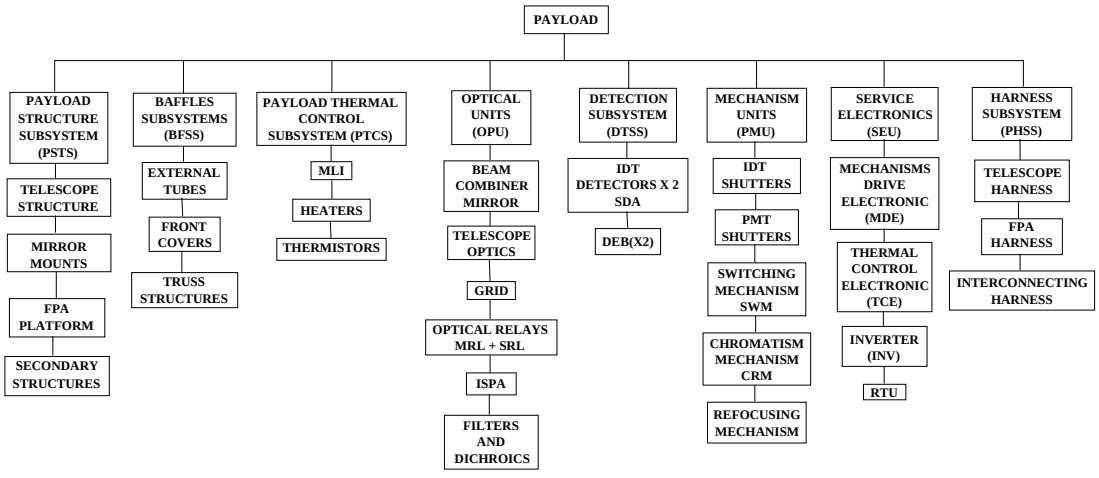

Figure 2.5. *Breakdown of the payload hardware at subsystem level (DEB: detection electronics box; FPA: focal plane assembly; IDT: image dissector tube; ISPA: internal star pattern assembly; MLI: multi-layer insulation; MRL: main relay lens; PMT: photomultiplier tube; RTU: remote terminal unit; SRL: star mapper relay lens).*

2.3. Payload Hardware

The payload system was divided into eight subsystems (see Figure 2.5). This section provides a brief description of these subsystems, outlining major design features and associated technology.

The payload structure: The payload structure was centred around a box built from five carbon-fibre reinforced plastic (type GY 70), single-skin panels, which provided all necessary interfaces to connect the three mirror mounts, the focal-plane assembly platform, and the various secondary structures. The carbon-fibre reinforced plastic elements gave the payload structure a low thermal susceptibility.

The focal-plane platform was a rigid, carbon-fibre reinforced plastic sandwich plate made of two face sheets of carbon-fibre reinforced plastic bonded on an aluminium honeycomb and equipped with specific inserts used to connect the different focal-plane assembly units—the optical relays, detectors, mechanisms, and electronic boxes. This platform was hard-mounted onto the telescope.

Each of the three telescope mirrors was supported by a mount consisting of a carbon-fibre reinforced plastic frame barrel rigidly connected to the main structure at three points. Three identical flexural-blade systems made of invar and titanium connected the mirror to its barrel.

In addition to the main structure, the secondary structures included the internal baffles, necessary for the protection against straylight, and the heater-mat carriers and covers, which were required to ensure light-tightness of the enclosure and to provide mechanical support to the thermal hardware multi-layer insulation, heater, thermistors and associated harnesses.

The optical units: The telescope optics consisted of the (flat) folding mirror, the spherical mirror, and the beam-combiner mirror, all made of zerodur and light-weighted by about 40 per cent. The optical surface quality of the folding and spherical mirrors was better than $\lambda/60$ rms at a reference wavelength of $\lambda = 550$ nm, and the overall optical quality of the telescope was $\lambda/20$ rms.

The grid assembly was based on a main substrate made of silica. The main grid and the two star mapper patterns were etched into the chromium layer on its front convex face using an electron-beam pattern generating technique. The rear side of the substrate constituted the field lens associated with the relay optics. A set of deviators folded the star mapper beam in the direction of the star mapper relay optics. These elements were mounted on an invar barrel, extended by the focal-plane baffle which protected the elements from stray light.

Relay optics imaged the main grid onto one of the image dissector tube photocathodes. One or other of the two optical chains was selected by means of a Suprasil switching prism, fixed onto a bi-stable positions mechanism, which allowed the beam to be switched between the nominal and redundant channels. Relay optics also conveyed the light from each of the two star mapper grids onto their respective blue/visual photomultipliers. Each of these star mapper relay optics was equipped with a dichroic

beam splitter, which provided the colour separation of the beam for the purposes of the Tycho experiment. The selection of the preceding or following star mapper was made electronically.

Also included in the optical units were the internal star pattern assembly which, in conjunction with the switching prism mechanism, gave the possibility of an in-orbit geometric calibration of the deflection coil currents of the main detectors, and the switchable chromaticity filters (one per image dissector tube relay optics), which gave the possibility of an in-orbit measurement of the system chromaticity.

The mechanism units: The re-focusing mechanism held the grid package and an associated folding mirror, which folded the resulting optical beam. This mechanism allowed movement of the grid position with respect to the telescope focal surface. The best focus position, maximising the signal modulation of the two fields of view, was determined in orbit.

The switching mirror mechanism provided the mechanical support to the switching prism, which permitted the selection of either one of the two main detectors.

There were two chromaticity mechanisms, one per image dissector tube channel, each of them being equipped with a chromaticity filter and a broad-band filter of identical optical path length. Switching from the broad-band filter to the chromaticity filter allowed the in-orbit calibration of the instrumental chromaticity.

There were four shutter mechanisms, preventing the detectors from damage induced by light overload as the fields of view scanned the Earth or the Moon.

The detection subsystem: The detection subsystem included the two primary detectors, each of them consisting of an image dissector tube, equipped with its high-voltage power supply and its pre-amplifier combined in a single package, and four photomultipliers, each of them integrated with its own high-voltage power supply and its own pre-amplifier. There were two detection electronic boxes, each of them dedicated to the operation of one main detector assembly and two star mapper detector assemblies (nominal or redundant chains).

The thermal control subsystem: The thermal control subsystem included the multilayer insulation blankets, the heater mats, and the thermistors. All components were installed on the secondary structure. The control law for the heaters was implemented in the satellite on-board computer. Control of heaters and thermistors was performed by the thermal control electronics, part of the service electronics. Twenty-one thermal zones were used to achieve payload thermal control, fifteen being devoted to the telescope enclosure and six to the focal-plane assembly.

The service electronic units: The service electronic units consisted of three boxes located on the upper platform of the spacecraft: (i) the inverter unit, which was used to convert the main DC bus regulated voltage into an AC voltage distributed to the payload electronic boxes (mechanism drive electronics, thermal control electronics, and detection electronic boxes); (ii) the thermal-control electronics, which controlled and monitored the temperature of the payload, using a control law which was implemented in the spacecraft on-board computer; and (iii) the mechanism drive electronics, which controlled and monitored the positions of the payload mechanisms.

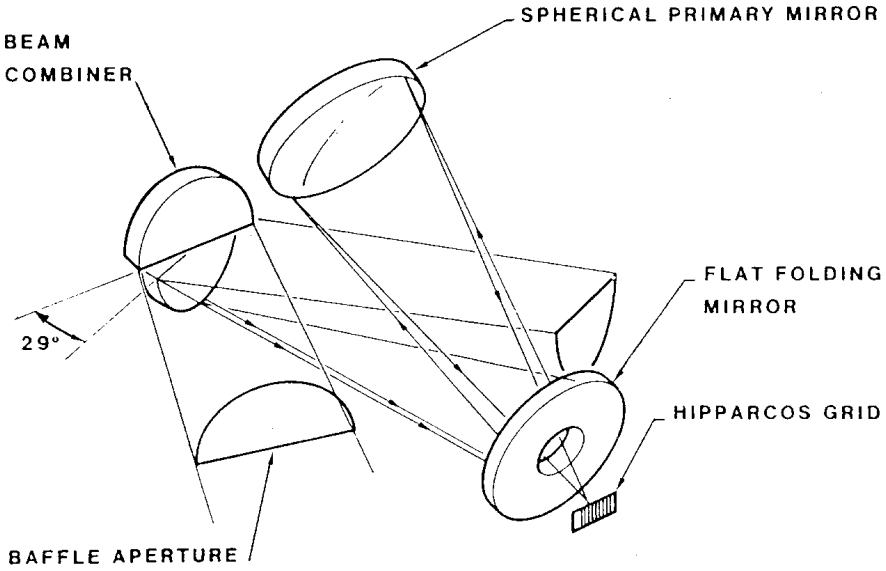

Figure 2.6. *Configuration of the Schmidt telescope. Light entered from the two baffle directions, and was brought together at the beam combiner, which was figured as a Schmidt corrector. The combined light was reflected from the folding and spherical primary mirrors onto the focal surface where the modulating grids were located.*

These three electronic boxes interfaced with the payload remote terminal unit, which was responsible for transfer of data commands and clocks from the spacecraft data-handling system to the electronic units of the payload, as well as the transfer of scientific, engineering and housekeeping data from the payload to the spacecraft data-handling system.

The baffle subsystem: The baffle subsystem consisted of two external baffles, which protected the payload from straylight originating from the Sun, the Earth, or the Moon. They were made of carbon-fibre reinforced plastic and were connected directly onto the spacecraft upper shelf. Each of these baffles was equipped with entrance covers, closed during ground handling and launch. They were opened in orbit by activation of associated pyrotechnic devices.

2.4. Telescope Mirrors

The telescope was based on the all-reflecting Schmidt concept, and consisted of three mirrors: a beam combiner, a primary spherical mirror, and a (flat) folding mirror (Figure 2.6). The folding mirror folded the optical beam to provide a more compact overall configuration. The beam combining mirror also performed the (off-axis) correction of spherical aberration.

A reflective coating was used for all three mirrors. It was chosen for its very high efficiency (in particular in the blue part of the spectrum), together with the fact that it had already been space qualified. It consisted of a layer of Ag, protected by a ThF_4 coating, on a layer of chromium to enhance its adherence. The metallic layer of this coating was grounded by bonding a grounding strap to an area, outside the useful coated

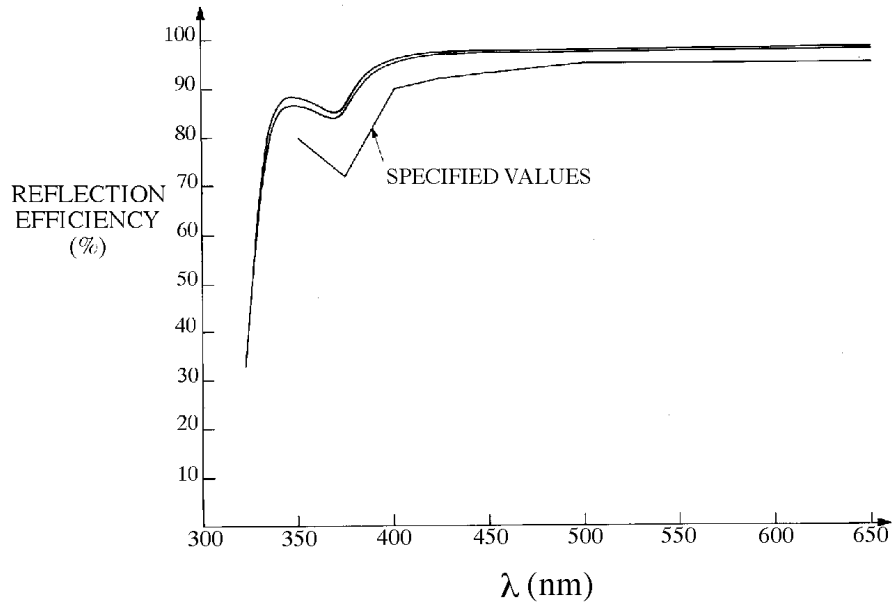

Figure 2.7. *Spectral reflectivity of the mirror coating as a function of wavelength.*

area, which was kept free of the dielectric protective layer. The performances of this coating, in terms of reflective efficiency is given in Figure 2.7. The mirror efficiencies are summarised in Tables 2.2–2.4 as part of the overall payload efficiencies.

The Beam Combiner

The beam combiner had three main functions: to combine the two fields of view; to define the entrance pupil; and to perform the correction of the aberrations of the spherical mirror.

The beam combiner mirror was made from a 'light-weighted' polished zerodur blank, 325.6 mm in diameter and 100 mm thick, cut into two halves and reassembled with a wedge angle of 29°. The optical surfaces of the half-mirrors were figured aspherically and the reflective coating defined the pupil area. The beam combiner assembly also included three fixation pads made of invar and bonded to the lateral side of the mirror. These pads interfaced with the beam combiner's isostatic mounts.

A beam combiner 'decentre sensor', consisting of a light source and a quadrant sensor, was bonded onto the two halves of the mirror and was used to align the spherical mirror's centre of curvature with the aspherical profile centre. The sensor was also used to verify alignment stability during on-ground operations.

The aspherical figuring of the beam combiner was of the Schmidt-Kerber type (see, for example, Buacher 1967). In this design, optical aberrations are minimised by corrections of the optical path at the level of the entrance pupil. The profile (Figure 2.8) was defined by its deviation with respect to the ideal flat surface:

$$X = \alpha\rho^4 + \frac{\beta}{2}\rho^2 \qquad [2.1]$$

where α is the aspherisation parameter ($\alpha = -5.16726 \times 10^{-12}$ mm^{-3}), β is the vertex curvature ($\beta = 3.47724 \times 10^{-7}$ mm^{-1}), and ρ is the radial coordinate in mm.

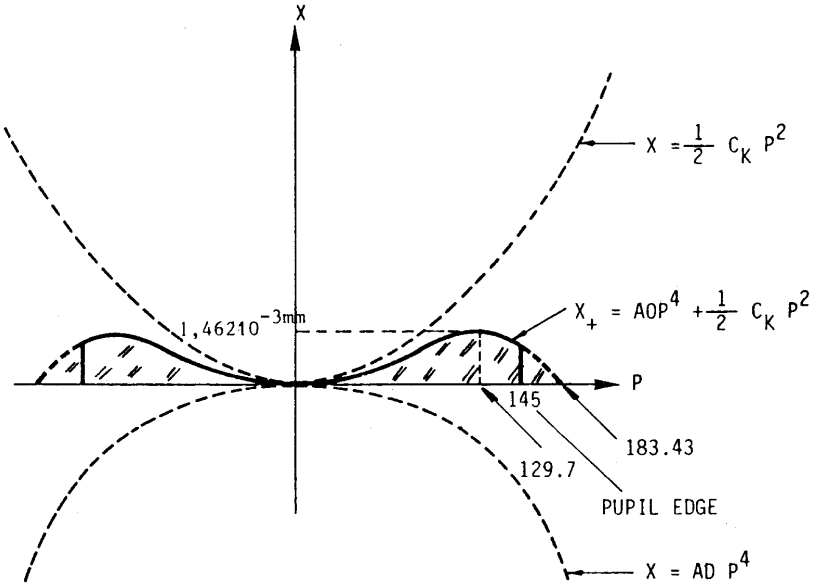

Figure 2.8. *Details of the Schmidt-Kerber profile of the beam combiner.*

Because of the incidence angles of ±14°.5 on the two segments of the beam combiner, the figuring should ideally be elliptical (non-rotationally symmetric) for a perfect correction. This profile was approximated by decentring the rotationally symmetric Schmidt-Kerber profiles of each mirror half by 4 mm from the optical axis, by removing an 8 mm slice while cutting the polished blank. The various steps of the manufacturing process are shown in Figure 2.9.

Deviation of the polished surface, after assembly, with respect to the best-fit Schmidt-Kerber profile (within 1 per cent of the nominal profile), was specified to be less than $\lambda/60$ rms (9.1 nm) at a reference wavelength of $\lambda = 550$ nm. The induced chromaticity was specified to be less than 1 milliarcsec.

Assembly of the two mirror halves was achieved by bonding with 64 glue spots, each 12 mm in diameter and 0.3 mm thick, to minimise wavefront distortions, without affecting the strength of the assembly. After assembly of the two halves of the beam combiner, the pupil projection onto a plane perpendicular to the optical axis, gave an external contour diameter of 290 ± 0.5 mm. Thus, the reflective coating external contour on the half mirror optical faces was actually elliptical.

The Flat Folding Mirror

The folding mirror was made from a flat, 'light-weighted' zerodur blank, 356 mm in diameter, 60 mm thick, with a conical central hole. Three fixation pads, made of invar, were bonded to the lateral side of the mirror. The mirror was polished by an annular lap technique, with appropriate compensation made for the weight of the fixation pads. Deviations of the resulting polished surface with respect to the best-fitting residual sphere (which had a radius of curvature greater than 100 km) were less than $\lambda/60$ rms. Induced chromaticity was less than 1 milliarcsec. The folding mirror was mounted to a plate, which had a large oval cutout for weight reduction. Two brackets were provided to hold the mirror in the mounting plate, and adjustment was possible from outside the barrel at three points.

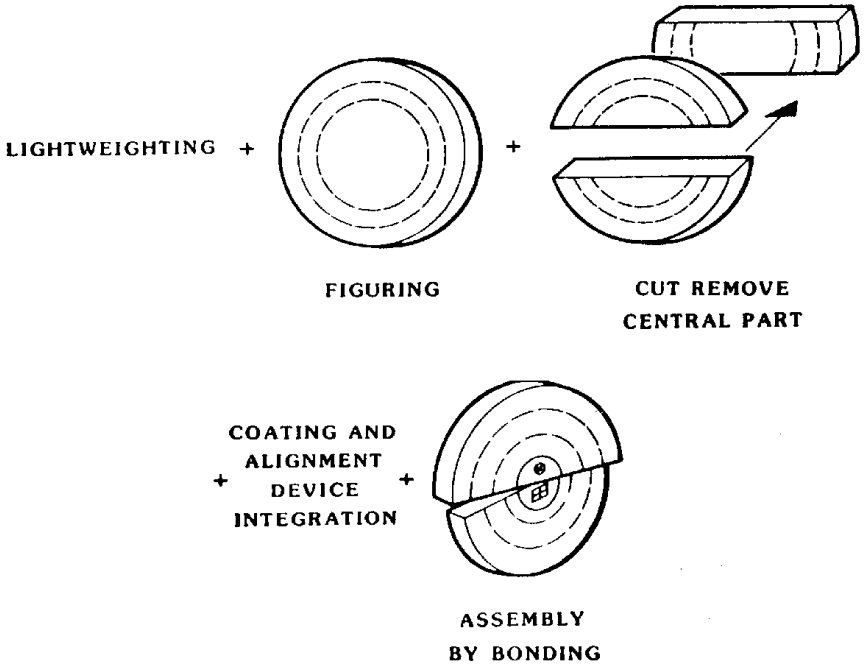

Figure 2.9. *Steps in the manufacture of the beam combiner. All three steps provided a considerable technical challenge in order to retain the overall high quality of the optical wavefront.*

The Spherical Mirror

The spherical mirror was made from a 'light-weighted' zerodur blank, 393 mm in diameter, 66 mm thick, with a small central hole (for alignment purposes). The optical surface was of concave spherical shape. Three fixation pads, made of invar, were bonded to the lateral side of the mirror. A lens, called the beam converger, was bonded to the central part of the rear side of the mirror, and this allowed for stability testing of the telescope, between the spherical mirror and the grid assembly.

The mirror was polished by conventional techniques, with appropriate compensation made for the weight of the fixation pads. Deviations of the resulting polished surface with respect to the best-fitting sphere (with radius of curvature 2800 ± 3 mm) were less than $\lambda/60$ rms. Induced chromaticity was less than 1 milliarcsec.

Beam Combiner and Mirrors Fixation Pads

The invar fixation pads of the mirrors and of the beam combiner were designed to minimise the wavefront distortion induced during the integration of the mirrors in their barrels with the isostatic mounts. They were bonded to the sides of the mirror with a glue film (type EC 2216) 0.3 mm thick. This resulted in a lack of symmetry in the (three-point) mounting of the two halves of the beam combiner.

The fixation pads were 50×70 mm^2 in size, with a thickness of 14.2 mm. They were tightened to isostatic mounts by twelve M4 studs, and positive locking was achieved by means of two expandable pins per pad. To avoid induced wavefront distortions, the

interface plane flatness was specified to be better than 2 μm, the studs were not fully secured to the pads, and expandable pins were located outside the main body of the pads. Overall wavefront error maps were measured as part of the verification procedures.

2.5. Modulating Grid and Baffle Unit

The grid assembly (Figure 2.10) was composed of the baffle unit and the grid unit. The main function of this assembly was to provide a modulated star signal which was analysed by the detection electronics (main detector assembly, star mapper detector assembly and detection electronic boxes). Consequently, the global performances of the payload were directly linked to the performance of this assembly. During the mission lifetime, the position of the grid unit with respect to the telescope focal surface could be adjusted by means of the refocusing mechanism, to compensate for secular shrinkage of the telescope structure due to outgassing, and other effects (see Chapter 10).

The Baffle Unit

The primary function of the baffle unit was to provide straylight protection of the modulating grid. A secondary function was to protect the grid against dust raised during integration and a specific 'dust cover' was implemented. This dust cover could be opened and closed manually from outside the payload, and was opened just before launch by disconnecting the actuating wire. The cover was equipped with a redundant spring system to keep it open during launch and thereafter throughout the mission. The baffle unit was also equipped with 'grid reference marks' and corresponding light sources, and a set of 'auto-collimation slits' and corresponding light sources.

The focal-plane baffle supported the light sources and optics used to illuminate the grid reference marks and auto-collimation slits, and also provided a base for the dust-cover mechanism. The complete baffle unit, with the exception of the dust cover, was made of invar.

The baffle structure itself was a tube, partly cylindrical and partly conical, from which a large part of the conical section had been removed. At the cylindrical part were lugs which formed the interface to the grid unit and the grid support of the refocus mechanism.

Inside the cylindrical part of the baffle, three diaphragms were positioned at distances of 6.5, 20, and 35 mm from the grid to provide straylight protection. The two baffle plates nearest to the grid surface were equipped with holes to fix the tubes in which the light-emitting diodes of the grid reference marks and auto-collimation sources were mounted.

The dust cover was mounted on the baffle tube with three screws and was operated manually via a double wire actuator system. It was designed to withstand vibration loads in both its closed and open positions. The pre-loading of the two springs was such that cover movement due to vibration was negligible. The dust cover was also approximately balanced about its hinge by the use of two counter-weights made of tungsten, fixed at the ends of two lever arms. In its closed position, the 'labyrinth'

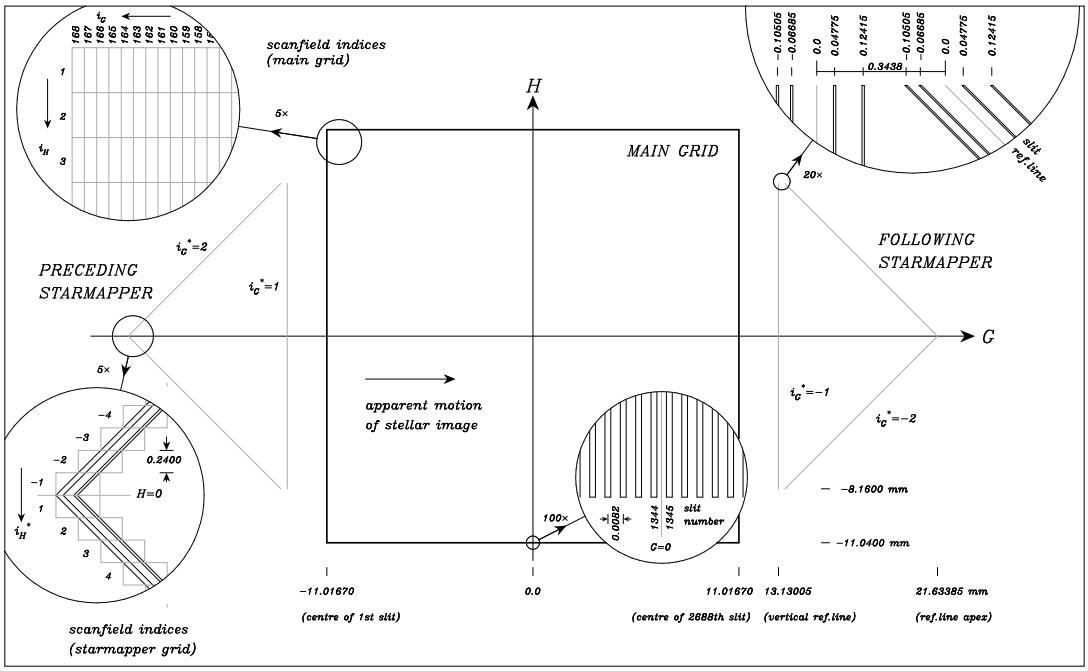

Figure 2.10. *General layout of the main and star mapper grids. The main grid covers a field of $0.^{\circ}9 \times 0.^{\circ}9$ (central square region) comprised of 2688 transparent and opaque slits (see central detail), layed down as 46×168 distinct 'scan fields' (see detail at top left). The two star mapper slit systems (two being provided for redundancy) each comprise 4 vertical and 4 inclined aperiodically spaced slits.*

formed between the edge of the cover and the edge of the third baffle plate prevented dust from entering the grid box.

The Auto-Collimation Sources

An auto-collimation device was provided within the payload to simulate a star image at the grid level. It was operated only while the satellite was on the ground. The sources were attached to the first baffle plate and illuminated by a light-emitting diode mounted in a tube between the first and second baffle plates. Each auto-collimation source consisted of a rectangular slit, $5 \times 200\ \mu m^2$ in size, and two prisms; one providing illumination of the slit and one projecting the auto-collimation source beam outward, in the direction of the optical axis. The dimensions were such that the auto-collimation source-slit appeared to be located on the grid surface. The photon flux, measured at the sub-assembly level, was more than 3×10^7 photon s^{-1}.

The auto-collimation source was made using an electron-beam pattern generator on a standard chromium-coated glass plate of the type used for integrated-circuit masks. After writing and etching, the plate was cut, ground to the required size, and bonded between the two prisms. This sub-assembly was then bonded to the first baffle plate, using a bonding jig to ensure accurate positioning. As the area available for bonding was only an annulus of 18 mm diameter, a titanium bracket was placed over the prisms to keep them properly located, even in case of a failure of the bond. A secondary purpose of this bracket was that of straylight protection.

The associated series of resistors and interconnections was located on a printed-circuit board that was attached to the linear actuator. The wiring between this printed-circuit board and the baffle unit was routed via a 15-pin connector, so that the baffle unit could be detached from the refocus assembly. The connector was located in the plane of the focal-plane assembly-platform in such a way that removal of the baffle unit was possible when the refocus assembly was mounted on the focal-plane assembly platform. The replacement of light-emitting diodes, bonded to the baffle, was possible during ground operations.

The Grid Unit

The grid unit was the main optical part of the refocusing assembly. It consisted of the optical block on which the main modulation grid and the star mapper patterns were written; the two star mapper deflectors; and the mounts for the optical block and for the star mapper deflectors. The grid transmissions for the main and star mapper detection chains are shown as part of the overall payload detection efficiencies in Tables 2.2–4.

The optical block was a piece of Suprasil 1, a high-quality silica. It served both as a substrate for the grid and the star mapper slits, and also as a field lens—i.e. the first element of the optics between the grid and the image dissector tube. The grid and the star mapper slits were written on a convex surface, matching the curved focal surface of the telescope. As this surface constituted a carrier for a pattern with sub-micron accuracy, which, to a large extent, defined the achievable accuracy of the mission, an extremely smooth surface finish was required. The optical block polishing was followed by a 'superpolish' treatment of the critical grid area defining the main field pattern. After polishing and cleaning, a layer of chromium was sputtered on the surface, followed by the deposition of a layer of electron-sensitive resist.

The rear side of the optical block had three parts. The central area, opposite the grid, was polished to a radius of curvature of 213.8 mm and served as a field lens. The parts opposite the star mapper patterns were flat and recessed to provide room for the star mapper deviators.

The optical block was bonded in the grid mount with the aid of a bonding rig that allowed accurate positioning of the optical block and the grid. An electrical contact between the chrome of the grid pattern and the grid mount was also provided.

A set of grid reference marks was provided within the grid assembly, allowing partial geometrical calibration of the detector assembly in flight. The grid reference marks were two holes, $275 \times 275\ \mu m^2$ in size, located on the grid surface. Each of them could be illuminated by one of two light-emitting diodes (for redundancy reasons) via an opal glass diffusor mounted on the first baffle plate.

The light-emitting diodes were mounted inside invar tubes, a mechanically rigid mounting that also prevented straylight from the light-emitting diode reaching the grid. The photon flux from these diodes, measured at the sub-assembly level, was more than 5×10^7 photon s^{-1}.

The grid pattern consisted of the main grid and star mapper grid patterns. The main characteristics of the parallel slits of the main grid are given in Table 2.5. Although the required grid pattern was uniform over the main field of view, it was written in discrete 'scan fields', 46×168 of these scan fields covering the full field of view (the dimensions

Table 2.5. Summary of the calibration results of the main grid.

Item	Performance
Slit geometry:	
average grid period	$8.20 \pm 0.001\ \mu$m
average slit width	$3.13 \pm 0.03\ \mu$m
slit width standard deviation	$< 0.033\ \mu$m (rms)
total number of slits	2688
number of scan fields	46×168
scan field dimensions	$131.2 \times 480\ \mu\text{m}^2$
Medium-scale grid irregularities:	
M_{pq}	$-0.038 < M_{pq} < 0.053\ \mu$m
gradient (scan field to scan field)	$0.009\ \mu$m (rms)
Small-scale grid irregularities:	
individual slit (random)	$0.015\ \mu$m (rms)
regular 'saw tooth step'	$0.000\ \mu$m (mean value)
irregular 'saw tooth step'	$0.016\ \mu$m (rms)
correlated scan field orientation	$0.009\ \mu$m (rms)
uncorrelated scan field orientation	$-0.009\ \mu$m (mean value)
Grid reference marks:	
shape	square
edge dimension	22.04–22.08 mm
centering accuracy	±0.001 mm
orientation	±0.25 arcmin

Table 2.6. Summary of the principal specifications for the star mapper grid.

Item	Specification
Medium-scale grid irregularities:	
vertical	$< 0.5\ \mu$m (max)
inclined	$< 0.5\ \mu$m (max)
transverse gradient (vertical)	$< 0.077\ \mu$m (rms)
transverse gradient (inclined)	$< 0.077\ \mu$m (rms)
Small-scale grid irregularities:	
vertical	$< 0.05\ \mu$m (rms)
inclined	$< 0.05\ \mu$m (rms)
magnification factor	< 0.15 (max)
scan field orientation (vertical)	$< 0.034\ \mu$m
scan field orientation (inclined)	$< 0.034\ \mu$m
slit width value	$6.20\ \mu$m
slit width variation	$< 0.35\ \mu$m (max)
Grid calibration:	
vertical	$< 0.055\ \mu$m (rms)
inclined	$< 0.077\ \mu$m (rms)

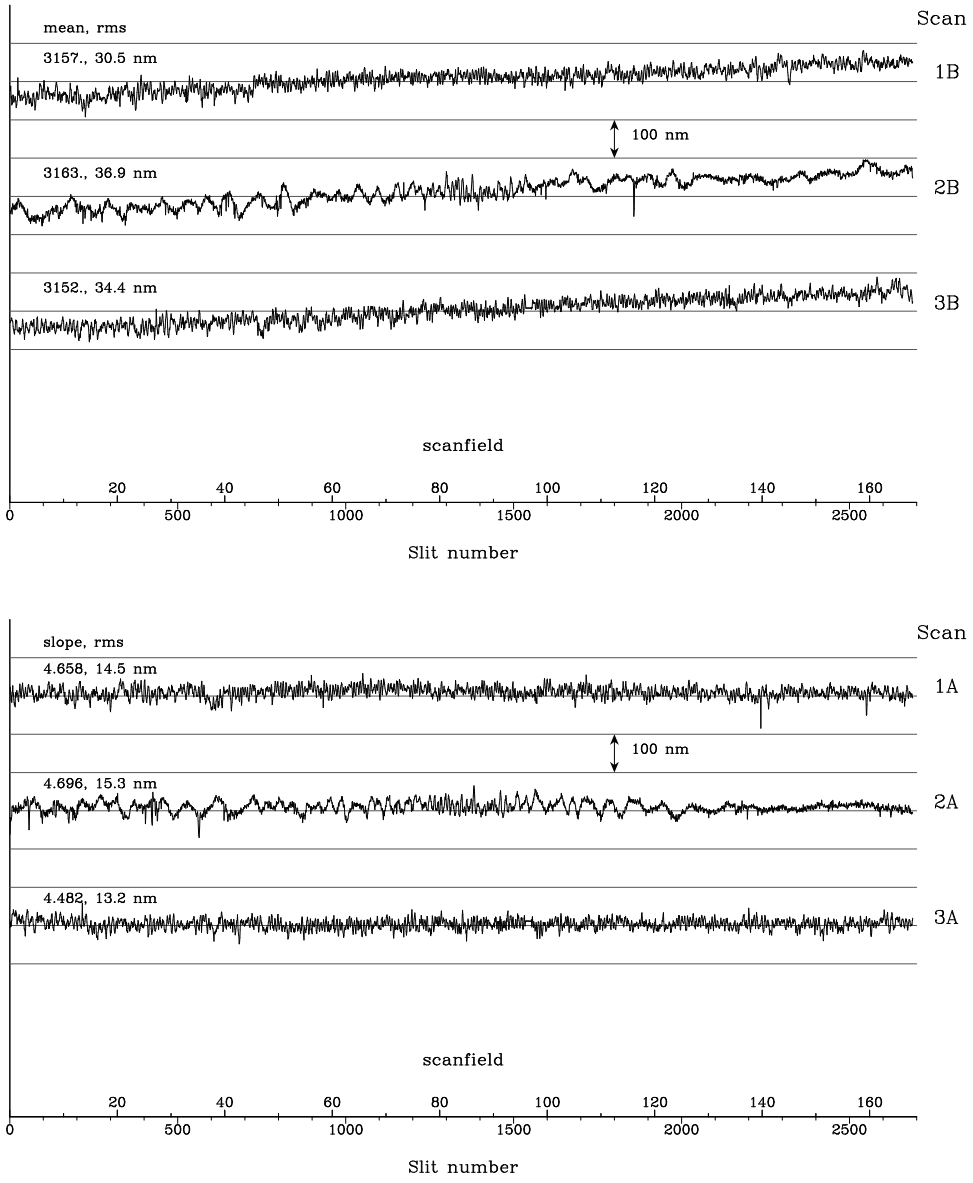

Figure 2.11. *Slit width variation across the main field. Top: as measured; bottom: after removal of the linear component. Nine calibration scans were made (on ground), three each (A, B, C) at i_H = 1 (1), i_H = 23 (2) and i_H = 46 (3) (see also Figure 2.10). The abscissa is given in both scan field and slit numbers, and the scale of the ordinate is shown in the figures. In the top figure the mean slit-width and associated rms values (in nm) are also given. In the bottom figure the (corrected) slope (in nm(width)/mm), and the rms values of the slit-width after removal of the slope, are given. The figure illustrates the high quality of the modulating grid, and the remaining medium-scale structure in the grid (due to the scan field construction) which was accounted for in the medium-scale calibration on ground and in orbit.*

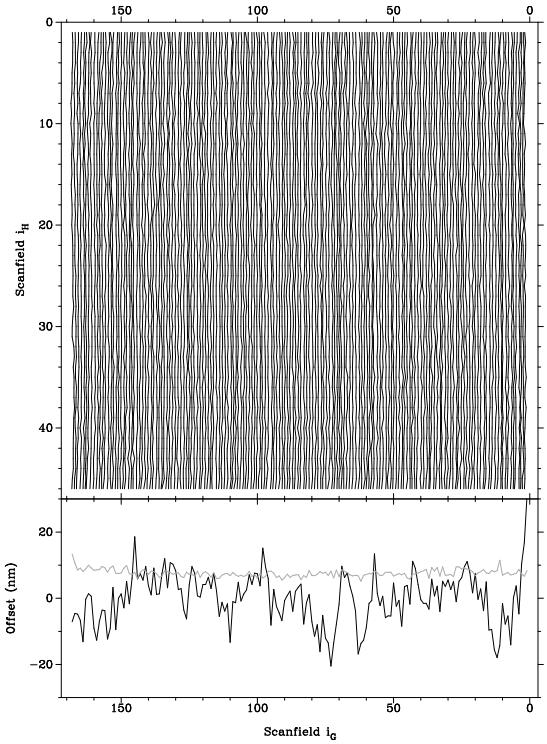

Figure 2.12. *The medium-scale irregularity of the main grid, in the scan direction. The geometry of the grid corresponds to the configuration shown in Figure 2.10. The scale in the upper figure is such that one scan-field 'unit' corresponds to 40 nm. The lower figure shows the mean value in the scan direction (solid line), and the standard deviation (dotted line).*

of each scan field were $131.2 \times 480\ \mu\text{m}^2$, with the longer dimension in the direction of the slits, i.e. normal to the scan direction). Two star mapper patterns lay on either side of the main grid—their principal characteristics are summarised in Figure 2.10.

Considerable attention was given to the manufacture and calibration of the grids, given that the final mission accuracies of around 1 milliarcsec corresponded to approximately 0.007 μm at the focal plane. Deviations of the main grid from a perfectly regular one were classified into large, medium, and small-scale grid irregularities. The large-scale grid irregularities were defined as deviations that could be expressed as a second-order polynomial fitted to the distortion map—these could be calibrated by the data reduction consortia during the 'great-circle' step of the data reductions. The medium-scale grid irregularities were defined as a matrix of M_{pq} elements, where each element represented the average distortion of the scan field (p,q) after removal of the large-scale component. The range of M_{pq}, and its field-to-field gradient, are tabulated in Table 2.5.

Small-scale grid irregularities were defined as the residual distortion, after the removal of the large- and medium-scale components. Their characterisation would have required a very large ground calibration effort, followed by the correction of the satellite data at a very high spatial resolution. The grid manufacture concentrated on producing a grid in which the small-scale irregularities could be neglected, a fact eventually confirmed in orbit. In the manufacturing and calibration process, the small-scale irregularities were split into various components (see Table 2.5). The 'individual slit' contribution

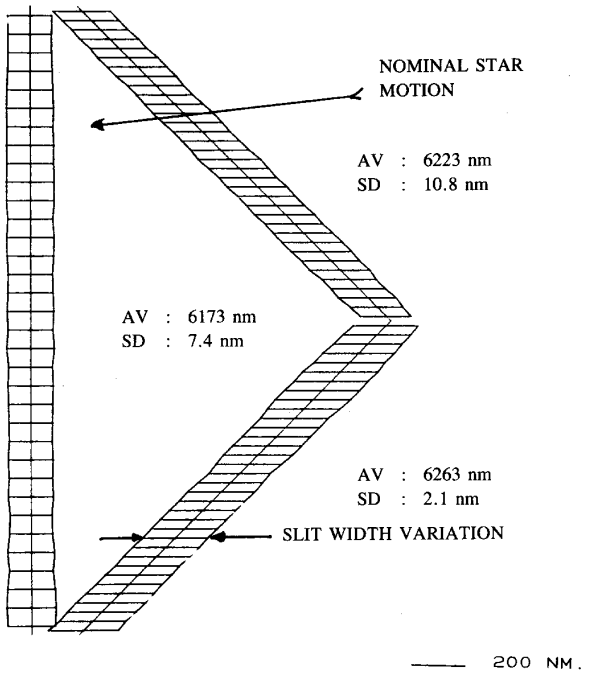

Figure 2.13. *Representation of the slit width variation for one vertical and one chevron slit of the preceding star mapper.*

arose from the imperfections in the slit edges. The regular and irregular 'saw tooth step' contribution was a result of the scan field 'scale' not being precisely matched to the scan field centre-to-centre spacing. The correlated and uncorrelated scan field orientations, measured in microns at the corners of the scan fields, arose from misalignments in the individual scan field orientations.

The grid pattern was written by means of an electron-beam pattern generator machine. A computer program for the writing of patterns with sub-micron accuracy on a curved surface was developed specifically for this purpose. According to the grid manufacturing plan, a first pilot series was produced in order to optimise the manufacturing process, followed by a second pilot series to finalise the process. This second pilot series was intended to lead to a grid of flight standard. A third pilot series was eventually produced, due to problems encountered during second-batch operations. Following the pilot series, a series of five flight-standard grids was made, from which the flight and the flight-spare grids were selected.

After writing, the grid was subjected to an extensive calibration process, in order to verify the quality of the writing. The measurements were made by optical and electron-beam methods. The main grid calibration results related to the slit width value, which was measured in three ways: using optical diffraction equipment, electron-beam pattern generator, and microscope. An optical inspection was also carried out to verify the pattern quality and to assess the distribution of any pattern defects, the pattern position and orientation, and the optical transmittance.

The electron-beam measurements used a dedicated software package. The principal element in this software package was the marker search by the electron-beam pattern

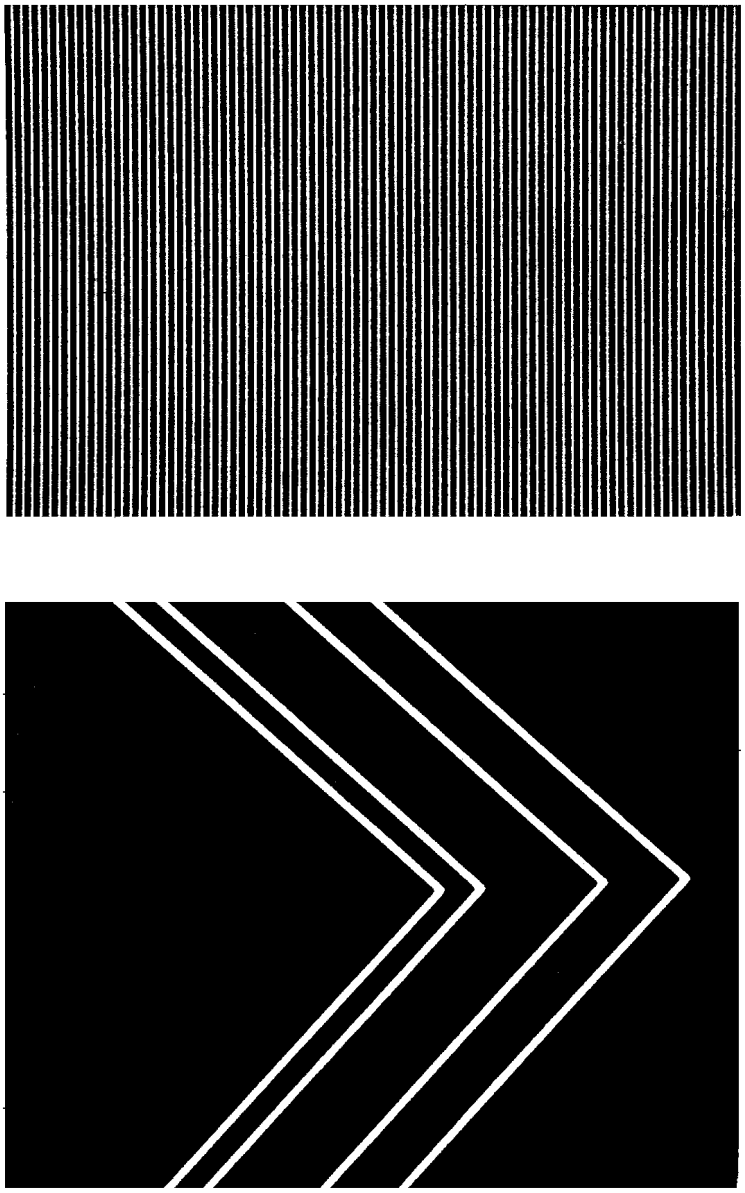

Figure 2.14. *Optical micrographs of part of the main modulating grid (top figure) and the star mapper grid (lower figure). The grids represented one of the main technical challenges of the Hipparcos payload, and were of an extremely high quality.*

generator. Another important element was the 'almost undeflected electron-beam operation', in order to minimise the contribution of main beam deflection errors. As a consequence, an *xy* table movement was required for each slit or marker measurement. The location of the position-calibration markers was obtained with an accuracy of 10 nm rms from its four marker edge positions. Each edge position was the average of 20 measurements on a centred 10 μm part of the marker edge. The marker search algorithm was based on a signal bandwidth reduction and a binary search scheme.

The slit position was obtained with an accuracy of 10 nm rms by the same marker search algorithm applied to both slit edges. The parameters were adapted to fit the nominal

slit sizes. In the main grid pattern, each slit edge position was derived from an average of 21 measurements over an edge distance of 6 μm, corresponding to the size of an imaged star in the direction of the slits. The position of each slit was obtained as the mid position of the slit edge positions, and the width of each slit was the difference of the corresponding slit edge positions.

The expected slit position was obtained for the known pattern positions in the grid coordinate system. The beamwriter coordinate system was transformed to the grid coordinate system by the compensation sequence of the beamwriter. The reference zero-point was the location of the position-calibration marker. The main grid and star mapper patterns for the electron-beam measurements have the same scan field xy arrangement as the one used during the pattern writing. Within a scan field, the slit position was defined by the x-position and the slit number.

The value of the measured slit position minus the expected slit position was obtained for the selected slit within the scan field. The positions measured within the main grid pattern relate to the matrix of 46×168 scan fields. For all scan fields, one slit at the scan field centre was measured. By repeated measurements with 8 slits per scan field, it was demonstrated that the same value of the scan field parameters had been achieved. It was demonstrated that just one measurement near the scan field centre was adequate to measure the scan field centre position. The idea behind this electron-beam measurement process was the 'step-on and repeat' process of the same scan field during writing, without a change in the scan field parameter settings. This procedure also helped to keep the electron-beam measurement time within reasonable limits, without a loss in accuracy of the position results obtained.

The grid calibration results are summarised in Table 2.5 for the main grid pattern, and the specifications related to the star mapper grid are summarised in Table 2.6. The electron-beam measurement data were recorded on magnetic tape for subsequent calibration studies, and distributed to the data reduction consortia, who used the geometrical calibration parameters during the ground processing of the satellite data. Examples of the grid calibration data for the main field are given in Figure 2.11 (the measured slit width variation across the grid), Figure 2.12 (the measured variation in the medium-scale irregularity across the grid), and Figure 2.13 (the measured slit width variations for the star mapper). Optical micrographs of part of the actual flight grid are shown in Figure 2.14.

The Star Mapper Deflectors

The light from the star mapper slits was deflected sideways, on to photomultipliers at either side of the refocus assembly, by star mapper deflectors mounted directly behind the optical block. Each star mapper deflector had a convex side, facing the optical block, which acted as a field lens. The other side, which was flat, deflected the light by 90°.

The star mapper deflectors were made from BAK 1 glass, which has a large refractive index, ensuring total internal reflection. The thermal expansion of 7.6×10^{-6} K^{-1} was accommodated by the deflector mount and the use of an appropriate flexible adhesive (Araldit AV138M). The bonding was carried out in a bonding jig to ensure proper alignment. The star mapper deflectors were appropriately masked to prevent straylight. In order to limit the Cerenkov effect, a further mask was directly replicated on the star mapper deflectors.

The Grid and Deflector Mounts

The grid mount was the housing for the optical block and formed the interface between the optical block, the baffle unit, links for parallel movement, and the star mapper deflector holders. The grid mount was a holder made of invar, suitable for carrying the optical block, without distortion and with the least possible introduction of displacements or stresses as a result of the thermal behaviour. This was achieved by using 24 bonding areas at the circumference of the lens. Mounting and dismounting of the grid unit and the baffle unit was possible while the refocus assembly remained attached to the focal-plane assembly platform.

In order to eliminate electrostatic charge build-up on the grid surface, four grounding wires were bonded to the grid (using Ecobond 55C), the other ends being bonded to the grid mount. The star mapper deflectors were mounted in their holders with Araldit AV138M glue with hardener HV 998. They were positioned with the help of an assembly-rig, and then bonded to the holder.

2.6. Relay Lens Systems

Various relay lenses and optical components were used to transfer the light modulated by the grid onto the detectors: the image dissector tube relay lenses, the photomultiplier relay lenses, the internal star pattern assembly (which was used for calibration purposes), and the associated filters and dichroics. A schematic layout of these various optical components is shown in Figure 2.15, which also shows the configuration of the B_T and V_T star mapper channels.

Image Dissector Tube Relay Lens

Optical design: The layout of the image dissector tube relay lens is shown in Figure 2.16. The energy contained in a circle of given diameter was computed from the geometrical size of the image blur. The spectral weighting factors used to represent a star of colour index $B-V = 0.5$ mag are given in Table 2.7. The results obtained are given in Table 2.8. The transmission budget for the image dissector tube relay lens is given as part of the overall payload transmission summarised in Table 2.2.

Multiple reflections within the relay lens system, and between the relay lens system and the other optical components, could induce 'ghost images', more or less focused, within the field. These were studied, and the relay lens design optimised to reduce the most severe ghost images (such as that arising between the lens system and the photocathode) to acceptable levels, by adding appropriate anti-reflection coatings to the lenses. The design also took into account an 'oversizing' to account for collection of the maximum amount of light, including that diffracted by the grid.

Each of the two image dissector tube relay lenses imaged the focal surface of the telescope onto the photocathode of the image dissector tube. The main housing of each lens assembly was machined from aluminium and supported the single lens mounts. A locking ring kept each set of lenses in a well-defined position. The outer faces were milled to a polygonal form. All attachment threads for fixation assemblies were reinforced with

Helicoil MN3. Shielding required for the protection of the glass against high-energy electrons creating Cerenkov radiation was also fixed to the housing with screws.

Between the two blocks of lenses, a deep cutout provided space for an aperture stop and filters. Each individual lens of the optical relays was mounted separately in a mounting ring to which the lens was bonded with Zeiss ADM5A glue. All mounting, securing, and locking rings had venting holes to allow depressurisation after launch. Each mounting ring had one radial fitting face and two plane parallel axial fitting faces. These machined faces were used for centering and tilt adjustment after bonding of the lens.

The image dissector tube relay lenses were fixed onto the focal-plane assembly platform by means of three similar feet, each with a titanium spring blade providing flexibility. Adjustment was permitted by built-in eccentric washers at the bases of these three blades, which could be positively locked after adjustment.

The image dissector tube switching prism was used in two different modes: in the nominal mode, the grid was imaged onto the photocathode of the main detector after reflection on its reflective front face, while in the internal star pattern assembly mode, the rear side of the reflective surface was used to image the internal star pattern onto the image dissector tube. Depending on the position of the prism, one detector viewed the grid, while the other viewed the internal star pattern, or vice versa.

The switching prism material was Suprasil 1 silica. The mirror support 'barrel' was made of invar. The sides of the prism were coated with an anti-reflective coating with a reflection loss of less than 0.5 per cent. On the outer side of the prism, an aluminium layer was deposited on the Suprasil, resulting in a reflection efficiency of better than 90 per cent, at wavelengths longer than 400 nm. This was followed by the deposition of the outer reflective layer, comprising a silver coating and a dielectric layer, which provided the reflection surface for the nominal path. The internal star pattern beam passed through the prism and was reflected by the aluminium layer.

The switching prism was bonded onto its invar mount with Zeiss Kleber No. 51 glue cured at room temperature. The cure time was 24 hours, and a film thickness of 0.1 mm was used. The bonded and mounted prism was balanced by a counterweight, adjusted by means of three screws permitting fine tuning of the prism's centre of gravity.

Photomultiplier Relay Lens

Each of the two photomultiplier relay lenses imaged the entrance pupil of the telescope onto the photocathode of two photomultipliers. The lenses, mirrors, filters, and the baffle were mounted in a U-shaped barrel with two exit lenses. Space for dichroic filters was provided in the barrel. The transmission budget of the photomultiplier relay lenses, for the B_T and V_T channels, is shown as part of the overall payload transmission in Table 2.3 and Table 2.4, respectively.

The main housing consisted of a U-shaped support machined in stainless steel. The necessary shielding to provide the protection against Cerenkov radiation was clamped to it. All optical parts were mounted separately on this main housing. After removal of the top cover, all optical elements were easily accessible for adjustment. All attachment points for fixation assemblies, optical parts, and the shielding were reinforced by increased wall thicknesses. The main housing also provided the necessary interface points for the fixation of the dichroic elements. All optical parts could be separately adjusted.

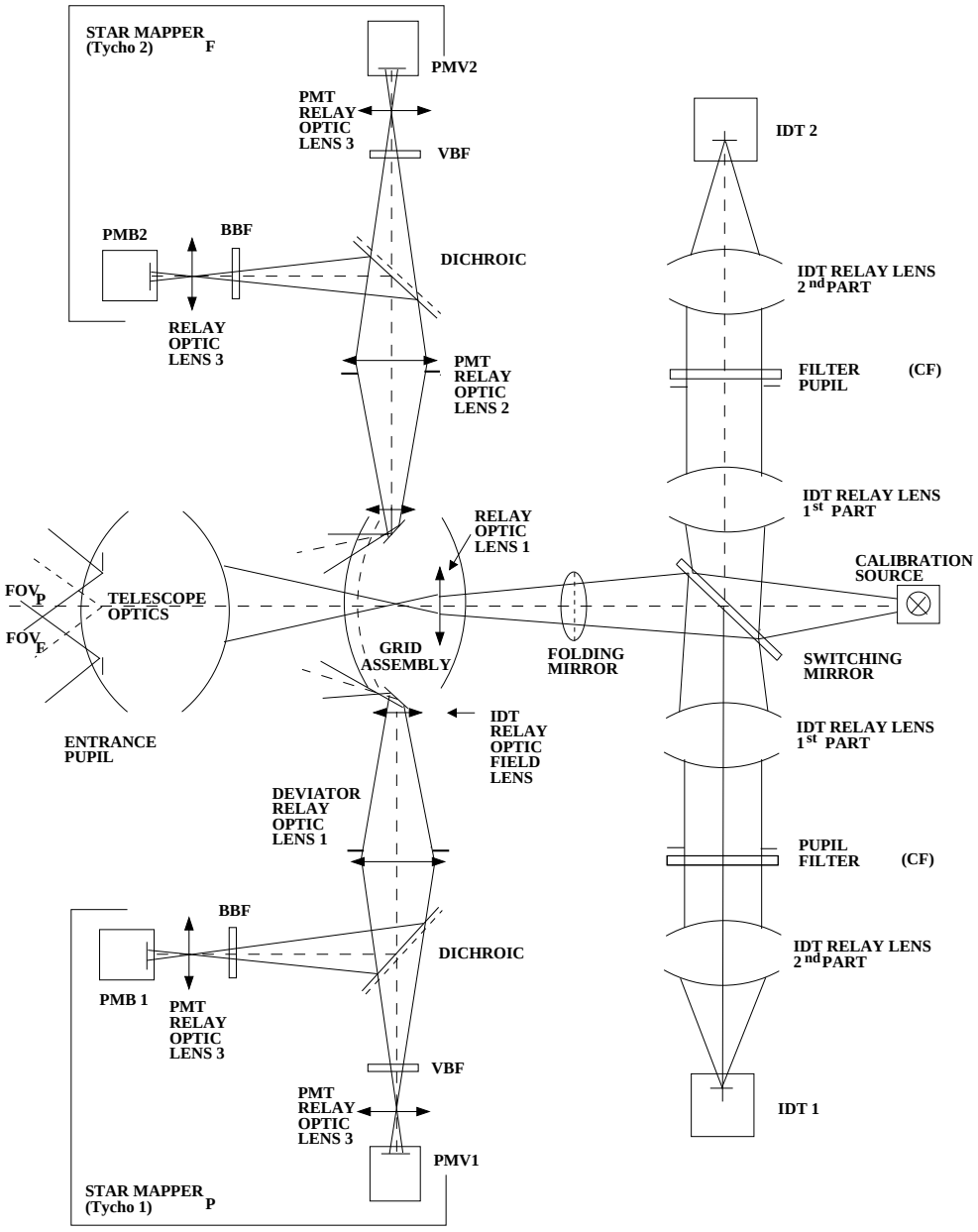

Figure 2.15. *Schematic of the optical units in the focal-plane assembly.*

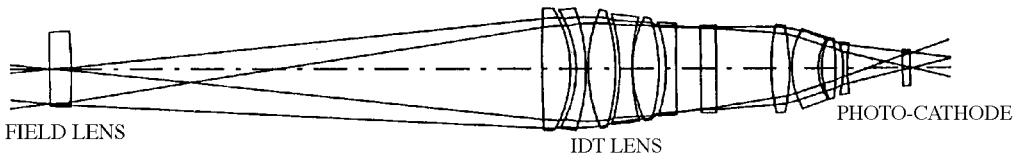

Figure 2.16. *Layout of the image dissector tube relay lens.*

The interface with the focal-plane assembly platform consisted of two spring blades for flexibility, and a third fixed point. Adjustment was achieved by eccentric washers at the base of the blades and fixed point, which were positively locked.

One lens had its own adjustment capability (shift of 2 mm in the X and Z directions and tilt of 5° about the X and Z axes). The bracket rested with its spherical face (the centre of sphere was the centre of the lens) in a spherical cap. Tilting and fixation of the lens was effected with four screws on the rear face of the mount. Lateral and vertical adjustment was made relative to a frame fixed to the barrel. Adjustment was positively fixed with tuned plates.

Internal Star Pattern Assembly

An internal 'fiducial' star pattern assembly was incorporated into the payload to allow in-flight calibration of the transformation from grid coordinates to deflection coil currents of the main detector assembly.

The internal star pattern was projected onto the photocathode of the main detector assembly to be calibrated. This assembly then scanned the fiducial star pattern, while the output data and the corresponding deflection currents were transmitted to ground. From these data, the relation between the deflection currents and the optical coordinates, as defined by the internal star pattern assembly, was derived. What were really needed however, were not the internal star pattern assembly coordinates, but the grid coordinates. For that reason, the optical path between the star pattern in the internal star pattern assembly and the main detector assembly was an exact duplicate of that between the grid and main detector assembly.

The switching between calibration and observation of the grid was done by the same switching mirror that deflected the grid output to either of the two redundant main detector assemblies. The thickness of the mirror was essentially zero, but the presence of the glass prism, supporting the mirror surface in the optical path between internal star pattern assembly and main detector assembly, made it necessary to apply a correction to the path length.

The internal star pattern assembly consisted of two major parts: a star source, containing the star pattern, a light diffusor, and two sets of light-emitting diodes; and a frame, supporting the star source and two folding mirrors. This frame also carried the electrical connectors. It had three adjustable feet, constituting the interface with the focal-plane assembly platform and providing an alignment facility.

During calibration, the star pattern was substituted for the main grid in such a way that the optical path from the star pattern to the main detector assembly optics was nominally equal to that from the grid. The only difference was that a correction was applied due to the fact that the glass prism, supporting the switching mirror, was in the internal star pattern assembly optical path and not in the grid one. The very limited space available made it necessary to fold the optical path twice, a function performed by two flat mirrors in the internal star pattern assembly. Also, the substrate carrying the star pattern had the same dimensions as that carrying the grid and was made from the same material.

The star pattern consisted of 275 μm square holes on a regular square grid with a 2.2727 mm pitch, resulting in a projected pattern of light spots with 1 mm pitch on

Table 2.7. Weighting factors for the different wavelengths used, defining the input flux corresponding to a star of colour index $B - V = 0.5$.

Wavelength (nm)	375	450	550	650	750
Weights	0.23	0.97	0.88	0.55	0.18

Table 2.8. Image dissector tube relay lenses encircled energy in the image plane (the image point is defined as the centre of 'gravity' of all points in the spot). In all cases, the energy within 80 μm diameter is close to 100 per cent.

Object Point		Image Point		Energy within
X	Y	X'	Y'	40 μm diameter
(mm)	(mm)	(mm)	(mm)	(per cent)
0.0	0.0	0.000	−0.001	99
6.0	6.0	−2.616	−2.615	99
6.0	0.0	−2.613	0.000	98
6.0	−6.0	−2.612	2.614	98
0.0	0.0	0.000	−2.615	100
0.0	−6.0	0.000	2.611	97
8.0	8.0	−3.492	−3.488	99
8.0	0.0	−3.485	0.001	98
8.0	−8.0	−3.485	3.488	98
0.0	0.0	0.000	−3.488	100
0.0	−8.0	0.000	3.483	97
11.0	11.0	−4.810	−4.803	96
11.0	0.0	−4.796	0.003	98
11.0	−11.0	−4.797	4.804	97
0.0	11.0	0.000	−4.800	100
0.0	−11.0	0.000	4.792	97
12.0	12.0	−5.242	−5.242	94
12.0	0.0	−5.232	0.004	98
12.0	−12.0	−5.235	5.244	96
0.0	12.0	0.000	−5.238	100
0.0	−12.0	0.000	5.229	97

the main detector assembly cathode. The pattern was defined by an electron beam pattern generator and etched in a chronium layer, vacuum deposited onto a bi-convex lens made of Suprasil 1 (fused silica). The material and the dimensions of this lens were the same as those of the grid substrate. The manufacturing of the star patterns was done in parallel with the manufacture of the main and star mapper grids.

The star pattern was mounted inside an invar tube and illuminated by four light-emitting diodes via a diffusor consisting of two opal-glass plates. The set of four light-emitting diodes was completely redundant, and the light-emitting diodes of one group were connected in such a way that, if one or more light-emitting diodes failed, the other ones would continue to emit light.

The frame was built up from three separate parts: the lower, middle, and top frames. The lower frame, connected to the focal-plane assembly platform by three flexible and adjustable feet, supported the middle frame and the connector bracket. The lower folding mirror was bonded to the bottom of the lower frame. The middle frame supported the star source and the top frame. The top frame was a bracket carrying the top folding mirror.

The main body and the mounting feet of the internal star pattern assembly were made from titanium. This metal was selected since its thermal expansion coefficient was sufficiently low to meet the stability requirement, while entailing a smaller mass penalty than that resulting from the use of invar. Pure titanium was used for the main body as this was more easily machinable. For the mounting feet, however, a titanium alloy TiAl6V4 was selected, as the greater strength allowed thinner blades, resulting in lower stresses in the focal-plane assembly platform. BK7 glass was used for the mirrors, as this had the same thermal expansion coefficient as titanium. The only part made out of invar was the star source housing, where a match with the much lower expansion of silica glass was required.

The optical block was made of Suprasil 1. It had a chromium layer coating with the star pattern at the front side of the optical block (R = 1400 mm), and an iraline coating at the rear side. The reflective coating consisted of three layers: chromium for adhesion, aluminium for reflection, and silica for protection.

The installation specification required provisions for shifting the internal star pattern assembly by 5 mm in three mutually perpendicular directions. Alignment devices between the flexible feet and the lower frame were used. As clamping by friction only was judged to be insufficient, shims were used throughout, even though this complicated the alignment. A further alignment possibility was provided by the rotation of the star source in the internal star pattern assembly frame. This was possible when the internal star pattern assembly was mounted on the focal-plane assembly platform.

Filters and Dichroics

In the chain of the image dissector tube relay optics, there was a switchable filter set, consisting of a chromaticity filter and a wide-band filter. There was a dichroic filter in the photomultiplier relay optics chain.

In order to calibrate the chromaticity of the payload in orbit (i.e. the geometrical shift in the grid coordinate position of stars of different colours—expected to be of the order of

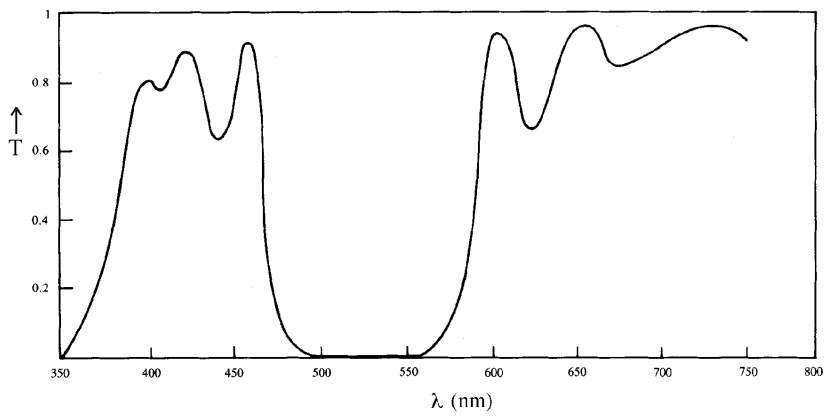

Figure 2.17. *Schematic transmission curve of the chromaticity calibration filter. The transmission characteristics of the filter resulted in two distinct images of each star, at two well-separated wavelengths, sufficient for the chromatically-induced displacements of the star images to be calibrated in orbit.*

1–2 milliarcsec, depending on star colour), a chromaticity filter was placed in the optical path.

The filter consisted of two wedges made of two different types of glass (PSK 53 and TiF 6), having the same refractive index at one wavelength, but different dispersions. The combination resulted in a plane-parallel, dispersing but non-deviating window. The two prisms, of 7°.5 angle, were 4 mm thick at mid-height, and were bonded together with SYLCO 14 cement, after a mirror coating of 90 nm spectral width around 520 nm was applied to the internal face of the PSK 53 glass. An anti-reflection coating in the range 350–800 nm was deposited on the external faces of the two prisms. The resulting transmission curve of the chromaticity calibration filter is shown in Figure 2.17.

The result is a double image of each star—a red and a blue image—on the image dissector tube, sufficiently displaced in the direction parallel to the slits to allow separate observation of the two images by the image dissector tube. This allowed the relative positions (via the modulation phases) of the two images of the star to be measured, and hence the chromaticity of the optical system.

In normal operations the chromaticity filter was not in the relay optics path. In order to compensate for the optical path length of the chromaticity filter, a wide-band filter was placed in the beam instead. The filter was made of 7.5 mm thick Suprasil 1 glass (to minimise 'darkening' caused by high-energy particle radiation in orbit), with an anti-reflection coating in the 350–800 nm range. Both the calibration filter and the wide-band filter had a face flatness of $\lambda/4$ peak-to-valley, and a face parallelism of better than 1 arcmin. The transmission curve of the wide-band filter is shown in Figure 2.18.

The dichroic filter, permanently present in the star mapper detection chain, had the effect of splitting the energy of the star mapper optical beam into two wavelength ranges, each range being directed to separate photomultiplier relay optics. Most of the light either went into the 'blue' photomultiplier channel (< 465 nm) by reflection, or to the 'visible' channel (> 475 nm) by transmission.

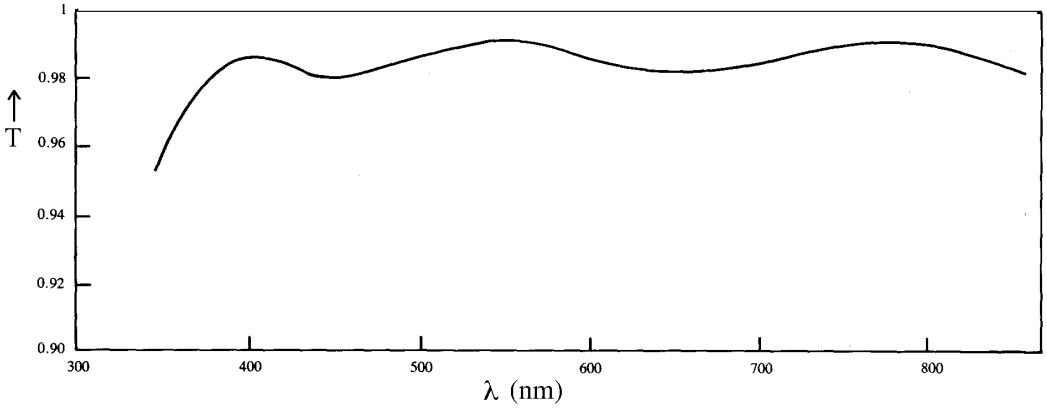

Figure 2.18. *Schematic transmission curve of the wide-band filter.*

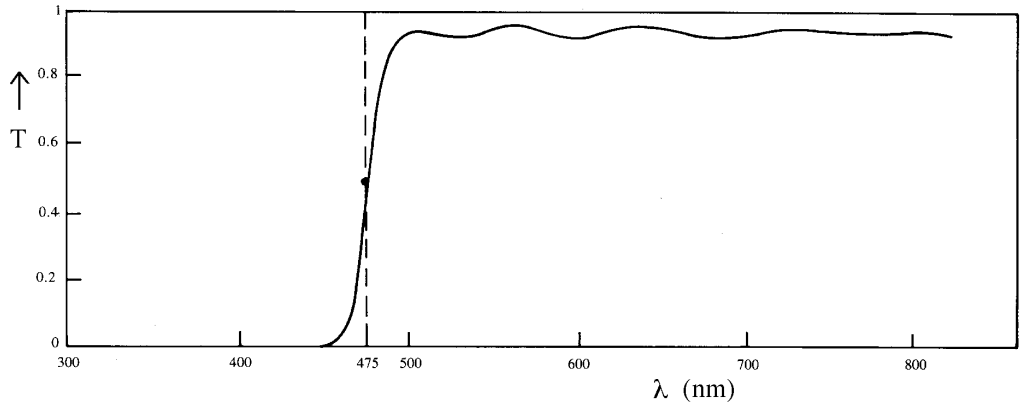

(a)

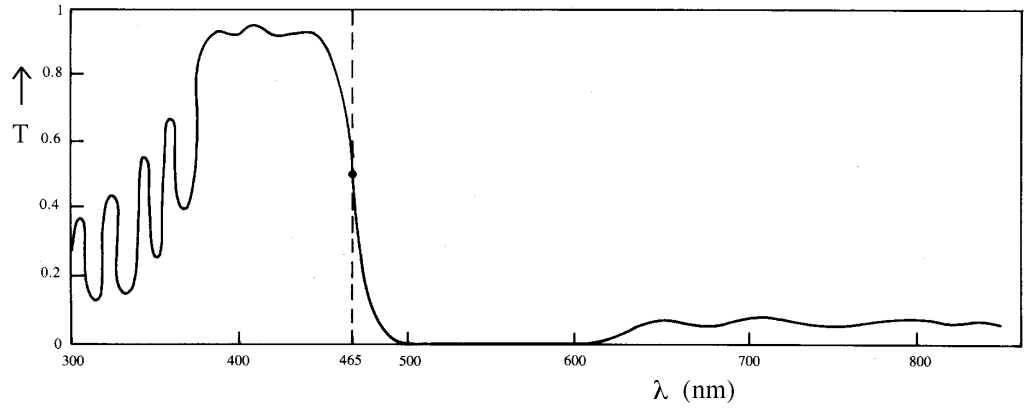

(b)

Figure 2.19. *Schematic transmission curves of the V_T (a), and B_T (b) star mapper channels.*

The dichroic filter was a coating deposited on 4-mm thick GG 475 glass. It worked at an incidence angle of 25°, where polarisation effects are limited. The 50 per cent point of this coating was at 465 nm in reflection and at approximately 475 nm in transmission. The second face of the dichroic filter was anti-reflection coated in the range 500–800 nm.

To increase the wavelength separation between the two parts of the spectrum, a blue filter was also included in the reflected path. This was a coating deposited on a 4-mm thick GG 375 Schott coloured glass window, giving zero transmission between 500–600 nm. An anti-reflection coating was applied to the second face in the range 350–500 nm. The dichroic coating and low-pass coating of the dichroic filter and blue filter were made of ZrO_2 and SiO_2, respectively, to get very hard layers, fully transparent as far as 300 nm. The flatness of the dichroic and blue filter face was $\lambda/2$ peak-to-valley. The resulting overall spectral transmission curves for the two channels are shown in Figures 2.19(a) and (b), (see also Table 2.3 and Table 2.4, which give the overall payload transmission, including the contribution of the dichroic filter).

3. THE PAYLOAD: DETECTORS, ELECTRONICS, AND STRUCTURE

Two different types of detectors were used for Hipparcos—the image dissector tube detector which sampled the modulated images of the stars as they crossed the main field of view, and the star mapper (photomultiplier) detectors, which sampled the entire field of the star mapper. The resulting signals provided the main sources of data analysed in the ground processing. There were two photomultiplier detectors for each star mapper channel, sampling the visual and blue wavelength ranges respectively. Mechanisms were used within the payload to protect the detectors as the fields of view swept across the illuminated Earth or Moon, to switch between the prime and redundant image dissector tube detectors (and introduce the corresponding internal star pattern assembly, used for geometrical calibration, into the field of view), to introduce the chromaticity calibration filter into the image dissector tube relay lens, and to adjust the focus position of the modulating grid. Each of the telescope's fields of view was protected by 'external' and 'internal' baffles, attenuating straylight from the Sun, Earth and Moon, and minimising the 'dead time' due to Earth and Moon occultations. Extremely high thermal and temporal stability of the relative positions of the optical components was also required.

3.1. Detectors

The function of both the main detection chain and the star mapper detection chain was the detection of the images of stars, which were modulated by the grid and focused by the relay optics, as described in Chapter 2. The photons detected were converted into electrical signals, and the processed signals were output according to a given protocol between the detection subsystem and the remote terminal unit.

The detection subsystem was located on the focal-plane assembly platform. It consisted of prime and redundant halves, each containing main and star mapper chains. As the power and switching of each section was independent, cross-strapping was provided, allowing either or both detection chains to be in operation in both halves of the subsystem. The star mapper detection chain was also responsible for the acquisition of data used for the Tycho experiment.

Main Detection Chain

The main detector assembly was an electro-optical and mechanical unit, whose function was to detect a light flux in a specific area and to convert this flux into an electrical signal. It contained the image dissector tube, the focus and deflection coils (including two-fold magnetic shielding), the high-voltage power supply (providing the required high voltages to the image dissector tube), the voltage divider network (providing the required intermediate high voltages to the individual dynodes of the image dissector tube), an isolation amplifier (providing the image dissector tube analogue output), and the pulse-amplifier and discriminator circuit (providing the image dissector tube pulse-counting output).

Under nominal operating conditions, only one of the two main detector assemblies was in operation, the other being available for redundancy reasons. The main detector assembly detected the light transmitted through the main grid from stellar images crossing the grid. The image dissector tube detected photons arriving at the photocathode in a small well-defined area, called the 'instantaneous field of view'. By appropriate control of currents through the deflection coils, this instantaneous field of view, of about 38 arcsec diameter, could be positioned to 'view' any location of the useful area of the photocathode. In this way, the detector was able to follow several stars on the main grid quasi-simultaneously, switching rapidly from one star image to another and detecting the photons from each star for a short period of time, defined by the star observing strategy.

The main detector assembly was designed to be used in both photon counting mode for faint stars and in analogue mode for bright stars. In photon counting mode, each photo-electron pulse is amplified, discriminated with an optimum threshold in order to improve the signal-to-noise ratio, and the output transmitted to a counter in the detection electronics box. In analogue mode, the photocathode current is amplified in the tube and the output current is directly converted into a digital word by means of a voltage-to-frequency converter in the main detector assembly. The output is transmitted to a counter in the detection electronics box.

The pulse counting channel counted the pulses at the anode of the image dissector tube caused by the photons which entered the instantaneous field of view. It consisted of two main parts: the part that brought the anode pulses into a shape suitable for a digital counting device; and a digital counter (the data compression circuit), which counted the resulting pulses. A block diagram of the pulse counting channel is shown in Figure 3.1.

The analogue channel (selected by telecommand) was designed to be used for the observations of the very brightest stars (brighter than about 1–2 mag), where the light input in the instantaneous field of view of the image dissector tube would be so high that a large number of pulses could no longer be recognised individually by the pulse counting channel. In order to avoid coupling problems with the pre-amplifier of the pulse counting channel, the current was measured on the last dynode of the tube.

A digital interface with the remote terminal unit provided data to the remote terminal unit and received memory load commands from it. The 16-bit memory load commands from this unit were converted into focus and deflection currents, or into high-voltage settings. Service signals (to clocks, power supplies, and test pulse generator) were also generated by the detection chain.

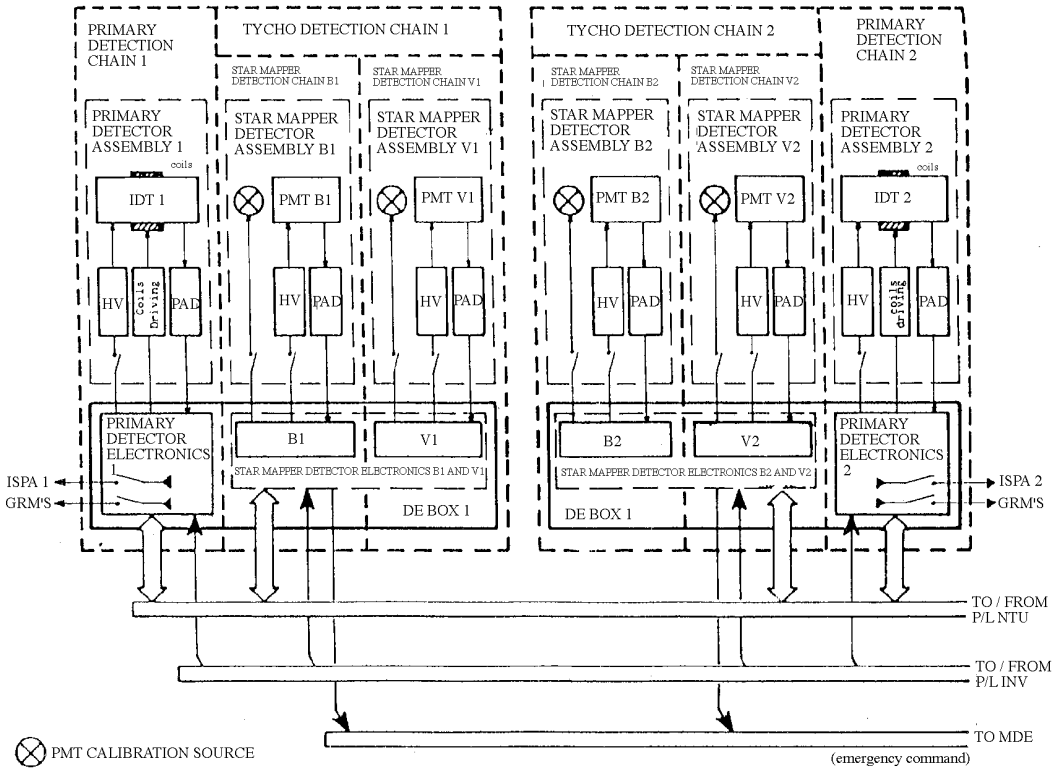

Figure 3.1. *Detection subsystem block diagram. The figure shows the schematic arrangement of the image dissector tube (IDT) and photomultiplier tube (PMT) detection chains, the latter used for the star mapper (Tycho) measurements. Each star mapper detection chain included a B_T and V_T channel, and each of the primary and star mapper detection chains was duplicated for redundancy reasons. (DE: detector electronics; HV: high voltage; ISPA: internal star pattern assembly; GRM: grid reference mark; P/L: payload; MDE: mechanism drive electronics.)*

The main detector assembly received its power from the detection electronics box and included its own high-voltage power supply, delivering the image section voltage, fixed at 400 V, and the multiplier section voltage, which could be adjusted by ±20 per cent around its nominal voltage of 1200 V by telecommand through the detection electronics box. The exact value of the high voltage was selected so as to have a nominal gain for the multiplier of 5×10^5.

For correct image dissector tube operation, the focus current had to be adjusted to obtain a good instantaneous field of view profile. The deflection currents of the image dissector tube were updated, during normal operations, at a frequency of 150 Hz (corresponding to 'slots' of the star observing strategy, as described in Chapter 8). These deflection currents defined the exact positioning of the instantaneous field of view at any instant.

Image dissector tube: The image dissector tube is a photomultiplier tube with a simple electromagnetic deflection system to sample one small part of its photocathode at a time. It had no memory to store an image, and so a strict sampling protocol was not required. The principle of operation is illustrated in Figure 3.2.

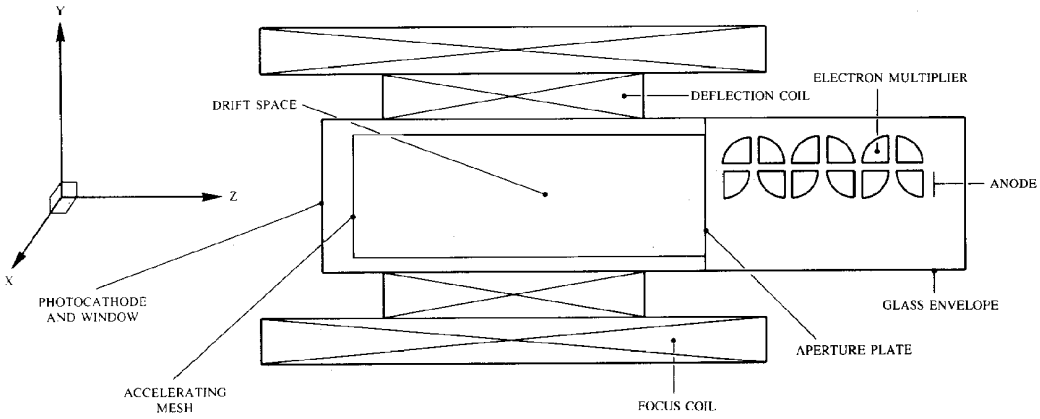

Figure 3.2. *Operating principle of the image dissector tube. Light reaches the photocathode from the left. The deflection coils ensure that light is detected from a small region of the photocathode, determined by the coil currents applied.*

The tube was constructed like a normal photomultiplier as far as the electron multiplier part was concerned. Between the photocathode and the first dynode, an electro-optical system was inserted for focusing and deflection. The electron multiplier and electro-optics were separated by an aperture plate with a dissecting aperture. In the case of Hipparcos, this aperture was circular with a diameter of 110 ± 2.5 μm (corresponding to about 38 arcsec on the sky).

The image dissector tube used for Hipparcos was a standard ITT (F4012 RP) tube without design modifications. The two-fold shielded focus and deflection coils were manufactured according to an existing design, with minor modifications to inner diameter and length of the assembly. The window was a plane-parallel (Dynasil 1000) fused silica plate carrying a semi-transparent S20 photocathode at the inner side of the tube. The photocathode was a thin light-sensitive layer which emitted electrons when photons were absorbed. The photocathode was deposited on a very thin transparent conducting layer, which compensated for the charge emitted by the photocathode.

The accelerating mesh was at a positive voltage with respect to the photocathode to extract the electrons from the photocathode area and to accelerate them in the direction of the drift space. A magnetic field was applied to the drift space by means of three coils (X-deflection, Y-deflection and focus). Emitted electrons followed orbits around the magnetic field lines and hit the aperture plane or passed through the aperture, depending on their points of origin on the photocathode.

Electrons passing through the aperture were collected by the first dynode, which produced secondary electrons with a certain efficiency. These electrons were collected by the second dynode and the process was repeated. At the end, all electrons produced were collected at the anode and the charge was amplified and processed further in the electrical system. The efficiency of the image dissector tube detector as a function of wavelength is given, as part of the overall payload transmission, in Table 2.2.

Star Mapper Detection Chain

The star mapper detector assembly was an electro-optical and mechanical unit, whose function was to detect a light flux and to convert this flux into an electrical signal. Four photomultipliers constituted the whole detection subsystem. In nominal operating conditions, two of the four star mapper detector assemblies were functioning, while the other two were available for redundancy reasons. In operation, the star mapper detector assemblies detected the light of stars that passed across the payload's star mapper grids. In each combination, the two photomultipliers were dedicated to a specific bandpass, with a wavelength centred at about 430 nm for the B_T photomultiplier chain, and at about 530 nm for the V_T photomultiplier chain.

Each star mapper detector assembly contained: a photomultiplier tube with shields against radiation and magnetic fields; high-voltage supply circuits (providing the required high voltage to the photomultiplier); a voltage divider chain (providing the required intermediate high voltages to the individual dynodes of the photomultiplier); a pulse-amplifier and discriminator circuit, for electrical processing of the electrical pulses produced in the photomultiplier, as a result of detection of photons at the photomultiplier photocathode; an anode-current monitor circuit, enabling the detection subsystem to generate an emergency command in case of over-exposure of the photomultiplier; and a light-emitting diode, providing optical test input to the photomultiplier.

Each detector assembly also had a mechanical structure, mechanical interfaces between the star mapper detector assembly and the focal-plane assembly, and electrical interfaces. The detection chain also generated service signals (to clocks, power supplies, and test pulse generator).

Photomultiplier tube: The photomultiplier tube used for Hipparcos was a special version of the Thorn-EMI 9924 B tube. The anode was modified as a result of extensive vibration tests performed by the manufacturer. The window was made as thin as possible, to reduce Cerenkov radiation caused by absorbed high-energy electrons. To increase the sensitivity, the window surface was vapour-blasted.

The photomultiplier had a 30 mm outer tube dimension, with a 23 mm effective cathode diameter. The photocathode had a bi-alkali spectral sensitivity. Photo-electrons, produced in the photocathode by incident photons, were amplified by means of 11 successive box-and-grid dynodes creating, on the photomultiplier anode, a charge pulse of $5 - 10 \times 10^6$ electrons per detected photon. The efficiency of the photomultiplier tube detectors as a function of wavelength is given, as part of the overall payload transmission, in Tables 2.3 and 2.4 for the B_T and V_T channels, respectively.

Detection Electronics Box and Signal Coding

The detection electronics box was an electronic unit whose main functions were: to interface with the remote terminal unit, inverter, and mechanism drive electronics; to interface with the main detector assembly and star mapper detector assemblies; to generate power supplies from the AC power; and to generate digital data from the star mapper detector assemblies and main detector assembly output.

Since the detection electronics box was the only interface for telemetry and telecommand, it received on/off commands for proper configuration of the detection subsystem, one 16-bit memory load command for the main detection chain (used for high-voltage setting, focus current, deflection current, and test generation operation), and one memory load command for the star mapper detection chain and test generation operation (this command was used for high-voltage setting of the B_T and V_T photomultipliers).

The detection electronics box was the interface for the transmission of scientific data. For each primary detection chain, sampled at 1200 Hz, the scientific data consisted of one serial digital 8-bit channel corresponding to the compressed data word in pulse-counting mode, and to the analogue-to-digital converter word in analogue mode (the pulse-counting or analogue-to-digital word was sent to the ground according to the status of an appropriate bit in the programme star file uplinked to the satellite).

For each star mapper detection chain, the scientific data, sampled at 600 Hz, consisted of one serial digital 16-bit word resulting from the concatenation of the two compressed 8-bit data words coming from the two star mapper detector chains—the most significant bits containing the V_T data, and the least significant bits containing the B_T data.

In photon counting mode, the 8-bit scientific data (for both the primary detection chain and the star mapper detection chain) represented the number of counts corresponding to the sampling period (1200 Hz for the primary detection chain, and 600 Hz for the star mapper chain), applying a 'semi-logarithmic' data compression. The maximum count rate that could be coded in pulse counting mode using this compression law was 8159 counts per sample, corresponding to a maximum flux for the image dissector tube data of 9 790 800 counts per second, and 4 895 400 counts per second for the star mapper data.

In this compression, the 8-bit word was the concatenation of a 5-bit mantissa, M, and a 3-bit exponent, E. The determination of E and M for counts, N, in the range $0 \leq N \leq 8159$ proceeded as follows: first the exponent E was determined such that $2^E \leq 1 + N/32 < 2^{E+1}$, then M was taken to be the integer part of $(N + 32)/2^E - 32$. Note that counts up to $N = 31$ were coded without loss of information ($E = 0$, $M = N$); this condition applied to all stars fainter than $B = 7 - 8$ mag.

Assuming image dissector tube count rates of between 2000–4000 counts per second for a star of $B = 9$ mag, depending on star colour, this implied that the analogue mode would be required for the observations of stars brighter than $B = 1 - 2$ mag. Similar considerations for the star mapper implied that the photon-counting channel would saturate for stars brighter than about $B = 2 - 3$ mag. In the case of the star mapper channel, no analogue mode was available, and stars brighter than the saturation threshold were not expected to yield valid data; this was not considered to be a limitation in the design, since the function of the star mapper was primarily one of real-time attitude determination, and the threshold limit for the use of stars as attitude 'reference' in the real-time attitude determination algorithm on-board was fainter than this saturation limit, actually about $B = 4 - 5$ mag, due to the range over which the reference star magnitude could be coded on board.

In practice, the analogue mode for the image dissector tube was not used, the photon counting mode being satisfactory even for the very brightest stars, while the star mapper observations were similarly only marginally affected for the brightest stars.

3.2. Payload Electronics and Mechanisms

The Payload Service Electronics

Mechanism drive electronics: The mechanism drive electronics unit supplied the motors for the mechanisms within the payload with suitable pulses. The programming was transferred via memory load telecommands from the payload remote terminal unit. The mechanism drive electronics unit also provided conditioned status information about the mechanisms to the remote terminal unit. Three different interface types were foreseen to drive the stepper motors, electromagnets, and torque motors.

The mechanism drive electronics unit contained two completely stand-by redundant mechanism control electronics, inclusive of AC/DC converters. Each one was able to drive and monitor all mechanisms. Mechanisms were driven by power pulses delivered by one of the two mechanism drive electronics sections. Both redundant chains were controlled and monitored by the payload remote terminal unit.

Thermal control electronics: The thermal control electronics provided the transformation of resistance values from housekeeping and temperature control thermistors into analogue voltages, the acquisition and processing of six memory load commands (containing control information for the heater DC-voltage levels and allocation of individual DC-voltage levels from the primary DC bus to payload heaters), and the generation of secondary DC-power for internal supply of the thermal control electronics powered by cold-redundant AC-buses.

The thermal control electronics included two redundant sections, with the exception of the housekeeping thermistor-conditioning circuits. These circuits were supplied with secondary power from both sets of thermal control electronics, which were dedicated to the 24 thermally controlled areas, nominal and redundant heaters, and thermistors. Both chains were controlled by the payload remote terminal unit.

Mechanisms

The following mechanisms were contained within the payload:

(1) the refocusing mechanism, which interfaced with the grid package and associated mirror necessary to fold the main beam. This mechanism allowed the focusing of the grid position with respect to telescope focal surface;

(2) the switching mirror mechanism, which provided the mechanical support to the switching prism. It allowed the optical beam to be switched to one of the two redundant main detectors;

(3) the two chromaticity mechanisms, one per image dissector tube channel; each was equipped with a chromaticity filter and a wide-band filter. Switching from the wide-band filter, which was used in normal operation, to the chromaticity filter allowed in-orbit calibration of the payload chromaticity;

(4) the four shutter mechanisms, which protected the detectors from light overload damage.

Refocusing mechanism: The main function of this mechanism was to allow the grid unit to be refocused during the mission to compensate for factors having long-term effects on the focus position, in particular moisture release and optical surface deformation as a result of radiation damage. The mechanism was split into four separate parts (Figure 3.3): the linear actuator, the linkage, the parallel movement element, and the mechanism frame.

The linear actuator comprised a stepper motor, a two-stage gear box, and some monitoring devices. The motor was activated via the mechanism drive electronics and drove the refocusing mechanism spindle. This spindle movement was transformed into a parallel motion of the grid, via the linkage, and the grid unit was moved along the optical beam axis direction. One cycle activation corresponded to four elementary motor steps, and induced a spindle displacement of 46 μm, which resulted in a grid movement of 1.2 μm. The total grid movement amplitude was $\pm$1.2 mm with respect to the mid-position.

The position of the spindle of the linear actuator was monitored by a linear potentiometer (a device capable of converting the movement along a straight line into a resistance change proportional to the displacement). The resistance range was about 1330 – 3670 Ω. The linear potentiometer did not give a very accurate indication of the refocusing mechanism's position (the accuracy was about 50 μm), and was used only as a real-time check that the refocusing mechanism was working nominally. A special coupling was used which freed at a force higher than about 20 N if the potentiometer jammed.

Each end of the linear actuator spindle stroke was monitored by two reed-switches, one being for redundancy reasons. The linkage was used to convert the displacement of the linear actuator into a reduced displacement of the grid barrel. The linkage was built from three spring blades. The two main blades were bolted to the mechanism frame and to the grid barrel, respectively, with zero-tolerance fixtures to ensure a high stability. The blades were fixed to each other at their other ends in a connecting block. From this block, a thinner spring blade went to the linear actuator. Parasitic rotation of the linkage-blades was prevented by two bearing wheels guiding the spindle of the actuator.

This linkage, made of titanium alloy, led to a reduction in the displacement, which varied from 1 : 4.08 to 1 : 4.76 in extreme positions. All connections between the parts of the linkage were made by electron beam welding performed in high vacuum. The parallel movement was required to shift the grid along its stroke without parasitic movements. To that extent, the guidance of the grid barrel was designed with circular springs to ensure low parasitic rotations around the optical beam axis. The parallel movement element was divided into the grid support unit and the folding mirror. The grid support unit consisted of the mounting for the grid mount and the barrel, which connected the membrane supports and the folding mirror system. Openings for the optical beams toward the main detector assembly and star mapper detector assembly were made in this barrel.

The attachment for the grid mount was on one side of a circular invar tube with two rigid lugs to connect to one of the springs, and four smaller lugs to fix the grid mount and the baffle unit. All fixtures were with zero tolerance. In this way, a stable base was created which allowed mounting and dismounting of the grid assembly with a good reproducibility. On the other side of the tube, four rigid lugs were available for connecting both the half membranes. There were also provisions for mounting the folding mirror and connection to the linkage.

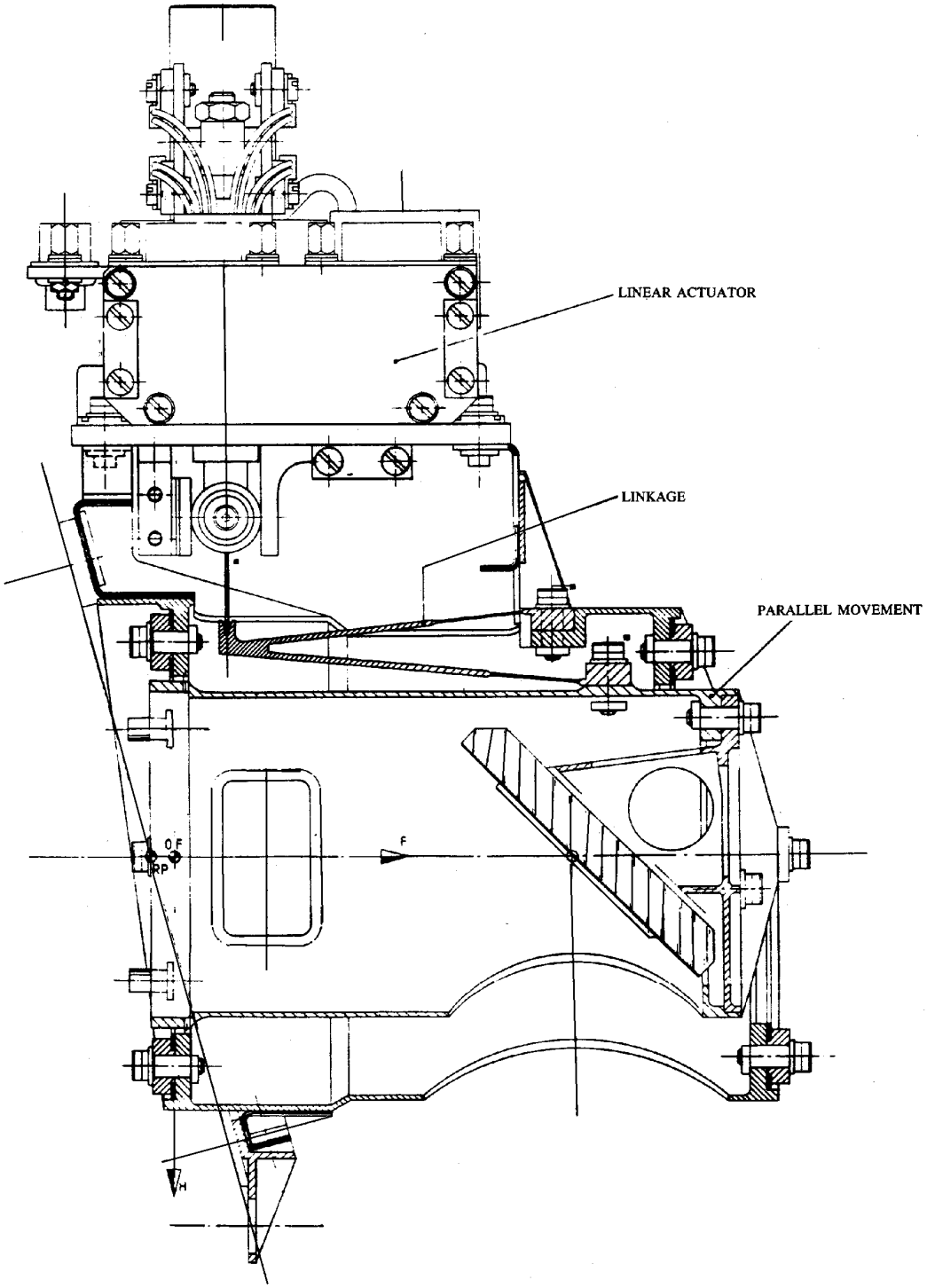

Figure 3.3. *General layout of the refocusing mechanism. The movement of the linear actuator in a vertical direction resulted in a much smaller movement of the refecting mirror, at the lower right, in a horizontal direction. The movement of the grid per refocussing step was 1.2 μm.*

The folding mirror was located at the back side of the grid barrel tube. This mirror, having an angle of 45° to the optical beam, deflected the main light beam towards the switching mirror and the main detector assembly packages. It was made of zerodur and was bonded in its mount, which was machined with sufficiently tight tolerances for there to be no need for adjustment. This mounting could be easily removed and re-installed with sufficient reproducibility, as a result of the zero-tolerance fixings.

The mechanism frame was the main structure to which the different assemblies were fixed: the parallel movement element with grid unit and baffle unit; the linear actuator; and the linkage. This frame was mounted onto the focal-plane assembly platform, using a device capable of adjusting the complete mechanism in three degrees of freedom to avoid the effects of shift and rotation during launch.

Flip-flop mechanisms: The basic function of each mechanism was to provide a two-position capability for the optical elements (filters and mirror) and the shutters. The principal differences between the types of mechanism were the rotation angle of the elements (45° for shutters and filters, and 90° for the switching mirror), the mass inertia and geometry of the different elements, and the accuracy and stability requirements for the different elements. The following operational modes were provided for each mechanism:

(i) normal mode, from rest to working position: on telecommand, the torque motor drove the element into its working position while torquing the spiral torsion spring. When the motor was switched off, the position was maintained by the attractive force between a permanent magnet fixed on the housing bracket and a soft iron core fixed to a paddle;

(ii) normal mode, from working to rest position: on telecommand, the torque motor drove the element back to its rest position. When the motor was switched off, the rest position was maintained by the rest torque of the spiral torsion spring;

(iii) back-up: the fail-safe device that provided partial drive redundancy consisted of the above-mentioned spiral torsion spring and an electromagnet mounted on the housing bracket. If a failure occurred in the nominal driving branch when the mechanism was in working position, the electromagnet could be activated. It produced a repulsive force, which compensated for the attractive force between the permanent magnet and associated soft iron core, and the spiral torsion spring drove the optical element back to its rest position.

The design was based on identical mechanisms for the main detector assembly and star mapper detector assembly shutters, and for the main detector assembly chromaticity filter. As far as the switching mirror was concerned, the design was adapted to more stringent accuracy and stability requirements.

Each mechanism consisted of a bearing box with an electrical torque motor as prime mover and a rotating shaft which carried the optical element. The mechanism housing was made of aluminium. The two mechanical end stops were located at the front of the mechanism in order to minimise the offset and the corresponding relative distortions between the moving element and its mechanical end stops.

The two end positions were maintained without power on the motor by means of the rest torque of the torsion spring in one position, and, in the other position, by the attractive force between a soft iron core fixed on the flip-flop disc and a permanent magnet fixed on

the mechanism bracket. The two ends of travel were monitored by means of reed end-switches mounted on the housing. The permanent magnet needed for activation of the reed switches was mounted on the flip-flop disc. A damping system was implemented on the flip-flop disc to reduce the rebounds generated in the mechanical end stops.

The mechanism bracket was made of invar to minimise the thermal load interaction between the mechanism and the focal-plane assembly. The aluminium housing was mounted on the bracket by means of three fixing points. A rigid fixing point was located at the front of the mechanism, and two flexible fixing points were located at the rear of the mechanism. The purpose of the two flexible fixings was to reduce the internal loads generated at this interface by the different expansions of the housing and the bracket under the given thermal environment.

Adjustment capabilities in the x, y, and z directions were achieved by means of shims. For x-direction adjustment, the shim was located between the flip-flop disc and the optical hardware; for the y-direction, on the fixing points between housing and fixing bracket; and for the z-direction, at the interface between the mechanism and the focal-plane assembly. The positioning accuracy caused by the x, y, and z adjustment operations was given by the shim manufacturing tolerances. Taking into account these tolerances the positioning accuracies of the flip-flop mechanisms were found to be within the specified initial positioning accuracy range. The interface to the electrical harness was provided by means of a 15-pin connector fixed to the housing.

3.3. Baffles

The 'External' Baffles

Each of the two baffles was divided into three major constituents: the support structure, the baffle tube, and the front aperture assembly.

The support structure was formed by six struts, four attachments to the spacecraft upper platform, and one adjustment device on each strut. It supported the other components and provided for ground alignment of the baffle optical axis. The struts, shown in Figure 3.4, were carbon-fibre reinforced plastic tubes of diameters 30 and 40 mm, with a wall thickness of 1.2 mm. They had titanium fittings at each end. The attachments were aluminium milled parts, screwed to the spacecraft upper platform attachment points. On them were fixed the lower adjustment devices. The lower adjustment device was formed by half spheres, spherical washers, and nuts. When the nuts were loose, any change in length induced by turning the nut moved the baffle as a rigid body, without introducing any load because of the isostatic function of a six-bar system. When all nuts were tightened, the struts were fixed in length and angular position.

The main optical requirement for the baffle tube was that all light from outside a given Earth angle envelope had to be intercepted by a set of fins. In addition, it supported the front aperture assembly. It was formed by nine segments—two of them were structural with 2 mm wall thickness, while the others were mainly optical with 0.52 mm wall thickness.

For stability reasons, there was no mechanical contact between the baffles and the payload structure. A 'labyrinth' system was provided by means of a carbon-fibre reinforced

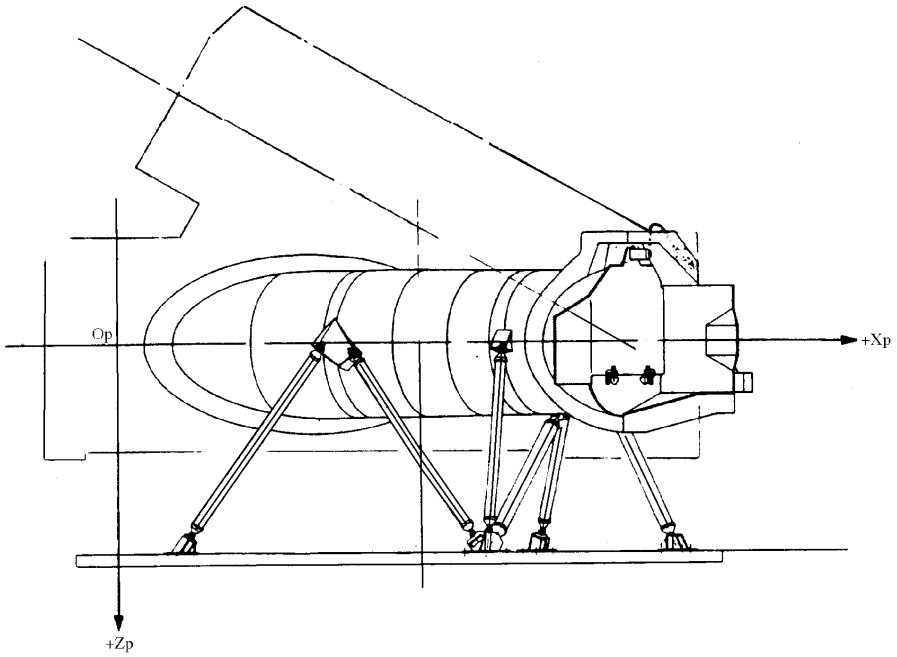

Figure 3.4. *The baffle assemblies. Light entered from the right of the figure. Internal 'labyrinths' suppressed the scattered light. The baffle assemblies were supported by struts to the spacecraft platform (below), mechanically decoupling them from the payload.*

plastic ring bonded on the baffle tube and the associated carbon-fibre reinforced plastic ring bonded on the payload structure. Four external brackets with aluminium reinforcements were bonded to the tube, onto which the upper adjustment devices were fixed.

In the front plate assembly, the front plate aperture defined the design beam envelope and the Earth angle envelope. The fixed screen and the cover in open configuration prevented any direct sunlight from reaching the front plate aperture. Moreover, the multi-layer insulation frame provided a flat mounting area for the shade structure thermal insulation. This assembly was formed by the front-plate fixed screen, the cover, hinges, the closing latch, the labyrinth, and the multi-layer insulation frame.

The front-plate fixed screen was a carbon-fibre reinforced plastic sandwich, fixed to the tube, on which the front plate aperture was machined. The hinges and the corresponding labyrinth and closing latch were fixed on the front plate. The cover was a carbon-fibre reinforced plastic sandwich panel connected to the front plate through the hinges and the closing latch in closed configuration. The other part of the labyrinth was fixed to it. There were two hinges in each baffle, so the system was redundant in driving torque, locking and monitoring.

During ground operations, and also throughout launch and the early operations, the baffles were closed by the covers, in order to protect the optics against contamination. When closed, the covers ensured the required telescope venting during launch and during transport by aircraft, through the labyrinth and venting holes. The covers were deployed in orbit by means of a pyrotechnic device. When opened, the cover prevented sunlight entrance into the baffle.

The 'Internal' Baffles

A set of internal baffles was connected to the main structure. Their prime function was to ensure separation of the half-pupil beams and of telescope inner enclosures, and consequently help to meet the light-tightness and straylight requirements. These baffles comprised:

(1) the straylight pupil baffle, consisting of carbon-fibre reinforced plastic plates (thickness 0.7 mm) assembled by means of bonded carbon-fibre reinforced plastic corner profiles. This baffle was located approximately half way between the beam combiner and the folding mirror, and was connected to the $+Z$ panel of the main structure and to the enclosure separator baffle by means of anchor floating nuts and screws;

(2) the enclosure separator baffle, consisting of a carbon-fibre reinforced plastic plate (thickness 0.7 mm) and parallel carbon-fibre reinforced plastic stiffeners (thickness 1.44 mm) bonded and riveted. This baffle was connected to the stiffener of the lateral panels by means of the two hard points and ten flexible blocks, cutting the enclosure into two parts: the beam combiner mirror plus folding mirror part, and the spherical mirror plus folding mirror part;

(3) the beam separator baffles, consisting of carbon-fibre reinforced plastic plate (thickness 0.7 mm) with a beam-shaped hole. These baffles were located around the two beam entrance apertures and were connected to lateral panels of the main structure by means of screws and floating anchor nuts;

(4) the pupil baffle, consisting of a box made from aluminium (type AG5) sheets of 0.3 mm thickness and black painted. Surrounding the beam combiner, it was connected to the barrel by means of blades;

(5) the grid baffle, attached to the grid assembly and described in Chapter 2;

(6) Cerenkov shielding: the external sides of the focal-plane assembly cover were equipped with shielding to protect the optics against Cerenkov radiation. The shielding, with a total weight of 2 kg, was made of aluminium sheets bonded on the external skin of the focal-plane assembly cover.

Straylight Performances

The main function of the baffles was to attenuate parasitic light coming from the Sun, the Earth and the Moon which would otherwise fall on the detectors. Straylight originating from the Sun was specified to be less than the average sky background (using a background figure of $B = 22.5$ mag arcsec^{-2} and a colour index of $B - V = 0.7$ mag), and straylight coming from the Earth or the Moon was specified to be less than ten times the background (defined to be the 'interruption limit'), when these bodies lay outside a rectangle of $\pm 24°$ (in the scan direction) by $\pm 13\overset{\circ}{.}5$ (in the transverse direction), centred on the optical axis.

The straylight performances of the payload, which also depended on mirror scattering, were measured before launch in a dedicated test using a light source representing the

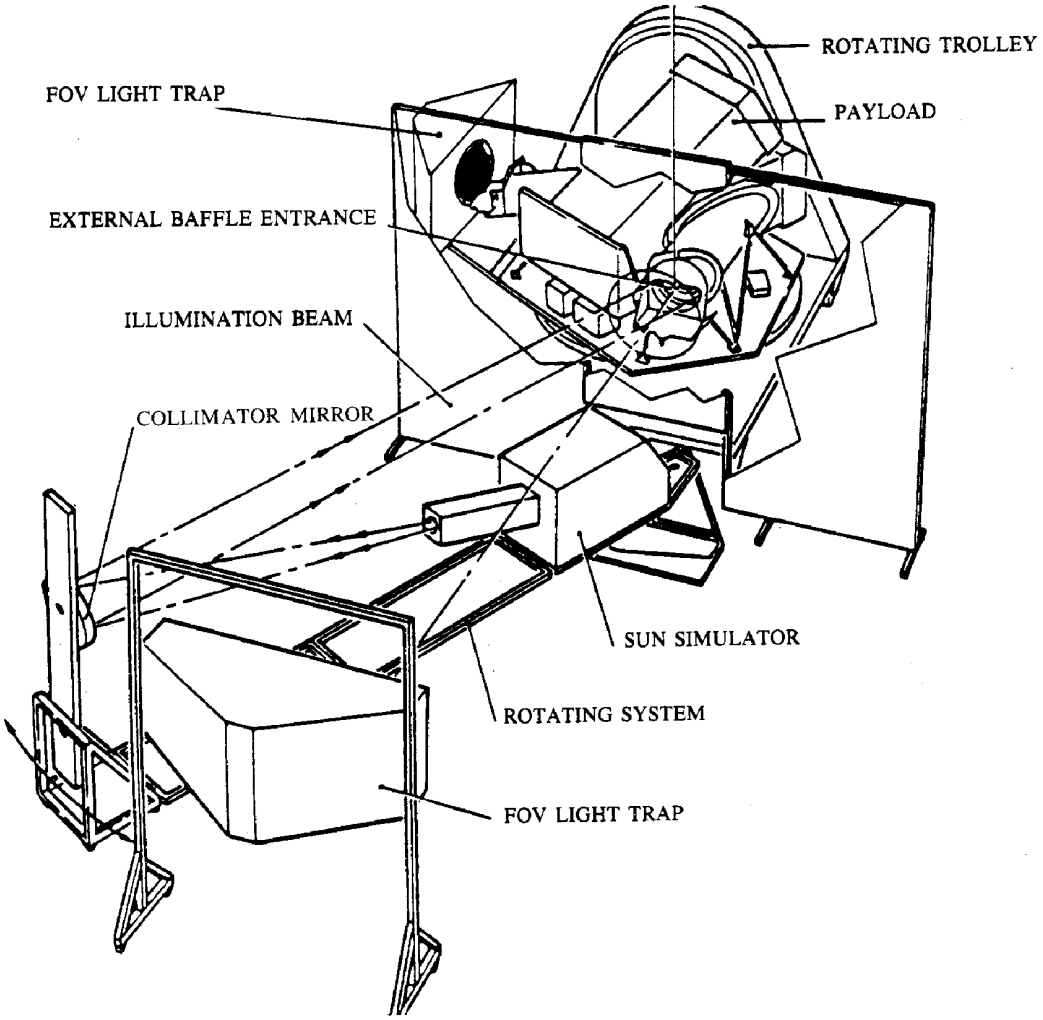

Figure 3.5. *Straylight test configuration. The rotating system moved the light source to different angles with respect to the viewing direction, leading to the production of the straylight attenuation curves shown in Figure 3.6. The light trap was directly in front of the entrance aperture, preventing other light from entering the payload.*

Moon directed onto the baffle aperture. The simulator was rotated around the baffle entrance along each of eight directions with respect to the scan axis, to provide representative positions of the illuminating source (see Figure 3.5). Measurements were corrected to account for the scattering of incident light due to the presence of air, and straylight performances for the Earth were computed from the measurements. Attenuation of the sun straylight was evaluated by simulating worst cases of sun aspect angle using the same simulator.

Measurements of the detected straylight intensity at a given position in the field of view, and of the incident light intensity on the baffle aperture, provided the data with which to determine the 'attenuation' in that direction, defined as the ratio of the equivalent straylight on the baffle aperture to the incident irradiance in the same direction (attenuations are therefore expressed in sr^{-1}). Figure 3.6 shows an example of an attenuation curve applicable to the case of the full Earth moving in the scan direction and crossing

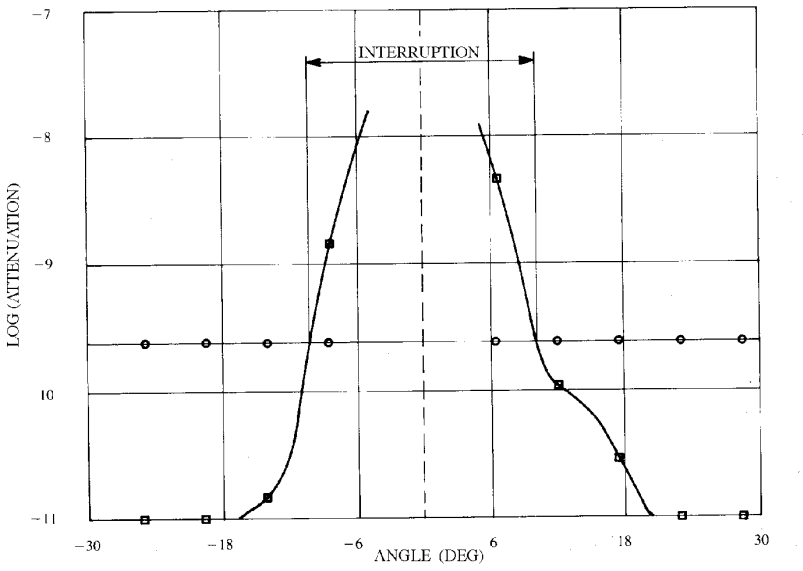

Figure 3.6. *Straylight attenuation curves. The squares show the measured attenuation, the circles show the accepted straylight 'interruption limit' of ten times the average sky background.*

the baffle axis. In this example, the straylight level is higher than ten times that of the sky background over a region 20°.3 wide, well within the specified 24°.

Straylight attenuation in the scan direction mainly influenced the duration of the interruptions of the observations. The corresponding dead time, averaged over the mission, was estimated to be about 5 per cent for a geostationary orbit. The number of interrupted scans, determined by the attenuation in the transverse direction, was predicted to be around 33 per cent, again for the nominal geostationary orbit.

3.4. Payload Structure

The payload structure subsystem provided the mechanical support for all other payload items—the telescope mirrors (the beam combiner, the folding mirror and the spherical mirror), the focal plane assembly platform (comprising the refocusing mechanism, the grid assembly, the relay optics, the detection subsystem, and the mechanisms), the thermal control hardware, and the harness.

The telescope structure was designed to maintain the accurate relative positioning of all optical surfaces, including the three telescope mirrors, and the elements of the focal plane assembly. Consequently, the structure had to be extremely stable over the entire period, from final alignment on ground until the end of mission in orbit. Such stringent alignment requirements had to be maintained in the face of the launch environment; thermal environment variation; mechanical interfaces with the satellite, focal plane assembly units and harness; variation of humidity; and the effect of gravity release.

The structure had to induce very low bending moments on the mirrors, to minimise optical surface deformations. Isostatic connection to the spacecraft was required; and the structure furthermore had to provide light tightness, maintain cleanliness, ensure

the easy implementation of thermal hardware and a maximum mechanical decoupling between structural and thermal hardware, and facilitate the integration.

The overall telescope structure was split into a primary structure (consisting of the main structure, the focal plane assembly platform and the mirror mounts), and a secondary structure (consisting of the internal baffles, the beam combiner and spherical mirror covers and focal-plane assembly cover, and the heater mat carriers). The following section provides a design description of the various sub-assemblies of the telescope structure.

Main Structure

The main structure was partially dismountable, with a door in the upper panel, providing easy integration without complex assembly tools, and access into the telescope structure during integration and test activities.

The overall optical layout, and the mass, stiffness, and stability requirements called for a box-type structure made with carbon-fibre reinforced plastic skin panels and stiffeners or carbon-fibre reinforced plastic shear panels linked by corner profiles and folded edges (see Figure 3.7).

For the five enclosure panels, a carbon-fibre reinforced plastic product was used, consisting of 12-ply multi-layers (using ultra-high-modulus GY 70 carbon fibre, which gave a very low coefficient of thermal expansion (of order 10^{-7} K^{-1}), with a high Young's modulus (about 10^5 N mm^{-2})). Where local reinforcements were needed, a number of carbon-fibre reinforced plastic face sheets were added (with the same lay-up) and bonded together.

The junction between the panels was achieved either by folded edges or by corner profiles bonded and riveted on panels, except for the door of the upper panel, which was dismountable and assembled with floating anchor nuts and expandable pins to avoid any relative movement of the carbon-fibre reinforced plastic parts.

The mounting hard points were bonded on carbon-fibre reinforced plastic skins and riveted together. Invar was used for the barrel interface because of its low coefficient of thermal expansion (2×10^{-6} K^{-1}), which was required for thermal stability and low bonding stresses in the expected thermal environment. Titanium was used for the interface structure for lightness. Fittings were designed to have a good torsion and bending stiffness, to avoid micro deformation due to local low stiffness and areas of stress concentration. The payload was bonded on the centreline of a carbon-fibre reinforced plastic supporting framework, which had a good bending and torsional stiffness.

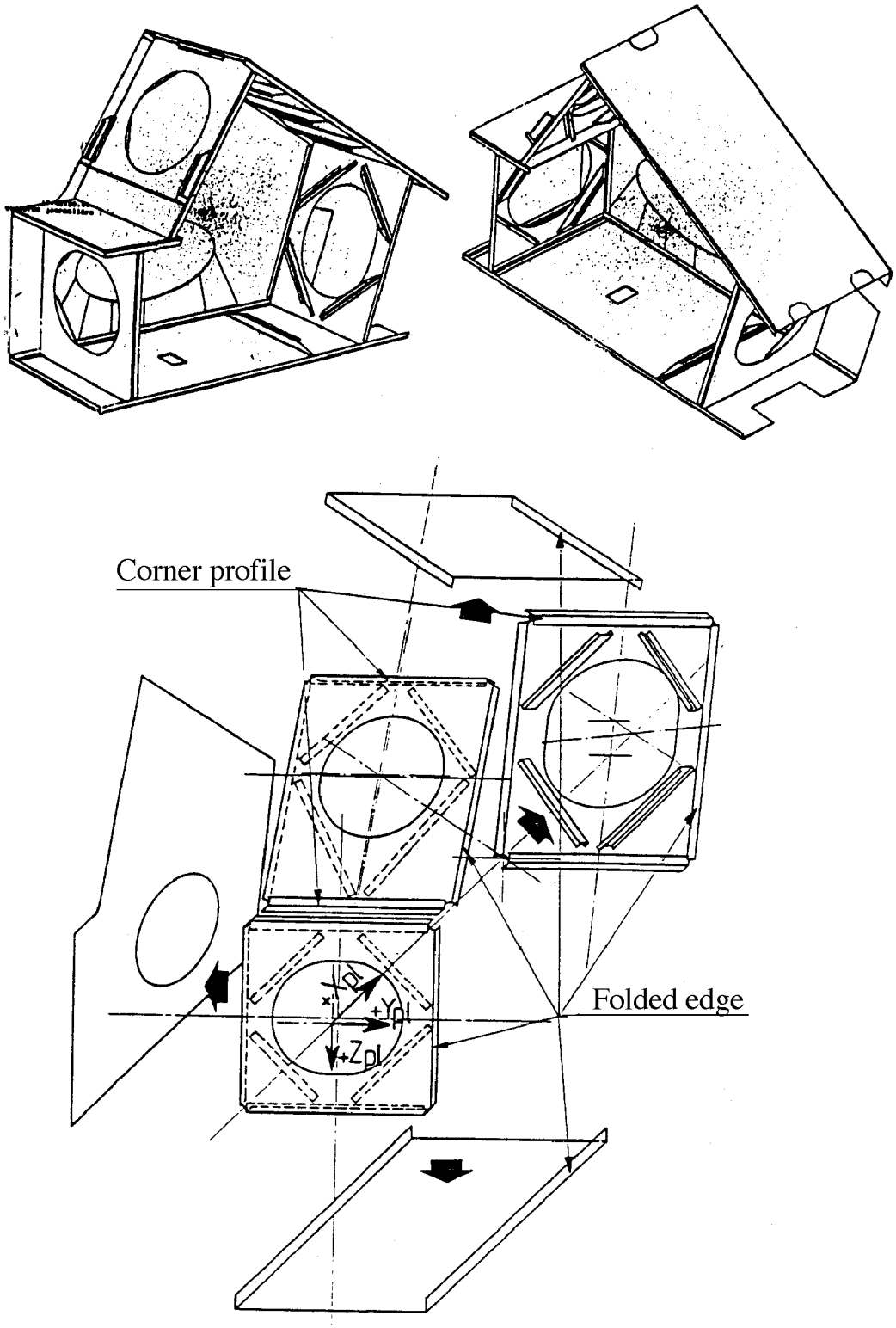

Figure 3.7. *The main structure. The structure was based around carbon-fibre reinforced panels, which were bolted together, with additional stiffeners in the areas of the aperture openings.*

Mirror Mounts

This sub-assembly consisted of a carbon-fibre reinforced plastic frame 'barrel' linked to the main structure by means of three rigid fixings, and three flexural pivot blade systems joining the mirror to the barrel.

The frame barrels were sandwich platforms with aluminium (AG5) honeycomb and carbon-fibre reinforced plastic skins. They had a hole in their centres, the external shapes being either triangular for the beam combiner and the spherical mirror, or quasi-circular for the folding mirror. In areas where loads were concentrated, there were carbon-fibre reinforced plastic thick plate reinforcements bonded on the sandwich. The different fixation hard points (with flexural pivot blade system and with telescope structure) were fixed with invar inserts, which were bonded and riveted on carbon-fibre reinforced plastic. The adjustment device for mirror and barrel alignment had six degrees of freedom, the adjustment being carried out by means of adjusting shims. Expandable pins were added to avoid relative component movements, in order to meet the long-term stability requirements.

A typical mirror mount set comprised three flexural assemblies, fixed symetrically at the periphery of the mirror. Each of the three assemblies was composed of a titanium cruciform section and an invar blade section. The cruciform section, attached to the mirror by 12 screws through an invar pad bonded on the mirror, behaved as a hinge around the radial direction and minimised the radial torque induced by barrel deformations. The solution of invar pads bonded to the mirror was selected because it was considered preferable to have separate thin pieces bonded to a mirror, instead of big pivot blades, during mirror polishing.

To improve long-term stability performance, positive fixings were implemented between pivots and pads by means of two expandable pins per pivot. The invar blade section was rigid around the axes tangential to the mirror edge. To minimise moments introduced during integration, the blade and the cruciform sections were assembled with spherical surfaces which had to be blocked, after alignment of the mirror, by means of a screw.

Focal-Plane Assembly Platform

This platform was designed to support 39 kg of equipment, and had to ensure a first frequency higher than 100 Hz. It was made of carbon-fibre reinforced plastic sandwich panel rigidly connected by eight points to the edges of panels of the main structure. Mounting of equipment and mechanisms onto the platform was achieved through some 110 bonded inserts equipped with studs.

The basic panel was made from aluminium honeycomb with carbon-fibre reinforced plastic skin, consisting of 18 ply multi-layers ultra-high-modulus GY 70 carbon fibre, which gave a very low coefficient of thermal expansion with a high Young's modulus. The focal-plane assembly platform's integration on the main structure required four degrees of freedom for alignment, where tilt adjustment was performed by means of adjusting shims. To avoid micro displacement of the focal-plane assembly platform with respect to the telescope, four expandable pins were added on four fittings. These fixing techniques provided a reproducibility that allowed mounting and dismounting activities to be undertaken without loss of the correct positioning.

Cerenkov Shielding

Some of the optical elements, such as the grid and the relay optics, generated photons (Cerenkov effect) and were expected to degrade in transmission ('darkening') as a result of irradiation by high-energy electrons in geostationary orbit. Such optical elements were protected by the so-called 'Cerenkov shielding'. A total of about 12 kg of protective material was placed around the relay optics and on the shade structure, complementing inherent shielding provided by the structure and the equipment surrounding the sensitive optical elements.

4. LAUNCH AND REVISED MISSION DEFINITION

Following a perfectly nominal launch of the Hipparcos satellite, by Ariane 4 flight V33, from Kourou on 8 August 1989, the satellite did not reach its intended geostationary orbit due to the failure of the apogee boost motor. The scientific mission was destined to be conducted from the highly elliptical non-nominal geostationary transfer orbit, with only small orbital changes possible (making use of the remaining hydrazine fuel intended for station keeping). The activities necessary to recover an operational mission, and to carry out the first phases of the planned mission operations—sun acquisition, real-time attitude determination, scanning law acquisition, and the start of the payload calibrations—are described. At this stage of the mission, the expected lifetime was highly uncertain, in particular due to the difficulty of predicting the long-term solar array performances in view of the hostile radiation environment in the geostationary transfer orbit.

4.1. Introduction

Hipparcos was launched as the lower passenger by Ariane 4 flight V33 at 23:25:53 UTC on 8 August 1989 from the launch site at Kourou, French Guyana. Hipparcos and the second passenger satellite (TV-SAT2) were injected by the Ariane launch vehicle without problems. The transfer orbit into which the satellite was launched had a period of about 10 hours reaching an apogee of 36 000 km (120 km lower than nominal) and a perigee of 200 km. The nominal injection attitude after launch was $\alpha = 200\overset{\circ}{.}816,\ \delta = -8\overset{\circ}{.}882$.

At first acquisition of signal at the Malindi ground station a spin rate of 6.92 rpm was calculated. The solar aspect angle was $70\overset{\circ}{.}5$, approximately 5° lower than expected. The estimated nutation at injection was about $1\overset{\circ}{.}0$, a value which reduced to $0\overset{\circ}{.}5$ through the first spin-up of the satellite.

On 10 August 1989 at 12:14:00 UTC, the telecommands to initiate the firing of the apogee boost motor were executed from the operations control centre at ESOC. However, no subsequent change in Doppler rate was observed at the supporting ground stations, and it was evident that the apogee boost motor firing had not taken place. The uplinked commands were immediately verified and confirmed to be correct, so the

failure was almost certainly on-board the satellite. Further unsuccessful firing attempts were conducted in subsequent orbits.

During the following weeks detailed investigations were performed in order to understand what had happened on-board. A reformatting of the telemetry allowed the sampling of the currents in the pyrotechnic relay unit at intervals of 5 ms. From the data downlinked during subsequent apogee boost motor firing attempts, it was possible to reconstruct the behaviour of the firing relays, and the fault was located to be somewhere in the pyrotechnics chain. A total of five firing attempts (each consisting of multiple firings) were made until 25 August 1989 without any success.

The most optimistic outlook for the mission at the time was that, if a 'hibernation mode' for the first long eclipse season could be devised (involving a reduction in spacecraft heating and deactivation of the payload to save power), there could be a chance of satellite survival until the next eclipses starting in mid-1990. By that time, it was expected that the on-board power generation would be so degraded that meaningful science data could no longer be collected.

Under the latter scenario, the outcome of the mission would have been reduced to something between 5 per cent and 10 per cent of the original mission objectives, but this would have still represented an achievement which would be hard to accomplish with ground-based astronomical observations. As a minimum, it was hoped that these measurements would still be useful in order to validate the Hipparcos mission concept. In reality, the mission lasted much longer.

4.2. Operations Until Revised Mission Implementation

This section summarises the main events which happened, day by day, through the attempts to fire the apogee boost motor, leading up to the decision to terminate further firing attempts, and concentrate on the implementation of a 'revised', or 'recovery', mission.

89-08-08: Launch of Ariane flight V33 at 23:25:53 UTC.

89-08-08: At 23:49:36 UTC, the spacecraft was successfully ejected from the launcher.

89-08-09: The first sun sensor data (at 00:21:00 UTC) registered a spin rate of 6.92 rpm and a solar aspect angle of $70\overset{\circ}{.}5$ (compared with the expected value of $75\overset{\circ}{.}15$). A series of spin-up manoeuvres were carried out to increase the spacecraft spin rate in a number of steps: firstly to 18.57 rpm, then to 62.33 rpm, followed by a correction manoeuvre to achieve the target spin rate of 60 rpm. At 02:52:00 UTC, the ground system derived an attitude (in right ascension and declination) of $\alpha = 204\overset{\circ}{.}9$, $\delta = -10\overset{\circ}{.}1$. The spacecraft was commanded to slew (in two stages) to the required attitude for the apogee boost motor firing attempt at apogee number 4 namely $\alpha = 213\overset{\circ}{.}91$, $\delta = -8\overset{\circ}{.}87$. Between the two slews, a spin trim manoeuvre to 60.13 rpm was performed. These manoeuvres were completed by 01:50:00 UTC on 89-08-10.

89-08-10: The first apogee boost motor firing attempt was performed at 12:14:00 UTC without success. At 21:45:00 UTC, the spacecraft was slewed to the required attitude for a second apogee boost motor firing attempt at apogee number 6, namely $\alpha = 212\overset{\circ}{.}29$, $\delta = -8\overset{\circ}{.}36$.

89-08-11: Three further apogee boost motor firing attempts were performed between 09:10:00 and 09:25:00 UTC, without success. At 10:15:00 UTC, the spacecraft was slewed to the required attitude for a further apogee boost motor firing attempt at apogee number 8, namely $\alpha = 211\overset{\circ}{.}49$, $\delta = -8\overset{\circ}{.}32$. In the event, the decision was later taken not to make a further attempt at apogee 8.

89-08-13: A further apogee boost motor firing attempt was performed at apogee number 11 (13:51:00 UTC), without success. During this attempt, a newly designed high-rate telemetry format (Format 4) was selected to allow oversampling of the apogee boost motor firing ignition current in order to investigate the failure. After the failed attempt, a slew manoeuvre to an 'average' attitude of $\alpha = 214\overset{\circ}{.}40$, $\delta = -9\overset{\circ}{.}60$ was deemed to be sufficient for subsequent firing attempts.

89-08-14: To reduce the strain on various components caused by the prolonged exposure to high spin rates, a spin-down of the spacecraft from 60 to 30 rpm was performed in two steps. The final attitude was $\alpha = 213\overset{\circ}{.}63$, $\delta = -9\overset{\circ}{.}50$.

89-08-17: Further apogee boost motor firing attempts were performed at apogee number 20 (between 11:55:00 and 12:05:00 UTC), without success. The Format 4 telemetry was used during the attempts to gather extra information.

89-08-18: It was decided that the next firing attempt should be made after heating the apogee boost motor. This was achieved by slewing the spacecraft such that the motor was oriented more toward the Sun (the solar aspect angle was reduced from 115 to 95°). This attitude ($\alpha = 277\overset{\circ}{.}8$, $\delta = -13\overset{\circ}{.}7$) was maintained for 6 days prior to the next apogee boost motor firing attempt.

89-08-19: The fill-in antenna was tested at 11:46 UTC.

89-08-24: The spacecraft was slewed to the apogee boost motor firing attitude ($\alpha = 217\overset{\circ}{.}69$, $\delta = -8\overset{\circ}{.}11$) changing the solar aspect angle from 103° to 113°.

89-08-25: The spin rate of the spacecraft was increased once more from 29.9 to 37.0 rpm at 08:20:00 UTC, prior to the fifth apogee boost motor firing attempt at apogee number 38 at 08:35:00 UTC. The Format 4 telemetry was used during this final attempt in order to gather extra information. One hour after apogee 38, a slew manoeuvre was performed to an attitude of $\alpha = 235\overset{\circ}{.}88$, $\delta = -14\overset{\circ}{.}73$. The attitude achieved meant that the daily drift of the solar aspect angle could be left uncompensated for several days thereafter.

89-08-26: The decision was taken to abandon any hope of successful boost motor firing, and all effort was dedicated to designing and optimising a 'recovery' or 'revised' mission operations scenario.

4.3. Apogee Boost Motor Failure Investigations

An enquiry board was set up in September 1989 to examine all aspects of the apogee boost motor anomaly, establish the most probable cause or causes, and to make appropriate recommendations to prevent re-occurrences.

The enquiry board identified and studied the most likely causes of the failure in the apogee boost motor pyrotechnic subsystem, which were: (a) mechanical failure of the

flexible explosive transfer assembly under vibration load; and (b) failure of the 'through-bulkhead initiators' (the pyrotechnic initiators). A characterisation programme to determine the detonator electrical resistance after firing was performed to establish whether the failure was of electrical or pyrotechnical nature. The characterisation programme consisted of manufacturing, testing and firing 40 detonators. Flexible explosive transfer assemblies were vibrated up to the qualification level of 20*g* at resonance, X-rayed and inspected. They did not show any deterioration. Then they were successfully fired. Study of the electrical resistance after the firing was in accordance with the telemetry values proving that the detonators had indeed been fired.

Through-bulkhead initiator tests were thorough and very complex. Drop tests were performed which proved that the through-bulkhead initiators were not damaged by such shocks. After the two through-bulkhead initiator firings performed in 1989, three more from the Hipparcos lot were fired and one of them failed. In total six through-bulkhead initiators from the Hipparcos lot were fired and two failed. However due to the limited number available it was not possible to conclude the direct cause of these failures.

The enquiry board, recognising that both redundant through-bulkhead initiators must have failed, concluded that the boost motor failure was related to the non-functioning of the through-bulkhead initiators.

4.4. Revised Mission Definition

Immediately following the first firing attempts, investigations were initiated to check the possibility of fulfilling at least part of the mission objectives within the given constraints. The prospects were not very promising, since the available hydrazine fuel (intended for station acquisition) would allow the orbit to be raised by not more than a few hundred kilometres: therefore, the satellite would be exposed to the effects of the van Allen radiation belts during each orbit. It was expected that the radiation would degrade the solar arrays to such an extent that the on-board power would not be sufficient for the satellite to survive the long eclipses (of over 100 minutes duration) starting in March 1990 (Figure 4.1).

A concentrated effort of ESOC, ESTEC, and industry experts was devoted to all relevant system, spacecraft, payload and associated operational aspects of a revised mission. At the same time, the Hipparcos Science Team performed investigations into the science implications of the revised mission. Their simulations indicated clearly that the ground station coverage should be increased to the maximum extent: only with close to full time station coverage, would it be possible to establish a full sky network of star measurements within a limited mission lifetime using the nominal attitude scanning law and star observation strategy which were implemented in the on-board software.

The objective of the mission redesign efforts was to recover as much as possible of the original Hipparcos mission objectives. The operational problems to be addressed were essentially those of a new mission with a few significant differences: (i) there was little flexibility left on the satellite system design: only limited on-board software modifications were possible within the practical constraints available; (ii) only narrow margins were available on the orbit selection because of fuel constraints; and finally, (iii) any day spent on the definition of the mission represented a full day of lost mission time.

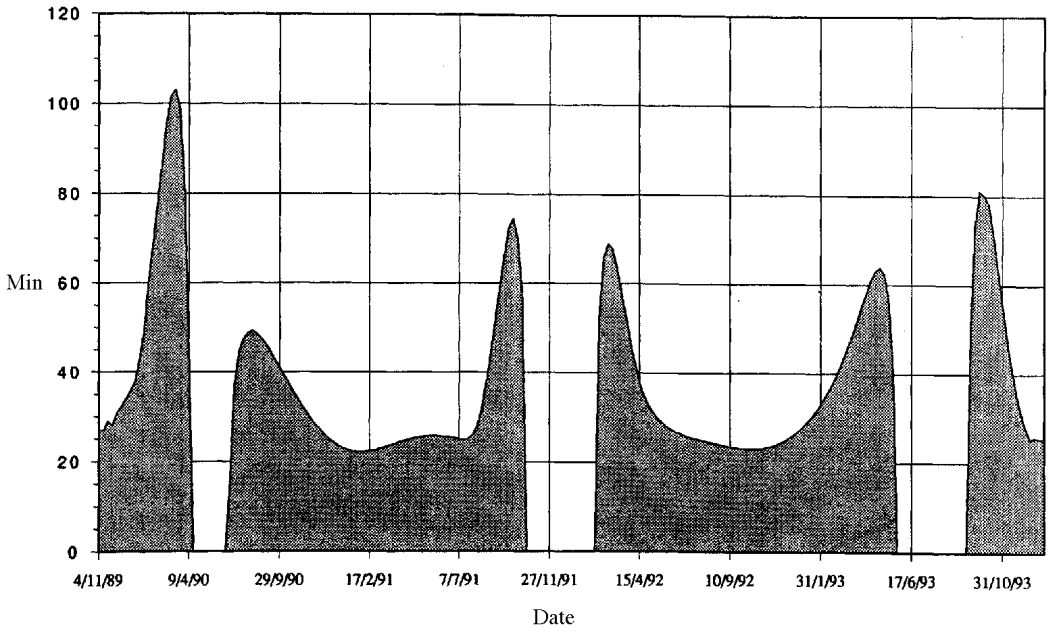

Figure 4.1. *Eclipse duration due to the Earth as a function of time throughout the operational period. The extended eclipse periods in early 1990, late 1991, early 1992, and early 1993 imposed constraints on the available satellite power, which had to be handled by shutting down specific on-board subsystems during some of these intervals.*

A number of problems and uncertainties contributed to generally pessimistic mission prospects at the time:

(i) the limited ground contact from the Hipparcos-dedicated antenna at Odenwald (about 32 per cent of the time) would not be sufficient for significant science data collection;

(ii) the limited station coverage from Odenwald would severely complicate the execution of the operations and endanger the satellite's safety outside the coverage interval, so a number of precautions would have to be implemented before each loss of contact (the satellite design was based on essentially full ground station coverage with occasional interruptions of not more than 0.5 hour);

(iii) the long periods without ground station contact would necessitate frequent initialisations of the autonomous attitude determination process from ground, which would further reduce the time for science data collection and would require a larger operations team;

(iv) the high radiation in the van Allen belts (which were crossed about four times per day) would increase the detectors background noise levels, complicating the autonomous star detection, and inducing a darkening of the payload optics which would degrade the photometric results;

(v) long eclipse periods would occur in March 1990. The associated power problems were expected to require a special and still to be designed 'hibernation mode';

(vi) the occultations caused by the Earth being in the field of view would be significantly longer and more frequent than in the nominal geostationary orbit. This would make the maintenance of the on-board attitude knowledge more difficult;

(vii) the Earth albedo effect would provide a thermal input to the payload in the perigee region. This could lead, for example, to significant distortions in the fine modulating grid of the payload;

(viii) the high perturbing torques in the perigee region would introduce difficulties for the attitude control. In any case, it would require the inhibition of the satellite emergency mode triggering on the basis of too high thruster actuation demands.

The following list summarises a few of the most significant mission design aspects studied at ESOC during the first few weeks after the failure:

(a) evolution of the geostationary transfer orbit and the satellite attitude orientation for subsequent apogee boost motor firing attempts and solar aspect angle violations;

(b) redesign of the attitude acquisition sequence (directly from the attitude required for apogee boost motor firing to the sun-pointing attitude);

(c) station coverage predictions of the transfer orbit and potential recovery orbits;

(d) eclipse and occultation predictions of the potential recovery orbits;

(e) potential implications of modifying the nominal scanning law and the star observation strategy;

(f) fuel budget requirements and predictions under the revised orbit and attitude acquisition strategies;

(g) strategies for covering the long periods without ground contact, and the implementation of a sparse programme star file as a means of survival of the on-board attitude knowledge;

(h) new attitude control parameters designed to cope with the high disturbance torques in the perigee region.

At the same time, ESTEC and contractor experts were evaluating the radiation effects of the van Allen belts on solar array and payload degradation. Thermal and power aspects of the new attitude acquisition strategy, and associated risks, were also being assessed and evaluated.

Immediately following the first apogee boost motor firing failure on 10 August 1989, a team of mission analysis and flight dynamics experts started investigations concerning potential recovery orbits. After it was found that 12-hour or 8-hour orbital periods were not practically feasible, the orbit selection concentrated on achieving a perigee altitude above 400 km taking account of fuel constraints and to reduce the influences of air drag and atomic oxygen with, at the same time, a synchronisation between the scanning law period (2 hrs 8 mins) and the orbital period: this was considered to be beneficial as it would limit the effects of albedo heating on the payload and minimise the duration of payload occultations in the perigee region by a proper tuning of the initial scan angle.

Fortunately, a 10 hour 39 min orbital period fulfilled both criteria, and was within reach of the available fuel resources. The necessary orbit adjustments were performed after implementation, validation and simulation of the required new software and control procedures, in a series of five manoeuvres during the period 7–18 September 1989 (see Figure 4.2).

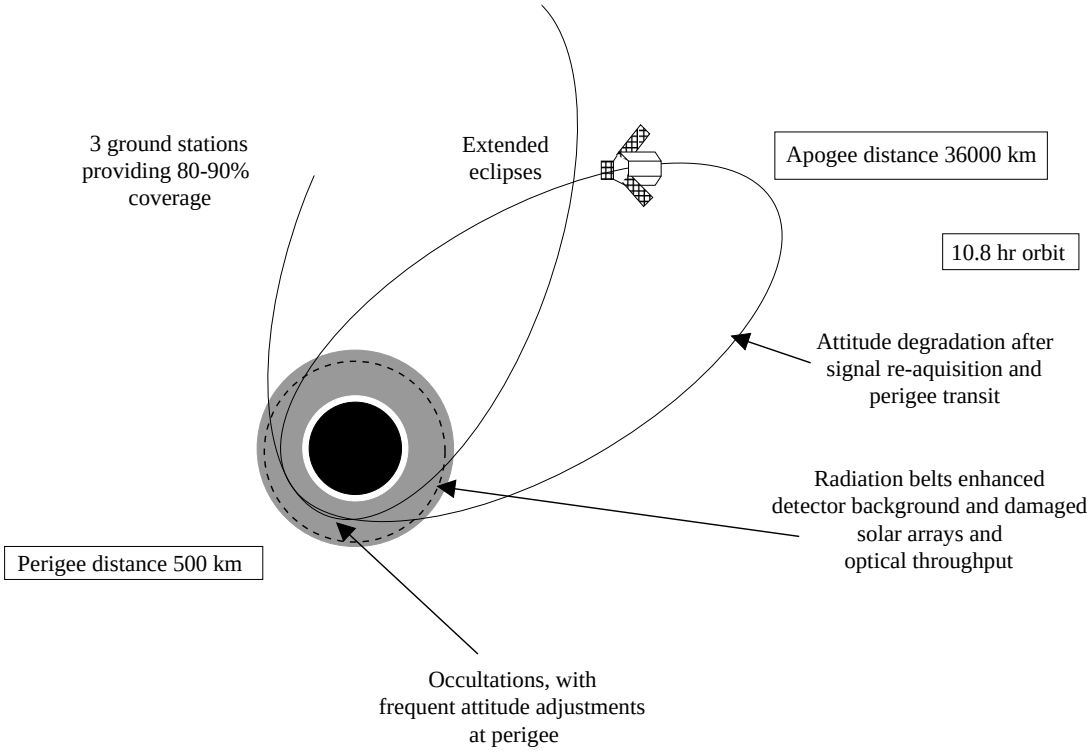

Figure 4.2. *The 'revised' or 'recovery' orbit from which the Hipparcos observations were conducted. The features of the orbit which provided considerable operational complications are indicated. The satellite could be observed for about 80–90 per cent of the time with three ground stations, compared with 100 per cent of the time in the intended geostationary orbit.*

4.5. Ground Station Utilisation

During the launch and early orbit phase, the ESTRACK launch and early orbit phase S-band network was used for telemetry acquisition, telecommanding and tone-ranging. The launch and early orbit phase ground stations were operated under control from the operations control centre. The launch and early orbit phase network consisted of the following ground stations: Kourou-100 (French Guyana), Malindi (Kenya), and Perth (Australia). Back-up support was given by the Odenwald ground station and the Villafranca transportable station when the satellite was visible.

For routine operations, the Hipparcos ground station network eventually consisted of five S-band stations: three stations belonging to the ESA ground station network (ESTRACK) and located in Germany (Odenwald), Australia (Perth) and French Guyana (Kourou). A fourth ground station, located in the U.S.A. (Goldstone) and belonging to the NASA deep space network, was added in the first half of 1990. The Kourou station, whose coverage was largely superseded by the Goldstone station, was subsequently taken out of the network in mid-July 1990. However, during the last months of the satellite's lifetime, Kourou was re-activated. All ground stations provided full tracking measurement, satellite data (telemetry) acquisition operations, and commanding for

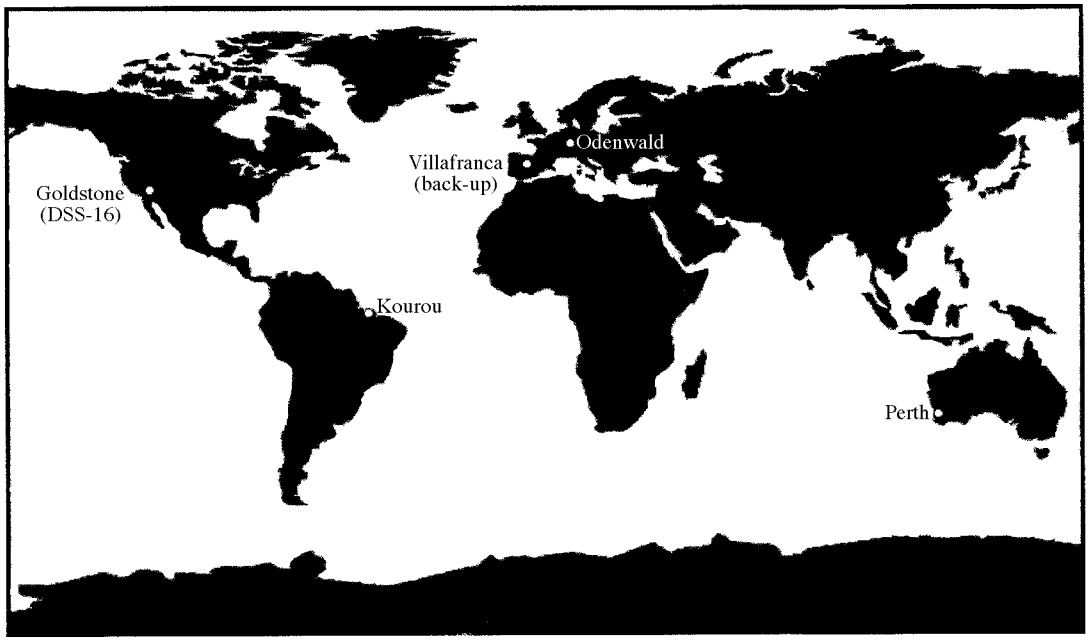

Figure 4.3. *Hipparcos ground stations. Only the Odenwald station had been originally foreseen for the geostationary orbit operations: the other ground stations were brought into the operational network only after a decision to proceed with the revised mission had been taken.*

the Hipparcos mission. A fifth ground station, located in Spain (Villafranca), provided a back-up to the Odenwald station. The ground station locations are illustrated in Figure 4.3.

The ground stations were operated in a transparent mode, i.e. the transactions between the operations control centre and the satellite were supported automatically with no local operator intervention at the station unless, in case of control centre or communication link failure, limited local commanding and telemetry readout functions were necessary to safeguard the satellite.

The ground communications facilities with the Kourou and Perth ground stations consisted of telecommand link for command transmission at 2 kbps using X25 level 3 protocol; low-rate telemetry link for telemetry transmission at 1.44 kbps using X25 level 3 protocol; high rate telemetry link for transmission at 23.04 kbps using X25 level 3 protocol (Perth and Kourou only); and voice loop, telex and telephone communications facilities.

The ground communication facilities with the Odenwald ground station consisted of telecommand link for command transmission at 2 kbps using X25 level 3 protocol; low- and high-rate telemetry link for telemetry transmission at 1.44 and 23.04 kbps using a digital PTT line with High Level Data Link Control (HDCL) protocol (integrated with the METEOSAT data traffic); ranging link allowing ranging request and measurement transmission using X25 level 3 protocol; link for antenna pointing transmission using X25 level 3 protocol; monitor and control link between the station computer at ESOC and the advanced monitor and control modules at the ground station, multiplexed with the high-rate telemetry.

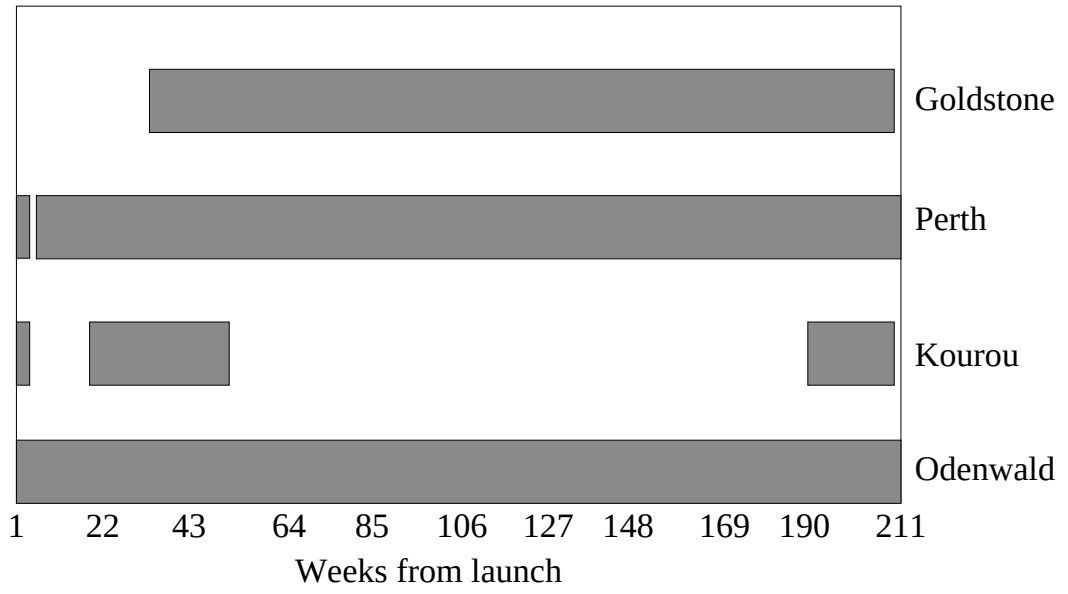

Figure 4.4. *Ground station support throughout the operational phase. The (baselined) Odenwald station was used throughout the mission. The Perth and Kourou stations were part of the ESA network. The Goldstone station was provided by NASA.*

The ground communication facilities with the Villafranca ground station, used as a back-up to Odenwald ground station, consisted of telecommand link for command transmission at 2 kbps using X25 level 3 protocol; low-rate telemetry link at 1.44 kbps using X25 level 3 protocol; communication of antenna pointing data; voice loop and telephone communications facilities in connection with back-up; commanding and telemetry quick-look functions.

The ground communication facilities with the Goldstone ground station consisted of telecommand link for command transmission at 2 kbps using X25 level 3 protocol; high-rate telemetry link for transmission at 23.04 kbps using X25 level 3 protocol; voice loop, telex and telephone communications facilities.

During the routine phase the ground stations at Odenwald, Perth, Kourou and Goldstone provided support. Routine phase back-up support was given by the Villafranca transportable station. The overall ground station support throughout the mission is illustrated in Figure 4.4.

The results for station coverage predictions did not vary significantly between the various possible orbits, and indicated that Odenwald would have contact with the satellite for not more than about 32 per cent of the time. Adding Perth and Kourou would extend the coverage to about 81 per cent (but even with those extra stations, long gaps of the order of 9 to 11 hours would have to be tolerated once every four days).

Preparations were immediately started to bring the Perth ground station on-line for telecommanding, high-rate telemetry reception and tracking purposes. This involved the installation at Perth of equipment which was used in pre-launch telemetry and telecommand interface tests between the satellite and the control centre at ESOC. In addition, dedicated communications lines were ordered from the PTT. Testing of the real-time interfaces with the control centre was performed during the first weeks of

September 1989. By mid-September, Perth was declared to be fully operational, and contact with the satellite was then available for about 62 per cent of the time.

Subsequently, similar activities were initiated to bring the Kourou Galliot station on-line for high-rate telemetry and telecommanding functions, the necessary equipment being procured or retrieved from other stations. By early November 1989, this station was also able to support all required real-time interactions between the satellite and ESOC. The support from Kourou was essential for obtaining a better understanding of the attitude control performance in the perigee region, as it was the only feasible station to provide occasional coverage in this region, being located near the equator.

Coverage was subsequently further improved by the assistance of NASA, through their offer of the Goldstone Deep Space Station (DSS-16) station in the Californian Mojave desert for the Hipparcos revised mission. In order to ensure that the data interfaces with ESOC were the same as for the other stations used in the Hipparcos revised mission, it was necessary to install ESA telemetry, telecommand, and data communications equipment on-site at Goldstone. The equipment was procured and integrated at ESOC before it was transported to Goldstone at the beginning of 1990. The real-time communications interface with ESOC was quite complex, and it took considerable effort on both ESA and NASA sides to get this station in a satisfactory operational condition (in the period from mid-March to the beginning of May 1990).

Since the Kourou station coverage intervals were almost completely contained within those of Goldstone, the Kourou support was not considered to be cost-effective within the existing network of stations. Kourou support to the Hipparcos revised mission was therefore terminated by mid-1990. During the last few months of the satellite's lifetime, the station was re-implemented into the ground stations network because of reduced Goldstone support due to competing demands.

Contact with the satellite became possible for about 90 per cent of the time and the duration of loss-of-contact periods was limited to not more than 1.5 hours: this eased the operations somewhat since the on-board attitude knowledge was less likely to be lost during the non-coverage periods. However, the complexity of the revised mission operations remained significantly above what would have been considered acceptable during the design phase. The coverage percentages are shown in Figure 4.5.

4.6. Mission Planning

The Hipparcos Mission Plan was regularly generated for a seven-day period starting always five days in advance, using a specifically designed software tool on the off-line computer system at ESOC. It included all orbit and attitude related events as well as ground-triggered ones (e.g. ground station non-availability).

The generation of a mission plan was based on both manual inputs e.g. payload calibrations, ground station availability times, and automatically computed events. Validity checks were performed according to pre-defined rules and any inconsistency was brought to the attention of the operator who could then modify the inputs. The output of the mission plan tool was a time-ordered sequence of events (ground station visibility, payload calibrations, antenna switching, occultations, eclipses and apogee/perigee control parameters changing) which could trigger possible satellite or ground segment

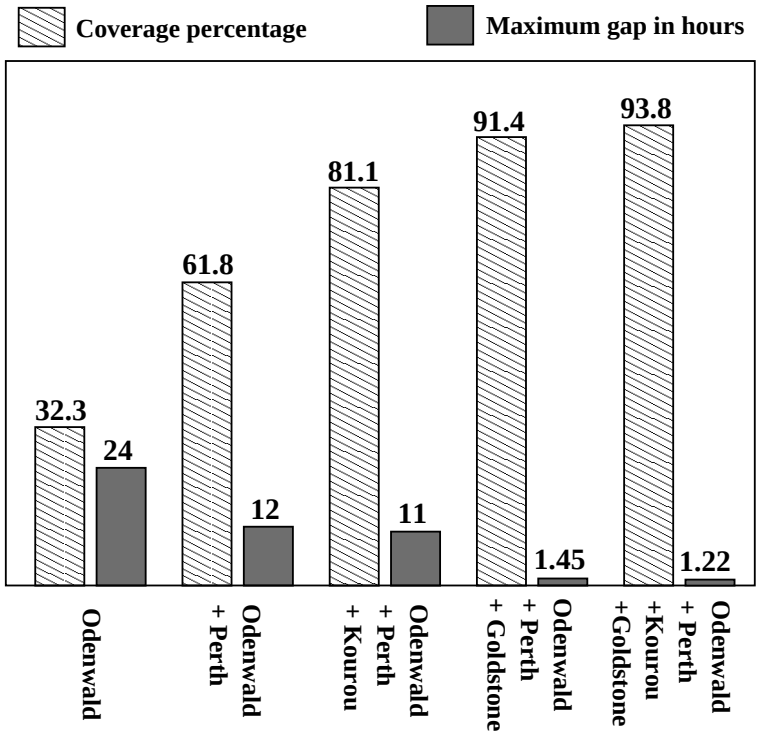

Figure 4.5. *Coverage percentage and maximum data gaps for the various ground station combinations. The Odenwald/Perth/Goldstone combination was used for most of the mission (the Kourou station adding little to this combination) with a resulting coverage of more than 90 per cent, and maximum data gaps around perigee of approximately 1.5 hours.*

related operations. From this mission plan, a chronological telecommand plan was produced automatically using pre-defined command sequences. Conflicts between the command sequences related to different events were resolved automatically according to pre-defined rules. The commands established in this manner were then transferred from the off-line computer to the on-line machine via a Hyperbus link, and were uplinked to the spacecraft at the specified times.

The mission plan had to be greatly enhanced to support routine operations for the non-nominal orbit with its period of 10 hours 39 minutes. In particular the list of computer generated events was augmented with the following items: (a) station coverage from Odenwald, Villafranca, Perth, Goldstone and Kourou; (b) spacecraft antenna to use in conjunction with the above stations; (c) periods of telemetry loss; (d) periods of commanding loss; (e) periods of perigee passage (spacecraft altitude below 6000 km); (f) periods of uninterrupted observation time; and (g) eclipse start/exit times.

The use of time-tagged commands had also been extended in order to perform spacecraft operations outside ground contact such as closing and opening of shutters for occultations, switching the perigee controller, updating the orbital oscillators, handling eclipses, etc.

A significant portion of the flight operations procedures had to be rewritten to take account of the new mission sequences adopted in the acquisition phase: the perigee raise and orbit adjustment manoeuvres, attitude acquisition sequence up to sun-pointing, and the sequence of events after solar array deployment. A considerable system analysis

effort involving individuals from ESOC, ESTEC and external experts was needed to ensure that the operations were compatible with the satellite design characteristics. All operations had to be arranged into sequences which would fit within the interval of ground station coverage (about 8 – 10 hours for Odenwald). Furthermore, it was essential that, before contact was lost, the satellite was brought into a safe configuration which would allow it to survive the long periods without ground contact.

The operations were by necessity extremely risky since the time pressure did not allow full assessment of all possible eventualities, nor to prepare for potential contingencies. Validation (as far as feasible) of the new procedures was carried out using the ESOC software simulator, often not more than one day prior to their execution in actual operations.

The failure or back-up modes for the real-time attitude control had to be revised as the nominal criterion (using the interval between thruster pulses) was no longer valid because of the high torques in the perigee region. The redesign of the operations for the revised mission had to take account of the following new constraints: (i) station contact was frequently interrupted: this resulted in the need for procedures to ensure the spacecraft and payload safety during periods without ground contact; (ii) eclipse periods were of a much longer duration (maximum of 104 minutes) and the more frequent occurrence demanded a careful monitoring of the on-board power generation and associated battery management functions; (iii) payload occultation periods occurred with higher frequency (up to 28 per day) and longer duration: this led to a higher risk in losing the on-board attitude knowledge and required more frequent support from ground. Also, more telecommand uplinks had to be prepared (to open and close the payload shutters); and (iv) crossing of the van Allen radiation belts often led to difficulties in attitude knowledge (re)-acquisitions and the data collected over these periods were not of the required quality to be forwarded to the scientific data analysis teams.

The operational support of the on-board attitude determination process was one of the most demanding tasks. Because of the long ground station loss-of-contact periods and due to the noise in the star mapper signals induced by the radiation belts, frequent loss of attitude knowledge had to be anticipated: in that case, ground control had to re-establish the on-board attitude knowledge using downlinked star mapper signals and a star pattern recognition technique. A new team for supporting these unforeseen activities around the clock was recruited and trained within a very short time. In the early days of the revised mission, this specific support was required after almost every perigee passage. New on-ground support software was implemented to prepare the manoeuvres required for achieving the recovery orbit, i.e. the perigee raise and the period adjustment manoeuvres, and the new attitude acquisition sequence.

The mission planning software had to be redesigned and extended to include many more unforeseen events related to the specific orbit characteristics and van Allen belts passage. These included (a) ground station coverage start and end times, (b) switching of the on-board torque model in the perigee region, (c) implementation of a special attitude control strategy in perigee region, (d) switching of shutters and antennae outside ground station contact periods, (e) calculation of revised eclipse durations, and (f) prediction of payload occultation intervals.

Updates to the on-board software were necessary in order to extend both the time-tagged telecommand and the programme star file buffers (see Section 8.4), which had to be sized to accommodate the many commands needed during the long periods without

ground contact. More sophisticated ground software was installed to allow real-time monitoring of the on-board attitude convergence using payload measurements.

The data interface definition between ESOC and the scientific data reduction consortia was also significantly affected by the revised mission: the necessary modifications to the interface were implemented and validated (using actual telemetry tapes) in the course of 1990.

4.7. Orbit Manoeuvres and Commissioning Activities

The initial payload switch-on and initialisation of the payload operations were conducted in the last week of September and the beginning of October 1989. The initialisation was severely hampered by extremely high solar activity with an exceptional solar flare occurring just at the time when the first star mapper samples were received: it was enough to ensure that no star transits could be observed.

After scanning law acquisition and successful calibration of the payload star mapper and main (image dissector tube) detectors, the actual scientific data collection started on 26 November 1989. The initial data recovery rate was about 50 per cent: this meant that 'good' data which could be used for the scientific data reduction were collected over about 48 hours during every four-day period, after which the ground station coverage pattern was repeated.

The computer system installed for the ground segment support was severely overloaded because of the many additional software tasks required, and the machine was replaced by a more powerful VAX computer in the beginning of 1990. This exchange resulted in extremely stable computer support conditions thereafter.

By summer 1990, the science data recovery rate had increased to about 65 per cent with the addition of the Goldstone station and because of further improvements and tuning of the operations support, mainly in the area of initialisation of on-board attitude determination and payload control.

Perigee Raising Manoeuvres

This section summarises the main events which happened, day by day, during the recovery mission implementation.

89-09-06: At 12:00:00 UTC, the spacecraft was de-spun from 37.03 to 30.05 rpm (12:00:00 UTC). The solar aspect angle at that time was 72°.46, with nutation less than 0°.05.

89-09-07: The decision having been taken to use almost all of the remaining hydrazine fuel to raise the perigee height, the first manoeuvre took place at 10:30:00 UTC and raised the perigee by 98 km.

89-09-08: A second perigee raising manoeuvre at 07:25:00 UTC raised the perigee by 102 km.

89-09-11: A third perigee raising manoeuvre at 09:14:00 UTC raised the perigee to the final target of 532 km.

Hydrazine Sun Acquisition

89-09-11: On the same day as the final perigee raising manoeuvre, the spacecraft was de-spun in two further manoeuvres. The first spin-down manoeuvre at 10:45:00 UTC reduced the spin rate from 29.49 to 19.90 rpm. The second spin-down manoeuvre at 11:45:00 UTC reduced the spin rate from 19.90 to 10 rpm.

89-09-12: Between 04:30:00 and 04:50:00 UTC, the two-stage slew to reorient the spin-axis to point at the Sun was performed. The first stage 'spin axis orientation' was performed using the on-board Earth/Sun sensor. The second stage 'hydrazine sun acquisition' used the sun acquisition sensor output. The solar panels were deployed at 05:02:00 UTC resulting in a decrease in the spin rate from 10.0 to 8.9 rpm. The fill-in antenna was then deployed.

89-09-13: The Perth ground station became operational for high-rate data telemetry.

Orbit Period Adjustment

89-09-14: The orbit was adjusted using the remaining hydrazine fuel to give a period which was commensurate with station coverage. In order to keep the spin rate within operational limits during the orbit period adjustment manoeuvres, the spacecraft was spun-up to 11.6 rpm. The first orbit adjustment manoeuvre started at 14:22:30.

89-09-15: The Perth ground station became operational for commanding.

89-09-16: The central on-board software was loaded and activated.

89-09-18: The central on-board software and payload were activated. The second orbit adjustment manoeuvre started at 13:52:00.

Hydrazine Fuel Dump

To prevent fuel sloshing during payload operations, the remaining hydrazine fuel supply was emptied out of the tanks while the spacecraft retained some degree of spin stabilisation. Following this, the helium pressurant was also drained.

89-09-19: Between 04:50:00 and 10:20:00 UTC, the first part of the remaining hydrazine was drained through cycles of firings of the hot gas thrusters. Nutation damping was performed using the cold gas thrusters.

89-09-20: Between 03:50:00 and 07:05:00 UTC, the second part of the remaining hydrazine was drained. Between 07:10:00 and 08:10:00 UTC, the helium was dumped. During the course of the fuel dumping exercise, the spin rate increased from 11.0 to 12.0 rpm.

Cold Gas Despin and Sun Acquisition

89-09-21: Between 09:30:00 and 14:14:00 UTC, the spacecraft was de-spun from 11.9 to 5.6 rpm using the cold gas thrusters.

89-09-22: Between 06:02:00 and 12:55:00 UTC, the spacecraft was de-spun in five manoeuvres from 5.6 to 0.2 rpm. After the third manouevre at 0.73 rpm, nutation damping was performed. At 13:03:00 UTC, the on-board sun acquisition software was triggered causing a final de-spin to the nominal spin rate of 168 arcsec s^{-1}. At 13:25:00 UTC, the on-board sun acquisition software was triggered orienting the spin axis of the spacecraft towards the direction of the Sun.

Real-Time Attitude Determination Initialisation

Real-time attitude determination activities proceeded as follows:

89-09-23: By collecting data at the nominal spin rate and at zero spin rate, a calibration of the biases of the sun acquisition sensor, and of the drifts on gyros 1 and 2, was performed. The sun acquisition sensor biases were uplinked to the spacecraft to optimise the sun-pointing accuracy, and the gyro drift estimates were used as first estimates for the ground real-time attitude determination software. Payload baffles were ejected on 26 September 1989, and star mapper transits were immediately detected.

89-09-27: The first attempt was made to run the ground real-time attitude determination software. Star pattern matching was achieved after tuning of the ground software. The basic angle separating the two fields of view was also calibrated.

89-09-30: The second attempt to run ground real-time attitude determination was aborted due to a solar flare giving extremely high background counts in the star mapper detectors. This phenomenon lasted several days.

89-10-04: The third attempt to run ground real-time attitude determination resulted in convergence of the ground software and an accurate attitude determination. Several attempts were made to command real-time attitude determination initialisation on-board. Convergence of on-board real-time attitude determination was not however assured, lasting for less than a minute after each attempt. The problem was subsequently traced to a problem in the ground software which was using the incorrect coordinate system for the on-board gyro drift representation.

89-10-08: The fourth attempt to run ground real-time attitude determination resulted in convergence of the ground software leading to the first successful initialisation of on-board real-time attitude determination at 10:30 UTC.

Between 9 and 31 October 1989, further successful attempts at real-time attitude determination initialisations were achieved, allowing payload calibration activities to proceed. In particular, a newly calibrated star mapper single-slit response was used to improve the performance of both real-time attitude determination and ground real-time attitude determination software.

During the same period, experiments were performed by varying the density of the programme star file. Real-time attitude determination performance was found to be

satisfactory even for losses of signal lasting longer than one complete orbit. Real-time attitude determination performance was shown to deteriorate through the van Allen belts. The need for real-time attitude determination initialisation activities after every perigee passage was demonstrated.

Scanning Law Acquisition

To bring the spacecraft from sun-pointing mode to the nominal scanning law in which the solar aspect angle was maintained close to 43°, it was necessary to perform a 'scanning law acquisition manoeuvre'. This manoeuvre was first performed on 1 November 1989, as part of the planned commissioning activities and subsequently repeated at various times in the mission when spacecraft contingencies required a return to sun-pointing mode.

The main sequence of events for the first scanning law acquisition manoeuvre were as follows:

08:15:00 The spacecraft was de-spun from 168.75 to 0.0 arcsec s^{-1}. This lasted two minutes, but there then followed a wait period of 25 minutes to account for damping of any overshoot and to prepare the next set of commands.

08:42:00 The spacecraft slewed about the −Y axis from a solar aspect angle of 0° one of 43°. A further wait period lasting 24 minutes was required to damp any overshoot.

09:22:00 The spacecraft was spun-up from 0.0 to 168.75 arcsec s^{-1}.

09:23:00 The spacecraft normal mode controller was selected to prevent any drift away from the nominal scanning law (see Chapter 8).

Before the manoeuvre start, preparation of nominal scanning law-based mission planning and programme star file was performed.

Real-Time Attitude Determination Initialisation at 43 Degrees

On 1 November 1989, having completed the scanning law acquisition manoeuvre, operations were immediately started to initialise real-time attitude determination at a solar aspect angle of 43° (i.e. according to the nominal scanning law).

Between 1 and 26 November 1989, further real-time attitude determination initialisation were achieved, allowing payload calibration activities to proceed. The commissioning phase was formally terminated on 26 November 1989, and routine operations started from that time.

Payload Calibration

The initial payload calibration activities were carried out between 4–26 November 1989, as described in detail in Chapter 5. Following this phase, routine science data collection was performed.

The following additional events took place in this period:

89-11-14: The parameters affecting the performance of the thrusters within the normal mode control software were altered for perigee passage. The transition between normal and perigee controllers was set at 18 000 km altitude.

89-11-15: Gyro 3 was activated for the first time, without problem.

89-11-20: The real-time attitude determination and central on-board software processing was enabled during the entire orbit for the first time.

89-11-23: A revised input star catalogue for the recovery mission was received.

89-11-24: The innovation thresholds within which the real-time attitude determination software would accept star mapper transit information were increased for both narrow and extended window modes.

89-11-25: Gyro 5 was activated for the first time, without problem.

5. INITIAL PAYLOAD CALIBRATION

This chapter summarises the initial activities performed at ESOC to calibrate and monitor the health of the payload prior to the start of routine operations. These calibration activities corresponded to mission critical performance aspects related to the detectors (noise, detector 'piloting', and single-slit responses of the star mapper), and to the optical distortion, focusing, chromaticity, and straylight.

5.1. Calibration Plan

Before the start of routine operations, a series of geometric and photometric calibrations were undertaken in orbit, in order to verify the payload performances in mission critical areas, and to determine the system response and geometrical transformation parameters necessary for the conduct of the mission itself. For the geostationary mission, about 20 days would have sufficed to calibrate both nominal and redundant detection chains. The revised orbit (with a period of 10.66 hours) caused this time to increase significantly due to the greatly reduced observation time, the satellite only being able to collect calibration data when: (a) there was ground station coverage, (b) there were no occultations by Earth or Moon, (c) on-board real-time attitude determination was converged, and (d) the satellite was outside regions of high background noise (the van Allen radiation belts).

The following geometric calibrations were performed by ESOC, according to the chronological order shown in Figure 5.1: (a) transformation of a star's grid coordinates into image dissector tube piloting currents (including non-linearity of the image dissector tube, rigid body displacement of the image dissector tube with respect to the grid, transverse offset of the transformation, and longitudinal offset of the transformation); and (b) chromaticity of the main field of view. In addition, the following photometric calibrations were performed: (c) detector noise, (d) modulation factors for the image dissector tube signal, (e) detector background and straylight counting rates, (f) sensitivity of the instantaneous field of view of the image dissector tube, and (g) single-slit response of the star mapper grids.

Many results from the calibration activities had a direct feedback into satellite operations. For example, the calibration of the star mapper single slit response was used to optimise

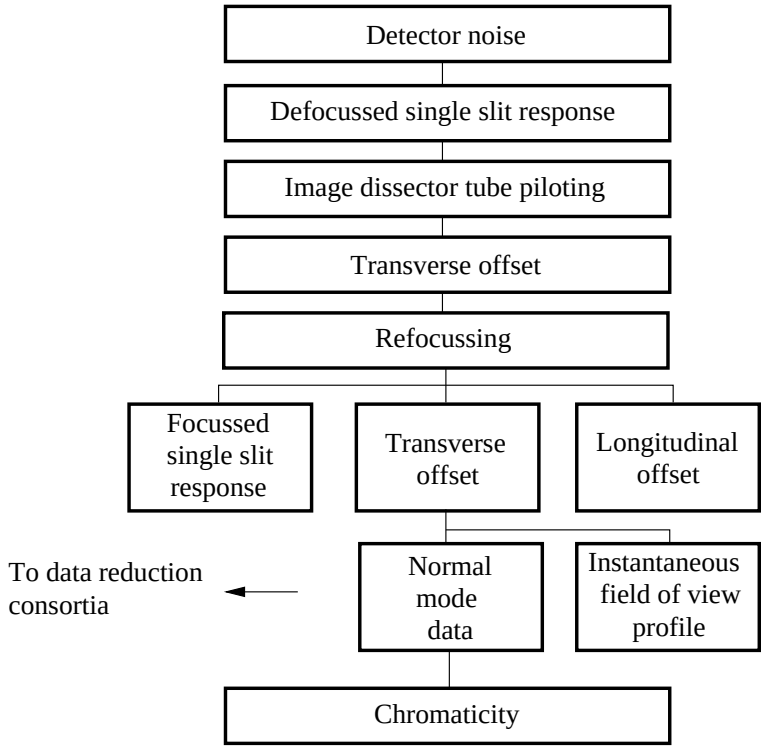

Figure 5.1. *Calibration operational plan.*

the on-board real-time attitude determination by improving the filter used to process star transits on-board. The results of the calibration of the grid to image dissector tube current transformation were regularly uplinked to the satellite to ensure optimum image dissector tube piloting.

5.2. Detector Noise

There were three detectors operating at any given time: the main grid image dissector tube, the star mapper B_T photomultiplier tube and the star mapper V_T photomultiplier tube. Each detector had a backup in case of failure making a total of six detectors on-board the satellite.

The purpose of the detector noise calibration was to measure the dark count rate of the three detectors as a function of several key parameters such as altitude, and to monitor the daily variation in the count rates. For the nominal mission this would have been rather straightforward. In the revised mission, the orbit with perigee height of about 500 km took the satellite through the Earth radiation (van Allen) belts. In addition, the calibration was performed at a solar maximum and several solar flares were observed e.g. 30 September and 20 October 1989.

Finally, various spacecraft configurations were used, in particular employing detection chains 1 and 2, shutters open and closed, and telescope baffle covers in place and released. Table 5.1 shows the results of several days processing for high altitudes (above 35 000 km). The effect of opening the shutters on 22 September was very small and

Table 5.1. High altitude count rates (above 35 000 km).

Date	Image dissector	Star mapper	Image dissector counts/sec	B_T channel counts/sec	V_T channel counts/sec	Baffle covers	Shutter status
89-09-18	1	1	1.5	8.3×10^2	7.1×10^2	In Place	Closed
89-09-19	1	1	1.9	5.2×10^2	4.8×10^2	In Place	Closed
89-09-22	1	1	3.2	8.3×10^2	7.2×10^2	In Place	Open
89-09-25	2	2	0.8	4.8×10^2	6.1×10^2	In Place	Open
89-09-30	2	2	25.0	5.7×10^4	8.4×10^4	Released	Closed

Table 5.2. Lower altitude count rates (below 35 000 km).

Date	Image dissector	Star mapper	Image dissector counts/sec	B_T channel counts/sec	V_T channel counts/sec	Altitude km	Time from perigee (hours)
89-09-21	1	1	6.6	2.4×10^3	2.0×10^3	30000	3.00
89-09-21	1	1	9.3	4.1×10^3	3.3×10^3	25000	2.21
89-09-21	1	1	22.4	1.1×10^4	8.4×10^3	20000	1.62
89-09-21	1	1	74.2	3.9×10^4	3.1×10^4	15000	1.16
89-09-21	1	1	70.6	3.6×10^4	2.8×10^4	12500	0.95
89-09-21	1	1	28.8	1.1×10^4	8.8×10^3	10000	0.77
89-09-21	1	1	11.8	5.8×10^3	4.6×10^3	8000	0.62
89-09-28	2	2	17.1	4.0×10^4	4.1×10^4	6000	0.49
89-09-28	2	2	169.5	6.1×10^5	4.1×10^5	5000	0.43
89-09-28	2	2	423.7	1.0×10^6	9.5×10^5	4000	0.36
89-09-28	2	2	613.1	1.3×10^6	1.3×10^6	3000	0.28

it was evident that chain 2 performed better than chain 1. The data obtained on 30 September showed the increase in the dark count rate when encountering a solar flare. Under these conditions, it was not easy to obtain good star mapper transits and the on-board real-time attitude determination found it difficult to maintain precise attitude estimates.

Table 5.2 gives the count levels at lower altitudes as a function of altitude for two different orbits (the satellite was not visible for the very low altitudes on 21 September). The passage through the upper radiation belt is clearly seen, with peak count rates obtained on all three detectors at about 15 000 km followed by the rates lowering to a minimum at about 8000 km before rising very rapidly in the lower belt. The values peaked at about 3000 km in the lower radiation belt but it was difficult to get coverage below that altitude due to a lack of ground stations close to the equator. The count rates fell again just below 3000 km before loss of telemetry from the satellite.

The high count rates in the photomultiplier tubes during passage through the van Allen belts, presented difficulties for real-time attitude determination (see Chapter 14). In the lower belt, noise levels were so high that they prevented any stars being detected in the star mapper data stream. This ‘blinding’ at a time when disturbance torques acting on the spacecraft were greatest rendered the real-time attitude determination periodically unable to function on-board after perigee, the real attitude being too far from that

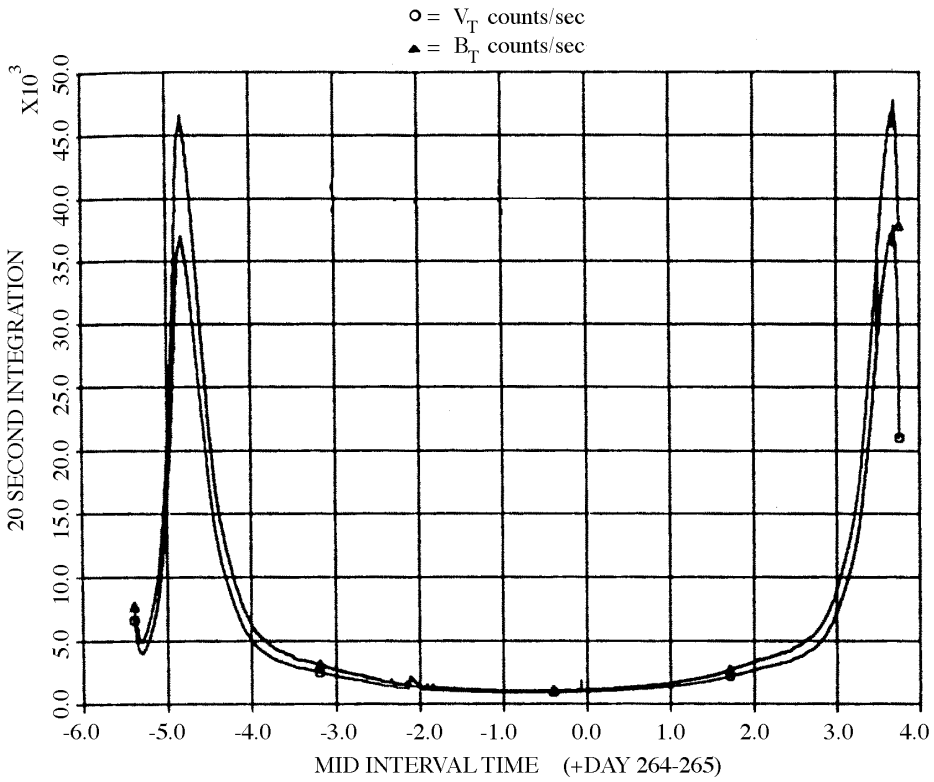

Figure 5.2. *Photomultiplier count rates for one orbit. The central region corresponds to low background count rates at apogee, with the peaks at each side of the figure corresponding to the high background count rates observed during the passage of the satellite through the outer van Allen radiation belts encountered close to perigee.*

estimated on-board. Under these conditions, manual intervention was required from ground to recompute the spacecraft attitude and correct the values held on-board. In the upper belt, it was usually possible to detect the brighter stars above the noise, allowing real-time attitude determination to operate normally. The peak noise and duration of the upper belt was highly dependent on solar activity.

Figure 5.2 shows the background rates obtained for the visibility period of a complete orbit. The two passages through the upper radiation belt are clearly visible.

5.3. Star Mapper Single-Slit Response

The on-board (and on-ground) real-time attitude determination system required accurate star mapper transit measurements. To compute reliable and unambiguous transit times, i.e. accurate times and a good certainty that the correct star had been processed, an accurate representation of the star mapper single-slit response, $S(x)$ defined in Equation 1.2, was necessary. The results of the calibration of this response were used to construct a filter that could be cross-correlated with the raw star mapper data by the on-board computer. The output of the filter allowed the transit time (position of peak) and star magnitude (height of peak) to be computed. The same filter was used by on-ground software during attitude initialisation (see Chapter 14).

The response itself was calibrated by analysing the transits of bright stars, $B < 6$ mag, across the star mapper slits. It was simple, using a filter based on *a priori* knowledge of the slit response and optimised for the actual scanning velocity of the satellite, to compute very accurate transit times for these stars. These transit times, together with pre-launch knowledge of the slit geometry, allowed the relative position of each sample with respect to the slit centres to be determined. All collected data were normalised and a least-squares estimator was used to fit a 12th order polynomial to the collected data subdivided according to B_T or V_T channel, and vertical or inclined slit system. Figure 5.3 shows four typical calibrated responses.

5.4. Initial Image Dissector Tube Piloting

The piloting of the instantaneous field of view of the image dissector tube to a star's image was performed by the on-board computer every $\frac{1}{150}$ s. To do this accurately, the following information was needed by the on-board computer: (i) *a priori* estimate of the star's position, (ii) knowledge of the satellite pointing direction, (iii) knowledge of geometric distortions in the optical system, and (iv) knowledge of the transformation between grid position and image dissector tube piloting currents.

Star Positions

The star positions were uplinked to the on-board computer in the form of a programme star file based on the pre-defined Hipparcos Input Catalogue of stars to be observed. This catalogue contained positional information for about 120 000 pre-selected stars down to a limiting magnitude of $B = 13$ mag. The programme star file produced from the Hipparcos Input Catalogue was defined relative to a nominal scanning law, i.e. the pointing directions of the two fields of view were pre-defined and uniquely identified the stars' expected transit times at the centre of the field of view together with the ordinate and drift angle at the time of transit. All this information was uplinked to the satellite for all stars to be observed. From this information, the stars' positions on the grid as a function of time from the expected transit time could be computed by the on-board computer:

$$\begin{aligned} \eta_N &= \omega_N (t - t_s) \\ \zeta_N &= \zeta_s + \mu_s \omega_N (t - t_s) \end{aligned} \qquad [5.1]$$

where:

(η_N, ζ_N) is the nominal position of the star on the grid (radians)

ω_N is the nominal scanning velocity (radians s^{-1})

t is time (s)

t_s is the expected transit time (s)

ζ_s is the expected ordinate at transit (radians)

μ_s is the drift angle of the star (radians)

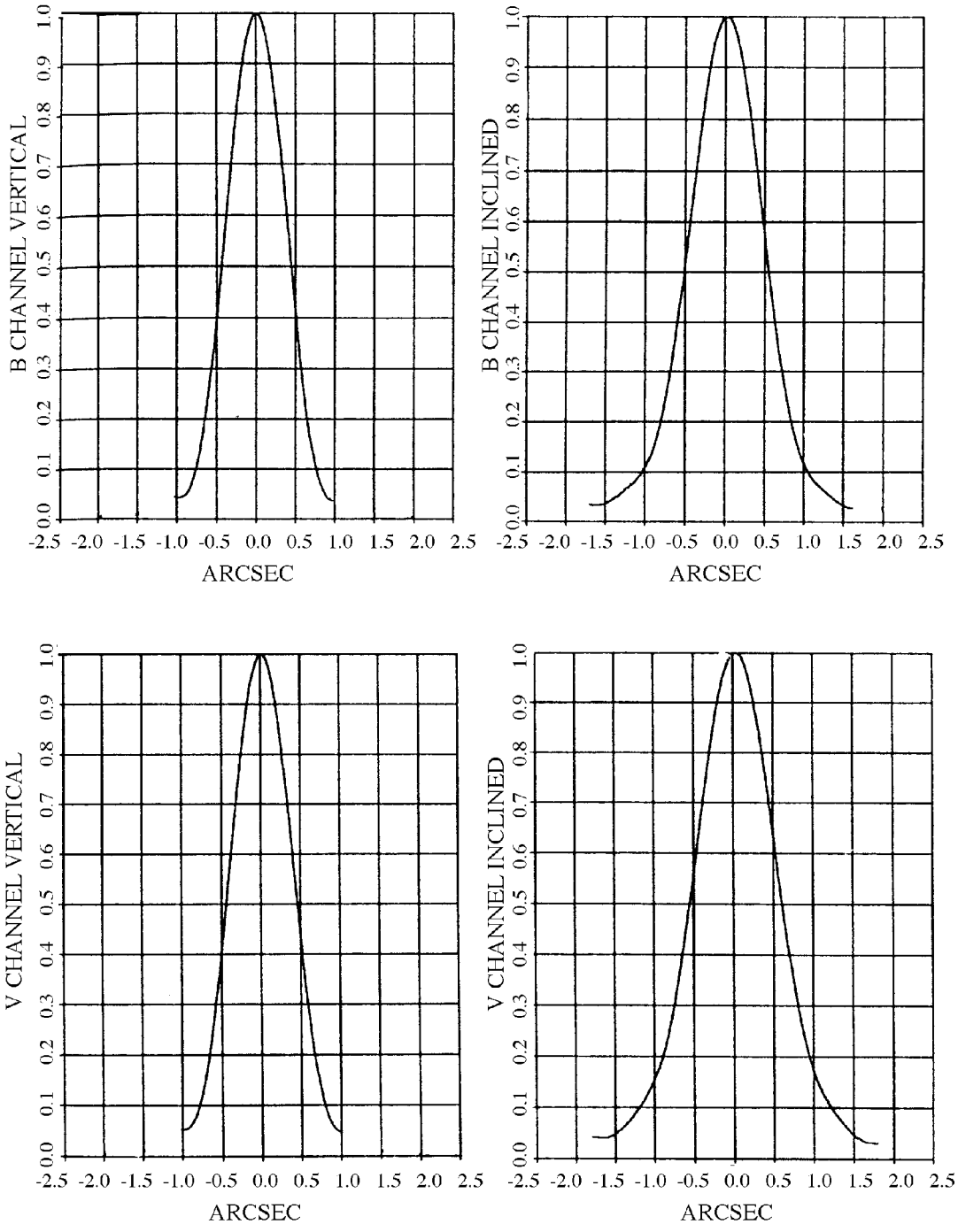

Figure 5.3. *Star mapper single-slit response for the B_T channel (upper pair), the V_T channel (lower pair), and for the vertical (left pair) and inclined (right pair) slits.*

Attitude De-Pointing and Optical Distortion

Equation 5.1 defines the position of the star on the grid assuming a perfect optical system, and assuming that the satellite did not deviate from the nominal scanning law. However, the satellite did not follow this law perfectly but was allowed to drift by up to 10 arcmin along any axis from the nominal. Also, during the initial payload calibration phase, there were the major effects of basic angle error and grid rotation to be compensated for. A final correction was made for the transverse offset of the image dissector tube.

The deviation from the nominal scanning law was computed on-board by the real-time attitude determination software as a set of three Tait-Bryan error angles (ϕ, θ, ψ) and their rates of change with time $(\dot{\phi}, \dot{\theta}, \dot{\psi})$. This is discussed in more detail in Chapter 14.

Applying all these effects together, the equations for the star's grid position (η_C, ζ_C) could be expressed as:

$$\eta_C = \eta_N + (\psi_i + f\frac{\delta\gamma}{2}) + (\mu_i + \mu_{Gi})\zeta_N - \mu_{Gi}\nu_i \qquad [5.2]$$
$$\zeta_C = \zeta_N - \nu_i - (\mu_i + \mu_{Gi})\eta_N - \mu_{Gi}(\psi_i + f\frac{\delta\gamma}{2}) + \delta\zeta_i$$

where:

$\delta\gamma$ is the correction for the basic angle error (radians)

μ_{Gi} is the grid rotation for field of view i (radians)

i is the field of view selector (1=preceding, 2=following)

f is +1 when $i = 1$, and −1 when $i = 2$

$\delta\zeta_i$ is the transverse offset for field of view i (radians)

and:

$$\mu_i = \cos(\frac{\gamma_N}{2})\phi + f\sin(\frac{\gamma_N}{2})\theta$$
$$\nu_i = \cos(\frac{\gamma_N}{2})\theta - f\sin(\frac{\gamma_N}{2})\phi \qquad [5.3]$$
$$\psi_i = \psi + \frac{1}{2}(\phi\theta - \mu_i\nu_i)$$

with γ_N the satellite's nominal basic angle (radians).

Grid Coordinates to Image Dissector Tube Piloting Currents

The electrical piloting of the instantaneous field of view to the computed position of the star's image was performed by the on-board computer using a 'coil current calibration matrix' of 11×11 points defining a regularly spaced mesh on the grid. For each point in the mesh, the electrical currents to pilot to that position were known. Thus, for any given position on the grid, the on-board computer performed a two-dimensional linear interpolation using the four surrounding points of the calibration matrix mesh to compute the best currents for the given position. The computation of the calibration matrix itself was performed by on-ground software in three steps: (i)

using an internal star pattern assembly; (ii) using grid reference marks close to the main grid; (iii) computing the coil current calibration matrix.

Internal Star Pattern Assembly

The calibration of the non-linearity of the image dissector tube piloting was performed using an internal star pattern assembly. This consisted of a pattern of 196 dummy light sources illuminated by two light-emitting diodes (see Section 2.6). These were imaged directly onto the photocathode of the image dissector tube by a switching mirror in the optical path. The on-board computer performed a special cross scan around each of these dummy light sources and on-ground software then analysed the raw telemetry generated and worked out the optimum currents that piloted the sensitive area of the image dissector tube to each of these dummy stars. The result of this calibration was a non-linearity matrix for the image dissector tube but still without any well-defined reference on the grid. This was provided by the next step.

Grid Reference Marks

The rigid body displacement of the image dissector tube with respect to the grid was computed using two fixed grid reference marks. These marks were built into the grid at known positions and illuminated by light-emitting diodes. In a similar way to the internal star pattern assembly calibration, the on-board computer scanned cross patterns around each of the reference marks and on-ground software then computed the best currents to pilot the sensitive area of the image dissector tube to each mark.

Coil Current Calibration Matrix Computation

The best currents computed in the grid reference mark calibration were used to define a transformation matrix that converted between the photocathode and the grid reference frames, i.e. the rotation and translation of the image dissector tube with respect to the grid were then known. The final step in the coil current calibration matrix computation was to use the non-linearity data obtained from the internal star pattern assembly calibration to compute the currents needed to scan to the fixed positions in the coil current calibration matrix mesh. This was achieved by performing a least-squares fit for the best currents using the four closest positions in the non-linearity matrix. If the results were in fairly good agreement with the previous coil current calibration matrix, then the new one was automatically uplinked from the on-ground software to the satellite without manual intervention. The complete cycle of telecommanding, ground processing and uplink of results could be performed automatically, driven by the mission planning software.

5.5. Transverse and Longitudinal Offsets

The first in-orbit calibration of the image dissector tube piloting was performed on 5 October 1989 and it was repeated on 19 October. As well as calibrating the non-linearity of the image dissector tube, through use of the coil current calibration matrix, it was also necessary to assess the constant offset in the transformation of a star's grid coordinates into image dissector tube piloting currents. Two offsets were assessed: in the transverse and longitudinal directions.

Transverse Offset

One effect, compensated for in Equation 5.2, was the addition of the transverse offset, $\delta\zeta_i$ for field of view i. This was caused by the photocentre of the star's image being offset from the telescope's chief ray due to the semi-circular geometry of the field of view entrance pupil. It was calibrated, in-orbit, by dedicated observations made with a modified programme star file. Instead of piloting the image dissector tube to the computed position of the star, the on-board computer piloted the image dissector tube to positions offset from the actual star image. This was achieved by the insertion of 'dummy' stars into the programme star file, with the same transit times as the actual star but with different ordinate values, ζ_s. A pattern of 10 of these 'dummy' stars was placed around each of the actual stars scheduled for observation (generally these were bright stars). By analysing the count rates at each of the 10 positions, the on-ground software could compute the offset from the actual star to the position that gave the highest count rate. By averaging many such observations, the mean offset for each field of view could be computed. The resulting offsets were then uplinked to the satellite.

Longitudinal Offset

The longitudinal offset of the image dissector tube piloting is not directly compensated for in Equation 5.2 as it was expected to be very small. This was verified, in-orbit, by dedicated observations with another modified programme star file. The special programme star file contained 'dummy' stars positioned close to an actual star with the same ordinate, ζ_s, but with modified transit times. Ground software, based on the transverse offset program, was used to compute the mean offset for each field of view. If the absolute value of the result had been the same for each field of view but with opposite sign, it would probably have been due to an error in the basic angle and could have been compensated for by modifying the value of $\delta\gamma$ used in Equation 5.2.

Image Dissector Tube Piloting Offset Results

The offset calibrations were performed four times during the calibration phase. The first calibration was carried out on 13 October 1989 before the telescope refocusing operations had been performed. Only the transverse offsets for each field of view were calibrated. The results obtained were -4.029 and -4.126 arcsec for the preceding and following fields of view respectively.

The transverse offsets were recalibrated on 1 November after refocusing, giving −3.766 and −4.251 arcsec for the preceding and following fields of view respectively. The longitudinal offsets were calibrated for the first time on 3 November after refocusing giving −1.004 and −0.380 arcsec for the preceding and following fields of view respectively.

An analysis was subsequently performed to investigate residual piloting offsets after the previous calibration. As a result, an empirical correction was introduced into the coil current calibration matrix computation. To verify this correction, both longitudinal and transverse offsets were recalibrated on 24 and 25 November 1989. The results for the transverse offsets were in good agreement with those previously obtained. Moreover the revised values for the longitudinal offsets showed a reduced spread of values about the mean, indicating that the empirical correction had been successful.

The grid rotation angle and basic angle (separating the two fields of view) were subsequently calibrated to high accuracy by the data reduction consortia. Corrected values were first used on-board on 23 January 1990, without empirical correction. The transverse offsets were recalibrated, giving −3.797 and −4.219 arcsec for the preceding and following fields of view respectively. These were the values used on-board throughout the rest of the mission. The longitudinal offsets were recalibrated giving −0.306 and −0.300 arcsec for the preceding and following fields of view respectively. The spread in the values obtained for the longitudinal offset showed a further reduction indicating a further improvement. It was not deemed necessary to re-compute any empirical corrections.

5.6. Focusing

The telescope could be refocused using a mechanism that allowed the grid assembly to move with respect to the telescope focal surface (see Section 3.2). This was necessary for two main reasons: (a) to enable the position of best focus to be determined at the start of the mission; and (b) to compensate for effects such as moisture release which altered the focus throughout the mission.

The quality of the focus for any given position of the grid assembly was assessed by ground processing of image dissector tube data collected for bright stars ($B < 9$ mag) in the central portion of a 3×3 subdivision of the main grid. As the focus was improved, the value of the first modulation coefficient, M_1 in Equation 1.1, increased. This value was determined by the ground processing software from 45 minutes of observations for each focus setting, as a function of star colour and field of view. Operationally, data was collected for ten different focus settings close to the predicted beginning-of-life position between 12 and 28 October 1989. The results are presented graphically in Figure 5.4 as a function of three colour groups.

The standard deviations of the residuals from a least-squares parabolic fit varied between 0.9 per cent and 1.9 per cent for the six cases considered.

There was evidence from this for a differential defocus, i.e. the position of best focus was not the same for each field of view. The position of best focus for the preceding field of view after launch was −44 μm and that for the following field of view was −26 μm. The actual position chosen as best overall focus immediately after launch, −35 μm, gave a differential defocus of ±9 μm. In December 1989, a revised grid scale factor was

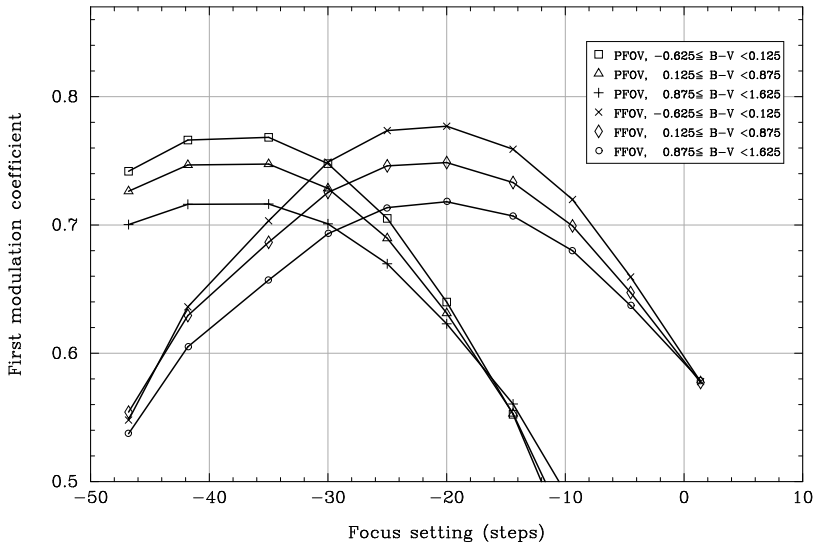

Figure 5.4. *The behaviour of the first modulation coefficient, M_1, versus focus position, and as a function of star colour and field of view. In the legend, PFOV and FFOV refer to results for the preceding and following fields of view respectively. Results are shown for three colour intervals in each case.*

computed by the data reduction consortia which improved the accuracy of observations. This had the effect of increasing the estimates of M_1 by approximately 5 per cent. The results from the calibration were in excellent agreement with pre-launch prediction of the optical performance. As stated above, the position of best focus evolved continuously due to moisture release and other effects (see Chapter 10). The refocusing calibration was performed at regular intervals throughout the mission with the objective of keeping the focus position on-board within one step ($\pm 1.2\ \mu$m) of the best focus position.

5.7. Instantaneous Field Of View Profile

The sensitivity profile of the image dissector tube was defined by a normalised transmission factor, $T(x)$, which defined the proportion of the observed star intensity obtained as the image dissector tube was depointed away from a star by x arcsec. It was important for the data analysis consortia to know this sensitivity profile, in particular for the processing of data for close double stars. The profile was calibrated, in-orbit, using a special programme star file containing 'dummy' stars deliberately positioned away from chosen bright stars. Ground software was used to compute the profile as a function of position in the field of view (on a 3×3 subdivision of the grid), star colour (3 colour groups), and offset distance (in arcsec).

Because of the instantaneous field of view profile's dependency on many parameters, over 20 hours of data between 9 and 21 October 1989 were collected and processed. The average of all profiles computed is shown in Figure 5.5.

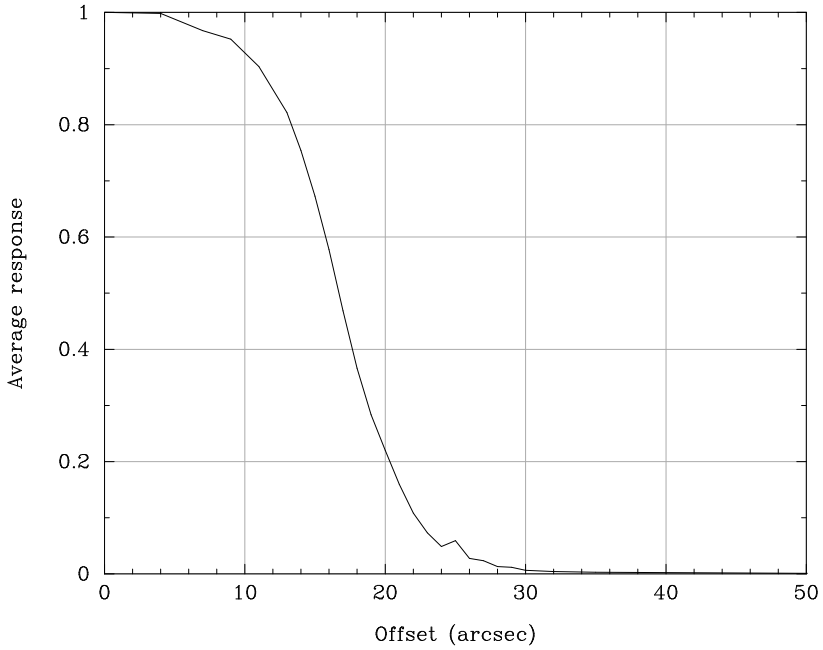

Figure 5.5. *Mean instantaneous field of view profile. The response profile is rather flat within ±10 arcsec from the centre, thereafter dropping steeply towards zero at around ±30 arcsec.*

5.8. Chromaticity

The chromaticity of the main field of view was defined to be the displacement of the photocentre of the image of a star of 'extreme' colour, $B - V = -0.25$ mag or $B - V = 1.25$ mag, compared with the photocentre of a star of typical colour, $B - V = 0.5$ mag. The (very small) chromatic displacement of the star images as a function of colour resulted from the form of the diffraction image, and was calibrated in-orbit using a special filter built into the payload (see Chapter 2). During calibration the filter was moved into the beam, by telecommand, between the grid and the image dissector tube. It caused the image of a star to be split into two images, red and blue, separated by approximately 60 arcsec. By piloting the image dissector tube to the two spots, quasi-simultaneously, data could be collected for further ground processing. This processing consisted of estimating the phase difference between the two image dissector tube signals using Equation 1.1 for each image separately. A resulting chromaticity map was built up, as a function of star colour and position in the field of view.

The associated image dissector tube signals for the two spots were measured, from which a phase difference for the two signals could be calculated. The phase differences were converted to chromaticity estimates by the following formula:

$$C_i = (\Psi_{1,i} - \Psi_{2,i}) \frac{\Delta\lambda}{\Delta\lambda_s} \qquad [5.4]$$

where $\Psi_{1,i}$ is the phase estimate for the blue spot associated with star i, $\Psi_{2,i}$ is the phase estimate for the red spot associated with star i, $\Delta\lambda$ is the effective wavelength difference

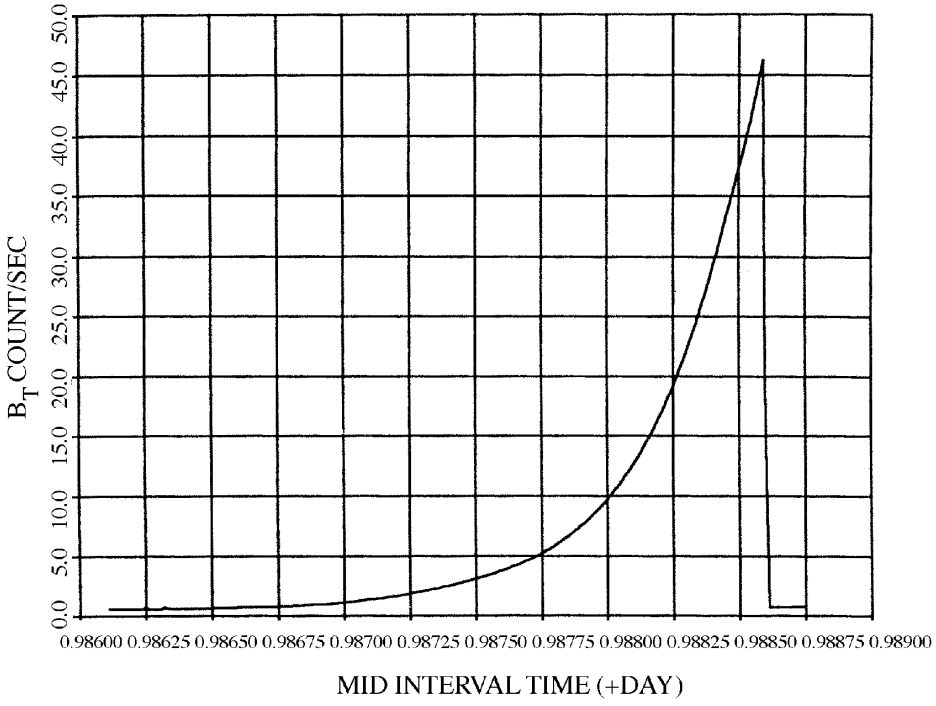

Figure 5.6. *Star mapper background (B_T) leading up to automatic shutter closure on 6 November 1989.*

between the images of a star of extreme colour and one of average colour, and $\Delta\lambda_s$ is the effective wavelength difference of the blue and red star images formed by the chromaticity filter assembly.

Each estimate was allocated a weight computed from the expected variance of the estimation. The final chromaticity map was produced by computing the weighted average of the individual chromaticity estimates in each of the mesh bins.

The first calibration was performed between 22 and 24 November 1989, giving an average value over both fields of view of −0.27 milliarcsec. Subsequently, more refined calibrations were performed by the data reduction consortia (see Volume 3), and the instrumental chromaticity was also estimated from the great-circle and sphere solutions.

5.9. Straylight

Straylight count rates for both star mapper and image dissector tube were calibrated. For the star mapper, background count rates entering and leaving an occultation were measured. Under normal operations, both image dissector tube and star mapper shutters were closed by ground command, for the protection of the detectors themselves. In addition, there was an automatic shutter closure facility on-board the satellite that closed the shutters if the count rate in the B_T channel became too high. This mechanism was exercised on 6 November 1989. The resulting rise in background rates culminating in shutter closure is shown in Figure 5.6.

The telemetry collected during the instantaneous field of view profile calibration also contained many observations away from programme stars permitting measurement of the sky background count rate on the image dissector tube. The algorithm used was to position a dummy star in the programme star file away from the programme stars. Analysis of the image dissector tube data was then performed and the modulation coefficients were computed. Any observation with $M_1 < 0.325$ was rejected and observations close together in time were averaged. In total, there were 3043 observations during this phase of the initial payload calibration, with a mean of 36 counts/sec and standard deviation of 16 counts/sec.

6. THE OPERATIONAL ORBIT

Planned to be operated in geostationary orbit by means of a single ground station, the satellite was actually operated from a highly elliptical (geostationary transfer) orbit. The parameters of the actual orbit are given, along with a summary of the features of the elliptical orbit which complicated the satellite operations and performances: the resulting radiation environment (considered in more detail in Chapter 7), eclipses (affecting the power budget), Earth and Moon occultations (affecting the observation programme), and the complex ground-station requirements—a single ground station would have resulted in a maximum of 30 per cent of useful data collection, and additional ground stations had to be rapidly brought into the telecommunication network. The problems affecting the satellite attitude control—perturbing torques especially those around perigee, and the consequences on the real-time attitude determination, and the (general) problem of micrometeoroid impacts—are discussed.

6.1. Orbital Elements

The orbital characteristics for the epoch 18 September 1989, when the revised mission manoeuvres had been completed, were as follows:

- perigee height: 526 km
- apogee height: 35 900 km
- orbital period: 640 min
- eccentricity: 0.72
- inclination: 6°.8
- ascending node: 105°
- argument of perigee: 214°

The observed evolution of some of these parameters during the mission is shown in Figure 6.1 and Figure 6.2. Additional information on the orbit evolution can be found in Volume 3, Chapter 8.

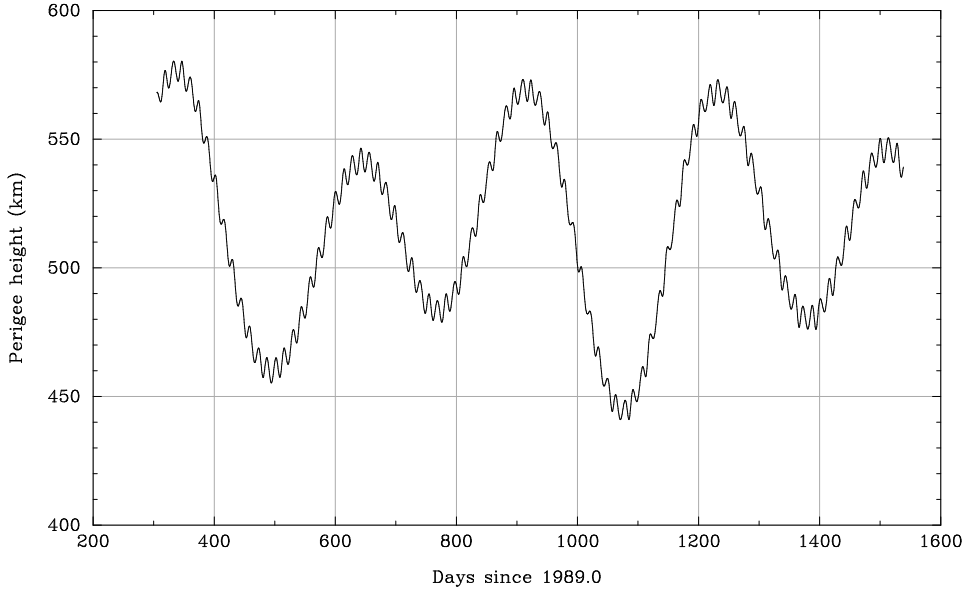

Figure 6.1. *Evolution of perigee height during the mission.*

For Hipparcos, a critical assessment of the accuracy and precision of the orbit data was essential. Preliminary analysis of the orbit determination accuracy assumed a perigee altitude of 600 km and three ranging stations. The covariance analysis showed that the semi-major axis could be determined to better than 10 m and the inclination to about $0\overset{\circ}{.}001$. The positional and velocity accuracy would vary along the orbit, as shown in Table 6.1. These data compared well with the orbit determination accuracy at that time:

- perigee/apogee altitude: ±150 m
- semi-major axis: ±50 m
- inclination: $\pm 0\overset{\circ}{.}2$
- apogee position: ±1.5 km
- apogee velocity: ±0.08 m s^{-1}

Specifications for the revised orbit included an instantaneous knowledge of the position to 1.5 km (in order to be able to account for positional observations of solar system objects), and the velocity to 0.2 m s^{-1} (in order to be able to correct for aberration). These criteria were achieved by the adopted ranging and orbital reconstruction procedures.

The orbit data, which included the time interval, the state vector components at a given reference time in the mean equinox of date frame, auxiliary Keplerian motion parameters, and Chebychev expansion of each of the six state components, was sent to the data reduction teams with the telemetry data.

Table 6.1. Variation in the position and velocity accuracy along the orbit.

Time since perigee (hours)	Position accuracy (km)	Velocity accuracy (m/s)
0.0	0.87	0.78
0.5	0.70	0.32
1.0	0.79	0.18
2.0	1.03	0.11
3.0	1.20	0.07
4.0	1.28	0.06
5.0	1.30	0.06

6.2. Radiation Environment

The revised orbit meant that the satellite was subject to a much higher particle radiation exposure than anticipated prior to launch. Consequently, radiation damage to the solar arrays and other payload and spacecraft equipment was higher than had been anticipated. In particular, the increased radiation led to the progressive degradation of the solar arrays, difficulties in maintaining the on-board attitude control and the failure of the satellite gyros. Details of the associated problems are presented in more detail in Chapters 7, 11, and 15.

6.3. Eclipses

In geostationary transfer orbit between zero and six eclipses due to the Moon occurred annually, with an average of three. The duration of these eclipses ranged from a few minutes to over four hours. Long eclipses occurred at the Sun-Moon-apogee-Earth conjunction. Eclipses by the Earth occurred about four times per day, with a duration range of a few minutes to more than one hour. Long eclipses occurred at a Sun-Earth-apogee conjunction. The duration of the eclipses are illustrated in Figure 4.1.

The distribution of eclipse durations are tabulated in Table 6.2. During its lifetime the critical eclipses for Hipparcos were March 1989 (eclipse duration 104 min), April 1993 (63 min) and August 1993 (82 min).

Coupled with the solar panel degradation problem was the fact that, in the elliptical orbit, the eclipses of the Sun by the Earth were much longer (up to 100 min) and much more frequent than in the geostationary case. During eclipses, the spacecraft could only function by extracting power from its batteries. Thus the power deficit problem was enhanced during the period of the longest eclipses and had to be solved with more drastic measures. Detailed power budgets and the relevant operational procedures were prepared to ‘hibernate’ the spacecraft in such cases when the batteries could not supply enough energy to maintain a fully nominal mission throughout the eclipse.

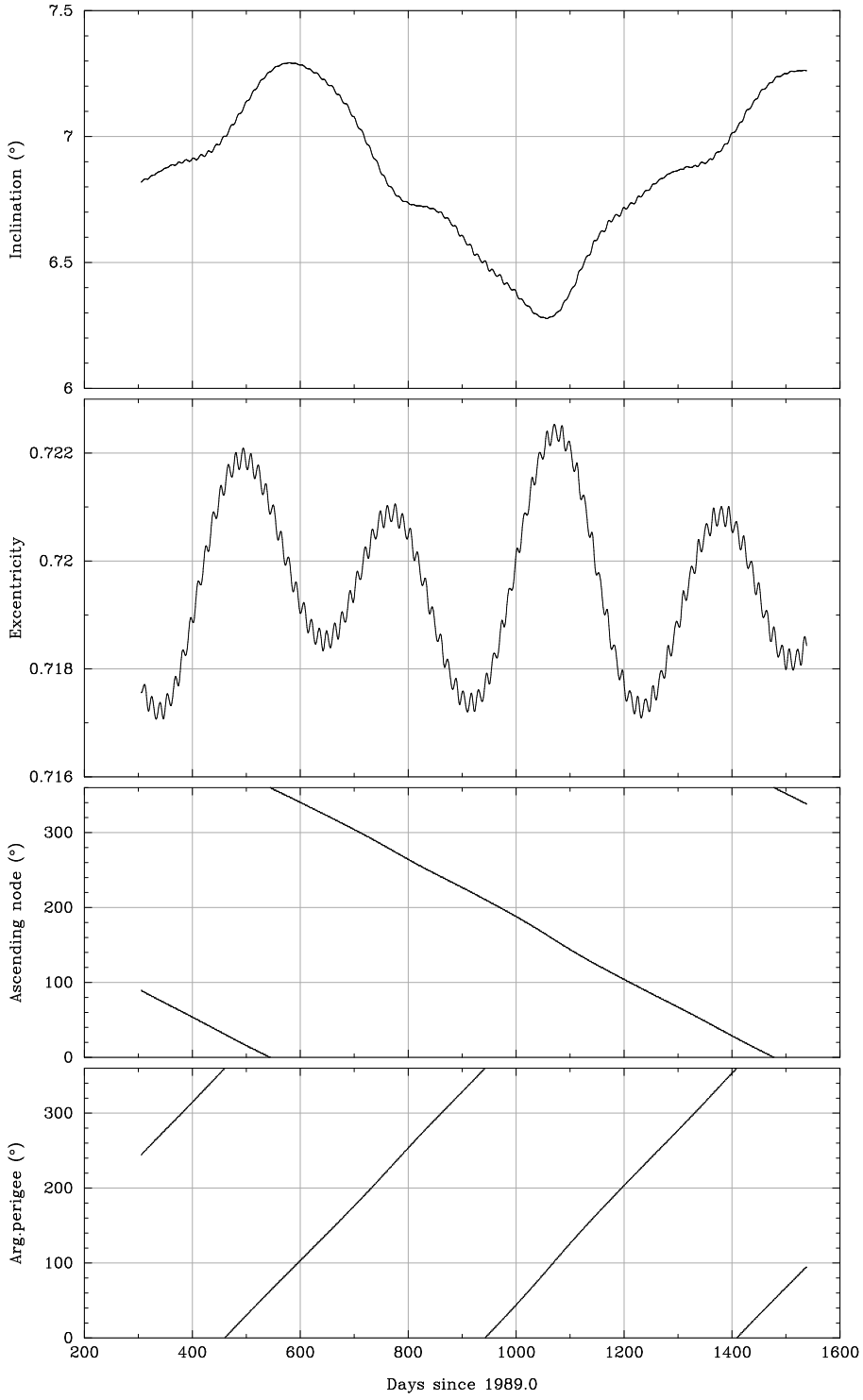

Figure 6.2. *Evolution of inclination, eccentricity, and angle during the mission.*

Table 6.2. Distribution of eclipse durations for a three-year mission in geostationary transfer orbit (approximately 2500 orbits).

Eclipse duration	%
0 to 20 min	18
20 to 30 min	44
30 to 60 min	26
over 60 min	12

In order to survive the long eclipse period (up to 104 min), a power saving strategy was developed, which guaranteed a positive power budget by decreasing or switching off loads. As a reference criterion the remaining time between end of charge of the batteries and the start of the next eclipse was taken. This time was calculated and extrapolated in real-time to ensure immediate implementation of the relevant power saving procedures. However, no such drastic measures were actually needed up to 30 March 1993, since even at the longest eclipse times the batteries were always fully charged before the next eclipse entry.

6.4. Occultations

Occultations occurred when one of the two fields of view crossed the Earth or the Moon. The payload detectors would have been damaged by these events, if they had not been shielded by shutters which closed at these times. The Earth occultations, like the eclipses, occurred more frequently and lasted longer in the elliptical than in the geostationary orbit, again reducing the amount and uniform time coverage of good science data. Also, when they occurred near perigee, they increased the risk of loss of attitude control by blinding the star mapper.

6.5. Ground Station Coverage

One of the most serious operational consequences of being in a geostationary transfer type orbit is that one ground station is not sufficient to track the satellite at all times. At the beginning of the mission, complete operational support was only available for about one third of the time, posing major problems on how to manage the mission outside visibility periods. The major problems to be solved were how to keep real-time attitude determination convergence until the next visibility period and how to protect the spacecraft, with appropriate reconfigurations of the subsystems, against such events as eclipses, occultations, perigee passages and possible on-board failures.

As described in Chapter 4 the number of ground stations was quickly increased to three. However, the lowest part of the orbit was only rarely trackable, and in any case only from Kourou (near the equator).

6.6. Perturbing Torques

In geostationary orbit, the only significant external disturbance torques acting on the spacecraft were expected to be due to the solar radiation pressure and the constantly spinning gyros. However, away from apogee of the revised orbit, other effects became significant, e.g. atmospheric, magnetic dipole and gravity gradient torques all played a role depending on the altitude and attitude of the satellite. Their combined effect degraded the on-board attitude control to the extent that ground support was often required. In addition, greatly increased cold gas consumption was necessary to control the attitude through these variable conditions, implying a shorter lifetime, based only on consumables. The higher torques also degraded the on-ground attitude determination.

6.7. Loss of Real-Time Attitude Determination

The difficulties involved in controlling the spacecraft attitude in the revised mission, arose from the critical link between the stellar measurements, the attitude measurements made on-board, and the attitude control. The approximate positions of all stars to be observed by the main detector were uplinked to the satellite in the form of expected times at which the stars were predicted to cross the star mapper slit measurement system, based on the nominal attitude of the satellite. The actual star transits across the star mapper slit system were detected and converted into actual crossing times. These times allowed the on-board computer to calculate the difference between the nominal and actual satellite attitude for a subset of the brighter programme stars.

Radiation from the van Allen belts blinded the photomultiplier which sampled the star mapper data: the on-board processor was then not able to filter out a star transit from the noise. At such times, the spacecraft was without external references and had to rely on the gyros alone for real-time attitude determination, except for increasingly refined modelling carried out towards the end of the mission allowing attitude control in the absence of one or more gyros (see Chapters 14–16). Close to perigee, the external disturbance torques were greatest, causing long thruster firings approximately once per minute. Studies later in the mission suggested that the gyro drifts also evolved more quickly around perigee. Both phenomena combined to cause a drift of the spacecraft without correction from the star mapper.

When the real-time attitude determination estimate differed by more than 10 arcsec from the actual spacecraft attitude, ground intervention was required to increase tolerances to the maximum value of 30 arcsec. If the real-time attitude determination estimate differed by more than 30 arcsec, further intervention was required using ground software to re-initialise real-time attitude determination. The resulting effects are described in more detail in Chapters 13 and 14.

6.8. Micrometeoroids

A potential hazard faced by satellite experiments is the impact of micrometeoroids. Although no specific events were ever attributed to micrometeoroid impacts on the Hipparcos satellite, a careful evaluation was made of the expected effects in advance of launch, both in order to assess possible attitude perturbations caused by impacts with the more common, lighter particles, and the risk of catastrophic damage by the rarer but more massive particles. In view of its applicability to other missions, a summary of the predicted effects are therefore given hereafter.

A dust experiment on HEOS-2 provided much data on the micrometeoroid environment in near-Earth orbit. The data could be categorised into three groups according to the observed rate. Event rates of 1 or more events per 15 min were classified as swarms, between 1 event per 15 min and 2 events per day was considered a group, and fewer than 2 events per day was attributed to random particles. Analysis of the event rates indicated that the apex particles (where the apex is the direction of the Earth's velocity around the Sun) were most frequent. Their average impact velocity was around 10 km s^{-1} resulting in a flux of $\phi_{apex} = 4 \times 10^{-4}$ m^{-2} s^{-1} $(2\pi \text{ sr})^{-1}$ for masses $\geq 10^{-12}$ g. The 'ecliptic-south particles', although almost as frequent as the apex particles, were much smaller and faster giving a correspondingly lower flux. These latter particles are believed to be fragmentation products from larger micrometeoroids.

An important result from the HEOS-2 experiment was that more than 80 per cent of all the detected particles arrived in swarms or groups. The groups showed a correlation with the Moon position suggesting a lunar origin—these particles may be ejected from the Moon's surface by impacting meteorites in the kg range. The swarms were found mainly in the near-Earth part of the orbit, and showed no lunar correlation prompting suggestions that they may be produced by meteors impinging on the Earth's atmosphere.

Simulations of the Effect of Micrometeoroids on Hipparcos

Simulations based on published data (Naumann, 1966) were undertaken before launch to assess the effect of micrometeoroid impacts on Hipparcos in orbit. The simulations were constructed as follows: (i) the satellite was hit by a random sized meteoroid at times which were uniformly distributed within the interval 0 to 10 000 s; (ii) the meteoroid velocity (v) was uniformly distributed in the range $\pm$ 47 km s^{-1}; (iii) each impact reached a target point on one of the solar panels at r = 1.8 m from the centre of the satellite and hits on the satellite body were neglected; (iv) the number of hits was calculated from the flux data as twice the product of the cumulative flux (for particles heavier than 1×10^{-15} kg), the total area of the solar panels (6.8 m^2) and the integration time. The factor of two arose from allowing both forward and backward hits; (v) the cumulative flux (given in impacts per m^2) of Landolt-Börnstein (1981) was used:

$$\phi = 5 \times 10^{-5} \left(\frac{m}{10^{-15}} \right)^{-0.4} \quad \text{for} \quad m < 1.4 \times 10^{-10} \text{ kg} \qquad [6.1]$$

$$\phi = 2 \times 10^{-1} \left(\frac{m}{10^{-15}} \right)^{-1.1} \quad \text{for} \quad m > 1.4 \times 10^{-10} \text{ kg}$$

This gave a change in angular momentum per hit of $\delta L = mvr$, and a change in angular velocity of $\delta\omega = \delta L / I$, where a mean value ($I = 400$ kg m^2) of the satellite's moment of inertia was used.

In this way successive impacts gave positive or negative increments of the angular velocity. In each time interval between hits, the velocity increment was integrated up to a change in angle. The nominal rotation of the satellite and the smooth perturbations due to solar radiation pressure were not included, so that the results only represent the additional effects caused by micrometeoroids.

The cumulative flux was also used to predict the masses of the impacting meteoroids. The data can be represented by the relation:

$$\left(\frac{m}{m_0}\right)^a = \frac{\phi}{\phi_0} = R \qquad [6.2]$$

where m_0 is the smallest mass considered, ϕ_0 is the flux of particles with $m > m_0$ and a is a negative constant. Two different values of a were used: $a = -0.4$ for m $< 1.4 \times 10^{-10}$ kg and $a = -1.1$ for higher masses (see Equation 6.1). Masses consistent with the flux data could be generated according to the formula:

$$m = m_0 R^{a^{-1}} \qquad [6.3]$$

when R is uniformly distributed between 0 and 1. To increase the number of data points, angle values were linearly interpolated between impact times such that one data point was obtained for every 10 s of the 10 000 s interval. A cubic spline was then fit with a knot every 100 s and the difference between the data and the spline function was then calculated. The residuals of this fit were taken as a measure of the micrometeoroid effect. A total of 1000 simulations of 10 000 s were made.

The results showed that the most frequent residual lay around 1×10^{-5} arcsec which was a factor of 10^{-3} smaller than the expected accuracy of the individual measurements made by the Hipparcos instruments. Only a few of the 1000 simulations had rms residuals in the vicinity of 10^{-2} and the median rms effect was 2.6×10^{-6} arcsec. In 2.5 years the simulations predicted about 500 impacts resulting in residuals $> 10^{-2}$ arcsec. The single largest impact during that period was predicted to produce residuals of the order of 10 arcsec.

The following analysis of the micrometeoroid problem also yielded similar results. Taking particles with mass $m = 10^{-12}$ g as representative, a satellite moment of inertia, $I = 350$ kg m^2, $v = 30$ km s^{-1} and an impact distance of $d = 1$ m from the center of mass yielded: $\delta\omega = mvd / I = 10^{-8}$ arcsec s^{-1}, with an average occurrence of about 1 event per 100 s. At the extreme end of the mass range (see Figure 6.3) particles of mass 10^{-3} g would give an increment to the spin velocity of approximately 10 arcsec s^{-1} about once per year.

The conclusion of these studies was that it was unlikely that most micrometeoroid impacts would have any major effects on the accuracy of the Hipparcos observations, but that larger, more infrequent events could significantly perturb the satellite attitude. In reality, it was difficult to ascribe any evolution of the satellite attitude unambiguously to the effects of micrometeoroids, and they certainly resulted in no evident threat or degradation of the mission performances.

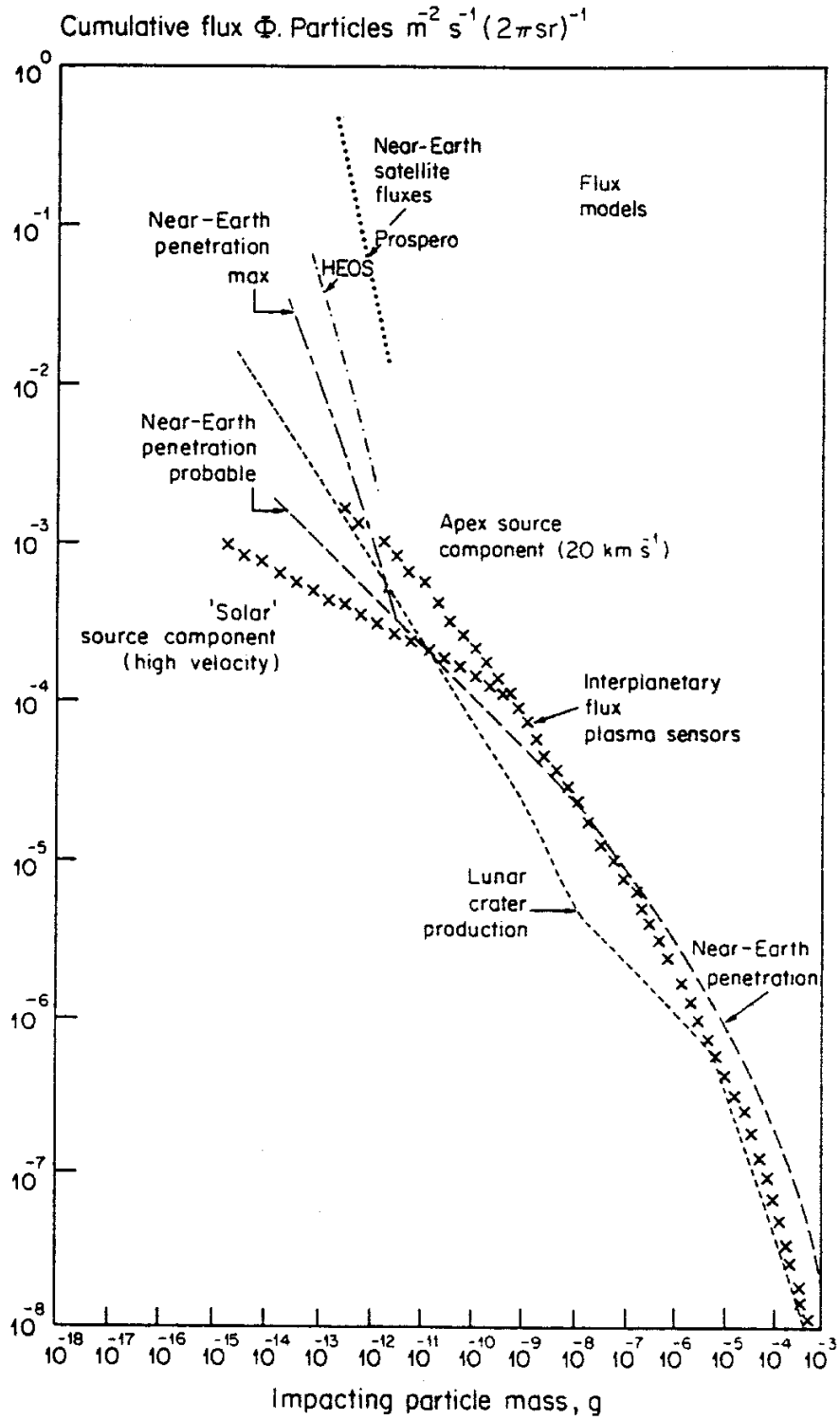

Figure 6.3. *Inter-comparison of models of the cumulative particle flux derived from near-Earth satellites, interplanetary probes and lunar flux measurements (from Cosmic Dust, J.A.M. McDonnell, 1978).*

The 1993 Perseid Meteoroid Shower

Although the Hipparcos mission was terminated before the 1993 Perseid shower, a careful evaluation of its potential effect was made, since periodic, seasonally correlated enhancements of meteoroid flux towards the Earth are quite normal, and are associated with trails of dust material along cometary orbits which the Earth crosses at fixed times of the year. The given maxima are very stable in terms of epoch, but they may increase considerably if the Earth crosses the path of the comet shortly after the comet itself.

As simulations had shown, the impact of meteoroid showers on the Hipparcos satellite during its mission were in general expected to be almost negligible. An exception to this might have been the 12 August 1993 Perseid shower, which was predicted to be unusually strong as a result of the perihelion passage of the Perseid's source comet, Swift-Tuttle, the previous year (31 December 1992). This expectation was based on analogy with the largest known meteor storm prior to this, the 17 November 1966 Leonid storm. Both the Leonids and the Perseids are of cometary origin, the former being associated with comet Temple-Tuttle with a period of 33.25 years, the latter with comet Swift-Tuttle with period 130 years. Prior to the storm of November 1966 there was a steady increase in Leonid meteoroid activity, a pattern also seen in the tenfold increase in Perseid activity in the previous two years. Less than one year prior to the Leonid storm the source comet passed its perihelion. The Perseid's source comet, Swift-Tuttle, passed its perihelion less than one year prior to expected storm activity.

At the time of the 1966 Leonid storm the Earth was within 450 000 km of the comet's orbital plane. During the Perseid storm the Earth would be within 140 000 km of the comet's orbital plane. The increase in meteoroid flux, above the mean background, for the Leonid 1966 storm was more than a factor of 1000. The increased Perseid activity was expected to be even greater than this. In particular the flux enhancement with respect to the average meteoroid background flux was expected to be of the order of 1000 or more (it has been shown that during periods of meteor storm activity, the impact probability increases by more than 10^4 over the sporadic background of meteoroids; see Beech, Brown & Jones, 1995). This would imply approximately 0.5 hits m^{-2} hr^{-1} by meteoroids of diameter larger than 0.1 mm on an exposed satellite surface. The impact velocity was expected to be of the order of 60 km s^{-1}, giving an equivalent penetration depth in Al of 5 to 10 times the diameter of the projectile. A 1 mm projectile could cause substantial damage, and even smaller particles of 0.1 mm diameter could disable sensitive spacecraft components such as the solar arrays.

Given the potential risk to the spacecraft and its components from the 1993 Perseid shower, ESOC carried out an assessment of the flux geometry for the predicted time of the Perseid storm relative to the spacecraft. The spin-axis of Hipparcos pointed towards the Sun and thus only the smaller side of the satellite (3.5 m^2) could be targeted by the meteoroids. The configuration between the meteoroids stream and the Sun indicated that the Perseid storm would not be dangerous to Hipparcos. Since the solar arrays were oriented towards the Sun, the solar arrays and the meteoroid stream were almost in the same plane (i.e. the Sun direction was $\alpha = 142°$, $\delta = 15°$, and the Perseid stream was $\alpha = 46°$, $\delta = 58°$). The angle between the two directions was about $80\overset{\circ}{.}5$ and thus the angle of impact would be about $9\overset{\circ}{.}5$ from the rear of the solar arrays, giving a reduction in the projected surface area of a factor of 6. On this basis it was considered that the overall risk to the spacecraft from this exceptional Perseid storm was not unduly alarming.

7. RADIATION BACKGROUND AND RELATED EFFECTS

The most critical problem faced by the satellite, and consequently also impacting on its operations, was the radiation environment in the geostationary transfer orbit. The regular crossings of the van Allen radiation belts meant that the satellite was repeatedly exposed to very high proton and electron radiation levels, much higher than those for which the satellite and payload were designed. The radiation damage resulted in the progressive degradation of the solar array performance (described in Chapter 11), heater anomalies (Chapter 12), the failure of the gyroscopes (Chapters 13–16), and eventually the loss of the mission through failure of the telecommunication subsystem. In addition, the radiation environment was responsible for an increased star mapper signal background which complicated and degraded the real-time attitude determination, as well as the Tycho data analysis.

7.1. Introduction

The Hipparcos payload was known and predicted to be sensitive to background signals induced by energetic electrons and protons. Radiation effects were an important consideration even in the planned geostationary orbit, and careful analysis of the focal plane shielding was made before launch.

After the failure of the apogee boost motor to raise the satellite into its planned orbit, there was concern that the considerably harsher radiation environment of geostationary transfer orbit would severely limit the mission lifetime due to solar cell degradation or component failure. It is likely that the eventual failure of four out of five gyroscopes was due to radiation damage to control electronics. There was an additional initial concern that the background signal induced in the telescope systems by energetic particle hits on the optics or the photomultiplier detectors would strongly limit the possible observation time during the orbit.

This chapter provides a summary of the radiation environment in near-Earth orbit, and details the effects of the radiation background on the satellite. From the perspective of understanding the radiation environment in geostationary transfer orbit, the Hipparcos observations over the mission lifetime yielded a long-term data set which strongly reflects the structure of the radiation belts, their dynamics and the effects of solar particle events.

7.2. The Radiation Environment in Space

The space radiation environment presents a hazard to most satellite missions, irrespective of the orbit. There are many high-energy particle populations in the different regions of space which can cause damage to spacecraft and instrument components. In addition they can give rise to detector interference, single-event upset and electrostatic charging.

Some regions, however, pose more of a threat to satellite experiments than others. For example, the trapping of charged particles, in particular electrons and protons, by the Earth's magnetic field, creates the toroidal radiation belts known as the van Allen belts. As a consequence of being in geostationary transfer orbit Hipparcos crossed the van Allen belts slightly more than four times per day. The inner belt, between 1000 and 4000 km from the Earth's surface, contains mainly high-energy protons, while the outer belt between 8000 and 12 000 km, contains high-energy electrons. The degradation of directly exposed subsystems, e.g. solar generators and electronic equipment, are important because of repeated exposure to radiation. Out of the van Allen belts, radiation rates are caused by particle events and galactic cosmic rays, and these can induce single event upsets.

During the early part of the mission, the effects of the radiation background on the solar array performance was considered to be a crucial factor in the overall satellite lifetime, and a particular effort was therefore devoted to understanding and predicting the solar array in-orbit power loss due to radiation damage. In practice, this was based on a correlation of laboratory solar-cell radiation damage data with an estimate of the radiation dose for the anticipated spacecraft trajectory. This estimate, therefore, also required an accurate knowledge of the spacecraft flight path exposure to the Earth's charged-particle trapping domains.

Steady improvements and refinements to our knowledge of the magnetosphere have been made since the discovery of the van Allen radiation belts in 1959. Static trapped-particle-environment models have evolved to the point where spatial and temporal variations may be allowed for. The radial electron and proton flux profiles depicted in Figure 7.1 demonstrate the complexity of the task and why different types of orbits will be damaging or benign. The prediction of solar particle event proton fluxes is more difficult, and present models are based on a probabilistic analysis involving mission duration and event confidence levels (Feynman *et al.*, 1992; Tranquille & Daly 1992). The high solar particle event doses in the lower energy range can be particularly damaging for spacecraft in eccentric or geostationary orbits (36 000 km) whereas spacecraft in low-inclination, near-Earth orbits (600 km) are protected from solar particle events by geomagnetic shielding effects.

The radiation belt models used in the analysis of the Hipparcos data are AE8 and AP8. AE8 (Vette 1991) is a model for the electron environment for energies of 40 keV to 7 MeV and altitudes of 1.2 to 11 Earth radii. Since solar activity can have a pronounced effect on the radiation environment experienced in an orbit the model comes in two forms. AE8MAX is appropriate for solar maximum conditions, while AE8MIN is for solar minimum. Similarly AP8 (Sawyer & Vette 1976) is a model of the trapped proton

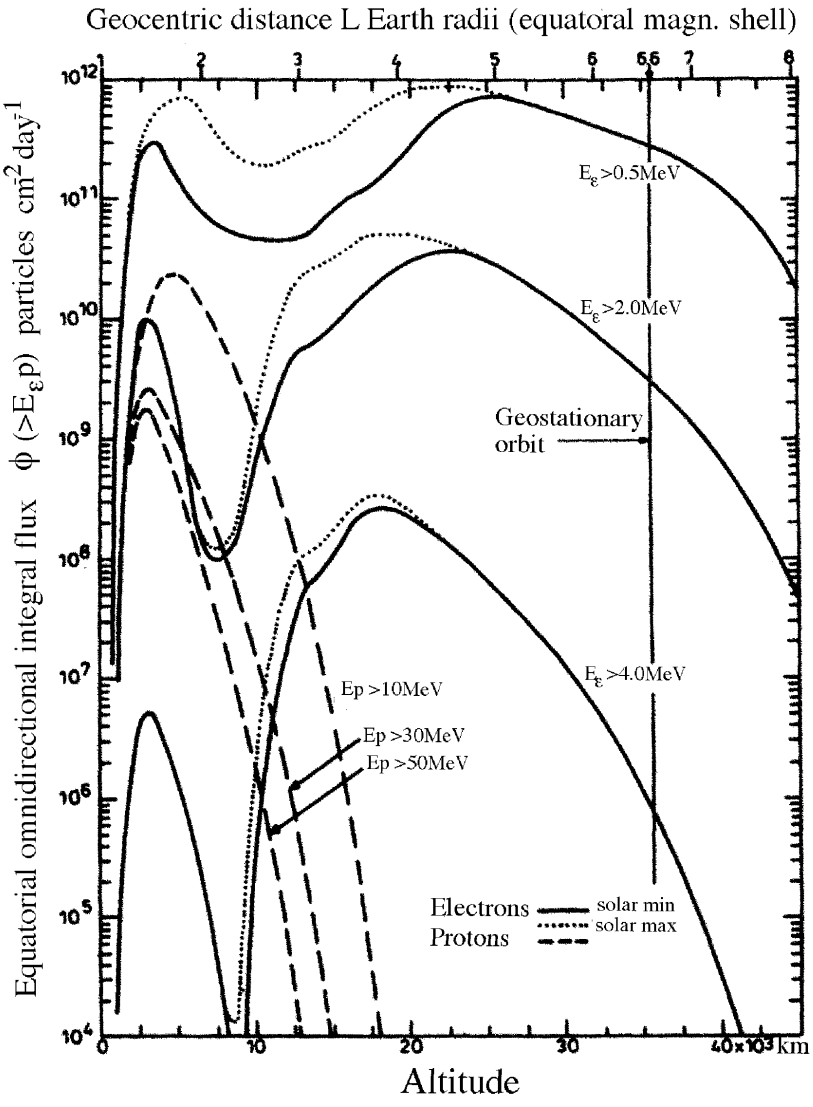

Figure 7.1. *The Earth's trapped electron and proton radial average flux profiles as a function of altitude (the Hipparcos satellite operated between 400 – 36 000 km). The different curves refer to different proton and electron energies (E_p and E_ϵ respectively). For electrons, the solid and dotted lines indicate the dependence at solar minimum and solar maximum respectively.*

environment for energies 100 keV to 400 MeV and altitudes of 1.15 to 6.6 Earth radii. This also has appropriate versions for solar maximum and solar minimum conditions.

An associated phenomenon—geomagnetic sub-storms—can lead to spacecraft anomalies and secondary solar-array damage. In this case occasional injections of hot plasma from the geomagnetic tail cause charging of surfaces to large negative potentials with respect to the surrounding plasma or different dielectric materials. Surfaces not neutralised by solar UV-induced photo-electron emission can develop large differential potentials leading to arc discharges. Electromagnetic interference from discharges is the cause of many anomalies on spacecraft and arcing can also damage exposed areas such as solar arrays. Special design features have to be incorporated to obviate this type of secondary damage and the associated electromagnetic interference.

Also troublesome are the solar eruptions producing energetic electrons, protons, α particles and nuclei such as C, N and O, although the most damaging components for spacecraft are typically protons. Galactic cosmic rays consist of approximately 90 per cent protons, 8 per cent α particles and 2 per cent nuclei of heavier elements. The energies are in the GeV range, but the fluxes are extremely low, around 2.5 particles cm^{-2} s^{-1}. However they are particularly penetrating and generate free charge in microelectronics, giving rise to single event upsets.

Protons

The energetic proton populations in space can be divided into three categories: (i) geomagnetically trapped radiation-belt protons with energies up to 300 – 400 MeV, which are primarily relevant for low-Earth and highly elliptic orbit missions; (ii) solar protons, notably those generated during a solar particle event. These may have energies from 10's to 100's of MeV, and occur sporadically. During a solar particle event, their fluxes can be extremely high. They tend to be deflected by the Earth's magnetic field (geomagnetic shielding) and thus pose a smaller threat to missions in low-Earth orbit. For missions with orbits outside the immediate vicinity of the geomagnetic shielding their effects can be crucial; (iii) protons originating from outside the solar system. These can be either galactic or extragalactic in origin. The galactic magnetic field can accelerate and contain protons with energies up to about 10^{19} eV, above which the particles are thought to originate outside the Galaxy. Such particles are extremely rare, such that they do not pose significant problems for satellites.

The daily positional proton flux encountered by Hipparcos is illustrated in Figure 7.2.

Electrons

In the vicinity of the Earth the largest contributor to the electron environment is the trapped radiation belt electrons, located in two zones: one at an altitude of L = 1.6 Earth radii, coincident with the proton belt, and an 'outer zone' at L = 4.5 Earth radii, where L is the geomagnetic dipolar field line equatorial radius. The largest electron fluxes are observed in the outer belt. Since the energy spectrum of trapped electrons drops exponentially, fluxes above 7 MeV are normally negligible. The dimensions of the two-component electron belt are much larger than those of the proton belt. The highest electron fluxes above the energy cutoff provided by typical spacecraft shielding are at least one order of magnitude higher than the respective maximum proton fluxes.

An important feature of the electron environment is its extremely dynamic nature. During disturbances, electron enhancements of several orders of magnitude can occur, and energies of tens of MeV have been observed. Current empirical models of the electron belts, however, consider the environment as static.

A population of high-energy electrons is also created during a solar flare. Due to the smaller magnetic rigidity of electrons, most of these remain trapped in the strong local solar magnetic fields—those that do obtain relativistic velocity and manage to escape lose much of their energy by emitting synchrotron radiation as they traverse the interplanetary magnetic fields. In the Earth's vicinity therefore the contribution to the high-energy radiation environment by solar flare originated electrons is very small. The same reasoning applies also to electrons arriving from outside the solar system.

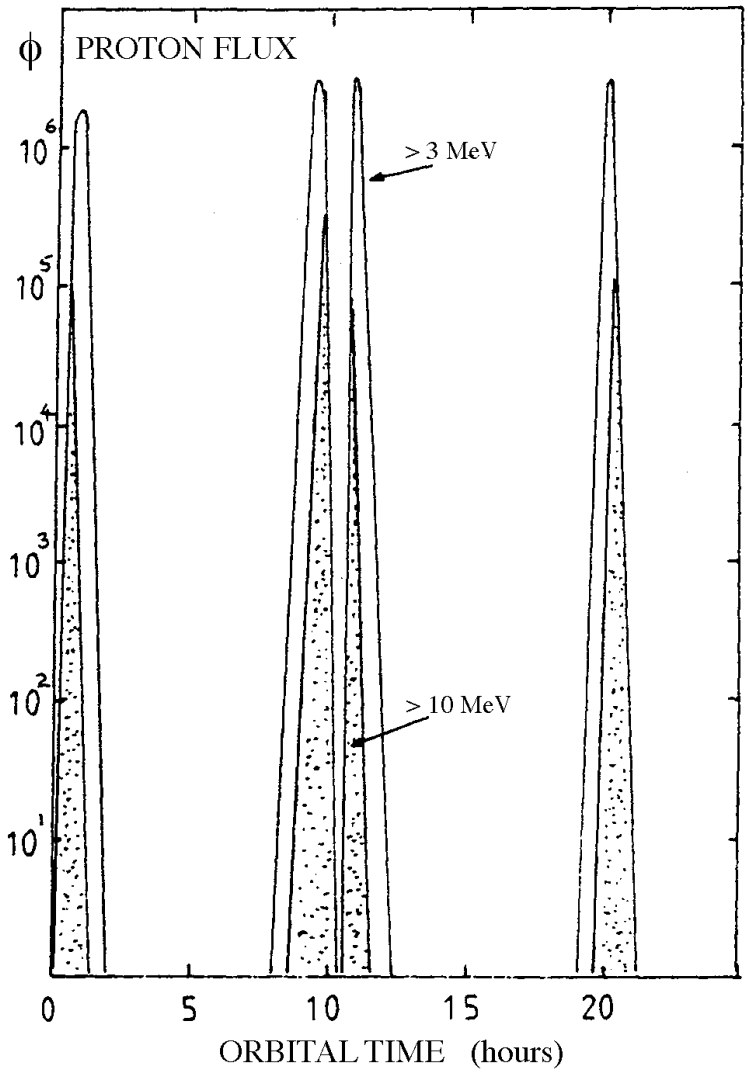

Figure 7.2. *The daily positional proton flux (in protons cm^{-2} s^{-1}) encountered by Hipparcos as it penetrated the van Allen belts four times per day in its elliptical orbit. The shaded regions correspond to the flux of > 10 MeV protons, and the open regions below the curves to > 3 MeV protons. Perigee passages correspond to the intervals close to 0 hrs and 10.7 hrs in the figure.*

Cosmic Ions

Cosmic ions also contribute to the charged particle environment in space, of which the most important are hydrogen and helium. The heavier nuclei are also of interest due to their high ionisation loss-rate in materials. There is also a small trapped heavy ion population in the radiation belts: the trapped anomalous cosmic rays. These particles in general tend to have low energies and consequently small ranges in matter compared to the equivalent shielding provided by most spacecraft, and are therefore of less interest from the radiation protection and monitoring point of view. However ions from outside the solar system, galactic cosmic rays, and accompanying solar particle events, are highly penetrating and deposit enough energy in sensitive nodes of microelectronic components to cause single event upsets or background.

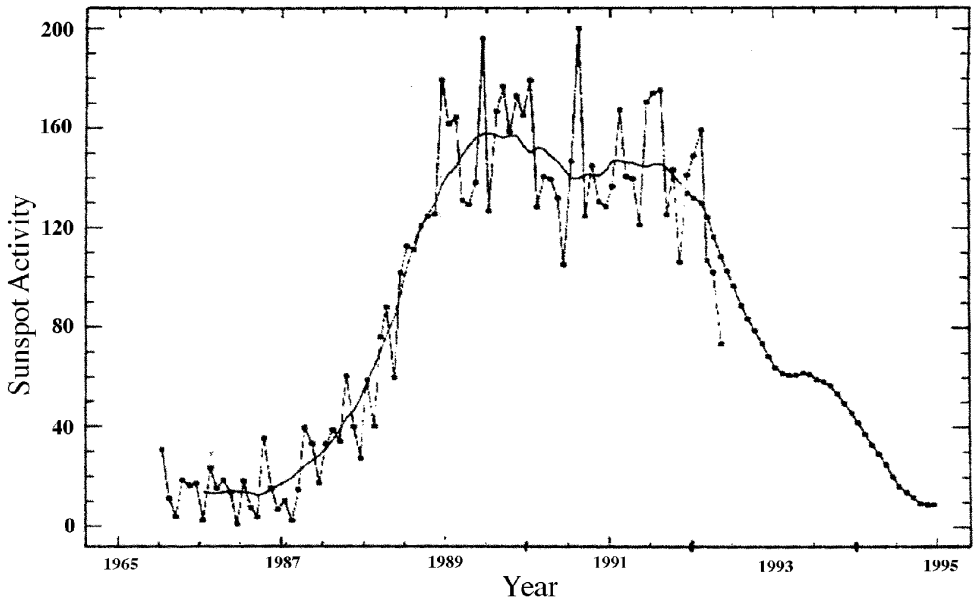

Figure 7.3. *Evolution of solar activity throughout the relevant solar cycle. The points give the monthly value of the sunspot number, the curve giving the smoothed values. The Hipparcos mission operated around the period of solar maximum.*

Solar Activity

Figure 7.3 shows the solar activity for the years preceding and during the Hipparcos mission. The solar maximum occurred during July 1989. After that the activity decreased. These determinations were made by the National Oceanic and Atmospheric Administration Center in Boulder, Colorado, U.S.A. In practice, Hipparcos was subject to three periods of intensive solar activity between the start of the mission and mid-1992—at the end of 1989, in the middle of 1990, and in the middle of 1991. Two exceptional solar proton events occurred in October 1989 and March 1991. The daily proton fluence is illustrated in Figure 7.4.

7.3. Modelling the Radiation Dose Absorbed by the Satellite

Following the implementation of the revised mission plan, studies were undertaken in an attempt to predict the future solar array performance as affected by the actual radiation background (see Chapter 11), and also the effects on the other spacecraft and payload electronics. This was carried out by comparing the effects of being in geostationary transfer orbit rather than its intended geostationary orbit using a simple scaling of the overall radiation dose levels. These studies resulted in a wide margin of uncertainty, but suggested that the electronic parts could withstand 32 months in the more severe environment.

Dose depth curves (Figure 7.5) were combined with a sector analysis to fit reality as close as possible. Sector analysis using a solid sphere dose depth curve corresponds to

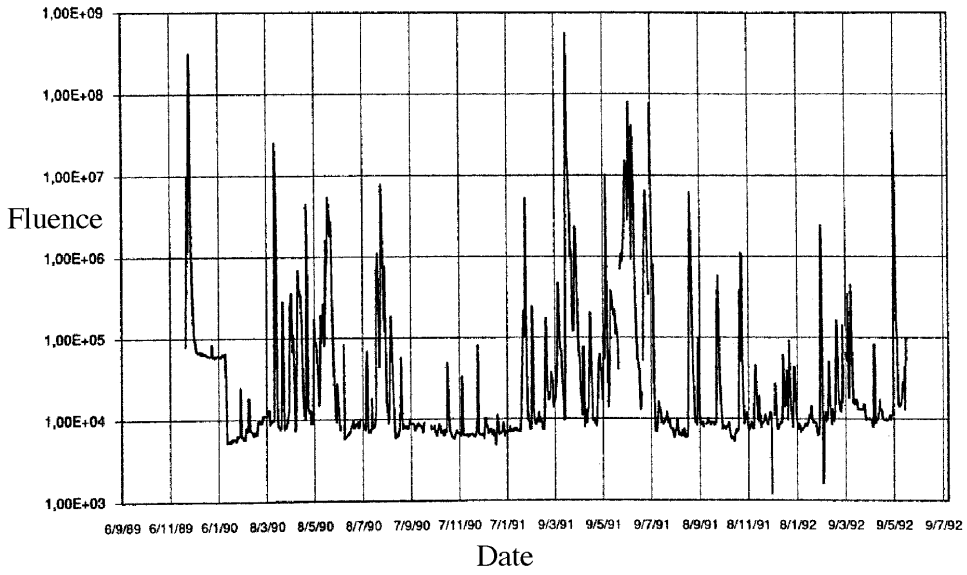

Figure 7.4. *Daily proton fluence during the mission, as indicated by solar activity reports communicated by the Observatoire de Paris-Meudon.*

an upper bound of total dose received, while sector analysis using a shell sphere dose depth curve corresponds to a lower bound but is closer to reality.

A margin of a factor of two had been applied when predicting the dose that a component could theoretically be exposed to, compared with its tested radiation hardness, meaning that the Hipparcos electronic parts were able to absorb at least twice the limiting dose specified for geostationary operation. Results are given in Figure 7.6, calculated for a 32 month mission according to the following two ratios:

$$\frac{\text{solid sphere dose}}{2 \times \text{specified geostationary dose}} \quad \text{and} \quad \frac{\text{shell sphere dose}}{2 \times \text{specified geostationary dose}}$$

The figure demonstrates that a significant divergence appears between the two extreme assumptions, depending on the equivalent aluminium thickness.

Another relevant aspect when interpreting various experimental data is the test conditions of components, particularly the dose rate used during irradiation tests. The dose rates in orbit are much lower than the testing dose rates, and experience in radiation testing shows that the behaviour of components under high dose rate conditions is worse than when using low dose rate exposures, except for a very few particular cases. This consideration gave an additional margin, difficult to assess quantitatively, which might also be expected to vary from one component to another.

For the studies of the radiation effects on the silicon solar-cell arrays, described in detail in Chapter 11, it was found to be desirable and possible to convert predicted integral proton and electron spectra outputs into a monoenergetic 1 MeV equivalent electron flux which, when time integrated, yields a 1 MeV equivalent electron dose flux (1 MeV electrons cm^{-2}). These flux values are readily and inexpensively simulated by van de Graaf accelerators, thereby enabling a solar cell's degradation characteristics to be assessed in the laboratory. The 'equivalence' concept holds good for penetrating radiation for which proton and electron irradiation produce the same qualitative solar-cell device degradation. The conversion of proton fluxes to equivalent 1 MeV electron

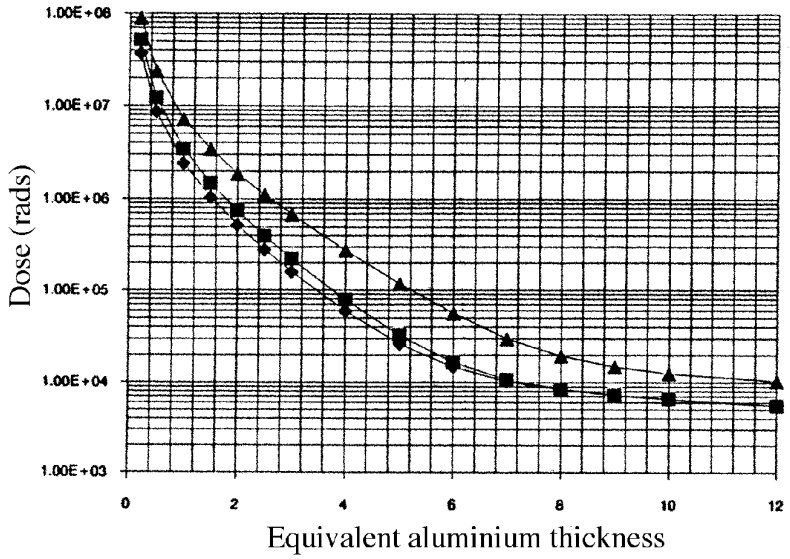

Figure 7.5. *Dose depth curves comparison for the actual Hipparcos orbit. Triangles and squares correspond to the dose curves for a solid sphere and a shell sphere respectively, the diamonds to two infinite slabs for comparison (see text for details).*

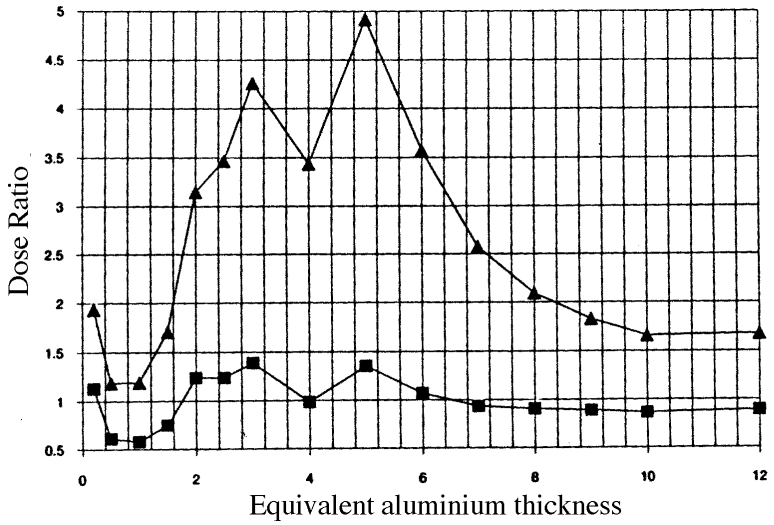

Figure 7.6. *Predicted dose ratio for a solid sphere (triangles) and a shell sphere (squares) with respect to twice the geostationary specified dose.*

fluxes is made by means of experimentally determined electron/proton damage ratio curves such as those depicted in Figure 7.7, from which it may be seen that 3000 1 MeV electrons are required to produce the same degradation as one 10 MeV proton in a 10 Ω cm n-p silicon solar cell. These proton-damage ratios are not universal constants, but have to be determined for each new type of silicon solar cell.

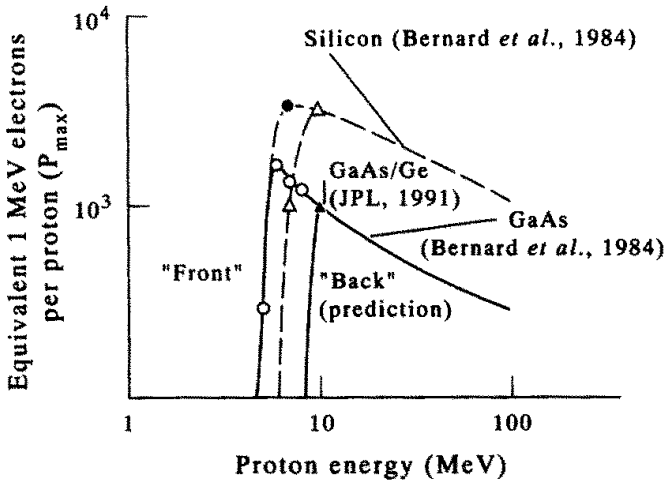

Figure 7.7. *Curves used to determine 1 MeV equivalent electron fluences as a function of proton energy. Different curves correspond to the effects of irradiation on the front and back sides of the panels (i.e. as a result of the shielding thickness). The curves permit the evaluation of the effects of orbital proton fluences in terms of equivalent 1 MeV electrons, and the subsequent testing of these cells using monoenergetic irradiation on ground. The 'silicon' curves correspond to the Hipparcos solar array, as used in the calculations described in the text. The GaAs/Ge relationships are shown for comparison.*

7.4. Effects of the Radiation Background on the Mission

Based on studies carried out before launch, the minimum shielding required to protect the sensitive spacecraft and payload components from radiation damage in the planned geostationary orbit was established to be equivalent to 8 mm aluminium. Particles penetrating normally (and therefore normal to the optical axis) retain most residual energy and are more numerous. This shielding corresponded to protons of about 40 MeV and electrons of roughly 3.5 MeV. However, electrons undergo considerable angular multiple scattering, and it is not possible to assign a unique penetration cut-off energy to them. Protons on the other hand travel in approximately straight lines. Near the end of their ranges they have a high linear energy transfer and a large contribution to the background signal is expected from fluorescence induced by protons within a few MeV of the penetration threshold.

Photomultipliers convert photon hits on a photocathode into an electrical signal via an amplified photo-electron cascade. Therefore radiation background signals can arise from: (a) secondary emission from photomultiplier window, cathodes or dynodes (internal electron-multiplying electrodes) induced by charged particle hits; (b) Cerenkov radiation in the spectral region of interest produced by charged particles passing through optical components (including the photomultiplier window); (c) fluorescence (scintillation) produced by charged particles in optical components; and (d) bremsstrahlung which can produce Cerenkov and fluorescence emissions via the generation of Compton-scatter electrons.

Secondary emission is most significant for low-energy particles. However, these are depleted in shielded situations. Secondary emission from the higher energy particles is generally inefficient compared to the other processes (Viehmann & Eubanks 1976).

Cerenkov radiation is a threshold effect requiring that the charged particle has a velocity exceeding the speed of light in the medium, which depends on refractive index. For most common glasses an electron need only have an energy above about 0.22 MeV to generate a Cerenkov flash. Protons on the other hand need energies above about 400 MeV. The direction relative to the particle track at which the light is emitted is a function of its velocity and the material's refractive index. A particle at the Cerenkov threshold velocity emits light in the forward direction while in common glasses the maximum emission angle, produced by highly relativistic particles, is about 45°.

Fluorescence is a continuous process with the amplitude of the photon emission dependent on the particle linear energy transfer. Photons are emitted isotropically. Even though the photon yield from an individual Cerenkov event may be larger than the yield from fluorescence, fluorescence may well produce the larger contribution. This is because of the very short duration and the directionality of Cerenkov emission, and because particles below the Cerenkov threshold can cause fluorescence.

Bremsstrahlung emission also has a significant angular spread. Although a Cerenkov event generates a large number of photons, the flash is extremely brief (100 ps) compared to the photomultiplier detection dead-time of 300 ns. A single Cerenkov event therefore only registers as a single count or 'spike' in the detector signal (Høg *et al.*, 1992; Howell & Kennel 1984; Viehmann & Eubanks 1976), and only the rate of Cerenkov events is registered.

Fluorescence is a much slower process lasting hundreds of micro-seconds and so contributes a larger count-rate. The slow rotation of the satellite and the fact that the planar shielding has its normal perpendicular to the rotation axis meant that over time the focal plane would view all directions. The rotation axis was in a sunward (but not exactly sun-pointing) direction so the rotation tended to expose the focal plane to most pitch angles (directions with respect to the magnetic field) over the 2 hour rotation.

Although the instantaneous environment seen by the telescope components had a directionality, time-averages and the large acceptance angle tended to make the response more isotropic. In the cases of electrons and bremsstrahlung, their multiple scattering and angular distributions further blurred directional effects.

In-Orbit Measurements

The 'star mapper chains' consisted of a series of 5 lenses, 2 filters and a pair of Thorn-EMI 9924B photomultiplier tube detectors. These detectors were specially built with thin windows to minimize Cerenkov radiation and fluorescence. Shielding of the Hipparcos focal plane star mapper optical components was approximately planar. The optical axis lay in a plane parallel to the plane of the shielding.

Figure 7.8 shows typical traces of the star mapper signal during four sequential orbits. The vertical lines indicate the times of perigee. Close to perigee the background signal is extremely high, corresponding to the inner, proton, radiation belt. The broad peaks of the electron belts on the outbound and inbound passages are apparent. As part of normal operations the instruments were shut down or data rejected during periods of

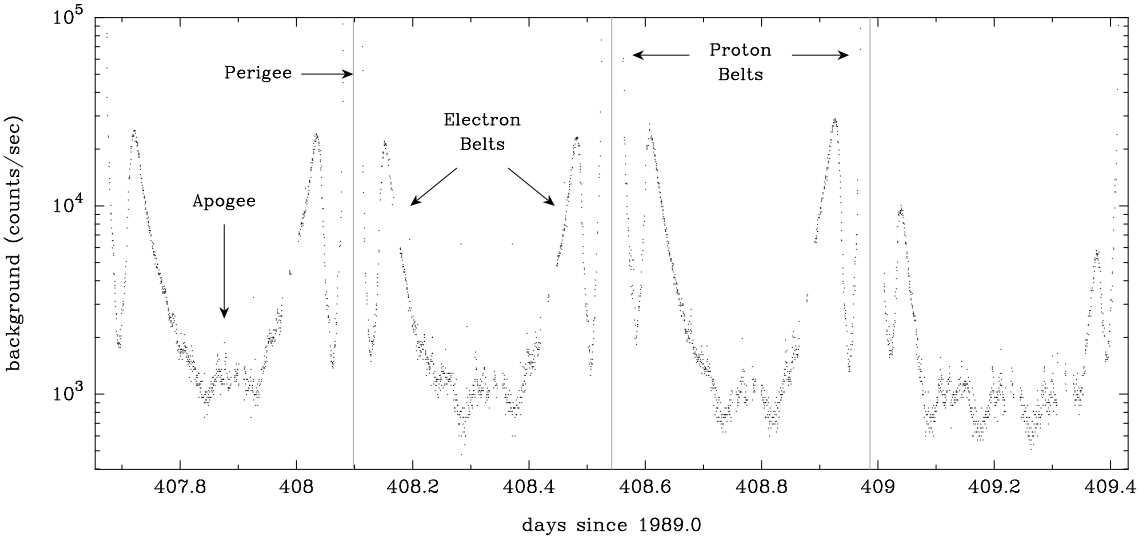

Figure 7.8. *Typical star mapper orbital background signal over a period of about 2 days. The vertical lines indicate the location of the perigee passages. The minima in the background signal correspond to the apogees of the orbit.*

very high background signal. Some data outages were also due to on-board anomalies which may themselves have been environmentally induced. Data were also not taken when the Earth or Moon were in the star mapper fields of view. Nevertheless, there were enough data in high-background regions to reveal clearly many interesting features. The background signal data consisted of 1000 points equally spaced in time per orbit, giving a resolution of about 38 s. The data set started close to the start of scientific operations, on 26 November 1989 and finished more than 3 years later on 17 March 1993, totaling 2722 orbits. Gaps totalled about 18 per cent of this time and were concentrated towards the end of the mission.

Interpretation of the Data

The data can be displayed as plots in terms of orbital time for various periods of interest. Figure 7.9 shows data for 20 orbits (9 days) of late March 1991. Also plotted on this figure are data from the particle detectors on the geostationary GOES satellite (Sauer 1987). These are for electron fluxes (cm^{-2} s^{-1} sr^{-1}) > 2 MeV divided by 10^3 and for proton fluxes (cm^{-2} s^{-1} sr^{-1} MeV^{-1}) of 11.6 MeV divided by 10 and of 60.5 MeV (the scaling is solely to fit the data in the figure). These GOES data show the onset of the well-known solar proton event on 23 March 1991 (Mullen *et al.*, 1991; Gussenhoven, Mullen & Violet 1994). The subsequent solar wind shock on 24 March resulted in the creation of an additional radiation belt (Blake *et al.*, 1992). The solar proton event is clear in the dramatically enhanced Hipparcos star mapper background signal rate. Also apparent is the dramatic fall in rate as perigee approaches, presumably due to geomagnetic shielding. This event also generated strong electron and proton drift

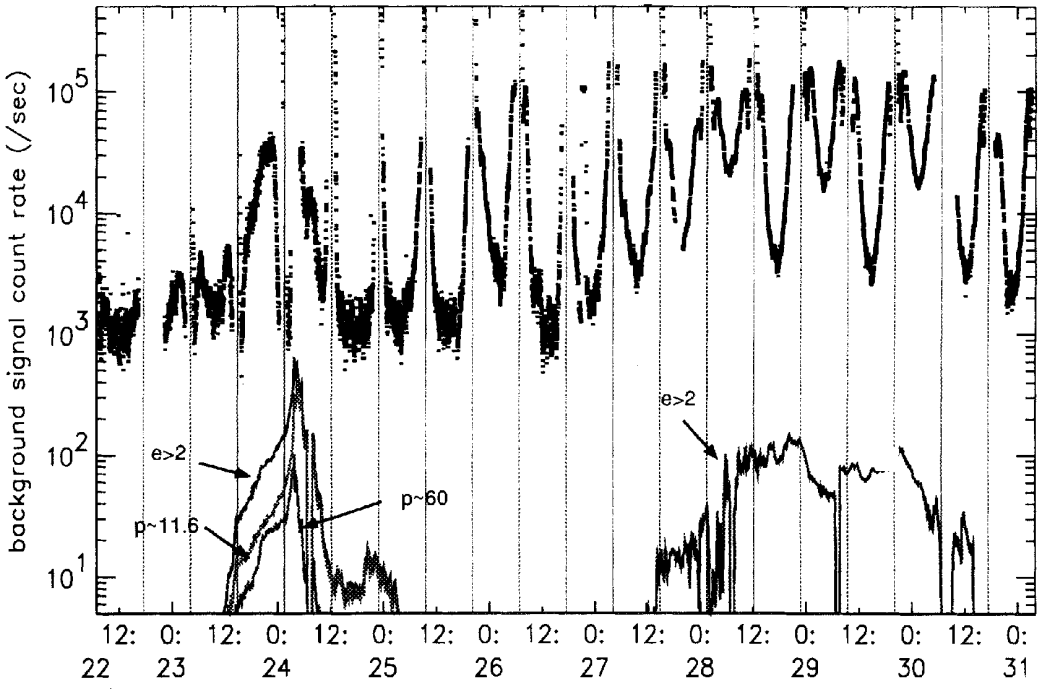

Figure 7.9. *Hipparcos star mapper background signal data for 20 orbits during late March 1991 (upper trace). The vertical lines indicate the periods of perigee passage: the star mapper background usually decreasing as the satellite altitude increases towards apogee. At the bottom of the figure are the corresponding GOES electron and proton data (scaled as described in the text). At the lower left, the three traces show the response to a large solar proton event, the three curves corresponding to electrons with energy above 2 MeV (upper), protons above 11.6 MeV (middle), and protons above 60 MeV (lower). To the bottom right of the figure are the GOES data corresponding to the subsequent geomagnetic storm (the curve is for electrons above 2 MeV) giving rise to a 1–2 order of magnitude increase in the star mapper background count rate.*

echoes at around 3:42 UT on 24 March (Blake *et al.*, 1992). Unfortunately the star mapper data for around this period are missing due to ground-station non-availability.

Earth occultation results in the absence of any inner-belt traces on the orbits shown in Figure 7.9, in contrast to Figure 7.8. On the orbits following 27 March an additional maximum is clearly seen, corresponding to the new belt and coincident with the enhancement of the GOES > 2 MeV flux shown at the bottom of the figure. A feature of the response in the days following 27 March is the way the background signal at 6 successive apogees 'oscillates' by close to an order of magnitude while the new belt magnitude and the GOES fluxes remain relatively stable. This is presumed to be a longitude effect caused by the tilt of the geomagnetic field; as the Earth rotates, successive orbits trace different paths through the geomagnetic field.

To relate the data better to radiation belt regions they were analyzed in terms of location in geomagnetic L space rather than time which compresses the lower altitude. The time of the data was used together with orbital ephemeris data to derive the L value corresponding to every data point. To do this the IGRF-1985 (International Geomagnetic Reference Field) model of the Earth's internally generated magnetic field was used together with the Olsen-Pfitzer-1977 quiet-time tilt-dependent model of the externally generated perturbation (Olsen & Pfitzer 1974) to compute B (the magnetic field strength) and L. This is the same procedure that has been used to order data from the

Combined Release and Radiation Effects Satellite (CRRES, Gussenhoven *et al.*, 1992; Brautigam, Gussenhoven & Mullen 1992). Since the orbit is of low inclination, L alone should produce reasonably good ordering of the data. However, as mentioned above, the tilt of the geomagnetic field and the 7° inclination combine with the Earth's rotation to produce a shift between orbits in L space. In other words subsequent apogees will not lie on the same L value. Around apogee, different orbital traces which were well ordered (overlapping) in orbital time were sometimes less well ordered when traced in L, indicating that the model fields were inadequate at high altitudes. At low altitudes, organising the data according to L was very effective at revealing the belt structures, even with patchy data. L distributions of the data for each orbit were derived by averaging the data in bins of 0.05 Earth radius in L. The complete mission background signal data and their temporal and L distribution are summarized in Figure 7.10. In this figure, as with other authors' method of plotting CRRES data summaries (Gussenhoven, Mullen & Violet 1994; Brautigam, Gussenhoven & Mullen 1992), the counts are displayed as a colour-scale with the vertical axis corresponding to the radial L variation (the bottom of the figure, $L = 1$, can be thought of as approximately the Earth's surface) and the horizontal axis corresponding to time, covering more than 3 years of data. To condense the plot and in order to remove residual longitude effects, the single-orbit L-distributions were averaged in 9-orbit segments, corresponding to the repeat period of 4 days. Just over 300 data segments are displayed horizontally, and there are 115 L bins within each segment.

The figure clearly illustrates the quiet period from September 1990 until the March 1991 event, the subsequent generation of the new radiation belt around $L = 2$, and the large event of July 1991 which was reported to remove some of the new belt (Gussenhoven, Mullen & Violet 1994).

This behaviour was also registered in the Hipparcos solar array degradation, which degraded at an unusually slow rate just before the March event and at a fast rate afterwards (Crabb & Robben 1993, see also Chapter 11). The Hipparcos data with its longer time-coverage also captured the events of April 1990, November 1991 and, largest of all, May 1992. The April 1990 event is seen to add slightly to the edge of the inner belt for a period of about a month. The November 1991 event produced a distinct narrowing of the second belt. The large May 1992 event, however, produced little lasting effect on the inner belt or the second belt which had all but decayed away by then.

Comparison with CRRES dosimeter data supports the view that both electrons and protons produced the background signal: the signal was strong in the inner belt below $L = 1.5$; it was temporarily very strong in the second inner ($L \simeq 2$) belt following the March 1991 event but subsequently decayed; and it responded readily to electron events seen by other spacecraft. In the CRRES data there is less obvious decay of the HiLET second belt (in the region $2 < L < 2.5$) than the LoLET second belt while the Hipparcos second belt decays noticeably. This would imply that protons are less important. However, the inner belt shows up stronger in the Hipparcos data than in the LoLET data. From this it appears that in this region Cerenkov radiation from very energetic protons is becoming an important component, while at higher altitudes, electrons and bremsstrahlung are the main contributors.

Because inner zone protons capable of generating Cerenkov radiation are of very high energy, the shielding around the telescope was largely ineffective. These protons therefore could access the telescope from a much greater range of directions. Using the

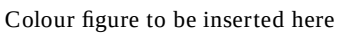

Figure 7.10. *The L-distribution of the Hipparcos background signal over most of the mission showing several solar proton events, and the creation and decay of the second inner belt around L = 2 around March 1991. The data are a 4-day (9-orbit) average, binned in 0.05* R_E *in ordinate. The red regions for L > 3 (corresponding to the outer electron belt) arise from injection events.*

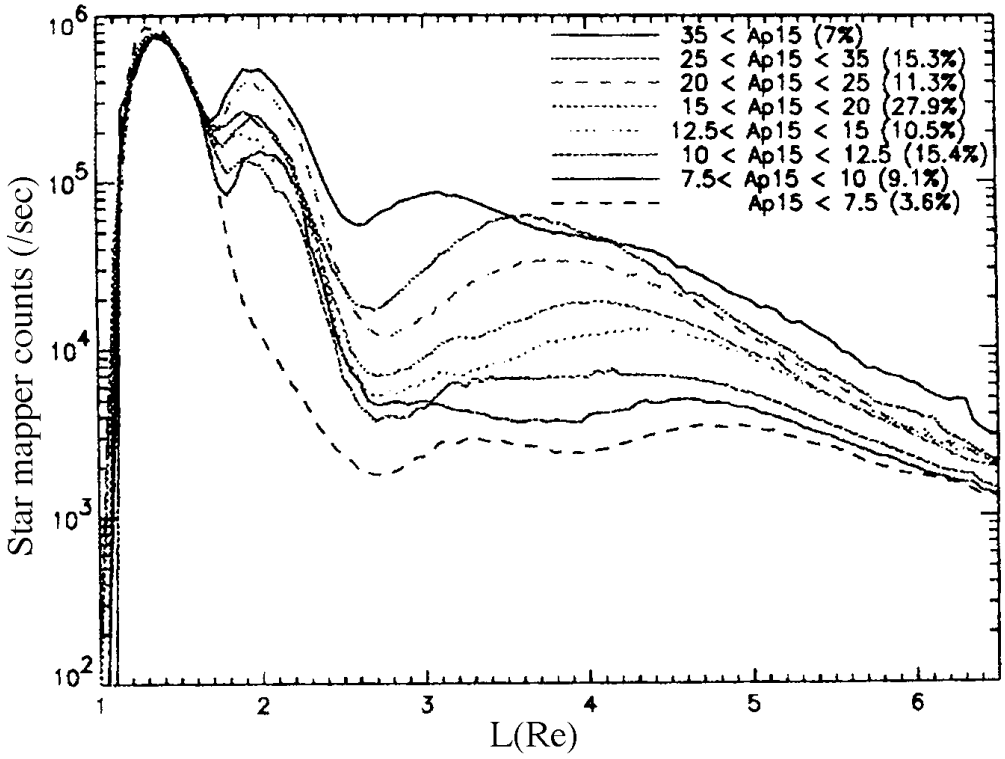

Figure 7.11. *Average radial L profiles of the star mapper background for various geomagnetic activity levels. It shows an increasing background trend for increasing value of the planetary A_P geomagnetic index. The percentages in parentheses indicate the fraction of the mission duration for the given index value.*

orbital L-binned data, average L-profiles of the background signal under various geomagnetic activity conditions were produced. The activity conditions were defined by the 1-day delayed 15 day average of the planetary A_P geomagnetic index available from the National Oceanic and Atmospheric Administration (NOAA), denoted A_P15. This scheme had previously been successfully applied to the sorting of CRRES high energy electron data (Brautigam, Gussenhoven & Mullen 1992).

Figure 7.11 shows the resulting activity ranges and in brackets the percentages of the total data which fall into each activity category. The lowest activity category corresponds to an almost total absence of an electron radiation belt ($2.5 < L$). There is a strikingly clean signature of the inner proton belt ($L \simeq 1.5$). The second inner belt ($L \simeq 2$) is also clear under higher activity conditions which are dominated by periods after March 1991. The lowest activity class is dominated by pre-March 1991 conditions, explaining the absence of the second inner belt. This type of geomagnetic activity separation is most useful for the outer regions since clearly perturbations to the inner regions persist during times of high and low geomagnetic activity. Beyond $L = 3$ there is a clean monotonic increase with A_P15 in the electron-induced background signal, most similar to the medium-energy models (2.2 – 3.1 MeV) of Brautigam, Gussenhoven & Mullen (1992).

Although there can be no real substitute for direct and unambiguous particle measurements for defining the environment, a by-product of the satellite's unplanned operation in geostationary transfer orbit was a long-term set of radiation background data giving

information on the radiation environment in important orbital regimes. These data are interesting in a number of respects. Comparison with data from an overlapping time period from CRRES facilitates the deduction of the cause of many elements of the background signal's spatial and temporal dependence. As with previous CRRES results, the data illustrate the highly dynamic nature of the electron component of the radiation environment. They show how the geostationary transfer orbit environment, thoroughly monitored for 14.5 months by CRRES, behaved in the 6 months before and 12 months after CRRES. In particular the long-term decay of the second inner ($L \simeq 2$) belt following the March 1991 event is seen, the very large event of May 1992 produced negligible effect on the belt structure and the November 1991 event produced a distinct loss from the second belt. Qualitatively, Hipparcos data and CRRES data are consistent during the overlapping period, especially the LoLET dosimeter in the outer zone and the secondary inner belt.

Comparison with GOES data following the March 1991 event reveals some interesting features at high altitudes in the background signal data related to geomagnetic field effects. In the inner parts of the orbit there was interesting evidence of geomagnetic shielding of solar proton events. While it is not possible to identify a unique particle species or detection mechanism, it is reasonable to conclude that the signal is from Cerenkov radiation and fluorescence caused by electrons, protons and bremsstrahlung.

In conclusion, although the geostationary transfer orbit environment can be a severe one, it has its quiet moments. It was never seriously contemplated to perform space-based astronomy from geostationary transfer orbit but these data and the eventual success of the Hipparcos mission show that it is feasible under certain circumstances. The possibility of operating in orbits which are normally considered too hazardous for spacecraft has obvious cost benefits, provided the protection aspects can be managed. These data are highly relevant for ESA's future space-based astronomy missions which will take place in highly-eccentric Earth orbits. They should yield important statistics for observation planning. They should also provide an interesting additional geostationary transfer orbit data set to add to those from CRRES. Finally they demonstrate the suitability of geostationary transfer orbit for radiation-belt and solar-terrestrial studies.

8. THE OBSERVATION PROGRAMME AND INTERFACE WITH THE INPUT CATALOGUE CONSORTIUM

This chapter describes the manner in which the satellite scanned the sky (the ecliptic-based scanning law). This scanning law ensured even coverage of the sky during the mission lifetime. The observation programme was nominally fixed before satellite launch, and the entire satellite operations and scientific observations were conducted on the basis of the pre-defined Hipparcos Input Catalogue. Nevertheless, considerable 'tuning' of the observing programme went on throughout the mission, especially during the early months of the mission. Very few objects had significantly erroneous positions or magnitudes, which were duly corrected as they became evident. Several updates of the global positions were made on the basis of the early data reductions, in order to improve the real-time attitude determination performances, and resulting photometric measurements. The parameters of the global observing programme were also adjusted throughout the mission taking into account the past and future (expected) observation times allocated to each object. The way in which the star observations were carried out—by interlacing observations of all stars simultaneously present in the combined field of view of the telescope—is described. Predicted appearances of the individual stars were computed on ground, on the basis of the Hipparcos Input Catalogue, and target observation times were pre-computed, based on the star's magnitude and priority and, ultimately, on the previous observing history of the star.

8.1. Scanning Law

Scanning Law Definition

Each object in the Hipparcos Input Catalogue was scheduled to be observed many times with different scanning orientations (typically some 100 times, although this varied considerably according principally to the object's ecliptic latitude) to increase the accuracy and precision of the parameters which would constitute the end results of the mission. This was achieved by constraining the attitude of the spacecraft to follow a complex 'revolving scanning' motion, called the nominal scanning law, which ensured reasonably even coverage of the sky over the lifetime of the mission whilst adhering

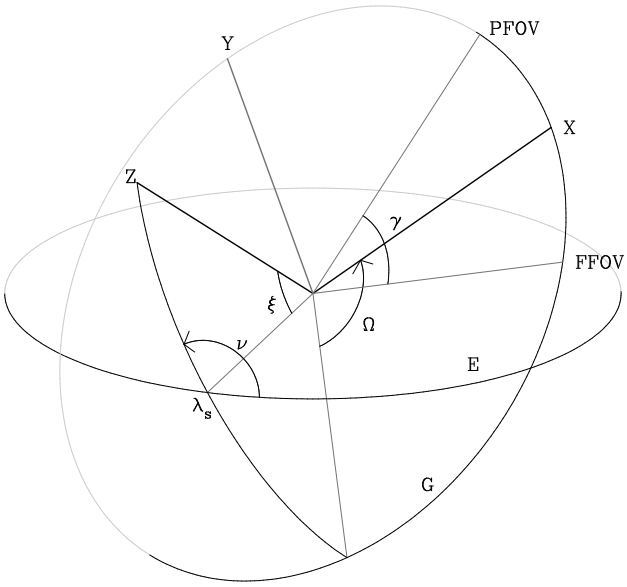

Figure 8.1. *Definition of the telescope reference frame (X, Y, Z). The spin axis of the satellite, Z, precessed around the sun line at a constant inclination angle of $\xi = 43°$, with the satellite rotating around this axis at a rate of R = 11.25 revolutions per day. E signifies the ecliptic plane, and λ_S the ecliptic latitude of the Sun. The precession angle, ν, and the heliotropic angle, Ω, define the elements of the scanning law through Equation 8.8. PFOV and FFOV refer to the preceding and following fields of view; G is the scanning great circle, and γ is the 'basic angle' between the two viewing directions.*

to thermal and other constraints. Three-axis control of the spacecraft was performed by regular firings of cold-gas thrusters (approximately every 10 min). In this way, the spacecraft rotated at 168°.75 per hour about its principal rotation axis, which itself was constrained to precess at roughly 6°.3 per day about a 43° half-cone centred on the Sun direction. It should be noted that the principles of the nominal scanning law, and of the programme star file and the star observing strategy, were not affected by the revised orbit.

The satellite attitude motion was most easily described in terms of the movement of the telescope with respect to the ecliptic reference system. The telescope reference frame (Figure 8.1) is the rectangular right-handed frame (OXYZ), where the origin, O, is the intersection of the two lines of sight, OP and OF, of the telescope; the plane (X,Y) is coincident with the plane (P,F); and the X-axis is the bisector of the basic angle POF. The satellite scanning motion was then defined as follows: the Z-axis of the telescope reference frame rotated at a constant angle $\xi = 43°$ around the Sun direction, following the Sun in its apparent motion along the ecliptic and performing $K = 6.4$ revolutions per year. At the same time, the satellite rotated around the Z-axis in the (X,Y)-plane performing $R = 11.25$ revolutions per day. The motions of the axes OP and OF of the preceding and following fields of view, which scanned the celestial sphere, resulted directly from this scanning motion.

Quantitative Description of the Scanning Law

In precise terms, the nominal sun line is defined by the following orientation:

$$\mathbf{s}(d) = \mathbf{l}\cos\lambda_s + \mathbf{j}\sin\lambda_s \qquad [8.1]$$

l j k being the ecliptic coordinate triad for the mean ecliptic and equinox of J2000.0, and:

$$\lambda_s = L + 2e\sin g + \frac{5}{4}e^2\sin 2g \qquad [8.2]$$

$$L = -1.386\,91 + 0.017\,202\,124\,0d \qquad [8.3]$$

$$g = -0.041\,14 + 0.017\,201\,969\,6d \qquad [8.4]$$

$$e = +0.016\,714 \qquad [8.5]$$

where d is the time in mean solar days from the reference epoch adopted for the nominal scanning law, defined as 1988 January 1, $12^h00^m00^s$ UTC (in practice, d was defined in terms of the satellite on-board clock).

The composition of the precession of the spin axis Z and the rotation of the Earth (and satellite) around the Sun resulted in a motion of the Z-axis on the celestial sphere, with a speed designated V_Z. The orientation of the telescope reference frame with respect to the heliotropic reference frame was described by the attitude angles v, ξ, Ω. The speed V_Z was kept approximately constant by modulating the precession angle v:

$$v = \overline{v} + a_1\cos(\overline{v}) + a_2\sin(2\overline{v}) + a_3\cos(3\overline{v}) + a_4\sin(4\overline{v}) \qquad [8.6]$$

where $\overline{v} = \overline{v}_0 + 6.4\lambda_s$, and the coefficients a_i are the following:

$$\begin{aligned} a_1 &= -0.163\,784\,59 \\ a_2 &= -0.013\,077\,77 \\ a_3 &= +0.001\,232\,43 \\ a_4 &= +0.000\,123\,41 \end{aligned} \qquad [8.7]$$

The instantaneous spin rate, ω_Z, was kept approximately constant by modulating the heliotropic attitude angle, Ω, as follows:

$$\Omega(d) = \Omega_0 + 2\pi R(d - d_0) - v\cos\xi + (b_1\overline{v} + b_2\cos\overline{v} + b_3\sin(2\overline{v}))\frac{\sin\xi}{K} \qquad [8.8]$$

where:

$$\begin{aligned} b_1 &= +0.082\,152\,69 \\ b_2 &= +0.990\,061\,17 \\ b_3 &= +0.040\,452\,13 \end{aligned} \qquad [8.9]$$

The parameters used in the nominal scanning law were the spin rate, $R = 11.25$ revolutions per day (168.75 arcsec s^{-1}), the revolving scanning angle, $\xi = 43° \pm 0°.5$, and the average precession rate, $K = 6.400 \pm 0.002$ revolutions per year. The principle of the

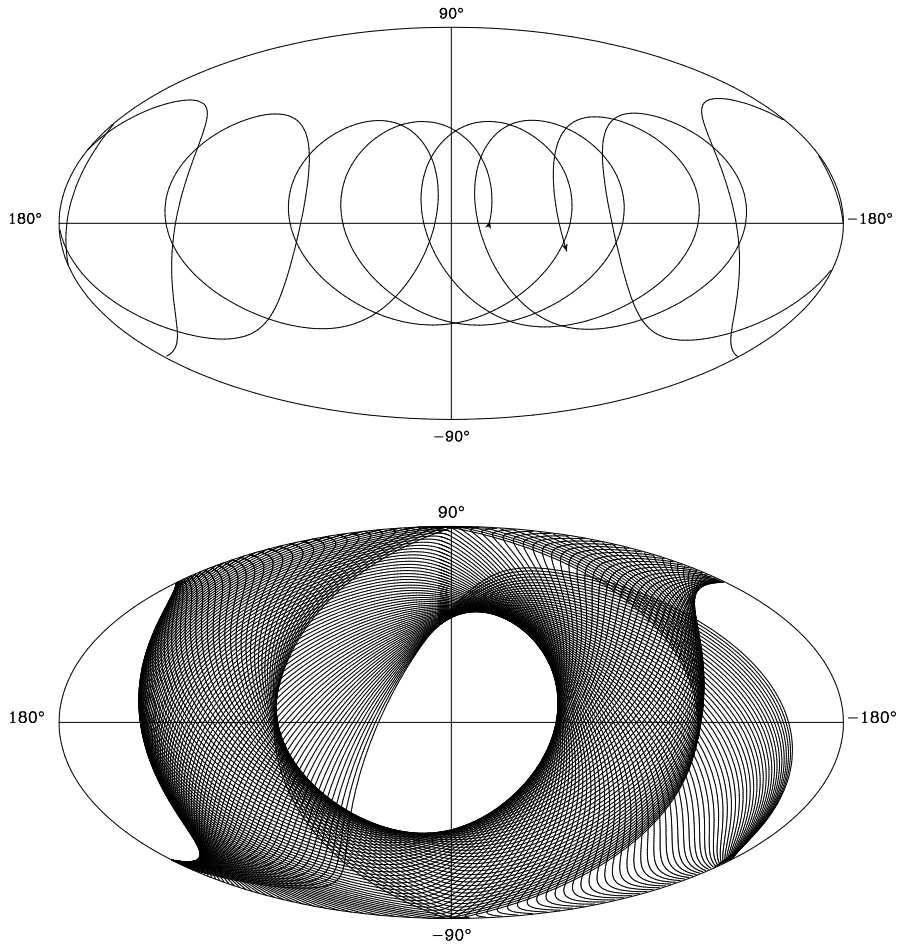

Figure 8.2. *The scanning motion of the Hipparcos satellite on the celestial sphere, shown in ecliptic coordinates. The top figure shows the path of the spin axis between 22 May 1990 and 23 September 1991. The scan direction is indicated by the arrows. The bottom figure shows one reference great circle for each orbit (5 revolutions of the satellite) for the period between 22 May 1990 and 14 July 1990. The actual scanning was 5 times denser.*

scanning measurements is illustrated in Figure 1.1, and the resulting scanning of the celestial sphere is shown in Figure 8.2.

The above description defines the 'nominal scanning law', i.e. the nominal paths of the fields of view on the sky throughout the mission. Deviations of up to ± 10 arcmin about the three satellite axes were tolerated in practice, attitude motion within these limits being controlled autonomously on-board by means of the attitude and orbit control system.

Optional Variations in the Definition

The choice of nominal scanning law parameters had been carefully analysed in the years preceding launch to ensure maximum homogeneity of coverage over the entire sky as well as accuracy of the final catalogue. The results of these studies optimised for the launch data of 8 August 1989, gave values of $\xi = 43°$ and $\overline{v}_0 = 40°$. The value of Ω_0 was less critical and could be defined by ESOC in orbit. The concept employed by ESOC during the commissioning phase after launch was to use the prescribed values of ξ and $\overline{v}_0$ to position the rotation axis of the spacecraft at the correct part of the 43° cone. At that time, using star pattern recognition techniques with the ground real-time attitude determination system, the phase of the fields of view as the spacecraft rotated could be calibrated and hence Ω_0 could be derived.

Although ESOC were in principle able to change the nominal scanning law through the ground software, mission constraints were prescribed which prevented any change to either ξ or $\overline{v}_0$. In addition Ω_0 should only be changed if necessary. Therefore in general, ESOC maintained a constant nominal scanning law throughout the routine (three-gyro) phase of the mission. The only times when it was deemed necessary to change Ω_0 during this period were during a small number of contingencies where the spacecraft assumed a non-nominal spin rate for a significant period of time. In order to re-acquire attitude control, ESOC had the choice of options, either to perform a large firing of the cold gas thrusters to slew the spacecraft around its principal rotation axis thereby re-acquiring the previous nominal scanning law attitude, or to calibrate the value of Ω_0 for the current phase and calculate a new mission plan and programme star file. In all cases where the drift around the rotation axis was more than one or two degrees, the second option was faster to implement, safer and less expensive in fuel.

During the two-gyro operations towards the end of the mission, significant drifts around the rotation axis occurred during every perigee, making re-calibration of Ω_0 necessary every orbit. A full discussion is given in Chapter 15. Moreover, the drifting phase angle also affected the accuracy of the on-board model for the precession around the 43° cone. The result was that the rotation axis itself was prone to drift. ESOC was then faced with a similar but more difficult decision concerning the method of re-acquiring attitude control under these conditions. The options in this case were to perform a large firing of the cold gas thrusters to slew the spin axis back to that position defined by $\overline{v}_0 = 40°$ or to calibrate the value of $\overline{v}_0$ for the current attitude and calculate a new mission plan and programme star file.

The second option was selected for the same reasons as for Ω_0 although it was realised that there may be a penalty to pay in terms of homogeneity of coverage. To monitor any possible biasing, the tables of nominal scanning law parameters used during the mission were monitored by the NDAC Consortium.

During the final brief period of attempted zero-gyro operations, efforts were made to initialise the real-time attitude determination in quasi sun-pointing mode where the solar aspect angle was close to but not exactly zero (see Chapter 16 for a more complete discussion). These attempts were largely unsuccessful, and further attempts were restricted to using a scanning law with $\xi = 0$.

Table 8.1. Nominal scanning law parameters during three-gyro operations.

Start time yy:dd	ξ deg	$\overline{v}_0$ deg	Ω_0 deg
1989:305	43.0	40.0	102.470
1990:178	43.0	40.0	138.850
1990:320	43.0	40.0	135.647
1991:160	43.0	40.0	134.167
1991:279	43.0	40.0	4.566

Table 8.1 lists the nominal scanning law parameters used during the three-gyro operational phase. Figure 8.3 depicts the nominal scanning law parameters for the two-gyro operational phase.

Orbital Oscillator

The nominal body rates of the spacecraft, defined in the nominal scanning law, were modelled on-board as a linear function of parameters referred to as the orbital oscillators S_v, C_v, which modelled the sine and cosine components of the phase angle of the nominal scanning law. The orbital oscillator values were propagated forward in time using an approximate formula, which would have led to a drift from the nominal scanning law unless accurate values were periodically uplinked from ground.

Defining:

Ω_N as the nominal scan rate of $168\overset{\circ}{.}75$ per hour

Ω_p as the precession rate of the spacecraft z-axis around the 43° cone ($\simeq 0\overset{\circ}{.}26$ per hour)

Ω_d as the spin rate accounting for precession ($\simeq 168\overset{\circ}{.}56$ per hour)

Ω_T as the transverse rate

ξ as the solar aspect angle (nominally 43°)

t_k as the on-board time sampled every $\Delta t = \frac{16}{15}$ seconds

$\Omega_N, \Omega_p, \Omega_d, \Omega_T$ were related via the equations:

$$\begin{aligned} \Omega_T &= \Omega_P \sin\xi \\ \Omega_N &= \Omega_P \cos\xi + \Omega_d \end{aligned} \qquad [8.10]$$

$S_v(k)$ and $C_v(k)$ were derived on-ground for time t_k as:

$$\begin{aligned} S_v(k) &= \sin(\Omega_d t_k) \\ C_v(k) &= \cos(\Omega_d t_k) \end{aligned} \qquad [8.11]$$

with the propagation coefficients:

$$\begin{aligned} S_d &= \sin(\Omega_d \Delta t) \\ C_d &= \cos(\Omega_d \Delta t) \end{aligned} \qquad [8.12]$$

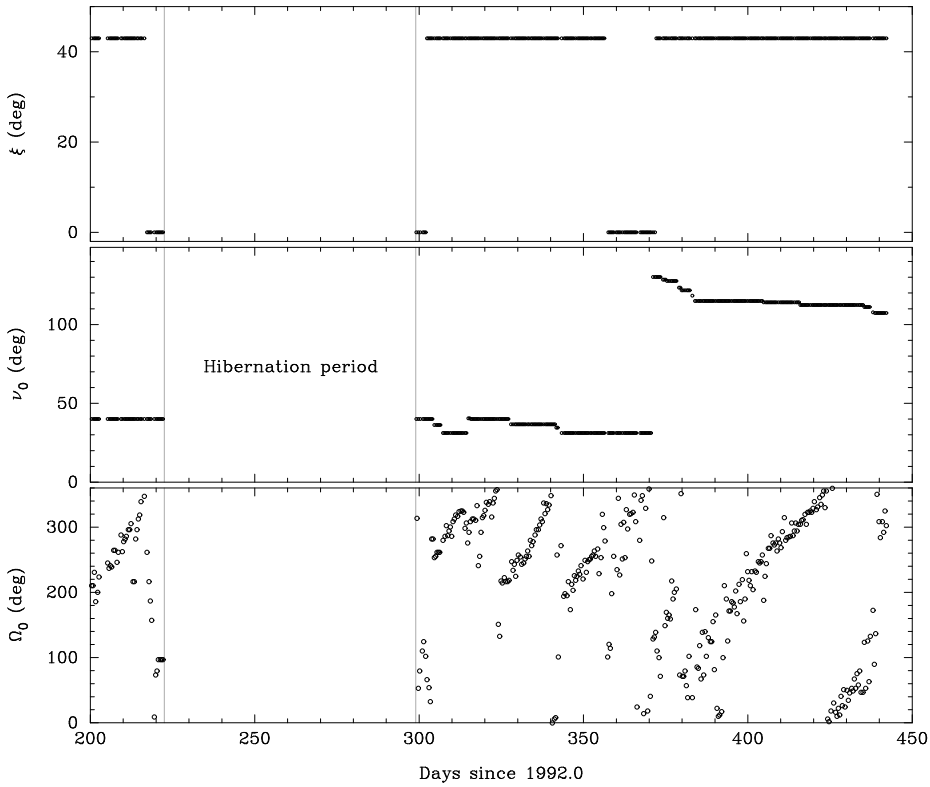

Figure 8.3. *Nominal scanning law parameters for the two-gyro operational phase. This phase occurred towards the end of the mission, following gyro failures which prevented continued three-gyro operations. The 'hibernation period' refers to an enforced period without scientific observations while the two-gyro operational mode was brought into service.*

$S_v(k), C_v(k), S_d, C_d$ were uplinked to the spacecraft and propagated on-board every Δt period as:

$$\begin{aligned} S_v(k) &= S_v(k-1)C_d + C_v(k-1)S_d \\ C_v(k) &= C_v(k-1)C_d - S_v(k-1)S_d \end{aligned} \qquad [8.13]$$

from which the nominal spacecraft body rates could be calculated:

$$\begin{aligned} \omega_X(t) &= \Omega_T S_v(k) \\ \omega_Y(t) &= \Omega_T C_v(k) \\ \omega_Z(t) &= \Omega_N \end{aligned} \qquad [8.14]$$

The on-ground orbital oscillator task was required to recalculate orbital oscillator values (S_v, C_v), propagation values (S_d, C_d) and transverse rate (Ω_T) and uplink these parameters to the spacecraft at regular intervals—nominally every 15 min—in both sun-pointing and normal modes. The orbital oscillator values calculated on ground corresponded exactly to the start time of a format on-board and were uplinked so that the new values were available on-board at precisely that time. The propagation values and transverse rate were less time-critical and were uplinked to be available on board shortly after the orbital oscillator values.

Uplink was performed automatically from ground through the mission planning system, although additional manual commanding was available if necessary. If for any reason, there was an interruption to commanding, there was no need to perform any emergency uplink of the orbital oscillator parameters since the on-board real time attitude determination showed no deterioration if the nominal scanning law rates were refreshed every hour or longer.

8.2. Star Observations

The star observing strategy algorithm, implemented in the on-board computer, made a selection, at regular time intervals, from the programme stars which crossed the field of view (information about the stars expected to cross the fields of view, on the basis of the nominal scanning law, was uplinked from the ground station to the satellite at regular intervals). The star observing strategy determined those stars that had to be observed, and allocated to them appropriate observation times.

The choice of the algorithm depended on optimisation criteria related to the performance of the mission, and on system constraints due to the hardware environment in which the star observing strategy had to operate. The main optimisation criteria were the following:

(1) minimisation of jitter effect: since observations of stars in the combined field of view were not strictly simultaneous, the attitude jitter of the satellite could introduce considerable noise in the measurements. The star observing strategy had to be able to minimise this effect by proper interlacing of star observations;

(2) distribution of observations between two viewing directions: implicit in the measurement concept was the capability of measuring relative angular distances between stars located far apart on the celestial sphere. It was one of the objectives of the star observing strategy to make sure that, when several stars were present in the combined field of view, angular distances were measured, whenever possible, between stars coming from the different fields of view;

(3) compatibility with the overall observing programme: in order to achieve the target precision at the end of the mission, stars of the various classes of magnitudes should have received, on average, a certain, predefined, global observation time. One of the functions of the star observing strategy was to ensure that stars received, during their crossing of the fields of view, a time allocation compatible with their global observation time;

(4) special emphasis on the observation of bright stars: observations of bright stars ($B < 9.0$ mag) were particularly valuable. Their positions could be measured with high precision, and these were subsequently used in the determination of the attitude of the satellite during the relatively long time periods (400 s on average) between attitude control jet firings. This ‘smoothing’ of the attitude determination provided, in turn, connections between pairs of bright stars not simultaneously present in the combined field of view. These additional connections considerably improved the final astrometric results. The star observing strategy was implemented such that bright stars were observed over as much of the scan as possible, i.e. as soon as they entered the field of view and until just before they left it;

(5) minimisation of errors due to grid imperfections: imperfections in the manufacture of the grid could induce errors in the phase measurements of a star. These errors were considerably reduced by a proper choice of the observation scheme.

The main system constraints related to the hardware environment in which the star observing strategy had to operate were the memory and time limitations of the on-board computer; the synchronisation with the telemetry format, the attitude and orbit control system, and the cold gas thruster firing; and constraints due to the downlink telemetry resources.

The Star Observing Strategy

The star observing strategy algorithm was built around a rigid time hierarchy and its operation was driven by three star-dependent parameters uplinked from ground. The time hierarchy was based on the following definitions:

(1) the sampling period, $T_1 = \frac{1}{1200}$ s, was the sampling time during which photoelectron counts were accumulated by the image dissector tube;

(2) the instantaneous field of view repositioning period, $T_2 = 8T_1 = \frac{1}{150}$ s, was the shortest time interval (or 'slot') during which the instantaneous field of view remained pointed on a given star. Each star was always observed for an integer number of slots, and the instantaneous field of view remained pointed at the same location on the grid throughout a slot. If a star was observed for more than one slot, the position of the instantaneous field of view was updated for the next slot;

(3) the interlacing period, $T_3 = 20T_2 = \frac{2}{15}$ s, was the period of time during which a group of up to 10 stars were observed;

(4) the observation frame period, $T_4 = 16T_3 = 2.133\ldots$ s, was the period of time during which essentially the same group of stars were observed in the same order and with a given observation time allocation (exceptions are discussed below);

(5) the transit time, $T_5 = 9T_4 = 19.2$ s, was roughly the time interval taken for any given star to cross one of the fields of view of the telescope.

Star-Dependent Parameters

The star-dependent parameters uplinked from ground, and on which the star observing algorithm operated, were:

(1) the selection index: the parameter used to calculate the priority with which a programme star must be observed with respect to the other programme stars simultaneously present in the field of view;

(2) the minimum observation time: the minimum number of slots of T_2 which, at frame level, had to be allocated to a star in order to achieve a sufficient precision in phase extraction (this was a function of the magnitude of the star);

(3) the target observation time: the observation time which, at frame level, had to be allocated to a given star in order to achieve, at the end of the mission, the global observation time associated with that star (this was also a function of the magnitude of the star).

The values of the star-dependent parameters could vary during the mission, to take into account the past and projected observational history of the star, but they were fixed during each crossing of the field of view by the star. The values of the minimum and target observation times for a star of given magnitude were determined on the basis of simulations carried out by the INCA Consortium and the data reduction consortia, and were uplinked during the mission from ESOC to the satellite, where the star observing strategy was implemented.

Other parameters included in the star observing strategy algorithm were: the predicted time of entrance of the star in the field of view; its magnitude; a flag indicating whether the star was observed in the preceding or following viewing direction; and a flag indicating whether the star should have been observed by the star mapper for attitude-measurement purposes (a subset of some 40 000 programme stars, in particular bright stars with good *a priori* positional accuracies, fell into this category).

During the operations, ESOC processed the data derived from the Hipparcos Input Catalogue and the observational history of the programme stars to produce a so-called 'programme star file', which contained the information to be uplinked to the satellite. The programme star file contained star identifications, magnitudes, field of view entering times, viewing direction flags (the transverse coordinate needed for detector piloting and real-time attitude estimation), and the current values of the three star-dependent parameters discussed above. A scheme for the data processing involved in the generation of the programme star file is shown in Figure 8.4.

Fully and Partially Observable Stars

When a frame of $T_4 = 2.133\ldots$ s was considered, stars that remained in the combined field of view during the entire frame were called fully observable stars; those that remained in the combined field of view only for a part of the frame, but not less than three interlacing periods ($3T_3$), were called partially observable stars—these could be stars that either left or entered the combined field of view during the frame period.

One way to visualise the flow of programme stars in and out of the combined field of view is by means of a time diagram, such as that shown in Figure 8.5. A star S_i entered the field of view at time t_0^i and left it at time $t_0^i + T_5$. The 'transit line':

$$f_i(t) = \frac{t - t_0^i}{T_5} \qquad [8.15]$$

represents the fraction of transit time spent by the star in the field of view:

$$0 \le f_i(t) \le 1 \qquad [8.16]$$

The stars that were present in the field of view at a given time t' could easily be identified by drawing the line $t = t'$: they are those whose transit lines are intercepted by $t = t'$.

By marking on the t-axis the time intervals corresponding to subsequent frames of $T_4 = 2.133\ldots$ s, one can also identify the stars present in a given frame. For example, in frame number 10 of Figure 8.5, there are three stars present in the combined field of view, of which two are fully observable stars and one is a partially observable star, leaving the field of view before the end of the frame period.

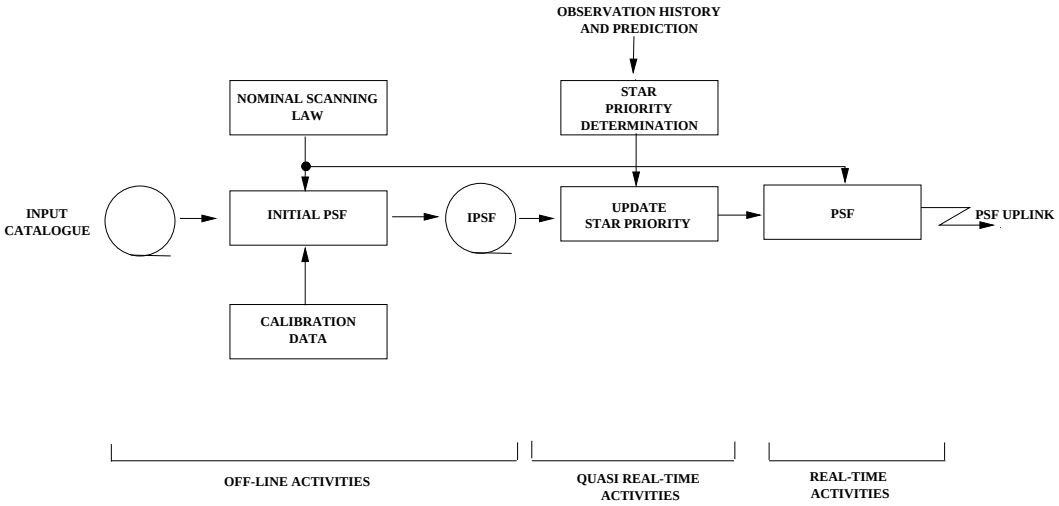

Figure 8.4. *Data processing involved in the generation of the programme star file (PSF).*

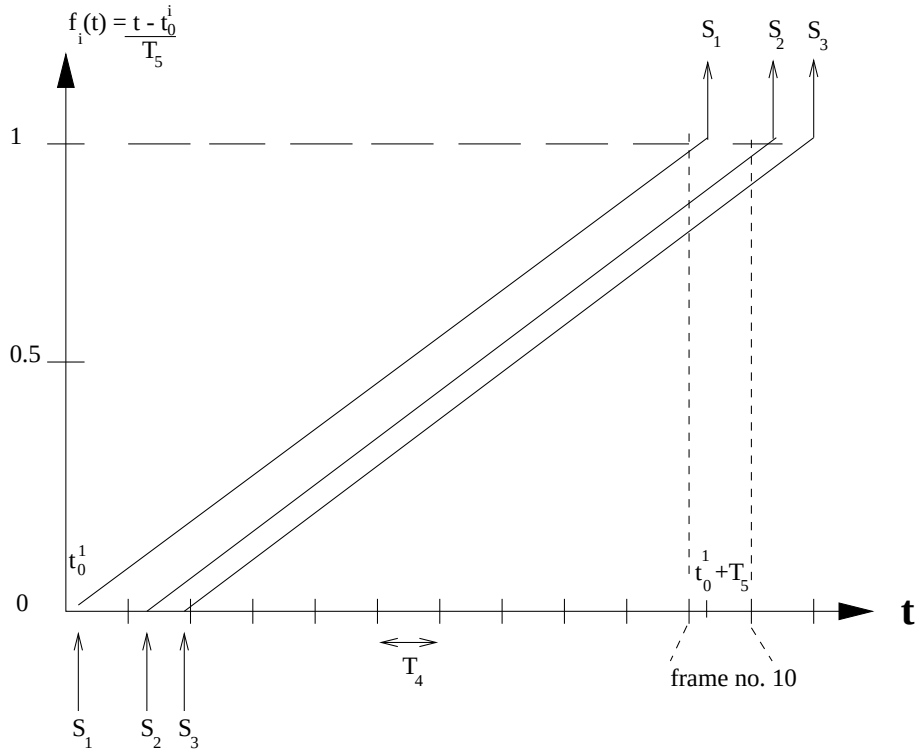

Figure 8.5. *The flow of programme stars in and out the combined field of view, illustrated by means of a time diagram. Stars S_1, S_2, S_3 enter the combined field of view at the bottom left of the diagram, and exit at the top right. An observation frame extends over an interval of T_4 (2.133 . . . s). See text for details.*

Star Selection

The star observing strategy algorithm involved both star selection and observation-time allocation. Star selection proceeded according to the following rules:

(1) from the data contained in the programme star file and the real-time attitude calculated on-board, the stars present in the combined field of view for the next frame were identified; the first 15 of them were retained for further selection;

(2) among the stars retained, the partially observable stars were identified and classified into 'leaving' and 'entering' stars;

(3) the fully observable stars were identified;

(4) if there was at least one fully observable star, up to two partially observable stars were selected (one leaving and one entering) provided that they were brighter than magnitude $B = 9$ mag, choosing the brightest in each class;

(5) if there was no fully observable star, up to two partially observable stars were selected (one leaving and one entering) choosing the brightest in each class;

(6) once the partially observable stars, if any, were selected, the selection of the fully observable stars proceeded as follows: (a) alternatively one star was selected from the preceding and one star from the following viewing direction, until one of the two groups was exhausted; then the remaining stars were added; (b) within each of the two groups, stars were selected according to their priority index, defined by:

$$P_i = (-1)^k \frac{t_k - t_0^i}{T_5} b_i \qquad [8.17]$$

where i is the star identification number of star S_i, k is the frame identification number, t_0^i is the time of entrance of star S_i in the field of view, t_k is the mid-time of frame k, b_i is the selection index, and T_5 is the transit time. Priority was then given to stars with the higher values of P_i. Due to the factor $(-1)^k$, priority indices changed sign from one frame to the next, in such a way that priorities alternated: the star with the highest priority in frame k was, as a rule, the star with the lowest priority in frame $k + 1$;

(7) the complete list of selected stars consisted of the partially observable stars, if any, plus a number of fully observable stars, if any, such that the total number of stars selected for observation during the relevant frame period did not exceed ten. The alternating priority parameter ensured that, in those (rare) cases where more than 10 stars were simultaneously visible in the combined field of view, those stars not observed during one frame period were observed during the subsequent frame.

Observation Time Allocation

Observation time was allocated over an interlacing period of $T_3 = \frac{2}{15}$ s. The resulting time allocation was repeated for the 16 interlacing periods contained in a frame, except for the change described at point (5) below. The observing time was allocated as follows:

(1) if there was no fully observable star in the field of view, 10 slots of $T_2 = \frac{1}{150}$ s were allocated to each partially observable star when two partially observable stars were

selected, or all 20 slots of T_2 to the one partially observable star, if only one partially observable star was selected;

(2) if there was at least one fully observable star in the field of view, two slots were allocated to each partially observable star selected. Once the observation time allocation to partially observable stars was completed, the remaining slots available were allocated to the selected fully observable stars as follows:

(3) each fully observable star was allocated, in sequence, its minimum observation time, until either the list of stars was exhausted or the number of slots available (20) in the interlacing period was exceeded. In the latter case, the remaining fully observable stars were dropped from the observation list and no longer considered. In the absence of any partially observable stars, at least two fully observable stars, if present, would always be observed, by allocating, if necessary, an observation time shorter than the minimum observation time (for the faintest stars the nominal minimum observation time was larger than 10 slots);

(4) the remaining slots, if any, were allocated one by one to the fully observable stars actually observed, on the basis of their so-called 'performance index' z_i, defined as:

$$z_i = \frac{n_i}{\underline{t}_i} \qquad [8.18]$$

where n_i is the actual number of slots which had already been allocated to the star in the interlacing period, and $\underline{t}_i$ is the target time. The first available slot was allocated to the star with the lowest performance index, and so on;

(5) if a partially observable star was actually observed, the 2 slots which were free when the star was *not* present in the field were allocated to the fully observable star with the lowest performance index—referred to below as its 'associated' fully observable star.

Execution of the Observing Sequence

The observation sequence was then executed in the following order:

(1) in each interlacing period fully observable stars were observed in order of entry;

(2) all slots devoted to the same star were contiguous;

(3) during the interlacing periods in which partially observable stars were present, the observation slots of each partially observable star were contiguous with the ones of its associated fully observable star;

(4) the entering partially observable star was observed after its associated fully observable star;

(5) the leaving partially observable star was observed before its associated fully observable star;

(6) if there was no fully observable star, the leaving partially observable star was observed before the entering partially observable star.

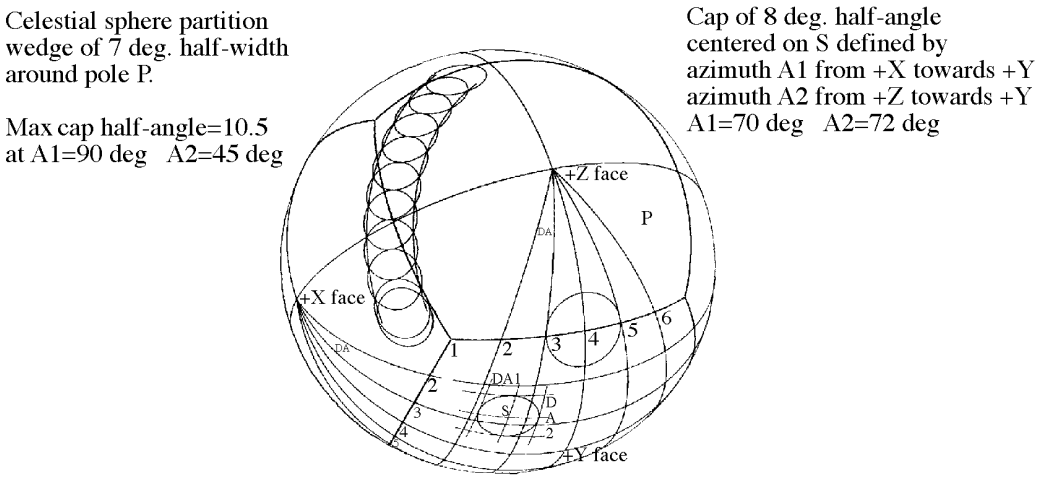

Figure 8.6. *Partitioning of the celestial sphere for the operational Hipparcos Input Catalogue implemented at ESOC.*

8.3. Input Catalogue Consortium Interfaces with ESOC

The Hipparcos Input Catalogue contained all relevant data for the 120 000 programme stars to be observed by the satellite. The stars chosen for the Hipparcos Input Catalogue fulfilled complex selection criteria related primarily to their scientific interest, but also taking into account other factors, such as their magnitude, their distribution over the entire sky, their proximity to other bright objects, and their role in the satellite attitude control and in the data processing. All these properties were then used to optimise the planned observation sequence obtaining the most homogeneous set of observations of objects on the entire sky over the lifetime of the mission.

The INCA Consortium provided ESOC with the main Hipparcos Input Catalogue, and a number of annexes including information on: (i) double and multiple stars; (ii) ephemerides for large-amplitude variable stars; (iii) approximately 13 000 additional stars with $B < 9.0$ mag not contained in the catalogue of programme stars but which were included as real-time attitude determination guide stars to provide more uniform sky coverage for the attitude control.

From the main catalogue ESOC generated an operational version which was partitioned according to a 'celestial cube' structure to ensure a fast access time. Conceptually the celestial sphere was first divided into six identical parts corresponding to the faces of a cube inscribed into the sphere. Each face was further divided into elementary zones of approximately $3° \times 3°$ by a grid of mutually orthogonal great circles (Figure 8.6). The main operational catalogue was augmented by an index file which contained a restricted set of data for each star, namely the position, magnitude, and HIC (Hipparcos Input Catalogue) number. The stars were ordered within the index file according to zone, the HIC number providing the key to the main catalogue.

In deriving the operational input catalogue various other parameters were computed, including, (a) variability flags, (b) target observation times, (c) lower and upper minimum observation times, (d) accuracy test vectors and (e) initial covariance matrices for the modulation strategy. The target observing time, $\underline{t}$, represented the mean time a star should be observed when crossing one of the fields of view. It was derived from the overall target time T (for the entire mission) and the average number $N(\beta)$ of crossings throughout the mission, where β was the ecliptic latitude of the star, and was given by:

$$\underline{t} = T / N(\beta) \qquad [8.19]$$

where T (in seconds) was a function of the Hipparcos magnitude (Hp):

$$\begin{aligned} T &= -750 + 560Hp - 89.5Hp^2 + 4.88Hp^3 \quad (Hp > 5.0) \\ T &= \ 420 \qquad\qquad\qquad\qquad\qquad\quad (Hp \leq 5.0) \end{aligned} \qquad [8.20]$$

$N(\beta)$ was derived by interpolation from Table 8.2.

Hipparcos Input Catalogue Updating

As the data reduction consortia processed the science data, more accurate positions were determined for the catalogue stars. These results were made available to ESOC for use in the programme star file, thereby improving the overall accuracy, not only of the instantaneous field of view positioning, but also of the real-time attitude determination performance, which in turn led to further improvements in overall mission accuracies. In addition, a small number of star positions and magnitudes had to be corrected at the start of the mission. Table 8.3 provides a summary of the principal catalogue updates carried out at ESOC during the mission.

Variable Star Ephemerides

Large-amplitude variable stars required special consideration since, to optimise observing time, it was important to be able to predict their apparent magnitudes. This was done by using specific variable star ephemerides, provided by the INCA Consortium. Once a variable star had been observed by the satellite, the data was processed at ESOC and the results were communicated back to the INCA Consortium, once per month, to further refine the ephemerides. Periodically, a new version of these ephemerides was sent to ESOC for use in generating the programme star file (see Table 8.3).

ESOC processed the observations of variable stars in two stages: (i) payload monitoring, performed in near real-time, and (ii) payload reporting, running off-line. The payload monitoring software is described in detail in Chapter 10. Every 60 s, the program selected one star observed in the preceding 30 s. The selection criteria were heavily weighted in favour of the large-amplitude variable stars, so that if one was present in the interval it was invariably selected for processing.

The second payload reporting program ran daily on the off-line main-frame computer at ESOC processing the previous 24 hours of payload monitoring results, and compiling statistics on various aspects of the general results. In addition, a longer run was performed every week specifically to obtain the large-amplitude variable star results.

Table 8.2. Mean scanning frequency as a function of ecliptic latitude.

$\|\beta\|$	0	10	20	30	40	47	55	65	75	85	90
$N(\beta)$	120	124	134	148	190	280	200	164	150	146	146

Piloting and Magnitude Monitoring

The main reason for running payload reporting every 24 hours was to obtain information concerning the intervals when image dissector tube piloting was 'good' in some sense. The intervals of 'good', 'bad' and 'unknown' image dissector tube piloting were used by the FAST and NDAC Consortia who only processed data when piloting was 'good'. A history of the piloting throughout the mission was held on a sequential file on the IBM main-frame. The information was also used by the observation modulation strategy software which updated observation priorities in the newly generated programme star file given the previous history of observations.

'Good' piloting was defined to be when the last three payload monitoring reports from both fields of view, showed agreement between predicted and measured *Hp* magnitudes to within 1.5 mag. 'Bad' piloting was defined to be when three consecutive payload monitoring reports from one field of view disagreed by more than 1.5 mag in their predicted and measured *Hp* magnitudes. 'Unknown' piloting was defined when there were no payload monitoring reports for over 45 min (usually during loss of signal around perigee). Piloting status flags in the telemetry data stream switched when any of these conditions were satisfied.

This piloting information was incorporated into the variable star reports which were generated in the weekly runs of payload reporting. The main processing steps within the payload reporting task which were relevant for variable star processing and image dissector tube piloting determination were:

(1) each payload monitoring record in the prescribed interval was extracted from the history file (normally extending some 20 days in the past);

(2) the predicted *Hp* magnitude was extracted from the input catalogue for the non-variable stars. For the variable stars the predicted *Hp* magnitude was calculated by linear interpolation from the ephemerides (data points separated by 10 days);

(3) the image dissector tube piloting at the time of observation was extracted from the piloting file if the data was available from previous results from payload reporting;

(4) the measured *Hp* magnitude was calculated (as described below). A record was written to the variable star report file containing the following information:
   - time of on-board observation;
   - Hipparcos Input Catalogue (HIC) identifier of monitored star;
   - blue magnitude of star;
   - colour of star;
   - sample count, i.e. observation time in units of 1/1200 s;
   - quality of preceding observation (see Chapter 10);
   - quality of image dissector tube piloting;

– field of view indicator (1 for preceding, 2 for following);
– observed intensity, I_0 in counts per s;
– measured modulation coefficient M_1;
– measured modulation coefficient M_2;
– predicted Hp magnitude;
– measured Hp magnitude;
– the difference between the predicted and measured Hp magnitudes.

The measured Hp magnitude as calculated above was dependent on (i) the measured count rate I_0; (ii) the field of view, $\epsilon = +1$ (preceding field of view), $\epsilon = -1$ (following field of view); (iii) the coordinates of the star on the main grid (G, H), and (iv) the colour index of star, $c = B - V - 0.5$.

A calibration of the transformation between measured count rates and Hp magnitude was conducted routinely by the FAST Consortium's 'first-look' facility at Utrecht. The calibration was performed using a least-squares fit, for photometric standard stars only, to the 17 unknown coefficients r_i in the following equations:

$$R = r_0 + r_1\epsilon + r_2 I_0 + r_3 I_0^2 + r_4 G + r_5 H + r_6 G^2 + r_7 GH + r_8 H^2 + r_9 G^3 + r_{10} G^2 H + r_{11} GH^2 + r_{12} H^3 + r_{13} c + r_{14} c^2 + r_{15} cG + r_{16} cH \quad [8.21]$$

and:

$$I_C = I_R \, R \, 10^{0.4(9-Hp)} \quad [8.22]$$

where I_C is the corrected value of I_0 for a star of Hipparcos magnitude Hp and I_R is a reference intensity for a star of magnitude $Hp = 9$ mag. ($I_R = 1760$ for the image dissector tube used throughout the mission). With I_R known and R calculated, the Hipparcos magnitude was given by:

$$Hp = 9 - 2.5 \log_{10}(I_0/(I_R R)) \quad [8.23]$$

Minor and Major Planet Ephemerides

In addition to the stars defined in the Hipparcos Input Catalogue, several solar system objects were contained within the original observing programme: 48 minor planets; the Jovian moon, Europa; and the Saturnian moon, Titan. In order to schedule these objects within the programme star file, accurate ephemerides for the major and minor planets were provided by the Bureau des Longitudes. These ephemerides were updated on a regular basis. In addition, a further Saturnian moon, Iapetus, was added to the observing programme part way through the mission. It had been expected that the Moon's brightness and separation from Saturn would make it a difficult candidate for observation. Nevertheless, the payload proved to be sufficiently sensitive to be able to make a series of good observations.

One other object which was added after the mission was started was the quasar 3C 273. This object, always considered to be at the very limit of the satellite's observational capabilities, was added in view of its possible role in defining an inertial reference system. As expected, however, the observations of this object provided very little additional weight in this respect.

Table 8.3. History of principal catalogue updates at ESOC.

Date	Description
01/12/89	Hipparcos Input Catalogue Version 6
20/12/89	Variable Star Ephemerides
23/03/90	Variable Star Ephemerides
21/06/90	Minor Planet Ephemerides
04/07/90	Hipparcos Input Catalogue Version 7
04/07/90	Variable Star Ephemerides
27/10/90	Variable Star Ephemerides
22/01/91	Variable Star Ephemerides
21/02/91	Hipparcos Input Catalogue Version 8
21/04/91	Hipparcos Input Catalogue Version 9
03/07/91	Minor Planet Ephemerides
03/07/91	Variable Star Ephemerides
06/08/91	Major Planet Ephemerides
06/08/91	Minor Planet Ephemerides
22/11/91	Europe, Titan, Iapetus Ephemerides
19/03/92	Variable Star Ephemerides
01/12/92	Hipparcos Input Catalogue Version 10
30/11/92	Minor Planet Ephemerides
16/12/92	Europe, Titan, Iapetus Ephemerides

History of Hipparcos Input Catalogue Updates during Operations

Table 8.3 lists the main updates which were made to the various catalogues and ephemerides throughout the mission. Versions 1 to 5 of the Hipparcos Input Catalogue were implemented at ESOC before launch. Smaller incremental changes were occasionally made at other times.

8.4. Programme Star File Generation

Basic Methodology

To hold the complete Hipparcos Input Catalogue (with details of the 120 000 stars and other objects to be observed) on-board and implement the observation strategy described in the previous section would have imposed too much of a computational burden on the on-board computer. The solution was to hold only the relevant star observation parameters for the next 20–30 minutes, and to refresh it by regular commands from ground. This buffer was called the ‘programme star file’.

The programme star file contained star identifications, magnitudes, field of view entry times, field of view identifications and the observation strategy parameters discussed in the previous section. The observation duration was calculated taking into account the brightness of the star (the fainter the star the longer the observation), its scientific

priority, the number of other programme stars within the field of view competing for the available observing time, and the number of times the star had already been observed during the mission. Because there were long periods without ground station support, some stars were under-observed over a particular time interval. Consequently, the relative importance of observing these stars later was increased. In this way, all the stars in the catalogue were observed sufficiently to provide reasonably uniform accuracies in position, parallax and proper motion, by the end of the mission.

The off-line IBM mainframe at ESOC prepared an on-ground 'extended programme star file', from where it was transferred to the Hipparcos dedicated control system on the real-time VAX. The extended programme star file contained not only data required by the on-board programme star file, but also additional data required for the on-ground payload monitoring software.

During the routine operational phase, the extended programme star file was generated on a daily basis, then transferred and uplinked regularly. In the two- and zero-gyro operational phases, where the nominal scanning law parameters were varying after every perigee, the extended programme star file could only be generated once the new nominal scanning law parameters had been determined. A history of the latest two weeks of data was maintained to allow post processing for payload calibration activities and maintenance of the modulation strategy. The creation of the daily extended programme star file is summarised as follows:

(1) a coarse selection was made of objects which would cross the field of view in the given period. The basic principle was to calculate the nominal scanning law attitude at very close intervals of time and for each field of view extract from the star catalogue the stars which were in the vicinity of the pointing directions. For each candidate star, an accurate transit time and ordinate was computed. If the ordinate was within the allowed range a star transit record was generated. This selection procedure was made efficiently through the use of the partitioned operational input catalogue (see Section 8.3);

(2) as soon as a star had been selected in the coarse selection phase, its accurate transit time was computed, taking account of: (a) proper motion in ecliptic longitude and latitude, (b) parallaxes for nearby stars, and (c) stellar aberration due to the combined motions of the spacecraft around the Earth and the Earth around the Sun;

(3) observation parameters were computed for each object to be observed on the main grid. These observation parameters were the minimum observation time expressed in a number of slots per interlacing period and the target observation time expressed in a number of slots per frame (2.133... s). These two parameters were used by the on-board star observation strategy to share the observation time between the programme stars present in the combined field of view (see previous section). For programme stars, these parameters were derived from the initial values modulated by the current observation history, characterised by the covariance matrix B (described in Section 8.5). For variable stars and solar system objects the observation parameters were only a function of the current magnitude and the ecliptic latitude.

In addition to nominal programme star files, ESOC were responsible for generating the special programme star files to support the initial calibration activities (Chapter 5). These programme star files were classified into two categories: those derived from the nominal scanning law, but with special requirements on the stars to be observed (e.g.

star magnitude, star density) and those derived from a non-nominal scanning law (e.g. the non-nominal sun-pointing operations with solar aspect angle $\xi = 0$).

Mission planning products acted as input for the extended programme star file generation since the mission plan (generated on a weekly basis) provided the times of any special calibration, Earth and Moon occultations when one or both fields of view were obscured, and ground station outage when a sparse programme star file was required (see below). A fuller description of the mission planning system is given in Section 4.6.

Real-Time Attitude Determination Guide Stars

Approximately 60 per cent of all programme stars were selected as guide stars for the on-board attitude control. The conditions for selection were that (a) the star had a variability range less than 0.02 mag; (b) its B_T magnitude was in the range 5.0–9.5 mag; and (c) its position accuracy was better than 0.8 arcsec. A component of a double or multiple star system could be selected if certain additional conditions were satisfied: (a) the distance to other components was larger than 23 arcsec; or (b) the difference in magnitude was larger than 1.5 for separations between 0.8 and 23 arcsec; or (c) for a separation not exceeding 0.8 arcsec, the root-mean-square of the separation and position accuracy did not exceed 0.8 arcsec.

Sparse Programme Star File

Significant modifications to the programme star file generation software were necessary for the revised mission. With the revised elliptical orbit, non-coverage periods lasting several hours were occurring routinely. Particularly, during the first months of the revised mission, before two further ground stations were made available on a regular basis, complete orbits were without coverage at times. Given that there was only sufficient memory for a nominal programme star file to last for about 20–30 min, real-time attitude determination would have diverged within a few minutes of the end of the programme star file. For an extended loss of coverage lasting 10 hours, the attitude of the spacecraft could have deviated from the nominal scanning law sufficiently to cause the on-board emergency sun acquisition mode to trigger.

This prompted the development of the so called ‘sparse programme star file’ for non-coverage periods to ensure permanent convergence of real-time attitude determination. This sparse programme star file consisted of only the brightest reference stars, spanning the non-visibility periods of up to 12 hours, thus providing continuous information for the attitude control system between two successive stations’ support.

Alternating Strategy

On 20 September 1991, the programme star file generation software was revised to include an alternating selection strategy for stars in the open cluster NGC 2516, where four stars in a small region of the sky were added to the programme to serve as calibration objects for the Fine Guidance Sensors on-board the Hubble Space Telescope.

Straightforward inclusion of these stars was not possible, as they exceeded the programme star file requirements for adequate observation time for each object. The solution was to allow approximately half the objects to be observed during one rotation

period of the spacecraft, then to allow those which were not observed in the previous period to be observed in the following. Subsequent scans across this area of the sky resulted in alternating selections of stars within the programme star file.

8.5. Modulation Strategy

Target observing times defined in Section 8.2 had been defined initially in order to achieve, as far as possible, uniform accuracy of the final Hipparcos astrometric data over the whole celestial sphere assuming nominal scanning. At the start of the mission, in order to fix those target times, it was necessary to compute, for each programme star, the 5×5 target covariance matrix, B, of the five astrometric unknowns (the ecliptic longitude and latitude, the ecliptic components of proper motion, and the parallax) based on the nominal scanning law. The memory of those target covariances was kept throughout the mission, while actual covariances were obtained via the routine updating process defined below. This process was equivalent to substituting each day in matrix B the actual observing times compared with the target ones. Comparing actual to target variances indicated whether stars were running under- or over-observed with respect to plans. Star-dependent parameters were then modified in the programme star file in order to give highest priority to the most important observations occurring over the coming hours.

The computation of the initial matrix B was performed at ESOC after receiving the main catalogue from the INCA Consortium. The most computationally efficient method to do this was to compute the matrix for each star in sequence, calculating all expected transit times over the predicted mission duration. The following steps were performed for each programme star:

(1) the information matrix $A(5,5)$ was initialised to zero;

(2) on the assumption that the parameters defining the nominal scanning law were fixed throughout the mission, the precession rates and rotation rates were used to extrapolate from the last observation to the next observation time. The use of the transit time was limited to the derivation of the inclination angle, i, which was defined to be the angle between the scan direction and the local ecliptic meridian at the time of observation. It followed that the level of accuracy was not as stringent as in the case of programme star file generation. In particular the effects of proper motion, parallax and aberration were neglected. It was however necessary to check whether the star crossed one or both fields of view setting n_i to 1 or 2 accordingly;

(3) for each transit, the five observation coefficients $a(1) \ldots a(5)$ were computed as follows. Defining:

(λ, β) as the star ecliptic longitude and latitude

λ_s as the sun ecliptic longitude

(X_0, Y_0, Z_0) as the orientation of the scan axis

T_i is the computed transit time (years)

T_0 is the expected mission mid-point time (years)

μ_s is the drift angle of the star (radians)

Then:

$$\cos i = X_0 \sin\lambda - Y_0 \cos\lambda$$
$$\sin i = \pm\sqrt{1 - \cos^2 i} \qquad [8.24]$$

where $\sin i$ takes the sign of Z_0. Finally:

$$\begin{aligned} a(1) &= \sin i \\ a(2) &= \cos i \\ a(3) &= (T_i - T_0)\sin i \\ a(4) &= (T_i - T_0)\cos i \\ a(5) &= \sin(\lambda_s - \lambda)\sin i - \cos(\lambda_s - \lambda)\cos i \cos\beta \end{aligned} \qquad [8.25]$$

(4) the information matrix was then updated using the number of observations n_i in the current revolution period, and the target observing time $\underline{t}$:

$$A(j,k) = A(j,k) + a(j)a(k)n_i\underline{t} \qquad [8.26]$$

(5) the symmetric matrix A was inverted to derive the covariance matrix B.

Routine Updating

Since the target observing time was derived from the covariance matrix of observations as available for each star in the main catalogue, the main catalogue at ESOC had to be updated on a daily basis taking account of the telemetered image dissector tube observation reports since the previous processing run. The processing of the image dissector tube observations was scheduled automatically on the off-line mainframe computer at ESOC. Again, this procedure only applied to the non-variable programme stars; solar system objects were not considered. The sequence of events was as follows:

- the image dissector tube reports were retrieved from the archive files on the front-end dedicated computer system and transferred to the off-line machine;
- the programme star file star identifiers (running from 0 to 255) were correlated with the HIC identifier in the extended programme star file, using the expected and observed transit times;
- the reports were archived and sorted according to HIC number;
- the total accumulated observation time was computed for every star each time it crossed one of the fields of view;
- the covariance matrices in the input catalogue records were updated according to the total observation times;
- a record was maintained of the last image dissector tube report to be successfully processed to allow the next processing run to continue from the correct time.

In order to update a covariance matrix, the HIC number in the (ground-based) extended programme star file record was used to extract the corresponding input catalogue record. The new covariance matrix was then computed using the old covariance matrix, the total observation time in this processing interval as well as certain additional data contained in the extended programme star file record.

Defining:

t_{obs} as the total accumulated observation time for the star in question as it transited a field of view

$\underline{t}$ as the target observing time per field of view transit (defined in the previous section)

$\vec{a}$ as the five observation coefficients, $a(1) \ldots a(5)$

B as the covariance matrix

Then B was updated using the following equations:

$$\begin{aligned} s &= \text{sign}(\underline{t} - t) \\ \vec{o} &= \sqrt{|\underline{t} - t|}\vec{a} \\ \vec{u} &= B\vec{o}^T \\ c &= -s\vec{o}\vec{u} + 1 \\ B &= B + \frac{s}{c}\vec{u}.\vec{u}^T \end{aligned} \qquad [8.27]$$

Consequences for the Revised Mission

On 9 May 1990, the revised observation modulation strategy taking account of the revised mission profile, was implemented within the flight dynamics system at ESOC. Significant revision to the strategy was necessary in order to account for long periodic losses of signal and loss of real-time attitude determination convergence around perigee when computing the initial covariance matrices, as follows:

(1) re-computation of the initial covariance matrix. The observation time which would be lost for each star due to perigee passage, ground station outages, occultations by the Moon and the Earth, and consequent loss of good measurements could not be predicted accurately over the projected 2.5 years of the revised mission. A coarse estimate was made of the loss, estimated to be between 20 and 30 per cent, depending on the ecliptic latitude of the star. For each star of the programme the overall target time T (see Section 8.3) was modified accordingly and the initial covariance matrix recomputed as a function of all nominal transits over the mission duration;

(2) recording of good observation periods. In the initial implementation of the modulation strategy it was assumed that all measurements would be of good quality. Access to the telemetry was required only to find how much time was effectively devoted to the observation of a star for a particular transit. In the actual mission the real-time attitude determination on-board diverged frequently mainly during perigee passage. This led to bad piloting of the image dissector tube and hence useless star measurements. The detailed time allocation recorded in the telemetry star observation reports was then of no value. Fortunately times of good observation periods could be provided by an already existing payload reporting program, running off-line on a daily basis (see Chapter 10). The modulation strategy package was modified to interface with this program, thus having access to the periods of ‘good’, ‘bad’ and ‘unknown’ piloting quality.

Results

Current values of the observation parameters were regularly communicated to the INCA Consortium for cross-checking that the modulation strategy was producing optimised observing times. Performance assessments made in May 1991 and March 1992 showed that the revised modulation strategy worked according to expectations. A detailed report of the May 1991 assessment study was given in Crézé & Chareton (1991). In particular

some stars which had been drastically under-observed in the early part of the mission slowly recovered the accuracy expected later in the mission as a result. The modulation strategy was eventualy switched off towards the end of 1992 when it became clear that no reliable long-term prediction of the nominal scanning law could be given in view of the gyro failures and consequent attitude control problems.

9. INTERFACES WITH THE DATA REDUCTION CONSORTIA

This chapter describes the key areas in the Hipparcos operations which required an exchange of information between the control team at ESOC and the various groups of scientists responsible for the data processing. Particular attention is paid to the nominal scientific data distribution to the Data Reduction Consortia. In addition to providing the input and final catalogues, the Data Reduction Consortia were able to supply refined payload calibration and other information which proved crucial for both the safety of the spacecraft and the quality of the final results.

9.1. Introduction

The satellite operating principle and the interfaces with the scientific data reduction consortia is illustrated in Figure 9.1. The satellite was fully controlled by ESOC, at Darmstadt (Germany). Using remote ground stations, all the necessary telecommanding was performed and all the telemetered data was received from the spacecraft at ESOC. The data was divided into several categories such as attitude control, spacecraft housekeeping, and science data. By monitoring this data (in real-time and off-line), it was possible, through ESOC's Hipparcos dedicated computer system, to control and operate the spacecraft in an optimum way. Of primary importance were spacecraft safety, on-board and on-ground systems maintenance, and effective science data return.

The Hipparcos Input Catalogue, as defined by the INCA Consortium, was used by ESOC for routine operations involving the generation of the programme star file, described in Chapter 8. Appropriate subsets of this file were uplinked to the satellite, along with the other telecommands necessary to maintain satellite operations. Typically, a 30-minute buffer of observations was maintained on-board, with observations being made continuously. After the on-board compression of the image dissector and star mapper data, the formatted scientific data was telemetered to ground. The telemetry allowed diagnosis of the performance of both spacecraft and payload, providing feed-back for telecommanding and future programme star file generation.

ESOC was also responsible for archiving all spacecraft data and for pre-processing and distributing the data to the data analysis consortia. Preliminary results from the data reduction consortia processing were then used to refine on-board parameters and the on-ground control. In particular, early observational results were sent to the Input

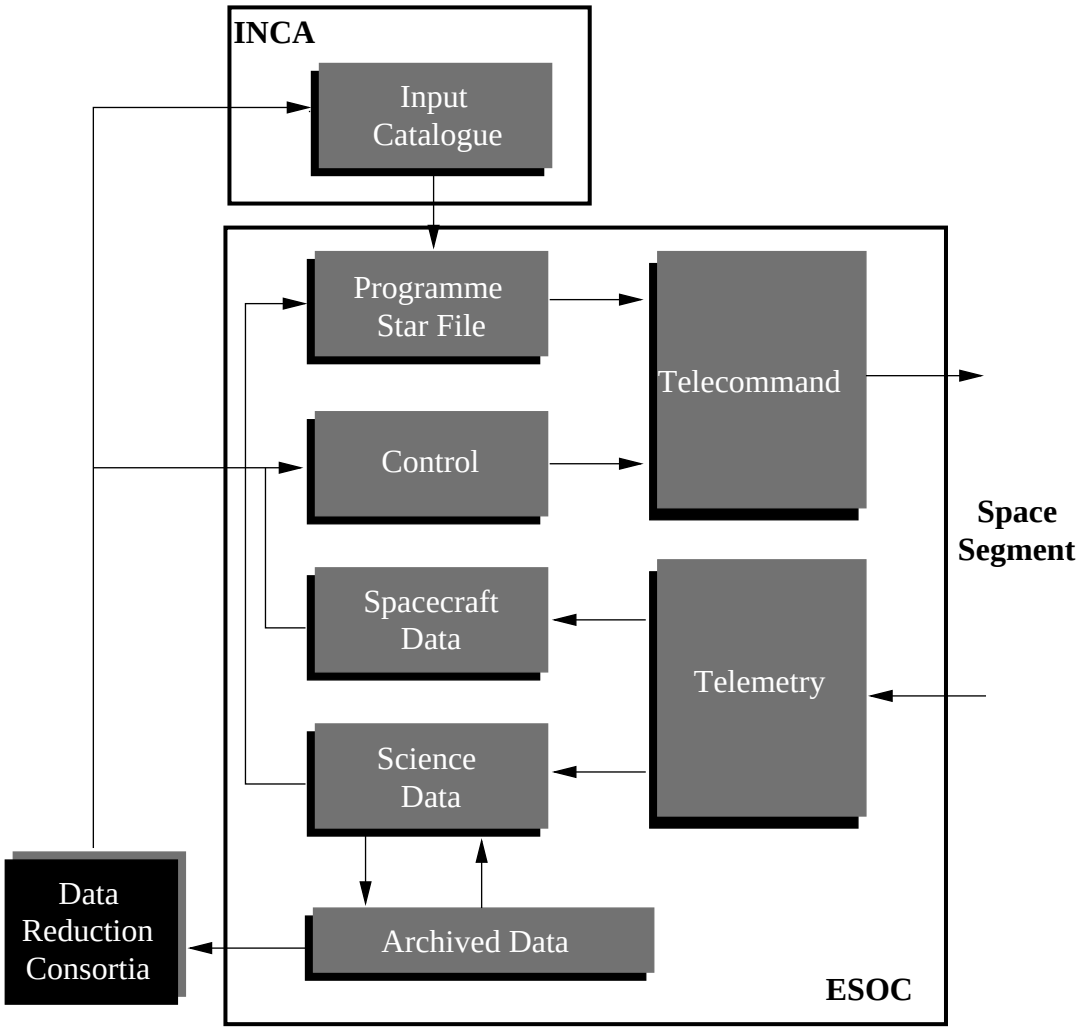

Figure 9.1. *Ground segment operating principle and data distribution. The Hipparcos Input Catalogue, constructed by the Input Catalogue Consortium (INCA), was the basis for the scientific observations and for the satellite attitude control. Data from the Input Catalogue were extracted in the form of the Programme Star File, uplinked regularly to the satellite. Scientific data from the satellite were formatted and archived at ESOC, and despatched to the data reduction consortia. Improved star positions were introduced into the operational scheme as the mission progressed.*

Catalogue Consortium for incorporation into an updated input catalogue for use in the programme star file, thereby improving the reliability of future observations through improved on-board attitude determination using the updated positions, improved detector pointing, and optimised assignment of observation times through the incorporation of improved magnitudes for large-amplitude variable stars.

A full description of the operational interfaces between ESOC and the Input Catalogue Consortium is given in Chapter 8. This chapter describes the interfaces between ESOC and the other Hipparcos scientific consortia, i.e. the FAST and NDAC Consortia, jointly (and in parallel) responsible for the analysis of the main mission data leading to the construction of the Hipparcos Catalogue, and the TDAC Consortium, responsible for the analysis of the star mapper data leading to the construction of the Tycho Catalogue.

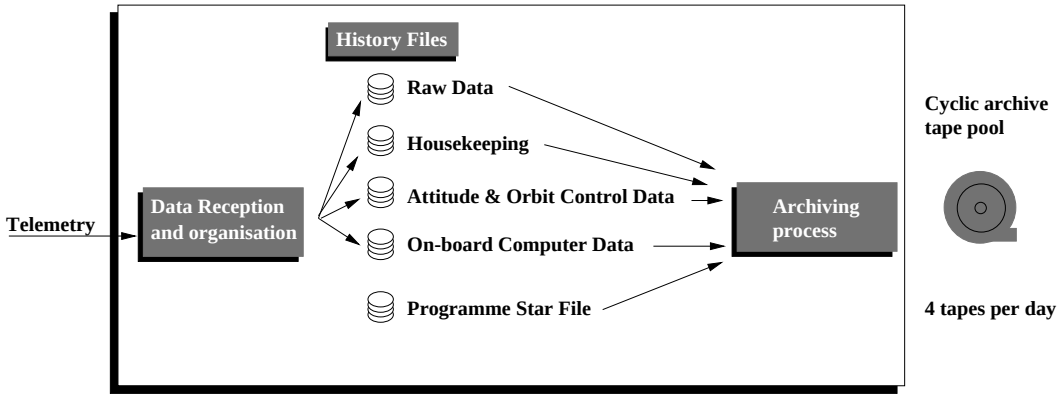

Figure 9.2. *Organising of the data archiving at ESOC. The various data streams from the satellite were merged with orbit data determined on-ground, and information from the programme star file, and despatched to the scientific consortia on magnetic tape.*

9.2. Data Distribution from ESOC to the Consortia

Scientific Data Distribution

ESOC archived all data coming from the satellite, and also took care of production and distribution of data tapes to the data reduction consortia. As a first step, archive tapes were produced on the Hipparcos real-time machine (VAX 8650) every 6 hours, without interfering with real-time operations. Each tape contained raw science data, housekeeping parameters, attitude and orbit control telemetry, on-board computer telemetry, and star information. The approximate volume of data on each tape was 100 Megabytes (see Figure 9.2).

The exact time spans of individual files contained in each of the master tapes of archive telemetry were held in an Oracle data base on the VAX. The running of a sequential tape production task caused the VAX data base to be queried and all new records to be transferred to the ESOC mainframe computer.

Two cartridge copies were made from each original archive tape: one going directly to a back-up store, and the other one was used to generate the scientific tapes. The off-line Comparex 8/96 machine was used for this second processing step. The archive cartridges were read to produce a set of disk files, where the derivation of the scientific data streams took place.

The recipients of the master set of data were situated at four sites in Europe, corresponding to two specific branches in the data reduction chain. Copies of the main mission data (i.e. data from the image dissector tube and selected data from the star mapper, ultimately leading to the Hipparcos Catalogue) were sent to the Royal Greenwich Observatory (RGO) for NDAC and to Centre National d'Etudes Spatiales (CNES) for FAST. Copies of the complete star mapper data records (ultimately leading to the Tycho Catalogue) were sent to two disinct institutes within the TDAC Consortium, the Astromisches Rechen-Institut in Heidelberg, and the Astromisches Institut in Tübingen.

From these four starting points the data were further distributed to groups contributing to the overall reduction and processing chain within the NDAC, FAST, and TDAC Consortia (see Volumes 3 and 4 for further details). In addition, subsets of the data were sent to the FAST Consortium's 'first-look' facility at SRON, Utrecht, for rapid but in-depth appraisal of the scientific data quality (see Section 9.3).

The Hipparcos tape production system for the data reduction consortia ran on the mainframe computer at ESOC. It consisted of six main components as follows:

(1) Tape Read: this read data from cartridges of archived telemetry into disk-based files. The files were organised as keyed sequential circular, and provided the input for the stream derivation task described below;

(2) Interactive Task: this provided a menu-driven interface allowing the user to configure the system for a single processing run and then to initiate processing by starting the Main Control Task or the Copy/Print Task. The different run types, 'First-Look', 'Sequential' and 'Ad Hoc' were all controlled at this level;

(3) Main Control: this acted as a scheduler for the following tasks. The status of the individual tasks was monitored by main control which could then spawn successive 'Read', 'Stream Derivation' and 'Write' operations depending on the return codes from the previous task;

(4) Tape Write: this wrote the reformatted telemetry onto magnetic tapes. The data was written when the system had sufficient data in its disk files to fill an output tape. The last tape written ended on the last full catalogue period present in the processed data. For sequential processing, two master tapes were produced, for the FAST and TDAC (Tübingen) groups;

(5) Copy/Print: this produced copies of the data reduction consortia tapes for the other groups (NDAC and TDAC Heidelberg) and printed tape labels and dispatch forms;

(6) Stream Derivation: this reformatted the telemetry in the format defined by the Hipparcos 'Data Delivery Interface Document', while performing quality checks and filtering the data. The main part of the processing was carried out in this task. Synchronisation of the various data streams to ensure that all streams covered exactly the same time intervals and removal of any spurious data was carried out here. Once the data had been checked for bad quality and valid satellite configuration, the remaining span was then divided into catalogue periods.

Final tapes for distribution to the scientific teams were created in an agreed interface format, specified completely by the Data Delivery Interface Document, which had been defined through dialogue and exchange of simulated data between ESOC and the Consortia well in advance of launch. The final tape contruction also added eclipse, orbit, payload monitoring and coil current calibration matrix files to the scientific streams. The scientific tapes were then distributed to the scientific consortia. Figure 9.3 shows the various steps in this tape production system.

ESOC also responded to specific requests from the consortia during the mission, to provide data tapes covering different time spans, used to evaluate anomalous trends in the behaviour of the payload or to validate specific aspects of the consortia software.

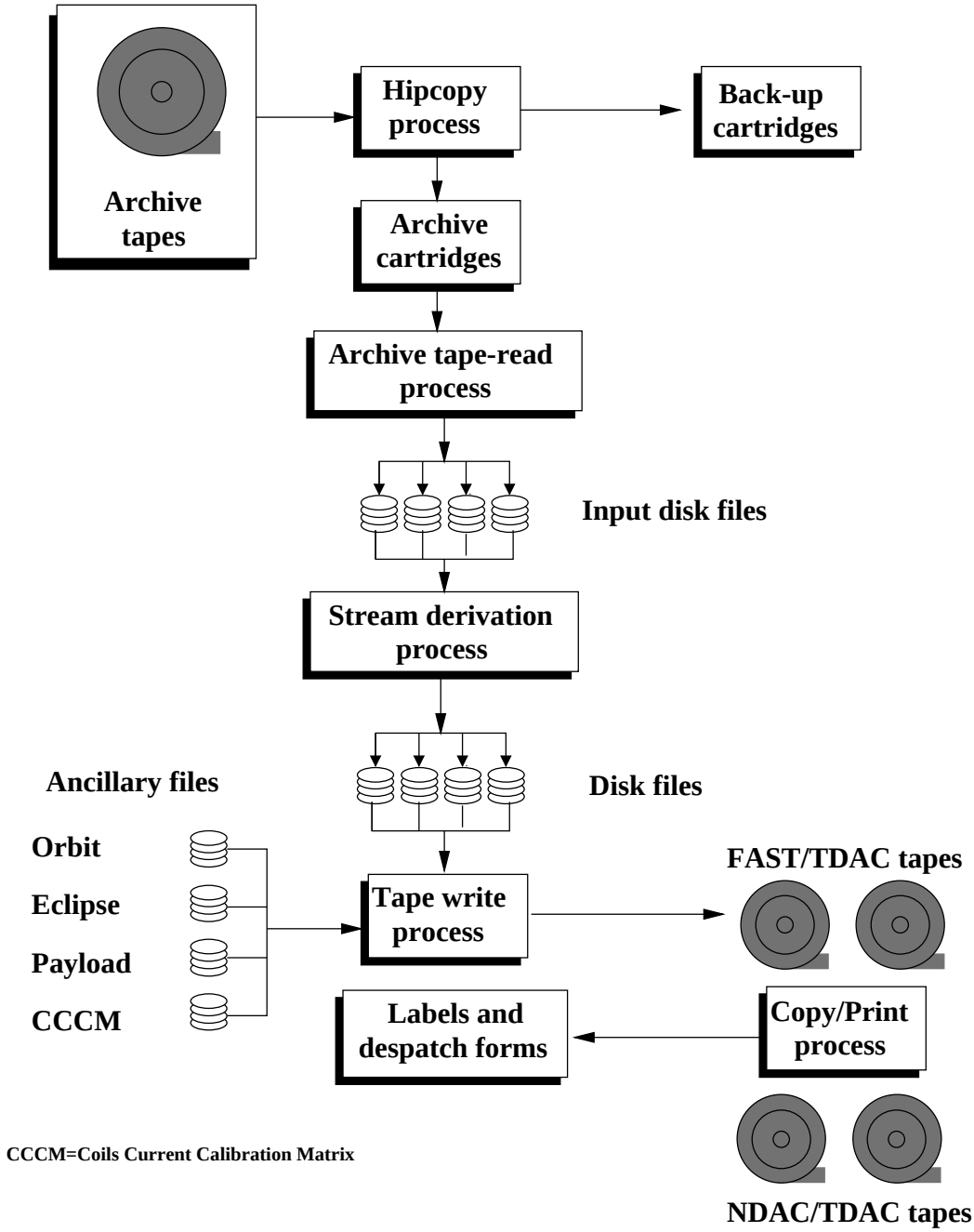

Figure 9.3. *ESOC tape production organisation, leading from the raw data received from the satellite to the magnetic tapes distributed to the data reduction consortia.*

The tape production system was designed with the nominal mission and nominal satellite configuration in mind. Certain changes were introduced as a result of the non-nominal orbit. The failure of on-board components also meant that certain parameters could no longer be reliably extracted from the telemetry. A method of inputting these 'adjustable parameters' was developed and extended throughout the mission as each new anomaly occurred. For example, gyro configurations, star mapper and image dissector tube selections plus additional nominal scanning law parameters were all entered. Checks on the satellite configuration were carried out by the stream derivation task. The changing, 'cross-strapping', patching and re-routing of the on-board systems demanded constant updates to the model against which the configuration was checked.

Once per week, several off-line tasks were performed to analyze all reports from the payload monitoring software in that period. One product from the analysis was a list of intervals in which the image dissector tube quality flag consistently showed that good scientific data was being collected. A file containing all such intervals over the entire mission was input to the tape production software. The consortia only processed data which was flagged as 'good' in this way.

The original raw telemetry was sorted and merged as follows: (i) decommutation into 'floating streams' corresponding to image dissector tube, star mapper data, housekeeping, attitude and orbital control system, and on-board computer data; (ii) association of telemetry reports from on-board computer streams with their corresponding data samples; (iii) extraction of star mapper data from the full star mapper data stream for transits of a magnitude-limited selection of programme stars; (iv) addition of orbit data and eclipse data; (v) addition of other ancillary data (payload monitoring results, coil currents calibration matrix data); and (vi) derivation of a data catalogue which described the payload and on-board computer status and identified periods of unchanging status. The files were transferred from ESOC to the consortia on magnetic tape.

The magnetic tapes were recorded at 6250 bytes per inch with a 7-bit ASCII character set. The maximum allowed blocksize in any file was fixed at 28 800 bytes and the maximum number of logical records were packed into each block. Each tape was self-contained and self-describing, with no multi-volume data sets.

There were two independent sources of timing information given on the tapes: the spacecraft (on-board) time and the ground station time. The ground station times had a resolution of 0.1 μs, but an absolute error of ± 1.0 μs which included a quantisation error of ± 0.2 μs associated with the clock. All telemetry frame times were retained and stored in compressed form with the attitude and orbit control system data stream. For each record of every stream only the initial ground station time and mean frame duration were stored in the telemetry header. The initial ground station time was not corrected for spacecraft-to-ground station propagation delay, nor for the internal ground station delay (these corrections were subsequently made by the data reduction consortia). The on-board time was stored in some records either as a 24-bit format counter or a 32-bit on-board time counter.

The structure of each tape was determined well in advance of satellite launch, following an extended period of dialogue between ESOC and the data reduction consortia, also involving the provision and analysis of simulated data, and leading to a complete specification of the tape structure and contents in the form of the Hipparcos 'Data Delivery Interface Document'.

At the start of every tape was a 'volume header' which gave a unique identifier to this tape, followed by a 'tape header' file which identified the tape as a Hipparcos tape, recorded the date of production and described the structure and contents of the rest of the tape. Every tape then consisted of a series of files, each preceded by a header whose purpose was to identify the consortia for whom the tape was made and to describe the type of file. The end of each file was marked with an end-of-file record which would list the number of blocks in the preceding file. All subsequent files fitted into this structure in a systematic way, no matter which combination of data streams was written to a particular tape. The tape contents generally consisted of the data catalogue, and science and ancillary files. The latter consisted of the image dissector tube file, star mapper file, raw housekeeping (including derived parameters), Tycho data file, attitude and orbit control system data, orbit data, eclipse data, coil currents calibration matrix and payload monitoring results.

Data catalogue file: The data catalogue file was a catalogue of payload status changes derived from the application of an algorithm to the housekeeping data stream. The aim of the data catalogue was to provide a log where the sequence of payload operations was available in a convenient form, and to aid direct access to parts of the data from a tape after it was transferred to disk. A catalogued period was defined as a period containing an integral number of consecutive telemetry formats during which no significant status change occurred. For each such period one record was added to the catalogue.

Telemetry header: All files which were pointed to by the data catalogue had records with a common header containing timing, datation and quality information. All timing information in the header referred to the start of a record. If part of the information for a particular record was missing from the telemetry stream, the timing would still be defined as if the record had been of perfect quality.

Image dissector tube file: Each image dissector tube record was formed by merging an image dissector tube observation report, its associated photon counts and relevant information from the Hipparcos Input Catalogue (in particular the details of the star observation strategy, described in Chapter 8, could be derived from this file). The file also included data received during calibrations of the grid reference marks and internal star pattern assembly (see Chapter 2), in which case the appropriate calibration reports were used. A flag in the image dissector tube header indicated which of the possible alternatives (i.e. normal image dissector tube, or calibration report) was contained in a particular file. Observation reports were merged into the image dissector tube reports without modification.

Counts were integrated over 1/1200 s and were compressed on board in one of two ways, depending on how the star was observed. In the analogue mode (for stars of magnitude brighter than 1.5) counts were 8-bit integers, with nominal quanta of 250 counts per sample period for image dissector tube number 1 and 220 counts per sample for image dissector tube number 2. For stars with magnitude fainter than 1.5, the photon counting mode was used in which counts were expressed as a 3-bit exponent (E) and a 5-bit mantissa (M). For N counts ($0 < N < 8159$), with $J_I = 32(2^I - 1)$ ($0 < I < 7$), if $J_I \leq N < J_{I+1}$ then $E = I$ and $M = (N - J_I)/2^I$. Any fractional part of M was truncated. To reconstitute the image dissector tube signal the algorithm was applied in reverse, with appropriate allowance for the effects of truncation and a non-linearity correction factor. This encoding method was also used for data samples in grid reference marks and internal star pattern assembly observation frames. In practice the analogue mode was never used (see Section 3.1).

Star mapper file: The star mapper file contained selected parts of the Tycho stream covering the calculated crossing times of selected programme stars merged with associated information from the programme star file. Crossing times were calculated for only one of the star mappers, whichever one was operational. For each transit 200 star mapper sample pairs (comprising B_T and V_T samples) were needed. To simplify the subsequent use of these records they were aligned on telemetry frame boundaries and contained 10 consecutive (i.e. separated by 0.04166... s) frames centered around the calculated transit ($T_{\rm calc}$). Star mapper records were stored in chronological order, and stars with $B > 10.25$ mag were disregarded. The transit in a given star mapper record occured at sample number $[(T_{\rm calc} - T_{\rm start}) \times 0.25] + 1.625$ within the record, thus the 200 samples of B or V could be extracted from the 250 samples in each record. The constant 1.625 was the delay between the accumulation of a sample and its appearance in the telemetry. The star mapper samples were encoded with the same semi-log compression law as for the image dissector tube photon-counting mode. There was no corresponding analogue mode for bright stars in the case of the star mapper data.

Tycho file: Each data record contained data extracted from one high-rate telemetry format, namely: (a) standard telemetry header and (b) the Tycho data stream of interleaved $B_{\rm T}$ and $V_{\rm T}$ star mapper counts, encoded with the same semi-log formula used for the image dissector tube data.

Raw housekeeping and derived parameters: This file contained housekeeping data extracted from the raw frame of the high telemetry format, and included additional information appended by ESOC to each record. There was a one-to-one correspondence between raw housekeeping records and the original raw formats. The contents of any bad or missing formats were set to zero. The additional information consisted of the temperature and powers associated with the 24 payload thermal control cells. The housekeeping data also included the complete spacecraft and payload memory-load-command readouts, along with other parameters which were duplicated in the data catalogue records.

Attitude and orbit control system file: The attitude and orbit control system parameters in each telemetry frame were extracted and stored, without modification, as a separate stream with one record per original format. The telemetered parameters were arranged into two groups: (i) those data expected to be of primary interest to the data reduction consortia, and (ii) housekeeping and status data which was not of primary relevance to the data reduction but may be necessary or helpful for scientific checks which were not foreseen at the time. Parameters associated with missing or bad frames were included and processed, but were tagged with an appropriate quality flag. These attitude and orbit control system files also contained the full datation of all incoming telemetry frames, although this was only expected to be used in the event that the on-board oscillator was unstable. Records were only created when the normal attitude and orbit control system format was being telemetered.

Orbit data: Orbit data were organised into a cumulative file covering the satellite lifetime. There was no relation or precise synchronisation between orbit records and telemetry records, thus the orbit data were not pointed to by the data catalogue, instead a description of the whole orbit file was contained in the first record. The time interval covered by a record was normally about 7–8 hours around apogee, and 0.5–1 hour around perigee.

Eclipse data: The eclipse file was another ancillary file pointed to by the tape header file and not by the data catalogue. It contained details of all eclipses that occurred during the mission.

Coil currents calibration matrix data: Real-time calibration generated one such record each time an internal star pattern or grid reference marks sequence resulted in an update of this calibration matrix.

Payload monitoring results: Payload monitoring generated long-term image dissector tube and star mapper reports, approximately one record per week.

First-Look Monitoring

Every week a special 'First Look' tape was sent from ESOC to SRON, Utrecht, a member of the FAST Consortium, for preliminary analysis of the science data. Unlike the main data processing which might only be processed weeks or months after the observations were made, the 'First-Look' task processed the data within a few days of delivery to assess the scientific data quality. Through rapid calibration of certain parameters associated with the instrument (e.g. basic angle, grid rotation, and single-slit response) ESOC were informed promptly if unexpected trends or disturbances were observable. ESOC were then able to examine the operations logs around the time of an event to see if there was a correlation with spacecraft activities at that time, and to take appropriate action if necessary. In addition, the 'First Look' facility provided payload calibration data to FAST, NDAC and ESOC.

Focus Evolution and Photometry Results

Results from the weekly payload monitoring analysis included an averaging of the intensities and grid modulation coefficients contained in the image dissector tube and star mapper reports. This gave an evaluation of the photometric degradation of the payload due to, for example, radiation darkening of the optics, or temperature instabilities. The best focus position evolved continuously throughout the mission, primarily due to moisture release. The refocusing calibration was performed every week throughout the mission (or more regularly in the case of anomalies) to monitor the best focus position and when necessary to change the actual focus position on-board. Details of the focus evolution and photometric degradation were communicated to Matra Marconi Space for further evaluation. A discussion of both phenomena is presented in Chapter 10.

9.3. Data from FAST to ESOC in Support of Satellite Operations

First-Look Monitoring Feedback

This interface (described above) proved to be very successful in identifying any trends in basic angle evolution and other payload phenomena. Already during the routine phase, as on-board heaters started to fail, Utrecht were able to provide important information when it was necessary for ESOC to perform special thermal control operations (see Chapter 12). Given that thermal instabilities could cause payload deformation, it was critical for ESOC to know within days rather than weeks if operations were degrading

the scientific data. This would allow corrective actions to be attempted. Additional important assistance was given in analysing the star mapper data during the two-gyro operational phase, as attempts were made to revive the spacecraft after hibernation (see Chapter 15).

Basic Angle and Grid Rotation

During the commissioning phase, it was necessary for ESOC to perform an initial coarse calibration of the basic angle (the angle between two fields of view) and grid rotation (the misalignment of the image dissector tube and star mapper grids with respect to the scanning plane), to refine the operations of the ground real-time attitude determination software. Thereafter, Utrecht were able to process the scientific data to yield more accurate values, which were fed back into the ground real-time attitude determination input data, giving rise to improved convergence of the attitude determination software. In addition, on 23 January 1990, the first calibrated grid rotation was used on-board resulting in a significant improvement in on-board real-time attitude determination performance. The real-time attitude determination 'innovations', which give a measure of the attitude corrections necessary between star mapper transits, were reduced from about ±5 arcsec to about ±2 arcsec. Subsequent monitoring of the basic angle by the consortia is described in Section 10.2.

9.4. Data from NDAC to ESOC in Support of Satellite Operations

Gyro Misalignment

The on-board real-time attitude determination system relied on integrated gyro outputs for determining the attitude between star mapper transits. The conversion of the satellite body rates around the operational gyro input axes was performed on-board and on-ground using a suitable projection matrix, and assuming the pre-launch calibration of the alignments. The NDAC Consortium, unlike the FAST Consortium, used the gyro output for the scientific data reduction. A by-product of the initial NDAC processing, conducted at the Royal Greenwich Observatory (RGO), was a calibration of the gyro misalignments with respect to the nominal positions. On 4 July 1991, the RGO was able to supply a newly calibrated projection matrix for uplink to the spacecraft. Subsequently, as the gyro configuration changed, due to gyro failures, particularly at the start of two-gyro operations, further projection matrices were supplied by the RGO for operational use.

External Disturbance Torque and Thruster Calibration

A further product of the NDAC processing, performed by the RGO, was a detailed study of the external disturbance torques acting on the spacecraft as well as the evolution of the thruster performance with time (see Volume 3, Chapter 8 for further details). The thruster performance results were used by ESOC to perform tuning of the thruster on-time coefficients as part of the on-board attitude control. One significant result was to show a difference in performance between the plus and minus thruster around each axis. This however could not be compensated for in the original real-time attitude

determination design since separate on-time coefficients were only available for each thruster axis and assumed identical performance for both thrusters around that axis.

This was valuable information in defining the real-time attitude determination algorithm for zero-gyro operations (see Chapter 16). The revised real-time attitude determination relied on an on-board disturbance torque model, which had to be updated on a regular basis from ground predictions. In addition, independent on-time thruster coefficients were applied for each thruster. The RGO participated with ESA and Matra Marconi Space in defining the new algorithm, using the experience already gained in determining the variability of the various torques around the orbit.

Although the disturbance torques around each of the spacecraft axes were broadly repeatable, with combined periods equal to the spacecraft rotation and orbital periods, the effect of the Earth's magnetic field, and a number of small partially-explained torques (such as gravity gradient and magnetic torques), could change fairly rapidly. For zero-gyro operations, this required a fast response time to re-calibrate and uplink the revised torques. To this end, the RGO supplied their on-ground attitude reconstitution software to ESOC for use in operations, to perform disturbance torque and thruster calibrations during every perigee passage for the next orbital period.

Preliminary Catalogue Results

NDAC were able to feed back their preliminary star positions and brightnesses to ESOC, via the INCA Consortium, to be used for the on-board programme star file. This was done in two stages as more results became available.

In February 1991, Input Catalogue Version 8 was received and implemented at ESOC, containing approximately half the programme stars updated from Hipparcos data. By November 1992, Input Catalogue Version 10 was received, with nearly all of the input catalogue stars now containing early Hipparcos results. The improvements in accuracy of the positions were, by that time (as expected), largely masked by the intrinsic performance accuracy of the real-time attitude determination. This and the greater reliability in the magnitude estimates allowed ESOC to tune the selection criteria for real-time attitude determination guide stars and to tune the on-board star mapper processing parameters to optimise the correct identification of guide stars in the star mapper data stream and virtually eliminate any possibility of mis-identifying stars, which could lead to an unexpectedly large innovation error in the on-board control.

All of the above support from the FAST and NDAC Consortia, when combined with additional work performed by ESOC and Matra Marconi Space, contributed strongly to the overall improvement in real-time attitude determination performance which was achieved by 1992, before significant problems with noisy gyros were experienced (see Chapters 14–15). By that time, real-time attitude determination innovations were consistently around ±1 arcsec, compared to the start of the mission figure of ±5 arcsec. Moreover the regularity with which real-time attitude determination was staying converged after perigee was also increased.

10. ROUTINE CALIBRATION AND PAYLOAD EVOLUTION

Continuous monitoring of the geometric and photometric performances of the payload was necessary throughout the mission. This was conducted partly at ESOC (in particular for the photometric aspects), and partly by the FAST Consortium as part of their 'first-look analysis' (in particular for the geometric aspects). The focus monitoring resulted in semi-regular focus adjustments to take account of progressive evolution of the payload structure, the results of which are described in detail, and which led to a comprehensive model of moisture release and optical degradation accounting for the observed focus evolution with time. The radiation darkening of the optics, especially of the star mapper relay optics, led to an evolution of the photometric performances, which had to be accounted for in the observation time allocation, as well as during the rigorous photometric calibration as part of the data reductions.

10.1. Routine Monitoring Activities at ESOC

Payload Monitoring

A subset of the software developed for calibration purposes was adapted and built into a separate payload monitoring program for use in near real-time. The selected stars were processed to estimate their intensities and modulation coefficients. The estimated values were compared with the expected values based on the photometric parameters defining the star (brightness and colour) and based on the calibrated response of the telescope and detectors. Reports were generated for each processed observation.

The software for this task ran on the Hipparcos dedicated computer system continuously throughout the mission. It performed many tasks associated with verifying the correct performance of the on-board science data collection and processing. Every 60 s, the program selected one star observed in the preceding 30 s. The selection criteria were based on the following: (i) stars present for less than a complete observation frame of 2.133... s were not used; (ii) multiple stars and minor planets were not used; (iii) large-amplitude variable stars were preferentially selected (in order to maintain up-to-date ephemerides for them); (iv) photometric secondary standard and constant stars were preferred over non-photometric stars; (v) brighter stars were preferred over faint

stars; (vi) if the previous star to be processed was observed in the following field of view, preference for the next observation was given to stars observed in the preceding field of view, and vice versa.

This last constraint was important for quick and reliable verification of the attitude control system (see below). One star was selected, out of those possible, in a pseudo-random manner where the probability of selection was weighted according to the above criteria. The largest weighting was given to large-amplitude variable stars, so they were almost always processed, if observed.

Regardless of star type, analysis proceeded as follows. The raw image dissector tube samples were extracted from the scientific telemetry, and the rotational (body) rates of the spacecraft were extracted from the attitude control system telemetry. The raw image dissector tube samples were then decompressed and corrected for detector saturation effects according to pre-defined decompression tables. The resulting data resulted in a modulated signal $I(t)$ of the form given in Equation 1.1. The five unknown parameters $I_0, M_1, M_2, \theta_1, \theta_2$ were estimated from a Fourier analysis of the signal. Except for the stars flagged *a priori* as variable, a check of the measurement quality was made. This was done by comparing the values of I_0 and M_1 against their expected values.

I_0 quality 0, 1, 2, 3 meant that the ratio of measured to expected I_0 corresponded to a magnitude difference of less than 1, 2, 3, or 4 respectively for $B < 10$ mag; or less than 2, 3, 4, or 4 respectively for $B > 10$ mag. M_1 quality 0, 1, 2 meant that the ratio of measured to expected M_1 lay in the range 0.8–1.2, 0.6–1.4, or 0.4–1.6 respectively for $B < 10$ mag; or in the range 0.6–1.4, 0.4–1.6, or 0.2–1.8 respectively for $B > 10$ mag; The I_0 and M_1 quality flags were summed to give the overall quality flag (setting an upper limit of 3), and the results were monitored in real-time by the spacecraft analysts but were also filed for later retrieval.

The quality flag information was used to determine if the on-board real-time attitude determination system was controlling the attitude adequately. If the attitude began to drift, this would affect the ability of the on-board software to pilot the image dissector tube to the correct portion of the grid. Consequently, the measurements taken under conditions of poor real-time attitude usually resulted in quality 3 star measurements in one or both fields of view. Only if results from both fields of view showed consistently quality 0 measurements was real-time attitude determination considered to be operating successfully.

A further off-line task analysed the payload monitoring results on a weekly basis compiling a list throughout the mission of intervals of ‘good’, ‘bad’ or ‘unknown’ piloting. This was supplied to the data reduction consortia to assist in the routine data reduction activities. Only intervals of ‘good’ data would be processed. When starting to process an interval of data, the algorithm assumed a status of ‘unknown’ until the first payload monitoring report. Piloting status would only change to ‘good’ if three consecutive observations in both fields of view were assigned as quality 0 measurements. Piloting status would only change to ‘bad’ once three consecutive observations in one or other field of view were assigned with non-zero quality flags. This proved to be an effective set of criteria for defining when real-time attitude determination was converged and useful scientific data was being obtained.

Focus Monitoring

The monitoring of the focus evolution and offset from current to best focus was done by means of the M_1 values computed by processing a four-hour batch of image dissector tube telemetry, in a similar manner to that described in Section 5.6. Since the position of best focus was evolving continuously the refocusing calibration was performed every week throughout the mission (or more regularly in the case of anomalies). The best focus position could be calibrated by computing the average grid modulation coefficients M_1 over a four hour period of data. These M_1 averages were then converted into a focus offset and hence, via the history of grid movements, into an absolute focus position using the calibrated curves shown in Figure 5.4.

The motor which changed the focus position, did so in steps of 1.38 μm, and the intention was to keep the focus position on-board within ± 1 step of the best focus position. In December 1989, the results from the ground software appeared to imply that the best focus position was changing at an increasing rate, in contradiction with pre-launch predictions. It was subsequently found that the change of focus was not actually taking place, but rather that the stepping motor was incapable of moving by only one step at a time. This was later confirmed by the manufacturer. Subsequently, only focus moves of two or more steps were commanded without further problems or degradation of the science data.

Background Noise Monitoring

The star mapper proved to be very sensitive to the radiation environment in the van Allen belts and during periods of high solar activity. The result was blinding close to perigee. Moreover the radiation environment could change rapidly, as a result of solar flares. This had a direct impact on the altitude at which re-initialisation of the on-board real-time attitude determination could be attempted following perigee passage, since ground-based star pattern recognition required frequent star transits to be identified in the star mapper data stream.

As a result, the overall star mapper signal in both channels was constantly monitored with a report produced every minute giving an integrated average to the ESOC flight control team. Only once noise levels were at an acceptable level, were ground real-time attitude determination initialisation procedures performed (see Chapter 14).

Spacecraft Performance Evaluation System

For Hipparcos, ESOC used a software system called the ‘spacecraft performance evaluation system’ for close to real-time anomaly analysis as well as long-term history performance evaluation studies. This service software, running alongside the spacecraft control and operating system (at the time the ESA standard for spacecraft control and operations), regularly transferred housekeeping telemetry, event data and generated telecommand history, from the on-line mission dedicated computers to the off-line spacecraft performance evaluation machine, via a high speed HYPERBUS inter-computer link.

Every hour, all spacecraft data collected by the real-time systems were checked and consolidated. After checking, the data were archived automatically in the Hipparcos data base. The system also maintained a copy of the on-line spacecraft control and operating system data base, updated via regular transfers, which gave the users means to manipulate the data, similar to those provided by the on-line control system.

At this point the data was available in an automatic cartridge storage and retrieval system. The associated software provided, on an off-line basis, certain functions to retrieve and manipulate the data. These included alphanumeric printouts, data retrievals over as long a time interval as desired (up to the duration of the entire mission), different time sampling strategies, tape production, graphical representation of parameters, etc. In particular it was possible to schedule the routine daily retrievals and graphical colour printouts and have them automatically produced by the system. As an example of its performance, the last version of the spacecraft performance evaluation system was able to scan through a complete year of data in little more than one day.

In addition, the system provided an operative language and compiler, allowing the definition and use of derived parameters in an easy and interactive way (a derived parameter is the result of an algorithm which involves the use of a certain number of already existing and defined telemetry parameters). All tools were widely and intensively used to evaluate spacecraft performance, accomplish subsystems trend analysis and were key instruments in the study and assessment of spacecraft anomalies. Specifically, the system was used on a daily basis to monitor the troublesome behaviour of the gyros and the degradation of the payload heaters in the thermal control electronics.

Since the beginning of the mission, the system provided flexible access to the complete satellite telemetry. This meant that it was able to support simultaneously several missions, and several users within each mission, in parallel. Taking advantage of this design feature, direct access to the system was made available to external users at ESTEC. Industrial firms involved in the project could also use it in a remote mode for their own studies and assessments.

10.2. Payload Calibration

Basic Angle and Grid Rotation

During commissioning activities, ESOC performed one preliminary calibration of the basic angle (the angle separating the two fields of view) using the ground real-time attitude determination system (see Section 14.3). The value obtained was 58° 30 arcsec, compared to an on-ground calibrated value of 58° 42 arcsec. The grid rotation estimate proved to be rather unreliable, although the maximum error of about 3 arcmin was in any case shown in simulations not to impact on ground real-time attitude determination accuracies.

During the remainder of the mission, more accurate calibrations were performed by the FAST Consortium's 'first-look' facility at Utrecht. The evolution in the basic angle is shown in Figure 10.1, using all points from the NDAC and FAST Consortium's great-circle reductions. After initially decreasing, the basic angle began to increase, having reached a minimum value of $58° 0' 31.''240$. The overall evolution of the basic angle was

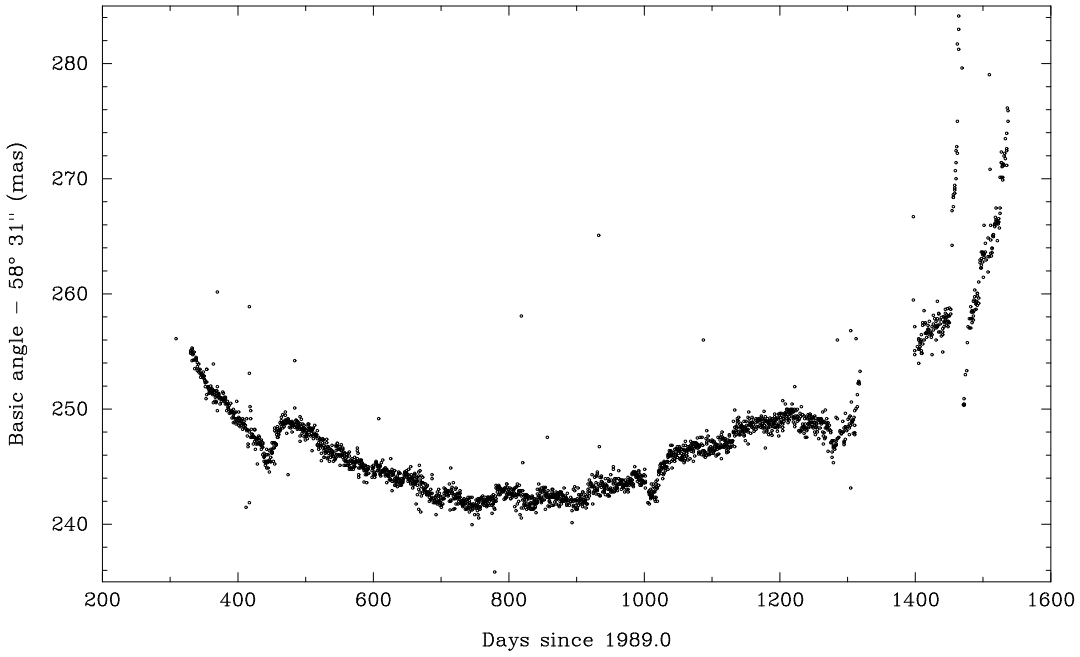

Figure 10.1. *Basic angle evolution as a function of time, determined from the preliminary great-circle reductions (see also Figures 10.12(a) and (b)). The smooth evolution with time results from contributions such as outgassing of the structure, radiation effects on the optics, and other ageing processes. Outlier points typically arise from thermal variations in the payload, described in further detail in Section 12.4. The overall evolution of the basic angle was well within specification, and well within the changes that could be modelled in the instrumental calibration on ground.*

well within the design specification, which called for a variation of below 1 milliarcsec within any 12-hour interval.

Instantaneous Field Of View Pointing

A description of the internal star pattern assembly and grid reference marks calibrations, relevant for the instantaneous field of view pointing calibration, was given in Section 5.4. The internal star pattern assembly calibration was repeated every two weeks throughout the mission. The grid reference marks calibration and coil currents calibration matrix uplink were performed daily. Typically, the standard deviation of the variation of the piloting currents was measured as 0.9 arcsec per day, i.e. the stability of both the image dissector tube pointing non-linearity, and the rigid body displacement, was very good.

Optics Darkening

Once per week, several off-line tasks were performed to analyse all data acquired by the payload monitoring software during that period. The products from the analysis included an averaging of the intensities and grid modulation coefficients contained in the image dissector tube and star mapper reports. This gave an overall evaluation of the photometric degradation of the payload due to, for example, glass darkening or

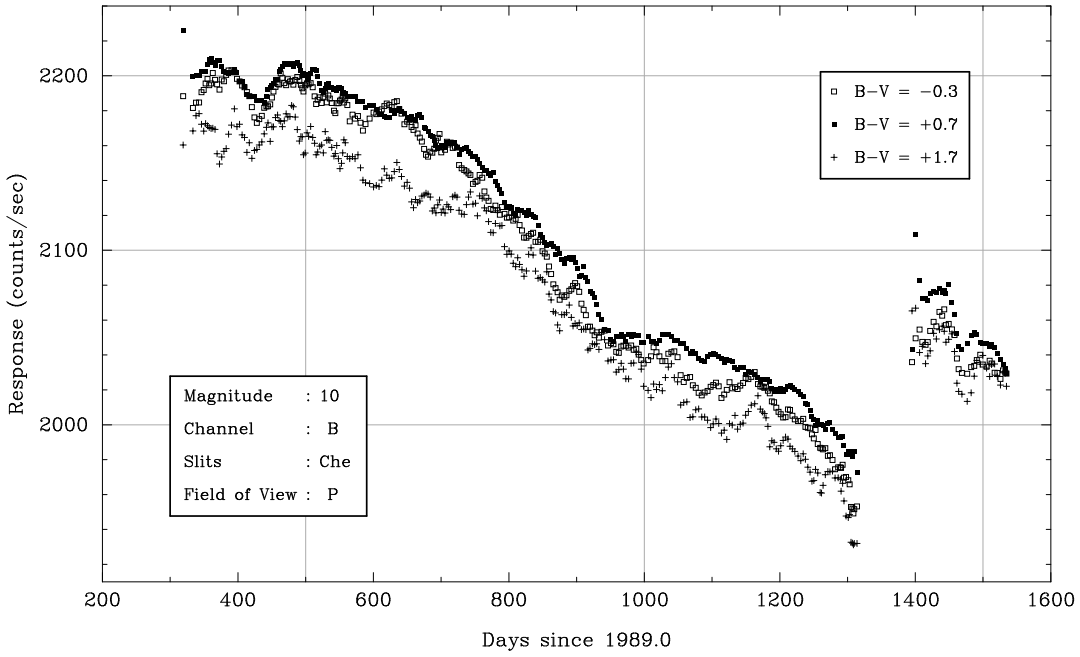

Figure 10.2. *Star mapper photometric response as a function of time, for three different ranges of star colour. The total degradation in the star mapper response throughout the mission amounted to about 10 per cent. The response improved towards the end of the mission, after the 'hibernation phase', probably because of the overall environment that the payload had been subjected to during the sun-pointing phase.*

temperature instabilities. Up to mid-February 1990 the individual star reports were processed in batches of 5000, and after that date, approximately once per week.

The results of the photometric calibrations are shown in Figure 10.2 for the star mapper response, and in Figure 10.3 for the image dissector tube response and for the first and second modulation coefficients. There was only marginal degradation throughout most of the three-gyro operations phase. However, by the beginning of 1992, the deterioration of gyro 5 began to affect real-time attitude determination accuracy which in turn affected the ground software which reduced the image dissector tube data. Further details of the evolution of the instrumental parameters are presented in Volume 3.

Other Payload Calibrations

ESOC was responsible for the initial calibration of the star mapper single-slit response profiles described in Section 5.3, the initial calibration of the instantaneous field of view profile described in Section 5.7, and for the initial chromaticity calibration activities described in Section 5.8. Subsequently, these parameters were calibrated in greater detail as part of the routine data analysis (see Volume 3).

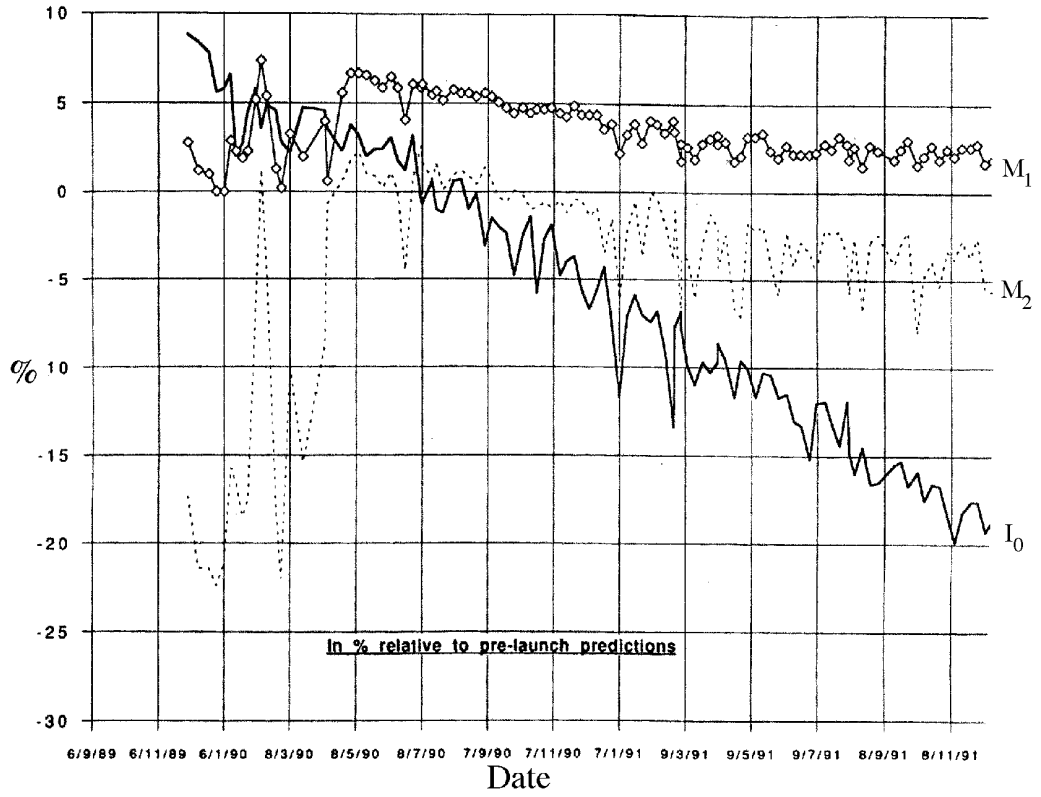

Figure 10.3. *Evolution of the image dissector tube response (I_0) and modulation coefficients (M_1 and M_2, with respect to the pre-launch predictions) with time.*

10.3. Focus Evolution

The variation of the best focus position was continuously monitored on ground through analysis of the modulation coefficients. It had been predicted that the best focus position would evolve with time due to moisture release from the carbon-fibre structure, and a focus mechanism was implemented within the payload to compensate for the expected structural evolution (to minimise the effects of a possible failure of this mechanism, it was set, pre-launch, to a position which would have given good modulation after several weeks in orbit).

In practice, significant deviations with respect to the predicted focus evolution appeared after 6 months in orbit, with the focus shift increasing more-or-less linearly from that date, and with both the amplitude and the time constant of the variation being greater than had been predicted before launch (Figure 10.4). This evolution was also accompanied by a 'differential defocus' between the best focus position of each of the two fields of view (see Figure 5.4). Consequently, the adopted focus position was taken to be the mean of the two optimum values, leading to a resulting decrease in the modulation coefficients for each of the fields of view. The details of the observed focus shift, and

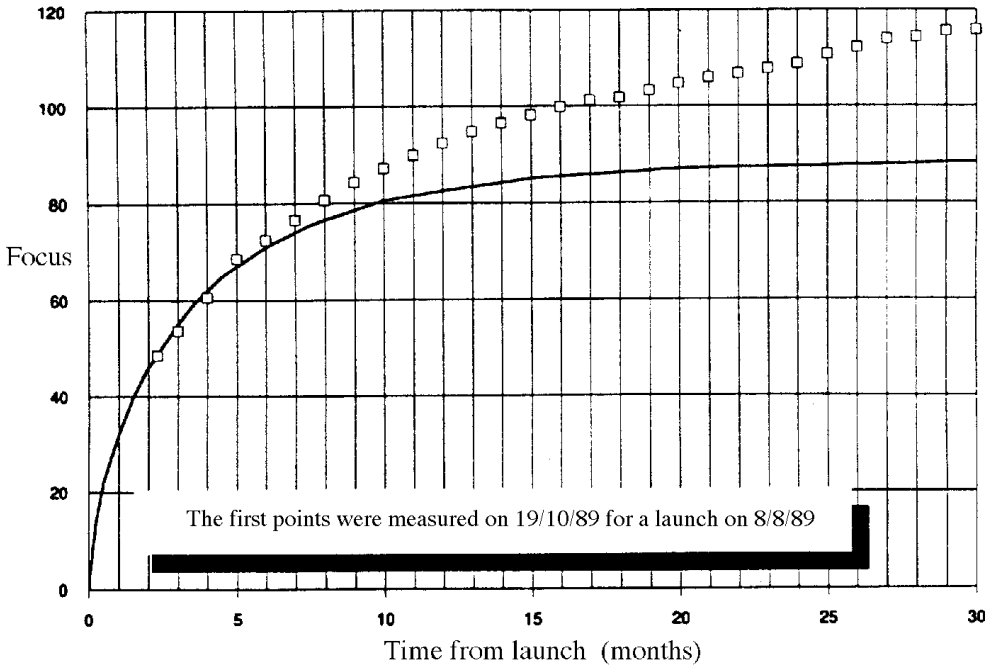

Figure 10.4. *Focus variation due to moisture release versus time. The solid line shows the pre-launch prediction of the best focus position, and the squares indicate the measured focus position.*

the conclusions of the specific study undertaken to understand the cause, are presented in detail in this section.

The theoretical behaviour of the telescope focus position was modelled prior to launch. It had been predicted to vary linearly with time, depending on the moisture content of the payload structural material. The moisture contained in the structure before launch was assumed to be homogeneously distributed, inside the material and between the payload panels, and was predicted to decrease with time as a result of 'outgassing', leading to a relationship of the form $M(t) = M_i \times G(t)$, where $M(t)$ is the moisture content at time t; M_i is the initial moisture content before the release started, and $G(t)$ is a time-dependent parameter approximated by:

$$G(t) = 1 - \exp\left[-7.3 \times \left[\frac{D \times t}{S^2}\right]^{0.75}\right] \qquad [10.1]$$

To model the evolution the following approximations were used:

$$G(t) = \frac{4}{\sqrt{\pi}} \times \frac{\sqrt{D}}{S} \times \sqrt{t} \qquad \text{for} \quad y \le y^* \qquad [10.2]$$

$$G(t) = 1 - \frac{8}{\pi^2} \exp\left[-\pi^2 \frac{D}{S^2} t\right] \qquad \text{for} \quad y \ge y^* \qquad [10.3]$$

where $y = \pi^2 Dt/S^2$ is a dimensionless function of time, $y^* = 0.52564$, $t^* = y^* S^2/(\pi^2 D)$, and D is the diffusivity of the material (in the direction normal to the surface). S is equal to the thickness k of the material when both sides are exposed to the same environment (free vacuum space in this case), and $S = 2 \times k$ when one side is obstructed (partial obstruction leading to an intermediate value).

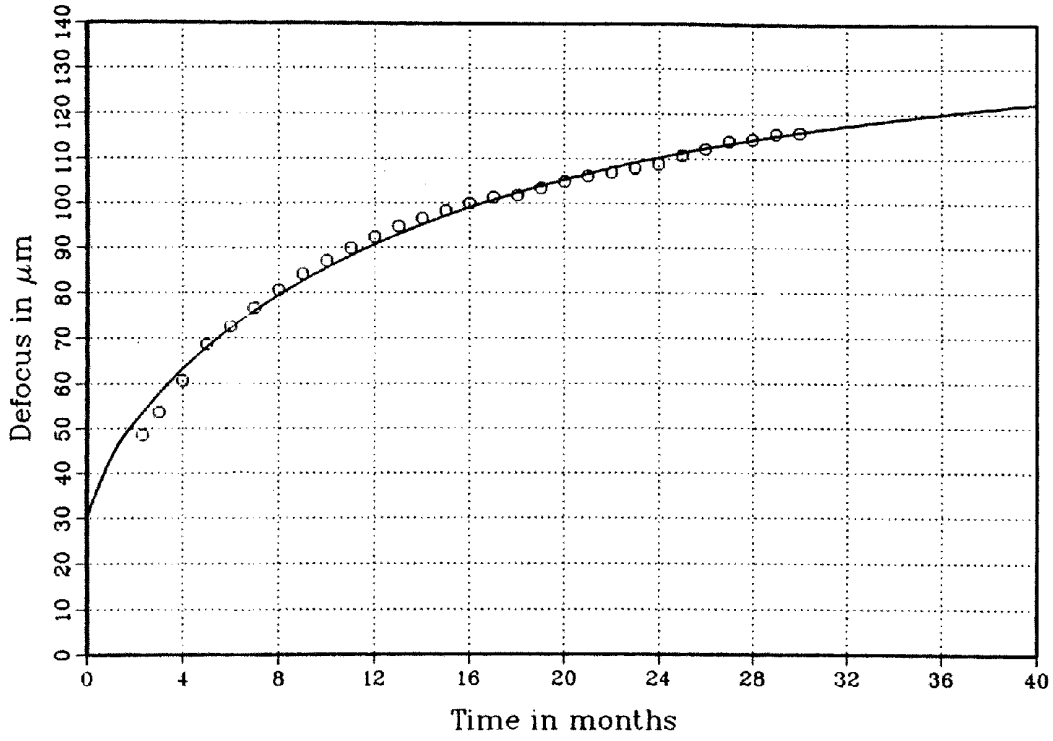

Figure 10.5. *Measured focus position and best fitting curve assuming pure moisture release according to Equation 10.6. This simple model fit to three free parameters did not provide a convincing physical explanation of the observed focus change.*

The diffusivity of the material depends on the temperature according to:

$$D = D_0 \exp\left[C\frac{T - T_0}{T \times T_0}\right] \qquad [10.4]$$

with C = 6000 K. A typical figure for carbon-fibre reinforced plastic is $D_0 = 3.8 \times 10^{-8}$ mm^2 s^{-1} at T_0 = 300 K. From the linear variation of the focus position with the moisture content, the actual focus position can be written:

$$F(t) = F_i + f_m \times G(t) \qquad [10.5]$$

where F_i is the initial focus position, and f_m is the amplitude of the variation of the focus position from the initial (moist environment) position to the final (completely dry) position, which is proportional to the final moisture content M_i. A best fit of the measured data with Equation 10.5 using for $G(t)$ the approximation given by Equation 10.1 yields:

$$F(t) = 30.3 + 104.2\ (1 - \exp(-0.134 \times t^{0.75})) \qquad [10.6]$$

where $F(t)$ is measured in microns and t in months. The plot of Equation 10.6 with the measured data indicates an apparently good fit for $t > 6$ months (Figure 10.5). However with three free parameters (F_i, f_m, and the exponent), a good fit is not necessarily consistent with the known physical properties of the system.

At the constant temperature of the telescope panels, 19 °C, the diffusivity is given by $D = 2.2 \times 10^{-8}$ mm^2 s^{-1} (from Equation 10.4), with the best fit provided by Equation 10.6 yielding a substrate thickness S = 3.42 mm. Being roughly twice the average panel thickness (1.7 mm), this result suggested that moisture release was taking place through

one side only, as if the secondary structure on the other side of the telescope panels (accommodating the heater mat carriers) was creating a hermetical sealing on the outer sides.

The most significant change of focus position occurred within about 6–8 months after launch (see Figures 10.4 and 10.5). For this interval, the approximation given by Equation 10.2 for the case $y \leq y*$ is applicable, since $t \leq t* = 324$ days on the basis of the above values of D and S. This indeed results in a rather reasonable fit, i.e. a linear dependence of the focus position with the square root of time:

$$F(t) = 5.7 + 27.7 \times \sqrt{t} \qquad [10.7]$$

as depicted in Figure 10.6(a). Equation 10.7 relates the amplitude of the variation of focus f_m to the thickness S as:

$$f_m \times \frac{4}{\sqrt{\pi}} \times \frac{\sqrt{D}}{S} = 27.7 \qquad [10.8]$$

Using the value of S deduced above, i.e. $S = 3.42$ mm, leads to $f_m = 175\ \mu$m, inconsistent with the value of f_m given by Equation 10.8, $f_m = 104\ \mu$m. On the other hand, with $S = 1.7$ mm (corresponding to moisture release through both sides) $f_m = 87\ \mu$m, very close to the pre-launch prediction of 89 μm. Figure 10.6(b) indicates that the focus evolution is well approximated by Equation 10.3 as:

$$F(t) = 5 + 90 \times \left(1 - \frac{8}{\pi^2}\right) \exp(-0.195 \times t) \qquad [10.9]$$

yielding approximately the same value for $t = 0$ ($F_i = 5\ \mu$m) as Equation 10.7, and also roughly the same amplitude of focus variation ($f_m = 90\ \mu$m). This tended to confirm the validity of the initial moisture release prediction, and suggested that conclusions drawn directly from the overall best fit to the measured data may be misleading.

The pre-launch prediction of the focus variation due to moisture release was based on the dry-out of several carbon-fibre reinforced plastic samples after thermal vacuum testing (weighed before and after the dryout sequence), and a test campaign including space conditioning at 50 °C over 5 days before the thermal vacuum test itself. A total focus variation of 38 μm was measured during the test. Samples of the carbon-fibre reinforced plastic were placed within the payload and weighed before and after the test. The prediction of the total focus variation of the telescope was obtained from $f_m \times (M_B / M_D)$ where M_B is the mass loss (before the thermal vacuum tests) of the carbon-fibre reinforced plastic samples after dry-out, and M_D is the mass loss of the samples during the thermal vacuum tests. This assumed that the amount of moisture release of the telescope structure during the thermal vacuum tests was equal to that of the samples. The time constant followed from an assessment of the diffusivity itself obtained from the measured focus variation over the space conditioning (33 μm during 5 days at 50 °C) and an assumed temperature of 20 °C during the orbital life. The resulting prediction was:

$$F(t) = 89 \times (1 - \exp(-0.427 \times t^{0.75})) \qquad [10.10]$$

with t in months. Closer analysis of the space conditioning sequence revealed an interval where the temperature was stable, and where a ‘pure’ moisture release effect presumably took place. Before and after this stable interval, thermoplastic effects due to the large temperature variations were superimposed on the moisture release effect. During this

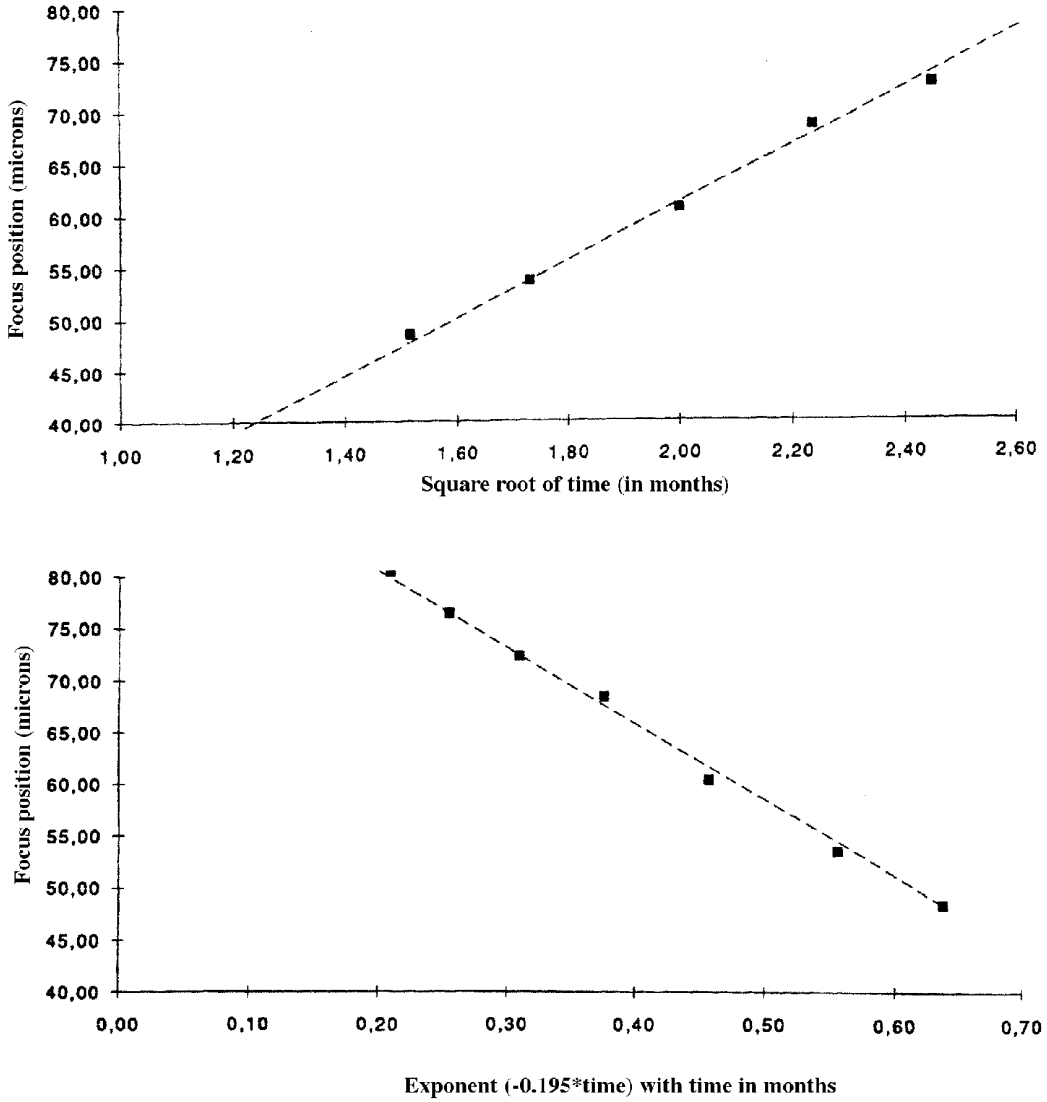

Figure 10.6. *(a) Linear approximation of the focus variation with* t^{-2} *and (b) linear approximation of the focus variation with* exp (*t*).

period, the focus position varied linearly with the square root of time as expected from Equation 10.2 such that:

$$F(t) = F_i + 2.626 \times \sqrt{F} \qquad [10.11]$$

As before, the total focus variation due to the moisture (f_m) is related to the thickness S and the diffusivity D as:

$$f_m \times \frac{4}{\sqrt{\pi}} \times \frac{\sqrt{D}}{S} = 2.626 \qquad [10.12]$$

With $D = 1.49 \times 10^{-7} \times 3600$ mm^2 hr^{-1}, at 49.5 °C, the measured temperature during the stabilised space conditioning, this gives S = 1.7 mm, f_m = 85 μm. This value was again close to the predicted one (89 μm) and also to the one obtained from the first points measured in-orbit (90 μm) assuming the same thickness S = 1.7 mm. The reassessed in-orbit 'prediction' at 19 °C was then:

$$F(t) = 89 \times (1 - \exp(-0.353 \times t^{0.75})) \qquad [10.13]$$

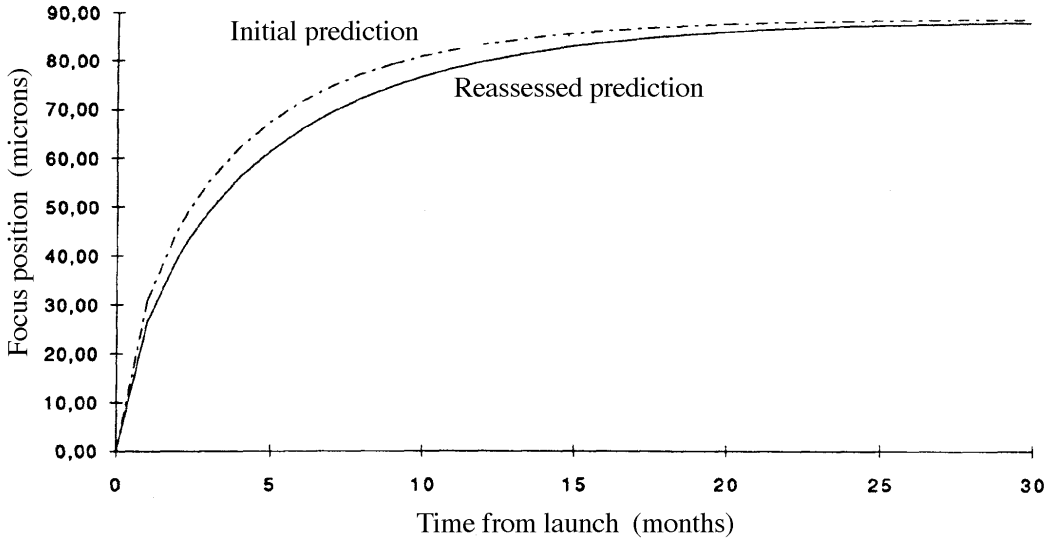

Figure 10.7. *Initial and reassessed moisture release predictions.*

very close to the initial prediction given by Equation 10.10 with, however, a slightly higher time constant (Figure 10.7).

Before turning to the origin of the discrepancy in the measured versus predicted focus evolution in-orbit, further evidence that the payload evolution had not been fully understood was given by the change in the modulation factors M_1, M_2 at the common best focus. The common best focus was adopted to be the mean of the best focus of the preceding and following fields of view. While the common best focus position had been evolving roughly according to the pre-launch predictions, the individual focus positions of the two fields of view were diverging, leading to a 'differential defocus', and a significant (and unexpected) degradation of the modulation coefficients with time (see Figure 10.3), albeit at a rate (-2.5 per cent per year for M_1) not large enough to severely impact the scientific data. The evolution of the differential defocus is shown in Figure 10.8.

Meanwhile the intrinsic optical quality of the telescope remained essentially unchanged since the beginning of the mission, as indicated by the stability of the modulation factors M_1, M_2 at the individual best focus for each field of view.

The differential defocus continuously increased with time, apparently linearly up to about 20 months after launch at a rate of $\simeq 0.66$ μm per month, thereafter remaining almost stable. This suggested a phenomenon other than moisture release was occurring, inducing deformations of the mirror surfaces, and resulting in changes of curvatures which were somewhat different for the two fields of view.

The identification of the increasing differential defocus with time suggested an average linearly varying defocus additional to the moisture release. The measured focus positions were found to be well represented by (Figure 10.9):

$$F(t) = 89 \times (1 - \exp(-0.353 \times t^{0.75})) + 0.82 \times t \qquad [10.14]$$

The additional linear variation amounted to 0.82 μm per month, corresponding to an increase of the telescope focal length. Two possibilities were considered: (a) stress release within the telescope mirrors, and (b) irradiation effects on the telescope mirrors.

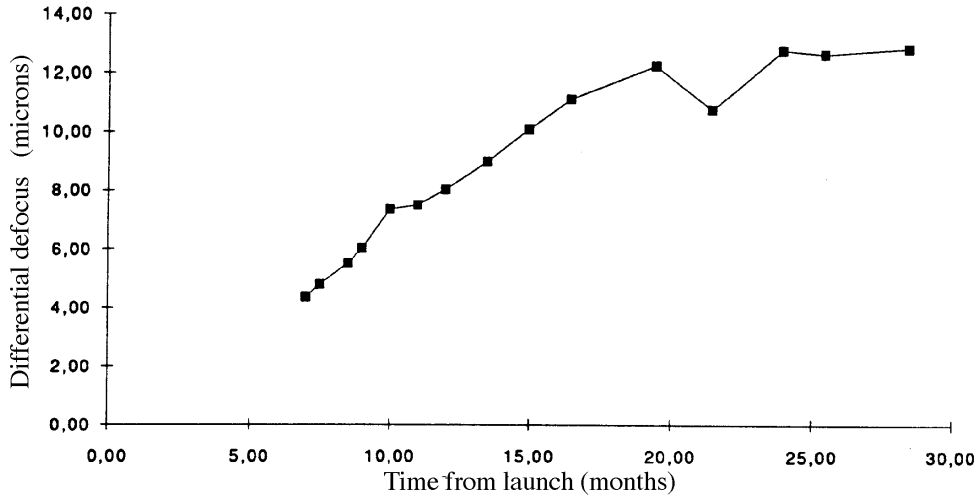

Figure 10.8. *In-orbit measured differential defocus.*

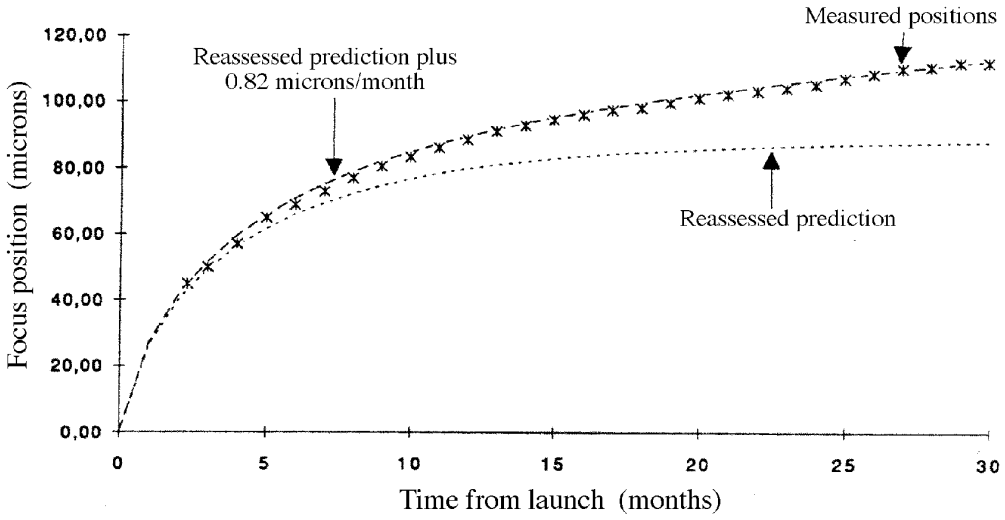

Figure 10.9. *Measured (crosses) and reassessed (lower curve) focus positions, and the reassessed focus position combined with an additional linear evolution due to optical deformation (upper curve).*

The latter was believed to be the origin of the phenomenon observed. This conclusion was based on test results obtained by bombarding samples of zerodur with very high doses (1–100 Mrads) of electrons representing 10–1000 years in low-Earth orbit (Rädlein 1991). This created a density increase of the top layers of the glass surface resulting in convex deformations of initially plane mirrors. For example, sags in the range of 1–10 μm were obtained with a zerodur disc of 100 mm diameter, and 5 mm thickness.

From Table 10.1 and Figure 10.10 it is apparent that the dose level, for 10 years in low-Earth orbit (1.3×10^4 Gy), is comparable to that observed by Hipparcos, after 2.5 years in its highly eccentric orbit, when shielded by 2.5 mm of aluminium over 4π steradians. However, the extrapolation of the sample results to the case of the Hipparcos mirrors is non-trivial. Several factors had to be considered, such as: (i) their diameter (300 mm)

Table 10.1. Dose levels.

Electron Dose 0.8MeV +0.3MeV	equivalent to time in orbit	Zerodur
20.5 Gy + 1.3×10^4 Gy	10 years	-1.6 μm
4.1×10^3 Gy + 1.3×10^6 Gy	10^3 years	-12.5 μm

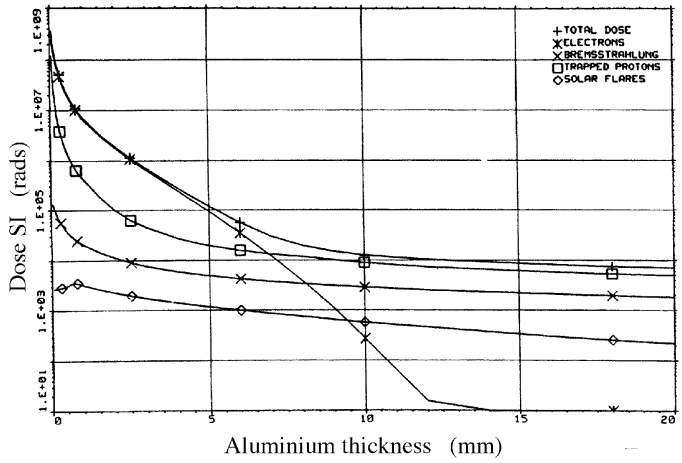

Figure 10.10. *The irradiance dose/depth curve for Hipparcos after 2.5 years in its highly eccentric orbit. The different curves indicate the effects of the different particle components*

and thickness (100 mm for the beam combiner, 60 mm for the spherical and folding mirror); (ii) the irradiation levels actually experienced by each mirror; (iii) the sensitivity to the irradiance dose (linear up to 10^5 Gy); and (iv) an understanding of the physical effects involved within the mirror substrates.

It was suspected that the spherical mirror was the most seriously affected one (on its back side), based on the sign of the additional linear variation. This acted as if the focal length of the telescope were increasing, at the rate of $\simeq$ 10 μm per year, i.e. as if the rear sides of the mirrors were more irradiated then the optical surfaces. Supporting this was the actual configuration of the payload hardware—the folding mirror was relatively well shielded, on its back side, by the focal plane assembly platform, whereas the beam combiner was least sensitive to surface deformations originating from irradiation due to its thickness. Moreover, both beam combiner and folding mirror were better shielded than the spherical mirror due to the spacecraft configuration.

Measurement of the mean scale value in the fields of view allows determination of the effective focal length in terms of the grid dimensions. This was done as part of the geometrical payload model described in Section 10.5, leading to the conclusion that the focal length did *not* change much over the mission. It would then appear that the dimensional variations of the structure, due to moisture release or some other process, continued over a much longer time than expected from the previous discussion.

Table 10.2. Photometric evolution.

Colour group	rate (per cent per day)	loss (per cent)
$-0.625 < B - V < 0.125$	−0.0343	29.94
$0.125 < B - V < 0.875$	−0.0356	31.08
$0.875 < B - V < 1.625$	−0.0313	27.39

10.4. Photometric Evolution

The photometric evolution of the image dissector tube was monitored using two independent sets of data: (i) the telemetry used for determination of the telescope focusing; and (ii) the post-processing of real-time payload monitoring results. The latter were also used to monitor the evolution of the star mapper photometry.

For off-line analysis the count rates were calculated assuming the following count rates for the three colour groups for stars of magnitude $B = 9.5$ mag:

$$-0.625 < B - V < 0.125\text{: } 1193.1 \text{ counts s}^{-1}$$
$$0.125 < B - V < 0.875\text{: } 1774.8 \text{ counts s}^{-1}$$
$$0.875 < B - V < 1.625\text{: } 3268.4 \text{ counts s}^{-1}$$

A quadratic curve for the colour dependency was assumed, and the expected value of I_0 was scaled for the magnitude dependency by:

$$10^{0.4(9.5-B)} \qquad [10.15]$$

Approximately 2.5 hours of image dissector tube data were processed, including all photometric constant and standard stars in the range $B = 1 - 9$ mag over the entire field of view. The mean weighted error in I_0 for each colour group in each field of view, $(I_0' - I_0)/I_0$, was calculated where I_0' was the measured intensity and I_0 was the predicted intensity. The final averaged results were then used to modify the three count rates mentioned above. By April 1992 the average rate of decrease was the same for each colour (see Table 10.2). This was in contrast to the first nine months of the mission where the rate of decrease had been more significant for the blue spectral region than for the others. The photometry losses were attributed to the decrease in optical transmittance of the associated relay lens system caused by irradiation effects.

10.5. Payload Modelling

As part of the normal data processing, a full geometric calibration was made of the parameters relating the sky coordinates to coordinates on the focal surface. This field-to-grid transformation was derived in the great-circle reductions described in Volume 3, Chapter 9. The development of the transformation parameters, as determined by the FAST and NDAC consortia, are described in Volume 3, Chapter 10.

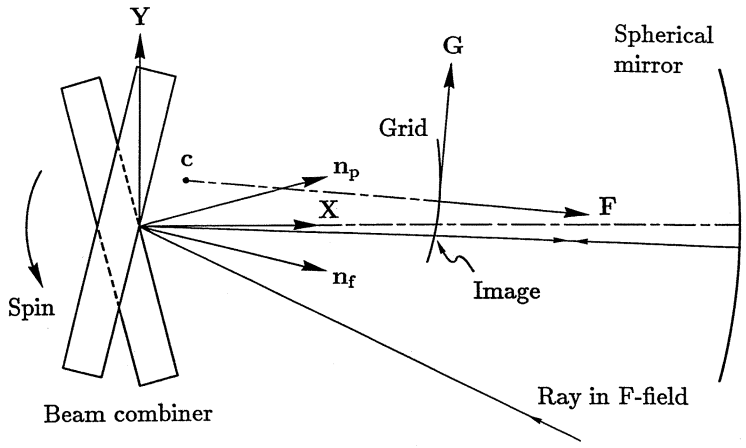

Figure 10.11. *Layout of the simplified geometrical model.*

As an aid for the interpretation of the transformation parameters a simple geometrical model of Hipparcos was developed (Lindegren *et al.*, 1992). By means of the model, basic geometric relations among the optical elements could be estimated and their temporal behaviour assessed. In particular it was of interest to study to what extent the observed transformation and its temporal variation could be attributed to simple geometrical effects, such as displacements and rotations of the optical elements.

The layout of the model is illustrated in Figure 10.11. The basic assumptions of the model are as follows: (i) all optical surfaces are perfect in shape, but may be displaced or tilted; (ii) only rays passing through the centre of curvature of the spherical mirror are traced; (iii) the aperture of the telescope is thus infinitely small, therefore the two segments of the beam combiner can be considered to be flat; and (iv) the imaging properties of this system are invariant to a parallel shift of the beam combiner surfaces, thus it is possible to position both at the centre of curvature of the spherical mirror.

Coordinate Systems and Transformations

The position and orientation of each element are described in a rectangular coordinate system, called the *laboratory frame*. On the other hand, all observations were made relative to the slits of the modulating grid. Nominally, the grid pattern consisted of a number of straight lines generated by an electron beam. The imaginary coordinate system in which the slits occupy their nominal positions is called the *electronic frame*. The model describes the transformation from laboratory coordinates to electronic coordinates; this is done via the intermediary *grid frame*, physically attached to the grid.

The origin of the laboratory frame [**X Y Z**] is chosen to be at the centre of curvature of the spherical primary mirror. This choice eliminates the need to specify any parameters for that mirror, thanks to the spherical symmetry and the assumed infinitely small aperture at the origin. The directions of the axes are defined by the beam combiner: the **Z** axis coincides with the intersection of the two beam combiner surfaces, **X** is the bisector of the mirror normals $\mathbf{n}_p$ and $\mathbf{n}_f$, which are separated by an angle of $\Gamma/2$. In the laboratory frame, the mirror normals are thus written:

$$\begin{aligned} \mathbf{n}_p &= \mathbf{X}\cos(\Gamma/4) + \mathbf{Y}\sin(\Gamma/4) \\ \mathbf{n}_f &= \mathbf{X}\cos(\Gamma/4) - \mathbf{Y}\sin(\Gamma/4) \end{aligned} \qquad [10.16]$$

The grid frame [**F G H**] is physically attached to the grid, with origin at the nominal centre of the grid and the (G, H) coordinates measured in the plane tangent to the grid at the origin, with the slits of the main grid parallel to the H axis. F is measured positively on the convex side of the grid. The radius of curvature, R, which should strictly be a model parameter, is consider a fixed parameter, since a very large change in R would be required to observe a measurable distortion. F can be related to (G, H) by:

$$F = \frac{-(G^2 + H^2)}{R + \sqrt{R^2 - (G^2 + H^2)}} \equiv F(G, H) \qquad [10.17]$$

The relation between the grid frame and the laboratory frame is given by six parameters specifying the displacement and rotation bringing a coordinate triad aligned with [**X Y Z**] into coincidence with [**F G H**]. To effect this realignment the following steps are applied: (1) displace the origin to (X_0, Y_0, Z_0); (2) rotate an angle ψ about the third axis; (3) rotate an angle θ about the second axis; (4) rotate an angle ϕ about the first axis. The resulting transformation is:

$$\begin{pmatrix} X \\ Y \\ Z \end{pmatrix} = \begin{pmatrix} X_0 \\ Y_0 \\ Z_0 \end{pmatrix} + \mathbf{A} \begin{pmatrix} F \\ G \\ H \end{pmatrix} \qquad [10.18a]$$

where:

$$\mathbf{A} = \begin{pmatrix} \cos\theta\cos\psi & \sin\phi\sin\theta\cos\psi - \cos\phi\sin\psi & \cos\phi\sin\theta\cos\psi + \sin\phi\sin\psi \\ \cos\theta\sin\psi & \sin\phi\sin\theta\sin\psi + \cos\phi\cos\psi & \cos\phi\sin\theta\sin\psi - \sin\phi\cos\psi \\ -\sin\theta & \sin\phi\cos\theta & \cos\phi\cos\theta \end{pmatrix} \qquad [10.18b]$$

Ideally, the slit centres should be straight and equidistant lines in the (G, H) plane. However, due to imperfections in the electron beam pattern generator used to produce the grid, they are not. It is therefore necessary to convert from electronic coordinates (g, h) (in which the slits occupy their nominal positions) to the geometrical coordinates (G, H). The transformation from (g, h) to (G, H) includes, in the real instrument, at least the small and medium-scale irregularities of the grid pattern. However, in the present idealised model, only the large-scale distortion caused by a tilting of the electronic frame [**f g h**] with respect to the grid frame is considered. This may be described by two successive rotations: (1) by the angle α about the third axis, and (2) by the angle β about the second axis, which brings [**F G H**] into coincidence with [**f g h**]. This gives the transformation:

$$\begin{pmatrix} F \\ G \\ H \end{pmatrix} = \begin{pmatrix} \cos\beta\cos\alpha & -\sin\alpha & \sin\beta\cos\alpha \\ \cos\beta\sin\alpha & \cos\alpha & \sin\beta\sin\alpha \\ -\sin\beta & 0 & \cos\beta \end{pmatrix} \begin{pmatrix} f \\ g \\ h \end{pmatrix} \qquad [10.19]$$

Calculating (G, H) from (g, h) may be achieved by iterating the equations:

$$\begin{aligned} G &= g\sec\alpha + F\tan\alpha \\ H &= h\sec\beta - F\sec\alpha\tan\beta - g\tan\alpha\tan\beta \\ F &= F(G, H) \end{aligned} \qquad [10.20]$$

starting from $F = 0$. The inverse conversion is obtained from Equation 10.17 and the inverse of Equation 10.19.

Model Parameters

The instrument model, in this simple approximation, can be parameterised by Γ, R, X_0, Y_0, Z_0, ϕ, θ, ψ, α, and β. This can be further simplified, since some of these parameters are redundant. The radius of curvature of the grid, R, is fixed. Y_0 and ψ are coupled since displacing the grid along the **Y** axis is equivalent to a simultaneous rotation of the grid and beam combiner about their respective **Z** axes, plus some second order adjustment of the distance between the two elements. Since a rotation of the beam combiner about **Z** does not change the field-to-grid transformation, Y_0 and ψ are in effect indistinguishable, and thus $\psi = 0$ is chosen. β does not enter the expression for g as a function of (F, G, H) and therefore cannot be determined from the observed distortion of the main field, thus $\beta = 0$ must be assumed. The remaining parameters (Γ, X_0, Y_0, Z_0, ϕ, θ, α) can be freely adjusted to represent the observed field-to-grid transformation as closely as possible.

Relation to the Instrument Frame

The laboratory frame is not directly accessible to observation. Rather, the great-circle reductions establish the relation between the (observable) electronic coordinates and an ideal system of angular coordinates in the two fields of view, the so-called *instrument frame*. In order to interpret the field-to-grid transformation in terms of the model parameters, it is therefore necessary to derive also the relation between the laboratory and the instrument frames.

Given the model, specified by the parameters listed above, the field-to-grid transformation is obtained by tracing a number of rays from different directions in either field of view through the origin $X = Y = Z = 0$ and up to its intersection with the grid surface. If **u** is the unit vector towards a star, the direction of the ray after reflection in the beam combiner is given by:

$$\mathbf{v} = 2\mathbf{n}\mathbf{n}'\mathbf{u} - \mathbf{u} \qquad [10.21]$$

where **n** is the mirror normal from Equation 10.16. After reflection in the spherical mirror, the ray returns to the origin in direction $-\mathbf{v}$. The ray's interception with the grid is computed from the parametric equation $|\mathbf{v}t - \mathbf{c}| = R$. **c**, the position of the centre of curvature of the grid, is obtained by setting $F = -R$ and $G = H = 0$ in Equation 10.18. Solving for t gives:

$$t = \mathbf{v}'\mathbf{c} + \sqrt{R^2 + (\mathbf{v}'\mathbf{c})^2 - \mathbf{c}'\mathbf{c}} \qquad [10.22]$$

The point of interception is $\mathbf{v}t$ in the laboratory system, which can be transformed to the grid frame and then to the electronic frame, via Equation 10.18 and Equation 10.19, yielding the (g, h) coordinates of the ray. To trace a ray in the opposite direction, starting in the laboratory frame, involves the application of Equations 10.20, 10.18 and 10.21.

The instrument frame [**x y z**] with associated field coordinates (w, z) are defined by the optics together with a reference value γ_0 of the basic angle and two features of the grid: (1) the chevron apex of the active star mapper, which defines the origin of the transverse field coordinate z; (2) the centre line of the main field, halfway between the 1344th and 1345th slits, which defines the origin of the longitudinal coordinate w.

The star mapper apex, in electronic coordinates, is $(g_A, 0)$ with $g_A = -21.63385$ mm; the centre line of the main grid is defined by $g = 0$. In the instrument system the two directions in space corresponding to the field point (w, z) are:

$$\mathbf{u} = [\,\mathbf{x}\ \mathbf{y}\ \mathbf{z}\,] \begin{pmatrix} \mp w \sin(\gamma_0/2) + \sqrt{1 - w^2 - z^2}\cos(\gamma_0/2) \\ +w \cos(\gamma_0/2) \pm \sqrt{1 - w^2 - z^2}\sin(\gamma_0/2) \\ z \end{pmatrix} \qquad [10.23]$$

where the upper/lower sign refers to the preceding/following field.

To calculate $[\,\mathbf{x}\ \mathbf{y}\ \mathbf{z}\,]$ in the laboratory system, the following procedure is adopted. A ray from $(g_A, 0)$ is traced through the preceding field. Let $\mathbf{a}_p$ be the resulting unit vector towards the point on the sky that is imaged on the star mapper apex. Similarly the corresponding direction $\mathbf{a}_f$ through the following field is traced. Then:

$$\mathbf{z} = \langle\, \mathbf{a}_f \times \mathbf{a}_p \,\rangle \qquad [10.24]$$

with $\langle\rangle$ denoting vector normalisation. Next we must find the two viewing directions $\mathbf{0}_p$ and $\mathbf{0}_f$, perpendicular to $\mathbf{z}$, which are imaged onto the main field centre line, $g = 0$. This may be done by writing $\mathbf{0}_p = \langle\, \mathbf{a}_p + \mathbf{z} \times \mathbf{a}_p s \,\rangle$ where s is a scalar to be found by solving the equation $g(\mathbf{0}_p) = 0$. The following viewing direction is similarly found by solving s in $\mathbf{0}_f = \langle\, \mathbf{a}_f + \mathbf{z} \times \mathbf{a}_f s \,\rangle$. The remaining instrument axes are then obtained as:

$$\begin{aligned} \mathbf{x} &= \langle\, \mathbf{0}_p + \mathbf{0}_f \,\rangle \\ \mathbf{y} &= \mathbf{z} \times \mathbf{x} \end{aligned} \qquad [10.25]$$

The basic angle is $\gamma = \arccos(\mathbf{0}_p' \mathbf{0}_f)$.

Model Fitting

Stellar observations on the main grid provide a determination of the longitudinal electronic coordinate g as a function of time. The basic assumption is that g increments by exactly 8.2 μm for each light modulation period. The observations are combined in the great-circle reductions to establish an empirical relation between g and (w, z) which may be expressed in terms of polynomial coefficients g_{ij}, h_{ij} in the simplified field-to-grid transformation formula:

$$g = -F_0 w + \sum_{i,j} (g_{ij} \pm h_{ij})\, w^i z^j \qquad [10.26]$$

where F_0 is the reference value for the equivalent focal length. Terms up to 4th order $(i + j < 4)$ were included. The lowest-order terms have a simple physical interpretation: by convention $g_{00} = 0$, which defines the origin of the w coordinate; g_{10} represents a correction to the scale value corresponding to F_0, while g_{01} represents a rotation about the optical axis of the (w, z) frame with respect to the grid. Among the differential terms, h_{00} represents half the correction to the reference basic angle γ_0, h_{10} represents half the difference in scale between the preceding and following fields, and h_{01} represents half the differential rotation of the (w, z) frame.

Given the coefficients g_{ij}, h_{ij} in Equation 10.26 and the corresponding reference values γ_0, F_0, the observed electronic coordinate g_O is obtained for an arbitrary position (w, z) in either field of view. From the geometrical model the 'calculated' coordinate g_C is obtained from Equation 10.23 and a tracing from $\mathbf{u}$ to the electronic frame. g_C depends

on the model parameters which are now adjusted to minimise the mean square deviation in both fields of view:

$$\mathrm{RMS}^2 = \frac{1}{2n^2} \sum_{\mathrm{FOVs}} \sum_{k=1}^{n} \sum_{l=1}^{n} [g_{\mathrm{O}}(w_k, z_l) - g_{\mathrm{C}}(w_k, z_l)]^2 \qquad [10.27]$$

Analysis of the coefficients was done with 98 rays (n = 7) with a digitisation step of 0.0022 in w and z.

The model was applied separately to the field-to-grid transformation data obtained by the NDAC and FAST consortia in their final iterations of the great-circle reductions. Since the consortia used slightly different representations of this transformation the NDAC version, defined by Equation 10.26, was chosen as a common convention for the purpose of this analysis. Converting the FAST results to the NDAC conventions involved a reversal of the axis directions, change of units, and the addition of the nominal transformation. In general a separate great-circle reduction was made for each 'orbit' of science data, i.e. for the (usually) several hours of data collected around each apogee passage in the $\simeq$ 10.7 hour period orbit. Consequently one independent determination of the model parameters Γ, X_0, Y_0, Z_0, ϕ, θ, and α could usually be made for each orbit during the periods when 'good' data were acquired. The results are plotted in Figures 10.12 and 10.13, with NDAC and FAST results on opposite pages. Tables 10.3–6 give examples of the pattern of residuals for the NDAC data at selected points of the mission.

Results

Comparison of the NDAC and FAST results in Figures 10.12–13 shows a remarkably good agreement in some of the parameters (Γ, X_0, Z_0), while systematic shifts are seen in other parameters; in all cases the evolution of the parameters is very similar in the two reductions. There is a striking difference in the amount of scatter, with the FAST results appearing to be significantly more precise. To some extent this reflects a true difference in precision: the FAST great-circle reductions are generally more precise than the NDAC ones, mainly due to the use of both signal harmonics in the FAST analysis (see below). However, the main difference in scatter seen in the diagrams is probably caused by the cubic terms of the field-to-grid transformation, which in NDAC were estimated independently for each great-circle reduction, while in FAST they were kept at constant values for certain time intervals (see Volume 3, Chapter 10).

The systematic shifts of some model parameters between NDAC and FAST may be caused by differences in the reduction procedures that are known to influence the determination of the field-to-grid transformations, such as:

- the FAST reductions used a weighted mean for the first and second harmonics of the main detector signal, whereas only the phase of the fundamental harmonic was used in NDAC data. The phase difference between the two harmonics is of the order of 10 – 20 milliarcsec and variable across both fields of view and with time;
- the observed phases were corrected for medium-scale irregularities of the grid, before they were used to determine the field-to-grid transformation parameters. The medium-scale irregularities were determined from the residuals of the provisional great-circle reductions, and may contain distortion components which are not orthogonal to the present model parameters;

- the determination of some parameters is sensitive to the adopted origin of the field coordinates (w, z), which depends on the assumed geometry of the star mapper grid and on details of the attitude determination, all of which differed somewhat between FAST and NDAC.

While the actual values of the model parameters must consequently be interpreted with some caution, their general evolution in time most likely represents a real physical development of the instrument.

Discussion

The evolution of all model parameters except X_0 are generally rather smooth up to day $\simeq$ 1270. However, there are a few significant jumps especially in Γ and Z_0, e.g. around day 450, 780, 820 and 1000. Some of them can be related to incidents in the thermal control system of the satellite. The evolution of X_0 is characterised by the sudden changes effected by refocusing operations, usually by +2 steps or 2.76 μm. Since X_0 is actually the optical distance between the grid and the curvature centre of the spherical mirror, it is concluded that the mechanical structure connecting the spherical mirror and the flat folding mirror was steadily shrinking; this is compensated by the periodic refocusing moving the grid away from the flat mirror. The rate of shrinking was $\simeq 1.3 \times 10^{-7}$ day^{-1} at the beginning of the mission and $\simeq 1.6 \times 10^{-8}$ day^{-1} two years later.

At the times of optimum focus, which presumably occurred half-way between successive refocusing events, the parameter X_0 equals the effective focal length of the telescope (the measuring-rod being the mean grid step of 8.2 μm). This quantity shows relatively small changes up to day $\simeq$ 1200, the total amplitude being less than 5 μm for most of the mission. This contradicts the tentative conclusion in Section 10.3 that there may be a secular drift of the focal length, by $\simeq$ 10 μm/yr, caused by irradiation of the spherical mirror.

The parameter α is constant to within the measurement errors which is to be expected if this particular distortion pattern was generated during the manufacturing of the grid. The offset in mean value between FAST and NDAC appears to be related to the adopted origin of the z coordinate.

The long-term drifts in X_0, Y_0 and Z_0 are all of the order of 0.1 μm day^{-1}. Also the mean drift in θ, when converted to a linear rate at a distance of 50–100 mm (the size of the grid assembly) is of similar size, while it is 30 times less in ϕ. The typical drift in Γ corresponds to only 10^{-5} μm day^{-1} at the edges of the beam combiner. With the exception of Γ the general tendency is for the drift rates to decrease with time, up to the anomalous behaviour from day 1270. From X_0, ϕ and θ a time constant of approximately one year can be inferred. This is roughly consistent with the assumption that the main changes in the supporting structure are caused by moisture release, as discussed in Section 10.3.

Of considerable interest is to see which terms in the field-to-grid transformation may be 'explained' in terms of the present model, i.e. as arising from simple translations and rotations of the optical elements. A closer examination of the residuals shows that the only terms that attain significant values in the model are: h_{00} (related to the basic angle), g_{10} (scale value), g_{01} (grid rotation about the optical axis), h_{01} (grid displacement along the Z axis), and the terms g_{20}, g_{11}, g_{02}, which may account for a tilting of the grid.

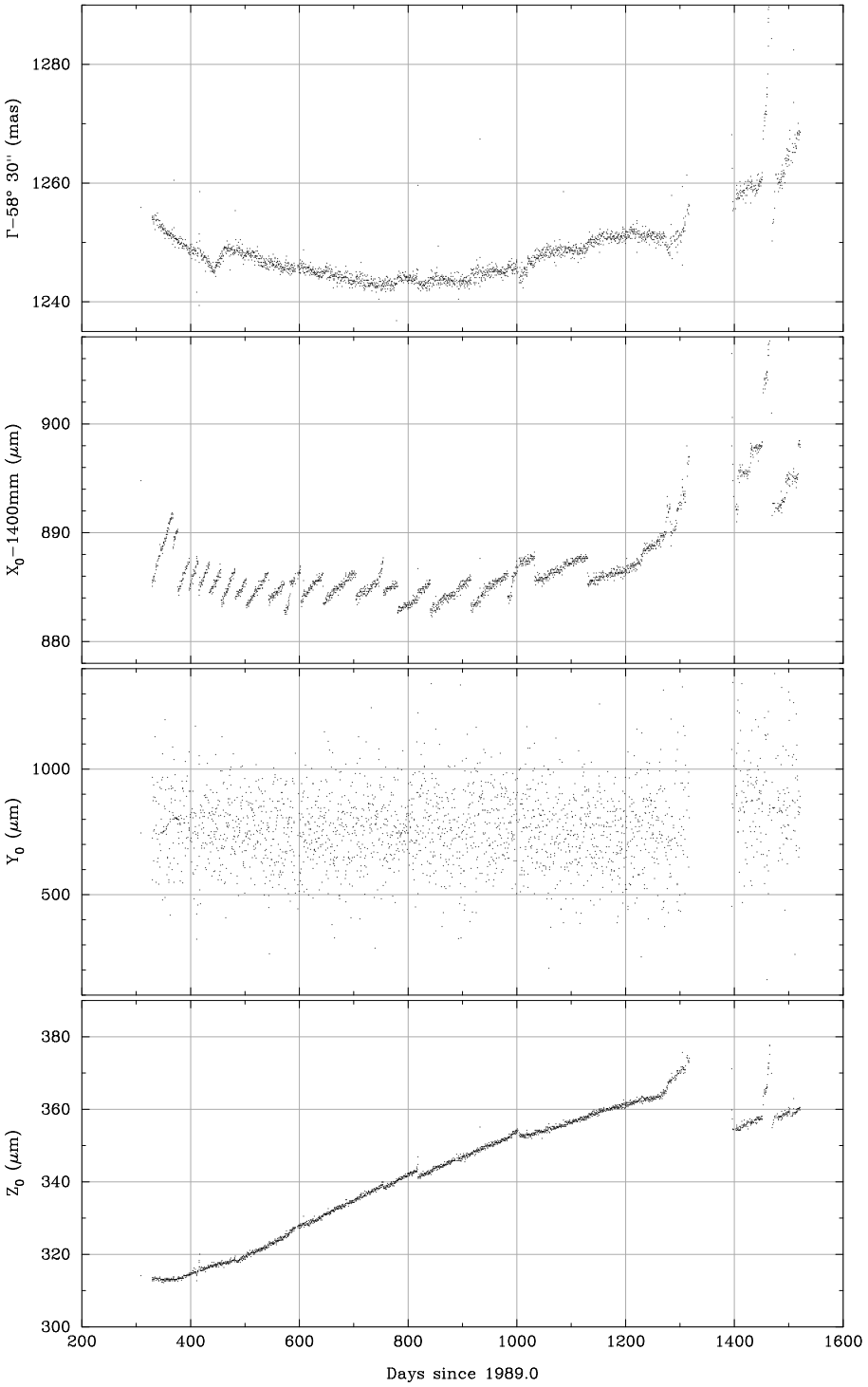

Figure 10.12(a). *Temporal evolution of the model parameters* Γ, X_0, Y_0 *and* Z_0, *using data from NDAC.*

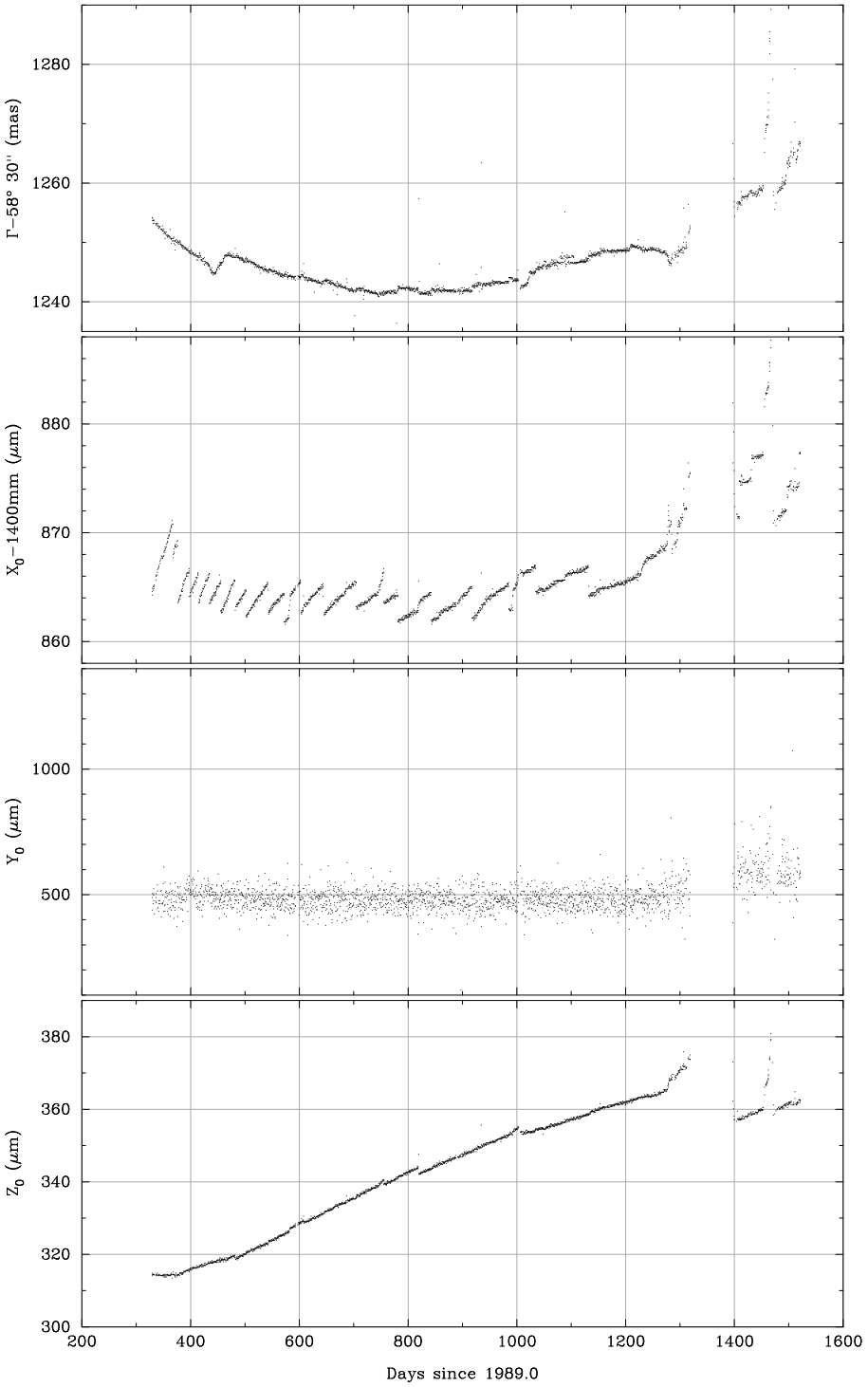

Figure 10.12(b). *Temporal evolution of the model parameters* Γ, X_0, Y_0 *and* Z_0, *using data from FAST.*

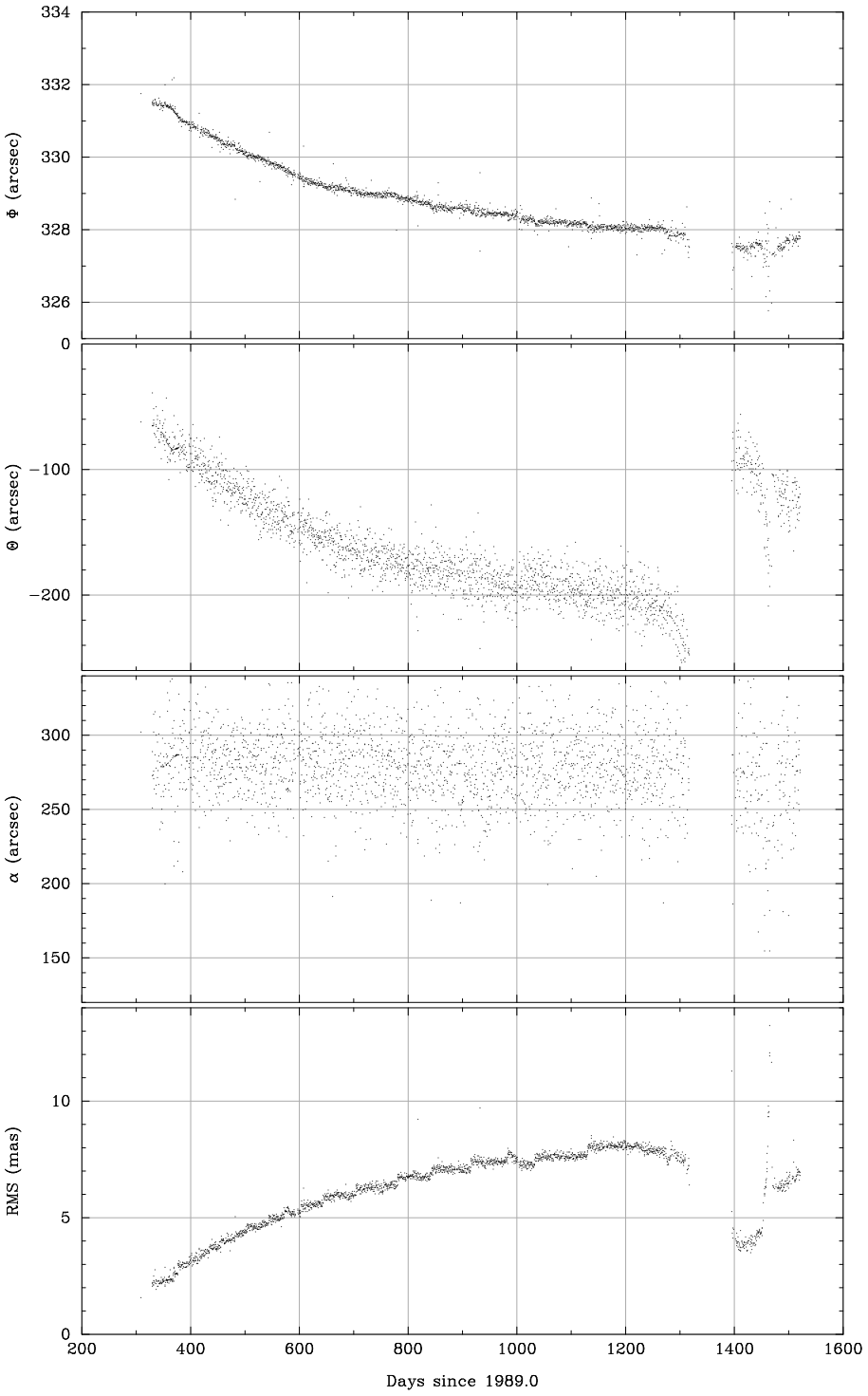

Figure 10.13(a). *Temporal evolution of the model parameters ϕ, θ and α, and of the rms residual of the model fits, using data from NDAC.*

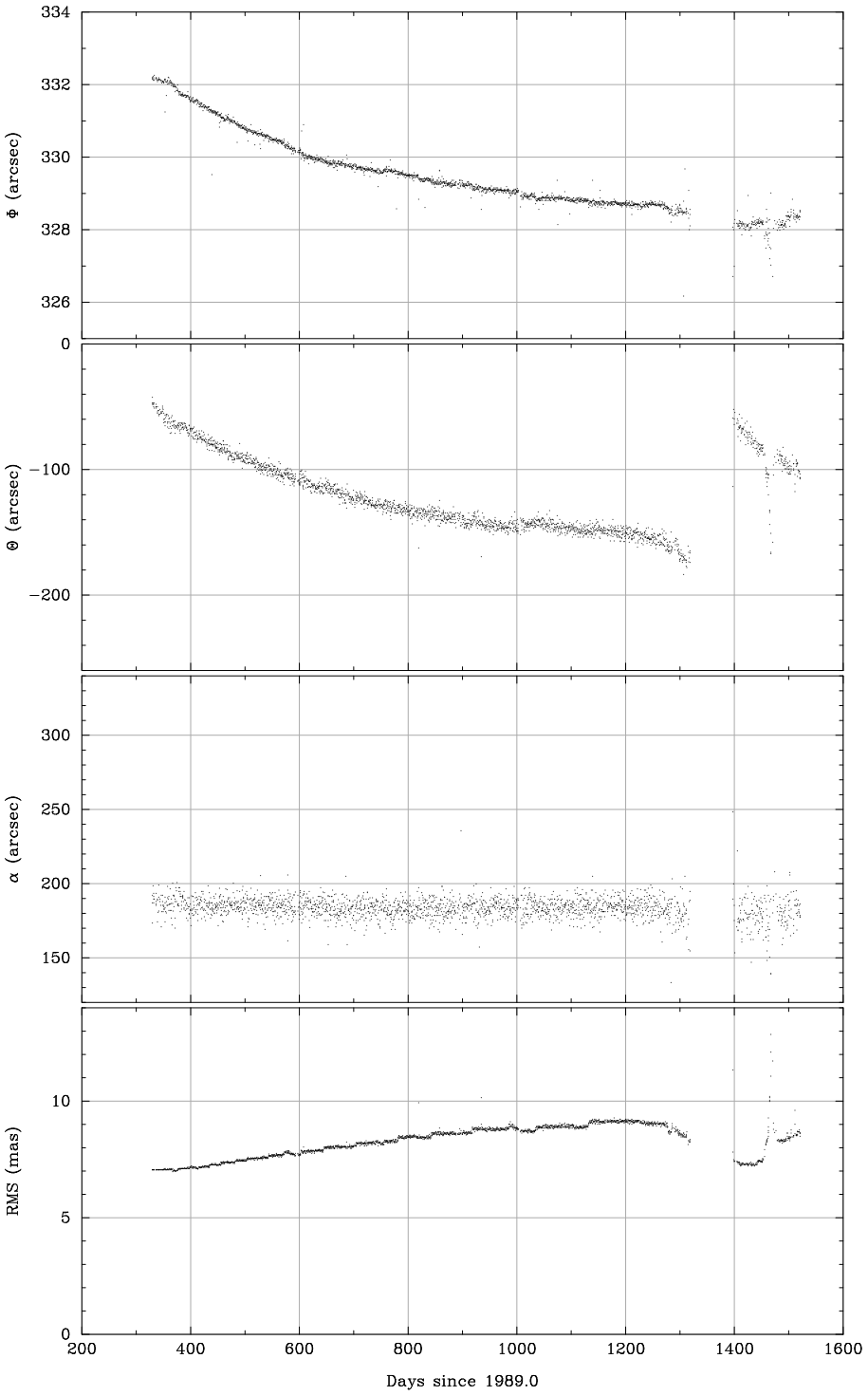

Figure 10.13(b). *Temporal evolution of the model parameters ϕ, θ and α, and of the rms residual of the model fits, using data from FAST.*

Table 10.3. Residuals $g_O - g_C$ (in milliarcsec) versus position in field (w, z) (in milli-rad) from the model fit to the NDAC transformation data for day 309 (5 November 1989, orbit 1).

$z \setminus w$	–6.6	–4.4	–2.2	0.0	2.2	4.4	6.6
Following field of view:							
–6.6	–3.53	–1.47	–0.68	–0.39	0.19	1.84	5.33
–4.4	–1.73	–0.61	–0.69	–1.20	–1.36	–0.37	2.54
–2.2	–0.16	0.26	–0.45	–1.51	–2.15	–1.57	0.99
0.0	1.02	1.00	–0.08	–1.45	–2.32	–1.91	0.57
2.2	1.67	1.46	0.25	–1.17	–2.03	–1.53	1.11
4.4	1.66	1.50	0.41	–0.81	–1.40	–0.57	2.47
6,6	0.83	0.97	0.26	–0.52	–0.60	0.83	4.52
Preceding field of view:							
–6.6	–2.90	0.30	1.71	1.73	0.73	–0.92	–2.83
–4.4	–0.56	1.87	2.70	2.30	1.05	–0.67	–2.47
–2.2	0.46	2.32	2.74	2.12	0.82	–0.78	–2.29
0.0	0.43	1.90	2.12	1.45	0.29	–1.00	–2.03
2.2	–0.40	0.88	1.07	0.56	–0.28	–1.07	–1.42
4.4	–1.76	–0.49	–0.13	–0.30	–0.62	–0.72	–0.21
6.6	–3.39	–1.94	–1.22	–0.86	–0.48	0.30	1.86

Table 10.4. Residuals $g_O - g_C$ (in milliarcsec) versus position in field (w, z) (in milli-rad) from the model fit to the NDAC transformation data for day 1196 (10 April 1992, orbit 2000).

$z \setminus w$	–6.6	–4.4	–2.2	0.0	2.2	4.4	6.6
Following field of view:							
–6.6	–17.77	–10.58	–4.88	–0.07	4.45	9.28	15.00
–4.4	–14.17	–8.41	–4.00	–0.36	3.10	7.00	11.91
–2.2	–11.50	–6.75	–3.23	–0.35	2.47	5.84	10.36
0.0	–9.94	–5.78	–2.74	–0.22	2.38	5.64	10.16
2.2	–9.66	–5.69	–2.71	–0.13	2.64	6.20	11.15
4.4	–10.85	–6.65	–3.33	–0.28	3.08	7.35	13.13
6.6	–13.68	–8.85	–4.77	–0.85	3.51	8.91	15.93
Preceding field of view:							
–6.6	5.11	6.61	5.14	1.72	–2.63	–6.88	–10.02
–4.4	10.45	10.00	6.84	1.99	–3.54	–8.71	–12.51
–2.2	13.20	11.37	7.08	1.36	–4.78	–10.32	–14.23
0.0	13.81	11.15	6.30	0.26	–5.94	–11.28	–14.74
2.2	12.71	9.78	4.91	–0.88	–6.58	–11.16	–13.61
4.4	10.31	7.68	3.36	–1.63	–6.26	–9.53	–10.41
6.6	7.05	5.28	2.07	–1.56	–4.58	–5.97	–4.72

Table 10.5. Residuals $g_O - g_C$ (in milliarcsec) versus position in field (w, z) (in milli-rad) from the model fit to the NDAC transformation data for day 1397 (28 October 1992, orbit 2452).

$z \setminus w$	–6.6	–4.4	–2.2	0.0	2.2	4.4	6.6
Following field of view:							
–6.6	–8.54	–6.22	–4.07	–1.66	1.40	5.54	11.16
–4.4	–6.62	–5.02	–3.60	–1.96	0.32	3.65	8.43
–2.2	–5.21	–3.99	–2.99	–1.78	0.04	2.87	7.14
0.0	–4.53	–3.37	–2.44	–1.35	0.33	3.01	7.08
2.2	–4.79	–3.36	–2.20	–0.89	0.98	3.82	8.03
4.4	–6.22	–4.20	–2.47	–0.62	1.76	5.09	9.77
6.6	–9.04	–6.10	–3.48	–0.77	2.46	6.59	12.06
Preceding field of view:							
–6.6	–0.37	3.29	3.98	2.54	–0.19	–3.33	–6.04
–4.4	4.22	6.20	5.41	2.72	–1.04	–5.01	–8.33
–2.2	6.80	7.55	5.74	2.23	–2.13	–6.48	–9.97
0.0	7.68	7.63	5.23	1.36	–3.15	–7.44	–10.65
2.2	7.14	6.73	4.20	0.40	–3.81	–7.59	–10.08
4.4	5.47	5.15	2.93	–0.35	–3.83	–6.66	–7.98
6.6	2.96	3.18	1.71	–0.60	–2.90	–4.33	–4.05

Table 10.6. Residuals $g_O - g_C$ (in milliarcsec) versus position in field (w, z) (in milli-rad) from the model fit to the NDAC transformation data for day 1466 (4 January 1993, orbit 2607).

$z \setminus w$	–6.6	–4.4	–2.2	0.0	2.2	4.4	6.6
Following field of view:							
–6.6	–23.42	–15.65	–8.90	–2.65	3.60	10.35	18.13
–4.4	–18.75	–11.80	–5.84	–0.37	5.11	11.11	18.15
–2.2	–16.18	–9.74	–4.29	0.69	5.70	11.24	17.82
0.0	–15.39	–9.18	–3.94	0.84	5.66	11.04	17.47
2.2	–16.08	–9.81	–4.49	0.38	5.32	10.81	17.38
4.4	–17.95	–11.32	–5.63	–0.37	4.96	10.87	17.87
6.6	–20.69	–13.41	–7.05	–1.12	4.91	11.52	19.24
Preceding field of view:							
–6.6	9.09	11.41	9.11	3.82	–2.77	–9.03	–13.28
–4.4	14.52	14.17	9.58	2.39	–5.73	–13.13	–18.14
–2.2	17.60	15.30	9.12	0.73	–8.21	–16.04	–21.11
0.0	18.69	15.13	8.07	–0.81	–9.87	–17.43	–21.84
2.2	18.13	14.01	6.78	–1.89	–10.36	–16.95	–20.01
4.4	16.25	12.28	5.58	–2.17	–9.34	–14.25	–15.25
6.6	13.40	10.28	4.83	–1.31	–6.47	–9.00	–7.23

The model cannot reproduce the remaining terms, in particular h_{10} (scale difference between the fields of view) and the cubic terms ($i + j = 3$).

The steadily growing rms residual seen in the bottom panels of Figure 10.12(b) and Figure 10.13(b) is mainly due to the increasing difference in scale between the preceding and following field of view, and to a smaller extent to the cubic coefficients g_{30}, g_{21} and g_{12}. The cubic terms are much more prominent in the FAST residuals than in NDAC, and have a rather significant magnitude already at the beginning of the mission, which explains the higher level of rms residuals in Figure 10.13(b) compared with Figure 10.13(a). In fact, the evolution of the rms residual in Figure 10.13(a) almost exactly mirrors the evolution of the differential scale h_{10} (see Volume 3, Chapter 10), suggesting that this is the main reason for the model mismatch. This is confirmed by a direct inspection of the residuals in Tables 10.3–6.

In contrast to the drifts discussed previously, the evolution of the differential scale and cubic terms, reflected in the increasing rms residuals, can only be understood in terms of deformations of one or several of the mirror surfaces. The scale difference between the preceding and following field of view must be caused by a difference in (mean) curvature between the two halves of one or more of the mirrors (beam combiner, flat folding mirror, or spherical primary mirror).

The differential scale (and consequently the rms residual) was significantly reduced from day 1397, immediately after the period of suspended operations (day 1315 to 1396), until day $\simeq$ 1450. This interval of reduced differential scale (1992.82 to 1992.97) coincides with the period of low ($\simeq -10\,^{\circ}$C) payload temperature shown in Figure 12.4. The sharp increase in differential scale thereafter coincides with the operation in sun-pointing mode (day 1453 to 1466), after which the parameters assumed more normal values. This suggests a thermal mechanism for the development of the differential scale, rather than radiation exposure, at least for the changes on a short time scale. Tables 10.3 to 10.6 show the residuals of the NDAC data at some key dates of this evolution:

Table 10.3: day 309 (beginning of mission);

Table 10.4: day 1196 (after gradual build-up of differential scale);

Table 10.5: day 1397 (immediately after suspension period, low payload temperature);

Table 10.6: day 1466 (end of sun-pointing period).

The residuals of the FAST data are not shown. They are similar to the NDAC residuals except that a strong cubic distortion is superposed, partly obscuring the evolution of the differential scale.

To produce a cubic distortion seems to require a 4th-order deformation of a mirror which is not in the plane of the entrance pupil, i.e. of the folding or spherical mirror. The required deformation is of the order of 50 nm peak value. The corresponding rms wavefront error would be of the order of $\lambda/30$, hardly enough to decrease the light modulation by a significant amount.

10.6. Star Mapper Sensitivity during Suspended Operations

During the first period of suspended operations (see Chapters 15–16) the payload was switched off to save power. When starting the two-gyro real-time attitude determination the star mapper process did not function until a minimum payload mean temperature was reached (approximately 5°C).

On 2 October 1992, the spacecraft was spun down from 0.45 rpm to the nominal spin rate, using modified on-board control software which used only the transverse gyros. Nutation damping was performed. No real-time attitude determination initialisation was possible due to the high background noise in the star mapper signal which was not, however, correlated with the actual solar activity.

A re-commissioning of the payload proceeded over the next three weeks to re-calibrate the single-slit response, basic angle, grid rotation, internal star pattern assembly, grid reference marks, transverse offset and focus position. No significant geometric deformations were detected, although the profile of the single-slit response was significantly broadened, accounting for the difficulties in successfully processing the star mapper data on-board and on-ground. At first, it was thought that the best focus position could be at fault and subsequently the focus position was moved ±80 steps from the previous best focus position. No improvement was seen however.

During the period of suspended operations, the payload had been cooled to −40 °C to reduce the load on the surviving payload heaters. There was no technical reason to believe that the cold payload temperature should affect the star mapper signal in this way. Nevertheless, the decision was taken to re-heat the payload on 25 October 1992. Within a few hours, the star mapper response had improved sufficiently to allow ground real-time attitude determination to initialise the on-board real-time attitude determination. The reason for the sensitivity to temperature of the star mapper detectors was never fully understood. While at low temperatures, the calibrations of the image dissector tube did not suggest any such problems.

After the period of suspended operations, the star mapper response improved significantly (see Figure 10.2), and other instrumental parameters also changed significantly (see Volume 3) for reasons presumably related to the thermal environment experienced during suspended operations, but which were not fully understood.

11. SOLAR ARRAY PERFORMANCE

The solar arrays provided power for the satellite and payload in all but the eclipse conditions (when the batteries were used). Degradation of the solar arrays occurred much more rapidly than had been predicted for the nominal geostationary orbit. During the early months of the mission, the available solar array power was expected to lead to a constraint on the overall mission duration. Modelling of the radiation damage, and predicting power margins and operational contingency procedures during extended eclipses, was therefore an important part of the operational procedure. This led to improved modelling of the degradation mechanisms, and good prediction of the available power during the later part of the mission.

11.1. Introduction

The power system comprised a solar array, associated sequential switching shunt regulator and battery discharge regulators which regulated the main bus potential to 50 ± 1 V in both sunlight and eclipse periods. Recharge of the power system batteries was achieved by allocating specific solar array cell strings or sections to this particular function.

The solar array consisted of three lightweight panels 120° apart. The panels were very similar to those used on most of the ESA communication spacecraft such as ECS and MARECS. These panels embodied six electrical sections of 142 series connected cells by 7 parallel cells for powering the main bus. A separate battery charge array was composed of six independent cell strings of 126 series connected cells which could be used for either sequential or parallel recharge of the two 28 cell 10 Ah nickel cadmium batteries of the system.

The solar cells were arranged to form main and charge sections. The solar array was based on proven solar generator design concepts, but with some important improvements, including the use of materials such as aluminium honeycomb, together with carbon-fibre reinforced plastic. This gave a lightweight, but highly-loadable structure. Some redesign on the hinge configuration was performed to minimise shock loads created during the latch up of a deploying panel at high satellite spin rates. Each panel was equipped with two hold-down units and one pyro-actuated cable cutter as a release unit.

For the electrical layout, the goal was to design a highly failure-resistant cell design. The solar generator design involved single stringing in all main sections, with individual blocking diodes to limit the effect of power loss in case of a short circuit, as well as an extra thick kapton insulation layer to give a high degree of protection against short circuits. Protection against adverse effects of shadowing of the inner parts of the solar array wings due to attitude control subsystem failure was achieved by incorporating shunt diodes for cell protection.

The protection against electrostatic discharge, which had caused many problems in the past, was designed with great care. To prevent charging of non-conductive structural parts of the front side of the panel, all areas not covered with solar cells were protected with an aluminised kapton foil, which was grounded to the structure of the solar array. The complete rear side, as well as the so-called 'edge members', were painted with conductive black paint. All panel wiring was carefully routed through the edge members and on the panel's rear side, wherever possible.

Mechanical Properties

Each of the three solar arrays was based on a lightweight structure built of aluminium honeycomb and carbon-fibre reinforced plastic: with kapton foil to electrically insulate the cell area from the array structure; special hinges to decrease latch-up shock loads during deployment at high spin rates (up to 10 rpm); and two hold-down points, with pyrotechnic cable cutter release mechanisms. Each of the arrays was 1690 mm long, 1190 mm wide, and 23 mm high. All three panels together weighed about 31 kg.

Electrical Properties

Each of the three solar arrays had two main sections, made up of seven strings with 142 serial connected cells (each string was equipped with a blocking and shunt diode), and two charge sections, each with 126 serial connected cells and shunt diodes to protect against shadowing effects. The cells were back-surface-reflecting high-efficiency units with a thickness of 180 μm. Electrostatic discharge protection was provided by means of grounded aluminised kapton on the panel's front side and conductive black paint on the rear and on edge members. An integrated thermocouple provided subsystem temperature data during the mission, and array deployment and successful latch-up was monitored by separate switches for each panel.

One of the consequences of the satellite being in a geostationary transfer orbit was that the efficiency of its solar panels was degraded by the repeated radiation exposure at a much higher rate than if the satellite had been in geostationary orbit. The consequence of this process led to a potentially shorter lifetime for the mission.

To estimate the lifetime of the satellite, periodic measurements were obtained from the open circuit voltage of the charge array strings. The first results from these calculations resulted in a very pessimistic forecast for the mission. The degradation was considered to be very high and a potential lifetime of only about 6 months was predicted. However, after first collection of real spacecraft data the degradation proved to be far less than the originally predicted values.

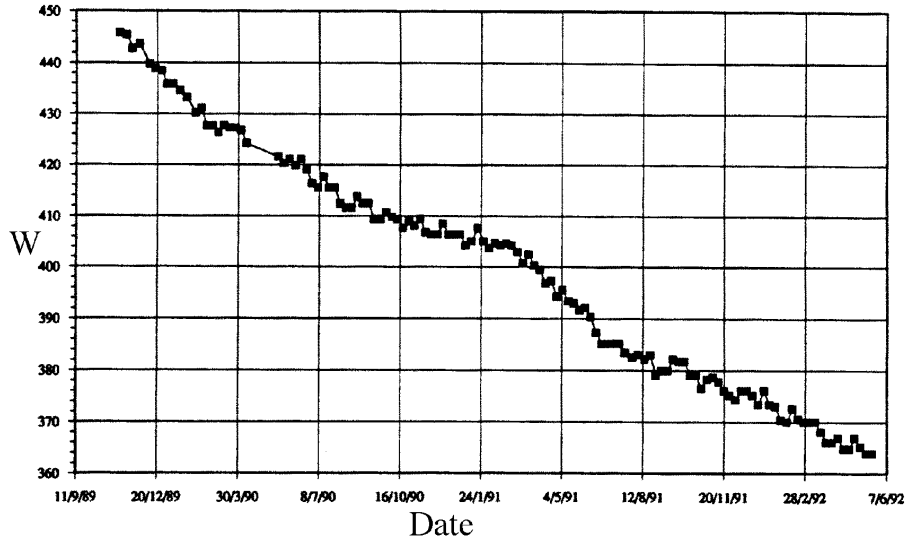

Figure 11.1. *Power provided by the solar arrays as a function of time. The decrease was predicted qualitatively and modelled accurately, as a consequence of radiation damage, as described in Section 11.3.*

11.2. Power Subsystem Degradation

The power supplied by the solar array is shown in Figure 11.1. The power drop from the beginning of the mission to June 1992 was 18 per cent of the initial value. The spacecraft required approximately 270 W in geostationary transfer orbit. Four out of six main sections were activated during the early stages of the mission.

The behaviour of the batteries remained nominal throughout the mission. The planned geostationary orbit would only have required battery operation during much shorter eclipses than those demanded in the case of the actual geostationary transfer orbit. Consequently they had not been designed with these cases in mind. The major constraints to the batteries efficiency under these circumstances were the long eclipse durations associated with a short sunlight time for charging, itself related to the battery power budget (during long eclipses, the satellite could only function by drawing power from the batteries) and the high battery charge/discharge cycle repetition rate.

The evolution of the maximum power margin provided by the batteries was monitored from the start of the mission. The maximum power margin is the difference between the maximum power that the batteries are able to supply during an eclipse, and the usual power consumption of the spacecraft during an eclipse, and is given by $P_{\text{max–margin}} = P_{\text{max}} - P_{\text{sat}}$ with $P_{\text{sat}} = 224$ W. P_{max} calculations took into account the charging current, the maximum charging time, the depth of discharge limit of 65 per cent, and the maximum power the battery discharge regulator could provide (440 W). For $P_{\text{max–margin}}$, P_{max} is the minimum value of 440 W, $P_{1\text{max}}$, $P_{2\text{max}}$, where:

$$P_{1\text{max}} = V_{\text{bat}} I_{\text{ch}} \frac{\eta_{\text{BDR}}}{HK} \frac{T_{\text{ch}}}{T_{\text{ecl}}} \qquad [11.1]$$

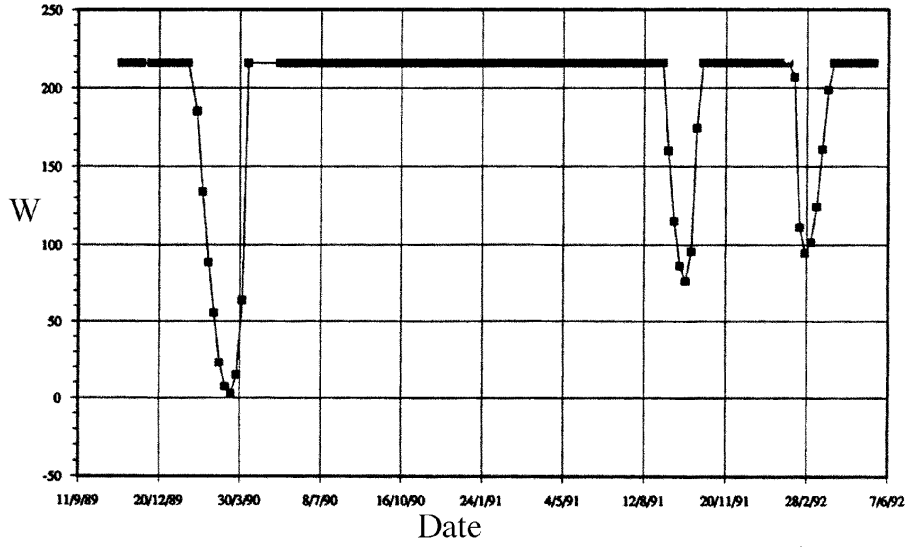

Figure 11.2. *Maximum power margin. The drops in the power margin correspond to the occurrence of the longest eclipse periods; shorter eclipses at other times had no effect on the power margin.*

$$P_{2\max} = V_{\text{bat}} \text{DOD} \frac{\eta_{\text{BDR}}}{H} (2 - 0.082) \frac{N}{T_{\text{ecl}}} \qquad [11.2]$$

V_{bat} is the battery voltage during eclipse = 37.5 V; T_{ch} is the charging time = 10.67–T_{ecl} hours; T_{ecl} is the eclipse duration in hours; H are harness losses = 1.01; K is the charge efficiency = 1.05; DOD is the depth of discharge = 0.65; I_{ch} is the charge current; N the battery nameplate capacity = 10 Ah; and 2 – 0.082 signifies the worst case of battery discharge regulator mismatch of 8.2 per cent. The charging current was directly calculated from the monitored short-circuit current, I_{sc}, which was a function of the solar array degradation and of the seasonal effects.

Prior to the March 1990 eclipse, simulations had indicated that power saving on board the spacecraft would be required to get through the long eclipses. Figure 11.2 shows that the three periods of longest eclipse were passed successfully without power saving. During the longest eclipse (up to 104 min) which occured on 19 March 1990, the margin decreased to 3 W, and the associated depth of discharge reached 60 per cent (Figure 11.3), although the specification limit of 65 per cent was never reached.

A similar study was performed with a linear extrapolation of I_{sc} degradation, and calculated eclipse durations, in order to assess the power margin during the following eclipses of April 1993 and September 1993. The results are shown in Figure 11.4. The batteries were expected to withstand both peaks without power saving on board the spacecraft, although with a power margin falling to about 9 W.

In its actual orbit the batteries underwent approximately 2000 charge/discharge cycles for the three-year mission compared to 125 charge/discharge cycles that had been anticipated in geostationary orbit. Since 25 000 cycles had been obtained in low-Earth orbit tests at 40 per cent depth of discharge over a three-year period at 5° and 25 °C, the charge/discharge factor was not a limiting factor in the satellite operations.

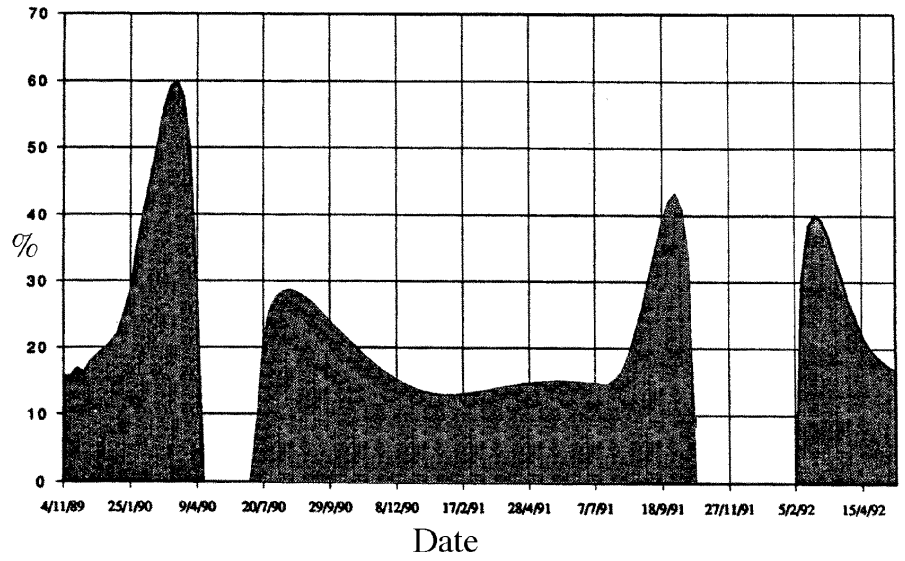

Figure 11.3. *Depth of discharge of the batteries, corresponding directly to the eclipse duration (see Figure 4.1). The maximum specified depth of discharge was 65 per cent. During the longest eclipse period in this interval (19 March 1990) the depth of discharge reached 60 per cent.*

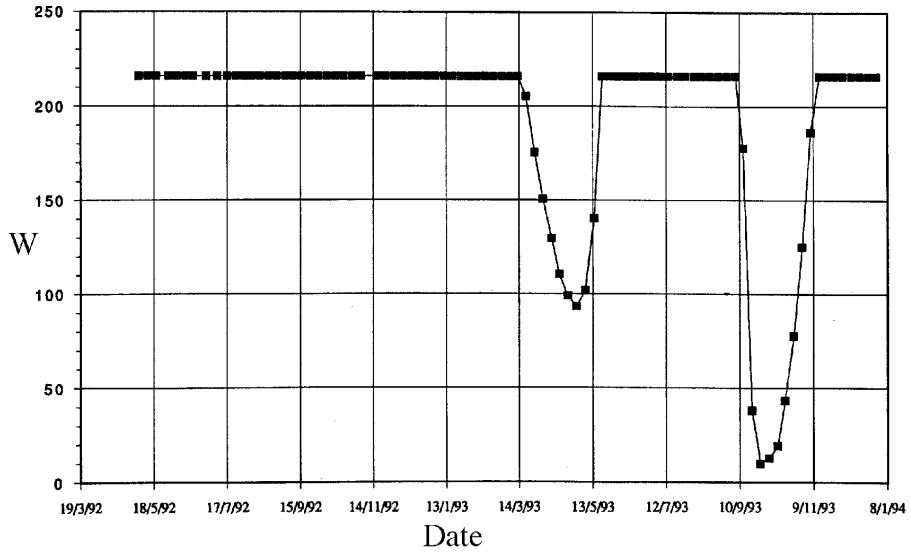

Figure 11.4. *Margin prediction for the future eclipses of April 1993 and September 1993. The first eclipse was passed without power saving (as predicted). Satellite operations terminated in August 1993, before the occurrence of the deeper eclipse.*

11.3. Solar Array Degradation

This section reviews the in-flight and predicted performance degradation of the spacecraft's solar array after three and half years in the very damaging radiation environment of its geostationary transfer orbit. The radiation environment provided a unique opportunity to study the on-board silicon solar cells up to equivalent 1 MeV electron fluence levels of $\phi = 1.26 \times 10^{16}$ e^- cm^{-2} for the short circuit current, I_{sc}, and 2×10^{16} e^- cm^{-2} for P_{max}/V_{oc}, the maximum power to open circuit voltage ratio, seldom attained by other spacecraft.

Radiation Model

Due to its geostationary transfer orbit (inclination 7°, perigee 651 km, apogee 35 835 km and period 10.68 hours) the satellite traversed the complete cross-section of the Earth's van Allen radiation belts. For the purpose of analysis, it was considered to have received intense one hour proton bombardment four times per day. This is depicted in Figure 7.2 which shows the daily positional proton flux encountered.

Although the computer routines used to assess the effects of the radiation environment embodied electron and solar flare components, these were insignificant compared to the proton contribution component of the 1 MeV 'equivalent' electron fluence aggregate. As an example, the daily trapped electron component only amounts to a fluence of 1.4×10^{11} 'equivalent' 1 MeV e^- cm^{-2} compared to 1.2×10^{13} e^- cm^{-2} for the daily proton component. Solar flares were also neglected since their annual contribution only amounts to the trapped proton daily fluence. This 1 MeV equivalent electron irradiation concept (Anspaugh 1991; Tada *et al.*, 1982; Anspaugh & Downing 1984) reduces both electron and proton irradiation effects over a wide energy range down to a single, convenient 1 MeV electron test energy and holds good so long as the electron and proton degradation characteristics take the same qualitative form (Figure 11.5 and Figure 11.6).

Laboratory Experiments

A series of laboratory experiments were carried out to investigate solar cell response to 1 MeV electron and 10 MeV proton irradiations. The two solar cell types tested were each the most radiation resistant of their class. They were the older generation 10 Ω cm silicon cell (Hipparcos type) and the more recent gallium arsenide/germanium (GaAs/Ge) cell; the latest advanced III-V compound cell to enter production. The silicon cells were manufactured by Telefunken System Technik (D) and the GaAs/Ge cells by Applied Solar Energy Corporation (USA).

More specifically the silicon cells were n-p 10 Ω cm, CZ silicon, measuring 2×4 cm^2 and 180 μm thick. They comprised a back surface Al reflector (for achieving lower operating temperature and hence more power output), a TiO anti-reflection coating and TiPdAg weldable contacts. Two thirds of the cells tested (75) were also fitted with nominal 150 μm thick cerium stabilised CMX cover glasses using DC93500 silicon adhesive. The average power output of these cells was 17.13 mW cm^{-2} (η = 12.7 per cent, 25 °C)

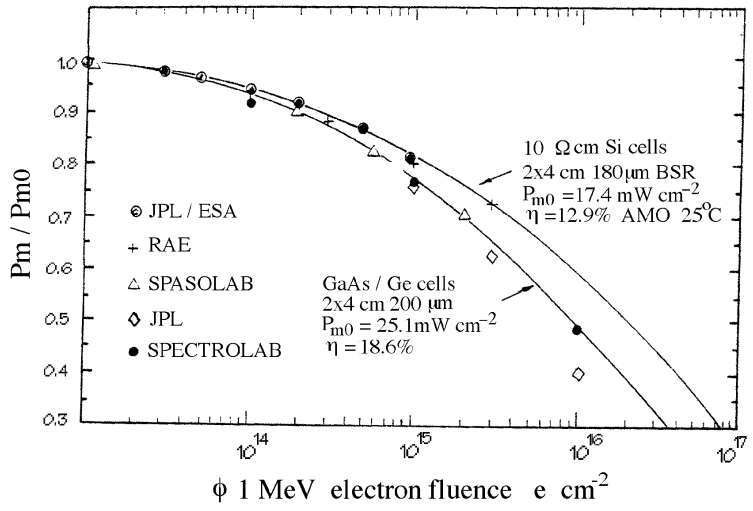

Figure 11.5. *Power loss versus 1 MeV electron fluence for Si and GaAs/Ge solar cells. The ordinate gives the ratio between the power at a given time (Pm), and the power originally provided by the solar arrays (Pm0). The abscissa refers to the equivalent electron fluence, discussed in Chapter 7. The upper curve gives the experimental results obtained for the Hipparcos (Si) cells, while the lower curve shows the degradation applicable to GaAs/Ge cells—although the latter degradation appears to be more significant, the equivalent 1 MeV electron fluence corresponding to a given proton flux is much lower for GaAs/Ge (see Figure 7.7).*

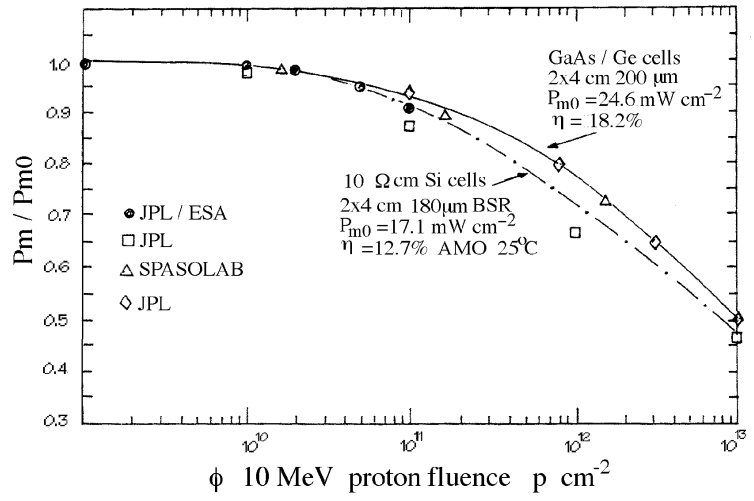

Figure 11.6. *Power loss versus 10 MeV proton fluence for Si and GaAs/Ge solar cells. Details are as for Figure 11.5.*

i.e. 170 W m^{-2}. The average uncovered cell weight was 439 mg yielding a power-to-weight ratio of 38.7 W kg^{-1} for the basic cell.

Six separate CMX cerium stabilised cover glasses were also supplied by Pilkington Space Technology (UK) for testing to facilitate differentiation of radiation-induced optical darkening from basic cell degradation.

The GaAs/Ge cells tested (60) were p-n, metal organic chemical vapour deposition cells (Cheng *et al.*, 1991) measuring 2×4 cm^2 and 200 μm thick. The GaAs to Ge interface was inactive. Half of the cells were covered with 50 μm thick cerium stabilised CMX cover glasses. The average power output of the cells was 24.60 mW cm^{-2} (η = 18.3 per cent, 25 °C) i.e. 246 W m^{-2}. The average uncovered cell weight was 886.9 mg yielding a power-to-weight ratio of 27.7 W kg^{-1} for the basic cell.

Solar Cell Performance Measurements

Solar cell I–V performance measurements were made using reliable pulsed or continuous xenon solar simulators as a light source. A primary standard cell of similar spectral response to that of the test cells was used to set the simulator intensity. The solar cells I–V characteristics were measured with a conventional four-probe measurement system and a power supply for a load. The solar cell temperature was controlled to 25 $\pm$ 0.2 °C during I–V measurements.

1 MeV Electron and 10 MeV Proton Irradiations

The 1 MeV electron irradiations of the covered silicon solar cells were performed using the JPL (USA) Dynamitron accelerator (Anspaugh 1991). The electron beam was spread into a wide uniform beam using an aluminium foil 127 μm thick. Beam intensity is highest at the beam centre and falls off to 91 per cent of the centre value at the edges. The cells were mounted on a copper cell-mounting plate using vacuum grease for good thermal contact. The cell-mounting plate was then bolted onto a fixed target plane in the irradiation chamber. This target plane was temperature controlled to hold the solar cell temperature at 28 °C during the electron irradiations and a Faraday cup was mounted in the centre of this plane for flux and fluence dosimetry. Cumulative fluence exposures were 1×10^{13}, 2×10^{13}, 5×10^{13}, 1×10^{13}, 2×10^{13}, 5×10^{13} and 1×10^{15} e^- cm^{-2}. All irradiations were carried out in vacuum at a pressure below 5×10^{-5} torr.

RAE (UK) subsequently repeated these tests on the uncovered Hipparcos Si cells using a water-cooled vacuum cell holder at their BICC van de Graaff accelerator in London. The 1 MeV electron fluence was extended to 3×10^{15} e^- cm^{-2}.

Spasolab irradiated their assignment of GaAs/Ge solar cells up to a 1 MeV electron fluence of 2×10^{15} e^- cm^{-2} using the University of Delft (NL) van de Graaff accelerator. This facility was also used to irradiate the covered silicon cells together with the individual CMX cover glasses up to very high fluences (3×10^{16} e^- cm^{-2}) to evaluate the radiation 'hardness' of the glasses and their adhesive (DC93500). This particular experiment was repeated, with the inclusion of directly glassed (electrostatically bonded with no adhesive) control cells, on account of the physical effects observed.

The 10 MeV proton irradiations were performed using Tandem van de Graaff accelerators (Anspaugh 1991; Anspaugh & Downing 1984). Beam energy was controlled

by 90° magnetic analysis and the accelerator energy was stabilised by a slit-feedback system to control the van de Graaff terminal voltage. All irradiations and dosimetry were performed in vacuum (less than 5×10^{-6} torr). The small focused proton beam produced by the accelerator was spread into a wide area uniform beam by means of scattering foils. The target plane was approximately 3 m from the scattering foils. The foils were chosen so that the beam intensity at the edge of a 10 cm diameter circle in the target plane varied no more than 7 per cent from the beam intensity at the centre.

The solar cell target plane was rotated at a rotation rate $d\Theta/dt$ proportional to $1/\sin\Theta$, thereby providing a good simulation of the omni-directional space radiation environment by rotation about only one axis. Fluence levels up to 1×10^{11} protons cm^{-2} were studied by JPL for the covered Si Hipparcos cells. Spasolab irradiated their GaAs/Ge cell assignment up to a 10 MeV fluence of 1.59×10^{12} protons cm^{-2} using the CEA accelerator near Paris.

The I–V characteristics of the irradiated cells were measured following 'cool-down' and performance stabilisation by photon irradiation (i.e. under simulated illumination at 25 °C for 48 hours).

In-Orbit Hipparcos Solar Cell Data

The most fundamental indication of the radiation influence was initially obtained from telemetry data of the open circuit voltage (V_{oc}, Figure 11.7) of the charge array strings. A further indication of the radiation environment effect was also regularly obtained from telemetry data of the short circuit current (I_{sc}, Figure 11.8) of one of the main solar array sections, this section being permanently dumped at launch as a result of lower on-board power consumptions than originally anticipated for the mission.

The I_{sc} and V_{oc} data were transmitted from ESOC on a regular basis after normalisation of the data to a solar aspect angle of 0°, air-mass-zero illumination and a cell temperature of 25 °C. The data was also correlated with solar intensity to account for the cyclic variation of the Earth-Sun distance. After February 1990, only solar arrays 1 and 2 were taken into account, since solar array 3 had suffered a thermistance failure. The nominal Hipparcos operating mode was with a solar aspect angle of 43° and a cell temperature of 33°. This was backed up by a 'safe mode' configuration with a solar aspect angle of 0° and a cell temperature of 55 °C. The flight data is probably accurate to ±2 per cent.

The final I_{sc} values result from the satellite sun-pointing mode during the final fifteen days. The operational voltage limit was taken to be 53 V which corresponded to a nominal voltage of 51 V, together with the voltage drop, the blocking diode and the charged quad. The average degradation was about 3 V per year, and extrapolation of the curve shown in Figure 11.8 indicated a lifetime up to the middle of 1994. However, since there was a direct correlation between the degradation of the solar generator and the solar particle flux (particularly the proton flux), the lifetime could be reduced in the event of stronger than predicted solar activity.

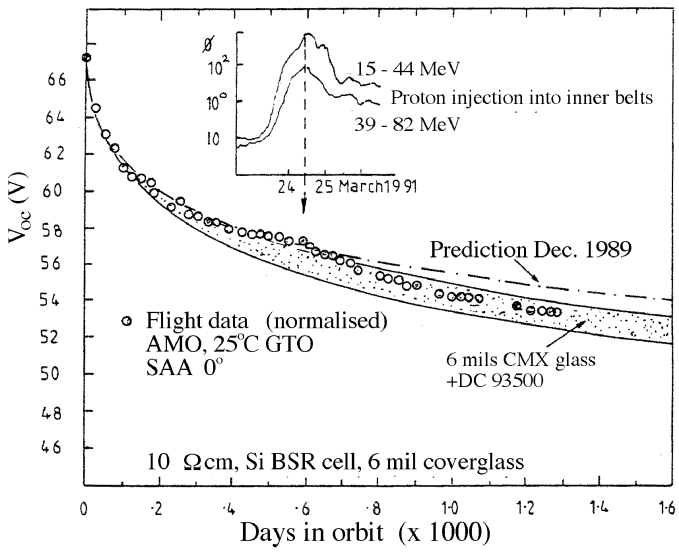

Figure 11.7. *Hipparcos in-flight solar array open circuit voltage (V_{oc}) degradation, normalised to 25 °C, 0° sun aspect angle (SAA), and air-mass-zero illumination (AMO). The dashed line indicates the degradation predicted early in the revised mission (in December 1989). The data points (open circles) correspond to the measured data. The shaded region corresponds to the final predicted performance described in the text, the uncertainty region corresponding to the tolerance on the cover glass thickness (nominally 6 mil; or 0.006 inches). The observed degradation corresponded fairly well with the final assessment of the cell performance.*

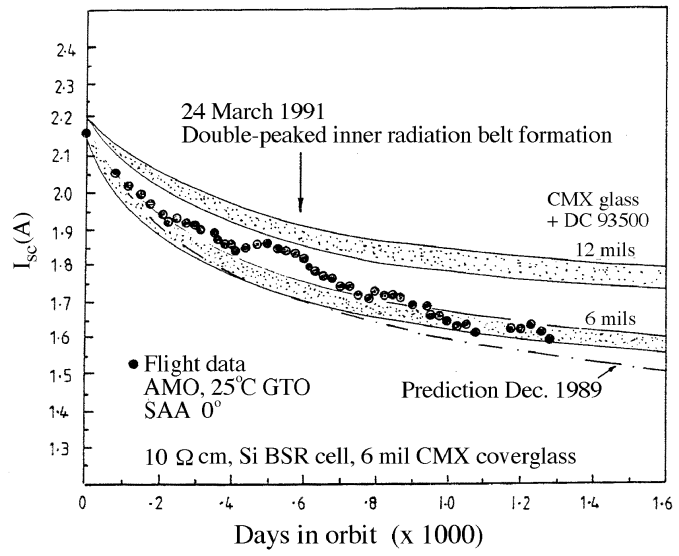

Figure 11.8. *Hipparcos in-flight solar array short circuit current (I_{sc}) degradation. Details are as for Figure 11.7. The observed degradation (solid circles) was less severe than the original (December 1989) prediction. The lower shaded region corresponds to the final model for the actual (6 mil thick) cover glass used for the Hipparcos solar arrays. The upper shaded region indicates the improvement in performance expected had 12 mil thick cover glass (used for GEOS) been used.*

Comparison of Results and Analysis

The results of the 1 MeV electron and 10 MeV proton irradiation experiments are depicted in Figure 11.5 and Figure 11.6 respectively. Additional data points were added from reliable reference sources to enhance the extrapolation of the degradation curves which were needed for making the in-orbit predictions. The partition of Si and GaAs/Ge cell data is distinct for both electron and proton irradiations and the data points from the various experimenters appear to be both complementary and in good agreement with each other. Considering the electron and proton fluence required to produce a 25 per cent loss of maximum cell power output ($P_m/P_{m0} = 0.750$), it is seen that in the case of the GaAs/Ge cells this is achieved for $\phi_1 = 1.3 \times 10^{15}$ e^- cm^{-2} and $\phi_2 = 1.3 \times 10^{12}$ protons cm^{-2} respectively. Thus the ratio $\phi_1/\phi_2 = 2.1 \times 10^{15}/7.5 \times 10^{11} = 2.80 \times 10^3$ e^-/proton, i.e. 2800 1 MeV electrons per 10 MeV proton. This data is consistent with the damage coefficients embodied in the NASA EQFRUX computer routine for silicon cells (Tada *et al.*, 1982) and the latest version applicable to GaAs/Ge solar cells (Anspaugh 1991). The character of these electron/proton ratios is depicted in Figure 11.9 as a function of proton energy and illustrates the proton energy cut-off levels achieved by using various cover glass shielding thicknesses.

Because of the non-uniform nature of the damage produced by low energy protons within the body of a cell, a similar data set had to be derived for short circuit current (I_{sc}) predictions (Tada *et al.*, 1982), i.e. the damage coefficients were partitioned as I_{sc} and P_{max}/V_{oc}.

By using the proton/electron belt radiation maps AP8 MAX and AE8 MAX in combination with the limited laboratory data available and appropriate EQFRUX computer routines, it was possible in December 1989 to make a prediction for the likely course of the Hipparcos solar array short circuit current and open circuit voltage performance degradation for the ensuing years.

These predicted degradation curves are shown in Figure 11.7 and Figure 11.8 for which it had been possible to include the observed flight data and additional refinements to the original predictions based on the latest available experimental data. The original predictions were reasonable; slightly pessimistic in one case and optimistic in the other. The updated prediction curves benefited from more recent laboratory data and higher particle fluences but another factor emerged to introduce another aspect of uncertainty; namely the thickness tolerance of the cell cover glasses and intervening optical DC93500 adhesive. Thus a nominal 150 μm CMX cover glass supply could have an allowable thickness variation from 130–170 μm, a 50 μm CMX cover glass 45–60 μm, a 300 μm cover glass 260–340 μm and so on. The extremities of the 'prediction' bands depicted in Figure 11.7 and Figure 11.8 represent the influence of the upper and lower values of the shielding specific mass.

The sudden discontinuity in the flight data on day 590 corresponds to the sudden solar storm commencement (Mullen *et al.*, 1991) and formation of a double peaked inner radiation belt. A similar effect was observed on the High Efficiency Solar Panel Experiment flown on CRRES (Ray *et al.*, 1993) for a period of 14.5 months i.e. from Hipparcos day 351 to 795. The radiation hardening which would have been achieved had 300 μm (12 mil) thick CMX cover glasses been used, is also shown in Figure 11.9.

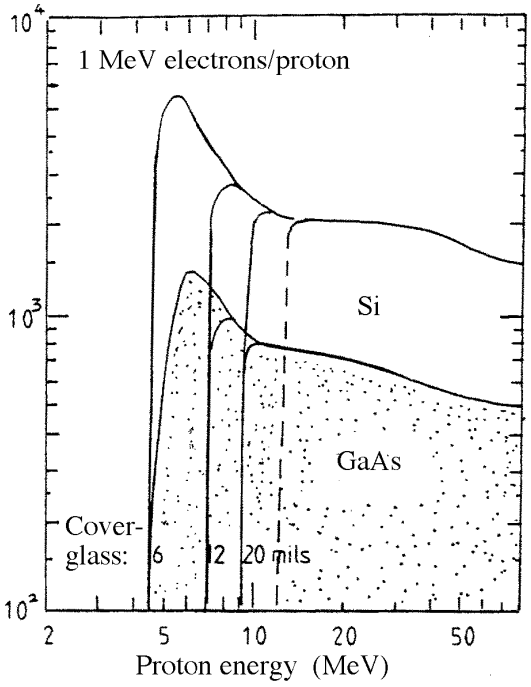

Figure 11.9. *The dependence of the number of equivalent 1 MeV electrons per proton as a function of proton energy, for various cover glass (shielding) thicknesses, and for Si and for GaAs solar cells. The figure illustrates the proton energy cut-off levels achieved by using various cover glass thicknesses. The Hipparcos cells corresponded to the 6 mil (0.006 inch ~ 150 μm) cover glasses on Si.*

Since the Hipparcos solar cell's operating point was now beyond the knee of its I–V curve it was possible to reconstitute its I–V characteristic by monitoring the battery recharge current in this region. This is shown in Figure 11.10 along with estimates of the associated 1 MeV equivalent electron fluences for I_{sc} and P_{max}/V_{oc} degradation.

As a consequence of the advanced stage of performance deterioration an interesting phenomenon was observed. The solar array delivered less power when pointed normal to the Sun (a safe mode in the event of gyro problems) than when in its normal operating mode (solar aspect angle = 43°). This arose because pointing at the Sun causes the cell's temperature to rise from 33 to 55 °C thereby lowering V_{oc} still further.

Concerning the durability of the cell's optical components at high fluence 1 MeV electron irradiation (Delft University), at $\phi = 3 \times 10^{16}$ e^- cm^{-2}, it was observed that several cover glasses had started to delaminate. This is shown in Figure 11.11. Subsequent microscopic examination and dissection revealed that advanced polymerisation and hardening of the DC93500 silicone adhesive had taken place and was followed by delamination at the cover glass/adhesive interface. The influence on the electrical performance of the cell was negligible (1 per cent). A repeat experiment was conducted with directly 'glassed' cells (i.e. electrostatically bonded with no adhesive) included as a control. These cells showed no such deterioration but several of the conventionally covered cells again displayed cover glass delamination. The six individual CMX cover glasses were also subjected to this high fluence level but exhibited no measurable deterioration of their transmission characteristics (Figure 11.12.)

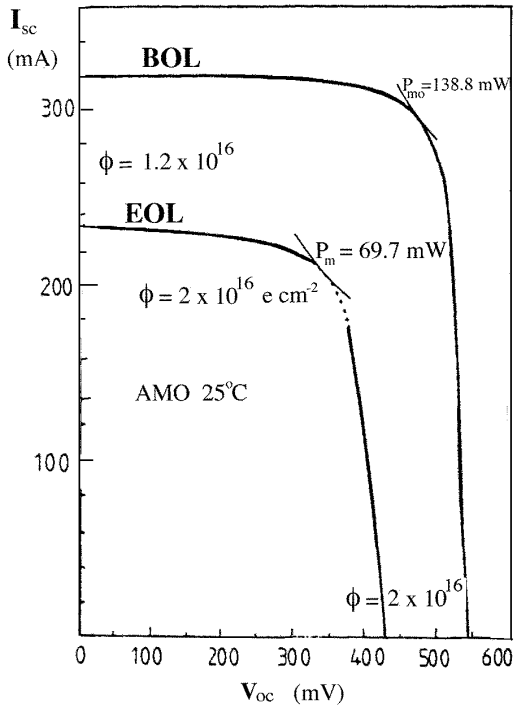

Figure 11.10. *Hipparcos solar cell I–V characteristics; at launch and after 1280 days in geostationary transfer orbit. V_{oc} and I_{sc} were measured for the array, and the figure indicates the estimated corresponding performance of the cell. The values of P_m indicate the maximum power points at the beginning-of-life (BOL) and end-of-life (EOL).*

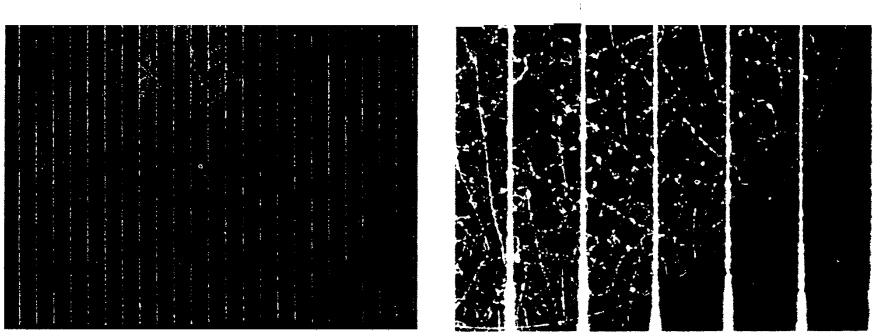

Figure 11.11. *Cover glass adhesive degradation. The vertical white lines are contacts on the solar cell (the separation between two such contacts is approximately 1 mm). The 'crazed' areas indicate delamination in the cover glass adhesive at very high radiation levels, typical of the end-of-life of the Hipparcos mission.*

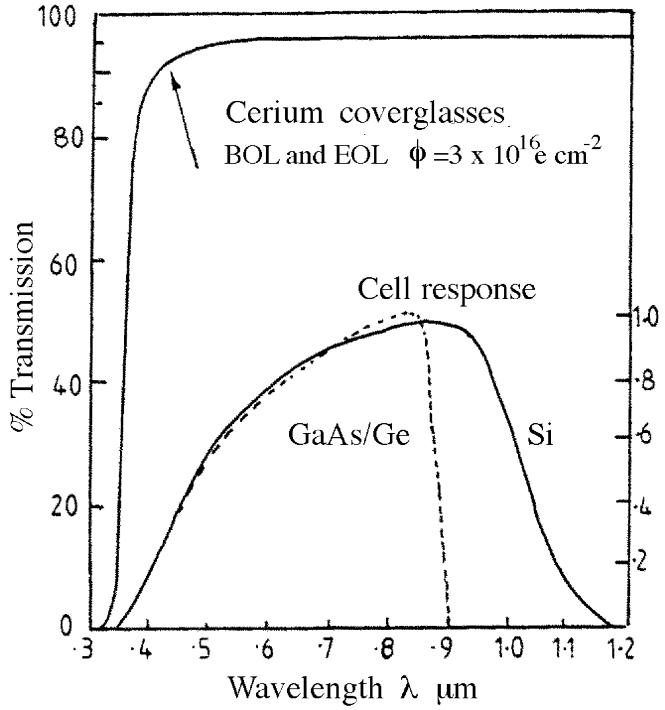

Figure 11.12. *Transmission characteristics of cerium stabilised cover glasses (corresponding to the Hipparcos cells) before and after high fluence 1 MeV electron irradiation. The upper curve is the same at the beginning- and end-of-life (BOL and EOL) indicating the stability of the cover glass. The lower curves indicate the intrinsic cell response as a function of wavelength—the cover glass is optimised to give the highest transmission over the relevant wavelength region.*

The study was concluded by making EQFRUX computer runs for both the Si and GaAs/Ge solar cells in order to compare their radiation hardness in geostationary transfer orbit for 1311 days as a function of cover glass/adhesive shielding. The resultant solar cell maximum power output curves are presented in Figure 11.13, each band extremity representing the permitted tolerance level for the nominal cover thickness indicated. Both cell types are thus expected to be very radiation resistant degrading at approximately the same rate as each other for a given cover shielding and with a marked fall off in hardness in both cases for cover glasses thinner than 150 μm. This is a direct consequence of the high non-linear rise in damage coefficient values at low proton energies (Figure 11.9).

In practice, these predictions were found to be somewhat pessimistic. The CRRES satellite, which operated for 14.5 months in a similar orbit, embodied the same cell types as employed in the present study (Ray *et al.*, 1993). Thus for the case of 300 μm (12 mil) cover glasses thickness the P_{max} of the GaAs/Ge cells degraded by 13 per cent compared to the 16 to 19 per cent predicted by Figure 11.13, while the P_{max} of the Si cells degraded by 16 per cent compared to the 23 to 27 per cent indicated by Figure 11.13. The qualitative 'fan effect' of Figure 11.13 was also confirmed.

In conclusion, the observed in-orbit radiation damage characteristics of the Hipparcos silicon solar cells were predicted reasonably well using proton and electron maps (AP8 and AE8) and NASA computer routines based on the equivalent 1 MeV electron irradiation concept. The accuracy was sufficient to facilitate optimum on-board power system

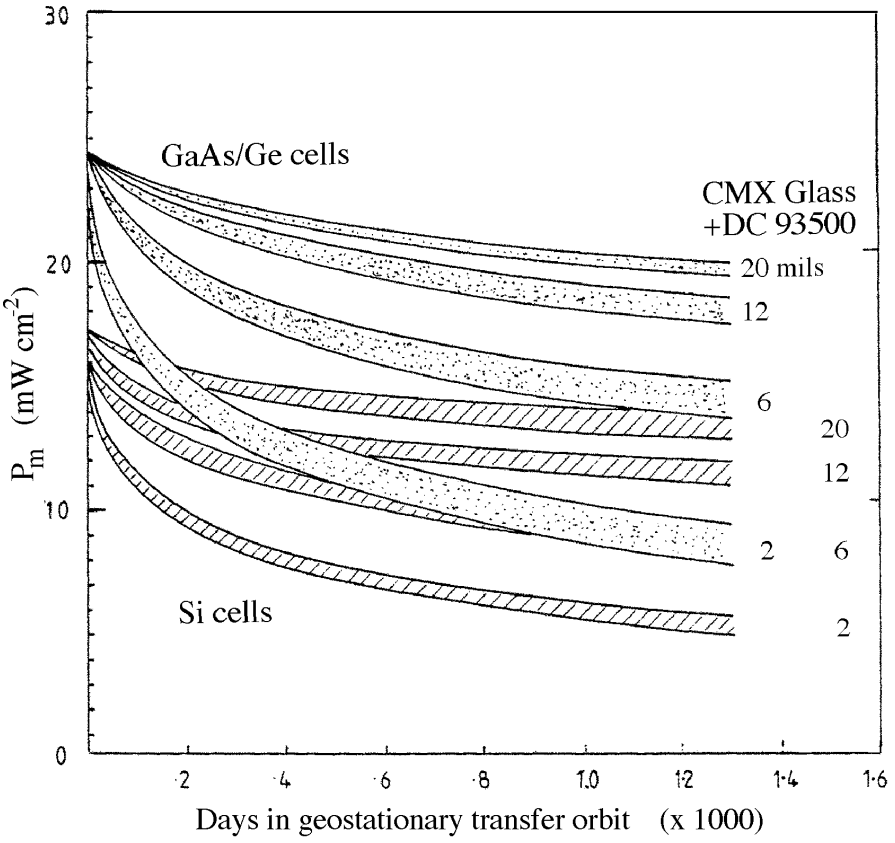

Figure 11.13. *The solar cell maximum power output (P_m) versus time, illustrating the radiation 'hardness' in geostationary transfer orbit for GaAs/Ge and Si arrays (the Hipparcos cells corresponded to the 6 mil (0.006 inch) Si cells, the other configurations being shown for comparison).*

management for the three and half years in geostationary transfer orbit. It was also concluded that the same computational procedure would be suitable for use with the next generation of radiation resistant, high power GaAs/Ge solar cells. Additional laboratory irradiation experiments would, however, be required at high proton/electron fluences and at low, near-shielding cut-off energies, to enhance the accuracy of predictions.

The single most important physical factor influencing the longevity of either cell type in space was found to be the choice of cover glass shielding. The wide range of manufacturing tolerances introduces an uncertainty in the cover glass thickness which must be taken into account. With regard to the durability of the optical cover glass/adhesive components, the use of cerium stabilised cover glass shielding was observed to be appropriate for this application.

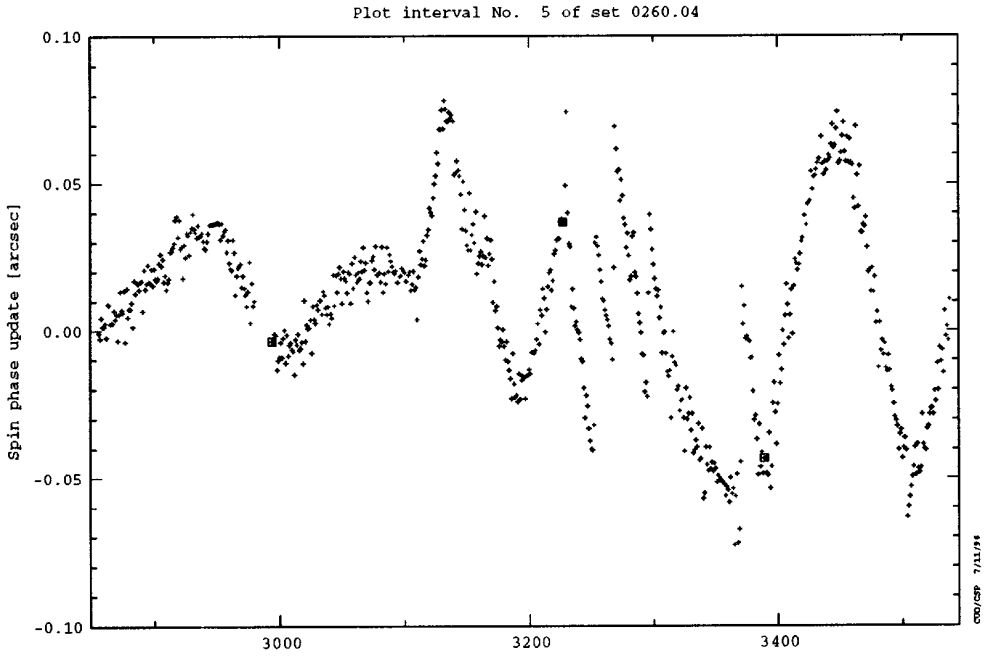

Figure 11.14. *Data interval illustrating the attitude jitter in the along-scan direction occasionally observed after the satellite emerged from eclipse to sunlight. The along-scan attitude is seen to develop smoothly up to frame number 3200, then a series of discontinuities or 'glitches' occur for the subsequent 100 frames (1 frame = 2.133 . . . s); thereafter the attitude develops smoothly again. Squares indicate times of thruster firings.*

11.4. Eclipse-Induced Attitude Jitter

During the on-ground attitude reconstruction, the NDAC Consortium reported intermittent short stretches of data during which the satellite along-scan (spin-phase) attitude updates derived in the great-circle processing showed an unexplained sawtooth behaviour: over some 5 min duration, a series of discontinuities of up to about 50 milliarcsec amplitude, separated by up to approximately 1 min, were observed (see Figure 11.14). The FAST Consortium subsequently confirmed the effect, and threw further light on the problem by noting that the phenomenon occurred some 100 observation frames (roughly 3 min) after the satellite emerged into sunlight after an eclipse period. A single opposite case was noted, less marked, and corresponding to an entry into umbra. It was tentatively proposed that thermal shocks were occurring in the optical structure. It should be noted that the problem affected an almost insignificant fraction of the entire data set, and the affected data were suppressed from the subsequent steps of the data analysis.

The following explanation was eventually formulated, although full confirmation would have required a more detailed study of the solar arrays, their attachment to the satellite, and their thermal environment entering and exiting the eclipses.

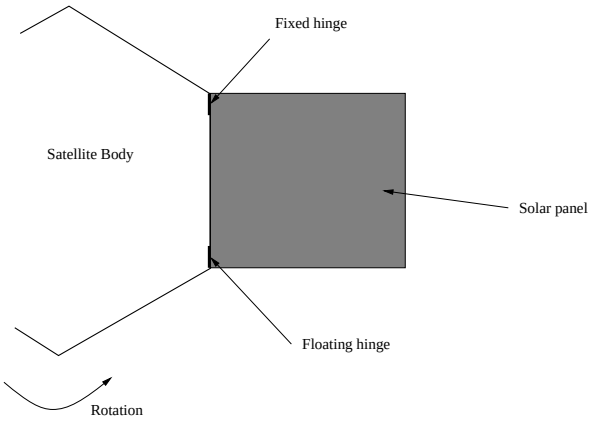

Figure 11.15. *The configuration of one of the solar arrays and its attachment to the body of the satellite. Thermal shocks after eclipses were considered responsible for small discontinuities in the along-scan attitude.*

For each of the three deployable solar panels, one of the hinges was rigidly fixed to the satellite body, while the other allowed some movement along the line of the attachment of the array to the satellite body, this construction allowing for differential expansion between the satellite body and the panels themselves (see Figure 11.15). The solar arrays are held by a carbon-fibre reinforced plastic structure having a very low coefficient of thermal expansion of about 1.5×10^{-6} K^{-1}. For a panel dimension of about 1 m, and a change in solar array temperature of about 100–150 K (the ambient temperatures being about 300 K in sunlit phase, and 170 K in eclipse) a change in dimension of some 0.2 mm (total) would result from passage from umbra to sunlight, and vice versa (the thermal variation of the satellite body was very much smaller because of its larger thermal capacity). It is considered likely that the resulting differential expansion occurred with a 'slip-stick' or 'stiction' behaviour, with the timescales involved (i.e. with the start of the phenomenon occurring 2–4 min after the thermal discontinuity, with an overall duration of a few minutes) well matched to the thermal time constant of the solar arrays provided in the manufacturer's reports.

The sharpness of the transition from umbra to sunlight depended on the satellite position along the orbit, and it was inferred that the effect would be more dramatic for shorter penumbra durations, or less dramatic for shorter total eclipse durations (where the maximum temperature excursion would not be reached). These features were qualitatively confirmed by the data analysis groups.

The transition from shade to sunlight had a more dramatic effect on the satellite motion than that from sunlight to shade. In the former case, with the arrays initially colder, the coefficient of friction between the affected surfaces would be larger than in the latter, and the stiction effect correspondingly larger. At the same time, the lower temperature would result in higher stresses in the hinges or joints (due to thermal contraction) and would thus also increase the friction between the moving surfaces. In summary, it was also considered likely that the effects on entering/exiting eclipse would indeed be 'asymmetrical'.

The magnitude of the phenomenon (50 milliarcsec discontinuities) was consistent with the slip-stick effect of the 10 kg solar array mass located 1 m from the satellite centre

of mass. The following analysis provided an order-of-magnitude estimate of the effect. The impulse of the moving element was estimated from:

$$i = m^* \Delta v \qquad [11.3]$$

where m^* is the solar panel mass. Assuming that the impulse duration corresponds to the fundamental frequency of the solar panel in the relevant plane:

$$\Delta v = 2\pi n^* \Delta u \qquad [11.4]$$

and assuming $n^* = 100$ Hz, $\Delta u = 0.2$ mm, $m^* = 10$ kg, gives $\Delta v = 0.1$ m/s and $i = 1.2$ kg m/s. The assumed n^* was taken as a realistic upper limit for the solar panels, but it could be as low as 10 Hz.

For a satellite moment of inertia of 1000 kg m^2 about the z-axis, the effect on the satellite movement is:

$$a\, i = I\, \Delta\Omega \qquad [11.5]$$

where a is the distance between the mass and the centre of gyration, and:

$$\Delta\theta = \Delta\Omega/(2\pi n) \qquad [11.6]$$

Assuming $n = 100$ Hz for the satellite (this could perhaps be in the range 30 – 200 Hz), and $a = 1$ m gives $\Delta\theta = 1.8 \times 10^{-6}$ rad = 0.4 arcsec.

There are certain complications in applying this simple model: (i) n and (especially) n^* are unknown; (ii) $a\, i$ is an upper limit due to the fact that plane of the panels are offset from the satellite centre of mass (a similar but smaller effect would therefore also be predicted about the other two axes); (iii) the combined effects of the three panels makes the results more complex; (iv) the above calculations led to an oscillatory motion of the given amplitude at the fundamental frequency, not a uni-directional displacement. But, in summary, it did not seem surprising that the effect was observable.

The solar array explanation seems most plausible, given the mass of the panels, rather than any effect of, say, the aluminium fill-in antenna albeit with its larger coefficient of thermal expansion. Effects on the payload itself were also considered to be unrealistic given the known thermal environment.

12. THERMAL CONTROL

To ensure the relative stability of the optical components within the Hipparcos payload, active and passive thermal control resulted in a temperature stability of better than 0.05 °C over short periods, and ±2 °C over the entire mission duration. Temperature measurements were collected at various points in the payload throughout the spacecraft's lifetime, and relayed both to the on-board computer (which monitors and regulates the thermal control) and the ground. Despite some loss of heater supply later in the mission, attributable to the excessive radiation damage experienced by the thermal control electronics, the payload thermal control proved to be extremely robust, permitting proper payload operation until the end of the mission.

12.1. Introduction

The thermal control of the Hipparcos payload was driven by very stringent requirements on the temperature stability of the payload structure, the optical elements and the detectors. Typical long-term temperature requirements were 20 ± 2 °C over the total mission duration when the payload was operational. Short-term temperature requirements on the mirrors were ±0.05 °C. These requirements could only be achieved by proper thermal design of enclosures, where the boundaries were used to balance internal and external thermal disturbances.

The payload structure was manufactured from carbon-fibre reinforced plastic with a very low coefficient of thermal expansion, using a box-type arrangement (see Figure 12.1). The optical elements and the detection systems were arranged inside the structure. In order to get isothermal boundaries, thin foil heater mats were placed on honeycomb panels (heater mat carriers), which were loosely connected mechanically to the carbon-fibre reinforced plastic structure. This design concept was chosen to minimise mechanical disturbance of the carbon-fibre structure due to thermal expansion of the honeycomb, and to keep the coefficient of thermal expansion constant by avoiding attaching a different material to the carbon-fibre structure. The entire payload was covered with multilayer insulation, except for two radiators, which were needed to dump the internally dissipated power of the detectors.

Depending upon the payload assembly, thermal control was achieved by either passive or active means, as shown in Table 12.1. The active thermal control relied on 21 'thermally

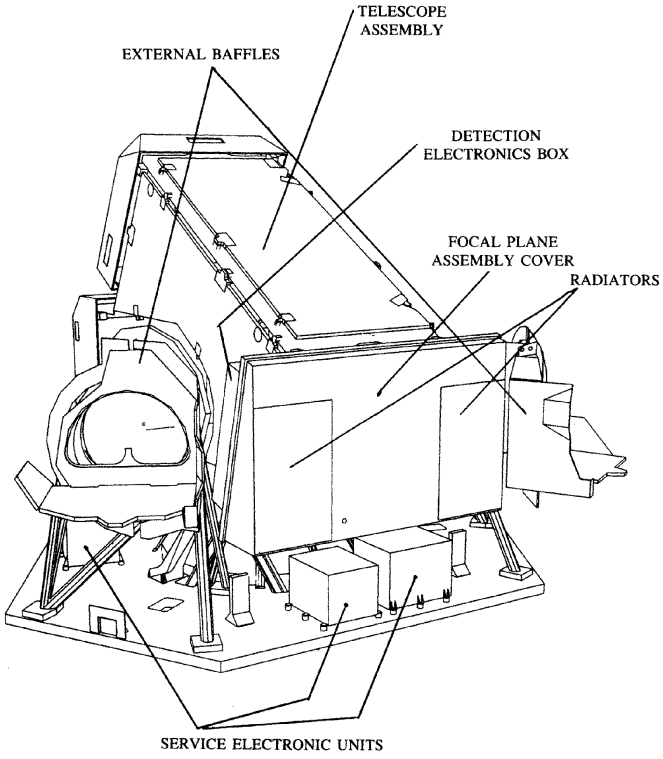

Figure 12.1. *Payload external configuration.*

controlled areas' (numbered from 1 to 24, with zones 4, 17 and 24 not used). Each area comprised a set of two heaters (nominal and redundant), physically implemented at the same location, and a set of two thermistors (nominal and redundant), implemented close to each other. These areas were controlled by the on-board computer through the thermal control electronics.

Active thermal control was provided to the payload, even when in the off state, by stand-by heaters controlled by the spacecraft electrical interface unit. There were two redundant automatic stand-by zones, corresponding to the telescope and the focal plane assembly. These zones were automatically regulated and the target temperatures were fixed; however, the heater's command could be over-ridden by ground command. There were two ground commanded stand-by zones (corresponding to the two detection electronics boxes).

For on-station payload operation, the heaters were controlled by a control law, monitored by the on-board computer, the principle of which is shown in Figure 12.2. Temperature measurements by the control thermistors were monitored by the thermal control electronics, and transmitted via the remote terminal unit to the on-board computer. The thermal control law, installed in the on-board computer, determined the respective power levels, which were sent back via the remote terminal unit and the thermal control electronics to the heater circuits. Updates were performed every 10 s. This system kept the mean temperature of the controlled area within 0.2 °C of the nominal values. Due to averaging, the individual optical elements within the enclosure were restricted to temperature excursions and temperature gradients of less than 0.05 °C.

Table 12.1. Characteristics of the payload thermal control.

Payload Assembly	Thermal Control	View to Space
Telescope assembly	active	yes
Focal plane assembly	active	no
Service electronics units	passive	no
Detection electronics boxes	active	no
Baffle assembly	passive	yes

12.2. Heater Design

The spacecraft thermal control provided a thermal environment to keep all of the spacecraft elements within their specified temperature limits throughout all the mission phases. In addition, it protected the payload from direct sun illumination in order to provide a more stable environment. The thermal control relied mainly on passive means, although for some critical elements supplementary heaters were provided. The thermal control electronics were in charge of controlling the tight payload thermal equilibrium. A certain number of areas had to be individually controlled in order to maintain the payload at the required temperature. Each of these areas contained a thermistor and a heater (see Figure 12.3 and Table 12.2).

The active thermal control worked mainly in the so-called proportional integral mode. Each heater was fed by a variable current level, which was driven in a closed-loop fashion by the reading of the relevant thermistor. For each cycle (10.66... s) the power fed to a heater was proportional to the difference between the actual temperature of the relevant controlled area and its target temperature. The overall control algorithm was located in the on-board computer, and based on so-called 'D-values' which for each heater identified a specific value of power (from 1–15) to be fed to the heater. Figure 12.4 presents the total power fed to the payload during the mission, expressed in units of D-values. In case of a degradation in the control area performance it was possible to inhibit the above described loop and put any control area in fixed power mode. This mode implied that the power applied to the heater was a constant value (on a scale of 1 to 15), defined on ground on the basis of the thermal history of the affected area.

12.3. Payload Thermal Control History

The first symptom of loss of heaters efficiency could be seen by the general increase of the on-board computer power level value fed to the heaters in order to keep each area at the target temperature. The second symptom was that once the maximum power level value had been reached or set manually (in fixed power mode) a decrease in the individual temperatures could be observed. The degradation could be observed by the need to increase the power load into the still functioning heaters to obtain a constant payload mean temperature (Figure 12.4, top), and the decrease of the payload mean temperature (Figure 12.4, bottom). During suspended operations, the mean payload temperature dropped to very low values since no on-board control on the thermal control electronics had been active.

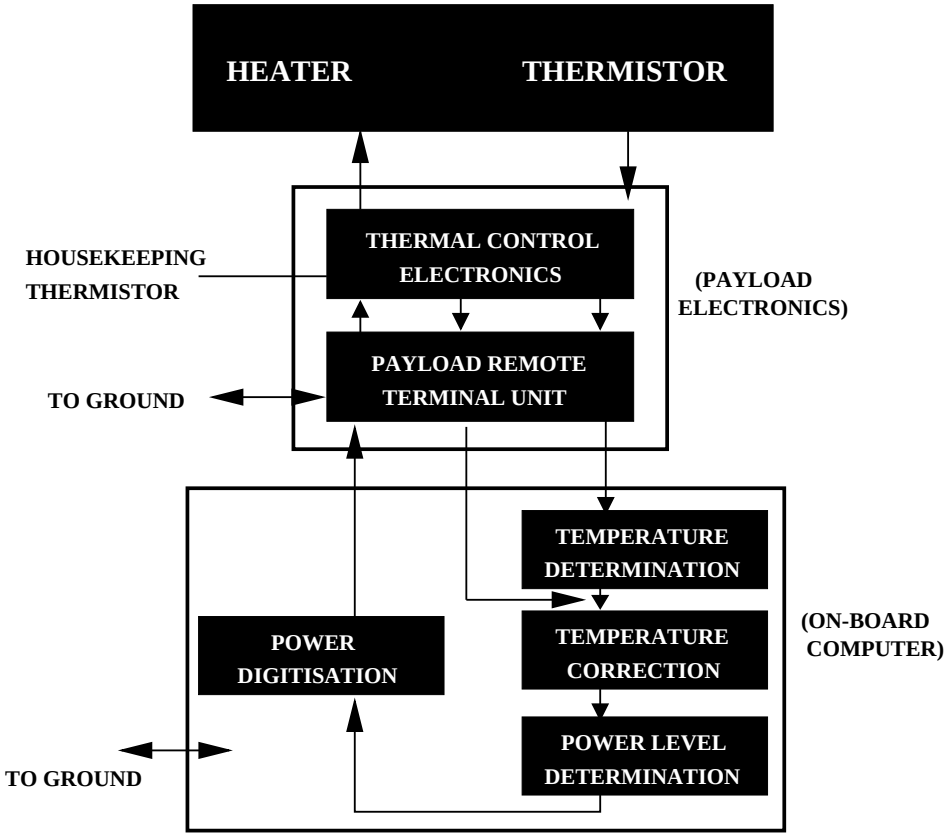

Figure 12.2. *Principles of the active thermal control.*

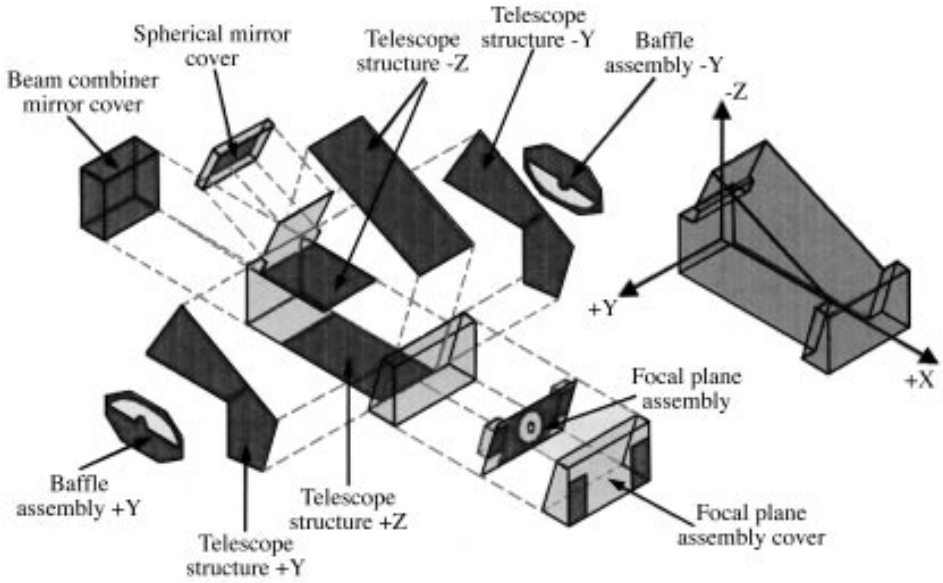

Figure 12.3. *Location of payload heaters.*

Table 12.2. Payload heater locations.

Payload Section	Heaters
Beam Combiner Mirror cover	heaters 1, 2, 3 and 5
Spherical Mirror cover	heater 7
Telescope Structure +Y	heaters 8 and 11
Baffle Assembly +Y	heater 15
Telescope Structure -Y	heaters 9 and 12
Baffle Assembly -Y	heater 16
Telescope Structure +Z	heaters 13 and 14
Telescope Structure -Z	heaters 6 and 10
Focal Plane Assembly	heaters 18, 21, 22 and 23
Focal Plane Assembly cover	heaters 19 and 20
Spares	heaters 4, 17 and 24

The following provides a summary of the changes occurring within the payload thermal control system during the mission (AR refer to formal 'Anomaly Reports', listed sequentially in Appendix B, and TCE refers to the Thermal Control Electronics):

90-07-19: AR number 37: loss of heater power supply on TCE 1 (area 17).

91-01-21: AR number 44: loss of heater power supply on TCE 1 (area 20).

91-01-25: Switch from TCE 1 to TCE 2.

91-09-18: TCE 2 area 20 set to fixed power mode value 11.

92-04-21: TCE 2 area 5 set to fixed power mode value 13.

92-07-06: AR number 61: TCE 2 loss of heater power supply (three heaters had now failed, three others were underperforming).

92-07-08: AR number 63: TCE 1 test (complete loss of the unit).

92-07-20: TCE 2 test (five heaters had now failed, two others were underperforming).

92-07-28: Payload TCE 1 and 2 tests (seven heaters had now failed).

92-09-02: Complete payload TCE 2 to fixed power mode.

93-02-10: TCE 1 and 2 test.

93-03-23: Payload off. TCE 2 left on.

93-03-24: TCE 2 configured to wide range to allow greater temperature variations.

93-03-30: All TCE 2 heaters to fixed power with value zero.

93-04-27: TCE 1 and 2 test. As further heaters had failed, all TCE 2 heaters were set to fixed power value 15.

93-06-07: TCE 2 test; out of 21 heaters only four were still functioning.

93-07-29: TCE 2 test.

During the mission lifetime a gradual degradation of the thermal control electronics 2 performance was noted since switch-on (on 25 January 1991), with occasional but significant peaks in the degradation rate (see Figure 12.4).

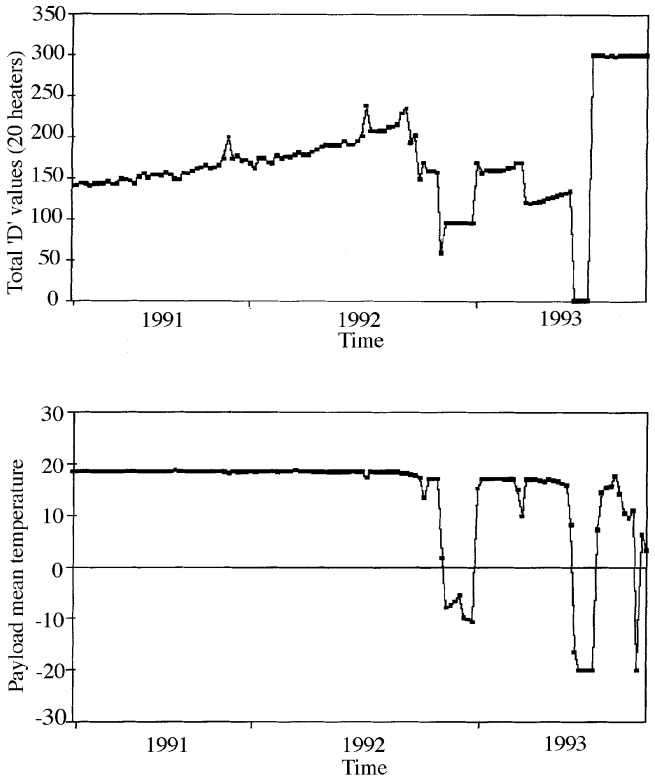

Figure 12.4. *Thermal control evolution throughout the mission. The top figure shows the total power fed to the payload, expressed in 'D values' (see text for details). The bottom figure shows the payload mean temperature (∘C) throughout the mission, including the low values experienced during suspended operations.*

12.4. Thermal Anomalies and the Basic Angle

The part of the payload most sensitive to temperature variations was the beam combiner. The basic angle, between the two viewing directions, had been specified to remain constant to within about 1 milliarcsec during a data set of up to 12 hours duration. It was therefore important to verify whether temperature control anomalies were the cause of rapid variations of the basic angle at the level of the great-circle reduction (see Figure 10.1, and also Volume 3, Chapter 9) observed on a few specific occasions during the mission.

Four thermistors controlled the surroundings of the beam combiner. Their temperature resolution was 0.03 K. It was found that temperature anomalies were indeed associated with significant variations of the basic angle. The characteristics of four such events during the first year of the mission are summarised in Table 12.3.

The basic angle results obtained in the FAST data reductions for the reference great circles around the above anomaly periods were investigated. In the basic data reduction treatment, the geometrical model (see Volume 3, Chapter 9) allowed only a constant value for the basic angle over the duration of one reference great circle. In most

Table 12.3. Payload temperature anomalies found during the interval studied.

year:day:hour	Temp. (K)	Anomaly Report (Appendix B)
1990:089:16	16.3	Payload remote terminal unit telemetry (AR26)
1990:118:11	20.5	On-board computer halted (AR29)
1990:243:14	17.9	Anomalous behaviour of on-board computer (AR38)
1990:322:04	19.0	

Table 12.4. Results for the reference great circle reductions solving for a variable basic angle. The model for the basic angle is $\gamma_0 + \gamma_1(t - t_0) + \gamma_2(t - t_0)^2$ where the times are expressed in days of 1990 (day 1.0 corresponding to 1 January 1990 0h UT). The angles are expressed in mas, mas/day and mas/day^2 (standard errors in parentheses).

t_0 (days)	$\gamma_0 - 58^\circ$ (mas)	γ_1 (mas/day)	γ_2 (mas/day^2)
89.715	31245.5 (0.3)	−3.8 (3.1)	18 (69)
90.121	31246.6 (0.3)	70.4 (1.7)	−452 (27)
90.560	31246.5 (0.4)	−7.0 (3.1)	60 (61)
118.575	31255.5 (0.3)	88.4 (4.1)	−1204 (132)
118.962	31248.3 (0.2)	−9.6 (1.4)	44 (18)
243.743	31249.0 (0.3)	86.8 (2.6)	−616 (40)
244.145	31243.9 (0.3)	−8.2 (1.8)	36 (21)
322.314	31244.7 (0.3)	80.6 (3.0)	−510 (54)
322.696	31242.4 (0.3)	−7.4 (1.3)	4 (15)

cases, during and after the anomaly, deviant values were found. Consequently, the great-circle reduction was repeated for all reference great circles associated with the temperature anomalies, and those immediately after. In these specific reductions, a quadratic variation with time was assumed for the basic angle. Although there was no reason to assume that such a model is particularly well suited to describe the basic angle variations, it had the advantage of being readily available in the software. A cubic model was not attempted because many of the data sets, in particular those during the most significant changes, were shorter than the minimum length required to apply such a model meaningfully. Table 12.4 gives the results obtained.

The basic angle indeed appeared to be responding to the temperature changes following a more-or-less fixed pattern: starting at a value of about 15 mas lower than the currently normal value, it increased quickly to a value above this normal value, and then returned to it much more slowly, on a time scale of about half a day. The rise sometimes seen at the end of the decreasing phase was never really significant, and was presumably an artefact of the quadratic model used to describe an exponential decrease.

In order to verify whether the low values at the start were real, or also due to the quadratic description, two of the reference great circles were reprocessed using only the first 4200 frames (i.e. one rotation plus one basic angle) allowing a constant basic angle and a linear variation with time. The results for these models were compared with those obtained previously, and confirmed the credibility of the initial low values of the basic angle.

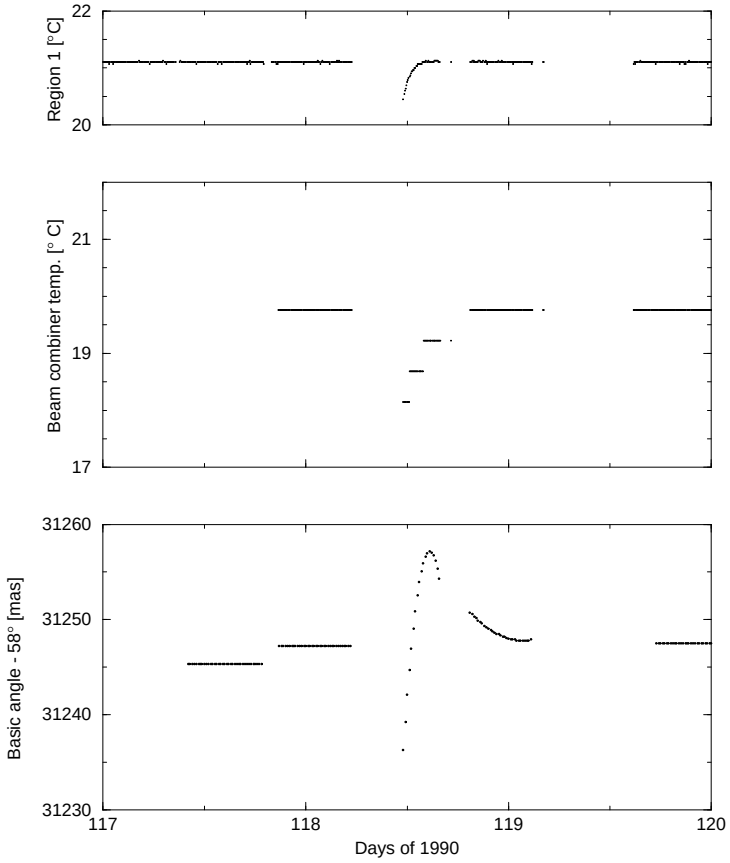

Figure 12.5. *Comparison of the temperature data of controlled region 1 (top), the beam-combiner housekeeping (thermistor) temperature reading (middle), and the basic angle variations arond the epoch 1990:118.*

Discussion

The behaviour of the basic angle during and after thermal control anomalies strongly suggests that two counteracting physical phenomena played a role, each with its own time scale. The first of these phenomena acted so as to decrease the basic angle, and responded (almost) immediately to changes in the temperature of the controlled regions, whereas the other phenomenon tended to increase the basic angle, and its effects were visible on a much longer time scale of about half a day.

It seems feasible that the more rapid effect was connected with the mounting of the beam combiner, and that the slower response was due to the interior of the beam combiner, possibly the glue cementing the two halves. In order to investigate this further, the output of the housekeeping thermistor on the beam combiner was checked. This thermistor was located on the back side of the beam combiner (near its edge) and is thus ‘halfway’ between the controlled regions and the interior. Although the resolution of the output was somewhat low (0.54 K), useful information could nevertheless be obtained.

Temperatures were derived from the telemetry values using the ESOC calibration curves. The temperatures from the thermistors were significantly lower than those of the controlled regions, which could be explained by the fact that the beam combiner radiated to the heat sinks presented by the baffles and open space.

In order to permit a better comparison, the controlled region temperatures, housekeeping thermistor temperature, and basic angle evolution for the two more obvious cases were combined. From this, it was clearly evident that the beam combiner temperature reacted much more slowly after a temperature anomaly (on a timescale of order 10 hours) than the controlled region temperature (on a timescale of 2–3 hours). This seemed to confirm the above hypothesis of a fast and a slower effect combined (see Figure 12.5).

An extra tilt of the beam combiner could explain the decrease in basic angle, but it would also have caused a very significant increase in differential field rotation. No evidence for this was found in the geometrical calibration, so that this explanation does not appear to be valid.

13. ATTITUDE AND ORBIT CONTROL SYSTEM AND PERFORMANCES

The attitude and orbit control system performed two major tasks. During the spin-stabilised phase, it provided a reference for the control of most of the flight-related functions, such as pointing antennas or solar panels, or orienting the apogee boost motor for orbit manoeuvres. During the three-axis stabilised phase, it coped with the most severe attitude requirements imposed by the payload, the attitude constraints being one of the limiting factors for the experimental accuracy demanded. In the framework of these overall tasks, the attitude and orbit control system carried out a variety of specific functions closely linked to the various operational aspects of the mission.

13.1. Functions of the Attitude and Orbit Control System

Spin-Stabilised Phase

During the spin-stabilised phase at the start of the mission, the attitude and orbit control system was involved in the separation of the satellite from the launch vehicle, the apogee boost motor ignition attempts, the perigee raising manoeuvres and sun acquisition. It was designed to provide:

(i) attitude control by maintaining the nutation angle within acceptable limits for all hydrazine propellant fill ratios and an inertia ratio below 1;

(ii) facilities to control the spin rate, employing 5 N hydrazine thrusters;

(iii) attitude information based on data from an Earth/Sun sensor, to allow the satellite attitude to be determined by the ground;

(iv) facilities to control the satellite spin axis by means of the 5 N thrusters;

(v) means to acquire and maintain the satellite east–west geostationary orbital position by means of 5 N hydrazine thrusters (not used in the revised mission);

(vi) means for a complete evacuation of all residual hydrazine propellant at the end of the spin phase;

(vii) back-up facilities to overcome failures, not handled by the ground station, which would lead to loss of the mission.

Three-Axis Stabilised Phase

During the three-axis stabilised phase, the attitude and orbit control system was involved in sun pointing, sensor calibration, scanning law initialisation, and normal operation. It was designed to:

(i) provide a stable sun pointing, by means of sun acquisition sensor data and 20 mN cold-gas thrusters, to enable gyro calibration and star pattern recognition;

(ii) slew the spacecraft rotation axis from the sun-pointing attitude to its position on the nominal scanning law;

(iii) control the satellite attitude, in order to follow the pre-determined scanning law with a maximum error cone semi-angle of 10 arcmin on the spin axis orientation, and a maximum error angle of 10 arcmin around the spin axis;

(iv) estimate the satellite attitude in real time with an accuracy such that the position of the telescope optical axes could be derived with an accuracy of better than 1 arcsec rms (cone semi-angle).

13.2. Equipment Description

The attitude and orbit control subsystem (Figure 13.1) comprised the control law electronics, the control and actuation electronics, the accelerometer package, the Earth/Sun sensor, the sun acquisition sensor, the attitude anomaly detector, the reaction control assembly and the inertial reference unit (the gyro measurement electronics and the gyro package).

Control Law Electronics

The control law electronics was the core of the subsystem. A microprocessor ran the attitude control software and interfaced with the rest of the spacecraft via the on-board data handling bus. Within the attitude and orbit control system, it interfaced with the control and actuation electronics and the gyro measurement electronics. Its main functions were subsystem telecommand and telemetry management, closed-loop attitude control, open-loop attitude manoeuvres, real-time attitude determination and subsystem configuration, and equipment monitoring.

The control law electronics was based on a TI SBP 9989 I^2L 16-bit microprocessor and a memory bank of 16 k PROM and 4 k RAM, with error detection and correction capability (16 bits of data and 6 bits for Hamming code implementation). The unit was internally fully redundant, and main and redundant functions were properly cross-strapped. The main functional blocks were as follows:

(1) telemetry and telecommand electronics: this module performed the on-board data handling bus interface, the acquisition of analogue data, relay status, and telemetry signals from the attitude and orbit control system, timing extraction from on-board data handling bus and distribution to the subsystem, and telecommand handling and distribution to the attitude and orbit control system users;

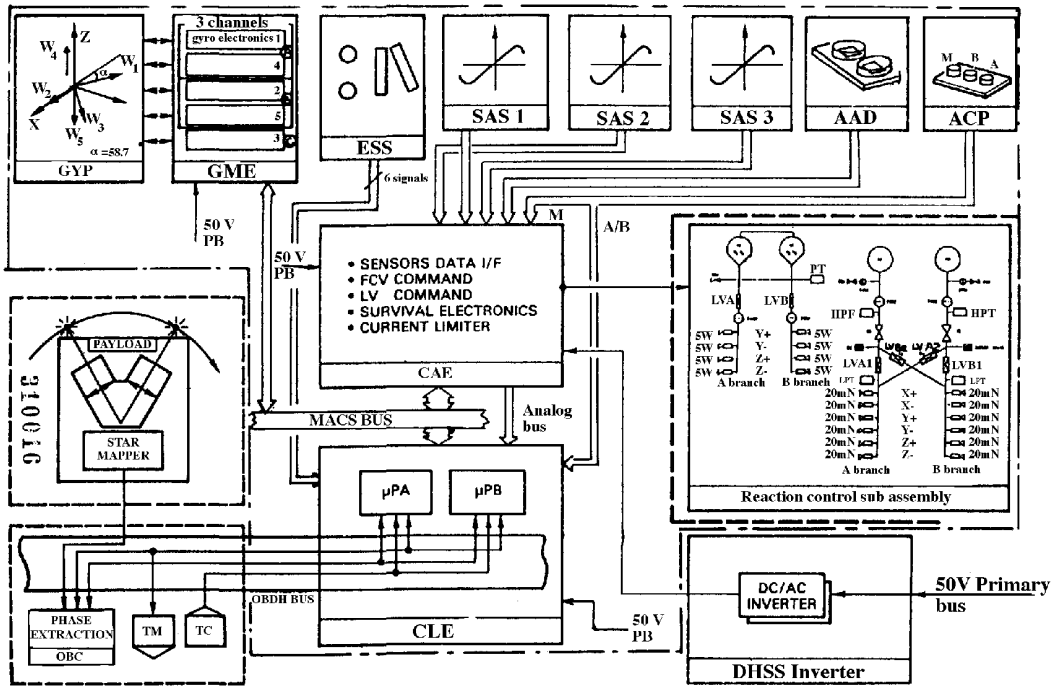

Figure 13.1. *Attitude and orbit control subsystem block diagram, showing the inter-relationship between the various on-board subsystems involved: AAD: attitude anomaly detector; ACP: accelerometer package; CAE: control and actuation electronics; CLE: control law electronics; DHSS: data handling subsytem; ESS: Earth/Sun sensor; GME: gyro mechanism electronics; GYP: gyro package; OBC: on-board computer; SAS: sun acquisition sensor; TM: telemetry; TC: telecommand.*

(2) central processing electronics: the central processing electronics board contained the microprocessor and power supply, the RAM array with error-detection circuitry, the interrupt controller, the memory page decoder, the up clock and general timing functions, the memory-mapped I/O interface, and the central processing electronics extension. The main functions of the central processing electronics extension were to interface with the attitude control system bus, the Earth/Sun sensor, telemetry and telecommand, failure detection, timing and switching, and PROM supply;

(3) the PROM board: the configuration of the board was based on 8 k × 8 PROM chips providing a 16 k × 16 array for the central processing electronics. They were supplied through a switching system providing power only to the addressed chips;

(4) the sensor acquisition electronics: this module performed the analogue-to-digital conversion of the various analogue signals of the subsystem, by means of a front-end operational amplifier array, an analogue multiplexer and a 12-bit analogue-to-digital converter. The result of the conversion could be sent on the modular attitude control system bus, via a dedicated telecom controller and bus driver/receiver. Timing and switching functions, along with interface to internal buses, were also implemented;

(5) switching electronics: this board was the power interface to the relay coils. It was driven by the central processing electronics extension that sent the proper line and column addresses in compliance with the matrix organisation of this board. The relay status acquisition electronics was also implemented;

(6) DC/DC converter: the converter module provided the supply voltages required by the various control law electronics circuits, together with the relevant current limitation monitoring and power management capabilities. The circuit also supplied the Earth/Sun sensor. The electrical power was provided by the 50 V DC main and redundant buses, and primary and secondary power lines were isolated.

Control Actuation Electronics

The control and actuation electronics interfaced with the control law electronics, via the internal bus. Its functions were to condition the outputs of the sun acquisition sensors, the attitude anomaly detector, and the accelerometer package, to drive the reaction control subsystem latch valves, flow control valves, and catalyst bed heaters in response to commands from the control law electronics, to provide sensor power switching, to provide hardwired emergency attitude control modes during on-station operation, overriding the control law electronics, and to provide automatic fault detection and recovery during the spin-stabilised phase, initiating automatic reconfiguration of the control law electronics and reaction control assembly. Furthermore, it performed subsystem initialisation at separation.

The AC/DC converter module provided the proper power supply lines to the box, and it was connected to the data handling subsystem inverter as power source. The galvanic isolation requirement was met by means of shielded transformers connected to the two AC lines. The cross-strapping function was implemented at a secondary level, after the current limitation functions. A dedicated converter section, with serial regulators, was implemented to provide power to the accelerometer package.

The reaction control assembly was supplied directly from the 50 V DC lines through the high-power and pulse-capability current limit circuits, able to deliver to the valve coils the proper current pulse. The ‘failure detection electronics’ was the module in charge of failure detection and hardwired back-up mode management. Due to the failure recovery philosophy adopted, this module was not redundant. It implemented five failure criteria: active nutation damping failure detection, thruster impulse monitoring, and pressure anomaly detection in the spin-stabilised phase, and thruster impulse monitoring and attitude anomaly detection in the three-axis stabilised phase.

Any criterion, if verified, generated a reconfiguration signal that could be overridden by on-ground commands. Each failure detection electronics block was fully independent and was driven by proper enable/disable telecommands, in such a way that at any mission phase a dedicated failure detection strategy could be selected.

Accelerometer Package

The accelerometer package was used as nutation sensor during the spinning phase. It comprised three Sunstrand QA 2000-type accelerometers (A, B, and M) and the relevant conditioning circuitry. The A and B output signals were sent to the control law electronics through sensor acquisition electronics, in order to drive the software-based active nutation damping function. The M output signal was routed to the control and actuation electronics, to be used in the hardware-based active nutation damping failure detection.

Earth/Sun Sensor

The Earth/Sun sensor provided the attitude and spin-rate measurement during the first part of the mission, when the satellite was spin stabilised. It employed the Galileo sensor flown on many telecommunications satellites. The attitude determination was performed by correlating the cross times of the Sun into the two sun slits and measuring the length of the Earth chord, by means of the two infrared telescopes and a timing circuitry in the control law electronics.

Sun Acquisition Sensor

The sun acquisition sensors gave the attitude and orbit control system a rough estimation (1°.6 accuracy) of the sun aspect angle along two axes for sun acquisition purposes, both in the nominal case or for emergency sun reacquisition. Each sensor was made up of 8 photovoltaic cells (4 main, 4 redundant) delivering a current proportional to the cosine of the angle between the sun line and the normal to the cell surface. The actual sensor configuration gave a field of view of more than 2 steradians and the full set of three units gave a spherical coverage around the satellite. The load resistor and the conditioning electronics were in the control and actuation electronics.

Attitude Anomaly Detector

The attitude anomaly detector monitored the satellite attitude in order to avoid the possibility of the sun damaging the solar generator or the payload. The device was based on a solar cell inside a baffling system. In normal conditions (normal mode), the Sun should have stayed at about 43° sun aspect angle. If the sun aspect angle drifted from this value by more than 3°, the sensor would issue a current pulse that would trigger the attitude anomaly detector criterion in the control and actuation electronics failure detection circuitry, commanding a reconfiguration strategy.

13.3. Reaction Control Assembly

The reaction control assembly provided impulses for velocity corrections, for satellite positioning, spin-up and spin-down, and for attitude control. The assembly consisted of two separate, functionally independent sub-assemblies which were used sequentially: a hot-gas reaction control assembly, which used hydrazine (N_2H_4) propellant, and a cold-gas reaction control assembly, which used nitrogen propellant. Each sub-assembly incorporated two redundant and independent functional branches.

Hot-Gas Reaction Control Assembly

The hot-gas reaction control assembly was a conventional monopropellant hydrazine system. The propellant was stored in two identical tanks, which operated in a blow-down pressure mode over a range from 22 to 5.5 bar. The tanks did not contain any positive expulsion devices. The hydrazine was pressurised by gaseous helium. The propellant/pressurant interface required for positive propellant expulsion was maintained

by the centrifugal acceleration produced by the satellite spin. The tank shape was conospherical to maximise expulsion efficiency. Both tanks were fed and pressurised by a single fill and drain valve and a common feed line. The fill and drain valve incorporated a 25 μm filter. Another line linked the pressurant ports.

Four thrusters were required to meet the subsystem attitude control and velocity requirements. Hydrazine was fed through a flow control valve and was chemically decomposed through a catalyst-induced combustion process inside the thrust chamber. The hot gases expanded through a nozzle and produced thrust. Thrust chamber assemblies incorporated electrical heaters, which raised the catalyst temperature to approximately 190 °C, prior to hydrazine injection into the combustion chamber. The thruster branches could be isolated from either tank by latching-type isolation valves.

The thruster assemblies were protected from particulate contamination by one 10 μm filter, located between tanks and isolation valves. In addition, one 10 μm filter was installed in the inlet of each thruster propellant valve, in order to provide increased component protection. A pressure transducer was located immediately downstream of the propellant tanks. Its reading, combined with that of tank temperature sensors, provided information to establish the propellant mass inside the tanks, throughout the hot-gas reaction control assembly life. The propellant feed-lines consist of 6.4 mm outer diameter titanium tubing. Hydrazine tubing, tanks, latching, and flow control valves were insulated and thermally controlled in order to prevent the hydrazine temperature dropping below its freezing point, at approximately 2 °C.

Mechanical connections between feed-lines and thruster valves, latching valves, and pressure transducer, consisted of standard flare-type fittings; all other joints were TiG welded. Every item of equipment had been qualified for previous space programmes.

Cold-Gas Reaction Control Assembly

The cold-gas reaction control assembly was a pressure-regulated system, using gaseous nitrogen propellant. The nitrogen was stored at a maximum pressure of 285 bar in two equally sized tanks. The tanks were not interconnected, and separate fill and vent valves were used in order to pressurise the tanks. These valves incorporated a 5 μm filter. Each tank fed one pressure regulator, which reduced the gas pressure from tank level to an average of 1.5 bar.

Impulse for all manoeuvres was provided by one of two redundant branches of six thrusters each. Gas was fed from the pressure regulators to the two thruster branches through a system of four isolation valves. These latching type valves permitted the isolation of either thruster branch and its feeding by either regulator. During normal operation, only one regulator would be used to provide regulated pressure. A high pressure, 10 μm filter was installed upstream of each pressure regulator. In addition, integral filters were installed in the inlets of the regulators and the propellant valves to provide additional protection. The pressure regulator incorporated a relief valve which prevented over-pressurisation of the low pressure line. Over-pressurisation could occur in two instances: in the case of pressure regulator leakage and/or temperature effects during which the thrusters were not operated, or in the case of pressure regulator failure. In the worst case, the low pressure line could experience pressures similar to those in the high pressure lines.

To vent the resulting mass flow, a so-called 'zero thrust device' (a calibrated T-fitting) was installed near the pressure regulators, so as to minimise the impingement of gas on spacecraft units. In the case of pressure regulator failure, the gas that exited the spacecraft through its vents may have caused disturbance torques in the order of 10^{-3} to 10^{-4} Nm. The high-pressure transducers located in each branch of the sub-assembly and the tank temperature monitors provided the information needed to establish the propellant mass inside the tanks throughout mission life. Low-pressure transducers were included in each half of the sub-assembly, to measure the regulated pressure and monitor regulator operations.

The feed lines consisted of 6.4 mm outer diameter titanium tubing. Mechanical connections were made by TiG welding with the exception of the thruster assemblies, pressure regulators, pressure transducers, and latching valves, which were installed using standard flare-type fittings. Except for the 20 mN thruster, all equipment had been qualified for previous programmes. An extensive qualification programme was performed for the cold-gas thruster.

Operating Modes

The hot-gas reaction control assembly was to have been used at the start of the mission during the transfer orbit, near synchronous orbit, and the initial geostationary orbit operations. In practice the sequence of operations for the revised mission were quite different (see Chapter 4).

The hydrazine thrusters were used to spin up the satellite after separation from the launch vehicle from 7 rpm to 60 rpm in a series of manoeuvres. After this the satellite spin axis was oriented for the apogee boost motor firing. In the course of various attempts to ignite the apogee boost motor, the spacecraft was de-spun from 60 rpm to 30 rpm. During the de-spin manoeuvres, the hydrazine thruster also provided active nutation damping. After all further attempts to ignite the apogee boost motor had ceased, virtually all of the remaining hydrazine was used to increase the perigee height of the transfer orbit in a series of three manoeuvres. The spacecraft was then de-spun to 10 rpm and oriented with its spin-axis pointing at the Sun. A final orbit manoeuvre was performed to synchronise the orbital period with the satellite's rotation period. The residual liquid hydrazine was then expelled from the sub-assembly, in order to avoid mass shifts caused by hydrazine sloshing during nominal operating modes and, thus, to avoid unwanted attitude jitter.

The subsequent control forces were provided by the cold-gas reaction control assembly. The satellite was further despun, reoriented, and stabilised. Emergency manoeuvres during routine operations were also served by the cold-gas reaction control assembly.

A summary of the mission phases, the thrusters used, and the thruster operating modes is presented in Table 13.1.

Assembly Performance

The hot-gas reaction control assembly thrusters provided a nominal thrust of between 2–6 N, depending on the supply pressure. Nominal specific impulse during steady-state operations ranged between 215–225 s. During pulsed mode operation, the specific

Table 13.1. Reaction control assembly mission summary.

Mission Phase	Mode/Manoeuvre	Thruster(s)	Operating Mode	System
Pre ABM Firing	Spin up (to 60 rpm)	$+z$	continuous	hot gas
	Spin axis orientation	$\pm y$	pulsed	„
	Active nutation damping	$\pm y$	pulsed	„
Revised Mission	Spin axis orientation	$\pm y$	pulsed	hot gas
	Active nutation damping	$\pm y$	pulsed	„
	Perigee raising	$\pm x, \pm y$	continuous	„
	Spin adjustment	$\pm z$	pulsed	„
	Despin (60 to 10 rpm)	$-z$	continuous	„
	Orbit period adjustment	$\pm x, \pm y$	continuous	„
	Hydrazine expulsion	$\pm y, \pm z$	continuous, pulsed	„
	Final despin (10 to 0 rpm)	$-z$	continuous	cold gas
	Attitude acquisition	$\pm x, \pm y, \pm z$	continuous	„
	Nominal mode	$\pm x, \pm y, \pm z$	pulsed	„
	Attitude reacquisition	$\pm x, \pm y$	continuous	„

impulse dropped to ranges varying from 180–220 s to 85–110 s, depending on the duration of the pulse.

The cold-gas reaction control assembly thrusters provided a nominal steady-state thrust in the range 5–28 mN, depending on supply pressure and environmental conditions. Specific impulse during steady-state operations was 66 s or higher, and during pulse-mode between 60–70 s, depending on pulse duration.

Mass Budget

The reaction control assembly total dry mass, i.e. excluding propellant and pressurant, was about 29 kg. Usable hydrazine propellant mass was 32 kg. Residual, unusable hydrazine and pressurant mass amounted together to 0.65 kg. Usable nitrogen mass was 9.4 kg, the residual mass in tanks at the end of the operative mission being about 0.4 kg.

13.4. Inertial Reference Unit

Gyros provided continuous three-axis rate and incremental attitude data during final despin and the three-axis stabilised mission phases. The gyro package (see Figure 13.2) consisted of five inertial class rate-integrating gyros, gyros 1 and 3 aligned midway between the $\mp x$ and $+y$ axes respectively, gyro 2 along the $+x$ axis, and gyros 4 and 5 along the $\pm z$ axes respectively. The adopted configuration was optimised for adequate redundancy and to minimise disturbance torques. The rate and attitude information was provided by the gyro measurement electronics to the control law electronics, via the internal attitude and orbit control system bus.

The inertial reference unit was the satellite measurement device for attitude and angular rates during commissioning and normal mode phases. The output of this unit, together with star mapper data, were processed by the control law electronics software. In nominal operating mode the results influenced the output of the scientific mission; therefore, the inertial reference unit performances were of extreme importance for the satellite. The inertial reference unit of Hipparcos was a direct derivation from the one flying on the French Earth observation satellite SPOT. With the progressive failure of the gyroscopes, these functions were ultimately fully transferred to the spacecraft/payload, where the star mapper readings provided very high accuracy attitude sensing, albeit at a low frequency.

Based on a SAGEM GYPSE gyrometer, the inertial reference unit was split physically into two boxes, gyro package and gyro measurement electronics, and functionally into five measurement chains organised into three independent channels. The gyro package contained the gyrometers with their mechanical support, thermal insulation, and the thermal control electronics; the gyro measurement electronics contained the inertial reference unit power supply DC/DC converter (from 50V DC bus), the switching electronics, the telemetry and telecommand, and the modular attitude control system bus interface, the spin motor power supply, the pick-off supply, the rebalance loop, the clock and general timing function, and the so-called angular rate digital integrator that senses the current flowing in the rebalance loop and converts it into a pulse train at a frequency proportional to the angular rate seen on the input axis of the relevant gyrometer; with a proper accumulator register read at a fixed time, it was possible to obtain the required information on attitude and angular rate.

The main measurement characteristics of the inertial reference unit were: angular resolution 0.032 arcsec in fine mode, and 0.26 arcsec in coarse mode; a full scale of $0^{\circ}\!.125\ s^{-1}$ in fine mode and $0^{\circ}\!.83\ s^{-1}$ in coarse mode, and a constant drift of less than 2° per hour.

As a consequence of the revised mission orbit, the performance of the gyros in the high radiation environment to which the satellite was exposed started to degrade shortly after the launch.

13.5. Gyro Performances

The first gyro problems were traced back to November 1989 when increasing noise on gyro 4 (z axis) was observed. By mid 1990, the gyro deteriorated to the point where it had to be taken out of the control loop and replaced by the redundant one (gyro 5). Gyro 5 soon developed the same problems as gyro 4. In July 1992, it deteriorated to the point of affecting the spacecraft attitude and had to be taken out of the control loop. The new two-gyro software was then implemented (see Chapter 15). In September 1992 both gyro 2 and 5 showed anomalous behaviour. At the end of the month gyro 1 had several spin-downs and broke completely two weeks later, and was replaced by gyro 3. In December 1992 gyro 2 showed large spikes, breaking down in March 1993. An overview of the gyro performance during the mission is shown in Figure 13.3. A summary of the behaviour of the various gyros is given hereafter.

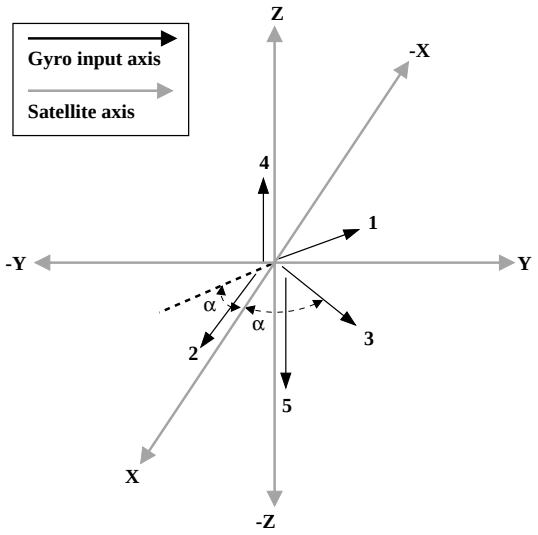

Figure 13.2. *The configuration of the five on-board gyros, illustrating the relationship between the gyro input axes and the satellite axes.*

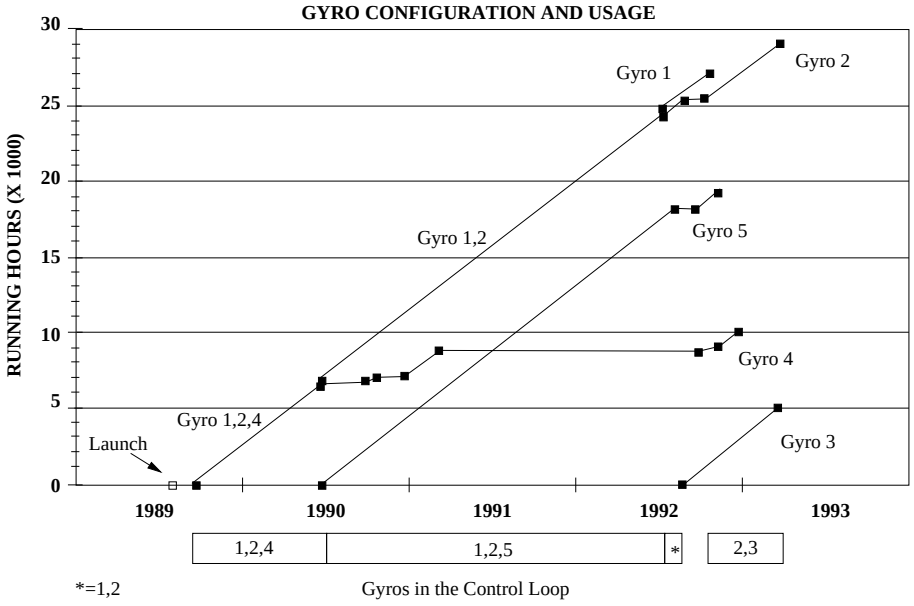

Figure 13.3. *The combination of gyros used at different stages of the mission. The bottom panel summarises which gyroscopes were operational during the mission. The upper panel indicates the cumulative running hours for each of the gyros. The two-gyro operations started towards the end of 1992.*

Gyro 1

July 92: Gyro 1 drift began to change erratically affecting real-time attitude determination performance.

92-09-25: The output of the gyro changed rapidly several times.

92-09-27: The output of the gyro again changed rapidly several times.

92-10-11: The gyro output went suddenly to zero. Several attempts were made to get the gyro working again, but with no success; finally the gyro was switched off. From that time, the gyro was used only for increasing the gyro measurement electronics box temperature as no real output could be obtained.

Gyro 2

92-08-11: The gyro was switched off by an automatic re-configuration order caused by an emergency sun reacquisition. The gyro was switched back on, but it developed the first spikes in the output and had to be switched off.

92-10-03: The gyro was switched off by an automatic re-configuration order caused by an emergency sun reacquisition. On the same day the gyro was switched on again, but there were several commanding problems due to the low gyro mechanical electronics box temperature; soon after the spikes in the output reappeared.

92-10-15: The gyro was switched off by an automatic re-configuration order caused by an emergency sun reacquisition. On the same day the gyro was switched on again, but soon after the spikes in the output reappeared. The same had to be repeated again later the same day due to a second emergency sun reacquisition.

92-10-27: The gyro output was tested via the gyro 2/5 de-multiplexing patch; this modification allowed the suppression of the output of gyro 2, gyro 5 or both.

92-10-13: The gyro output developed several spikes, but it recovered after the switch-off of gyro 5.

92-12-22: The spikes on the output of the gyro became severe enough to cause a loss of real-time attitude determination convergence outside perigee.

Gyro 3

91-07-28: During a regular gyro destorage, the gyro heater did not operate. The heater did not operate throughout the rest of the mission.

91-09-27: A test was conducted on the gyro to see if it would operate correctly at a lower temperature.

92-08-13: The gyro was switched on to replace gyro 2.

92-10-27: The gyro was switched off to allow the testing of gyros 2 and 5; it was turned back on at the end of the test.

Gyro 4

November 89: First noise on the gyro was observed.

90-06-26: The gyro output presented large variations for the first time.

90-06-29: The gyro was switched off and replaced by gyro 5.

90-10-18: A week long gyro destorage was started, where the gyro was left running outside the control loop.

90-11-15: During a normal gyro destorage, the output variations re-appeared several times.

90-12-20: During a normal destorage, the output did not change from zero and it took three attempts to finally get a correct spin rate. The gyro was then left on, but not in the control loop.

From 91-01-12 to 91-02-26: Occasional changes in the gyro spin rate caused the real-time attitude determination loop to diverge although it was not in the control loop.

91-03-01: The gyro was finally switched off.

92-10-04: Due to the problem with gyros 2 and 5, the gyro was switched on to get a correct spin-rate estimate. Then the gyro was switched off.

92-10-11: The gyro was again switched on.

92-10-27: The gyro was switched off.

92-11-13: The gyro was switched on to replace gyro 5 after an emergency sun reacquisition.

From 92-11-26 to 92-11-29: Gyro output variations were observed.

92-12-22: The gyro was finally switched off. On the same day, an emergency sun reacquisition occurred; the gyro was again switched on to increase the gyro mechanical electronics box temperature, but the output stayed at zero. After the temperature had stabilised, the gyro was switched off. From this day on, the gyro was used only for increasing the gyro mechanical electronics box temperature as no real output could be obtained.

Gyro 5

90-06-29: The gyro was switched on to replace gyro 4.

92-03: Deterioration on gyro 5 started to have a noticeable impact on overall real-time attitude determination performance.

92-07-03: The first large spikes occurred, causing the divergence of the on-board real-time attitude determination loop.

92-07-10: The gyro was taken out of the control loop but left on and was replaced by the two-gyro real-time attitude determination patch.

92-08-04: The gyro was switched off by an automatic reconfiguration order caused by an emergency sun reacquisition. The gyro was switched back on and large spikes were observed on its output.

92-08-08: Gyro 5 recovered sufficiently to return to three-gyro operations.

92-08-11: Scanning law acquisition manoeuvre return to 43° nominal scanning law. Glitches on gyro 5 output caused an emergency sun reacquisition. The spacecraft was then spun up and the gyro left off. From this day on, the gyro was not used again for the actual control of the satellite.

92-08-14: The gyro was switched on for a test and was then switched off again.

92-10-02: The gyro was switched on after an emergency sun reacquisition.

92-10-03: The gyro was switched off by an automatic reconfiguration order caused by an emergency sun reacquisition. On the same day, the gyro was switched on again but there were several commanding problems due to the low gyro mechanical electronics box temperature.

92-10-15: The gyro was switched off by an automatic reconfiguration order caused by an emergency sun reacquisition. On the same day, the gyro was switched on again with the same commanding problem experienced a few days earlier. It happened again later the same day due to a second emergency sun reacquisition.

92-10-27: The gyro output was tested via the gyro 2/5 de-multiplexing patch.

92-11-13: The gyro noise increased and the output indicated a spin-down to a level equal to 60 per cent of the nominal rate. After a check carried out with the star mapper output, the gyro was switched off.

92-12-22: After emergency sun reacquisition occurred the gyro was switched on to increase the gyro mechanical electronics box temperature, but the output stayed at zero. The gyro was left on, although the output had been disabled via the gyro 2/5 de-multiplexing patch and it was only being used to increase the gyro mechanical electronics box temperature.

Gyro Drift

Studies showed that on short timescales, gyro drifts were sensitive to long eclipses which gave rise to thermoelastic effects. During eclipses, the variation in drift for a thirty minute eclipse was approximately 10^{-7} arcsec s^{-1}. The estimated gyro drift over longer timescales (from the beginning of the mission) is illustrated in Figure 13.4. The larger discontinuities coincide with on-board gyro reconfigurations, since different operational gyros gave rise to different biases. The cause of the smaller variations was investigated. Thermal effects were believed to be the cause of this behaviour.

13.6. Gyro Related Ground Investigations

Ultimately the successive failures of the gyros was to lead to the complete redefinition of the on-board and on-ground real-time attitude determination systems using firstly two and then no gyros in the control loop (see Chapters 15 and 16 respectively). Before or in parallel with this development, a series of less drastic measures were taken to minimise the risk to the spacecraft of maintaining three-gyro operations.

Ground Procedures and Software Changes

In February 1991, while both gyro 4 and gyro 5 were switched on (with gyro 5 in the control loop), the specialised real-time attitude monitor software at ESOC was enhanced to perform limit checking on both gyros and to raise an alarm should the operational one go out of limits. The spacecraft controller would then have been able to swap the failing gyro out of the control loop before significant deviations from the nominal scanning law could accumulate, possibly leading to an autonomous triggering of the emergency sun reacquisition manoeuvre. This software was made largely redundant after gyro 4 was

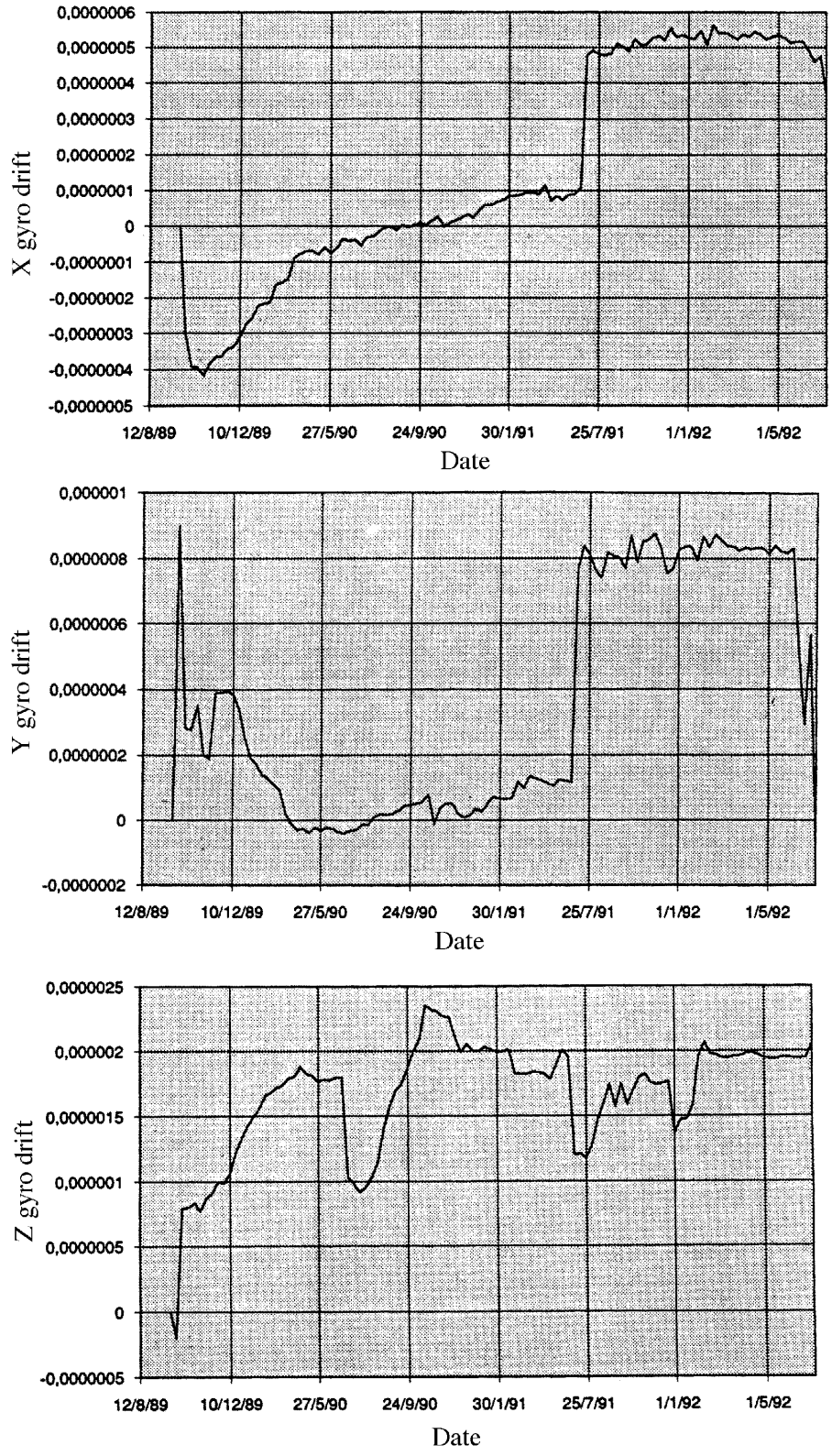

Figure 13.4. *Drifts for the x, y and z gyros (top to bottom), as estimated by the on-board real-time attitude determination system. The drifts are given in the on-board units of radians per AOCS cycle (16/15 s). The discontinuity in the drifts in July 1991 is associated with the upgrade of the orientation matrix for the gyros. The discontinuity in the z gyro drift in June 1990 is due to the change from gyro 4 to gyro 5.*

switched off and the monitoring of the gyro 5 output was achieved via the gyro 5 filter on-board software patch, described below.

In March 1992, in response to increased noise on gyro 5 having a detrimental effect on the real-time attitude determination performance, it was believed that any changes to the gyro drifts around perigee was most likely due to biased corrections by the real-time attitude determination (see Chapter 14). Therefore the ground procedures were changed to allow the resetting of the on-board drift estimates as soon as possible after perigee to the last values observed before perigee. Subsequent careful monitoring for drift evolution was then performed throughout the orbit to ensure that the best drift estimates were maintained.

Gyro 5 Filter On-Board Patch

Matra Marconi Space, as spacecraft prime contractor, were responsible for the development of a series of on-board software patches.

This patch was designed to reject all gyro 5 pre-processed outputs that were outside a given window (for example $168.^{\circ}75\ \mathrm{hr}^{-1} \pm 10^{\circ}$). In case a bad value was detected (outside the ground defined window) it was then replaced by the previous value. This patch became practically obsolete when the frequency of occurrence of bad values increased.

Gyro 2/5 De-Multiplexing On-Board Patch

Gyro 2 and 5 were part of the same inertial reference unit channel. It appeared that their output were at times swapped causing erroneous performance by the real-time attitude determination. A modification was then designed so that the software gave the option to read only one gyro output. This software became obsolete when the gyro electronic problem worsened and mechanical problems appeared.

Other Satellite Missions

In the case of Hipparcos the failures of the gyroscopes were characterised by high output noise, high amplitude output spikes, repeated spin-rate anomalies, followed (except for one out of five gyroscope systems) by a final spin-down. The thermal control of the remaining gyroscope system failed and its output was severely degraded.

Hipparcos was not the only mission to be affected in an adverse manner by failure of the gyroscope systems. Three of the four gyroscope systems on board the German satellite ROSAT showed output transients whose polarity was correlated with the immediately preceding angular manoeuvre. Two gyroscope systems exhibited apparent spin-rate anomalies, leading to final spin-down for one of them. However, similar gyroscope systems flying on other European satellites showed very few in-orbit anomalies.

An inter-agency ‘gyroscope systems working group’, maintained by ESA, CNES (F), DARA (D), and DRA (UK) from 1992 until mid-1993, conducted systematic investigations of Hipparcos and ROSAT flight data through contracts placed with gyroscope manufacturers. These investigations were later supported by the Laboratoire de Recherches Balistiques et Aérodynamiques (F). A general conclusion reached by all parties to the

investigation was that the primary source of all the failures lay in the electronics of the gyroscope system and not in its electro-mechanical gyroscope unit.

The in-orbit failures of the Hipparcos satellite were investigated by Matra Marconi Space, who integrated the inertial reference unit and supplied most of the gyroscope electronics, and SAGEM (F), the gyroscope manufacturer. All anomalous behaviour and failures of the gyroscope systems could be explained in terms of radiation-induced degradation of electronic components. This was deduced from the abnormal orbit flown and the time which elapsed before the most serious failures were observed, about three years after launch, after the nominal lifetime had expired.

Causes of failure were traced to the spin motor supply circuitry, while other failures were thought to have most probably originated in sensitive electronic interfaces. Anomalies occurring in the ROSAT satellite were investigated by GEC-Ferrari (UK). These concluded that the most probable cause of failure was the electronic circuitry supplying the spin motor, although other electronic failures were also noted. The recommendations for improving gyroscope systems, resulting from this inquiry, were passed to ESA projects and industry.

13.7. Gas Consumption

The cold-gas mass (M_{cg}) in the tanks was calculated as follows:

$$M_{cg} = \frac{PV}{zrT} \qquad [13.1]$$

where P is the tank pressure (Pa), V is the tank volume (m^3), z is the compressibility factor for nitrogen, T the temperature (K) and r a constant. The evolution of the cold gas, since October 1989, is shown in Figure 13.5. By May 1992 tank 1 was almost empty, with only 0.6 kg remaining. Tank 2 still had 4 kg out of the original 5.07 kg.

The average consumption was 0.15 kg per month. The consumption followed a linear law. Extrapolating that law predicted an attitude and control ability until after 1994, well beyond the final termination of satellite operations in August 1993.

13.8. Normal Mode Controller

The primary output from the on-board real-time attitude determination system (see Chapter 14) were the estimated angular deviations from the nominal scanning law (error angles) and their rates of change (error rates). These error angles and error rates were combined within the 'normal mode' control software to produce error signals. When an error signal exceeded the preset threshold level, thruster firings were commanded on all three axes. The lengths of the pulses were determined as a function of the angles, rates and a preset estimate of the disturbance torque.

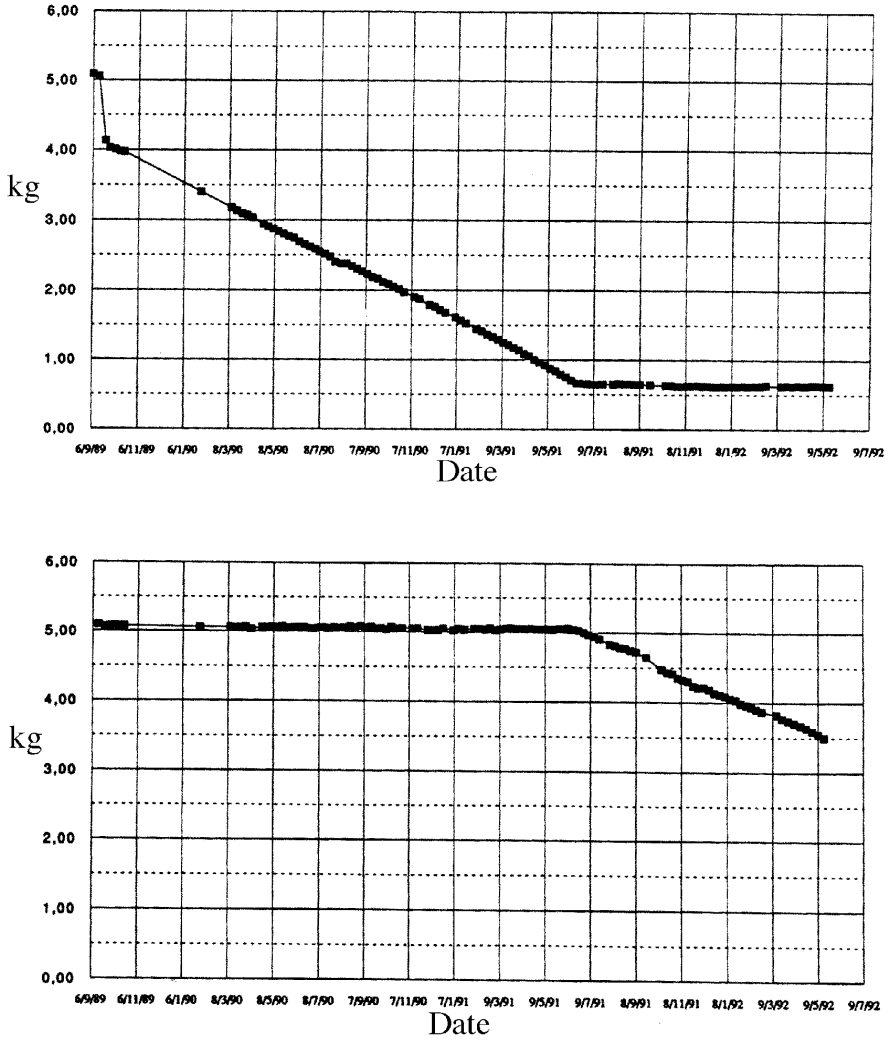

Figure 13.5. *Hipparcos cold gas consumption: (a) tank 1 and (b) tank 2.*

On-board Disturbance Torque Modelling

The disturbance torque estimates were based on the assumption that the satellite would operate from a geostationary orbit. Therefore the on-board disturbance torque model was designed to give a first-order estimate only, based on the expected predominant torques, i.e. a constant torque arising from the moments of the spinning gyros, and a periodic torque arising from radiation pressure. In practice, other torques such as gravity gradient, magnetic torques, and atmospheric drag (near to perigee) played a very significant role at lower altitudes resulting in modifications to the normal mode control around perigee.

The radiation pressure torque varied according to the geometric surfaces of the spacecraft which were exposed to sun-light. Consequently, the torques around the spacecraft x and y axes had a periodicity equal to that of the spacecraft rotation rate (2 hours 8 min). Due to the approximate 120° rotational symmetry of the spacecraft about the z axis, the radiation pressure torque around the z axis had a periodicity of 1/3 of the spacecraft rotation period. It was sufficient for the normal mode control to assume a sinusoidal model for the radiation pressure torque.

The orbital oscillator parameters, $S_v(k)$, $C_v(k)$, described in Chapter 8, were used to model the phase angle of the periodic torques around the x and y axes. For the z axis, a further two phase angle parameters were required. Recalling that $S_v(k)$ and $C_v(k)$ are the sine and cosine of phase angle $\Omega_d t_k$ respectively, it was possible to model the disturbance torques around the z axis using a phase angle of $3\Omega_d t_k$. Therefore the on-board computer was capable of evaluating:

$$S_{v3}(k) = \sin(3\Omega_d t_k) \qquad [13.2]$$
$$C_{v3}(k) = \cos(3\Omega_d t_k)$$

by addition and multiplication only, using the standard trigonometrical expansions of $\sin(3\theta) = \sin((\theta + \theta) + \theta)$ (similarly for cosine).

On-board Algorithm

The following variables (updated every $\frac{16}{15}$ s) were input from other areas of the control software:

$\phi(k)$, $\theta(k)$, $\psi(k)$: x, y and z error angles from real-time attitude determination (see Chapter 14).

$\dot{\phi}(k)$, $\dot{\theta}(k)$, $\dot{\psi}(k)$: x, y and z error rates from real-time attitude determination.

$S_v(k)$, $C_v(k)$, $S_{v3}(k)$, $C_{v3}(k)$: Orbital oscillator outputs (see Chapter 8 and above).

The following on-board constants were used:

K_x, K_y, K_z: X, Y and Z rate gains

μ_x, μ_y, μ_z: X, Y and Z thresholds

A_x, A_y, A_z: coefficients of ϕ_k, θ_k, ψ_k

B_x, B_y, B_z: coefficients of T_x, T_y, T_z

C_x, C_y, C_z: coefficients of $\dot{\phi}_k$, $\dot{\theta}_k$, $\dot{\psi}_k$

T_{xc}, T_{yc}, T_{zc}: constant disturbance torque estimates

T_{xss}, T_{yss}, T_{zss}: disturbance torque sine coefficients

T_{xsc}, T_{ysc}, T_{zsc}: disturbance torque cosine coefficients

Defining additionally:

ϵ_x, ϵ_y, ϵ_z: error signals

T_x, T_y, T_z: external disturbance torque estimates

$t_{\mathrm{on},x}$, $t_{\mathrm{on},y}$, $t_{\mathrm{on},z}$: calculated on-times

the error signals were given by:

$$\epsilon_x = \phi_k + K_x \dot{\phi}_k$$
$$\epsilon_y = \theta_k + K_y \dot{\theta}_k \qquad [13.3]$$
$$\epsilon_z = \psi_k + K_z \dot{\psi}_k$$

The thruster on-time calculation was only performed if an error ϵ exceeded in magnitude its corresponding threshold μ.

(i) Disturbance torque estimates:

$$\begin{aligned} T_x &= 2\ T_{xc} + T_{xss}\ S_v(k)\ T_{xsc}\ C_v(k) \\ T_y &= 2\ T_{yc} + T_{yss}\ S_v(k)\ T_{ysc}\ C_v(k) \\ T_z &= 2\ T_{zc} + T_{zss}\ S_{v3}(k)\ T_{zsc}\ C_{v3}(k) \end{aligned} \qquad [13.4]$$

(ii) On-time calculation:

$$\begin{aligned} t_{\mathrm{on},x} &= A_x\ \phi_k + B_x\ T_x + C_x\ \dot{\phi}_k \\ t_{\mathrm{on},y} &= A_y\ \theta_k + B_y\ T_y + C_y\ \dot{\theta}_k \\ t_{\mathrm{on},z} &= A_z\ \psi_k + B_z\ T_z + C_z\ \dot{\psi}_k \end{aligned} \qquad [13.5]$$

At the start of the mission, an upper limit of 500 ms and a lower limit of 50 ms was imposed on any calculated on-time.

Ground Disturbance Torque Calibration

The disturbance torque coefficients T_{xc}, T_{yc}, T_{zc}, T_{xss}, T_{yss}, T_{zss}, T_{xsc}, T_{ysc} and T_{zsc} were regularly calibrated on ground and uplinked at the same time as the orbital oscillator coefficients. The torque estimation was performed by fitting sine curves to the measured angular accelerations derived from gyro data. In the course of the mission, this ground based calibration was enhanced to include gravity gradient torques, thereby allowing accurate calibrations to be performed over more of the orbit. Ultimately, this disturbance torque estimation procedure underwent significant modification for the two-gyro operations (Chapter 15).

Perigee Control

As mentioned above, the disturbance torques around perigee were arising from other effects such as gravity gradient and atmospheric drag. Consequently, the disturbance torque model was redundant in this region and the on-times had to be much greater to combat the torques encountered. A different set of on-time coefficients were set on-board before each perigee passage. In particular, the coefficients B_x, B_y, B_z were set to zero and the values of C_x, C_y, C_z were increased.

13.9. Thruster Monitoring and Normal Mode Software Patch

At the start of the mission, particular attention was paid to fuel consumption around perigee, since the mission lifetime could have been decided on cold-gas consumption. Early in 1990, the on-ground real-time attitude monitoring software was modified to give extra thruster performance monitoring. As a result of this and other studies, the altitude at which the switch from normal mode to perigee mode control occurred was optimised to minimise ‘double-sided’ firings. Such double-sided firing occurred when the perigee control software commanded too large an actuation causing a rapid change in error signal from one error threshold to the other. This was indicative of inefficient control. However, the perigee control parameters could not readily be made weaker since they would have to command long enough actuations to avoid continuous and

inaccurate control at closest perigee approach. Another aspect of both the normal and perigee control software was the coupling of actuations around all three axes. Although less efficient in fuel consumption, this coupling was effected to allow longer periods of science observations without the jitter caused by an actuation.

However, as the data reduction consortia began to process the science data it was noticed within their own on-ground attitude reconstitution, that the small actuations around the z axis which were being commanded because the x and y error signals were hitting the threshold were very often entirely superfluous, wasting fuel and hindering the derivation of accurate scan-rate measurements.

Subsequently, Matra Marconi Space were commissioned to produce an on-board attitude and control software patch called the 'z thrusters de-coupling and accumulator patch', consisting of two different modifications to the normal mode controller. The first change compared the computed z thruster on-times with a given threshold, and if this was not exceeded, no firing was actually performed. The second modification accumulated all z thruster on-times and compared them with another threshold; when the given value was exceeded, the software inhibited the z normal mode control (no further firings allowed). This was to avoid excessive z-thrust (spin-up/spin-down of the spacecraft) in case of a z-gyro failure. As this could possibly have occurred outside ground station contact, it avoided the possibility of a significant loss of propellant as a result of a single failure. Both thresholds could be modified and reset via ground commands. The hardwired on-board safety protection had been disabled because of the nature of the orbit.

13.10. Disturbance Torques

The third attitude and control software modification developed by Matra Marconi Space, the 'spy' patch, allowed the storage of N words (16 bits) each cycle of the attitude and control software memory. These data were stored in a random access memory (RAM) area specified by a low and a high limit. This could be dumped using the normal attitude and control software dump routine. The patch had been primarily developed to gather data around the non-visibility periods (perigee) in order to obtain more information about the torques acting on the spacecraft causing attitude divergences almost every perigee. The nature of the disturbance torques is discussed fully in Volume 3, Chapter 8.

13.11. Real-Time Attitude Determination

The definition of the revised mission and the subsequent performance of the attitude and orbit control system hardware had a profound effect on the performance of the on-board real-time attitude determination system as well as the ground real-time attitude determination system used for initialisation of the on-board system. In particular, the failures of the gyros led to major re-design work being required on both systems. The three gyro systems, upgrades and re-design for two- and zero-gyro operations are described fully in Chapter 14 (three gyros), Chapter 15 (two gyros) and Chapter 16 (no gyros).

14. REAL-TIME ATTITUDE DETERMINATION WITH THREE GYROS

This chapter describes the details of the attitude determination and control using the nominal three-gyro configuration. In acquiring the scanning law—a procedure which would have been required just once in the nominal geostationary scenario, but which had to be repeated many hundreds of times throughout the revised mission (attitude knowledge was lost during perigee passages and during periods of high star mapper background levels)—a series of procedures had to be followed: initial star transit recognition, star pattern matching, and precise attitude determination. Since the procedures had to be used repeatedly, considerable effort went into their optimisation.

14.1. Introduction and Overall Concept

The spacecraft was constrained to rotate once every 2 hours 8 min about its principal spin axis, and this spin axis precessed about a 43° half-cone centred on the Sun. This motion was called the nominal scanning law, and was defined in a heliotropic reference frame (see Chapter 8 for details). The heliotropic attitude angle Ω was defined with respect to an initial heliotropic angle Ω_0, which was not known before the initial star pattern recognition. The actual orientation of the satellite (x, y, z frame) with respect to the predefined nominal scanning law (X, Y, Z frame) was described using the Tait-Bryan error angles ϕ, θ, ψ shown in Figure 14.1.

In practice, the spacecraft was allowed to deviate from the nominal scanning law by up to 500 arcsec, before being corrected by the cold-gas thrusters (approximately every 10 min). This ‘normal mode’ control is described in more detail in Chapter 13.

Since the image dissector tube could only sample one star at a time, the instantaneous field of view was controlled by the on-board computer to track the programme stars for short intervals, switching rapidly from one to the other. The computer had to be able to calculate the expected position of a star on the grid at any given time. Excessive memory would have been required to hold the entire catalogue on-board permanently and to calculate the expected times. Instead a memory buffer of transit times (the programme star file, described in detail in Chapter 8) for the next 30 min of observations was maintained and regularly refreshed by ground command. The transit times were

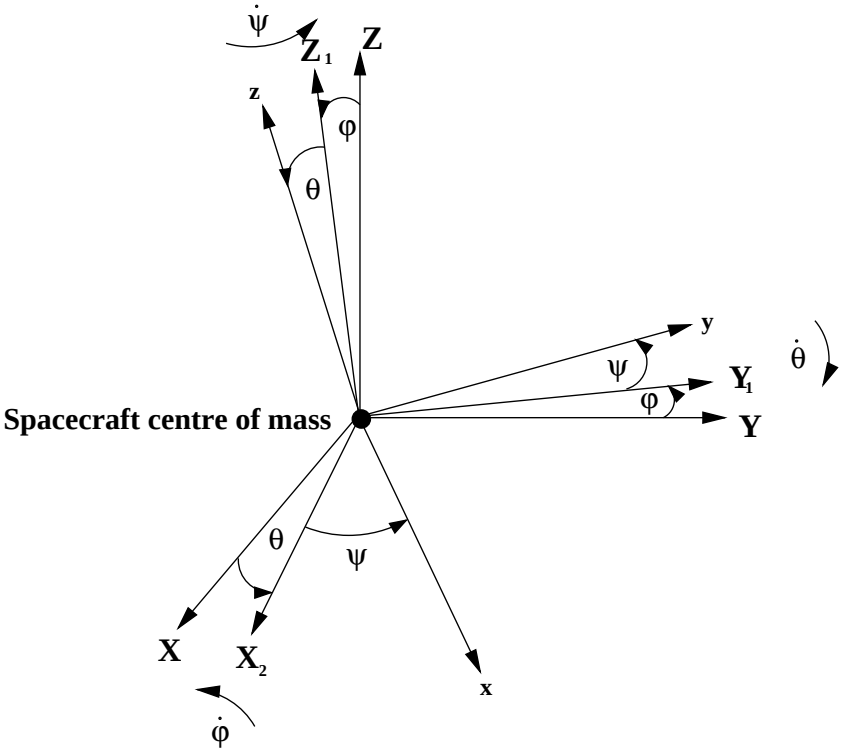

Figure 14.1. *Tait-Bryan error angles of the spacecraft frame (x, y, z) relative to the nominal scanning law frame (X, Y, Z).*

calculated in advance on ground at ESOC, assuming that the spacecraft was perfectly following the nominal scanning law.

The on-board computer therefore required detailed knowledge of the attitude, both for spacecraft control and for image dissector tube piloting. This was achieved through on-board software called the real-time attitude determination system, which received inputs from three operational rate-integrating gyros every 1.066 . . . s. The gyro data, after pre-processing, allowed the determination of the rotation rates about the three principal orthogonal axes of the spacecraft. Real-time attitude determination was able to integrate these measurements, taking into account knowledge of the thruster firing times to predict the attitude at any time. This alone however did not provide sufficient accuracy for the image dissector tube piloting. The gyros themselves were subject to biases (known as gyro drifts) in their rate estimation which led to a steadily increasing error in the attitude determination. The real-time attitude determination was capable of compensating for these gyro drifts assuming they were accurately determined. In practice, these drifts varied with time due to thermal distortion from the external environment and 'random walk' effects. The only way for real-time attitude determination to calibrate the drifts was to use a second independent data source.

This source came from the measurements of the stars across the star mapper grid, consisting of two sets of four aperiodically spaced slits (see Chapter 2). One set was vertical with respect to the scanning direction, the other arranged in a ±45° chevron (see Figure 2.10). The errors between the expected and measured transit times of the stars across these two sets of slits were used, via Kalman filter techniques on-board, to refine the attitude determination to approximately 1 arcsec accuracy. The modulated

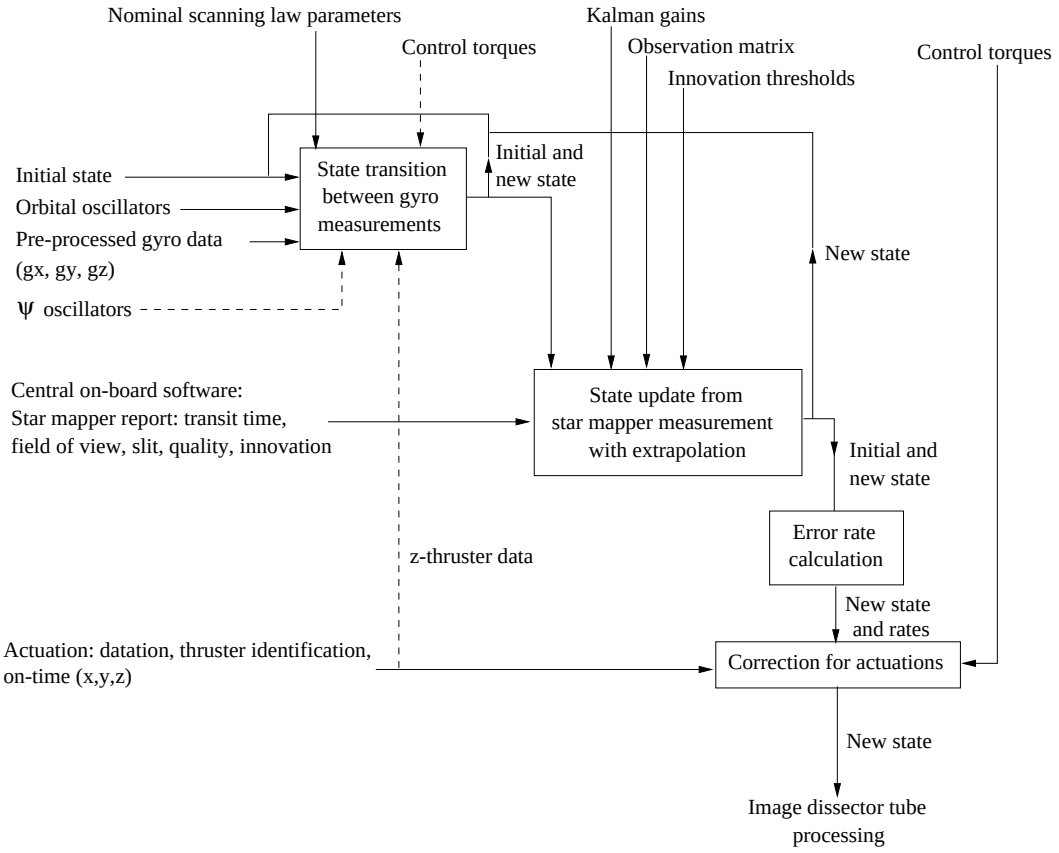

Figure 14.2. *The interconnection of on-board tasks related to the real-time attitude determination using gyros. The dashed lines indicate the additional input required for the implementation of the two-gyro attitude control described in Chapter 15.*

light from the star mapper grid was sampled by two photomultiplier tubes operating in two different spectral bands.

Each set of four slits was separated in a 1:3:2 ratio. Thus when starlight crossed the four slits, a distinctive pattern was discerned by the on-board software, which filtered the raw data assuming an ideal single-slit response profile. The resulting modulated signal was characterised by one main lobe and several side lobes. The height and width of these lobes were checked against various accuracy criteria before being passed to real-time attitude determination for use in determining the attitude. Such tests included determining the height of the main lobe against the value expected for a star of that brightness.

The various elements of real-time attitude determination are shown in Figure 1.5, and the interconnection of on-board tasks related to the real-time attitude determination using gyros is illustrated in Figure 14.2.

When a star had been successfully identified in one or other of the fields of view, the transit time was measured by the position of the main lobe in the filtered data. By comparison with the expected transit time as given in the programme star file, a measurement of the attitude error was derived using a Kalman filter. In this filter, under three-gyro control, six values were estimated: three angles which defined the error

between the current spacecraft attitude and the nominal scanning law (the Tait-Bryan error angles), and three gyro drifts converted into rates along the principal spacecraft axes.

As a result of tuning since the start of the mission involving ESOC, Matra Marconi Space and the scientific consortia, the real-time attitude determination system was capable of working to an accuracy of 1 to 2 arcsec in attitude determination if stars were being successfully identified in the star mapper processing. However, if errors had built up to over 10 arcsec, star measurements could no longer be used by real-time attitude determination, which diverged from the real attitude. This happened after 50 per cent of all perigee passes, where higher disturbance torques and noise in the star mapper signal (caused by van Allen belt radiation) made divergence more likely.

As a protection against falsely identified stars, the attitude determination on board normally rejected any star transit times which showed that the spacecraft attitude relative to the nominal scanning law had drifted by more than 10 arcsec since the last star transit was processed by real-time attitude determination. During normal operations this was not expected to happen, because the gyro drifts were accurate to less than 5 milliarcsec s^{-1} and real-time attitude determination received star transit data every 10 s on average.

Should anomolous conditions cause such an error to build up, it was possible to increase this 10 arcsec limit ('narrow window') to 30 arcsec ('extended window') to allow real-time attitude determination to use these larger transit time errors to update its attitude knowledge. If the errors were greater than 30 arcsec, then intervention was required from ground, because the on-board software was no longer capable of processing the correct buffer of raw star mapper data for stars to be detected. A suite of programs called the ground real-time attitude determination system was developed and used at ESOC for this purpose. This software was designed to process on-ground all star mapper data and estimate the attitude independently of any real-time attitude determination results.

14.2. On-board Real-Time Attitude Determination using Three Gyros

On-board real-time attitude determination involved estimating in real-time a state vector consisting of:

- ϕ: Tait-Bryan error angle around the spacecraft x-axis;
- θ: Tait-Bryan error angle around the spacecraft y-axis;
- ψ: Tait-Bryan error angle around the spacecraft z-axis;
- d_x: gyro drift around the spacecraft x-axis;
- d_y: gyro drift around the spacecraft y-axis;
- d_z: gyro drift around the spacecraft z-axis.

Data from three gyros gave angular velocities (spacecraft body rates) about all three axes. This allowed a complete prediction of the attitude from one processing cycle (16/15 s) to another, assuming the previous attitude estimate was correct. Small corrections to these predictions were made by comparing expected and measured star mapper crossing times.

Real-Time Attitude Determination Definitions

The following variables were input to the real-time attitude determination algorithm:

$G_x(k+1)$, $G_y(k+1)$, $G_z(k+1)$: angular measurements currently available from the gyro data cyclic acquisition software.

t_d: star detection time derived from the on-board star mapper processing.

R: star angular measurement derived from the on-board star mapper processing.

(ϵ, f): star mapper slit identifier of the detected star:
- $\epsilon = 0$: vertical slit
- $\epsilon = -1$: inclined slit, upper half of field of view
- $\epsilon = +1$: inclined slit, lower half of field of view
- $f = +1$: preceding field of view
- $f = -1$: following field of view

IQ: star quality:
- IQ = 1 for a quality 1 star (more accurate on-ground position, typically better than 0.4 arcsec)
- IQ = 2 for a quality 2 star (less accurate on-ground position, typically in the range 0.4–0.8 arcsec)

T: time of real-time attitude determination estimate (multiple of the real-time attitude determination cycle time t_i).

$S_v(k)$, $C_v(k)$: sine and cosine values produced by the orbital oscillator, but corresponding to the previous time interval (see Chapter 8).

$t_{on,x}$, $t_{on,y}$, $t_{on,z}$: the X, Y, and Z cold-gas thruster on-times provided by the nominal mode control algorithm (see Chapter 13).

Ω_T: transverse rate defined by Equation 8.10.

Ω_N: estimate of the absolute Z-axis nominal scanning law spin rate provided by the on-board computer.

The following on-board constants were used:

t_i: the cycle time (16/15 s) between inputs from the inertial reference unit.

KG_1 (6,6): the 6×6 matrix of fixed gains associated with quality 1 stars.

KG_2 (6,6): the 6×6 matrix of fixed gains associated with quality 2 stars.

One column of KG_1 or KG_2 was used in a star mapper update of the real-time attitude determination filter estimate. The column used was determined by the slit identifier as follows:
- column 1: $(\epsilon, f) = (0, 1)$
- column 2: $(\epsilon, f) = (-1, 1)$
- column 3: $(\epsilon, f) = (1, 1)$

– column 4: $(\epsilon, f) = (0, -1)$
– column 5: $(\epsilon, f) = (-1, -1)$
– column 6: $(\epsilon, f) = (1, -1)$

The rows corresponded to the six components of the filter state vector:

$$V = \begin{pmatrix} \phi(k+1) \\ \theta(k+1) \\ \psi(k+1) \\ d_x(k+1) \\ d_y(k+1) \\ d_z(k+1) \end{pmatrix} \quad [14.1]$$

where $d_x(k+1)$, $d_y(k+1)$, $d_z(k+1)$ were the current estimates of the gyro drifts.

H (6,6): star mapper observation matrix. The row used in a star mapper update was determined by the slit identifier (exactly as for the column of KG_1). The columns corresponded to the six components of the filter state.

T_{ax}, T_{ay}, T_{az}: control torques applied about the spacecraft x, y and z axes.

I_{xx}, I_{yy}, I_{zz}: principal moments of inertia about the x, y and z axes.

μ: innovation threshold for narrow and extended windows.

Defining additionally:

$\omega_X(k)$, $\omega_Y(k)$, $\omega_Z(k)$: angular rates with respect to inertial space expressed in scanning law X, Y and Z axes and relating to the previous time interval.

$d_x(k+1)$, $d_y(k+1)$, $d_z(k+1)$: current estimates of drift rates about the spacecraft x, y, and z axes.

R_I: the innovation to be used in the filter star update, i.e. the difference between the extrapolated star mapper measurement and the linear approximation of the star mapper measurement using the present real-time attitude determination attitude estimates.

The following outputs were obtained:

$\phi(k+1)$, $\theta(k+1)$, $\psi(k+1)$: current estimates of attitude error angles.

$\dot{\phi}(k+1)$, $\dot{\theta}(k+1)$, $\dot{\psi}(k+1)$: current estimates of attitude error rates.

$\phi_m(k+1)$, $\theta_m(k+1)$, $\psi_m(k+1)$: modified (predicted) estimates of attitude error angles around actuation.

$\dot{\phi}_m(k+1)$, $\dot{\theta}_m(k+1)$, $\dot{\psi}_m(k+1)$: modified (predicted) estimates of attitude error rates around actuation.

Three-Gyro Real-Time Attitude Determination Algorithm

At each sampling interval the real-time attitude determination produced estimates of the Tait-Bryan angles and their derivatives from the output of the gyro data cyclic acquisition software (see Figure 14.2).

The first step was the calculation of the nominal scanning law rates about the theoretical X and Y axes using the output of the orbital oscillator:

$$\begin{aligned} \omega_X(k) &= \Omega_T \; S_v(k) \\ \omega_Y(k) &= \Omega_T \; C_v(k) \\ \omega_Z(k) &= \Omega_N \end{aligned} \qquad [14.2]$$

where $\Omega_T = 168^\circ\!.75 \text{ hr}^{-1}$, and $\Omega_T = \Omega_p \sin\xi$ with $\xi = 43^\circ$ (see Chapter 8 on the orbital oscillator and its scheduling). The estimates of the Tait-Bryan angles were then calculated according to the matrix estimate equation:

$$\begin{pmatrix} \phi(k+1) \\ \theta(k+1) \\ \psi(k+1) \\ d_x(k+1) \\ d_y(k+1) \\ d_z(k+1) \end{pmatrix} = \begin{pmatrix} 1 & \omega_z t_i & 0 & -t_i & 0 & 0 \\ -\omega_z t_i & 1 & 0 & 0 & -t_i & 0 \\ 0 & 0 & 1 & 0 & 0 & -t_i \\ 0 & 0 & 0 & 1 & 0 & 0 \\ 0 & 0 & 0 & 0 & 1 & 0 \\ 0 & 0 & 0 & 0 & 0 & 1 \end{pmatrix} \begin{pmatrix} \phi(k) \\ \theta(k) \\ \psi(k) \\ d_x(k) \\ d_y(k) \\ d_z(k) \end{pmatrix}$$
$$+ \begin{pmatrix} G_x(k+1) - \omega_X(k)\; t_i - G_y(k+1)\; \psi(k) \\ G_y(k+1) - \omega_Y(k)\; t_i + G_x(k+1)\; \psi(k) \\ G_z(k+1) - \omega_Z(k)\; t_i - G_x(k+1)\; \theta(k) \\ 0 \\ 0 \\ 0 \end{pmatrix} \qquad [14.3]$$

Finally, estimates of the first derivatives of the Tait-Bryan angles were calculated by:

$$\begin{aligned} \dot{\phi}(k+1) &= (\phi(k+1) - \phi(k))/t_i \\ \dot{\theta}(k+1) &= (\theta(k+1) - \theta(k))/t_i \\ \dot{\psi}(k+1) &= (\psi(k+1) - \psi(k))/t_i \end{aligned} \qquad [14.4]$$

When star information was available from the on-board computer it was used to update the gyro-based estimates of the Tait-Bryan angles and their derivatives. As a result of the necessary processing time, there was a delay between the detection time and the time the star information was available in the real-time attitude determination. Therefore, the star measurement was extrapolated to make it consistent with the time of the most recent gyro measurement. This extrapolation was a function of the change in $\phi(k+1)$, $\theta(k+1)$ and $\psi(k+1)$ over the relevant time interval:

$$\begin{aligned} R_E = R &+ H(*,1)\; \dot{\phi}(k+1)\; (T - t_d) \\ &+ H(*,2)\; \dot{\theta}(k+1)\; (T - t_d) \\ &+ H(*,3)\; \dot{\psi}(k+1)\; (T - t_d) \end{aligned} \qquad [14.5]$$

where the $*$ represents the relevant row of the observation matrix as determined by the slit identifier. If the extrapolation procedure had been invalidated by a thruster actuation, the star information was ignored. When this was not the case the difference between the extrapolated star measurement and its linear approximation was given by:

$$R_I = R_E - (H(*,1)\; \phi(k+1) + H(*,2)\; \theta(k+1) + H(*,3)\; \psi(k+1)) \qquad [14.6]$$

If this innovation was less than the innovation threshold μ, the Tait-Bryan angles together with the estimates of the gyro drift were updated according to the filtering equation:

$$\begin{aligned}
\phi(k+1) &= \phi(k+1) + \mathrm{KG}_1(1,*)\ R_I \\
\theta(k+1) &= \theta(k+1) + \mathrm{KG}_1(2,*)\ R_I \\
\psi(k+1) &= \psi(k+1) + \mathrm{KG}_1(3,*)\ R_I \\
d_x(k+1) &= d_x(k+1) + \mathrm{KG}_1(4,*)\ R_I \\
d_y(k+1) &= d_y(k+1) + \mathrm{KG}_1(5,*)\ R_I \\
d_z(k+1) &= d_z(k+1) + \mathrm{KG}_1(6,*)\ R_I
\end{aligned} \qquad [14.7]$$

If the innovation was greater than the innovation threshold the star information was ignored. In Equation 14.7 the update is associated with a quality 1 star. For a quality 2 star KG_1 was replaced by KG_2 in the above equations.

Additional Attitude Prediction in the Case of Actuation

The output of the real-time attitude determination was used in the attitude and orbit control system control loop and in the pointing of the image dissector tube beam. As the normal pointing of the image dissector tube beam used information two time cycles out of date, an additional attitude prediction was necessary around a thruster actuation to prevent the situation where the image dissector tube beam was pointed without accounting for the thruster firing.

The real-time attitude determination outputs corresponding to the observation frame $(k+1)$ preceding the actuation, and to the observation frame $(k+2)$ including the actuation were extrapolated from the nominal real-time attitude determination estimates according to equations of the form:

$$\begin{aligned}
\dot{\phi}_m(k+2) &= \dot{\phi}_m(k+1) = f(\dot{\phi}(k+1),\ t_{\mathrm{on},x},\ T_{ax},\ I_{xx}) \\
\dot{\theta}_m(k+2) &= \dot{\theta}_m(k+1) = f(\dot{\theta}(k+1),\ t_{\mathrm{on},y},\ T_{ay},\ I_{yy}) \\
\dot{\psi}_m(k+2) &= \dot{\psi}_m(k+1) = f(\dot{\psi}(k+1),\ t_{\mathrm{on},z},\ T_{az},\ I_{zz})
\end{aligned} \qquad [14.8]$$

and:

$$\begin{aligned}
\phi_m(k+2) &= \phi_m(k+1) = g(\phi(k+1),\ \dot{\phi}(k+1),\ \dot{\phi}_m(k+1),\ t_{\mathrm{on},x},\ t_i,\ T_{ax},\ I_{xx}) \\
\theta_m(k+2) &= \theta_m(k+1) = g(\theta(k+1),\ \dot{\theta}(k+1),\ \dot{\theta}_m(k+1),\ t_{\mathrm{on},y},\ t_i,\ T_{ay},\ I_{yy}) \\
\psi_m(k+2) &= \psi_m(k+1) = g(\psi(k+1),\ \dot{\psi}(k+1),\ \dot{\psi}_m(k+1),\ t_{\mathrm{on},z},\ t_i,\ T_{az},\ I_{zz})
\end{aligned} \qquad [14.9]$$

Modified Attitude Prediction

If during a given cycle k, the scanning law control determined that an actuation was necessary this actuation was synchronised with the observation frame cycle $(k+1)$. The real-time attitude determination outputs corresponding to cycle k preceding the actuation and to cycle $(k+1)$ including the actuation were extrapolated from real-time attitude determination estimates and from applied thruster on-times. The real-time attitude determination outputs corresponding to cycle $(k+2)$ following the actuation were then nominal again.

For cycle k, preceding the actuation, real-time attitude determination outputs were given by:

$$\begin{aligned}
\dot{\phi}_m(k) &= \dot{\phi}(k) + T_{ax} t_{\mathrm{on},x} \\
\dot{\theta}_m(k) &= \dot{\theta}(k) + T_{ay} t_{\mathrm{on},y} \\
\dot{\psi}_m(k) &= \dot{\psi}(k) + T_{az} t_{\mathrm{on},z} \\
\phi_m(k) &= \phi(k) - \tfrac{1}{2} T_{ax} t_{\mathrm{on},x}^2 - T_{ax} t_{\mathrm{on},x} t_i \\
\theta_m(k) &= \theta(k) - \tfrac{1}{2} T_{ay} t_{\mathrm{on},y}^2 - T_{ay} t_{\mathrm{on},y} t_i \\
\psi_m(k) &= \psi(k) - \tfrac{1}{2} T_{az} t_{\mathrm{on},z}^2 - T_{az} t_{\mathrm{on},z} t_i
\end{aligned} \qquad [14.10]$$

For cycle $(k+1)$, including the actuation, real-time attitude determination outputs were given by:

$$\begin{aligned}
\dot{\phi}_m(k+1) &= \dot{\phi}(k+1) + T_{ax} t_{\mathrm{on},x} \\
\dot{\theta}_m(k+1) &= \dot{\theta}(k+1) + T_{ay} t_{\mathrm{on},y} \\
\dot{\psi}_m(k+1) &= \dot{\psi}(k+1) + T_{az} t_{\mathrm{on},z} \\
\phi_m(k+1) &= \phi(k+1) - \tfrac{1}{2} T_{ax} t_{\mathrm{on},x}^2 \\
\theta_m(k+1) &= \theta(k+1) - \tfrac{1}{2} T_{ay} t_{\mathrm{on},y}^2 \\
\psi_m(k+1) &= \psi(k+1) - \tfrac{1}{2} T_{az} t_{\mathrm{on},z}^2
\end{aligned} \qquad [14.11]$$

The modified estimates were computed only for on-board computer acquisition purposes. They were never used in the nominal attitude prediction.

14.3. On-Ground Real-Time Attitude Determination

The initial on-ground attitude initialisation could be split into two distinct phases:

Initial Star Pattern Recognition: This phase generated off-line pairings between observed star transits and star identifications from a catalogue, identifying both the slit system crossed and the field of view of observation. This allowed the initial attitude of the scanning law to be determined, and provided initialisation for the next phase of the attitude determination.

The on-ground initial star pattern recognition was divided into five stages, each of which passed its output data as input to the next stage. These stages were:

(a) telemetry pre-processing and star mapper filtering;
(b) slit distinction and gyro correction;
(c) field of view separation;
(d) star pattern matching against a star catalogue;
(e) initialisation of the nominal scanning law.

All of the above steps were necessary if Ω_0 was unknown (as it was at the start of the mission). Generally however, under three-gyro control, attitude drifts after perigee were less than 100 arcsec. Therefore in general, ESOC maintained a constant value of Ω_0 throughout the routine (three-gyro) phase of the mission. The only times when it was deemed necessary to change Ω_0 during this period were during a small number of contingencies where the spacecraft assumed a non-nominal spin rate for a significant period of time. In order to re-acquire attitude control, ESOC had the choice of options, either to perform a large firing of the cold gas thrusters to slew the spacecraft around its

principal rotation axis thereby re-acquiring the previous nominal scanning law attitude, or to calibrate the value of Ω_0 for the current phase and calculate a new programme star file. In all cases where the drift around the rotation axis was more than one or two degrees, the second option was faster to implement, safer and less expensive in fuel. This implied that in those cases where Ω_0 was known, only the first two stages up to 'slit distinction and gyro correction' needed to be taken before moving on to precise attitude determination.

Precise Attitude Determination: This activity paired, in close to real-time, observed star transits and star identifications from the operational catalogue, identifying the slit system crossed, whether the upper or lower half of the chevron slit system was crossed, and the field of view of observation. This information was used to generate a precise attitude in near real-time and to estimate the gyro drifts. Linear extrapolation was used to predict the spacecraft attitude at a precise time (approximately 25 s in the future) and the attitude along with the gyro drifts were uplinked to the spacecraft to be received on-board at precisely the time at which the attitude was valid. This uplink allowed initialisation of the on-board real-time attitude determination.

The precise attitude determination was divided into four distinct stages, each of which passed its output data as input to the next stage. These stages were:

(a) star pattern monitoring;
(b) fine attitude estimation;
(c) basic angle calibration;
(d) initialisation of the on-board real-time attitude determination.

The basic angle calibration was a subsidiary task, only used at the start of the mission and thereafter infrequently. The other stages were all critical to real-time attitude determination initialisation.

Telemetry Pre-processing and Star Mapper Filtering

This stage of the initial star pattern recognition involved the collection of both star mapper and attitude and orbit control system telemetry data, together with processing of the star mapper data. This was a time-critical task which ran throughout the attitude determination. The raw data from the satellite telemetry were received as telemetry 'bundles'. Each bundle contained 0.666... s of raw telemetry data equivalent to 16 telemetry formats (1 format = 41.666... ms). Data from the on-board attitude and orbit control system required by tasks in the attitude initialisation chain were extracted and made available to all tasks.

The star mapper samples for both the B_T and the V_T channels were also extracted and placed in a circular buffer. Every raw star mapper sample in the V_T channel was tested against a threshold (usually corresponding to $V_T = 9$ mag). This threshold was adaptive to reflect changes in the background noise level, for example as experienced as the spacecraft passed through the van Allan radiation belts. A sample exceeding this threshold could be from a peak from a star crossing one of the slits (vertical or inclined). Therefore a window of data around this sample was correlated with a four-peaked matching filter function which corresponded approximately to the expected signal from a bright star. The uneven spacing of each slit system (and also of the matching filter function) gave one correlation peak with distinct determinable side lobe peaks for a valid star transit.

A transit was identified if a correlation peak was found with the same time datation in both the B_T and the V_T channels. The height and location of the peaks allowed a transit time and approximate B_T and V_T magnitudes to be determined, which were passed to the next task in the initialisation chain. It was of course possible to have peaks from more than one transit after correlation. In this case each transit was identified by the algorithm except where there was interference between main peaks and side lobes of other peaks.

Figure 14.3 shows the star mapper data for the V_T channel contained in a 0.666... s bundle of raw telemetry data. The crossing by a bright star of one of the slit systems is clearly seen and would have been detected by the correlation process. Figure 14.4 also shows the star mapper data for the V_T channel contained in a 0.666... s bundle of raw telemetry data. The solitary large spike would have exceeded the raw threshold thus triggering the star mapper filtering. However in this case no peaks would have been detected after correlation. Figure 14.5 shows similar data for the B_T channel in which multiple transits can be seen.

Slit Distinction and Gyro Correction

The transit data from the filtering process described above did not contain entirely accurate information, since the correlation function was not optimal for a given transit crossing for the following reasons: (i) the exact focus of the telescopes was not known at the start of the mission; (ii) the filter was matched to the nominal rotation rate of the satellite, so that deviations from the nominal rate would smear the response; (iii) the star mapper photometric performance and slit characteristics were different for the vertical slits and the inclined slits. There was no *a priori* information about the slit system crossed and hence a correlation function had to be used for an 'average' slit performance.

The first two error sources led to a magnitude bias while the third led to a bias between the magnitude calculated by a star transit of the vertical slit system and the magnitude calculated by a transit of the same star through the inclined slit system. Successive transits of the same star image across the vertical and inclined slit systems were separated by between 0.3 and 7.2 s (see Figure 2.10). A star crossing the centre of the star mapper slit system would transit the second slit systems 7.2 s after it transited the first whereas this time separation was 0.3 s for one crossing at the extremes of the star mapper. The slit distinction algorithm attempted to 'pair' transits separated by no more than 7.2 s by comparison of their magnitudes. Two transits occurring within 7.2 s of each other were paired if their B_T and V_T magnitudes and colour ($B_T - V_T$) were equal within certain tolerances; these tolerances being set to take account of the errors referred to above. Each member of the pair was then tested separately to ensure that it could not form part of any other pair. Any pairs containing a transit that could belong to more than one pair were discarded and their data were not used by following tasks.

This process led to approximately 40 per cent of transits being discarded. Real-time slit distinction was not possible: on receipt of data from a bright star transit crossing the first slit system at most 7.2 s delay could occur before data were received from the second slit crossing. Besides, following 'pairing' of two transits a further delay of 7.2 s after reception of the second transit of the pair was needed to ensure that the pairing was unique. Once a successful pairing had been found a revised magnitude estimate could be formed by taking the arithmetic mean of the two magnitudes of the two transits

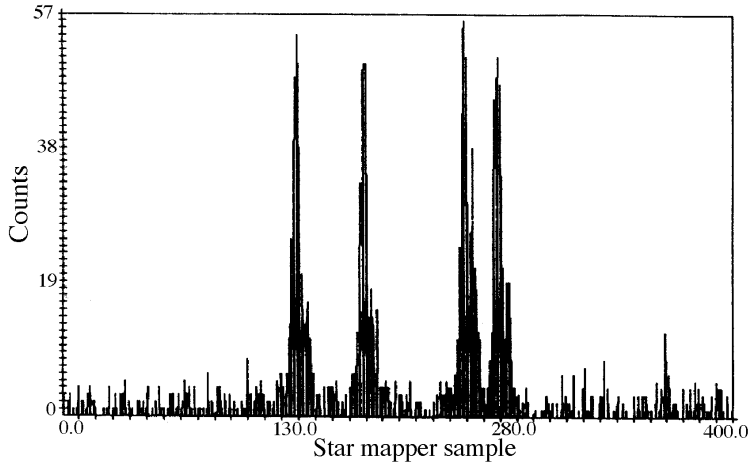

Figure 14.3. *A typical bright star crossing the four slits of the star mapper, as sampled in the V_T channel in a 0.666 . . . s 'bundle' of raw telemetry.*

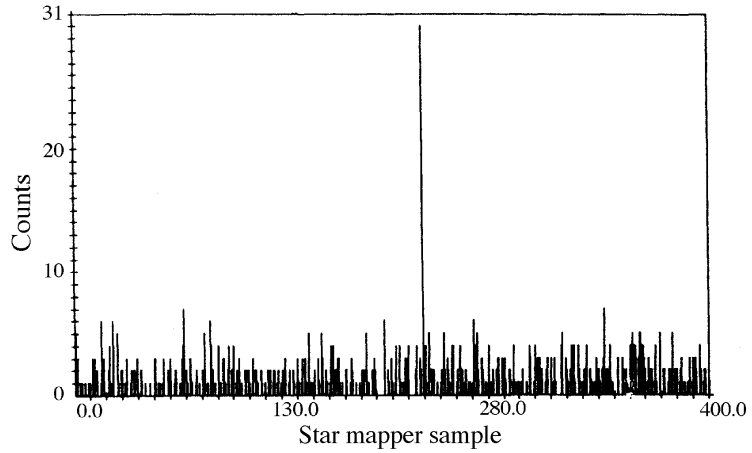

Figure 14.4. *Star mapper data (V_T channel) showing the occasional appearance of solitary noise spikes in the star mapper telemetry. Such an outlier would trigger star mapper filtering, but would not result in a false star transit being detected.*

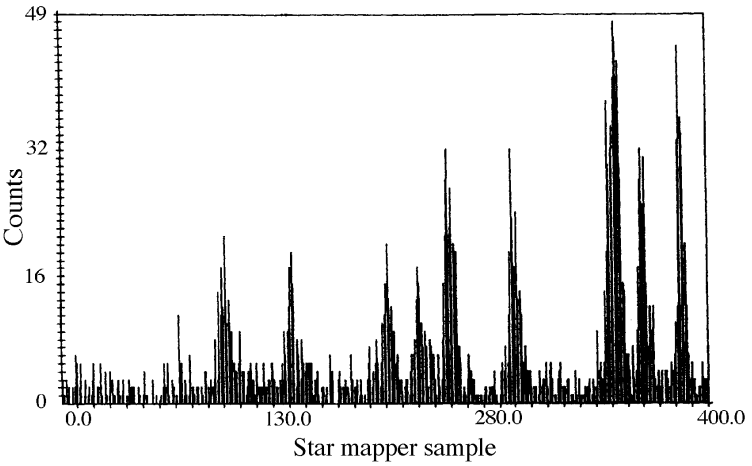

Figure 14.5. *A typical example of several stars crossing the different star mapper slits (B_T channel) at nearly the same time. The ground real-time attitude determination system could, in almost all cases, separate the multiple star transits without confusion.*

forming the pair. As later tasks wanted to match transits between fields of view and with a star catalogue a map from a vertical crossing to a phase round a great circle was performed. This map could be improved if variations in the spacecraft scan rate as detected by the on-board z-gyro were used to give a corrected vertical slit crossing time. This correction was performed at this stage by accessing the attitude and orbital control system gyro data stored by the telemetry pre-processing.

Field of View Separation

As explained above, this stage was only necessary if Ω_0 was completely unknown.

The two fields of view of the payload scanned approximately the same strip of sky with a phase difference equal to the basic angle. In practice the following field of view did not exactly scan the same strip of the celestial sphere as the preceding field of view, although there was generally sufficient overlap to match patterns of stars observed in the two fields of view.

Data from the slit distinction algorithm were collected over a time interval of around 1 hour. The data thus collected were used to construct two fields of equal duration whose start times were separated by the minimum time over which the basic angle could be scanned—about 20 min. These were called field 1 and field 2.

A succession of time offsets were added to the gyro corrected transit times in field 1. These time offsets were such that: (i) each offset was within a predefined tolerance around the nominal time taken to rotate through the basic angle; (ii) after adding the time offset to the transit times in field 1 at least one transit in field 1 had exactly the same time associated with it as a transit time in field 2. All such time offsets were considered.

For each offset a count was made of the number of transits that 'aligned', i.e. whose transit times, magnitude and colour were equal within specific tolerances. For alignment counts above a predefined threshold of 5 a residual was calculated which was equal to the root of the mean sum of squares of the time separations between aligned transits.

For all time offsets which produced an alignment count greater than 70 per cent of the maximum count, that which resulted in the lowest residual was selected as the best offset and the transits from field 2 which were matched were taken as an identified pattern of stars from the following field of view only.

In practice the field of view separation algorithm proved itself to be both robust and accurate, even though it was not essential to have error-free results at that stage. As a by-product of the field of view separation the average scan rate over the basic angle was calculated.

Star Pattern Matching Against a Star Catalogue

As explained above, this stage was only necessary if Ω_0 was completely unknown.

The transits identified by the field of view separation algorithm as being in the following field of view were used as input to the star pattern matching algorithm. This task attempted to identify these transits by matching with stars from a 360° catalogue strip. The pole of this strip was given by the predicted z-axis of the satellite, corresponding to

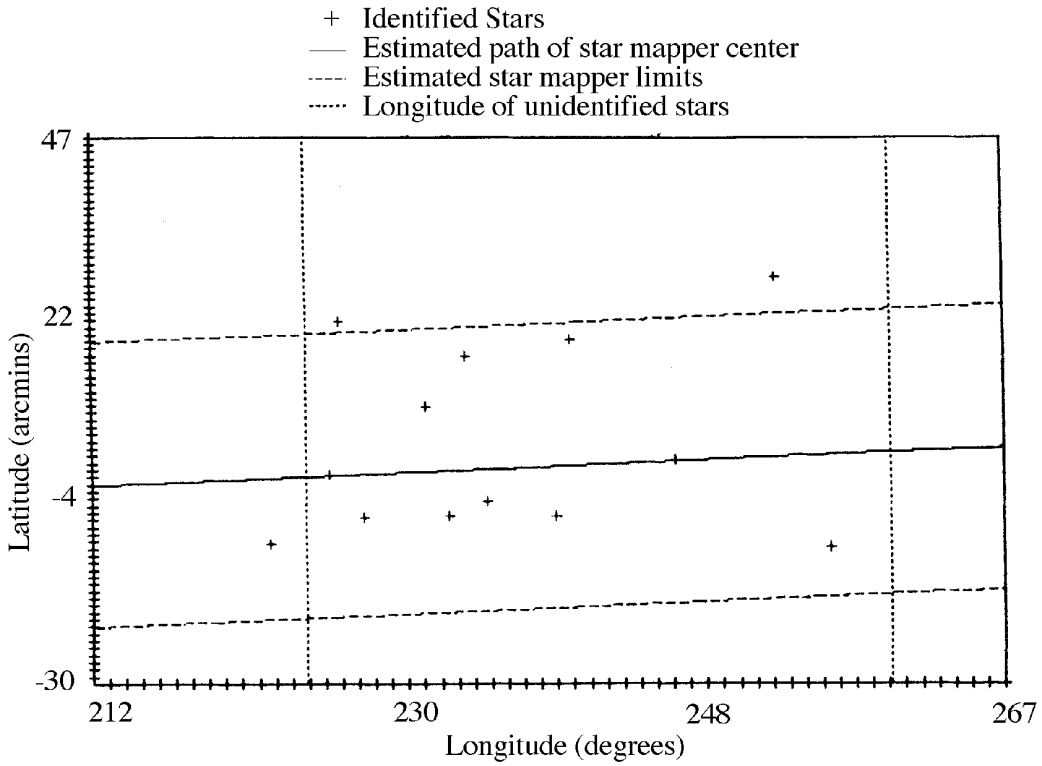

Figure 14.6. *An example of graphical output from the ground real-time attitude determination star pattern matching facility. Star transits were paired, where possible, with stars in the star catalogue strip (see text for details). Longitude and latitude were measured with respect to the pole of the star catalogue strip. Successfully identified stars are denoted by crosses. Unidentified stars are denoted by vertical 'longitude' lines.*

the nominal scanning law Z-axis. It was found in practice that a maximum strip width of 2° was needed for the algorithm.

The gyro corrected vertical transit times were mapped onto a great circle using the rotation rate estimate derived from the field of view separation results.

A similar technique to that used in field of view separation was then applied to match the pattern of star transits with a star catalogue strip covering the possible scanned band of the celestial sphere. To avoid possible confusion within the algorithm stars of similar magnitude separated by less than 2 arcsec along the strip were removed before matching was attempted. All valid offset angles between 0 and 360° were considered and the best offset determined using the same criteria as defined for field of view separation.

Because this matching was CPU-intensive the processing was performed on a fast off-line machine, with input data transfer through a high-speed computer link. The algorithm was demonstrated to be accurate in operations, coping with any possible 'missing' stars in both the catalogue and the set of transits. To give the user confidence in the match given by the algorithm the location of the identified stars along the strip were plotted. A 'best fit' path of the star mapper centre was drawn and the 40 arcmin star mapper extent shown. Figure 14.6 shows an example of this. Unidentified transits are depicted by a dashed vertical line.

Initialisation of the Scanning Law

Again, as explained above, this stage was only necessary if Ω_0 was completely unknown.

The value of the Ω_0 of the nominal scanning law was not known before initial star pattern recognition. However if Ω_t is the heliotropic angle derived from the nominal scanning law for the attitude initialisation zero time assuming $\Omega_0 = 0$, Ω_m is the offset calculated from the following field of view to the star catalogue strip, Ω_s is the offset of the centre of the star mapper vertical slit system from the spacecraft *x*-axis, then the initial heliotropic angle is given as: $\Omega_0 = \Omega_m - \Omega_t + \Omega_s$ and thus from this point on the scanning law could be determined.

Star Pattern Monitoring

Whereas the initial star pattern recognition identified detected transits retrospectively, the aim of star pattern monitoring was to identify transits as close to real time as possible. It did this by maintaining a sliding window of six matched vertical transits in each field of view. New transit pairs which had been identified by the slit distinction algorithm in near real-time were received. The vertical transit time was mapped to an angle round the great circle and added to the existing pattern in both fields of view. A pattern match was attempted on each field of view using a similar—though not identical—algorithm to that used to calculate Ω_m, based on a small range of offsets centred around the previous offset for each field of view.

If the transit was identified in one and only one of the fields of view it was accepted. The window for that field of view was updated by releasing the 'oldest' star and adding the new identification. The transit pair data and star identification were passed to the fine attitude estimation task.

Once an accurate value for Ω_0 was known (either from previous spacecraft operations or as a direct result of the full initial star pattern recognition just described) the two field of view windows required by star pattern monitoring were easily initialised. The offset calculated in star pattern matching was used to calculate offsets to the catalogue strip for each field of view. The set of following field of view transits from field 2 of the separation algorithm (see field of view separation above) was used to initialise the following field of view, and the remaining transits in field 2 were assumed to be rich in preceding field of view transits and these were used to initialise the preceding field of view. If the on-board real-time attitude determination needed to be subsequently re-initialised, providing the nominal scanning had been maintained, the star pattern monitoring could be re-initialised using the nominal scanning law to determine the offsets to the catalogue strip for each field of view.

Up to 20 transit pairs identified by slit distinction were used as trial patterns for both fields of view and pattern matching was attempted. If a pattern was identified uniquely in both fields of view then the star pattern matching task was initialised and could begin near real-time identifications. Otherwise further transit pairs were collected from slit distinction and further pattern matches attempted. Figure 14.7 shows the results from initialising one of these windows in this manner. Here a succession of closely spaced offsets, each giving an alignment count of 11 transits, can be seen. The residual is plotted on top of this and the local minimum, corresponding to the best pattern match,

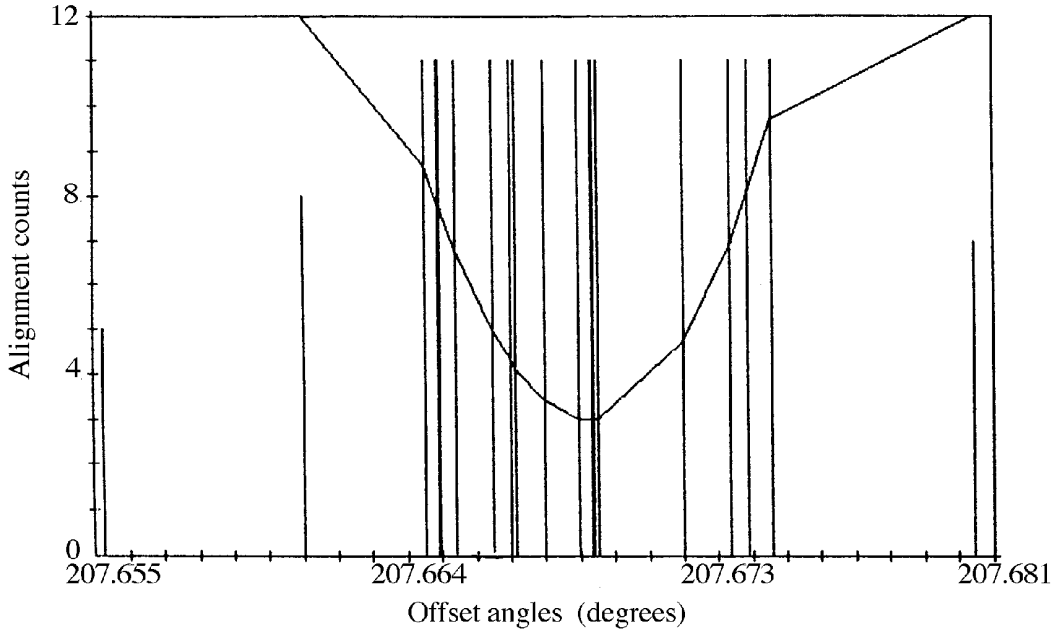

Figure 14.7. *An example of graphical output from the ground real-time attitude determination star pattern monitoring facility, during the initialisation phase. The angular offset from the strip origin which gives the best pattern match is that showing the maximum alignment count and lowest residual (see text for details).*

is located toward the centre of this offset grouping. (This is also the behaviour observed for field of view separation and star pattern matching.)

The star pattern monitoring task ran throughout the remainder of the operations. A graphics display was used to illustrate the real-time identifications. An example is shown in Figure 14.8. The display is split up into 5 sections: the top panel displays the incoming transits as a function of time. Each incoming star transit is represented by a separate point. The symbol used for the star shows whether the transit has been identified and if so in which field of view. The two central graphs display the identifications in each field of view. The left hand graph displays the following field of view and the right hand graph the preceding field of view. Each identified transit is plotted in star catalogue coordinates in the appropriate field of view. The path of each field of view across the catalogue strip can therefore be seen—this was useful for determining the best half-width to use for the strip. The lower two graphs show the residuals for the two fields of view as functions of time. The residuals will be small—any increase in the residuals shows a deterioration in the quality of the pattern match possibly because of star misidentification.

Fine Attitude Estimation

The requirement for the fine attitude estimation algorithm was to estimate in near real time the spacecraft attitude, body rates and gyro drift rates. At this stage, the attitude was determined by defining three Tait-Bryan attitude angles (ϕ, θ, ψ) in an inertial reference frame.

(ϕ, θ) defined the scan plane orientation and ψ defined the rotational phase of the spacecraft. Hence (ϕ, θ) oscillated about zero, while ψ changed secularly at the same

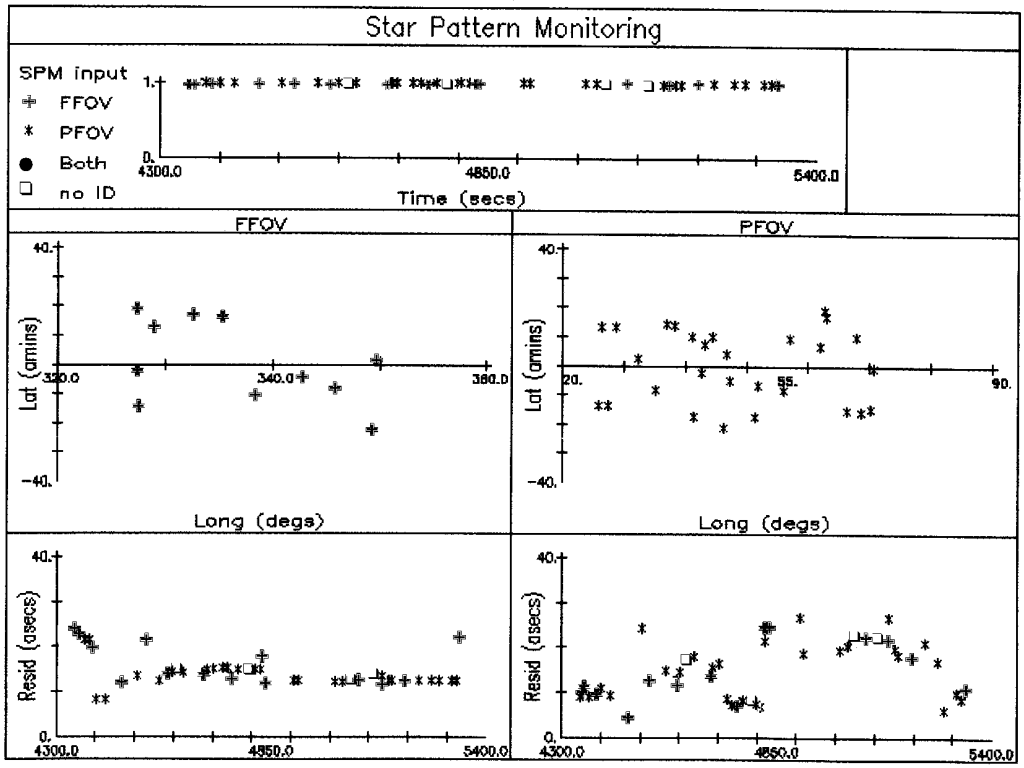

Figure 14.8. *An example of graphical output from the ground real-time attitude determination star pattern monitoring facility, during the routine monitoring phase (see text for details).*

rate as the rotation rate of the spacecraft (168.75 arcsec s^{-1}). The three axis rotation rates were determined from the three operational gyro outputs.

The attitude and rates were determined using the identified star transit pairs (inclined and vertical transits), generated by the star pattern monitoring program, with gyro rate and thruster actuation data extracted from the attitude and orbit control system telemetry stream by the telemetry pre-processor. This information was processed in real-time using a Kalman filter method, to update the spacecraft state estimate, where the state was described by: (i) the attitude (Tait-Bryan angles in either sun-pointing or 43° inertial reference frame); (ii) the body rates about the spacecraft axes, (ω_x, ω_y, ω_z); and (iii) the gyro drift rates about the gyro input axes.

The initial state estimate assumes: $\phi = \theta = 0$; $\psi = 180°$; $\omega_x = \omega_y = 0$; $\omega_z = 168.75$ arcsec s^{-1} and gyro drift rates from pre-calibrated values or previous attempts to initialise real-time attitude determination.

Besides the state estimation processing, the current attitude knowledge was applied to the identified transit pair to determine which inclined slit, upper or lower, was crossed. Transits lying within approximately 5 arcmin of the spacecraft equator were rejected. As the estimation converged, this rejection deadband was reduced, more transits could be processed and the estimation accuracy thereby increased.

The filter processing consisted of the following steps: (a) state and state covariance transition between star transit pairs, with allowance for thruster actuations between

transit pairs; (b) pre-processing of star transit pair data and gyro rates to generate a measurement for input to the Kalman filter; and (c) state vector and covariance matrix update resulting from a new measurement.

State and State Covariance: The state vector and state covariance transition between star mapper measurements was performed as a series of transitions over intervals without actuations, with covariance updates at actuations. Between measurements a discretised linear state model was used, which could be derived from kinematic and dynamical (Euler equations) relationships for the attitude and the body rates respectively. The drift rates were modelled as a random walk with the drift noise incorporated into the model's system noise. Gyro reaction torques and solar radiation pressure torques were taken account of in the forcing function which was used to perform the transition of the state vector. Other disturbance torques (e.g. gravity gradient and magnetic) were modelled as torque noise within the overall system noise.

The performance of the Kalman filter could be tuned by varying the power spectral densities in the system noise matrix. There were six power spectral densities which could be independently tuned: three for the torque drifts and three for the gyro drifts. The power spectral densities used affected the performance of the filter; if they were too large the filter tended to track the raw measurements (including noise), if they were too small the filter response would be slow and the estimates would lag behind the optimal values. The effects of actuations were allowed for by updating the state covariance at the time of the actuation. Specifically, the rate covariance on the axis about which an actuation torque acts was relaxed—the covariance was reset to a comparatively large preset value. The state and the remaining state covariance components were not updated.

Measurement pre-processing: This covered the calculation of a measurement, measurement observation matrix and measurement covariances given a star transit pair and/or the attitude and orbit control system gyro output history. The different measurement types generated were:

(i) transverse measurement (ζ_m), giving the longitude of the star measured from the spacecraft equator, which was a function of:

- inclined/vertical star transit times;
- estimated attitude (ϕ, θ, ψ) in the catalogue strip reference frame at the vertical slit transit time;
- estimated body rates at the vertical slit transit time;
- star latitude and longitude in the catalogue strip reference frame;
- inclined/vertical slit mounting angles in the spacecraft reference frame.

(ii) phase measurement giving the phase of the spacecraft x-axis measured from the catalogue strip reference x-z plane about the scan axis direction. Whereas star transit pairs for both preceding fields of view and following fields of view were processed to give transverse measurements, only transits of one field of view were processed to give phase measurements. This measurement incorporated the scan phase and scan rate knowledge. By considering only one field of view, possible bias effects due to uncertainty in the basic angle separating the two fields of view were removed from the scan phase and scan-rate estimates. After initial calibration of the basic angle at the start of the mission (see next section), this bias was removed and it was safe to use measurements from both fields of view for updating the state vector;

(iii) gyro rates for the two equatorial and the z-axis gyro at a given time.

The measurements were treated as scalars rather than as a 5-dimensional measurement vector.

State Vector and Covariance Matrix Update: The updating of the state and state covariance from the measurement, measurement covariances and observation matrices was performed using the standard Kalman Filter algorithms. The state vector was updated using the differences (innovations) between the observed measurements and those predicted from the previous estimate of the state. The star pattern monitoring may have sent a small number of misidentified stars which led to unexpectedly large differences in the measurements. If these differences had been used the convergence of the filter would have been badly disrupted. To avoid this, a measurement innovation threshold could be set for each of the three types of measurement. These thresholds could be altered during the operation of fine attitude determination to protect the accuracy of the estimates. Using the conventional Kalman Filter equations, it was found that the gyro drift estimates were particularly sensitive to high innovations. Reasonably accurate initial estimates were obtained for these drifts and a way needed to be found to protect those values from excessive alteration at the start of fine attitude estimation when the initial attitude and rates were not so well known. The solution was to modify the measurement innovations going into the drifts estimates by factors which could be tuned during operation of fine attitude estimation. Initially these values were set low to fix the drifts at a constant value until such times as the Tait-Bryan angles and body rates have begun to converge. They could then be increased, once the innovation thresholds were low enough to protect against star misidentifications, so that more accurate final values for the drifts could be obtained.

Convergence of fine attitude estimation was usually achieved within 20 min, but times varied considerably depending on the frequency of star transits. Convergence was improved by having a mixture of transits in both fields of view. Examples of the Tait-Bryan angles, body rates, gyro drifts rates and innovation levels are given in Figure 14.9 to Figure 14.12 for a typical real-time attitude determination initialisation attempt at 43° from sun-pointing.

Basic Angle Calibration

As described in the previous section, a difference between the actual and the measured basic angle (nominally 58°) led to a bias in the predicted attitude (particularly the Tait-Bryan angle ψ). The solution was to collect transits once fine attitude estimation was converged and process them using a least-squares method to derive a better estimate of the basic angle, which could then be used to further improve the convergence of fine attitude estimation. The process consisted of three activities: collecting star transit and attitude information from fine attitude estimation; pre-processing the fine attitude estimation results to obtain a 'batch' of measurements; and estimation of the basic angle and grid rotation parameters by the application of a batch weighted least-squares method.

Once fine attitude estimation was approximately converged, it was possible to collect transit information including: transit time; field of view (following or preceding); catalogue position of observed star; current orientation of the scan plane as estimated by fine attitude estimation; and current rotation rate about the spacecraft z-axis.

These data were collected over 40–60 min by which time approximately 100 measurements should have been collected. During this period only phase measurements from

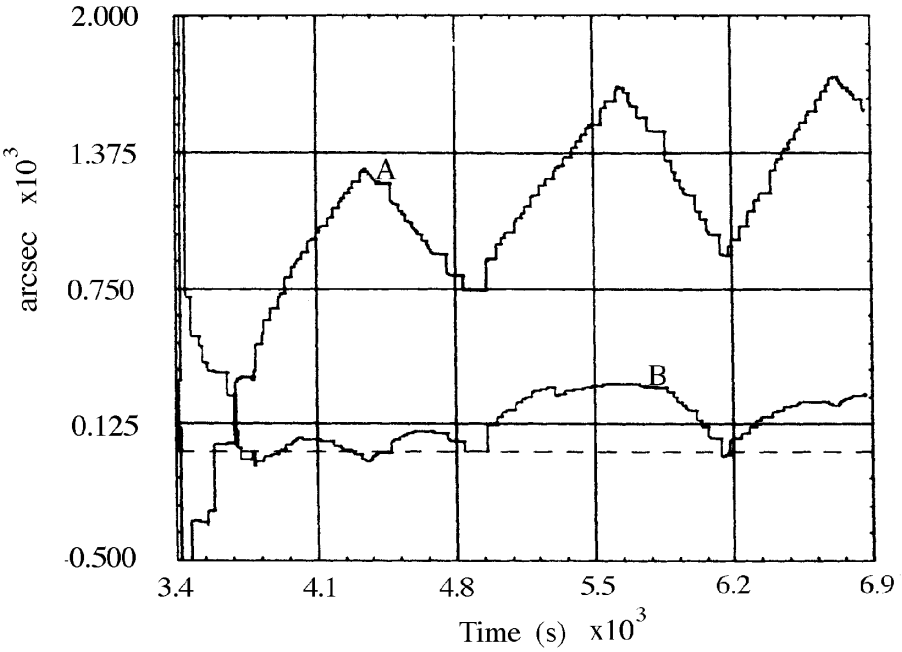

Figure 14.9. *On-ground estimates of the ϕ (A) and θ (B) Tait-Bryan attitude angles from the ground real-time attitude determination fine attitude estimation facility. The discontinuities result from thruster actuations.*

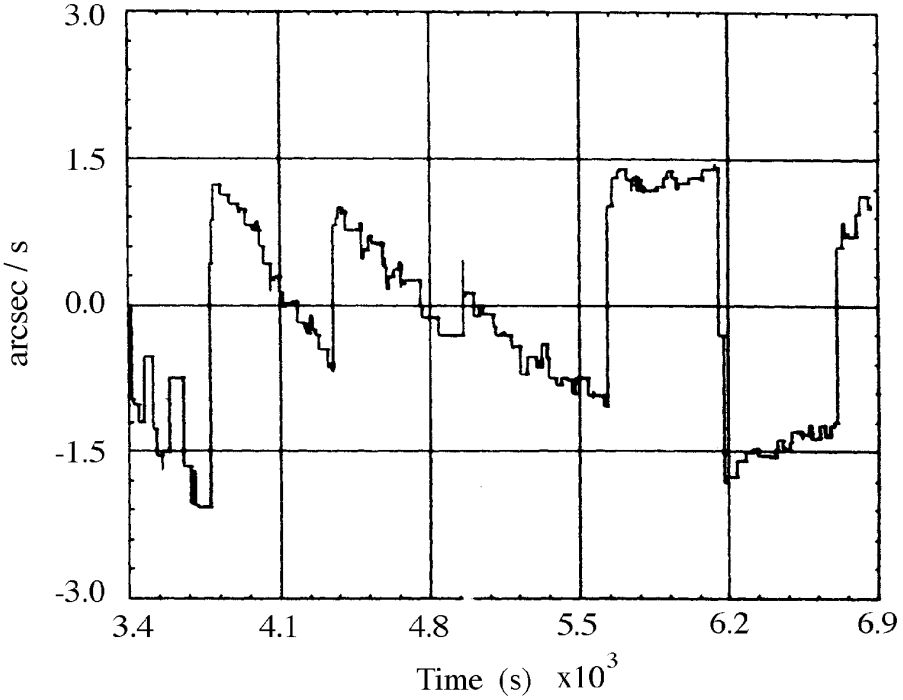

Figure 14.10. *On-ground estimate of body rate about the spacecraft y-axis from the ground real-time attitude determination fine attitude estimation facility.*

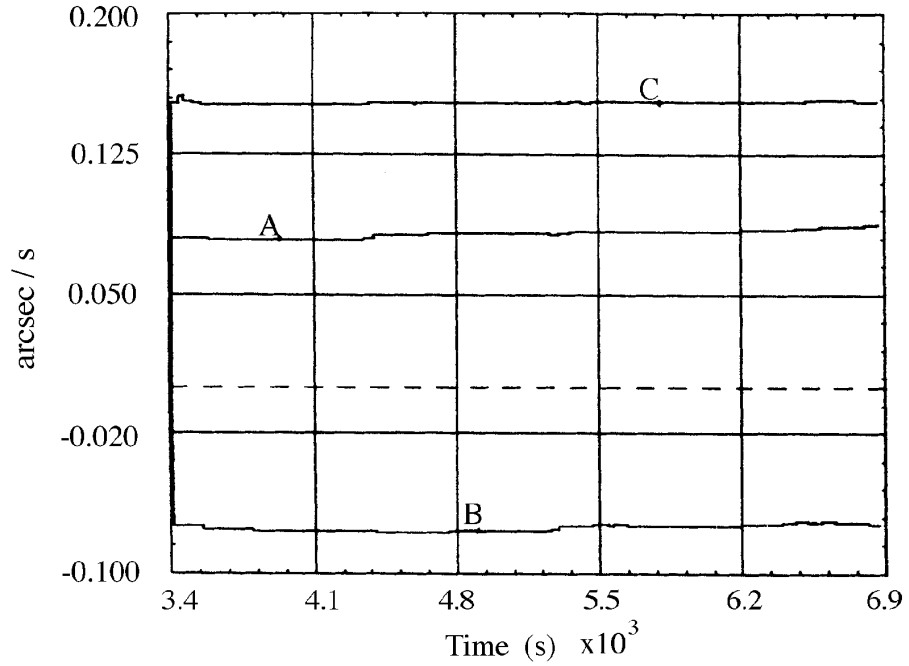

Figure 14.11. *On-ground estimates of the drift rates of gyro 1 (A), 2 (B) and 4 (C), from the ground real-time attitude determination fine attitude estimation facility.*

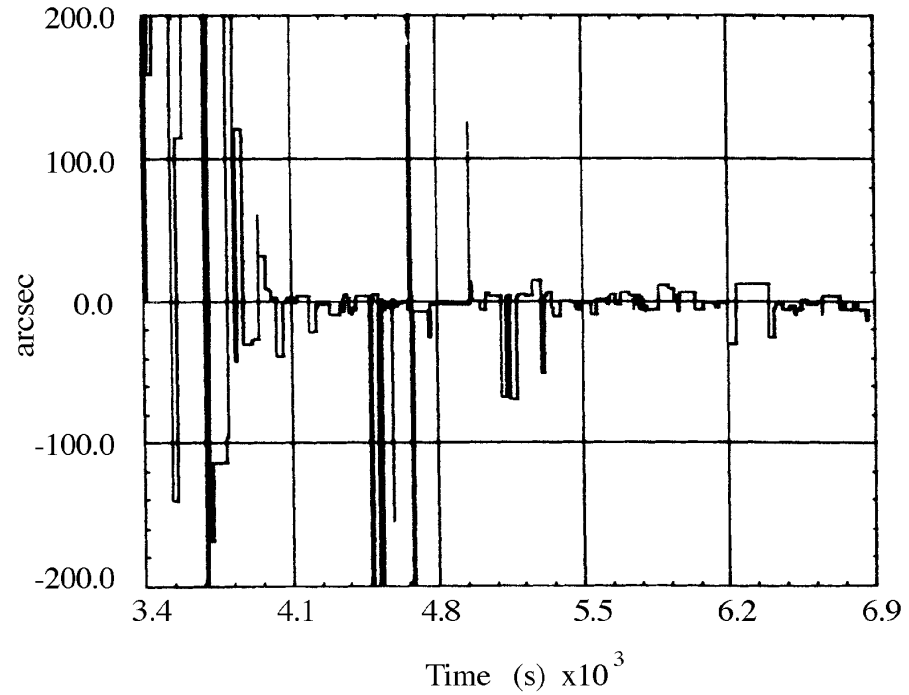

Figure 14.12. *On-ground transverse measurement innovation used in the Kalman filter within the ground real-time attitude determination fine attitude estimation facility. Convergence of the algorithm to a stable attitude estimate is seen as the size of the innovations reduces towards zero.*

one field of view could be used to update the state vector. This eliminated possible biases in the state vector estimates.

At the end of this collection period, the raw measurement data were pre-processed. Near-simultaneous (within a specified time tolerance) transits of the vertical star mapper slits of the two fields of view (preceding and following) were required. For each preceding/following pair selected, the expected star separation was calculated from the known star catalogue positions. The transverse coordinates of each star at the corresponding vertical slit transit time were calculated using the attitude estimated by the fine attitude estimation program and the catalogues star positions. The mean scan rate over the interval spanned by the results stored on disk was computed by integrating the instantaneous z-axis body rate results—as calculated by fine attitude estimation—with time and dividing by the interval duration. These measurements were then combined in a least-squares formulation which provided estimates of the rotation angle of the grid (nominally zero) and the basic angle.

The basic angle was calibrated at the start of the mission while the spacecraft was sun-pointing. The value obtained was 58° 30 arcsec, compared to an on-ground calibrated value of 58° 42 arcsec. The grid rotation estimate proved to be unreliable. The maximum error of 3 arcmin was in any case shown in simulations not to impede convergence of fine attitude estimation. Convergence of fine attitude estimation during operations assumed that the value was zero and no problems had been met. The new value for the basic angle was thereafter used by fine attitude estimation. Subsequent attempts to re-initialise real-time attitude determination were performed using phase measurements from both fields of view without impeding convergence. Within a few weeks of the start of the mission, the data reduction consortia had derived a more accurate value for the basic angle, which was used by the ground real-time attitude determination system.

Initialisation of the On-Board Real-Time Attitude Determination

The final stage of the on-ground attitude initialisation was to provide for the spacecraft an instantaneous attitude estimate in terms of the Tait-Bryan error angles plus the three gyro drifts projected onto the spacecraft axes.

The spacecraft attitude estimated on-ground at any given time would have been derived from data collected on-board the spacecraft at some earlier time. Although this time delay could be calculated by using the computer clock and the correlation between the spacecraft clock and UTC, further time delays would occur in uplinking the attitude to the spacecraft. The following solution was adopted.

A future time, t_1 was selected according to the following criteria: t_1 was at least 20 s in the future; it corresponded exactly to an on-board telemetry format start time (1 telemetry format = 10.666... s); and the total delay from the time, t_0, of on-board acquisition of the data used for the attitude estimate to the time t_1 was calculated. The attitude estimate and the estimated body rates calculated by the fine attitude estimation task and valid for time t_0 were used to linearly extrapolate through the time interval (t_1 - t_0) to give an attitude estimate valid for time t_1. The attitude estimate for time t_1 was converted to the ecliptic reference frame and compared with the nominal scanning law attitude for time t_1 to derive the Tait-Bryan error angles ϕ, θ, ψ. These Tait-Bryan error angles together with the gyro drift estimates calculated by fine attitude estimation were uplinked to the spacecraft.

The uplink command was time-tagged to expire 5 s before the time t_1, but was format synchronised so that the command was only executed at the start of a format. This ensured that the uplinked attitude estimate was accepted on-board at precisely the time at which the estimate was valid.

Note that the above method did not remain valid if there was an actuation of the on-board thrusters during the interval $t_1 - t_0$, as this would invalidate the extrapolation. Thruster actuations were monitored on-ground and the uplink was only performed during a period when no actuations were expected. The Tait-Bryan error estimate had to be within 28 arcsec of the true attitude for the on-board real-time attitude determination to converge following the uplink. To meet this requirement it was essential to keep the time interval $t_1 - t_0$ as small as possible. This illustrates the time-criticality of the on-ground processing from the telemetry pre-processing and star mapper filtering task through to the final attitude estimation. The value of $t_1 - t_0$ was monitored during operations and the uplink was only permitted when this value was less than 60 s. Under conditions of normal computer load this criterion was easily met. Figure 14.13 and Figure 14.14 show the effect of the attitude initialisation uplink on the on-board real-time attitude determination.

Subsequent Ground Operations

Following the uplink the on-board real-time attitude determination took over control of the spacecraft. During the period of attitude initialisation a programme star file was prepared on ground containing expected star transit data and this was uplinked to the spacecraft before the attitude initialisation. If the value of Ω_0 was already known, the programme star file could already be generated in advance of the start of real-time attitude determination initialisation procedures. In general, therefore, during the three-gyro operations, the programme star file was generated automatically every 24 hours on the off-line mainframe computer, transferred to the real-time system and uplinked to the spacecraft, regardless of the status of real-time attitude determination.

The on-board real-time attitude determination was enabled after the attitude initialisation, controlling the spacecraft using observations of reference stars across the star mapper and data from the attitude and orbit control system. The on-ground attitude estimation process continued and the difference between on-ground and on-board estimates of the Tait-Bryan error angles and gyro drifts were monitored along with the on-board innovations to allow the on-ground support team to assess the convergence of the on-board algorithms. When the initial Tait-Bryan uplink was large (of the order of $0^\circ.5$) then it was necessary to wait until the on-board controller had recovered the initial attitude error and then fine-tune by uplinking a further set of Tait-Bryan error angles before switching control to the on-board algorithm.

Once real-time attitude determination had been seen to converge on-board, the image dissector tube should be capable of tracking stars. The image dissector tube was the primary detector for the scientific data, and its correct operation was an indication of real-time attitude determination convergence. Thus once the attitude and the gyro drifts were known on-ground, the values could be uplinked to the spacecraft for use by real-time attitude determination and normal operations could continue. In this way, the attitude was accurately known and the gyro drifts could be continually calibrated.

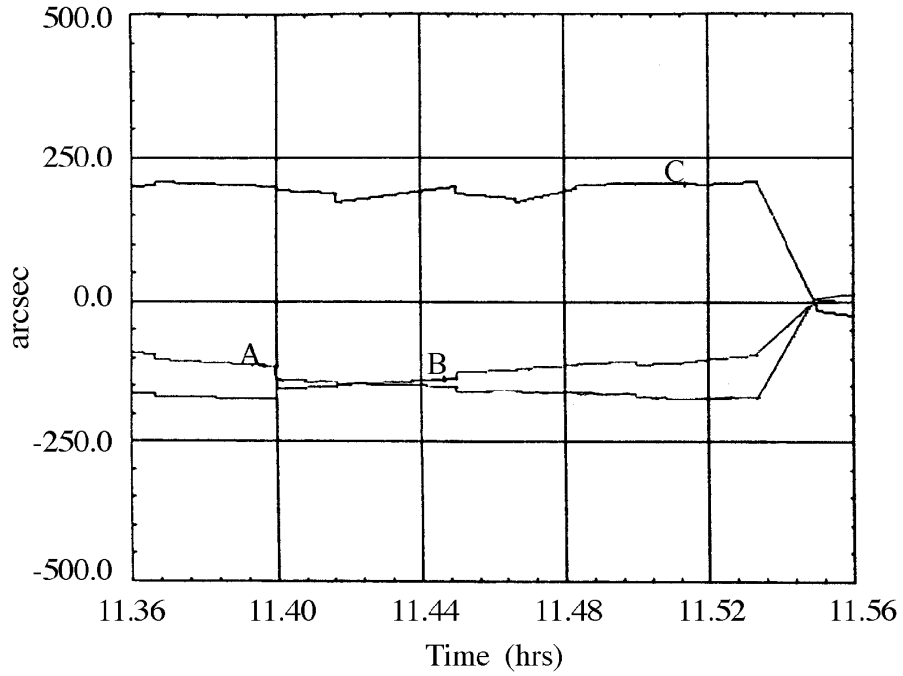

Figure 14.13. *Tait-Bryan angle uplink. The figure shows three lines denoting the differences between the on-board and on-ground estimates of the Tait-Bryan error angles ϕ, θ, ψ (lines A, B, C respectively). All three curves reduce to zero at uplink (to the right of the diagram).*

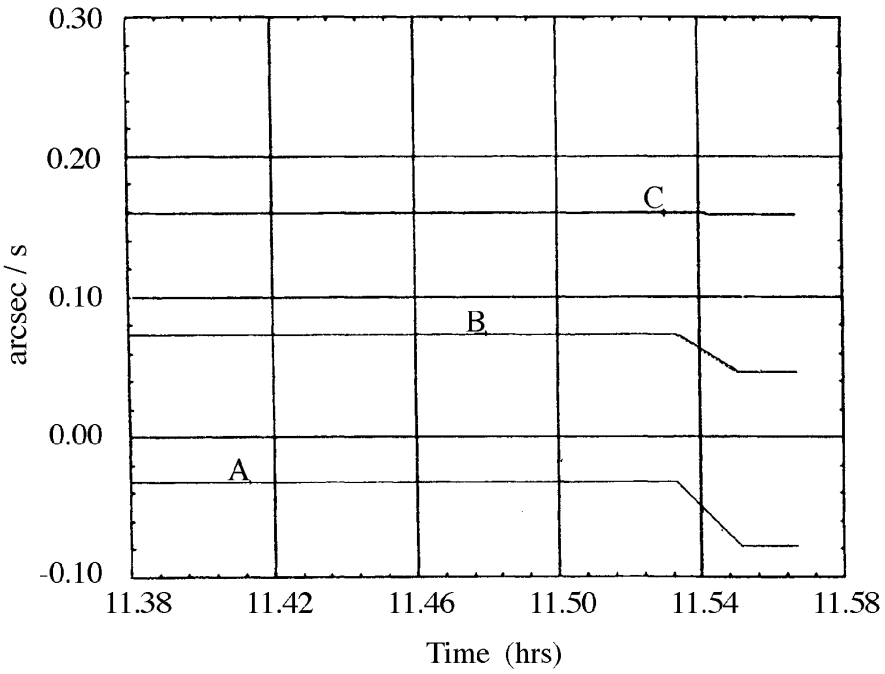

Figure 14.14. *Gyro drift relative to the spacecraft axes, as used on-board, for the x, y and z drifts (labelled A, B, C respectively). Values change after the uplink of new values from ground.*

14.4. Real-Time Attitude Determination Performance

In addition to ground real-time attitude determination, software ran continuously to monitor the attitude and the behaviour of the gyros and thrusters. Various alarms were to be triggered, on-board and on-ground, when an attitude anomaly occurred, such as a failed gyro or jammed thruster. If the spacecraft was visible from one of the ground stations, procedures could be implemented to minimise attitude drift. On-board, there were other safety measures, which could be triggered automatically or manually from ground, to protect the spacecraft should it start to drift for any reason. A sun sensor was used to protect the spacecraft from drifting more than 3° off the nominal scanning law with the immediate danger of the sun shining directly into the telescope, damaging the grid or detectors. If the spacecraft drifted past this threshold a so called emergency sun reacquisition order was triggered on board. The spacecraft then immediately slewed back to sun-pointing.

Data Recovery Percentages

The revised orbit induced real-time attitude determination divergence after approximately half of all perigee passes. The requirement to re-initialise real-time attitude determination prompted the decision to introduce a shift team of flight dynamics specialists to support spacecraft operations. Real-time attitude determination performance was continually monitored using the image dissector tube observations as the definitive criterion for convergence, i.e. if stars were being consistently observed by the image dissector tube, then real-time attitude determination must be converged. Once real-time attitude determination diverged (most often seen immediately after perigee) re-initialisation would take place using the ground real-time attitude determination software.

The overall percentage of science data achieved over the mission is shown in Figure 14.15. The figures are derived from ESOC's ground-based payload monitoring software (described in Chapter 10). 'Good' data refers to periods when stars were consistently observed by the image dissector tube during coverage periods. 'Bad' data refers to periods when real-time attitude determination diverged (usually immediately after perigee) during coverage periods. 'No data' refers to periods without ground station or computer support. The hibernation periods refer to those times when the spacecraft was spun up between three- and two-gyro phases and between two- and zero-gyro phases.

Once all three ground stations were made available, 'good' data recovery was around 71 per cent during the three-gyro operations (71 per cent of 24 hours per day). 'Good' data was recovered 87 per cent of the coverage time.

The time to perform real-time attitude determination re-initialisation varied greatly. This was due to two primary factors: (a) star mapper noise in the van Allen belts and (b) occultations after acquisition of signal.

The star mapper was particularly sensitive to background radiation in the van Allen belts. When highly active, after a solar flare, the star mapper could be blinded for

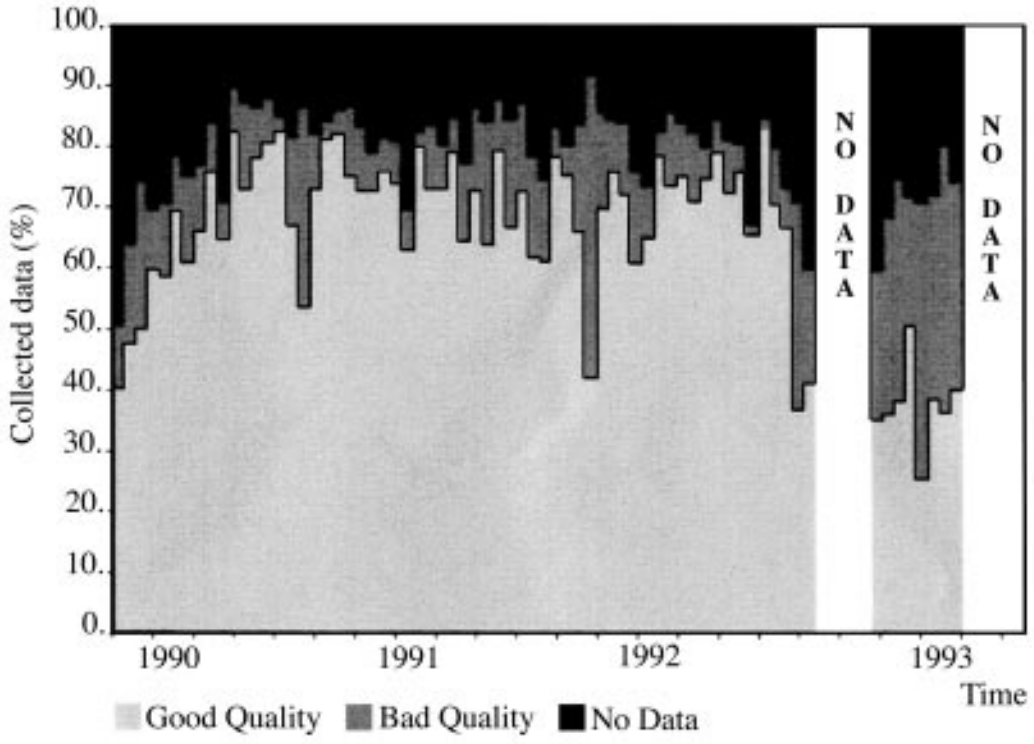

Figure 14.15. *Science data recovery as measured at ESOC.*

several hours per orbit due to the high background count rate. In the most extreme cases of solar activity, the star mapper would be blinded for the entire orbit, making convergence of real-time attitude determination impossible. Blinding of the star mapper also affected the ground real-time attitude determination software which filtered the star mapper data stream. Only once the noise was sufficiently low was it profitable to start real-time attitude determination re-initialisation procedures.

Seasons occurred where real-time attitude determination convergence could be recovered by switching to extended window after perigee. These seasons could last days or, latterly in spring 1992, weeks. At other times, real-time attitude determination would require initialisation every pass. These seasons were however unpredictable in their occurrence and were the subject of studies performed at ESOC and Matra Marconi Space. Resulting from these studies and input from the data reduction consortia, a significant number of changes (such as improved torque modelling and thruster calibration) were made to on-board and on-ground software which over the course of the mission improved the accuracy of real-time attitude determination in the apogee region and the chances of maintaining convergence though perigee. This had a direct consequence of improving the quantity and quality of the science data.

Typically at the start of 1990, the real-time attitude determination innovations (average difference between predicted and actual transit times converted to angular separations) were between 1 and 5 arcsec. By the beginning of 1992, the innovations were consistently around 1 arcsec, although the size began to increase again with the deterioration of gyro 5.

The principal improvements are described in the subsequent sections.

Central On-Board Software Patch and Parameter Tuning

As described in Chapter 9, in January 1990, the first calibrated grid rotation from the FAST Consortium was used on-board resulting in a significant improvement in on-board real-time attitude determination performance. The resulting innovations, which give a measure of the attitude corrections necessary between star mapper transits, were reduced from an average distribution of around ±5 arcsec, to around ±2 arcsec.

In March 1990, a new version (4.02) of the central on-board software was uplinked to the spacecraft. The new patch contained the following changes:

(a) extensions of the time-tagged buffer with an increase of allocated space from 640 words to 1504 words;

(b) extension of the memory area for the star data blocks which was increased from 1983 star data blocks (11898 words) to 2314 star data blocks (13884 words);

(c) improved star mapper filtering to eliminate false star mapper identifications in high noise.

The first change was necessary to perform efficient operations through long ground station outage. The second change allowed a denser selection of real-time attitude determination reference stars through long ground station outage (the 'sparse programme star file' described in Chapter 8). Clearly, the likelihood of maintaining real-time attitude determination convergence was proportional to the frequency of good star mapper measurements.

The third change was necessary since it became clear that high star mapper noise during van Allen belt passage was occasionally causing the on-board software to make a 'false star' detection. This erroneous measurement could be seen as real-time attitude determination as a larger than average innovation. Although the largest errors would be trapped by setting an appropriate innovation rejection threshold on-board, moderate sized errors were still apparent leading to increased noise in the overall real-time attitude determination performance. After the on-board patch was included, a clear reduction in the largest innovations was seen. Moreover, it became possible to make better use of the 'extended window' innovation threshold of 30 arcsec during high noise to help re-converge real-time attitude determination.

In May 1990, a swap from the B_T to the V_T channel for star mapper processing was made. This was due to the higher response in the V_T channel giving a higher number of successfully processed stars.

Over the following months, other tuning of on-board software parameters associated with star mapper rejection criteria was made. Statistics of reasons of star mapper measurement rejection were compiled over several weeks, correlating them to background noise and magnitudes of the reference stars. In this way, certain magnitude dependent parameters relating to expected height and width of the filtered signal were tuned. The result was a steady increase in the frequency of successful star mapper measurements for use by the real-time attitude determination system.

Reference Star Rejection Criteria

It was observed early on in the mission that the faintest real-time attitude determination reference stars were invariably rejected in the star mapper processing (95 per cent). Therefore, in March 1990, the limiting magnitude of such reference stars (flagged in the programme star file) was reduced from 10 to 9 mag. The result was a reduction in the load on central on-board software processing, allowing more of the brighter stars to be successfully processed.

Hipparcos Input Catalogue Updates

As described in Chapter 9, the NDAC Consortium was able to feed back their preliminary star positions and magnitudes to ESOC, via the INCA Consortium, to be used for the on-board programme star file.

In February 1991, Version 8 of the Hipparcos Input Catalogue was received and implemented at ESOC, containing approximately half the programme stars with positions updated from the preliminary data reductions. By November 1992, Version 10 was received, with nearly all of the programme stars containing updated results. The improvement in accuracy of the positions was, by that time, superior to the intrinsic performance accuracy of the real-time attitude determination.

This and the greater reliability in the magnitude estimates allowed ESOC to tune the selection criteria for attitude guide stars and to tune the on-board star mapper processing parameters to optimise the correct identification of guide stars in the star mapper data stream and virtually eliminate any possibility of mis-identifying stars, which could lead to an unexpectedly large innovation error in the on-board control.

Occultations and Eclipses

An occultation occurred when the Earth or Moon crossed one of the fields of view of the telescope (the definition of the nominal scanning law prevented the Sun from ever doing so). Light from either body could have damaged the sensitive detectors, hence shutters were closed to protect them. Unfortunately that meant that no stars could be seen by either the image dissector tube or star mapper and real-time attitude knowledge could deteriorate, resulting ultimately in divergence.

Occultations by the Earth or the Moon required that the star mapper shutters be closed for up to 30 min at a time, near the perigee region. These would often hinder ground real-time attitude determination re-initialisation procedures. At times, it would be necessary to restart the procedure, if the occultation interrupted the star pattern recognition before convergence of the ground software could be achieved.

In 1991, the mission planning software at ESOC was modified to allow the shutters to remain open during occultations whenever a dark area of the Earth's surface occulted one or both fields of view. Since there was no risk to the instruments from the dark side of the Earth, real-time attitude determination was more likely to be maintained using star measurements from the other field of view. This was particularly valuable at

lower altitudes, where the Earth's disc was much larger and the occultation duration consequently longer.

Gyro Projection Matrices

As described in Chapter 9, in July 1991, the NDAC Consortium was able to supply a newly calibrated gyro projection matrix for uplink to the spacecraft, to account for gyro misalignments with respect to the nominal positions.

Gyro Drift Monitoring and Correction

As described in Chapter 13, from March 1992 onwards, ground procedures were changed to allow the resetting of the on-board drift estimates as soon as possible after perigee to the last values observed before perigee. Subsequent careful monitoring for drift evolution was then performed throughout the orbit to ensure that the best drift estimates were maintained.

15. REAL-TIME ATTITUDE DETERMINATION WITH TWO GYROS

Radiation damage was considered to be responsible for the progressive failure of the gyroscopes. In the nominal mode of operation these gyros were essential for acquisition and maintenance of attitude knowledge and control. In principle the satellite itself, with adequately known external and internally-actuated torques, allows the integration of its attitude evolution with less noise than integration of the gyro outputs. However, this would require both a very accurate starting point and very sophisticated modelling. The accuracy of such a description of attitude evolution could only be maintained through the observation of star transits across the star mapper grids. The time between these events must be sufficiently short for the integration to maintain the required accuracy. In the originally intended geostationary orbit it seems likely that this notion would have provided the incentive to operate with the gyros turned off, thus suppressing jitter and parasitic torque. In the actual geostationary transfer orbit the long interruptions of star transit observations coincided with the least known, yet highest perturbing torques, which would inevitably cause loss of attitude to the point of requiring reinitialisation. Thus for a less than three-gyro mode of operation not only a model to replace the real-time onboard input of the absent gyro was needed, but also a much faster, and thus more sophisticated attitude determination and initialisation on ground. As redundancy in the gyroscopes disappeared, a substantial effort was put into developing the procedures to work with only two gyroscopes, and eventually without gyroscopes altogether. The two-gyro mode was fully implemented, and eventually used for the last months of scientific observations.

15.1. Two-Gyro Operations Development History

In June 1990, gyro 4, which monitored the scan rate about the principal spin axis, failed. It was replaced in the attitude control loop by the backup unit, gyro 5. Before the failure, gyro 4 had exhibited a large and fluctuating noise envelope (exceeding 1 arcsec s^{-1} amplitude at times). Subsequent monitoring showed that gyro 5 exhibited similar noise characteristics to those of the failed gyro.

Given the repeated apparent run-downs of gyro 4 and the anomalous noise properties of gyro 5, there was a high risk that both could fail irreparably. In order to continue

the mission without any z-gyro (the z referring to the z-axis in the spacecraft reference system used for real-time attitude determination, as described in Chapter 14), a series of studies were performed. They resulted in an attitude control software modification, called the 'two-gyro patch', and a number of ground software changes/updates which allowed the continuation of the mission using only two gyros.

The revised on-board real-time attitude determination algorithm replaced the z-gyro input by a simple sinusoidal model for the disturbance torque around the z-axis near apogee, combined with a revised Kalman filter to estimate not only the z-axis Tait-Bryan error angle (as for the three-gyro real-time attitude determination) but also the difference between the nominal and actual spin rate and the acceleration around the z-axis. Both the Kalman filter state vector and the sinusoidal model had to be initialised from ground after every perigee using the revised ground real-time attitude determination software. The on-board attitude control logic, indicating the changes necessary in going from three-gyro to two-gyro operations, are shown in Figure 14.2.

The patch was run successfully in parallel with the actual real-time attitude determination in order to validate both the on-board and ground modifications. These changes were extensively tested during the second half of 1991 and proven to function correctly.

On 10 July 1992, after continuous poor performance, gyro 5 was removed from the control loop and the two-gyro real-time attitude determination system was used to control the spacecraft for the first time. By 11 July 1992, after parameter tuning on-board and refinement of ground procedures, the first scientific data were obtained. The concept of two-gyro real-time attitude determination had been proven, and when converged, gave better performance than the three-gyro real-time attitude determination with the noisy gyro 5.

Although it had been proved that the ground software developed during 1991 and 1992 was adequate for initialising real-time attitude determination, it was far from optimal. Moreover, although giving generally better performance in the apogee region, the two-gyro real-time attitude determination suffered two distinct disadvantages:

(a) divergence after occultations was frequent, leading to lost science data before the ground real-time attitude determination software could re-initialise on-board real-time attitude determination;

(b) there was little control of the spin rate through perigee, leading to a lengthy procedure of real-time attitude determination initialisation after every perigee. This procedure took between 1.5 and 2 hours at that time, in comparison with 20–40 min with the three-gyro real-time attitude determination (with a high probability that real-time attitude determination would remain converged after perigee). Given that typically 9.5 hours was covered by ground station per orbit, a loss of 1 to 2 hours science data per orbit was considerable.

After an emergency sun reacquisition on 4 August 1992, in which the satellite spin axis was autonomously slewed to the Sun direction, a recovery in the performance of gyro 5 prompted a return to three-gyro real-time attitude determination operations on 8 August 1992. However, on 11 August after a scanning law acquisition manoeuvre to return to the nominal scanning law, gyro 5 failed for the last time causing an emergency sun reacquisition and a spin-up to 0.45 rpm. The decision was taken to extend the spacecraft spin-up phase as much as possible, i.e. until the increasing solar aspect angle reached the limit of 43°. There were two main reasons for doing so:

(a) the early operational experience with the two-gyro real-time attitude determination before the emergency sun reacquisition occurred, proved to be valuable in highlighting various improvements which could be made to speed up real-time attitude determination initialisation. While the spacecraft was spin-stabilised, it was safe enough to remove the flight dynamics team from operational shift work to daytime development of enhanced ground real-time attitude determination software, thereby increasing the speed of production of the software by a factor of 3 to 4. As stated above, these changes increased the speed and reliability of real-time attitude determination initialisation once the operations were resumed;

(b) it was hoped at that time that the mission lifetime would be dictated by the gas consumables. Given that no gas was being used in the spin-up phase, by delaying spin-down, one was actually extending the lifetime of the mission with a subsequent improvement in the final accuracies of the proper motions.

This approach was agreed between ESOC, ESTEC and the data reduction consortia. The spacecraft remained spun up until 1 October 1992, when the increasing sun aspect angle necessitated an additional manoeuvre to sun-pointing mode. By this time, most of the planned software changes had been completed. Full operations resumed with the new system, collecting science data for approximately four more months.

15.2. Operational Requirements

In running with two-gyro control, several new operational procedures had to be performed:

(a) the higher disturbance torques close to perigee caused a net angular acceleration around the rotation axis. These acceleration terms were difficult to model and predict as there was no ground station coverage possible at so low a height (500 – 600 km). Nominally, the scan rate was constrained by the on-board attitude control software to be within approximately 2 per cent of the nominal rate of 168.75 arcsec s^{-1}. Without the z-axis gyro input, much larger excursions were expected. As far as possible, these excursions had to be minimised through perigee;

(b) on receiving signal from the spacecraft after perigee it was necessary to measure the scan rate on-ground and correct it, if necessary, by direct thruster command;

(c) the spacecraft lost real-time attitude determination control through perigee. Therefore it was necessary to estimate on-ground the attitude, body rates, (particularly around the z-axis) and correct the on-board values in real-time. It was also necessary to be able to reset the drift values on the remaining gyros;

(d) most importantly, after re-initialisation, the revised real-time attitude determination software on-board had to be capable of remaining converged on the correct attitude estimate to allow scientific data to be collected, accurate attitude information being necessary for the image dissector tubes to pilot successfully.

On-Board Memory Constraints

Memory space on-board was limited. Some of the spare memory already provided additional gyro/thruster monitoring during loss of signal, preventing an irretrievable spin-up of the spacecraft should the second spin-rate gyro fail. A highly sophisticated model would not fit the available space that was left. The model that was adopted is described in detail in the next section.

The revised on-board software was devised to fit into the available spare memory and could be run in parallel with the nominal three-gyro system. This allowed, during the first half of 1992, the new software to be tested on-board in a monitoring mode, i.e. the attitude was estimated without using the (still) operational spin-axis gyro. However this information was merely dumped in the telemetry and was not used to control the spacecraft. Rather the nominal on-board system continued to control the satellite until the time that the z-axis gyro failed.

Ground System Requirements

In addition to the dramatic changes required to the on-board real-time attitude determination, the ground system also required significant modification.

Raw star mapper data were only processed by the telemetry pre-processing and star mapper filtering task in the ground real-time attitude determination chain (see Chapter 14). Therefore it had to perform the scan-rate estimation if no z-gyro was operational. This led to the following constraints on the scan-rate estimation algorithm:

(a) the algorithm performance had to comply with the real-time constraints of the ground attitude determination within the resource limitations imposed by the available hardware and other essential control tasks running in parallel;

(b) implementation of the scan-rate estimation algorithm had to involve minimum changes to the existing telemetry pre-processing and star mapper filtering software. Algorithms and techniques employed in the nominal algorithm had to be retained wherever possible and interfaces to the original software kept simple. This reduced problems of integrating and testing new software and minimised development time. This was important at the start of the development since the lifetime of the remaining z-gyro was unknown;

(c) the scan-rate estimation algorithm could not rely on *a priori* knowledge of either the expected transit time or detailed characteristics of the slit system being crossed, since this information was only derivable from subsequent tasks in the ground system;

(d) the interfaces to other tasks in the ground attitude system had to be unaltered wherever possible to minimise software changes.

The operational constraints imposed on the on-ground real-time attitude determination gave it distinctive problems in star recognition which were quite different from either the on-board real-time attitude determination system or the post-processing work performed by the scientific data reduction consortia. For example, on-board real-time attitude determination could not successfully recognise stars in the star mapper data unless it could calculate the spacecraft attitude accurately. Ground real-time attitude

determination had to identify stars, with little or no *a priori* information concerning the spacecraft rotational phase around the spin axis. Besides, ground real-time attitude determination had also to be able to operate under these new conditions with very much larger deviations in the spin rate. Ground real-time attitude determination had also to straddle the twin hurdles of providing sufficiently robust and accurate attitude determination, when the finite resources of the on-board system were unable to cope, and performing it in near real-time. This latter constraint was not imposed on the data reduction consortia who were able to re-constitute the attitude off-line to much higher accuracy, given the good *a priori* attitude information of the on-board system, that enabled the image dissector tube piloting for the acquisition of good scientific data.

15.3. On-Board Software

On-Board Real-Time Attitude Determination using Two Gyros

As discussed above, given that on-board memory was limited, changes to the real-time attitude determination algorithm were limited in scope. A full description of the design concepts of real-time attitude determination was given in Chapter 14. This section concentrates on the differences between the three- and two-gyro systems.

In the nominal on-board system, the state vector in the Kalman filter consisted of the three Tait-Bryan error angles and three gyro drifts. All six were defined with respect to a co-rotating cartesian coordinate system. The integrated gyro outputs were used to estimate the attitude evolution and the star mapper transit times were used as measurements to update the state vector.

Without a z-gyro, it was necessary to include the angular rate around the z-axis within the state vector and to allow that to be updated by the star mapper measurements. Studies by Matra Marconi Space showed that it was feasible to replace the z-gyro rate inputs by a dynamic model predicting ψ, the Tait-Bryan error angle around the z-axis. The vector would be increased to dimension 8 to include separately first and second-order terms in ψ and the z-gyro drift would be replaced by $d\psi/dt$ and $d^2\psi/dt^2$.

Consequently the revised state vector was:
- ϕ: Tait-Bryan error angle around the spacecraft x-axis;
- θ: Tait-Bryan error angle around the spacecraft y-axis;
- ψ_1: Tait-Bryan error angle around the spacecraft z-axis (first-order term);
- ψ_2: Tait-Bryan error angle around the spacecraft z-axis (second-order term);
- d_x: gyro drift around the spacecraft x-axis;
- d_y: gyro drift around the spacecraft y-axis;
- d_z: scan rate drift from nominal (168.75 arcsec s^{-1});
- γ_z: rate of scan rate drift.

Above 20 000 km where the radiation pressure was the dominant disturbance torque, the acceleration around the z-axis could be successfully modelled by a harmonic of three times the nominal scan-rate. Such a model already existed on-board in the ‘normal mode’ control software for use in optimising thruster on-times (see Chapter 13), but up to now had not been used for attitude determination. The time dependency of the model was provided by the variables $(S_{v3}(k), C_{v3}(k))$, which were already derived for

three-gyro operations (see Equation 13.2). The two new coefficients required to define the amplitude and phase of this oscillatory model (A_d, B_d) were stable over at least one orbit. With frequent on-ground calibration (a procedure carried out since the start of the mission) such a model was used by providing a separate correction term for ψ (denoted ψ_d) outside the Kalman filter, where (at time t_k):

$$\psi_d = A_d\ C_{v3}(k) + B_d\ S_{v3}(k) \qquad [15.1]$$

Therefore:

$$\psi = \psi_1 + \psi_2 + \psi_d \qquad [15.2]$$

Gyro data from two transverse gyros gave angular velocities (body rates) about the x and y axes. Gyro processing was performed using an updated gyro projection matrix to obtain estimates of the spacecraft body rates (G_x, G_y, G_z) around all three axes:

$$\begin{aligned} G_z &= \omega_Z\ t_i \\ G_x &= a_1 G_1 + b_1 G_2 + c_1 G_3 + d_1 G_z \\ G_y &= a_2 G_1 + b_2 G_2 + c_2 G_3 + d_2 G_z \end{aligned} \qquad [15.3]$$

where ω_Z is the nominal scanning law Z rate, (the z error-rate effect was negligible) and G_i ($i = 1, 2, 3$) are gyro increments over $t_i = 16/15$ s for the (x, y) plane gyros. The coefficients of non-selected gyros were set to zero by telecommand.

The spacecraft attitude and remaining gyro drift rates were predicted as follows:

$$\begin{pmatrix} \phi(k+1) \\ \theta(k+1) \\ d_x(k+1) \\ d_y(k+1) \end{pmatrix} = \begin{pmatrix} 1 & \omega_Z\ t_i & -t_i & 0 \\ -\omega_Z\ t_i & 1 & 0 & -t_i \\ 0 & 0 & 1 & 0 \\ 0 & 0 & 0 & 1 \end{pmatrix} \begin{pmatrix} \phi(k) \\ \theta(k) \\ d_x(k) \\ d_y(k) \end{pmatrix} + \begin{pmatrix} G_x(k+1) - \omega_X(k)\ t_i - G_y(k+1)\ \psi(k) \\ G_y(k+1) - \omega_Y(k)\ t_i - G_x(k+1)\ \psi(k) \\ 0 \\ 0 \end{pmatrix} \qquad [15.4]$$

$$\begin{pmatrix} \psi_1(k+1) \\ \psi_2(k+1) \\ d_z(k+1) \\ \gamma_z(k+1) \end{pmatrix} = \begin{pmatrix} 1 & 0 & t_i & 0 \\ 0 & 1 & 0 & t_i^2/2 \\ 0 & 0 & 1 & t_i \\ 0 & 0 & 0 & 1 \end{pmatrix} \begin{pmatrix} \psi_1(k) \\ \psi_2(k) \\ d_z(k) \\ \gamma_z(k) \end{pmatrix} + \begin{pmatrix} -G_x(k+1)\theta(k) \\ 0 \\ 0 \\ 0 \end{pmatrix} \qquad [15.5]$$

Spacecraft body rates around all three axes could therefore be estimated as:

$$\text{rate}(k+1) = (\text{attitude}(k+1) - \text{attitude}(k))/t_i \qquad [15.6]$$

In the event of actuation, for the following cycle, corrective terms were added to Equation 15.4 such that:

$$\begin{aligned} \psi_1(k+1) &= \psi_1(k) + d_z(k)\ t_i - g_x(k+1)\ \theta(k) + T_{az}\ t_{\text{on,z}}(t_i - t_{\text{on,z}}/2) \\ d_z(k+1) &= d_z(k) + \gamma_z(k)\ t_i + T_{az}\ t_{\text{on,z}} \end{aligned} \qquad [15.7]$$

where T_{az} is the mean thruster acceleration on-board parameter (fixed) over actuation, $t_{\text{on,z}}$ is the applied thruster on-time. Consequently, an accurate thruster calibration was required and this was performed and provided to ESOC by the data reduction consortia (see Chapter 9).

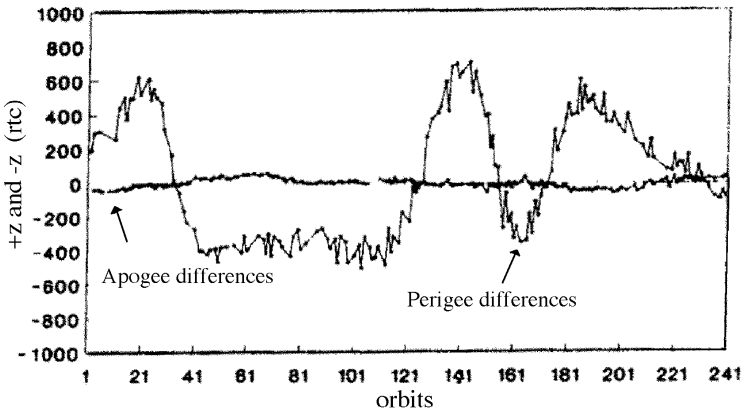

Figure 15.1. *z-thruster on-time differences (expressed in rtc units of 1/75 s) as accumulated around perigee and apogee for 240 orbits. See text for details.*

Measurement extrapolation and innovation (R_I) computation were performed in a similar manner to that used for three-gyro real-time attitude determination except that new fixed gain sets $\mathrm{KG}_{\mathrm{new}}$ were used. Attitude updates were consequently computed as:

$$X^{+}_{\mathrm{new}} = X_{\mathrm{new}} + R_I \ \mathrm{KG}_{\mathrm{new}}(\mathrm{slit}, \mathrm{quality}) \qquad [15.8]$$

where:

$$\begin{aligned} X_{\mathrm{new}} &= (\phi, \theta, \psi, d_x, d_y, x_z, \gamma_z) \\ \psi_1^{+} &= \psi^{+} - \psi_d \\ \psi_2^{+} &= 0 \end{aligned} \qquad [15.9]$$

Modification of the attitude for on-board computer extrapolation on cycles around actuation was performed as for three-gyro real-time attitude determination.

Perigee Scan-Rate Control

Through perigee passage, the complex disturbance torques around the z-axis were not modelled on-board to sufficient accuracy for attitude determination. In addition the accelerations could not be determined in the Kalman filter from star transit measurements because the star mapper electronics were blinded by noise from the van Allen belts.

It was soon realised that a further z-gyro failure could result in an irretrievable spin-up of the spacecraft. A software patch was implemented which allowed the accumulation of the $+z$ and $-z$ thruster on-times. Should either exceed a certain threshold which was reset every orbit, further firings of the z-thruster would be inhibited. This facility had the additional benefit of giving, on readout, information about the torques around the z-axis. The difference between the $+z$ and $-z$ total on-time allowed the determination of the total spin-up/down of the spacecraft if actuations about the z-axis were inhibited. Figure 15.1 shows a graph of on-time differences around perigee and apogee over 240 orbits (approximately 107 days). Thruster units (rtc) are in 1/75 s, which equated to a change in angular velocity of approximately 0.12 arcsec s^{-1} rtc^{-1}. Apogee differences always remained small. However perigee differences could be as great as 800 rtc units (100 arcsec s^{-1} change from the nominal rate of 168.75 arcsec s^{-1}).

No direct information was available about the likely phase angle drift around perigee, but drifts of several degrees were expected. To get more information on this aspect and provide a better overall understanding of the torques in this region, a further on-board software patch was later implemented, which allowed the storage and later dumping of telemetry parameters during loss of coverage. This 'spy patch' allowed ground to replay selected gyro and thruster information around the perigee region, giving more insight and more accurate predictions of scan-rate and scan angle deviations.

15.4. On-Ground Software

Scan-Rate Estimation and Correction

Ground real-time attitude determination, required a more sophisticated approach than that employed on-board, where the star mapper would not only measure the virtual transit time of a star as it crossed one of the sets of four slits, but would measure the spread in the four peak data stream to obtain the spin rate directly. This involved determining the best correlated signal as a function of the position and spread of the four-peak signal. Support was also required from ground in re-calibration and maintenance of the on-board harmonic model.

After the perigee passage the spacecraft would have an unknown scan rate about the z-axis. Once the ground station had acquired a signal from the spacecraft and the background noise had decreased to an acceptable level, the scan rate could be estimated. This was a time-critical task which directly affected the quantity of scientific data which could be collected in each orbit. It was an additional task to the standard operations and thus had to be performed as quickly as possible, but without sacrificing the accuracy of the achieved scan-rate after firing the thrusters.

The basis of the method was to estimate as accurately as possible the time taken to cross between the first and fourth slits. Since the distance between these slits had been accurately calibrated in orbit, this transit time allowed the scan rate to be calculated.

The approach in the nominal three-gyro system was carried out in the telemetry processing and filtering task (see Chapter 14) as follows:

(1) star mapper data for both the B_T and the V_T channels (sampled at 600 Hz) were extracted from the telemetry frames and placed in a circular buffer;

(2) each data sample from the V_T channel was tested against a threshold (nominally corresponding to V_T = 9 mag). This threshold was adaptive to reflect changes in the background noise level;

(3) a window (nominally 500 data samples) was created for further processing;

(4) the V_T channel data (which had a better signal-to-noise ratio than the B_T channel) was correlated with a four-peaked matching filter function corresponding to an average single-slit response based on the nominal vertical and chevron slit responses (see Figure 5.3). For the star mapper the slit separation in data samples was 20, 60, 40. For

computational efficiency a 'folded' signal was first calculated:

$$E_i = S_i + S_{i+20} + S_{i+80} + S_{i+120} - 4B \qquad (i = 8, N - 127) \qquad [15.10]$$

where S_i is the raw star mapper data sample, B is the background noise, and N is the number of samples in the window. This folded signal was then correlated with a single peaked matching filter for one slit, to provide the full correlation;

(5) the correlation peak was calculated by parabolic interpolation and checks were performed to ensure that sufficient side lobe peaks were found at the correct locations, with an appropriate relationship between the main peak height and the side lobe peak height;

(6) the B_T channel data were correlated using the estimated scan-rate to check that a correlation peak was found with the same datation as for the V_T channel.

The algorithm to determine the scan rate was based on the above method. Essentially steps 4 and 5 were repeated assuming different scan rates, though a modified correlation algorithm was used as defined below. For scan rates where the algorithm showed a star transit, parabolic interpolation of the peak heights as a function of scan-rate was used to give a new maximum peak height; the corresponding scan-rate became the estimate.

The slit system had been defined such that at the nominal scan-rate of 168.75 arcsec s^{-1} a star would cross the slits in 0.2 s. Since the sampling rate was 600 Hz this corresponded to 120 data samples. A scan-rate step of 168.75/120 = 1.40625 arcsec s^{-1} was chosen. This meant that the number of data samples between the first and fourth slits was always an exact integer value. For calculating the scan-rate interpolation problems were avoided by only using data from the outer slits.

For the scan-rate estimation:

$$G_i = S_i + S_{i+120+k} - 2B \qquad [15.11]$$

where:

$$k = \frac{(168.75 - v)}{168.75} \times 120 \qquad [15.12]$$

and v is the variable scan-rate incremented by 1.40625 arcsec s^{-1}.

The output correlated signal was then calculated as:

$$M_i = \sum_{j=-6}^{6} F_j G_{i+j} \qquad [15.13]$$

for all i, where F_j is the response for the average slit derived from the responses for a vertical slit and a chevron slit. This was represented by a function with 13 discrete points. M_i is the output signal which could be used to calculate the scan-rate. To verify the crossing was a star transit and not a noise spike it was necessary to check for side lobes. This could only be achieved if the complete signal was correlated i.e. for the second and third slits as well.

The folded signal for the second and third slits was:

$$H_i = w_1 S_{i+k_1} + w_2 S_{i+k_1+1} + w_3 S_{i+k_2} + w_4 S_{i+k_2+1} - 2B \qquad [15.14]$$

where w_i are the weighting factors dependent on the scan rate being processed, calculated using linear interpolation. k_1 and k_2 are also scan-rate dependent centred around 20 and 80 respectively. Then:

$$N_i = \sum_{j=-6}^{6} F_j H_{i+j} \qquad [15.15]$$

and the sum $O_i = M_i + N_i$ was checked for the requisite number of side lobes. The heights of the side lobes were checked as before. The positions of the side lobes, which are a function of velocity, were also checked.

The estimated scan-rate was updated if there was only one good transit in the data window. This avoided incorrect estimates due to transit coupling or interference between main peaks and side lobes of the other peaks.

As presented above, the scan-rate should have been controllable within ±30 arcsec s^{-1} of the nominal 168.75 arcsec s^{-1}. 51 trial scan-rates were processed by the algorithm. The accuracy of the scan-rate estimation required at this stage was of the order of 0.5 arcsec s^{-1}. This allowed the nominal scan-rate to be achieved with sufficient accuracy.

Once a consistent estimate of the scan-rate had been achieved, the number of scan-rates processed was reduced to 11. This gave a band of approximately 7 arcsec s^{-1} around the latest estimate. This very significantly reduced the processing time required. More side lobes were checked for than in the nominal telemetry pre-processing and star mapper filtering to eliminate spurious harmonics.

Once 5–10 min of closely correlated scan-rate estimates had been achieved, the thruster on time required to correct the scan-rate would be calculated. Before the scan-rate correction was sent, the number of scan rates processed would be increased to cover the nominal scan-rate case. The software would then automatically track the thruster firing and calculate new scan-rates for each transit received. Once the scan-rate had settled down the number of scan-rates could be reduced back to 11.

When a scan-rate close to the nominal value had been reached the software had to calculate an accurate estimate of the full spacecraft attitude. The telemetry pre-processing and star mapper filtering task had now to calculate precisely the same information as for the nominal mission. Thus for each transit an accurate estimate of the star transit time over the virtual slit centre and the B_T and V_T magnitudes were required. Since tasks further down the chain process the z-gyroscope data this was now replaced by the scan rate estimate.

The B_T and V_T magnitudes were calculated using only data from the outer slits, and so avoided inaccuracies due to data interpolation.

Tests were performed at non-nominal scan-rates using the attitude and payload simulator in ESOC, which was adapted for the purpose. Various scan-rates were used. The maximum deviations from the nominal rate used were 30 arcsec s^{-1}, corresponding to the expected maximum error in correcting the scan-rate after perigee. Some results are summarised in Table 15.1.

Scan-rates are measured in arcsec s^{-1}. Over runs of typically an hour or more, star transits of varying brightness taken from the Hipparcos Input Catalogue, were simulated at these different scan-rates. For each star, a rate estimate was produced. Their mean

Table 15.1. Results from on-ground simulations (see text).

Simulated	Mean Error	Standard Deviation
200.0	-0.14	0.30
168.75	-0.09	0.14
138.75	-0.13	0.27

and standard deviation were computed. As expected, the error in determining the correct scan rate grew as the scan rate moved further away from the nominal. However, the accuracy was still good enough even at highly irregular scan-rates to allow for the rate to be corrected by direct thruster commanding.

For the later stages, with near-nominal scan-rates the on-ground Kalman filter was capable of smoothing out irregularities in the rate estimates.

Ground Real-Time Attitude Determination

The remaining tasks in the ground real-time attitude determination chain (described more fully in Chapter 14) are now summarised. One new task was developed to support the ground real-time attitude determination: 'star pattern offset matching' which is described below.

Slit distinction and gyro correction: The slit distinction algorithm remained unaltered from the nominal case. The gyro correction algorithm 'corrected' the transit times of vertical slit crossings to remove the effects of spin-rate variation i.e. it produced a set of pseudo vertical transit times as if the spacecraft had been spinning at a constant rate. Although the algorithm for gyro-correction remained unaltered for the non z-gyro case the (less accurate) scan-rate estimations were used rather than the measured gyro rates; this had implications for the next task in the chain.

Star pattern monitoring: Star pattern monitoring used star pattern recognition to identify each transit pair and determine the field of view of observation. The algorithm mapped the transit times to angles around a great circle. This mapping was less precise when no gyro data was available for the transit time correction. Consequently larger tolerances were needed in the pattern recognition, which raised the probability of confusion or misidentification. An enhanced algorithm was implemented to improve the performance of this task, both in the initialisation phase and during the normal real-time execution. In addition, the user interface was re-worked to provide greater flexibility in obtaining the initial star through parameter options and through improved alphanumeric and graphical displays.

Fine attitude estimation: In the nominal ground real-time attitude determination, a nine element state vector defining Tait-Bryan attitude error angles, body rates and gyro drifts was used in a Kalman filter, receiving measurements from star mapper transit times and the gyros rates at those transit times. Changes were necessary for the new version to allow the star mapper scan-rate estimates to replace those from the z-gyro. Obviously, the estimation of the z-gyro drift was suppressed and the gyro misalignment projection matrix adjusted accordingly. The user interface was altered to allow the spacecraft operator to monitor closely the estimated scan-rate. In tests it was found that a misidentification could have serious impacts for the scan-rate estimate and hence after parameter tuning, a much smoother scan-rate estimate was obtained, obviously at

the cost of sensitivity. Another significant enhancement was the inclusion of actuation on-times to improve ground body rate estimates.

Real-time attitude initialisation: This task provided an instantaneous estimate of the on-board real-time attitude determination state-vector which was valid at precisely the time that the data were accepted on-board.

The real time attitude initialisation software was updated to calculate the values for the new state vector implemented in the on-board real-time attitude determination for the non z-gyro case.

For state vector initialisation:

(i) ϕ_n, θ_n and ψ_n the angular errors, were derived as the difference between the attitude as calculated by fine attitude estimation and the expected attitude from the nominal scanning law;

(ii) transverse gyro rates and drifts were calculated by fine attitude estimation;

(iii) ψ_d was derived as follows:

$$\psi_d = A_d \cos 3\Omega_d t + B_d \sin 3\Omega_d t \qquad [15.16]$$

where Ω_d = 168.56 arcsec s^{-1} (the scan-rate including precession, A_d and B_d were calculated by orbital oscillator routines (see below);

(iv) ψ_2 was set to zero;

(v) then $\psi_1 = \psi_n - \psi_d$;

(vi) $\dot{\psi}$ was provided by fine attitude estimation (from the scan-rate estimate calculated by telemetry pre-processing and star mapper filtering);

(vii) ψ_2 was set to zero;

(viii) $\ddot{\psi}$ was set to zero.

On-Board Torque Model Support

The ground software for computing orbital oscillator parameters refreshed the on-board real-time attitude determination orbital oscillator model, ($\cos\Omega_d t$, $\sin\Omega_d t$) at 15 min intervals (see Chapter 8). For the new on-board real-time attitude determination the deterministic ψ model coefficients, A_d, B_d had also to be maintained. But:

$$\ddot{\psi}_d = \frac{T_z}{I_{zz}} \sin(3\Omega_d t + \gamma_{z0}) \qquad [15.17]$$

where T_z is the torque around the z-axis, I_{zz} is the z inertia, and γ_{z0} the phase of the torque model about z. By double differentiation of the equation for ψ_d, expressions for A_d and B_d were derived. T_z and γ_{z0} were in any case calculated by the ground software.

Star Pattern Offset Matching

This program provided a more efficient way of determining the initial heliotropic angle Ω_0 to within $0\overset{\circ}{.}1$ accuracy. During three-gyro operations, this task was performed in two steps (Chapter 14): field of view separation, and star pattern matching. These two tasks were performed off-line once sufficient star transits had been identified as a result of star mapper filtering and slit distinction. Typically around 20 identified stars were required before a reliable star pattern match could be performed. The process involved considerable manual intervention and a stable scan rate (taking approximately 30 min). Fortunately, during three-gyro operations, Ω_0 remained constant except during rare contingencies. Subsequently, this task was rarely required.

It was clear that, for two-gyro operations, changes of several degrees in Ω_0 could be expected after every perigee. It therefore became productive to look for ways to improve the speed and reliability of this part of the ground procedure. This was achieved by taking a more statistical approach to the determination of Ω_0. The ground system assumed knowledge of the spacecraft z-axis orientation (even if Ω_0 was unknown). Consequently, matching of star mapper transits could be limited to a strip on the sky rather than the complete celestial sphere. The 'star pattern offset matching' algorithm would make no *a priori* assumptions concerning the field of view in which a particular star transit was seen; rather the algorithm would identify all stars around the sky-strip with similar magnitude (in both B_T and V_T) and calculate, for each candidate star, and for both fields of view, the value of Ω_0 which would allow the specified star to be observed in the specified field of view at the measured transit time.

In this way, all the measured star transits gave rise to several candidate values for Ω_0. However when these were binned into small intervals (typically $1°$) and displayed as a histogram, a clear peak around the true value was invariably apparent (unless the scan rate was not well controlled to the nominal value at the time).

The real-time 'star pattern monitoring' task was adapted to allow the input value of Ω_0 to be changed on-line. Consequently, the operator at the start of initialisation procedures could attempt to establish a match with 'star pattern monitoring' based on the value of Ω_0 in the previous orbit. Simultaneously the same star data were being used off-line to build up a histogram of potential Ω_0 values. Typically a trend was visible with as few as 10 transits. Assuming the operator was unsuccessful in obtaining a good match from the previous value of Ω_0, a new value could be used in real-time as soon as it became apparent.

Additional Changes

Additional ground software changes to support the two-gyro real-time attitude determination operations were:

(i) modifications to nominal scanning law routines to allow slow precession from sun-pointing to $43°$ maintaining real-time attitude determination convergence in the event that no other way could be found to recover from an emergency sun pointing manoeuvre taking place. This modification was never used operationally;

(ii) an additional command was developed to reset the deterministic z-axis error angle on-board. This allowed the inhibition of the z-axis precession around the 43° cone for use during long losses of signal. This operation is described more fully below;

(iii) gyro configuration checking was suppressed in other gyro monitoring software;

(iv) programme star file observation covariance matrices used for the modulation strategy (see Chapter 8) were re-calculated for the extended mission;

(v) given that several attitude and orbit control system software patches were now active, a new facility was developed for the ground system to perform the selection and automatic uplink of the software patches to the spacecraft. This was first used for the two-gyro patch and the decoupling of the z-thrusters.

15.5. Operational Experience

Parallel Tests During Three-Gyro Operations

The on-board software was designed to run in parallel with the nominal real-time attitude determination software. It was implemented and had been initialised on several occasions, for performance testing, using the new ground real-time attitude determination system. Figure 15.2 shows a graph of the nominal and new ψ Tait-Bryan error angles over 40 min on 26 September 1991.

The nominal real-time attitude determination was converged throughout this period (as in all tests performed with the spacecraft). However, at the start of this graph, the new real-time attitude determination was diverged. After 13 min, ground real-time attitude determination software had calculated and reset the new state vector to the correct value. For the remainder of this period, the two methods kept good agreement, even across two z-thruster firings (shown by the discontinuous changes in gradient).

It was also interesting to compare the performance of the individual components making up the new ψ estimate over the same period. Figure 15.3 shows the values of ψ_1 and ψ_d. ψ_d is the sinusoidal curve. The effectiveness of the ψ_d model in describing the disturbance torques in the apogee region was seen by the fact that the ψ_1 term was nearly linear between thruster firings. ψ_2 remained much smaller throughout. In tests, the new real-time attitude determination was found to remain converged throughout the apogee region (i.e. for several hours). Like the nominal real-time attitude determination, it was however incapable of surviving the perigee region, below 6000 km, where the disturbance torques were greatest.

It was necessary to close the shutters on the payload detectors, whenever the Earth or Moon crossed one of the fields of view. During these occultations, real-time attitude determination ran on gyro and thruster data alone. With three operational gyros, this presented no problems. However, without a z-gyro, z-thruster on-times affected the rate estimates after a firing. Figure 15.4 shows one such firing taking place during an occultation with a subsequent divergence of the new real-time attitude determination from the nominal.

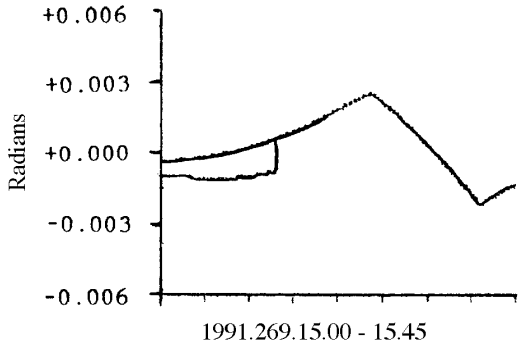

Figure 15.2. *Convergence of the z-axis Tait-Bryan error angle ψ after ground real-time attitude determination correction.*

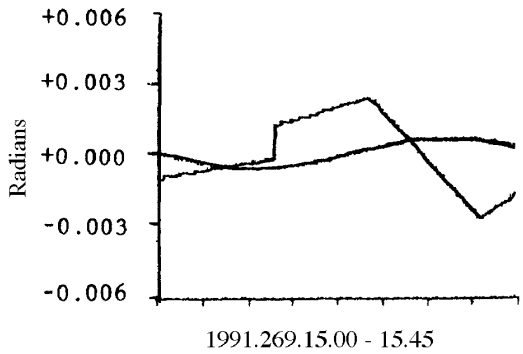

Figure 15.3. *Contribution of ψ_1 (linear part) and ψ_d (smooth curve) to the total Tait-Bryan error angle ψ over the same period as in Figure 15.2. ψ_d is the periodic term reflecting the evolving disturbance torques. ψ_1 is the linear term which was corrected from ground, and which changed gradient after each thruster actuation.*

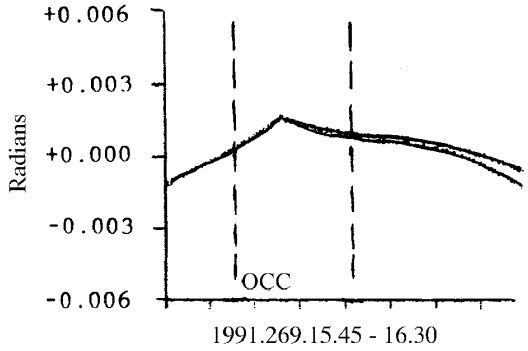

Figure 15.4. *Divergence of ψ after a thruster firing during an occultation (the region within the vertical dashed lines, OCC), where no star transits were available to correct the rate estimates.*

Full Two-Gyro Operations

Once two-gyro operations resumed after the hibernation period, it was seen that the performance of real-time attitude determination, when converged, was greatly improved, as measured by the size of the innovations (once more generally below 1 arcsec). This could be directly attributed to the substitution of a noisy gyro 5, by a smooth, although simplified, disturbance torque model around the spacecraft z-axis. This torque model

was designed specifically to model the radiation pressure torque at apogee. As a result, real-time attitude determination performance would deteriorate as the altitude of the spacecraft dropped near perigee due to the increase in size in un-modelled torques and high star mapper background noise. During perigee, there was no possibility that real-time attitude determination would remain converged due to a total absence of information about orientation around the z-axis: no gyro, a blind star mapper and an uncalibrated disturbance torque model. It was expected that the spacecraft would spin-down or spin-up through perigee by as much as 30 arcsec s^{-1} every orbit.

Hibernation studies had suggested that it might be possible to partially predict in an empirical manner the likely amount of spin-up/down. In practice, this proved to be ineffective. Initially, much higher changes in spin rate were seen (50 – 60 arcsec s^{-1}). This was traced in part to futile attempts by the on-board normal mode control software to take erroneous real-time attitude determination output and fire the z-thrusters, sometimes exacerbating the change in spin rate. A procedure was put in place, involving resetting various real-time attitude determination variables on-board which completely disabled the z-thruster around perigee. This decreased the size of the spin-rate changes, as well as saving gas. However, predictions still proved unreliable and manual compensation through perigee for possible spin rate changes was abandoned. Correction of the spin rate was earlier made easy by the use of gyro 4. Although too unreliable for use with real-time attitude determination, the deteriorated gyro output could be used when telemetry was re-acquired after perigee, while the star mapper was still blinded and unusable by the ground software.

On 22 December 1992, gyro 4 failed completely, thereby making it necessary to run ground real-time attitude determination to obtain spin-rate estimates based on the four peak separation of a star mapper transit. Although the on-ground star mapper filter was capable of determining the scan rate over a wide range of potential values, it was inefficient in the high noise regions of van Allen belts. Moreover, occasional deviations from the nominal scan rate of up to 50 arcsec s^{-1} were still apparent making an initial estimate very difficult. Extra facilities were quickly added to allow a graphical display of particularly bright star mapper transits. This allowed a crude visual estimate of the scan rate to be obtained, even in high noise, so that scan rate corrections could be achieved as quickly as possible after perigee.

At the start of two-gyro operations, some difficulty was found in initialising the on-board real-time attitude determination system from ground. The errors in the on-ground attitude determination, particularly in the rate estimation around the z-axis, were higher than for three-gyro operations. Given that the delay of between 30 and 60 s from the time of last good star observation to the execution time of the on-board initialisation command, errors were building in the on-ground extrapolation of the on-board state vector. The result was that the attitude was sufficiently accurate to be within the 30 arcsec innovation threshold on-board, but produced a large initial innovation before bringing the on-board estimate within the narrow threshold range of 10 arcsec. This innovation was also used, to update the transverse gyro drifts (see Equation 15.8) when in fact the drifts were reasonably stable over the short period of the initialisation. The now erroneous drift values subsequently led to erratic convergence of the on-board system or even divergence again. Work continued to improve the accuracy of the ground software. However an additional measure was taken by devising a second set of fixed gains for use on-board. This set was used during initialisation procedures and contained much smaller gains for updating the gyro drifts. The first gain sets produced for the two-gyro operations had assumed gyro drift gains 100 times higher

than those used during three-gyro operations. Values closer to the previous sets used in three-gyro operations were re-adopted for the new 'extended window' set. These safeguarded the gyro drifts during initial convergence. Once convergence was achieved and the innovation threshold was set to narrow range, a more sensitive set of gains was implemented on-board to produce smoother performance of the attitude determination during science data collection.

Further tuning of the gains was carried out as the performance of the remaining gyros worsened to lessen the effects of erratic drifts diverging the on-board system. In addition calibration studies by ESOC and the Royal Greenwich Observatory (RGO) resulted in more accurate z-thruster performance figures being used on-board.

After 1 November 1992, it was necessary to make occasional changes to the initial precession angle defining the z-axis position on the 43° cone around the sun vector. This was to safeguard the spacecraft through long losses of signal (more than 5 hours around perigee). During a long loss of signal, the nominal scanning law precession rate was set to zero. Without this, a spin-up/down of the spacecraft through perigee could have resulted in a large change to the initial heliotropic angle, which defined the orientation of the spacecraft x and y axes. In the worst case, the initial heliotropic angle could have changed by up to 90°. In this case the last orbital oscillator command sent before loss of signal would have driven the z-axis perpendicular to the nominal scanning law. Left without correction over a typical lost pass, (12 hour loss of signal), the z-axis could drift in solar aspect angle by more than 3° and would consequently have come dangerously close to triggering an emergency sun reacquisition order.

Figure 14.15, showing the overall science data return, clearly indicates that significantly less data were collected per orbit. Overall 'good' data were returned 37 per cent of the total time, or 51 per cent of the covered time. There were three main reasons for this: (1) the real-time attitude determination initialisation procedure was required every orbit; (2) despite the improvement made during the hibernation period, the initialisation procedure was still lengthier than during three-gyro operations; (3) real-time attitude determination divergence after occultations was rather frequent (over 50 per cent of the time), usually occurring over the longer ones where a thruster firing took place in the middle.

Occultations occurred in seasons: sometimes only at perigee, thereby securing uninterrupted coverage for most of the orbit; sometimes occurring in pairs every revolution of the spacecraft, making data return exceptionally poor. Analysis was performed by the NDAC Consortium and ESOC into the possibility of slewing the spacecraft around the 43° nominal scanning law cone to avoid occultations, but it was concluded that this would be detrimental to the overall observation programme.

Software changes were made to improve the performance of the ground real-time attitude determination software immediately after occultations in an effort to reduce the time to re-initialise real-time attitude determination. Steps were also taken to understand the disturbance torques and thruster performance better in the hope of improving the probability of real-time attitude determination survival through occultations. Such improvements were still on-going when further gyro failures necessitated the use of the zero-gyro real-time attitude determination system.

16. REAL-TIME ATTITUDE DETERMINATION WITH ZERO GYROS

In response to the continuing deterioration of all gyros, the zero-gyro operations and software were developed, in principle allowing the real-time attitude control to function with perturbing torque models in place of the gyro data. Catastrophic failure of the telecommunications subsystem terminated the mission before this mode was used. The procedures used to handle these contingencies are nevertheless described.

16.1. Activities during Suspended Operations

On 18 March 1993, the total failure of gyro 2 prompted an emergency sun reacquisition and a spin-up to 0.25 rpm of the spacecraft. This state was maintained until 11 June 1993, when attempts began to operate under the zero-gyro real-time attitude determination control. There were two principal reasons for the delay:

(1) the software for on-board and on-ground real-time attitude determination without gyros was still under development. However, operations resumed when sufficient (if not optimised) ground software was in place for support;

(2) there were concerns that solar panel degradation was too great to allow the spacecraft to be fully operated during the long eclipse season (ending on 21 May 1993). In practice, the degradation was less than that predicted.

The return to full operations was further hampered on 5 and 6 May 1993 by the discovery that both star mappers were partially damaged (no output on the B_T channel of star mapper 1 and the V_T channel of star mapper 2). The only operational solution was to use two different telemetry formats. The first (prepared on-ground and loaded on-board) combined both star mapper outputs but at the cost of the image dissector tube data. This format was required for use in the ground real-time attitude determination system to perform initial star pattern recognition. The second (available on-board) was combining star mapper 2 and image dissector tube 2 data for use once real-time attitude determination convergence was achieved and good science had to be collected. Because the ground software had to work with both formats, a further re-design was necessary.

Event History during Suspended Operations

The progressive failures occurring during the last months of attempted operations were attributed to radiation damage of the associated electronics. A summary of the problems encountered during the period in which zero-gyro operations were attempted is given hereafter, with further details of the various anomalies given in Appendix B.

93-03-18: Gyro 2 failure (Anomaly 77): the on-board system automatically triggered an emergency sun reacquisition.

93-03-19: The spacecraft was spun-up to 0.25 rpm and the gyros switched off to save power. Nutation damping was then performed.

93-03-23: The decision was taken to suspend spacecraft operations. The payload was switched off, with the thermal control electronics branch 2 left on.

93-03-24: Thermal control electronics 2 was configured to wide range.

93-03-28: The nominal antenna switching command failed (Anomaly 78).

93-03-30: All thermal control electronics 2 heaters were set to fixed power with value zero, i.e. switched off, due to power constraints.

93-04-01: Both antenna switching commands failed.

93-04-05: Commands 62 and 65 were used to switch antennas.

93-04-23: Due to the orbital rotation of the Earth around the Sun, the solar aspect angle of the spin axis had been steadily increasing at approximately 1°/day. Power efficiency of the solar panels was highest near the nominal 43° solar aspect angle. This prompted the design and implementation of a series of manoeuvres to reduce the solar aspect angle, which was already larger than 43°, without de-spinning the satellite. This was performed by direct thruster commanding, using the sun acquisition sensor as guidance. Nutation damping was also performed at this time.

93-04-27: The increased efficiency of the panels at 43° combined with the decreasing eclipse durations, allowed the payload thermal control electronics 1 and 2 to be switched on and tested. Consequently, the thermal control electronics 2 heaters were set to fixed power value 15.

93-05-04: The payload was switched on. A preliminary check showed that the image dissector tubes were undamaged by the suspended operations.

93-05-05: Star mapper 2 V_T channel had ceased to function (Anomaly 79).

93-05-06: Star mapper 1 B_T channel had ceased to function (Anomaly 79).

93-05-10: Further manoeuvres were performed to reduced the solar aspect angle and perform nutation damping.

93-05-11: The control law electronics branch A failed (Anomaly 80). The switch to the redundant branch B was made.

93-05-12: A new telemetry was introduced (format 4) combining the star mapper 1 and star mapper 2 telemetry.

93-05-13: Further manoeuvres were performed to reduced the solar aspect angle and perform nutation damping.

93-05-14: The battery discharge regulator 1 module 2 overvoltage status changed.

93-05-17: Further manoeuvres were performed to reduced the solar aspect angle and perform nutation damping.

93-05-24: The eclipse season ended. Gyros 1 and 4 were switched on to increase the gyro electronics box temperature. No usable output was obtained.

93-05-25: Further manoeuvres were performed to reduced the solar aspect angle and perform nutation damping. Gyros 2 and 5 were switched on to increase the gyro electronics box temperature. No usable output was obtained.

93-05-26: Gyro 3 was switched on but within a few hours was showing very high noise (Anomaly 81). The gyro was declared unusable and switched off.

93-05-27: The zero-gyro real-time attitude determination software patch was loaded on-board.

93-06-02: Further manoeuvres were performed to reduced the solar aspect angle and perform nutation damping. The new sun acquisition manoeuvre 4 software patch was loaded on-board.

93-06-04: Further tests were performed with gyros 1, 3 and 5.

93-06-05: The inertial reference unit was completely switch-off.

93-06-06: The attitude control software crashed when the new sun acquisition manoeuvre 4 software was enabled. The problem was traced to an invalid checksum and corrected.

93-06-09: Further manoeuvres were performed to reduced the solar aspect angle and perform nutation damping.

93-06-11: Prior to the resumption of scientific operations, the spacecraft was de-spun from 0.25 rpm to 0.15 rpm.

93-06-12: The spacecraft was further de-spun to 0.05 rpm, and an emergency sun reacquisition was commanded from ground to bring the spacecraft to the safe sun-pointing mode. Operations with the zero-gyro real-time attitude determination system began.

16.2. On-Board Software

Zero-gyro Real-Time Attitude Determination

A full description of the design concepts of real-time attitude determination was given in Chapter 14. Although the basic concepts of filtering were the same in three-, two- and zero-gyro systems (see Figure 14.2), the zero-gyro real-time attitude determination system constituted a complete re-design of the on-board real-time attitude determination.

The body rates derived from gyro measurements were replaced on all three axes by angular accelerations which were integrated using discretised perturbation equations on-board. The result of these calculations was an on-board attitude state vector containing Tait-Bryan attitude error angles and body rate estimates which were corrected using Kalman filter techniques by the star mapper measurements. Further parameters were introduced to account for thruster misalignments and differences in performance.

As with the two-gyro system, the design had to take into account the limited memory space for the on-board software.

A critical new component of the system was an on-board acceleration model for all three spacecraft axes. Although the two-gyro system could work with a sinusoidal on-board disturbance torque model (see Chapter 15), the disturbance torques around the x and y axes were far from sinusoidal. The most accurate solution possible was to compute the predicted angular accelerations arising from external disturbance torques by using empirical tables of points spanning on average two hours and refreshed by ground command (two hours was the maximum allowable given the memory space and the resolution of points required). Each table was capable of being refreshed in two halves thereby avoiding discontinuities when the tables were reset. The on-board angular acceleration tables were computed on-ground from predicted disturbance torques, calibrated from the most recent history of the attitude.

The following revised state vector had to be initialised using the modified ground real-time attitude determination system:

- ϕ: Tait-Bryan error angle around the spacecraft x-axis
- θ: Tait-Bryan error angle around the spacecraft y-axis
- ψ: Tait-Bryan error angle around the spacecraft z-axis
- $\dot{\phi}$: error rate around the spacecraft x-axis
- $\dot{\theta}$: error rate around the spacecraft y-axis
- $\dot{\psi}$: error rate around the spacecraft z-axis
- γ_x: angular acceleration around the spacecraft x-axis
- γ_y: angular acceleration around the spacecraft y-axis
- γ_z: angular acceleration around the spacecraft z-axis

Each component of the state vector v was broken down into a predicted (deterministic) component v_d taking the spacecraft dynamics into account, and the other was a corrective term v_1 taking into account uncertainties in the modelling:

(a) nominal scanning law rates ω_X, ω_Y, ω_Z were computed as for the three-gyro real-time attitude determination (see Equation 8.14);

(b) the deterministic components of the angular accelerations ($\gamma_{d,x}$, $\gamma_{d,y}$, $\gamma_{d,z}$) were derived from the on-board acceleration tables, via quadratic interpolation based on the neighbouring points at the time of computation;

(c) the other deterministic components of the state vector, namely the Tait-Bryan error angles (ϕ_d, θ_d, ψ_d) and error rates ($\dot{\phi}_d$, $\dot{\theta}_d$, $\dot{\psi}_d$) were propagated forward from time t_k to time t_{k+1}. Defining the time step $t_i = 16/15$ s, then the propagation equations were:

$$\begin{pmatrix} \phi_d(k+1) \\ \theta_d(k+1) \\ \psi_d(k+1) \\ \dot{\phi}_d(k+1) \\ \dot{\theta}_d(k+1) \\ \dot{\psi}_d(k+1) \end{pmatrix} = \begin{pmatrix} 1 & \omega_Z\ t_i & 0 & t_i & (1+\Gamma_1)\omega_Z\ t_i^2/2 & 0 \\ -\omega_Z\ t_i & 1 & 0 & -(1+\Gamma_1)\omega_Z\ t_i^2/2 & t_i & 0 \\ 0 & 0 & 1 & 0 & 0 & t_i \\ 0 & 0 & 0 & 1 & \Gamma_1\ \omega_Z\ t_i & 0 \\ 0 & 0 & 0 & \Gamma_2\ \omega_Z\ t_i & 1 & 0 \\ 0 & 0 & 0 & 0 & 0 & 1 \end{pmatrix} \begin{pmatrix} \phi_d(k) \\ \theta_d(k) \\ \psi_d(k) \\ \dot{\phi}_d(k) \\ \dot{\theta}_d(k) \\ \dot{\psi}_d(k) \end{pmatrix} + \begin{pmatrix} \gamma_{d,x}\ t_i^2/2 - \omega_X\ t_i \\ \gamma_{d,y}\ t_i^2/2 - \omega_Y\ t_i \\ \gamma_{d,z}\ t_i^2/2 \\ \gamma_{d,x}\ t_i \\ \gamma_{d,y}\ t_i \\ \gamma_{d,z}\ t_i \end{pmatrix} \quad [16.1]$$

(d) the correction components of the state vector, namely the Tait-Bryan error angles (ϕ_1, θ_1, ψ_1), error rates ($\dot{\phi}_1$, $\dot{\theta}_1$, $\dot{\psi}_1$) and angular accelerations $\gamma_{1,x}$, $\gamma_{1,y}$, $\gamma_{1,z}$ were propagated forward in a similar manner to above:

$$\begin{pmatrix} \phi_1(k+1) \\ \theta_1(k+1) \\ \psi_1(k+1) \\ \dot{\phi}_1(k+1) \\ \dot{\theta}_1(k+1) \\ \dot{\psi}_1(k+1) \\ \gamma_{1,x}(k+1) \\ \gamma_{1,y}(k+1) \\ \gamma_{1,z}(k+1) \end{pmatrix} = \quad [16.2]$$

$$\begin{pmatrix} 1 & \omega_Z\ t_i & 0 & t_i & (1+\Gamma_1)\omega_Z\ t_i^2/2 & 0 & t_i^2/2 & 0 & 0 \\ -\omega_Z\ t_i & 1 & 0 & -(1+\Gamma_1)\omega_Z\ t_i^2/2 & t_i & 0 & 0 & t_i^2/2 & 0 \\ 0 & 0 & 1 & 0 & 0 & t_i & 0 & 0 & t_i^2/2 \\ 0 & 0 & 0 & 1 & \Gamma_1\ \omega_Z\ t_i & 0 & t_i & \Gamma_1\omega_Z\ t_i^2/2 & 0 \\ 0 & 0 & 0 & -\Gamma_2\ \omega_Z\ t_i & 1 & 0 & -\Gamma_2\ \omega_Z\ t_i & t_i & 0 \\ 0 & 0 & 0 & 0 & 0 & 1 & 0 & 0 & t_i \\ 0 & 0 & 0 & 0 & 0 & 0 & 1 & 0 & 0 \\ 0 & 0 & 0 & 0 & 0 & 0 & 0 & 1 & 0 \\ 0 & 0 & 0 & 0 & 0 & 0 & 0 & 0 & 1 \end{pmatrix} \begin{pmatrix} \phi_1(k) \\ \theta_1(k) \\ \psi_1(k) \\ \dot{\phi}_1(k) \\ \dot{\theta}_1(k) \\ \dot{\psi}_1(k) \\ \gamma_{1,x}(k) \\ \gamma_{1,y}(k) \\ \gamma_{1,z}(k) \end{pmatrix}$$

where:

$$\Gamma_1 = \frac{I_{yy} - I_{zz}}{I_{xx}}$$
$$\Gamma_2 = \frac{I_{xx} - I_{zz}}{I_{yy}} \quad [16.3]$$

are ratios involving the principal spacecraft moments of inertia (I_{xx}, I_{yy}, I_{zz});

(e) corrections for actuations are performed on the vector (ϕ_d, θ_d, ψ_d, $\dot{\phi}_d$, $\dot{\theta}_d$, $\dot{\psi}_d$) using:

$$\begin{aligned} \phi_d' &= \phi_d + \lambda_x(T_{ax}\delta_{tx} + T_{ax}\ t_{\text{on},x})(1 - \tfrac{1}{2}(t_{\text{on},x} + \delta_{tx})) \\ &\quad + \lambda_{xz}(T_{az}\delta_{tz} + T_{az}\ t_{\text{on},z})(1 - \tfrac{1}{2}(t_{\text{on},z} + \delta_{tz})) \\ \theta_d' &= \theta_d + \lambda_y(T_{ay}\delta_{ty} + T_{ay}\ t_{\text{on},y})(1 - \tfrac{1}{2}(t_{\text{on},y} + \delta_{ty})) \\ &\quad + \lambda_{yz}(T_{az}\delta_{tz} + T_{az}\ t_{\text{on},z})(1 - \tfrac{1}{2}(t_{\text{on},z} + \delta_{t_z})) \end{aligned}$$

$$
\begin{aligned}
\psi_d' &= \psi_d + \lambda_z(T_{az}\delta_{tz} + T_{az}\ t_{\text{on},z})(1 - \tfrac{1}{2}(t_{\text{on},z} + \delta_{tz})) \\
\dot{\phi}_d' &= \dot{\phi}_d + \lambda_x(T_{ax}\delta_{tx} + T_{ax}\ t_{\text{on},x}) + \lambda_{xz}(T_{az}\delta_{tz} + T_{az}\ t_{\text{on},z}) \\
\dot{\theta}_d' &= \dot{\theta}_d + \lambda_y(T_{ay}\delta_{ty} + T_{ay}\ t_{\text{on},y}) + \lambda_{yz}(T_{az}\delta_{tz} + T_{az}\ t_{\text{on},z}) \\
\dot{\psi}_d' &= \dot{\psi}_d + \lambda_z(T_{az}\delta_{tz} + T_{az}\ t_{\text{on},z})
\end{aligned}
\qquad [16.4]
$$

where:

- T_{ax}, T_{ay}, T_{az} are the calibrated accelerations of the $+x$, $+y$, and $+z$ thrusters respectively;
- λ_x, λ_y, λ_z are set to 1 if the actuation is on a positive thruster. If the actuation occurs on the negative thruster, $\lambda = T_a(-)/T_a(+)$ (the ratio of the negative thruster to the positive thruster);
- λ_{xy}, λ_{yz} are corrective coupling terms;
- δ_{tx}, δ_{ty}, δ_{tz} are thruster time offsets which are independent of the length of any actuation;
- $t_{\text{on},x}$, $t_{\text{on},y}$, $t_{\text{on},z}$ are the computed thruster on-times;

(f) the new updated Tait-Bryan error angles and error rates combined the deterministic and corrective terms:

$$
\begin{aligned}
\phi(k+1) &= \phi_d(k+1) + \phi_1(k+1) \\
\theta(k+1) &= \theta_d(k+1) + \theta_1(k+1) \\
\psi(k+1) &= \psi_d(k+1) + \psi_1(k+1) \\
\dot{\phi}(k+1) &= \frac{(\phi(k+1) - \phi(k))}{t_i} \\
\dot{\theta}(k+1) &= \frac{(\theta(k+1) - \theta(k))}{t_i} \\
\dot{\psi}(k+1) &= \frac{(\psi(k+1) - \psi(k))}{t_i}
\end{aligned}
\qquad [16.5]
$$

(g) the measurement extrapolation and innovation computation were similar to the filter used for three-gyro real-time attitude determination. However the state vector (ϕ, θ, ψ, $\dot{\phi}$, $\dot{\theta}$, $\dot{\psi}$, $\gamma_{1,x}$, $\gamma_{1,y}$, $\gamma_{1,z}$) was now updated using a (9×6) array of fixed gains (9 elements to the state vector and 6 different star mapper slits). As before, separate gain sets were included for Quality 1 and Quality 2 stars;

(h) after update, the corrective terms had to be recalculated before the next cycle:

$$
\begin{aligned}
\phi_1 &= \phi - \phi_d \\
\theta_1 &= \theta - \theta_d \\
\psi_1 &= \psi - \psi_d
\end{aligned}
\qquad [16.6]
$$

Sun Acquisition Sensor Controller

There was a need to maintain the spacecraft stability and achieve a certain operational safety with a zero-gyro system. The questions how to manoeuvre the spacecraft and how to maintain the attitude of the spacecraft at any solar aspect angle still needed an answer. Looking for alternative ways of operations, the spacecraft equipment used only for launch and early orbit phase was examined and the sensing and measuring devices still operational in the spacecraft were scrutinised. Finally, using existing features, a way to maintain and correct the measured angles with respect to the Sun was achieved using the sun acquisition sensor aligned with the z-axis. The resulting modification was called the sun acquisition sensor controller (modified sun acquisition manoeuvre 4).

The sun acquisition sensor was capable of sensing the direction of the Sun along two perpendicular axes, provided that the solar aspect angle, (the angle between the Sun and the spacecraft z-axis) never exceeded approximately 70°. Each of the two aspect angles output from the sun acquisition sensor formed a sine wave whose frequency and amplitude were a function of the spacecraft spin rate and of the solar aspect angle. The faster the spacecraft was spinning, the higher the frequency of the sine waves; the further the Sun was from the spacecraft z-axis, the bigger the amplitude. If the spacecraft could have two reference sine waves representing together the nominal spin-rate and the nominal spacecraft angle with respect to the Sun, those references could be compared with the actual waves seen by the solar aspect angle. Then, if deviations induced by external factors could be corrected, the sun acquisition sensor and spin rate would be maintained under control.

The new sine models were propagated using the same orbital oscillator coefficients that controlled the precession of the z-axis around the 43° cone centred on the Sun. Also, the attitude and orbit control system supported an operational mode used for early orbit sun acquisition able to correct deviations in x and y axes by firing the relevant thrusters, with the property that it was triggered by error signals coming from the solar aspect angle. When combining both of the above, an alternative way to control the spacecraft attitude could be derived.

16.3. On-Ground Software

Ground Real-Time Attitude Determination

The major changes in the ground real-time attitude determination chain (described more fully in Chapter 14 and Chapter 15) are now summarised. One new task was developed to support the ground real-time attitude determination: ‘full sky matching’ which is described below.

In order to perform initial star pattern recognition, it was necessary to have information from both B_T and V_T channels to provide not only brightness but colour information. Without both, the range of candidate stars for each match would have been too large to achieve a successful match sufficiently quickly. Once a match was achieved however and the on-board real-time attitude determination was successfully initialised, the knowledge of which stars should be observable in the immediate future meant that the ground

system should be able to continue to run in monitoring mode with only one star mapper channel, thus freeing up the space in telemetry for the necessary science data from the image dissector tube (on-board processing actually used only one star mapper channel).

Telemetry processing and filtering: The software needed to be able to work with star mapper 1 and/or star mapper 2 depending on the selected telemetry format with independent filtering of B_T and V_T channels. In addition a more responsive background noise estimation algorithm was added which additionally filtered out the occasional 'spikes' seen in the telemetry stream leading to a more accurate estimate of the star brightnesses. The opportunity was also taken at this time to install an improved graphical interface for initial scan rate determination.

Slit distinction and gyro correction: The two star mappers worked with two distinct sets of slits (Chapter 2) with the stars crossing first star mapper 2 (B_T channel) followed by star mapper 1 (V_T channel). The time separation between the vertical and inclined slits for one star mapper was between 0.3 s and 7.2 s (at the nominal scan rate) depending on the position of the star with the respect to the scan plane. In matching stars across two star mappers, separations of up to 38 s had to be allowed for. The ground software needed the ability to perform slit distinction for two non-synchronised star mapper channels (B_T and V_T). This involved a complete redesign of this element of the system to allow the determination of the times for each star to cross all four star mapper slits (vertical or inclined) as well as correct the crossing times for actuations.

Since the separation between the two vertical slit transits in each channel were well defined, the algorithm was based on matching the vertical V_T channel transits to the vertical B_T channel transits. When a matching pair of vertical transits had been identified, the inclined transit partners had to be searched among the past transits of the vertical B_T channel transit and the future partners of the V_T channel transit. A suitably long time gap had to be maintained to ensure that all the transits used in a match could only occur for one star and that there was no possibility for ambiguity.

The time to transit all four slits of the vertical slit system gave a coarse estimate of the scan rate which could be used to correct the transit times for scan-rate variation before star pattern matching was attempted.

Full sky matching: The lack of gyro information around any of the three axes meant that significant excursions of the spin axis from the nominal scanning law could be expected after every perigee passage. During three- and two-gyro operations, initial star pattern matching had assumed a known solar aspect angle ξ and initial precession angle $\overline{v}_0$ (see the nominal scanning law definitions in Chapter 8). This new off-line program was developed to determine ξ and $\overline{v}_0$ to within 1° accuracy, using statistical star pattern recognition techniques similar to that employed for the 'star pattern offset matching' task (Chapter 15).

The software required a list of successful star mapper transits from the previous 'slit distinction and gyro correction' task. Both star mapper channels had to be in telemetry. The full sky matching algorithm then pre-selected only rarer stars which were above a certain brightness threshold or colour index to limit the list of potential candidate matches. By way of preparation, a specially filtered version of the Hipparcos Input Catalogue was prepared during the suspended operations phase, with corresponding brightness and colour thresholds.

The algorithm proceeded to match the reduced list of star transits against the filtered input catalogue to produce, for each transit, a list of potential matching stars. Individual candidates for different transits were then considered in a pairwise manner. If the combination of transit times and angular separation were such that the star could have been observed at those times in one or other of the two fields of view, the cross product of the two star vectors (giving the spin axis orientation) was calculated and stored. Once all possible combinations had been considered, the resulting cross product vectors were binned in small areas (typically $2° \times 2°$) of the celestial sphere and displayed graphically as a colour coded density map. A clear peak around the true spin axis orientation was invariably apparent.

The algorithm used for the two-gyro operations to determine the initial heliotropic angle Ω_0 was incorporated into the new software. Once ξ and $\overline{v}_0$ had been identified in this way, the same transits could be used to determine Ω_0. With this knowledge of the 'best fit' nominal scanning law parameters to the current attitude, the real-time star pattern monitoring was able to be initialised.

Typically a good match was obtained with 10 to 15 rare transits, which took between 3 and 5 minutes to collect, assuming that the spacecraft z-axis did not drift by more than 3° in that period.

Star pattern monitoring: The original algorithm for star pattern matching was capable of working with one star mapper channel information or two by suitable changing of on-line parameters. It was however fully expected that the number of ambiguities in matching would rise when only one star mapper channel was available.

Fine attitude estimation: The on-ground Kalman filter was adapted to replace the gyro information by the same theoretical disturbance torque model as was used on-board. Additional thruster misalignments and calibration results were modelled in the attitude and body rate prediction. It was possible to obtain a coarse estimate of the spacecraft body rates by calculating the time for a star to transit all four slits of the vertical and inclined slit systems of one of the star mappers. The time to cross the vertical slits gave the scan rate around the z-axis. The angular speed across the inclined slits, less the scan rate, gave a body rate about an axis perpendicular to the plane containing the z-axis and the star mapper field of view direction. These two measurements were input to the Kalman filter.

Real-time initialisation: The final task was required to reset the new format on-board state vector. Previous versions of the task had performed automatic uplink of the state vector command as soon as a star transit had provided a recent update to the on-ground attitude estimate. This was to prevent accumulation of error due to extrapolation. A manual override was now added to allow the operator to manually command within a few seconds of receiving an on-ground update, after verifying its accuracy. The task was also capable of finding the best fitting nominal scanning law parameters before the programme star file was generated. This would minimise attitude corrections with a subsequent saving in fuel and time.

On-Ground Attitude Reconstitution

A very significant step was the inclusion of the NDAC Consortium's on-ground attitude reconstitution software at ESOC for use in calibrating external disturbance torques and thruster performance. The experience of the Royal Greenwich Observatory (RGO) in

calibrating the external torques and thruster throughout the mission provided considerable insight into the problems confronting the development of the zero-gyro systems. Studies with Matra showed that it was likely that the disturbance torques would require calibration every orbit to provide accurate enough information for the on-board acceleration tables.

The RGO collaborated closely with ESOC to establish a way of installing an adapted version of their system within the ground control system using an additional high performance work-station. They also provided test data for both the on-board and on-ground systems, through the system.

Discrete Disturbance Torque Model

In addition to the off-line on-ground attitude reconstitution software described above, a new program was developed to uplink the commands necessary to refresh the on-board acceleration tables at regular intervals, using input from on-ground attitude reconstitution results. This software had to note when one of the two tables had expired and uplink the next set of data while the other table was active. These tables were obviously dependent on the nominal scanning law and could only be uplinked once the first coarse attitude estimates had been achieved on-ground.

Modified Sun Acquisition Sensor Support

The two new sine wave models for the sun acquisition sensor controller required to be calculated and refreshed once the current nominal scanning law parameters had been defined. These coefficients were calculated off-line and uplinked by manual command.

Additional changes

The nominal focus monitoring task had used gyro derived rate information. This information was replaced by the telemetered real-time attitude determination error rates.

The real-time telemetry and telecommanding chain underwent numerous changes for zero-gyro operations, including:

- additional routing of telemetry to the new workstation required for the ground real-time attitude determination and on-ground attitude reconstitution software and receipt of commands;
- development of a telemetry template and format to allow the recovery of both star mapper streams;
- development of a filing system for the new workstation, keeping a local copy of all required telemetry. Details of on-board time and frame number were also stored;
- conversion of the data reduction consortia tape production software to produce disk format output for transfer to the workstation. The data fed the on-ground attitude reconstitution software. This data reduction consortia tape software incorporated flags for the solar aspect angle and the telemetry mode;
- modification of the uplink system to decompose all commands before transmission.

16.4. Operational Experience

The spacecraft remained spinning at 0.25 rpm until 11 June 1993 when the on-ground software was completed. An initial de-spin to 0.15 rpm was then performed with nutation damping. The next day the spacecraft was de-spun to 0.05 rpm and emergency sun reacquisition was triggered to bring the spacecraft to sun-pointing mode. Earlier fears that the power margin at sun-pointing would be so low that a quick manoeuvre to the nominal 43° solar aspect angle would be required, were unfounded. It was therefore agreed to remain sun-pointing and to attempt to converge real-time attitude determination. The ground real-time attitude determination software worked as expected and was able to perform star mapper filtering with the two semi-functioning star mappers. The attitude was subsequently determined and initialisation of real-time attitude determination on-board attempted. It was then found that the on-board software was incapable of responding accurately to the frequent thruster firings caused by the initialisation command, resulting in an unpredictable divergence after each command.

Within a few hours the ground software was modified to limit changes in the uplinked on-board state vector in such a way as to reduce thruster on-times at the normal mode boundary. In the following days further modifications were made to the on-board and ground real-time attitude determination software.

On-board real-time attitude determination: Convergence of real-time attitude determination under simulations showed sensitivity to star mapper transit frequency. Some attempts were made to incorporate Tycho catalogue stars into the program star file at sparse areas. This was not tested with the spacecraft however. Having verified the performance of the ground real-time attitude determination software in determining body rates, some changes to the on-board Kalman gain set were made to increase the sensitivity to innovations of the transverse body rates on-board. This helped by allowing the real-time attitude determination to stay converged after initialisation from ground, making it possible to collect real-time attitude determination converged data every pass for further analysis. From this it was possible to correlate later divergences with firings, leading to the conclusion that a new thruster calibration was required. Insufficient data for use with calibration software on-ground, was obtained before the end of the mission.

Ground real-time attitude determination: After real-time attitude determination operations resumed, some significant changes were made when it was found that a less strict approach to using three out of four sets of slit crossings still maintained star pattern monitoring and allowed more measurements for on-ground attitude convergence. A further modification was made which limited the commanded change to the on-board state vector to lie just outside the normal mode control bounds. In this way, convergence of the on-board body rate estimates could be maintained. An additional command was added to allow only the on-board body rates to be initialised, while maintaining the old attitude.

Short periods of converged real-time attitude determination were achieved, ranging from 15 minutes to 1 hour, over the next days in sun-pointing mode. The frequency with which these periods of convergence could be achieved was steadily increasing, with the further tuning and familiarisation with the new operations mode.

Throughout this period, investigations by ESOC, Matra Marconi Space and the RGO were on-going concerning the fragility of the on-board real-time attitude determination. It was concluded that the *a priori* thruster calibration made by RGO did not adequately reflect the true thruster performance after such a long sun-pointing with a very different thermal environment. ESOC and RGO worked toward a revised thruster calibration by using the NDAC Consortium's on-ground attitude reconstitution software on the short intervals of real-time attitude determination-converged data obtained.

On 15 June 1993, the spacecraft was manoeuvred to the nominal 43° solar aspect angle having spun down the spacecraft to zero, before invoking the sun acquisition manoeuvre controller with fixed 43° sun acquisition sensor bias. The manoeuvre had an overshoot of $4-5°$ due to initial inaccuracies in the sun acquisition sensor calibration and the spacecraft was returned to sun-pointing. A second attempt some hours later was successful. The modified sun acquisition manoeuvre controller with oscillating sun acquisition sensor biases was successfully used and maintained the spacecraft safely through the next perigee.

Ground real-time attitude determination attempts were unsuccessful due to the high frequency of firings and the very high transverse rates ($20-30$ arcsec s^{-1}) experienced by the spacecraft at that time. Moreover, the fuel consumption under this controller proved to be unexpectedly heavy (30 grams per day). The reason for both phenomena was that the simple sinusoidal model of the sun acquisition sensor bias on-board did not adequately reflect the real sun acquisition sensor output for the spacecraft spinning at 43°. This was a recognised problem beforehand, however neither the sun acquisition sensor calibration nor the simulations had shown that the effect would be so severe.

On 16 June 1993, the spacecraft was manoeuvred back to sun-pointing mode, to improve overall real-time attitude determination performance there. A revised strategy was devised for operating at 43°, using various combinations of control thresholds timed with the phase of the sun acquisition sensor which would have reduced both fuel consumption and transverse rates. This was not attempted however until the overall real-time attitude determination performance could be improved.

17. END OF MISSION ACTIVITIES AND CONCLUSIONS

Satellite operations were continued under increasingly difficult technical circumstances, in the face of solar array and power degradation, gyroscope and thermal control failures, all attributable to the harsh radiation environment in which the Hipparcos satellite was destined to carry out its measurements. Nevertheless, operations were maintained for a total duration of four years, longer than the nominal 2.5-year operational period intended before launch, and long enough for all of the scientific mission goals to be significantly surpassed. Operations were terminated on 15 August 1993, after repeated attempts to communicate with the satellite on-board computer were finally abandoned. The end of the satellite operations was accompanied by a series of diagnostic tests undertaken to establish the final performances of several of the spacecraft and payload subsystems. An assessment of the overall satellite reliability, the data archiving policy, and some considerations of the mission in retrospect are presented.

17.1. End-of-Life History

On 24 June 1993, the central on-board software halted. Subsequent attempts to reload prime and redundant computers failed. Without the central on-board software, no scientific data could be obtained. Investigations indicated that the fault lay with a failed opto-coupler in the on-board computer. These components are radiation sensitive and may have been the cause of the earlier demise of on-board computer 2. It was decided to cool the spacecraft to improve the performance of the opto-couplers.

On 8 July 1993, on-board computer 1 accepted a run command and restarted. Over the next few days, the entire central on-board software was reloaded, although the command failure rate remained high. Once the central on-board software was reloaded and started, investigation began into reducing the high command rejection rate. The problem was traced to the checksum packet at the end of each command being corrupted. It was then possible to load some parameters by slightly modifying the values, thereby changing the checksum. The payload was re-heated to allow ground real-time attitude determination to be performed and to attempt real-time attitude determination initialisation. This was partially successful with real-time attitude determination remaining converged for one hour in one period. However, commanding was still failing

frequently, making initialisation and maintenance of real-time attitude determination convergence impossible for most of the time.

It was realised that a central on-board software patch would be required to provide robust enough commanding for a reasonable science return. Before this possibility had been properly assessed, however, a further deterioration in the on-board computer became apparent, when the last checksum packets were rejected without exception, making any further commanding of that type impossible. A swap of central data units was performed, without improvement. This required that on-board computer 1 would have to be restarted. This was not possible.

No solution was found to work around the failure of the two on-board computers, and the decision was taken by the ESA Project Manager and the ESOC Spacecraft Operations Manager to terminate operations. Before shut down, certain end-of-life tests were carried out, and subsequently the spacecraft was spun up to 10 rpm—there being insufficient fuel to de-orbit the satellite or to change the perigee height significantly. At mission termination all end-of-life tests had been completed and the payload was turned off. The attitude and control system remained on, and the power and data handling sub-systems were nominal. No fuel remained in one tank, while the other had 20 bars (0.75 kg of cold gas) remaining.

Operations of the Hipparcos satellite ceased on 15 August 1993 at 16:00 UTC, when the transmitter was switched off for the last time.

17.2. End-of-Life Tests

In the last two weeks of operations, the satellite was subject to a series of engineering tests. These tests were used to assess the conditions of the various subsystems after the four year period in the revised transfer orbit with its regular passages through the van Allen belts. The tests involved many on-board re-configurations in order to verify units which had never been used before, or units that had already failed in the past and had been substituted by the back-up ones. All test were carried out via mode 3 memory load commands since packet commands were not usable due to the on-board computer failure.

The following sections describe the tests that were carried out, ordered by subsystem. Unless specifically noted otherwise, the tests carried out were terminated after the stated number of cycles (rather than failing at that point).

Payload

Image Dissector Tube 1: the status of image dissector tube 1 was last verified on 29 July 1993 using the internal star pattern assembly. Image dissector tube 1 was still working, but both the electronics and the high voltage power supply voltage readouts were not correct, probably due to a faulty input multiplexer on the payload remote terminal unit.

Image Dissector Tube 1 Chromaticity Filter: the image dissector tube 1 chromaticity filter underwent a destructive test starting on 12 August 1993. It was commanded to the calibration position and then to the wide band again (using a purpose built command

sequence) for 288 cycles without any problem. The sequence contained the memory load, reset, and execute commands spaced to allow the verification of each, and the verification of the filter position via the telemetry.

Image Dissector Tube 1 Shutter: the image dissector tube 1 shutter underwent a destructive test starting on 10 August 1993. It was commanded open and then closed again (using a purpose built command sequence) for 244 cycles without any problem. The sequence contained the memory load, the reset, and the execute commands spaced to allow the verification of each, and the verification of the status of the shutter via the telemetry.

Image Dissector Tube 2 Shutter: the image dissector tube 2 shutter underwent a destructive test starting on 4 August 1993. The shutter was commanded open and then closed again (using a purpose-built command sequence) for 60 cycles before the telemetry readout stopped updating. Then, the internal star pattern assembly light sources were turned on to verify the position of the shutter. The sequence contained the memory load, the reset, and the execute commands spaced to allow the verification of each, and the verification of the status of the shutter via the telemetry.

Internal Star Pattern Assembly: the internal star pattern assembly lights underwent a destructive test starting on 13 August 1993. The switching mirror was moved toward image dissector tube 1 thus allowing image dissector tube 2 to detect the light; then the internal star pattern assembly lights were switched on and off again (using a purpose built command sequence) for 720 cycles without any problem. The commands were verified via the light's associated telemetry parameter and via the image dissector tube raw output.

Electro-Magnetic Torquer: the status of the mechanism drive electronics 2 electromagnetic torquer was last verified on 13 August 1993. The test showed that, apart from the star mapper 2 shutter which went to an intermediate position, none of the mechanisms actually worked.

Mechanism Drive Electronics: the status of the mechanism drive electronics 1 and 2 were last verified on 13 August 1993. The test confirmed that the units were still in working condition, although the secondary voltage of mechanism drive electronics 1 had dropped to 1.44 V instead of the 1.88 V registered at the time of its first anomaly.

Refocusing Mechanism: the functioning of the refocusing mechanism was last tested on 11 August 1993. The results of this test confirmed the correct functioning of the refocusing mechanism, but they showed a discrepancy in the maximum and minimum limits reachable by the grid as the calibration curve indicated a minimum of 20 per cent and a maximum of 80 per cent of the allowed range which were not achieved.

Thermal Control Electronics: the status of the thermal control electronics 1 was last verified on 6 August 1993. The results of this test were in line with the previous tests conducted on thermal control electronics 1, and they confirmed that the unit was not working. The status of the thermal control electronics 2 was last verified on 29 July 1993 for each of the 21 actively controlled areas. Of the 24 controlled areas (21 with connected heaters and 3 spare with no heaters) only 4 still functioned.

Star Mapper 2 Shutter: the star mapper 2 shutter underwent a destructive test starting on 14 August 1993. The shutter was commanded open and then closed again (using a purpose built command sequence) for 160 cycles without any problem. The sequence

contained the memory load, the reset, and the execute commands spaced to allow the verification of each, and the verification of the status of the shutter via the telemetry.

Radio Frequency

Transmitter 2: the status of transmitter 2 was last verified on 14 August 1993. The results of this test indicated that transmitter 2 was working without any problem, but it also showed a lower on-board automatic gain control reading for receiver 2. This situation did not appear to hinder the commanding function of the satellite, and it had already been observed in the past during ground station checks.

Solar Arrays

Solar Panel Degradation Test: the degradation level of the solar arrays was last verified on 10 August 1993 using the open circuit test. The results of this test indicated that there was no major change in the performance of the solar arrays since the previous tests had been conducted.

Solar Panel Shadowing Test: the solar panel shadowing test was carried out on 12 August 1993, using the modified sun acquisition manoeuvre phase 4 controller. Using the modified sun acquisition manoeuvre phase 4 control loop, the spacecraft was first moved to 55° where its status was checked out; using the same method, the satellite was then moved to 65° where the charge current started to drop, but no discharge was observed. The satellite was finally moved to about 75° where the charge current dropped completely, and the batteries started to discharge. Once the desired solar aspect angle had been reached, the attitude control software was configured to standby mode 2, and the spacecraft was spun up to about 500 arcsec s^{-1}. Shortly afterwards, sun acquisition sensor 3 entered its shadow area, and the spacecraft started to drift while it was trying to re-acquire the Sun; from the output of both sun acquisition sensor 1 and sun acquisition sensor 2 it was seen that the satellite completed a revolution around the *x* axis. As soon as sun acquisition sensor 3 re-acquired the Sun, an emergency sun reacquisition was initiated from ground, and the satellite was brought back to the Sun. At the end of the test, no noticeable difference was seen in the behaviour of the solar arrays.

Attitude and Orbit Control System

Accelerometer Package and Earth/Sun Sensor: the Earth/Sun sensor 2 and the accelerometer package B, were last tested during the spin-up manoeuvre carried out between 13 and 14 August 1993. The results of this test showed that the units were still working, although it was not possible to fully test the Earth/Sun sensor due to the satellite's sun-pointing position and spin rate.

Control Processing Electronic Cross Strap Configuration: the two control law electronics systems were last tested in a cross-strapped configuration on 12 August 1993. The results of this test verified the feasibility of this unorthodox configuration.

Gyro Oversampling: the gyros outputs were last tested, using the 10 Hz oversampling system (format 3), on 4 and 5 August 1993; the data samples related to the tests were forwarded to ESTEC, Matra Marconi Space and the 'Laboratoire de Recherches Balistiques et Aérodynamiques' for further analysis.

Gyro Heaters: the status of the gyro heaters was verified in two parts on 27 July and 5 August 1993, due to the gyro mechanism electronics temperature problem. The results of this test confirmed the correct functioning of the heaters of gyros 1, 2, 4 and 5 and the failure in the heater of gyro 3.

Latching Valve: the status of the latching valve A1 was last verified on 29 July. The results of this test confirmed the correct functioning of the latching valve.

Spin-up Manoeuvre: the spacecraft was spun-up to its final rotation speed of 10 rpm in several steps starting on 13 August 1993, via direct thruster firing commands. As a first step, the satellite was moved 8° away from the sun-pointing position using the sun acquisition manoeuvre phase 4 controller and direct thruster firing commands on the $-x$ axis. Once the rates had abated to an acceptable level, the first $+z$ direct thruster firing command was sent bringing the spin rate to 0.25 rpm; this first manoeuvre also introduced a nutation of about 9° half-cone which had to be reduced before progressing any further.

After the nutation had been successfully reduced to less than 1° half-cone, a second step was started bringing the spin rate to 1 rpm. A third step brought the satellite to 3.02 rpm, and was immediately followed by another step which should have brought the satellite to a spin rate of about 5 rpm. During this period, in order to prepare for a different test, a series of attitude and orbit control system re-configurations were carried out; unfortunately, one of them caused the manoeuvre to abort prematurely (the attitude and orbit control system telemetry format was changed from high rate to low rate). Once the re-configuration was completed the spin-up was resumed with a fifth step which brought the rotation rate from 3.75 to 5.1 rpm.

Two more steps were carried out, bringing the spin rate to 9.07 rpm. On 14 August, a spin-down was performed to introduce nutation around the z-axis in order to verify the accelerometer package; during this manoeuvre, tank B was emptied, and had to be swapped for tank A. The de-spin was manually stopped at about 8.52 rpm as there was little or no effect on the nutation amplitude. The last step of the spin-up manoeuvre, was then carried out bringing the spin rate to its final value of 10.04 rpm and leaving about 21 bars in tank A.

Data Handling Subsystem

Central Decoding Unit: the status of central decoding unit 2 was last verified on 23 and 24 July 1993. The result of the test indicated that there was a problem with the commanding chain of central decoding unit 2 (mode 3 commands), thus making it completely unusable.

Memory Bank Module: the status of memory bank module 3 was last verified on 23 and 24 July 1993. The results of these tests indicated that memory bank module 3 was working correctly.

Spacecraft Remote Terminal Unit 2: the status of spacecraft remote terminal unit 2 was last verified on 14 August 1993. The results of this test indicated that spacecraft remote terminal unit 2 worked without any problem.

17.3. Satellite Reliability Assessment

A summary study of the reliability of the Hipparcos satellite during its three years of operation in geostationary transfer orbit compared to the expected reliability after three years in the nominal geostationary orbit was undertaken by Matra Marconi Space. The following hypotheses were assumed for the study: (a) the computed anomalies referred to satellite anomalies only, with ground-segment anomalies not taken into account, and (b) the satellite was considered to be one instrument, rather than an association of different subsystems each with their own reliability.

Figure 17.1 represents the evolution of the reliability of the satellite versus time in geostationary orbit (nominal mission), and the geostationary transfer orbit (revised mission). Figure 17.2 represents the evolution of the failure rate versus time in geostationary transfer orbit (revised mission). It is apparent that the reliability decreased quickly and remained very low after three years in geostationary transfer orbit (between 0 and 0.2) compared to the expected reliability (around 0.6) for the nominal mission in geostationary orbit. The failure rate continuously increased.

17.4. Data Archiving Policy

In accordance with the general data archiving policy at ESOC, the raw satellite data will be archived for a period of 10 years. It is, however, considered most unlikely that access to the raw satellite data at ESOC would again be needed. The data processing tasks undertaken by the data reduction teams were so lengthy, and so complex, that a repeat of the Hipparcos data analysis starting from the raw data will almost certainly never be embarked upon. Intermediate data archives generated by the data reduction teams would be the natural starting point for further analysis, should this ever be considered appropriate.

17.5. Miscellaneous Considerations

Design and Development of the Satellite

Concerning the relationship between the instrument design, manufacture and operation on the one hand, and the data analysis effort on the other, several features of the Hipparcos mission implementation contributed to the mission's success:

(i) acceptance of the mission within the ESA scientific programme was only undertaken after a very thorough scientific and technical evaluation of the end-to-end system (up to the final product) had been made;

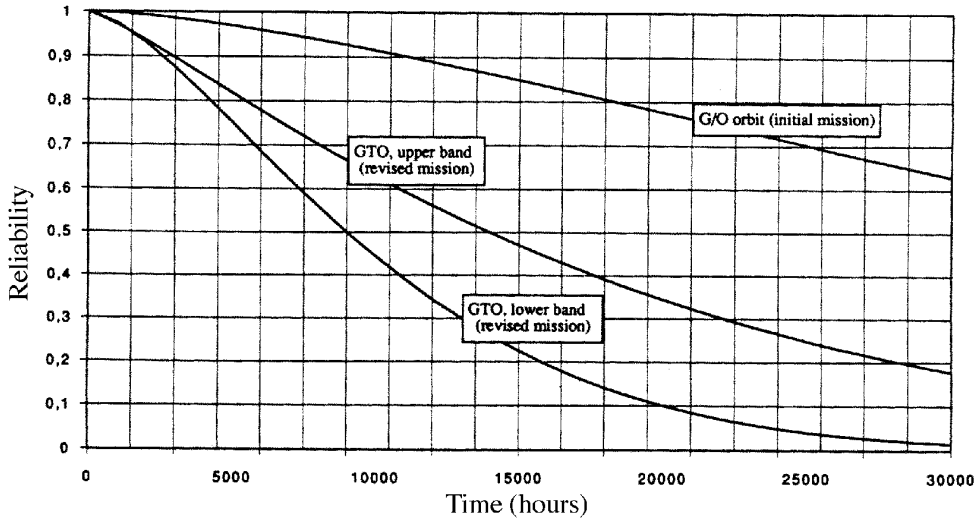

Figure 17.1. *Evolution of the nominal reliability of the satellite as anticipated in geostationary orbit (top curve), and as inferred in the geostationary transfer orbit.*

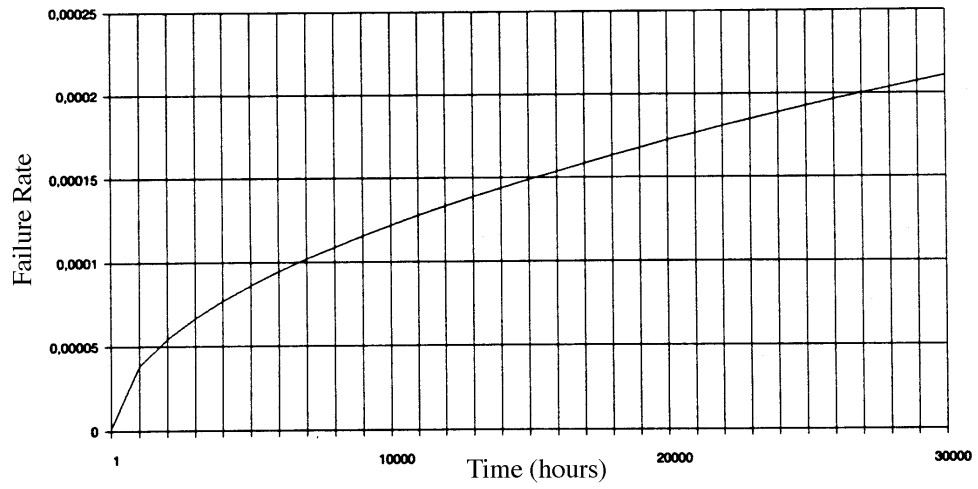

Figure 17.2. *Failure rate, expressed as the probability of a satellite failure occurring per hour, versus time.*

(ii) sole responsibility for the total success of the spacecraft and payload was entrusted to a single prime contractor, who placed great emphasis on the overall (system) error budgets;

(iii) the observing programme definition and data analysis preparations took place in parallel with the satellite design and manufacture;

(iv) for about a year during the early satellite design phase, the industrial prime contractor employed the services of a Science Advisory Group, comprising some of the same scientists that advised ESA through their participation in the Hipparcos Science Team;

(v) a single scientific advisory group with responsibility for all scientific aspects of the mission (the Hipparcos Science Team), and an ESA project scientist with overall responsibility for all scientific aspects of the project from the start of the mission to the final catalogue publication, were important elements in the proper functioning of this very complex mission.

Some of these aspects are not 'standard' ESA policy. Thus while the Hipparcos spacecraft and payload were constructed and calibrated by a single prime contractor, ESA is more typically requested to provide experimental opportunities on specified platforms, with the scientific space research laboratories building the scientific instruments.

It may have appeared superficially questionable for both customer and manufacturer to be advised by the same individuals. That this structure worked may be attributed to the fact that the scientists and engineers concerned, whether employed by the prime contractor, as part of ESA's Project Team, or through scientific institutes as members of the Hipparcos Science Team, were capable of pursuing the difficult challenges of the mission in a collegial atmosphere oriented towards success. This atmosphere tended to dominate the very few incidents where commercial or other aspects surfaced.

A constructive rivalry was present throughout the mission between the scientific consortia, and it engendered a positive collaborative spirit that has been with the Hipparcos mission since its inception. The mission has also maintained a persistent level of independent parallel dedicated effort, conducted in a manner that may well have differed from that encountered in missions where the Agency leaves the scientific instruments to the respective institutes and the platform to the contractor, finding itself in the middle with the task of integration.

Satellite Margins

With the final results in the hostile geostationary transfer orbit being basically superior to those targeted at the time of the project's acceptance by ESA, it is natural to reflect on what the final astrometric results would have been had the correct orbit been achieved. At the same time the question of whether the mission was 'over specified', with corresponding cost implications, should be posed. Although it seems evident in retrospect to conclude that some specifications could have been relaxed while still meeting the target mission goals in the nominal orbit, the full answer to these questions is not so trivial. The satellite would undoubtedly have survived for significantly longer, providing high quality data for perhaps 1.5 – 2 times as long as it did. However that fact was not fully apparent during the satellite design phase: the consumption rate of the cold-gas in particular was the most obvious life limiting factor, budgeted by the prime contractor and installed with a corresponding safety margin. Performing the analysis of this budget

to the level required to make a significantly more precise cold-gas budget would very soon surpass in cost the savings that might be made on cold-gas mass. In particular, improvements beyond the already very sophisticated attitude control strategy were not foreseen, and would have required an in-depth study of ideas like gyroless operations, before creative hopes could have been turned into reality.

There was actually one significant concern that was eliminated by the failure of the apogee motor: the contribution to the pre-launch error budget arising from a potentially significant jitter source through the interior 'bouncing' of the remaining propellant flakes after burnout. Design efforts had been aimed at making the power spectrum of the jitter as weak as possible at the higher frequencies, and the apogee boost motor residuals were the most significant remaining jitter concern. For the same reason the hot-gas (hydrazine) system for orbit manoeuvres was replaced by the cold gas for the operational phase of the mission. The cold-gas thrusters were specifically designed for the low thrusts required, again basically to minimise their impulsive character. Even now it is not clear how much the apogee motor residuals would have affected the measurements. Undoubtedly, the absence of the boost motor mass, and the presence of the residuals, would also have affected the cold-gas consumption. The benefits of a smooth attitude motion, free from such residuals, had been anticipated, but these could never be guaranteed.

In most other respects any 'over specification' can only be identified in retrospect. The photon noise budget, for example, took into account the radiation darkening of the optical elements, allowing for a certain number of solar events during the period of solar maximum which could never be properly predicted before launch. Indeed, for most identified error sources, a small margin was normally demanded, and the cumulative effects proved significant, outweighing the negative effects of a reduction of observing time due to the lack of full orbital coverage.

The mission operational life had been specified as 2.5 years, and the survival for almost 4 years in this harsh environment is certainly more than might have been hoped. Yet a specification of mission survivability for at least 3 years is not the same as specifying its demise after 3.1 years, as evident from experience with other missions such as IUE. It was also clear from the beginning that a longer mission duration would lead to improvements in the proper motions according to time to the power of 1.5, rather than with time to the power of 0.5 as for the parallaxes and positions. These facts may well have provided at least the scientific advisors with an incentive to optimise the margins affecting the mission duration, but only to convincing levels for the prime contractor and the ESA Project Team.

The fact that the mission, even in its adverse orbit, fully surpassed its original goals is basically due to its impressive survival of the harsh conditions, with an unprecedented creativity of the operations team in overcoming increasingly failing hardware. Thus in the end the mission provided as much data as foreseen, but stretched over a somewhat longer time.

Orbit and Perturbing Torques

The successful operation of the Hipparcos satellite in its geostationary transfer orbit provided an unprecedented experiment providing insight into operational possibilities for scientific missions in this harsh environment. It gave information about the radiation conditions at solar maximum in considerable detail, and also gave details of the decay

of semiconductor-based systems with inadequate shielding. The radiation-induced deterioration of the optics, including induced stresses deforming the highly accurate mirrors, was modelled in detail.

The carefully designed thermal control subsystem performed well within the revised mission, avoiding significant deterioration of the science data. Also the detailed description of the disturbing torques, such as due to the magnetic field and gravity gradient torques, will facilitate the future design of attitude control systems for very demanding missions in such orbits. In order to avoid the atmospheric drag, which is very difficult to model, the minimum perigee height should be around 550 km.

Many other aspects of the satellite functioned flawlessly, including the image dissector tube and photomultiplier (star mapper) detectors, and their associated electronics.

The mass implications for going to geostationary orbit instead of operating in the transfer orbit are very significant, amounting to almost 50 per cent. It may be that the dedicated design of a mission and its associated hardware might be optimised for such an orbit, with resulting benefits even when taking into consideration the significant additional operational constraints. Mission planning with more forward uplink, supporting significant periods of loss of direct satellite contact, could minimise operational implications in a manner which was impossible for Hipparcos. Improved uplink and downlink storage capabilities on board, and increased uplink and downlink budgets during periods of visibility, may evolve in the future to make that less of a drawback.

A future astrometric mission aiming at improved accuracies of tens of microarcsec will face as large an advance in terms of precision as has been achieved with Hipparcos. It is not at all evident that such goals could be achieved with 'only' a Hipparcos-type understanding of the hardware and mission analysis. The demands of such a mission would evidently not tolerate a geostationary transfer orbit operation, and a geostationary or L2 orbit would be vastly preferable, given the environmental stability. A solid boost motor would not be employed, although this choice for Hipparcos was determined by its record for dependability as well as cost. In retrospect it might well have been a better choice to have included a larger supply of hydrazine; even the rather low thrust of the hydrazine thrusters was good enough for the perigee raise manoeuvre in only a few orbits. The high thrust of the original solid fuel boost motor also resulted in certain design constraints: acceleration forces of more than 6g, and the potential jitter source of the motor residuals referred to above. A lower thrust propellant would demand a longer period required to reach the final orbit, but already with the solar generators deployed.

Another issue that will merit a more detailed analysis for a future high-accuracy astrometric mission is operation with the gyroscopes turned off. A rotating spacecraft which 'observes' its own attitude with high accuracy is potentially a better gyro than almost any 'regular' high accuracy gyroscopes system. The performance would mainly depend on the maximum unmodelled angular accelerations, i.e. on external disturbing torques and moments of inertia. These contributions can be kept small enough when the satellite is kept well away from the Earth surface, but become too complicated to handle in a geostationary transfer orbit.

While clearly required during the early orbit and station acquisition phases, gyroscopes present two drawbacks thereafter: residual torques (depending on the configuration of the active gyros), consuming cold gas or other attitude actuations, and moving parts, at undesirable angular frequencies which may generate jitter in the measurements. For

a future mission targeting two orders of magnitude higher precision such concerns will need to be carefully addressed.

Understanding the Hipparcos Payload

A driving concern during the design and construction of the satellite and payload was always that of some unforeseen and 'indescribable' effect appearing in the satellite or in its data stream. In engineering terms, the mission's success centred around the concept of a measurement apparatus, mechanically defining a measurement reference (albeit with an optical readout, to about 1 nm in a device of 1.5 metre in size). This concern resulted in the satellite and payload specifications being formulated in very fine detail (reflected in the 'Invitation to Tender' prepared by ESA for industry in 1981). While all significant effects were indeed duly accounted for, at least three smaller unforeseen effects became apparent in the data. Although these were so well 'documented' in the measurements themselves, and facilities existed in either the on-board or on-ground data analysis, or on-board hardware, to correct for them, their unforeseen appearance should be noted:

(i) differential grid rotation: this had not been anticipated, although the software for both data reduction consortia were very easily able to accommodate the unforeseen effect of different rotation angles of the main grid about the optical axis for the two different fields of view;

(ii) (differential) flexure of mirrors due to radiation exposure. The effect is described in Chapter 10. In addition to a common linear component, an additional differential effect was caused by non-uniform shielding of the back of the folding flat mirror, and caused both a differential evolution of the focus for the two fields and an evolving discrepant phase difference between the first and the second harmonic of the modulation. Such an effect qualified as one of the effects for which it was mandatory to downlink the raw photon counts, rather than just compressed modulation parameters;

(iii) along-scan attitude jitter due to mechanical relaxation in the solar arrays due to thermal effects after emergence from eclipses (see Chapter 11). In practice, this affected an almost insignificant fraction of the overall data set, which was easily recognised as corrupted, and duly discarded.

With the emphasis of the satellite design being focussed on the accurate control of random and systematic errors, it is noted that two other means of suppressing potential systematic errors were discussed in advance of launch, but never implemented:

(i) the sense of the satellite rotation was not strictly part of the instrumental design, and thus reversing the spin could have helped determine and suppress errors affected by the spin sense, or by the sequence of observations resulting from a particular spin sense. This was considered (but never placed as a requirement) during the mission design and planning, but was abandoned around 1986 for reasons of induced additional complexity in the on-board and on-ground software. In practice, no effect that could only be traced by spin reversal had been identified, and even in retrospect, no parameter affecting the final results has been identified that could have been (better) determined by means of spin reversal;

(ii) another feature that might have been exploited more rigorously was the *independent* use of the first and the second harmonics of the modulation by the main grid at the

level of the great circle-reductions and the sphere solution. These measurements almost correspond to independent instruments, the discussion of which might well have contributed to the detailed understanding of the payload. That little, if any, astrometric weight was lost using the adopted data reduction procedures is, however, evident.

On-Ground Versus In-Orbit Calibration

A sizeable ground-based calibration programme was carried out for Hipparcos, in common with all space programmes, and these revealed certain payload problems, most notably a problem of vignetting in one of the fields of view due to misalignment. Thermal cycling was also demonstrated to leave hysteresis in the glue originally selected for the mounting pads, a problem avoided by an alternative choice of glue, and resulting in the spare flat folding mirror becoming the flight model. Although effective in putting a well adjusted and properly verified payload together, the on-ground calibration thereafter strictly provided only starting values for the parameters to be evaluated in flight. Without exception the in-orbit calibration proved more extensive than what had been achieved on ground: in particular improved photometric and spectral responses were derived in orbit. These in-orbit improvements were not surprising, and even modifications to certain of the calibration parameters had been foreseen—thus it was considered unlikely that the payload would retain its calibrated parameters through the heavy load phase of launch and early orbit manoeuvre, and moisture outgassing was expected to lead to an evolution of the best focus position after launch.

The only on-ground calibration that was not fully re-performed in flight, although it was subject to considerable verification using the in-flight data, was the medium-scale grid calibration. The verifications carried out confirmed the details of the on-ground calibration, and proved the grid to be of very high quality. Any remaining grid-induced errors were not capable of even marginally acting as an additional ‘noise source’ in the data.

On-Board Data Compression

At the time of the mission design the downlink budget, amongst other things, was driven by a requirement to avoid significant data processing on board: this was considered to be too high a risk for such an advance in measurement precision in an area that had been hampered historically by significant systematic errors. Any data reduction on board (beyond the actual coding of the photon counts as used for Hipparcos) would implicitly have imposed some model into the data. ‘Undoing’ such a model on-ground would have been impossible, and this risk far outweighed other considerations such as the consequent demands on the downlink budget, both in terms of photon counts (the dominant contribution to the telemetry), as well as in many instrumental parameters, such as the on-board thermistors.

Subsequent experience of the Hipparcos data analysis has confirmed that the end result of the complex data reductions has indeed led to an understanding and modelling of the missions measurements, the payload mechanics, the optics, and the detection systems, and that these may be considered to have been essentially ‘perfectly’ understood, resulting in photon noise largely dominating the final error source. That experience was guided throughout the scientific data reductions by the detailed comparisons between the two reduction consortia. It seems evident that any errors that would have remained in any (encoded) data analysis algorithms would have seriously weakened this

conclusion. While the data could have been downlinked after compression of the photon counts according to Equation 1.1, such a conclusion might not have been reached without the 'luxury' of the raw data, and indeed without the two reduction consortia with basically independent approaches to the data analysis.

17.6. Overall Success of the Hipparcos Mission

Targeted for an operational lifetime of two and a half years, more than three years of high-quality star measurements were eventually accumulated. The Hipparcos mission finally superseded all of its original scientific goals, resulting in milliarcsec astrometric measurements of positions, distances and space motions for more than 100 000 stars, and an additional catalogue of high-precision astrometric and photometric data for more than one million stars.

APPENDIX A

THE ESA-ESOC OPERATIONS TEAM

The following is a list of people in the Hipparcos launch team and recovery mission team at ESOC. Many other permanent and contract staff were also involved in such areas as ground station manning, general technical and administrative support. Their contribution is also recognised and appreciated. The launch team is listed by technical area including company affiliation where appropriate. When no such company information appears, it should be inferred that the person in question was permanently employed by ESA.

Launch Team

Flight Control

D. Wilkins		Flight Operations Director
W. Wimmer		Deputy Flight Operations Director
M. Barrett		Ground Operations Manager
J. Dohm		Ground Operations Manager
E. Garcia		Ground Operations Manager
D. Heger		Spacecraft Operations Manager
H. Nye		Spacecraft Operations Manager
M. McCaig	Vega	Spacecraft Operations Engineer
J. Nolan	Vega	Spacecraft Operations Engineer
C. Sollazzo		Spacecraft Operations Engineer
R. Leroux	Thomson	Spacecraft Analyst
P. Vogt	Elekluft	Spacecraft Analyst
E. Schambion	Thomson	Spacecraft Controller
R. Southworth	Thomson	Spacecraft Controller
J. Kouwenberg		Mission Planning
R. Maertens		Mission Planning
J. Murray	Thomson	OCC Support
A. Vega-Izquierdo		OCC Support

Mission Analysis

J. van der Ha		Ground Segment Manager
H. Klinkrad		Mission Analysis
G. Janin		Mission Analysis

Flight Dynamics

R. Muench		Flight Dynamics Coordinator
L. Fraiture		Flight Dynamics Coordinator
M. Soop		Flight Dynamics Coordinator
A. Schütz		Flight Dynamics Coordinator
L. Agrotis	Logica	Orbit Determination
J. Dow		Orbit Determination
O. Mikkelsen	CRI	Orbit Determination
S. Pallaschke		Orbit Determination
W. Peterhaensel	mbp	Orbit Determination
M. Schaefer		Orbit Determination
H. Deasy	Captec	Attitude Determination
R. Ellis	Science Systems	Attitude Determination
G. Gienger		Attitude Determination
J. Palmer	Logica	Attitude Determination
M. Walker	Science Systems	Attitude Determination
N. Wiengarn		Attitude Determination
A. Batten	Science Systems	Attitude Support
J. MacLaren	Logica	Attitude Support
A. McDonald	Logica	Attitude Support
F. Tesseyre		Attitude Support
J. Allan	Logica	Payload Support
P. Davies	Logica	Payload Support
F. Hechler		Manoeuvre Optimisation
T. Morley		Manoeuvre Optimisation
R. Mugellesi		Manoeuvre Optimisation
J. Bishop	Science Systems	Manoeuvre Support
P. Mahr		Manoeuvre Support
H. Stace	Logica	Manoeuvre Support
P. de Broeck†		Quality Assurance
P. Kristiansen	CRI	Quality Assurance
W. Meyer	mbp	Quality Assurance
H. Mueller	mbp	Quality Assurance
H. Ruegheimer	mbp	Quality Assurance
S. Baltzer		Task and Data Handling
P. Gladney	CRI	Task and Data Handling
T. McFarlane	Science Systems	Task and Data Handling

Software Support

N. Head		HDCS Software Coordinator
R. Blake	Logica	HDCS Software Support
G. Di Girolamo		HDCS Software Support
J. Harborne	Logica	HDCS Software Support
M. Keenan	Logica	HDCS Software Support
K. Keyte	Logica	HDCS Software Support
C. Spanholtz	Logica	HDCS Software Support
A. Wollenberg	Logica	HDCS Software Support
P. Maigne		MSSS/SCOS Software Coordinator
M. Ahier	Logica	MSSS/SCOS Software Support
J. Bowers	Logica	MSSS/SCOS Software Support
B. Mullet		MSSS/SCOS Software Support
F. Prati	CAP-SESA	MSSS/SCOS Software Support
H. Thielmann	CAP-SESA	MSSS/SCOS Software Support
M. Vanhamme	CAP-SESA	MSSS/SCOS Software Support
T. Velin	CAP-SESA	MSSS/SCOS Software Support

Computer Support

H. Loetterle		Computer Coordination
P. Neumeister		Computer Coordination
K. Stehling		Computer Coordination
R. Gale	Serco	Computer Operations
N. Godfrey	Serco	Computer Operations
C. Clark	Science Systems	DMSS Computer Software Support
J. Franks		DMSS Computer Software Support
P. Hughes	Science Systems	DMSS Computer Software Support
T. Norris	Science Systems	DMSS Computer Software Support
I. Diddams	Science Systems	MSSS Computer Software Support
J. Everitt	Science Systems	MSSS Computer Software Support
B. Komasa		MSSS Computer Software Support
S. Lane	Shade	MSSS Computer Software Support
A. Habermann	Serco	OPSLAN Support
S. Jespersen	CRI	OPSLAN Support
H. Hammann		Off-line Mainframe Support
F. Kelly	Cara	Off-line Mainframe Support
T. Kennedy	Cara	Off-line Mainframe Support
S. Llorente		Off-line Mainframe Support

Engineering Support

T. Beck		Engineering Support
W. Wittwer		Engineering Support

Network Support

A. Martin-Crespo		Malindi Ground Station
J. Comas-Bullo		Malindi Ground Station
G. Wittig		Odenwald Ground Station
N. Bobrinsky		Kourou Ground Station
P. Fauquet		Kourou Ground Station
A. Nicot		OCC
H. Dorner	Elekluft	OCC Maintenance
H. Groll	Elekluft	OCC Maintenance
D. Rossin	Elekluft	OCC Maintenance
J. Schloesser	Elekluft	OCC Maintenance
T. Spoerer	Elekluft	OCC Maintenance
D. Weinitschke	Elekluft	OCC Maintenance
P. Jensen		Simulations Support
S. Rodgold		Simulations Support
G. Schreiber	Elekluft	Simulations Support
M. Sheldon	Serco	Simulations Support
J. Fay		DPSS Support
J. Huber	Elekluft	DPSS Support
A. Kabir	CAP-SESA	DPSS Support

GTS Support

G. Schellenberg		GTS Coordinator
W. Waechter		GTS Support

Revised Mission Operations Team

Dietmar Heger		1989–93	MOD	Spacecraft Operations Manager
Howard Nye		1989–90	MOD	Spacecraft Operations Manager
Jozef van der Ha		1989–93	MOD	Ground Segment Manager
Hans-Heinrich Klinkrad		1989	MOD	Mission Analysis
Oscar Ojanguren		1989–93	MOD	Spacecraft Operations Engineer
Claudio Sollazzo		1989–93	MOD	Spacecraft Operations Engineer
Mike McCaig	Vega	1989–90	MOD	Spacecraft Operations Engineer
John Nolan	Vega	1989–90	MOD	Spacecraft Operations Engineer
Joerg Fischer	mbp	1990–93	OAD	Flight Dynamics Engineer
„	Vega	1993	MOD	Spacecraft Operations Engineer
Rene Leroux	Thomson	1989–90	MOD	Spacecraft Analyst
Peter Vogt	Elekluft	1989–90	MOD	Spacecraft Analyst
Richard Southworth	Thomson	1989–90	MOD	Spacecraft Controller
„	„	1990–91	MOD	Spacecraft Analyst
Mario Monaldi	Vitrociset	1989–90	MOD	Spacecraft Controller
„	„	1990–93	MOD	Spacecraft Analyst
Eric Schambion	Thomson	1989–91	MOD	Spacecraft Controller
„	„	1991–93	MOD	Spacecraft Analyst
John Barry	Thomson	1989–93	MOD	Spacecraft Controller
Rudi Ciarletta	Vitrociset	1989–93	MOD	Spacecraft Controller
Alan Flowers	Thomson	1989–92	MOD	Spacecraft Controller
Trevor Thomson	Serco	1990–93	MOD	Spacecraft Controller
Aldo Ingegnieri	Vitrociset	1990–91	MOD	Spacecraft Controller
Mike Seidel	Elekluft	1991–93	MOD	Spacecraft Controller
Lance Hayward	Serco	1991–93	MOD	Spacecraft Controller
Frank Lautenschlaeger	Thomson	1992–93	MOD	Spacecraft Controller
Andrew Andris	Elekluft	1993	MOD	Spacecraft Controller
Steve Grant	Serco	1993	MOD	Spacecraft Controller
Alain Schütz		1989–93	OAD	Flight Dynamics Coordinator
Paul de Broeck†		1989–92	OAD	Flight Dynamics Quality Assurance
C. van der Beken		1989	OAD	Flight Dynamics Engineer
Alastair McDonald	Logica	1989–93	OAD	Flight Dynamics Engineer
Alan Batten	Science Systems	1989–93	OAD	Flight Dynamics Engineer
Poul Kristiansen	CRI	1989–93	OAD	Flight Dynamics Quality Assurance
John Auburn	Science Systems	1989–91	OAD	Flight Dynamics Engineer
Philip Davies	Logica	1989–90	OAD	Flight Dynamics Engineer
John Allan	Logica	1989	OAD	Flight Dynamics Engineer
„	„	1990–93	DPD	Software Support
Jimmy MacLaren	Logica	1989	OAD	Flight Dynamics Engineer
Kevin Galloway	Science Systems	1989–91	OAD	Flight Dynamics Engineer
Beatrice Mueller	mbp	1989–90	OAD	Flight Dynamics Engineer
Lisa Retbøll	Logica	1989–90	OAD	Flight Dynamics Engineer
Steen Retbøll	CRI	1990–93	OAD	Flight Dynamics Engineer
Mark Thomas	Science Systems	1990–92	OAD	Flight Dynamics Engineer
Dom Lindars	Logica	1990	OAD	Flight Dynamics Engineer
Paul Shah	Logica	1990–91	OAD	Flight Dynamics Engineer

Nick White	Logica	1990–92	OAD	Flight Dynamics Engineer
„	„	1992–93	DPD	Software Support
Vippin Gupta	Science Systems	1991–93	OAD	Flight Dynamics Engineer
Juan Morras	GMV	1991–93	OAD	Flight Dynamics Engineer
Karen Rollin	Logica	1991–93	OAD	Flight Dynamics Engineer
Mike Walker	Science Systems	1992–93	OAD	Flight Dynamics Engineer
Carsten Petersen	CRI	1992–93	OAD	Flight Dynamics Engineer
Pedro Schoch	GMV	1992–93	OAD	Flight Dynamics Engineer
Francisco Martinez	GMV	1993	OAD	Flight Dynamics Engineer
Rainer Kresken	mbp	1993	OAD	Flight Dynamics Engineer
Johann Schoenmaekers		1993	OAD	Flight Dynamics Quality Assurance
Nigel Head		1989–91	DPD	Software Support Coordinator
Angela Wollenberg		1991–93	DPD	Software Support Coordinator
Jon Harborne	Logica	1989–90	DPD	Software Support
Charles Spanholtz	Logica	1989–90	DPD	Software Support
Rick Blake	Logica	1989–92	DPD	Software Support
Mike Keenan	Logica	1989–90	DPD	Software Support
Honour Luckins	Logica	1990–91	DPD	Software Support
Mark Hampson	Logica	1990–91	DPD	Software Support
Matthew Couch	Logica	1991–92	DPD	Software Support
Stuart McMillan	Logica	1992–93	DPD	Software Support
John Calladine	Logica	1992–93	DPD	Software Support

Acronyms:

DMSS	Distributed Mission Support System
DPD	Data Processing Division
DPSS	Data Packet Switching System
GTS	General Technical Services
HDCS	Hipparcos Dedicated Control System
MOD	Mission Operations Department
MSSS	Multi-Satellite Support System
OAD	Orbit and Attitude Division
OCC	Operations Control Centre
OPSLAN	Operational Local Area Network
SCOS	Spacecraft Control and Operations System

APPENDIX B

SATELLITE ANOMALIES

In addition to the failure of the apogee boost motor, a total of 82 anomalies occurred throughout the routine mission, arising mainly from 'single event (radiation) upsets' or hardware failures on-board or on-ground. They are summarised here sequentially, but organised by subject whenever appropriate. The formal Anomaly Report (AR) number and applicable date(s) are given.

Sun acquisition sensor **AR number 1 (89-10-10)**

During the hydrazine sun acquisition manoeuvre the sun acquisition sensor outputs, used to monitor the manoeuvre performance, did not give the expected output. There appeared to be no overlap in the sensor coverage between sun acquisition sensor 1 and sun acquisition sensor 3, and furthermore the maximum output of sun acquisition sensor 1 was much less than expected. The only impact was that eclipse emergency mode would be affected. To cover this possibility, the sun acquisition sensor 3 output was recalibrated during the scanning law acquisition manoeuvre in October 1991.

Solar array panel 3 microswitch status **AR number 2 (89-10-10)**

After the solar array panels deployment, the telemetry indicated a 'no-latch' status on panel 3. Power supply analysis confirmed, however, that the panel had deployed.

Automatic reconfiguration order **AR number 3 (89-10-11)**

After the fill-in antenna deployment commands were executed on-board, an automatic reconfiguration order was issued by the attitude control software, reconfiguring the attitude and orbit control system to the redundant branch. A reconfiguration to the attitude and orbit control system prime branch took place and no operational impact occurred.

Battery 1 & 2 end of charge **AR numbers 4, 7, 40, and 42**

The batteries did not reach the commanded end-of-charge voltage on several occasions, resulting in a thermal runaway of the batteries temperatures. The charge had to be terminated from ground. The end-of-charge voltage settings were revised, taking into account the different thermal environment of this orbit.

Bad telemetry with ranging transponder on **AR number 5 (89-10-11)**

The telemetry quality changed from 'good' to 'bad' with every telecommand transaction when the ranging transponder was on and high data rate selected. This anomaly was already detected during ground test, but not reflected in relevant documentation. The operational procedures were updated such that ranging and commanding were exclusive.

Tank temperature **AR number 6 (89-10-11)**

Two temperature parameters of the hot gas tanks showed inconsistent values. A thermistor failure of one temperature reading seemed to have been the cause. The fault had no impact on the mission.

Emergency sun reacquisition order **AR number 8 (89-10-11)**

After acquisition of signal, following a perigee and eclipse pass, an emergency sun reacquisition order was triggered and a reconfiguration to the B branch was initiated. From an investigation of the telecommand history file, the workstation event log, and the Hipparcos dedicated control system message file, it was possible to confirm that the emergency sun reacquisition order disable command sent was rejected by the satellite due to sequence counter error.

Real-time attitude initialisation **AR numbers 9, 10 and 11 (89-10-12)**

Several attempts to achieve real-time attitude convergence during sun-pointing operations failed due to early loss of signal or too high background noise on the star mapper.

Image dissector tube piloting **AR number 12 (89-10-19)**

Using the computed coil currents calibration matrix from the latest grid reference marks and internal star pattern assembly results, the image dissector tube data generated from the on-board processing of real stars indicated that the instantaneous field of view was not correctly piloted over the image dissector tube. Based on Matra inputs, the coil currents calibration matrix calculations were revised curing this anomaly.

Excessive star mapper noise **AR number 13 (89-11-09)**

The problem of no real-time attitude determination due to excessive star mapper noise, arising from solar flares and excitation of van Allen belts, occurred repeatedly in the non-nominal orbit, and led to loss of observing time throughout the mission.

Single event upsets **AR numbers 14–15, 18, 20–21, 28–29, 34, 38, 45–49**

The anomalies related to the single event upsets were of a recurring nature and were recovered by, for example, reloading the on-board computer, the programme star file, or by resetting the logic of the unit affected. Two anomalies were detected during subsequent reloading of the on-board computer and were of non-reoccurring nature (AR number 21 and AR number 46).

Star mapper shutter closure **AR number 16 (89-11-09)**

On 6 November 1989, the mechanism drive electronics 1 over-exposure flag triggered, indicating that the star mapper shutter had not closed before the occurrence of an occultation. Subsequent analysis showed that the shutter did not close at the expected time since the time-tagged command had an incorrect time entered for execution by the mission plan.

Multiplexer failure **AR number 17 (89-12-04)**

Multiplexer channel 8 of input multiplexer 2 failed. All subsequent telemetry acquired through this channel was therefore false.

Focus activation **AR number 19 (90-01-04)**

The focus monitoring performed during periods with a step-by-step activation of the refocusing mechanism indicated that the on-board focusing operation was not working properly. Investigation confirmed that the origin of the anomaly was in the refocusing mechanism itself. The design of this mechanism was such that a motor rotation of 60° corresponded to a grid movement of a refocusing step (1.4 μm) and a rotation of 13.5° at the level of the wheel acting as magnetic brake. During ground testing the refocusing mechanism had been activated in a step by step manner. No malfunction was detected, except that the magnetic brake was found to be too small. The permanent magnets had been replaced by stronger magnets. After this change, the refocussing mechanism was not re-tested in a step by step manner, but only by several steps and no malfunction was detected. Due to the stronger magnets, the step by step mode did not function and had to be replaced by at least a two step operation. To allow a better fit between the actual defocus curve and the model (straight line), the last 30 days of observations (instead of 50 days) were used to compute the next grid displacement.

Image dissector tube analogue mode **AR number 22 (90-01-31)**

The bright star Alpha Centauri was scheduled to be observed in the analogue mode, but the analogue mode triggered too early, thus corrupting the observation of the preceding star (a faint one) which was supposed to be observed in the photon-counting mode. Thereafter, all stars were observed in photon-counting mode.

Central on-board software error **AR number 23 (90-02-14)**

This anomaly was detected whilst preparing special procedures for the ‘long’ eclipse season. A cross-correlation was made between the power the central on-board software commanded to the thermal control electronics and the actual thermal control electronics input current. From the averaging of the thermal control electronics input current over time it was determined that the thermal control electronics consumed about 47 W. The central on-board software however indicated consistently, via the thermal report packet, that it was sending approximately 60 W. The calibration curve to determine the central on-board software telemetered power used a least significant bit of 0.004 W. A new calibration curve was calculated and implemented with a least significant bit of 0.003 W which corrected the anomaly.

Emergency sun reacquisition order **AR number 24 (90-02-14)**

On the morning of 12 February 1990 the automatic commanding task failed to send the commands to disable/enable the emergency sun reacquisition order for the upcoming eclipse. Following an investigation it was discovered that no eclipse commands had been scheduled by the mission planning task for all eclipses after midnight on 11 February 1990. The source of the problem was identified as a typing error in the sequence activity file used by the mission planning task to attach command sequences to activities such as occultation, eclipses and calibrations. Prior to the generation of the mission plan, on 9 February 1990, for the coming week, the sequence activity file was modified to support Goldstone. The fields for occultation, eclipses and calibrations were not modified and hence not checked following the generation of the new mission plan. On generation of the mission plan the software failed to find a match for the eclipse activity sequence and hence failed to generated the appropriate commands.

Unexpected closing of shutters **AR number 25 (90-03-07)**

At 05:28 UTC of 12 February 1991 the image dissector tube 2 shutter closed followed within 10 s by the closing of the star mapper 2 shutter. After investigation of the telemetry, mission plan, command history and time-tag display, it was concluded that: (a) the shutter closure was not triggered by the bright object detector; (b) the mission plan did not identify any commands to be uplinked at this time; (c) the command history did not show any command being uplinked at this time (manually) or as a time-tagged command to be executed at this time; (d) the time-tag displayed confirmed (c) above. The two commands to close the shutters were sent about 6.5 days earlier just as a change of ground stations from Odenwald to Kourou took place. Unfortunately Kourou had portable simulator system data on-line at the time the two commands were uplinked automatically. Therefore, the on-board time from which the Hipparcos dedicated control system calculated the execution time of the time-tagged commands was based on the format counter from the portable simulator system data instead of the satellite data.

Payload remote terminal unit **AR number 26 (90-04-02)**

In the prime payload remote terminal unit, which provided the data interface between the payload and the satellite central processor, the remote control core failed causing the loss of all payload housekeeping telemetry. A reconfiguration to the back-up unit had to be implemented.

Solar array 3 temperature **AR number 32 (90-05-15)**

The average temperature readings over one spacecraft revolution (128 mins) from the three solar arrays should have been within one least significant bit (4°) of the calibration curve. Moreover, the measured minimum and maximum temperatures for each solar array should have been identical for this time period. However, after 6 February 1990, the average temperature of solar array 3 started to differ from the temperatures of array 1 and 2. By 14 February 1993 the difference was almost 4.6° in the average temperature. The temperature difference was caused by power not being dumped on this panel. Thus the temperature was lower than on the other panels.

Star mapper rejection of very bright stars **AR number 33 (90-05-28)**

This anomaly refers to the rejection of very bright stars on the basis of 'main lobe truncation at the border'. The observed anomaly was a direct effect of the central on-board software patch which was implemented to correct for false stars detection during high background noise periods. The objective of this patch was the deletion of all star transits which were characterized by only one valid maximum after correlation. All the star transits which were rejected for the above mentioned reason were assigned an error code which, for simplicity reasons, was the same as the one allocated for the 'main lobe truncation error'. The majority of these rejections were due to the star side lobes being below the minimum allowed threshold. However, this problem applied only to a limited number of bright stars. This anomaly had no impact on the mission.

Gyros 3 and 4 **AR numbers 35 (90-07-03) and 52 (91-08-06)**

The satellite was equipped with five rate-integrating gyros. Two of these measured rates around the spin axis (gyros 4 and 5), one being for back-up. The other three gyros were in the plane perpendicular to the spin axis (gyros 1 to 3), one being the back-up for the other two. Gyro 3, which acts as a back-up to gyro 1 or 2, suffered a failure in its electronics such that the operating temperature of 70 °C could not be reached, and this implied that no gyro back-up in the plane perpendicular to the spin axis existed any more. Gyro 4 (along the spin axis) showed erratic behaviour on several occasions which caused irregular attitude control firings leading to loss of real-time attitude convergence. Reconfiguration to gyro 5, the back-up spin-axis gyro, was performed in order to continue the nominal mission. This of course implied that no back-up existed any more for this axis. With the possibility of a further gyro failure, investigations and modifications were carried out to operate the spacecraft with only two gyros. Software modifications to the on-board control logic and the ground supporting software modules were developed to cope with a possible gyro 5 failure. Further modifications were developed should gyro 1 or 2 fail.

Loss of spacecraft attitude **AR number 36 (90-08-22)**

After the perigee pass in the evening of 16 August 1990 and the subsequent crossing of the inner and outer van Allen belt, the spacecraft had diverged from its optimal pointing, necessitating an uplink of the Tait-Bryan error angles. The error angles were uplinked at 23:15 UTC causing several attitude and orbit control system parameters to raise out of limit alarms because of large thruster firings around all three axes. Moreover, no convergence of real-time attitude had been achieved. During the subsequent validation of the ground data used to uplink the error angles, the limited history file did not contain the magnitude of the uplinked angles, but it was believed that the magnitude had been approximately 0.9°.

Payload thermal control **AR numbers 37 (90-09-04) and 44 (91-01-28)**

Several heater and/or thermistor failures occurred in the payload active thermal control. As a consequence, a reconfiguration to the back-up thermal control electronics had to be performed. On the second unit, some thermistors also failed. These were excluded from the control loop by setting the relevant heaters to a fixed power level.

Radio frequency 1 **AR number 39 (90-09-04)**

The on-board automatic control gain of receiver 1 and 2 showed high variations whenever telecommands were being uplinked. The variations were in the order of −21 dbm. The analysis of this anomaly concluded that the automatic control gain bandwidth was too wide and out of specification. However, no evidence of a generic problem with the telemetry, tracking and command transponder design and corresponding specifications was found, as the automatic control gain malfunction and corresponding discrepancies were not critical with respect to the overall uplink function.

Payload mechanism drive electronics 1 **AR number 41 (90-09-26)**

On 24 September 1990 at 17:26 UTC, mechanic drive electronics 1 secondary voltage (parameter J001) dropped from 2.44 V to 1.88 V, falling below the nominal operating range ('out of limits' status). A short test showed that both shutters (image dissector tube and star mapper) were still able to work (opening and closing properly) under this anomalous voltage. However, the decision was taken to switch to redundant unit mechanic drive electronics 2 and the spacecraft was subsequently reconfigured at 19:23 UTC. On 14 March 1991 tests were performed and proved that mechanic drive electronics 1 was in fact functioning thus implying a fault in the multiplexer of the payload remote terminal unit.

Loss of attitude **AR number 50 (91-06-17)**

Ultimately triggered by high solar activity, severe problems were experienced with real-time attitude determination from 5 – 11 June 1991. On 6 June at 18:16 UTC the spacecraft attitude was lost after a series of large innovations caused real-time attitude determination to diverge.

Erroneous orbital oscillator command **AR number 53 (91-10-08)**

On 29 September 1991 at 17:01 UTC an orbital oscillator command was executed on-board with a value for the z component of the torque six orders of magnitude larger than the nominal calculated value, (this command was ground-calculated and uplinked every 15 mins for time-tagged execution on board) triggering a z thruster firing request of 213.33 s.). The spacecraft started to move away from its nominal spin-rate of -168.75 arcsec s^{-1} through zero and to the other direction. Corrective action was taken to bring the spacecraft back to safe sun-pointing configuration.

Suspect pre-processed gyro readings **AR number 54 (91-10-15)**

During the recovery from the 'erroneous orbital oscillator anomaly', the pre-processed on-board estimates of the body rates were shown to be inconsistent with the actual gyro outputs. In particular, the x and y body rates were about eight times larger than expected. The attitude control software was in standby mode 2 at the time. Confirmation was needed that the software mode standby mode 2 assumed the gyros to be in coarse range.

Gyro heating **AR number 55 (91-10-15)**

On 30 September 1991 at 02:10 UTC gyros 1, 2 and 5 were switched on as part of the recovery following the anomaly AR number 53. The temperature behaviour of all gyros was not as expected, since normally a continuous and smooth increase of temperature up to 70 °C was observed followed by a steady state lasting approximately 10–15 min. The anomaly had no impact on the mission.

Status reading of switching mirror **AR number 56 (91-10-15)**

On 30 September 1991 at 07:14 UTC when the payload was switched on following the recovery from the 'erroneous orbital oscillator command' (see AR number 53), the telemetry readings of the switching mirror both indicated a 'CLOSED' status, which did not reflect a valid position. However, from science data analysis it could be verified that the switching mirror was pointing towards detector 2 as it was commanded before payload switch-off. The anomaly had no impact on the mission.

Image dissector tube 1 voltages **AR number 57 (91-10-15)**

On 10 October 1991 at 11:42 UTC a procedure to switch image dissector tube 1 on and to perform a calibration was implemented to verify correct functioning of the detector chain before the switching mirror was moved. After switching the image dissector tube 1 electronics on, the secondary supply voltages telemetered in parameters G007 (image dissector tube 1 +15/ – 12 V) and G008 (image dissector tube 1 +6/ – 5.2/ + 30 V) indicated a low out of limit. The procedure was terminated and image dissector tube 1 was switched off again. The anomaly had no impact on the mission since only image dissector tube 2 was normally used for the operations. A telemetry problem (faulty payload remote terminal unit multiplexer) was suspected and confirmed on 29 July 1993 implying that image dissector tube 1 could have been used operationally.

Battery charge during perigee **AR number 58 (92-01-13)**

Since the end of the eclipse season, 21 October 1991, it was noted that both batteries were commanded to 'charge' by the on-board logic. This change of status was only happening during perigee (non-visibility periods) and was observed at almost every pass. Because no eclipses occurred during that time, the only change of spacecraft status was caused by occultations where the payload shutters were closed and opened via time-tagged commands. This abnormal behaviour was explained by orbit geometry. The spacecraft was crossing the Earth albedo and during these periods, the already degraded solar panels generated less power. Thus, high power demanding commands were enough to trigger the battery logic. The anomaly had no impact on the mission.

Gyro 1 real-time attitude drift **AR number 59 (92-06-11)**

At acquisition of signal from the Goldstone ground station at 23:23 UTC on 9 June 1992, following 6 hours of non-coverage, the gyro 1 drift had changed from its previous recorded value of 0.16 to 0.12 arcsec s^{-1} and was further decreasing. Correction to the 'old' drift value was uplinked at 23:25 UTC. However, the drift rate started to decrease again, until real-time attitude diverged (at about 01:00 UTC on the next day) and the drift started to increase. The anomaly had no impact on the mission.

Telemetry after radio frequency switching **AR number 60 (92-06-23)**

On 6 June 1992 at 18:04:50 UTC, the command to change transponder 1 to the fill-in antenna and transponder 2 to the cardioid antenna was executed from the on-board time-tag buffer previously loaded by the uplinked mission plan (one command for the two functions). The subsequent telemetry readout showed that transponder 1 was connected to the fill-in antenna. However, the telemetry readout for transponder 2 did not indicate the expected change to the cardioid antenna, but remained on the fill-in antenna. Since the on-board automatic control gain had changed as expected after the antenna switch command was executed it was concluded that the radio frequency switch had functioned as expected, the anomaly seemed to be a 'false' telemetry readout.

Thermal control electronics **AR number 61 (92-07-07)**

Temperatures of the telescope focal plane and the beam combiner decreased below specified minimum even after the maximum power to some of the control area heaters were applied. No action could be taken besides a close monitoring of the relevant thermal areas since thermal control electronics 2 was replacing thermal control electronics 1 after the failure of the heaters used for the same areas.

Gyro 5 **AR number 62 (92-07-07)**

From 3 July 1992, occurrences of 'false' gyro readouts were experienced. These readouts resulted in spurious z-thruster firings and in most cases caused real-time attitude to diverge. The attitude had to be subsequently corrected by ground intervention.

Gyro 5 and two gyro implementation **AR number 63 (92-07-10)**

On 10 July 1992 after acquisition of signal by Goldstone at 00:30 UTC 'glitches' in the raw output of gyro 5 occurred for approximately one hour during the outer van Allen belt crossing. The same was experienced during the following Odenwald pass. In both cases the z thruster firings were inhibited by the action of the on-board z thruster accumulator patch which stopped the firings when the accumulated thruster on-time reached the limit (60 s). However, because the normal mode z error angle was outside limits, and could not be corrected by the disabled z thruster, continuous demands to fire the z thruster were present, which resulted also in x and y thruster firings. The thruster firings were short but continuous until the 'glitches' disappeared, then the on-board software patch was reset from ground thus re-enabling the z thruster firings. At 16:01 UTC gyro 5 was taken out of the control loop and its function replaced by the two-gyro patch. Real-time attitude convergence was maintained confirming that the new on-board software was working correctly.

Attitude and orbit control system **AR number 66 (92-08-05)**

On 4 August 1992, just before loss of signal at the Odenwald ground station at 13:21 UTC, attitude and orbit control system telemetry packets were not present in the downlink. Furthermore, an attitude control software error was observed as well as several central on-board software errors. Special support was immediately requested from the Perth station, and the data received between 13:59 UTC and 14:16 UTC (loss of signal at Perth) confirmed that no communication was available between the

central on-board software and the attitude control software. At about 14:06 UTC, power was generated by the solar arrays and the batteries were discharging. This was a clear indication of a serious attitude anomaly. Goldstone was requested to provide emergency support some four hours ahead of schedule starting at 14:48 UTC. This allowed an immediate reconfiguration of the attitude and orbit control system to the redundant branch to be carried out, and by 17:17 UTC good attitude and orbit control system telemetry was again received. It was then confirmed from sun sensor and gyro data, that the spacecraft was badly nutating (half-cone of about 19°). At 17:57 UTC a ground commanded emergency sun reacquisition brought the spacecraft to a safe sun-pointing mode. Thereafter the spacecraft was configured for sun-pointing operation. The spacecraft was moved back to the nominal scanning law at 43° and convergence was achieved on 11 August 1992. Another emergency sun reacquisition was caused by the failure of gyro 5 a few hours later. After a 3-month hibernation period routine operations at 43° were resumed on 29 October 1992.

Gyro 5 and gyro 2 failure **AR number 67 (92-08-12)**

At 10:45 UTC on 11 August 1992, gyro 5 failed (output data corruption), inducing high torques around all three axes. At this time, the two gyro real-time attitude convergence had not been achieved. Immediate ground interventions failed to reduce the rapidly increasing body rates. The on-board anomaly detector triggered the emergency sun reacquisition and the spacecraft returned to a safe sun-pointing mode. In order to safeguard the attitude at sun-pointing for the upcoming perigee passage including an eclipse, the spacecraft was spun up to about 0.4 rpm which would guarantee stable dynamic behaviour. However, during the spin-up nutation had arisen and could not be damped before the loss of signal. Goldstone was requested to provide emergency support some three hours ahead of schedule starting at 17:04 UTC. At acquisition of signal another anomaly, this time on gyro 2, was detected. The gyro 2 output was corrupted in an identical manner to gyro 5. The additional failure of gyro 2 complicated the nutation control from ground, which was finally achieved around 18:00 UTC.

On-board computer 1 **AR number 68 (92-09-07)**

On 5 September 1992 at acquisition of signal by Perth (02:24 UTC) a continuous stream of memory error alarms was received. The error was identified as related to the programme star file buffer area, which was not being used in the present mode. An attempt to reset the on-board computer was unsuccessful; a reset of the programme star file buffer did not clear the problem. In addition on-board computer 1 could not be commanded to monitoring mode. A central on-board software reload was commanded, but the watchdog 1 could not be enabled. Power was removed and enabled into on-board computer 1 to reset the watchdog 1 signal. After a period of loss of signal (05:45 to 06:50 UTC), several attempts were made to bring on-board computer 1 to a proper initial state (therefore disabling the watchdog) by removing/restoring power to on-board computer 1, but all subsequent attempts to reconfigure the watchdog failed. Commands were verified through the demodulator and frame synchronizer channels, other possible sources of error were checked (receiver, decoder chain, etc.) and discarded. At this point a reconfiguration to the redundant unit (on-board computer 2) was carried out. A reload of the central on-board software software was performed without problems. Watchdog 2 was enabled successfully on the first attempt. Reconfiguration was finished at 09:08 UTC.

On-board computer 2 **AR number 69 (92-09-22)**

On 16 September 1992, a test was performed on on-board computer 2 in order to check all of its functions, whilst the watchdog was disabled. All functioned nominally and it was therefore concluded that on-board computer 1 was usable having the watchdog disabled. To finally validate the proper function of on-board computer 1, a switch-over was attempted. However, the command necessary to reset on-board computer 2 did not work. On-board computer 2 remained then the operational unit.

Gyro 1 spin-down **AR number 70 (92-09-28)**

Since 25 September 1992 three spin-downs of gyro 1 had taken place. The first occurrence lasted about 3 mins with a maximum variation of 36 arcsec s^{-1}. This was followed 15 mins later by a second spin-down of a smaller magnitude. The third occurrence was noticed two days later.

Gyro 1 breakdown **AR number 71 (92-10-14)**

On 10 October 1992 at 23:26 UTC gyro 1 stopped functioning completely. The gyro stopped spinning, and could not be started again. All attempts, including change of attitude and orbit control system from branch A to branch B and switching off/on the power supply channel, failed. Gyro 4, fed by the same channel, was switched on and spun up nominally. This excluded a failure of the power supply.

Emergency sun reacquisition order **AR number 72 (92-10-14)**

On 14 October 1992, an emergency sun reacquisition order was triggered at eclipse exit which reconfigured the spacecraft to the attitude and orbit control system branch B. Emergency sun reacquisition order had to be disabled by time-tagged command for each eclipse period while sun-pointing because at this attitude the on-board attitude anomaly detector sensor was illuminated by the Sun and triggered. The required uplink times had been miscalculated, thus emergency sun reacquisition order was not disabled during the eclipse period and consequently triggered.

Emergency sun reacquisition order **AR number 73 (92-11-13)**

On 10 November 1992, emergency sun reacquisition order triggered at 15:33 UTC as a consequence of a command resetting the z gyro drift rates to zero. The spacecraft returned to sun-pointing mode and reconfiguration from attitude and orbit control system branch A to branch B was immediately performed. Real-time attitude determination at sun-pointing was initialised at 20:31 UTC. At 20:48 UTC the manoeuvre to return the spacecraft to the nominal scanning law (43° solar aspect angle) was started and successfully terminated at 21:36 UTC. Real-time attitude determination was initialised at 22:06 UTC and science data collection re-commenced.

Gyro 5 **AR number 74 (92-11-13)**

The noise of gyro 5 raw output increased suddenly on 18 November 1992 at about 03:45 UTC and remained high until loss of signal (06:02 UTC). At acquisition of signal (06:51 UTC), the gyro output noise characteristic had not changed, but also high spin variations between 100 and 200 arcsec s^{-1} were observed. Furthermore, gyro 2 (sharing the same power supply as gyro 5) had similar spin variations. Gyro 4 was switched on, confirming a constant spacecraft spin rate. Gyro 5 was switched off at 10:31 UTC and gyro 2 output immediately recovered.

Gyro 2 spikes **AR number 75 (92-12-28)**

At acquisition of signal (17:44 UTC) on 22 December 1992, gyro 2 raw output data showed an increasing noise envelope. At around 18:40 UTC, spikes on the gyro data similar to the previously observed spikes on gyro 5 triggered the emergency sun reacquisition order which returned the satellite to sun-pointing mode. The satellite was reconfigured and gyros 2 and 3 switched on. The noise (spikes) on gyro 2 was still present, but disappeared after the temperature of the gyro electronics had passed 22 °C.

On-board computer 2 **AR number 76 (93-02-18)**

On 16 February 1993 at 08:17 UTC a few packet commands were rejected on-board due to checksum error. The number of rejections varied depending upon the command uplink rate, but with increasing tendency. The anomaly was present with all four ground stations. No evidence of a ground problem was detected. On 17 February 1993 starting at 13:15 UTC, a reload of on-board computer 2 was attempted but failed because some of the load commands were rejected on-board. The ground system was again thoroughly checked, including a further attempt to reload on-board computer 2 with the back-up system resulting again in on-board command rejections. A reconfiguration from on-board computer 2 to on-board computer 1 was done followed by a successful reload of on-board computer 1. Science collection re-commenced at 18:15 UTC.

Gyro 2 failure **AR number 77 (93-03-18)**

On 18 March 1993 at 20:26 UTC gyro 2 failed causing an emergency sun reacquisition. Prior to this, increased noise had been observed on the raw gyro output data. Attempts to restart gyro 2 (and any of the previously failed gyros) were unsuccessful. Only gyro 3 started. The satellite was spun up to 0.25 rpm followed by nutation damping.

Antenna switch command failure **AR number 78 (93-03-30)**

On 28 March 1993 the command to connect transponder 1 to the fill-in antenna and transponder 2 to the cardioid antenna failed execution. The command was sent as a time-tagged command from the on-board computer. The command was transmitted from ground for immediate execution, but failed again. The back-up command was then used and correct antenna switching was achieved. From then on, only the back-up command was used to switch antennae. A possible explanation could be a fault in the relevant on/off module. An on/off module was a module of the payload remote terminal unit responsible for the distribution of the commands (de-multiplexer).

Star mapper 1 and 2 partial failures **AR number 79 (93-05-25)**

On 5 May 1993 star mapper 2 was switched on and it was found that the V_T channel was no longer working. The following day star mapper 1 was tested and it was found that on this unit the B_T channel did not work. Ground real-time attitude determination required both channels to identify star magnitude and colour to perform correct star pattern matching. The ground software was then modified to operate with both star mapper streams available in telemetry (B_T channel of star mapper 1 and V_T channel of star mapper 2).

Suspect control law electronics **AR number 80 (93-05-27)**

The processor of the control law electronics of the attitude and orbit control system branch A stopped twice during the week 28 June to 4 July 1993. Once without any error messages and once with the error indicating a 'CPU overload'. The attitude and orbit control system was configured into a cross-strapped mode using the branch B control law electronics and the branch A control actuation electronics, which retained all safety aspects in case of attitude anomaly detection.

Gyro 3 noise **AR number 81 (93-05-31)**

On 26 May 1993 gyro 3 was switched on at 07:02 UTC and showed nominal behaviour. During the early morning hours of 27 May increasing noise (spikes) appeared, reaching peak values of more than 50 arcsec s^{-1}. The gyro was switched off at 08:12 UTC.

On-board software 1 and 2 failure **AR number 82 (93-06-28)**

On 24 June 1993 at 14:41 UTC central on-board software 1 halted with an error message indicating an 'illegal instruction' in memory. Prior to this, three error messages were received indicating checksum errors at the same location. Several further attempts to start either central on-board software 1 or central on-board software 2 during the following days were unsuccessful.

APPENDIX C

REFERENCES

Anspaugh, B.E., 1991. *Proton and electron damage coefficients for GaAs/Ge solar cells*, Proceedings IEEE, PVSC, Las Vegas.

Anspaugh, B.E., Downing, R.G., 1984. *Radiation effects in Silicon and Gallium Arsenide solar cells using isotropic and normally incident radiation*, JPL Publication 84-61.

Auburn, J.H.C., Batten, A.J., McDonald, A.J.C., 1991. *Hipparcos attitude determination with two gyros and a star mapper*, Proc. 3rd International Symp. Spacecraft Flight Dynamics, Darmstadt, Germany, ESA SP-326, 213.

Batten, A.J., McDonald, A.J.C., 1989. *Hipparcos precise attitude determination: methods and results*, Int. Symp. Space Dynamics, Toulouse, France.

Beech, M., Brown, P., Jones, J., 1995. *The potential danger to space platforms from meteor storm activity*, Quarterly Journal of the Royal Astronomical Society, 36, 127.

Bernard, J., Reulet, R., Crabb, R.L., 1984. Proc. 4th European Symp. Photovoltaic Generators in Space, ESA SP-210, 407.

Blake, J.B., Gussenhoven, M.S., Mullen, E.G., Fillius, R.W., 1992. *Identification of an unexpected space radiation hazard*, IEEE Trans. Nucl. Sci. NS-39, 6, 1761.

Brautigam, D.H., Gussenhoven, M. S., Mullen E.G., 1992. *Quasi-static model of outer zone electrons*, IEEE Trans. Nucl. Sci. NS-39, 6, 1797.

Buacher, J., 1967. *Les combinaisons optiques: practique des calculs*, Editions de la Revue d'Optique Theorique et Instrumentale.

Cheng, C. *et al.*, 1991. *Improved MOCVD technology in high-throughput high-efficiency GaAs/Ge solar cell manufacture*, Proceedings IEEE, PVSC, Las Vegas.

Crabb, R.L., 1994. *Solar cell radiation damage*, Radiat. Phys. Chem. 43, 93-103.

Crabb, R.L., Robben, A.P., 1993. *In-flight Hipparcos solar array performance degradation after three and a half years in GTO*, Proc. European Space Power Conference, Graz, ESTEC/XPG-WPP-054.

Crézé, M., Chareton, M., 1991. *Accuracy uniformity of Hipparcos parallaxes and proper motions: strategy and current status*, Highlights of Astronomy, Vol 9, Bergeron J. (ed).

Daly, E.J., *et al.*, 1994. *Radiation-belt and transient solar-magnetospheric effects on Hipparcos radiation background*, IEEE Trans. Nucl. Sci. NS-41, 6, 2376.

Davies, P.E., McDonald, A.J.C., 1991. *Results of the Hipparcos In-Orbit Payload Calibration*, Journal of the British Interplanetary Society, 44, 37.

Feynman, J., Armstrong, T.P., Dao-Gibner, L., Silverman, S., 1992. *New interplanetary proton and fluence model*, J. Spacecraft, 27, 403.

Gussenhoven, M.S., Mullen, E.G., Sperry, M., Kerns, K.J., Blake, J.B., 1992. *The effect of the March 1991 storm on accumulated dose from selected satellite orbits: CRRES dose models*, IEEE Trans. Nucl. Sci. NS-39, 6, 1765.

Gussenhoven, M.S., Mullen, E.G., Violet, M.D., 1994. *Solar particle events as seen on CRRES*, Adv. Space Res., 14, (10)619.

Howell, L.W., Kennel, H.F., 1984. *A stochastic model for photon noise induced by charged particles in multiplier phototubes of the Space Telescope Fine Guidance Sensors*, NASA TP-2337.

Høg, E. *et al.*, 1992. *Tycho data analysis: overview of adopted reduction software and first results*, Astron. Astrophys., 258, 177.

Lindegren, L. *et al.*, 1992. *Geometrical stability and evolution of the Hipparcos telescope*, Astron. Astrophys., 258, 35.

McDonnell, J.A.M., 1978. *Cosmic Dust*, John Wiley & Sons.

Mullen, E.G., Gussenhoven, M.S., Ray, K., Violet, M., 1991. *A double-peaked inner radiation belt: Cause and Effect as Seen on CRRES*, IEEE Trans. Nucl. Sci. NS-38, 6, 1713.

Naumann, R.J., 1966. *The near-Earth meteoroid environment*, NASA TN D-3717.

Nieminen, P.J., 1995. *Standard radiation environment monitor detector design and simulations*, ESTEC Working Paper 1829.

Olsen, W.P., Pfitzer, K.A., 1974. *A quantitative model of the magnetospheric magnetic field*, J. Geophys. Res., 79, 3739.

Rädlein, E., 1991. *Simulation der Wechselwirkung von Weltraumstrahlung mit Glas und Glaskeramik*, Dissertation zur Erlangung des Grades eines Doktor (publication in English issued from the Conference of Physics of Non-Crystalline Solids, 4–9 August 1991, Cambridge.

Ray, K.P., Mullen, E.G., Trumble, T.M., 1993. *Results from the high-efficiency solar panel experiment flown on CRRES, (Phillips Laboratory USAF)*, IEEE Trans. Nucl. Science, 40, 6, 1505.

Sauer, H.H., 1987. *A personal computer-based GOES data archive*, NOAA Technical Memorandum ERL-SEL-74.

Sawyer, D.M., Vette, J.I., 1976. *AP-8 trapped proton environment for solar maximum and solar minimum*, NSSDC 76-06.

Soo, D., Schuyer, M., 1994. *Preparing for the Future*, ESA Publication, Vol. 4, No. 2.

Tada, J., *et al.*, 1982. In *Solar Cell Radiation Handbook, 3rd Edition*, NASA JPL Publication 82-69 and Addendum 1 JPL Publication 82-69.

Tranquille, C., Daly, E.J., 1992. *An evaluation of solar proton event models for ESA missions*, ESTEC Working Paper 1647.

Vette, J.I., 1989. *Trapped radiation models: development of improved models of the Earth's radiation environment*, Technical Note 1, Chapter 4.

Vette, J.I., 1991. *The AE8 trapped electron model environment*, NSSDC Report 91-24, NASA/GSFC.

Viehmann, W., Eubanks, A.G., 1976. *Noise limitations in multiplier phototubes in the radiation environment of space*, NASA TN-8147.

APPENDIX D

BIBLIOGRAPHY

This bibliography applies to both the technical (this Volume) and scientific (Volumes 3–4) aspects of the Hipparcos mission, and includes refereed papers, conference proceedings, and articles of a more popular nature, published up until the end of 1996.

Amoretti, M., Badiali, M., Cardini, D., Emanuele A., 1985. *The signal of the Hipparcos nominal system*. Proc. Marseille Coll. 'Processing of Scientific Data from Hipparcos', Second FAST Thinkshop, 21–25 January 1985, Kovalevsky, J. (ed.), 49.

Arenou, F., 1993. *Contribution à la validation statistique des données d'Hipparcos: Catalogue d'Entrée et données préliminaires*. Thèse de doctorat, Observatoire de Paris.

Arenou, F., Grenon, M., Gómez, A., 1992. *A tridimensional model of the galactic interstellar extinction*. A&A, 258, 104.

Arenou, F., Lindegren, L., Frœschlé, F., Gómez, A.E., Turon, C., Perryman, M.A.C., Wielen, R., 1995. *Zero-point and external errors of Hipparcos parallaxes.* A&A, 304, 52.

Arenou, F., Morin, D., 1988. *The INCA data base for the Hipparcos mission*. Astronomy from large databases: scientific objectives and methodological approaches, Garching, Murtagh, F., Heck, A. (eds), 269.

Argue, A.N., 1985. *Report by INCA subgroup 2130 (link to extragalactic reference objects)*. Proc. Aussois Coll. 'Scientific Aspects of the Input Catalogue Preparation', 3–7 June 1985, Turon, C., Perryman, M.A.C. (orgs), ESA SP-234, 237.

Argue, A.N., 1986. *Hipparcos: link with the extragalactic reference frame*. IAU Highlights of Astronomy Vol. 7, Swings, J.P. (ed.), 719.

Argue, A.N., 1986. *The reconciliation of optical and radio positions.* IAU Symp. 109, 'Astrometric Techniques', Gainsville, 9–12 January 1984, Eichhorn, H.K., Leacock, R.J. (eds), 757.

Argue, A.N., 1988. *Report to subgroup 2130 (link to extragalactic objects)*. Proc. Sitges Coll. 'Scientific Aspects of the Input Catalogue Preparation', 25–29 January 1988, Torra, J., Turon, C. (eds.), 439.

Argue, A.N., 1990. *A strategy for linking Hipparcos to an extragalactic reference frame*. IAU Proc. 'Inertial coordinate system on the sky', Lieske, J.H., Abalakin, V.K. (eds.), 323.

Argue, A.N., 1991. *Hipparcos: its link to an extragalactic reference frame*. Proc. IAU Coll. 127 'Reference systems', Hughes, J.A., Smith, C.A., Kaplan, G.H. (eds), US Naval Observatory Publ., 63.

Argue, A.N., Baxter, R.D., Morgan, B.L., Vine, H., 1982. *The selection of stars for linking the Hipparcos frame to extragalactic radio sources by Space Telescope (progress report)*. Proc. Strasbourg Coll. 'Scientific Aspects of the Hipparcos Space Astrometry Mission', 22–23 February 1982, Perryman, M.A.C., Guyenne, T.D. (eds), ESA SP-177, 53.

Argue, A.N., White, G.M., 1992. *Link to an inertial system*. Highlights of Astronomy, 9, 429.

Argue, A.N. *et al.*, 1984. *A catalogue of selected compact radio sources for the construction of an extragalactic radio/optical reference frame*. A&A, 130, 191.

Arlot, J.E., Bec-Borsenberger, A., Dourneau, G., 1991. *Observations of the planetary satellites Europa and Titan by Hipparcos.* Proc. IAU Coll. 127, 'Reference systems', Hughes, J.A., Smith, C.A., Kaplan, G.H. (eds), US Naval Observatory Publ., 202.

Baarda, W., 1968. *A testing procedure for the use in geodetic networks.* Neth. Geodetic Commission, Publ. on Geodesy. Vol. 2, 5.

Baarda, W., 1973. *S-transformation and criterion matrices.* Neth. Geodetic Commission, Publ. on Geodesy. Vol. 5, 1.

Bacchus, P., 1974. *Space astrometry project: optical concept.* Proc. Frascati Symp. 'Space Astrometry', 22–23 October 1974, Nguyen, T.D., Battrick, B.T. (eds), ESA SP-108, 31.

Bacchus, P., 1974. *Space astrometry project: reduction by multilateration.* Proc. Frascati Symp. 'Space Astrometry', 22–23 October 1974, Nguyen, T.D., Battrick, B.T. (eds), ESA SP-108, 37.

Bacchus, P., 1982. *Caractéristiques des étoiles doubles observables par Hipparcos.* Proc. Strasbourg Coll. 'Scientific Aspects of the Hipparcos Space Astrometry Mission', 22–23 February 1982, Perryman, M.A.C., Guyenne, T.D. (eds), ESA SP-177, 153.

Bacchus, P., Lacroute, P., 1974. *Prospects of space astrometry.* in New Problems in Astrometry, Gliese, W., Murray, C.A., Tucker, R.H. (eds), 277.

Badiali, M., Amoretti, M., Cardini, D., Emanuele, A., 1986. *Tests on the Hipparcos real system*. Proc. Bari Coll. 'Processing of Scientific Data from Hipparcos', Third FAST Thinkshop, 3–6 November 1986, Bernacca, P.L., Kovalevsky, J. (eds), 305.

Badiali, M., Cardini, D., Emanuele, A., Prezioso, G., Pannunzio, R., 1991. *Expected performances of Hipparcos satellite in detecting double star systems.* Advances in Space Research, 11-2, 71.

Baglin, A., 1988. *Hipparcos mission and fundamental physics.* Proc. Sitges Coll. 'Scientific Aspects of the Input Catalogue Preparation', 25–29 January 1988, Torra, J., Turon, C. (eds.), 103.

Barbieri, C., Bernacca, P.L. (eds.), 1979. Proc. Padova Coll. on European Satellite Astrometry. University of Padua.

Barbieri, C., Nota, A., 1983. *The sky background from a space station*. Proc. Asiago Coll. 'Processing of Scientific Data from Hipparcos', The FAST Thinkshop, 24–27 May 1983, Bernacca, P.L. (ed.), 135.

Barthés, D., Davies, P., Ménessier, M.O., 1991. *Luminosity of large amplitude variable stars: comparison between ground-based predictions and observations by the Hipparcos satellite*. Advances in Space Research, 11-2, 67.

Bässgen, G., Wicenec, A., Andreasen, G.K., Høg, E., Wagner, K., Wesselius, P., 1992. *Tycho transit detection*. A&A, 258, 186.

Bastian, U., 1985. *Treatment of the Hipparcos grid step ambiguity problem*. Proc. Marseille Coll. 'Processing of Scientific Data from Hipparcos', Second FAST Thinkshop, 21–25 January 1985, Kovalevsky, J. (ed.), 295.

Bastian, U., 1986. *Hipparcos, der 100000-Sterne-Satellit.* Sterne und Weltraum 25, 524.

Bastian, U., 1994. *Hipparcos, ein Astrometrie-Satellit der ESA*. Astronomie und Raumfahrt, 33, 4.

Bastian, U., 1994. *Hipparcos-Mission abgeschlossen*. Sterne und Weltraum 33, 12.

Bastian, U., Born, E., Agerer, F., Dahm, M., Großmann, V., Makarov, V., 1996. *Confirmation of the classification of a new Tycho variable: HD 32456 is a 3.3-day Cepheid.* Inf. Bull. Variable Stars, No. 4306.

Bastian, U., Lederle, T., 1985. *The ARI catalogue of astrometric data for the Hipparcos Input Catalogue*. Proc. Aussois Coll. 'Scientific Aspects of the Input Catalogue Preparation', 3–7 June 1985, Turon, C., Perryman, M.A.C. (orgs), ESA SP-234, 185.

Bec-Borsenberger, A., 1985. *Petites planètes du programme Hipparcos.* Proc. Aussois Coll. 'Scientific Aspects of the Input Catalogue Preparation', 3–7 June 1985, Turon, C., Perryman, M.A.C. (orgs), ESA SP-234, 175.

Bec-Borsenberger, A., 1988. *Petites planètes et satellites à observer par Hipparcos.* Proc. Sitges Coll. 'Scientific Aspects of the Input Catalogue Preparation', 25–29 January 1988, Torra, J., Turon, C. (eds.), 303.

Bec-Borsenberger, A., 1992. *Solar system objects observed by Hipparcos.* A&A, 258, 94.

Bec-Borsenberger, A., Bange, J-F., Bougeard, M-L., 1995. *Hipparcos minor planets: first step towards the link between the Hipparcos and the dynamical reference frames.* A&A, 304, 176.

Beeckmans, F., 1980. *The astrometry satellite Hipparcos.* ESA Journal, 4, 15.

Belforte, P., 1986. *Report on the attitude reconstitution task*. Proc. Bari Coll. 'Processing of Scientific Data from Hipparcos', Third FAST Thinkshop, 3–6 November 1986, Bernacca, P.L., Kovalevsky, J. (eds), 41.

Belforte, P., Canuto, E., Carlucci, D., Fassino, B., 1983. *The jitter error in grid coordinate estimation*. Proc. Asiago Coll. 'Processing of Scientific Data from Hipparcos', The FAST Thinkshop, 24–27 May 1983, Bernacca, P.L. (ed.), 197.

Belforte, P., Canuto, E., Donati, F., Villa A., 1983. *An approach to on-ground attitude reconstitution: preliminary results.* Proc. Asiago Coll. 'Processing of Scientific Data from Hipparcos', The FAST Thinkshop, 24–27 May 1983, Bernacca, P.L. (ed.), 163.

Belforte, P., van der Marel, H., Canuto, E., 1986. *On two different ways of modelling the Hipparcos attitude*. Proc. Bari Coll. 'Processing of Scientific Data from Hipparcos', Third FAST Thinkshop, 3–6 November 1986, Bernacca, P.L., Kovalevsky, J. (eds), 81.

Bernacca, P.L. (ed.), 1983. *Processing of the scientific data for the ESA astrometry satellite Hipparcos.* Proc. Asiago Coll. 'Processing of Scientific Data from Hipparcos', The FAST Thinkshop, 24–27 May 1983, Bernacca, P.L. (ed.).

Bernacca, P.L., 1985. *Progetto Hipparcos.* Letture, Giornale di Astronomia, 375.

Bernacca, P.L., 1985. *Project Hipparcos.* Astrophys. Space Sci., 110, 21.

Bernacca, P.L., Kovalevsky, J. (eds), 1986. *Processing of scientific data for the ESA astrometry satellite Hipparcos.* Proc. Bari Coll. 'Processing of Scientific Data from Hipparcos', Third FAST Thinkshop, 3–6 November 1986.

Bernstein, H.H., 1985. *Numerical results on astrometric parameters and accuracy assessment*. Proc. Marseille Coll. 'Processing of Scientific Data from Hipparcos', Second FAST Thinkshop, 21–25 January 1985, Kovalevsky, J. (ed.), 291.

Bernstein, H.H., Hering, R., Walter, H.G., 1988. *Astrometric parameters of visual double stars derived from simulated Hipparcos measurements.* Astrophys. Space Sci., 142, 161.

Bertani, D., Cetica, M., Iorio-Fili, D., 1985. *Optical model for the Hipparcos telescope in its real configuration*. Proc. Marseille Coll. 'Processing of Scientific Data from Hipparcos', Second FAST Thinkshop, 21–25 January 1985, Kovalevsky, J. (ed.), 43.

Bertani, D., Cetica, M., Iorio-Fili, D., 1986. *Field to grid transformation for the real Hipparcos system*. Proc. Bari Coll. 'Processing of Scientific Data from Hipparcos', Third FAST Thinkshop, 3–6 November 1986, Bernacca, P.L., Kovalevsky, J. (eds), 315.

Bertani, D., Cetica, M., Iorio-Fili, D., Borriello, L., 1986. *The Hipparcos telescope relay response in real configuration*. Proc. Bari Coll. 'Processing of Scientific Data from Hipparcos', Third FAST Thinkshop, 3–6 November 1986, Bernacca, P.L., Kovalevsky, J. (eds), 297.

Bertotti, B., Farinella, P., Milani, A., Nobili, A.M., Sacerdote, F., 1984. *Linking reference systems from space*. A&A, 133, 231.

Betti, B., Migliaccio, F., Sansò, F., 1986. *A rigorous approach to attitude and sphere reconstitution in the Hipparcos project*. Proc. Bari Coll. 'Processing of Scientific Data from Hipparcos', Third FAST Thinkshop, 3–6 November 1986, Bernacca, P.L., Kovalevsky, J. (eds), 391.

Betti, B., Mussio, L., Sansò, F., 1983. *A new proposal of sphere reconstitution in the Hipparcos project*. Proc. Asiago Coll. 'Processing of Scientific Data from Hipparcos', The FAST Thinkshop, 24–27 May 1983, Bernacca, P.L. (ed.), 281.

Betti, B., Mussio, L., Sansò, F., 1985. *Experiments with the arcwise sphere reconstitution*. Proc. Marseille Coll. 'Processing of Scientific Data from Hipparcos', Second FAST Thinkshop, 21–25 January 1985, Kovalevsky, J. (ed.), 263.

Betti, B., Sansò, F., 1983. *A detailed analysis of rank deficiency in the Hipparcos project*. Proc. Asiago Coll. 'Processing of Scientific Data from Hipparcos', The FAST Thinkshop, 24–27 May 1983, Bernacca, P.L. (ed.), 317.

Betti, B., Sansò, F., 1985. *A continuous model for the arcwise sphere reconstitution*. Proc. Marseille Coll. 'Processing of Scientific Data from Hipparcos', Second FAST Thinkshop, 21–25 January 1985, Kovalevsky, J. (ed.), 255.

Betti, B., Sansò, F., 1986. *A possible use of the results of Hipparcos project in satellite-to-satellite tracking.* Manuscripta Geodaetica, 11, 188.

Betti, B., Sansò, F., 1986. *The continuous analogue of the sphere reconstruction in Hipparcos project*. Manuscripta Geodaetica, 11, 133.

Blaauw, A., 1982. *Trigonometric parallaxes: the stellar content of the volume of space covered by Hipparcos and some of its astrophysical implications.* Proc. Strasbourg Coll. 'Scientific Aspects of the Hipparcos Space Astrometry Mission', 22–23 February 1982, Perryman, M.A.C., Guyenne, T.D. (eds), ESA SP-177, 97.

Bois, E., 1987. *First order theory of satellite attitude motion, application to Hipparcos.* Celestial Mechanics, 39, 309.

Bois, E., 1987. *Théorie analytique de la rotation d'un satellite artificiel: application à Hipparcos.* Thèse de Doctorat nouveau régime, Observatoire de Paris.

Bonnefoy, R.B., Fade, G., Gricourt, C., 1985. *The scientific payload of the Hipparcos astrometry satellite*. Proc. 36th Congress International Aeronautical Federation, Pergammon.

Borriello, L., 1986. *Imaging approach to multiple star recognition*. Proc. Bari Coll. 'Processing of Scientific Data from Hipparcos', Third FAST Thinkshop, 3–6 November 1986, Bernacca, P.L., Kovalevsky, J. (eds), 189.

Borriello, L., 1987. *Hipparcos: the imaging approach to multiple star recognition*. Fourth Int. Conf. on Image Analysis and Processing, Cefalu.

Borriello, L., 1987. *Hipparcos: the imaging approach to multiple star recognition: the algorithm and the results.* IAU Coll. 97, Bruxelles.

Borriello, L., d'Alessandro, F., Murgolo, F.P., Prezioso, G., 1985. *Hipparcos: the reduction chain of observations and double star recognition using an image processing approach*. Second Int. Workshop on Data Analysis in Astronomy, Vulcano.

Bouffard, M., 1985. *Hipparcos: the first satellite devoted to global astrometry.* 19th European Space Symp., NASA GSFC Publication.

Bouffard, M., Zeis, E., 1983. *The Hipparcos Satellite*. Proc. Asiago Coll. 'Processing of Scientific Data from Hipparcos', The FAST Thinkshop, 24–27 May 1983, Bernacca, P.L. (ed.), 31.

Brosche, P., Geffert, M., 1988. *A small extragalactic link for Hipparcos.* Proc. Sitges Coll. 'Scientific Aspects of the Input Catalogue Preparation', 25–29 January 1988, Torra, J., Turon, C. (eds.), 475.

Brosche, P., Sinachopoulos, D., 1988. *The optical fraction of a Hipparcos sample of wide binaries.* Astrophys. Space Sci., 142, 255.

Bucciarelli, B., Lattanzi, M.G., Migliaccio, F., Sansó, F., Sarasso, M., 1991. *A comparison between two strategies of data reduction of the Hipparcos mission*. Advances in Space Research, 11-2, 79.

Bucciarelli, B., Lattanzi, M.G., Tommasini, T., 1986. *Sphere reconstitution: parallel methods and numerical experiments.* Proc. Bari Coll. 'Processing of Scientific Data from Hipparcos', Third FAST Thinkshop, 3–6 November 1986, Bernacca, P.L., Kovalevsky, J. (eds), 97.

Burnage, R., Fehrenbach, Ch., Duflot, M., 1988. *Vitesses radiales pour Hipparcos.* Proc. Sitges Coll. 'Scientific Aspects of the Input Catalogue Preparation', 25–29 January 1988, Torra, J., Turon, C. (eds.), 427.

Calaf, J., 1988. *Orbital elements and ephemerides of the minor planets included in the Hipparcos mission*. Proc. Sitges Coll. 'Scientific Aspects of the Input Catalogue Preparation', 25–29 January 1988, Torra, J., Turon, C. (eds.), 321.

Canuto, E., DeLuca, A., Fassino, B., 1983. *The photon noise error in grid coordinate estimation.* Proc. Asiago Coll. 'Processing of Scientific Data from Hipparcos', The FAST Thinkshop, 24–27 May 1983, Bernacca, P.L. (ed.), 187.

Canuto, E., Donati, F., 1986. *On-ground attitude reconstitution of the Hipparcos satellite*. Proc. Second Int. Symp. on Spaceflight Dynamics, Darmstadt, 379.

Canuto, E., Donati, F., 1991. *The On-Ground Attitude Reconstitution of the Hipparcos Satellite*. Proc. Third Int. Symp. on Spacecraft Flight Dynamics, ESA SP-326, 97.

Canuto, E., Donati, F., 1992. *The on-ground attitude reconstitution of the Hipparcos satellite*. International Journal of Modelling and Simulation, 12, 125.

Canuto, E., Fassino, B., 1986. *IDT data processing in the presence of veiling glare*. Proc. Bari Coll. 'Processing of Scientific Data from Hipparcos', Third FAST Thinkshop, 3–6 November 1986, Bernacca, P.L., Kovalevsky, J. (eds), 207.

Canuto, E., Fassino, B., Villa, A., 1983. *The star mapper data processing.* Proc. Asiago Coll. 'Processing of Scientific Data from Hipparcos', The FAST Thinkshop, 24–27 May 1983, Bernacca, P.L. (ed.), 155.

Caprioli, G., 1983. *Precise apparent places of stars by vector transformation*. Proc. Asiago Coll. 'Processing of Scientific Data from Hipparcos', The FAST Thinkshop, 24–27 May 1983, Bernacca, P.L. (ed.), 255.

Carlucci, D., Donati, F., 1981. *Attitude estimation for a spinning satellite from gyroscope and star mapper data*. Proc. IFAC 8th World Congress, Tokyo, XVI, 64.

Carlucci, D., Donati, F., 1981. *Data processing for high accurcay star mapper.* Proc. IFAC 8th World Congress, Tokyo, XVI, 70.

Carlucci, D., Donati, F., Fassino, B., 1984. *The Hipparcos astrometry satellite: closed-loop digital attitude control using gas jets.* Proc. IFAC 9th World Congress, Budapest, III, 12.

Catullo, V., 1985. *Apparent places of stars as seen by the Hipparcos satellite*. Proc. Marseille Coll. 'Processing of Scientific Data from Hipparcos', Second FAST Thinkshop, 21–25 January 1985, Kovalevsky, J. (ed.), 329.

Cayrel de Strobel, G., 1982. *Hipparcos could make the distance of the Hyades into a conventional constant*. Proc. Strasbourg Coll. 'Scientific Aspects of the Hipparcos Space Astrometry Mission', 22–23 February 1982, Perryman, M.A.C., Guyenne, T.D. (eds), ESA SP-177, 173.

Clausen, K., Perryman, M.A.C., 1989. *The Hipparcos mission*. IAF Proceedings. Vol. 22, Acta Astronautica, 229.

Cordoni, J.P., Mennessier, M.O., 1986. *Les catalogues d'étoiles variables et le satellite astrométrique Hipparcos.* Bull. Inf. CDS, 30, 55.

Crézé, M., 1985. *Optimising the Hipparcos Input Catalogue through simulations.* Proc. Aussois Coll. 'Scientific Aspects of the Input Catalogue Preparation', 3–7 June 1985, Turon, C., Perryman, M.A.C. (orgs), ESA SP-234, 79.

Crézé, M., 1988. *Algorithm for PSF generation*. Proc. Sitges Coll. 'Scientific Aspects of the Input Catalogue Preparation', 25–29 January 1988, Torra, J., Turon, C. (eds.), 135.

Crézé, M., 1992. *Hipparcos et la dynamique galactique*. 'Hipparcos, une nouvelle donne pour l'astronomie', Benest, D., Frœschlé, C. (eds.), Editions Société Française des Spécialistes d'Astronomie, 499.

Crézé, M., Chareton, M., 1988. *Basic ideas of simulations and observability of INCA stars.* Proc. Sitges Coll. 'Scientific Aspects of the Input Catalogue Preparation', 25–29 January 1988, Torra, J., Turon, C. (eds.), 49.

Crézé, M., Chareton, M., 1992. *Accuracy and uniformity of Hipparcos parallaxes and proper motions: Strategy and current status.* Highlights of Astronomy, 9, 393.

Crézé, M., Chareton, M., Oblak, E., 1985. *Optimising the observing strategy through simulations.* Proc. Aussois Coll. 'Scientific Aspects of the Input Catalogue Preparation', 3–7 June 1985, Turon, C., Perryman, M.A.C. (orgs), ESA SP-234, 97.

Crifo, F., 1988. *Completeness of the Survey.* Proc. Sitges Coll. 'Scientific Aspects of the Input Catalogue Preparation', 25–29 January 1988, Torra, J., Turon, C. (eds.), 79.

Crifo, F., Grenon, M., Jahreiß, H., McLean, B., 1991. *Search of the latest non-astrometric Hipparcos stars in the HST Guide Star Catalog.* Advances in Space Research, 11-2, 137.

Crifo, F., Gómez, A., Arenou, F., Morin, D., Schrijver, H., 1992. *Reliability of the Hipparcos Input Catalogue tested by the 'First Look'.* A&A, 258, 116.

Crifo, F., Gómez, A., Morin, D., Turon, C., 1985. *The Hipparcos Input Catalogue: an example of intensive use of the SIMBAD data base*. Mem. Soc. Astr. It., 56, 377.

Crifo, F., Turon, C., Grenon, M., 1985. *Definition of the survey.* Proc. Aussois Coll. 'Scientific Aspects of the Input Catalogue Preparation', 3–7 June 1985, Turon, C., Perryman, M.A.C. (orgs), ESA SP-234, 67.

Cruise, A.M., 1982. *Hipparcos: space-age astrometry.* Nature, 298, 324.

Daalen, D.T. van, 1983. *General considerations on reduction on circles.* Proc. Asiago Coll. 'Processing of Scientific Data from Hipparcos', The FAST Thinkshop, 24–27 May 1983, Bernacca, P.L. (ed.), 235.

Daalen, D.T. van, 1985. *The current state of the reduction on circles.* Proc. Marseille Coll. 'Processing of Scientific Data from Hipparcos', Second FAST Thinkshop, 21–25 January 1985, Kovalevsky, J. (ed.), 193.

Daalen, D.T. van, 1986. *The astrometry satellite Hipparcos: its possible contribution to geodesy: the geodesists contribution to Hipparcos.* Proc. First Marussi-Hotine Symp., Sansò, F. (ed.), Rome, 259.

Daalen, D.T. van, Bucciarelli, B., Lattanzi, M.G., 1986. *Rank deficiency during the sphere reconstitution*. Proc. Bari Coll. 'Processing of Scientific Data from Hipparcos', Third FAST Thinkshop, 3–6 November 1986, Bernacca, P.L., Kovalevsky, J. (eds), 369.

Daalen, D.T. van, van der Marel, H., 1986. *Geodetic, geometric and computational aspects of Hipparcos.* Manuscripta Geodaetica, 11, 146.

Davies, P.E., Burrows, C.J., 1988. *The Hipparcos main mission accuracy simulation*. Journal of the British Interplanetary Society, 41, 435.

Davies, P.E., van der Ha, J.C., 1986. *Real-time payload monitoring of the Hipparcos satellite*. Proc. Bari Coll. 'Processing of Scientific Data from Hipparcos', Third FAST Thinkshop, 3–6 November 1986, Bernacca, P.L., Kovalevsky, J. (eds), 325.

Delaney, W., 1985. *Double star analysis strategy.* Proc. Marseille Coll. 'Processing of Scientific Data from Hipparcos', Second FAST Thinkshop, 21–25 January 1985, Kovalevsky, J. (ed.), 153.

Didelon, P., Egret, D., 1987. *Cross-matching SIMBAD and the Guide Star Catalogue for the Tycho Input Catalogue: first tests.* Bull. Inf. CDS, 32, 27.

Dommanget, J., 1982. *The interest of double star observations by Hipparcos.* Proc. Strasbourg Coll. 'Scientific Aspects of the Hipparcos Space Astrometry Mission', 22–23 February 1982, Perryman, M.A.C., Guyenne, T.D. (eds), ESA SP-177, 161.

Dommanget, J., 1985. *Concerns, realisations and prospects of the double star sub-group of the Hipparcos INCA Consortium*. Proc. Aussois Coll. 'Scientific Aspects of the Input Catalogue Preparation', 3–7 June 1985, Turon, C., Perryman, M.A.C. (orgs), ESA SP-234, 153.

Dommanget, J., 1985. *Hipparcos astrometric binaries.* Astrophys. Space Sci., 110, 47.

Dommanget, J., 1985. *Observabilité par Hipparcos des étoiles doubles spectroscopiques.* Proc. Aussois Coll. 'Scientific Aspects of the Input Catalogue Preparation', 3–7 June 1985, Turon, C., Perryman, M.A.C. (orgs), ESA SP-234, 165.

Dommanget, J., 1985. *The sub-group double stars of the Hipparcos INCA consortium*. Proc. Aussois Coll. 'Scientific Aspects of the Input Catalogue Preparation', 3–7 June 1985, Turon, C., Perryman, M.A.C. (orgs), ESA SP-234, 153.

Dommanget, J., 1988. *Concerns, realisations and prospects of the sub-group double stars of the Hipparcos INCA consortium II*. Proc. Sitges Coll. 'Scientific Aspects of the Input Catalogue Preparation', 25–29 January 1988, Torra, J., Turon, C. (eds.), 191.

Dommanget, J., 1988. *Known and unknown double and multiple stars in the Hipparcos mission*. Proc. Sitges Coll. 'Scientific Aspects of the Input Catalogue Preparation', 25–29 January 1988, Torra, J., Turon, C. (eds.), 221.

Dommanget, J., 1988. *The contribution of the Hipparcos mission and of the CCDM Catalogue to the study of wide systems.* Astrophys. Space Sci., 142, 23.

Dommanget, J., 1989. *Hipparcos: demi-échec ou demi-succès?* Ciel et Terre, 105, 111.

Dommanget, J., 1989. *The CCDM astrometric catalogue for double and multiple stars.* Contributions of the Van Vleck Observatory, 8, 77. (Star catalogues: A Centennial Tribute to A.N. Visstosky).

Dommanget, J., 1990. *Hipparcos ou la persévérance maitrisant l'infortune…* Ciel et Terre, 106, 69.

Dommanget, J., 1992. *L'astronomie des étoiles doubles visuelles.* Comptes Rendus de la Seizième Ecole de Printemps de Goutelas: Hipparcos, une nouvelle donne pour l'Astronomie, 243 & Comm. de l'Obs. R. de Belg., Serie B, No. 162.

Dommanget, J., 1995. *Is this orbit really necessary? (III). On the use of Hipparcos double star measurements for orbit computation*. A&A, 301, 919.

Dommanget, J., Lampens, P., 1992. *L'apport scientifique de la mission Hipparcos dans le domaine des étoiles doubles visuelles.* 'Hipparcos, une nouvelle donne pour l'astronomie', Benest, D., Frœschlé, C. (eds.), Editions Société Française des Spécialistes d'Astronomie, 287.

Dommanget, J., Lampens, P., 1993. *How double star astronomy may develop after Hipparcos.* Astrophys. Space Science, 200, 221, & Comm. de l'Obs. R. de Belg., Serie B, No. 161.

Dommanget, J., Nys, O., 1993. *Etoiles doubles nouvelles découvertes au cours de la préparation du catalogue d'entrée Hipparcos.* Bull. Inf. CDS, 43, 27.

Dommanget, J., Nys, O., 1994. *Catalogue des composantes d'étoiles doubles et multiples (CCDM) - première édition*. Comm. de l'Obs. R. de Belg., Série A, No. 115, 1. (Deposited at the CDS, Strasbourg, under the reference: I-211).

Dommanget, J., Nys, O., 1994. *Erreurs relevées dans le Catalogue Index*. Bull. Inf. CDS, 45, 7.

Dommanget, J., Nys, O., 1995. *Catalogue d'entrée Hipparcos: Corrections et données complémentaires.* Bull. Inf. CDS, 46, 13.

Dommanget, J., Nys, O., 1995. *Catalogue of the components of double and multiple stars (CCDM), First Edition*. Bull. Inf. CDS, 46, 3.

Dommanget, J., Nys, O., 1996. *Catalogue d'Entrée Hipparcos: corrections et données complémentaires (II)*. Bull. Inf. CDS, 48, 19.

Donati, F., 1986. *Some considerations about the Hipparcos reference system*. Proc. Bari Coll. 'Processing of Scientific Data from Hipparcos', Third FAST Thinkshop, 3–6 November 1986, Bernacca, P.L., Kovalevsky, J. (eds), 377.

Donati, F., Belforte, P., Canuto, E., Carlucci, D., Villa, A., 1984. *High accuracy on-ground attitude reconstitution for the ESA Hipparcos astrometry mission*. Proc. IFAC 9th World Congress, Budapest, III, 18.

Donati, F., Canuto, E., 1985. *Report on the task attitude reconstitution*. Proc. Marseille Coll. 'Processing of Scientific Data from Hipparcos', Second FAST Thinkshop, 21–25 January 1985, Kovalevsky, J. (ed.), 111.

Donati, F., Canuto, E., 1985. *Report on the task raw data treatment*. Proc. Marseille Coll. 'Processing of Scientific Data from Hipparcos', Second FAST Thinkshop, 21–25 January 1985, Kovalevsky, J. (ed.), 117.

Donati, F., Canuto, E., Belforte, P., 1985. *Modelling the Hipparcos attitude motion in solar eclipse conditions.* Proc. Marseille Coll. 'Processing of Scientific Data from Hipparcos', Second FAST Thinkshop, 21–25 January 1985, Kovalevsky, J. (ed.), 113.

Donati, F., Canuto, E., Carlucci, D., Villa, A., 1983. *The CSS approach to attitude reconstitution and raw data treatment*. Proc. Asiago Coll. 'Processing of Scientific Data from Hipparcos', The FAST Thinkshop, 24–27 May 1983, Bernacca, P.L. (ed.), 147.

Donati, F., Canuto, E., Falin, J.L., Frœschlé, M. Kovalevsky, J., 1992. *On-ground attitude determination in the Hipparcos mission*. Highlights of Astronomy, 9, 405.

Donati, F., Canuto, E., Fassino, B., 1985. *First improvement of the accuracy of the Input Catalogue star coordinates by star mapper data reduction*. Proc. Marseille Coll. 'Processing of Scientific Data from Hipparcos', Second FAST Thinkshop, 21–25 January 1985, Kovalevsky, J. (ed.), 115.

Donati, F., Canuto, E., Fassino, B., Belforte, P., 1986. *High accuracy on-ground attitude reconstitution for the ESA astrometry Hipparcos mission*. Manuscripta Geodaetica, 11, 115.

Donati, F., Frœschlé, M., Falin, J.L., Canuto, E., Kovalevsky, J., 1992. *Attitude determination in the Hipparcos revised mission*. A&A, 258, 41.

Donati, F., Sechi, G., 1992. *Method of comparison between determinations of the Hipparcos attitude*. A&A, 258, 46.

Eeg, J., 1986. *On the adjustment of observations in the presence of blunders.* Geodaetisk Institut, Technical Report 1, Copenhagen, Denmark.

Egret, D., 1985. *Les données existantes pour les étoiles candidates au catalogue d'entrée*. Proc. Aussois Coll. 'Scientific Aspects of the Input Catalogue Preparation', 3–7 June 1985, Turon, C., Perryman, M.A.C. (orgs), ESA SP-234, 105.

Egret, D., 1985. *The Tycho Input Catalogue and the Guide Star Catalogue of the Space Telescope*. Proc. Aussois Coll. 'Scientific Aspects of the Input Catalogue Preparation', 3–7 June 1985, Turon, C., Perryman, M.A.C. (orgs), ESA SP-234, 231.

Egret, D., 1988. *The INCA catalogues: complementary data and output format.* Proc. Sitges Coll. 'Scientific Aspects of the Input Catalogue Preparation', 25–29 January 1988, Torra, J., Turon, C. (eds.), 405.

Egret, D., 1992. *Le programme Tycho.* 'Hipparcos, une nouvelle donne pour l'astronomie', Benest, D., Frœschlé, C. (eds.), Editions Société Française des Spécialistes d'Astronomie, 119.

Egret, D., Didelon, P., McLean, B., 1988. *Tycho Input Catalogue: cross-matching the GSC with the SIMBAD database*. Proc. Sitges Coll. 'Scientific Aspects of the Input Catalogue Preparation', 25–29 January 1988, Torra, J., Turon, C. (eds.), 419.

Egret, D., Didelon, P., McLean, B.J., Russell, J.L., Turon, C., 1992. *The Tycho Input Catalogue. Cross-matching the Guide Star Catalog with the Hipparcos INCA Data Base.* A&A, 258, 217.

Egret, D., Gómez, A., 1985. *Astrophysical aspects of the contents of the Input Catalogue*. Proc. Aussois Coll. 'Scientific Aspects of the Input Catalogue Preparation', 3–7 June 1985, Turon, C., Perryman, M.A.C. (orgs), ESA SP-234, 87.

Egret, D., Halbwachs, J.L., Bässgen, G., Bastian, U., Didelon, P., Høg, E., McLean, B., Schwekendiek, P., Turon, C., Wagner, K., Wicenec, A., 1992. *The Tycho Input Catalogue compared with the first results of Tycho star recognition.* ESO Conference and Workshop Proceedings No. 43, 'Astronomy from Large Databases II', 259.

Egret, D., Høg, E., 1988. *The Tycho survey of stars brighter than eleventh.* IAU Proc. 'Mapping the sky', Debarbat, S., Eddy, J.A., Eichhorn, H.K., Upgren, A.R. (eds.), 265.

Estalella, R., Paredes, J.M., Rius, A., 1983. *Flux density monitoring of radio stars observable by Hipparcos at S-band and X-band.* A&A, 124, 309.

Estalella, R., Paredes, J.M., Rius, A., 1985. *Radio observations of Hipparcos stars.* Proc. Aussois Coll. 'Scientific Aspects of the Input Catalogue Preparation', 3–7 June 1985, Turon, C., Perryman, M.A.C. (orgs), ESA SP-234, 255.

Evans, D.W., van Leeuwen, F., Penston, M.J., Ramamani, N., Høg, E., 1992. *Hipparcos photometry: NDAC reductions.* A&A, 258, 149.

Falin, J.L., 1992. *La mission Hipparcos.* 'Hipparcos, une nouvelle donne pour l'astronomie', Benest, D., Frœschlé, C. (eds.), Editions Société Française des Spécialistes d'Astronomie, 11.

Falin, J.L., Kovalevsky, J., 1985. *Etat d'avancement de la chaine de traitement des données du consortium FAST.* Proc. Aussois Coll. 'Scientific Aspects of the Input Catalogue Preparation', 3–7 June 1985, Turon, C., Perryman, M.A.C. (orgs), ESA SP-234, 37.

Fassino, B., 1986. *Report on the grid coordinate task.* Proc. Bari Coll. 'Processing of Scientific Data from Hipparcos', Third FAST Thinkshop, 3–6 November 1986, Bernacca, P.L., Kovalevsky, J. (eds), 51.

Feaugas, J.-C., 1985. *Hipparcos: simulation des observations sur une longue période.* Proc. Aussois Coll. 'Scientific Aspects of the Input Catalogue Preparation', 3–7 June 1985, Turon, C., Perryman, M.A.C. (orgs), ESA SP-234, 91.

Fehrenbach, C., Burnage, R., Duflot, M., 1985. *Vitesses radiales pour Hipparcos avec les prismes objectifs.* Proc. Aussois Coll. 'Scientific Aspects of the Input Catalogue Preparation', 3–7 June 1985, Turon, C., Perryman, M.A.C. (orgs), ESA SP-234, 213.

Fehrenbach, C., Duflot, M., 1982. *Proposition de mesure de vitesses radiales stellaires pour le programme Hipparcos.* Proc. Strasbourg Coll. 'Scientific Aspects of the Hipparcos Space Astrometry Mission', 22–23 February 1982, Perryman, M.A.C., Guyenne, T.D. (eds), ESA SP-177, 221.

Feissel, M., Gómez, A., 1978. *The contribution of Hipparcos to the study of open clusters.* IAU Coll. 48, 'Modern Astrometry', Vienna, 12–14 September 1978, Prochazka, F.V., Tucker, R.H. (eds.), 591.

Fitzgibbon, J., 1988. *The Hipparcos dedicated control system*. Journal of the British Interplanetary Society, 41, 469.

Fontijn, L.A., van Agthoven, H.J., van der Kraan, M.R., 1986. *E-beam calibration of the Hipparcos grid pattern*. Proc. SPIE Symp., Santa Clara, 632.

Fricke, W., 1985. *Fundamental catalogues: past, present and future*. Cel. Mech., 36, 207.

Frœschlé, M., 1988. *Bilan des interruptions d'observation du satellite Hipparcos.* Proc. Sitges Coll. 'Scientific Aspects of the Input Catalogue Preparation', 25–29 January 1988, Torra, J., Turon, C. (eds.), 159.

Frœschlé, M., 1992. *Le systéme de référence Hipparcos.* 'Hipparcos, une nouvelle donne pour l'astronomie', Benest, D., Frœschlé, C. (eds.), Editions Société Française des Spécialistes d'Astronomie, 197.

Frœschlé, M., Canuto, E., Donati, F., Falin, J.L., Mignard, M., 1991. *Amélioration des positions des étoiles Hipparcos par l'utilisation des observations star-mapper.* Advances in Space Research, 11-2, 59.

Frœschlé, M., Dupic, J., Falin, J.L., Mignard, F., 1986. *Simulation des données de télémetrie ESOC.* Proc. Bari Coll. 'Processing of Scientific Data from Hipparcos', Third FAST Thinkshop, 3–6 November 1986, Bernacca, P.L., Kovalevsky, J. (eds), 129.

Frœschlé, M., Falin, J.L, Mignard, F., 1986. *Simulation des données pour les tâches étoiles doubles et magnitudes.* Proc. Bari Coll. 'Processing of Scientific Data from Hipparcos', Third FAST Thinkshop, 3–6 November 1986, Bernacca, P.L., Kovalevsky, J. (eds), 145.

Frœschlé, M., Kovalevsky, J., 1982. *The connection of a catalogue of stars with an extragalactic reference frame*. A&A, 116, 89.

Frœschlé, M., Kovalevsky, J., Mignard, F., 1983. *Effects of various types of noise on phase determination*. Proc. FAST Thinkshop, Asiago. University of Padua, Bernacca, P.L. (ed.), 209.

Frœschlé, M., Kovalevsky, J., Mignard, F., 1985. *Les corrections de l'effet de voile (veiling glare) dans les observations Hipparcos.* Proc. Aussois Coll. 'Scientific Aspects of the Input Catalogue Preparation', 3–7 June 1985, Turon, C., Perryman, M.A.C. (orgs), ESA SP-234, 133.

Frœschlé, M., Mignard, F., 1981. *Numerical simulation of the signal and data processing of the Hipparcos satellite*. Appl. Opt., 20, 3251.

Gall, J.Y. le, 1983. *L'image de diffraction polychromatique de la mission d'astrométrie spatiale Hipparcos.* Thèse, Université de Paris-sud.

Gall, J.Y. le, 1985. *Hipparcos payload modelling.* Proc. Marseille Coll. 'Processing of Scientific Data from Hipparcos', Second FAST Thinkshop, 21–25 January 1985, Kovalevsky, J. (ed.), 29.

Gall, J.Y. le, Saisse, M., Tayeb, C., Frœschlé, M., Mignard, F., 1983. *A photon journey through Hipparcos: from the payload to the signal.* Proc. Asiago Coll. 'Processing of Scientific Data from Hipparcos', The FAST Thinkshop, 24–27 May 1983, Bernacca, P.L. (ed.), 51.

Galligani, I., Betti, B., Bernacca, P.L., 1986. *The sphere reconstitution problem in the Hipparcos project*. Manuscripta Geodaetica, 11, 124.

Gazengel, F., Spagna, A., Pannunzio, R., Morbidelli, R., Sarasso, M., 1995. *The Hipparcos multiple stars: reduction methods and preliminary results.* A&A, 304, 105.

Gerbaldi, M. *et al.*, 1985. *Astrophysical parameters for Ap and Am stars with Hipparcos.* Proc. Strasbourg Coll. 'Scientific Aspects of the Hipparcos Space Astrometry Mission', 22–23 February 1982, Perryman, M.A.C., Guyenne, T.D. (eds), ESA SP-177, 111.

Gómez, A.E., 1988. *Fulfilment of astrophysical programmes.* Proc. Sitges Coll. 'Scientific Aspects of the Input Catalogue Preparation', 25–29 January 1988, Torra, J., Turon, C. (eds.), 63.

Gómez, A.E., 1988. *The INCA data base: source of the Input Catalogue*. Proc. Sitges Coll. 'Scientific Aspects of the Input Catalogue Preparation', 25–29 January 1988, Torra, J., Turon, C. (eds.), 33.

Gómez, A.E., Crifo, F., 1985. *Present status of the Input Catalogue*. Proc. Aussois Coll. 'Scientific Aspects of the Input Catalogue Preparation', 3–7 June 1985, Turon, C., Perryman, M.A.C. (orgs), ESA SP-234, 57.

Gómez, A.E., Crifo, F., 1988. *Hipparcos: an example of astrophysical uses of astrometric data*. IAU Symp. 133, 'Mapping the Sky', Paris, 1–5 June 1987, Débarbat, S., Eddy, J.A., Eichhorn, H.K., Upgren, A.R. (eds)

Gómez, A.E., Luri, X., 1992. *Hipparcos et la détermination de la magnitude absolue*. 'Hipparcos, une nouvelle donne pour l'astronomie', Benest, D., Frœschlé, C. (eds.), Editions Société Française des Spécialistes d'Astronomie, 367.

Gómez, A.E., Torra, J., 1987. *Hipparcos: the Input Catalogue*. Rev. Mexicana Astron. Astrof., 14, 441.

Gómez, A.E., Turon, C., 1995. *The Luminosity determination, based on observations made with the ESA Hipparcos satellite*. Highlights of Astronomy, Vol. 10, 399.

Granès, P., Mignard, F., 1983. *The Hipparcos photometric system*. Proc. Asiago Coll. 'Processing of Scientific Data from Hipparcos', The FAST Thinkshop, 24–27 May 1983, Bernacca, P.L. (ed.), 99.

Grenier, S., 1988. *Radial velocities obtained at the Haute-Provence Observatory from the Marly Slit spectrograph for B0 to F5 stars.* Proc. Sitges Coll. 'Scientific Aspects of the Input Catalogue Preparation', 25–29 January 1988, Torra, J., Turon, C. (eds.), 433.

Grenon, M., 1985. *New ground-based photometric observations.* Proc. Aussois Coll. 'Scientific Aspects of the Input Catalogue Preparation', 3–7 June 1985, Turon, C., Perryman, M.A.C. (orgs), ESA SP-234, 117.

Grenon, M., 1985. *Standard stars for the on-orbit photometric payload calibration*. Proc. Aussois Coll. 'Scientific Aspects of the Input Catalogue Preparation', 3–7 June 1985, Turon, C., Perryman, M.A.C. (orgs), ESA SP-234, 113.

Grenon, M., 1986. *Hipparcos: preparation of the mission: earth-based photometry.* IAU Highlights of Astronomy Vol. 7, Swings, J.P. (ed.), 691.

Grenon, M., 1988. *The Hipparcos and Tycho photometric systems.* Proc. Sitges Coll. 'Scientific Aspects of the Input Catalogue Preparation', 25–29 January 1988, Torra, J., Turon, C. (eds.), 21.

Grenon, M., 1988. *The new ground-based photometric measurements.* Proc. Sitges Coll. 'Scientific Aspects of the Input Catalogue Preparation', 25–29 January 1988, Torra, J., Turon, C. (eds.), 343.

Grenon, M., Mattei, J., Mennessier, M.O., 1992. *The Input Catalogue tested by the first Hipparcos observations - Photometry and variable stars.* Highlights of Astronomy, 9, 388.

Grenon, M., Mermilliod, M., Mermilliod, J.C., 1992. *The Hipparcos Input Catalogue*. *III*. *Photometry.* A&A, 258, 88.

Grewing, M., Høg, E., 1986. *Hipparcos/Tycho: photometry and astrometry for more than 500 000 stars.* IAU Highlights of Astronomy Vol. 7, Swings, J.P. (ed.), 707.

Großmann, V., 1993. *Tycho photometry: calibration and first results.* IAU Coll. 136, 'Stellar photometry — current techniques and future developments', Butler, C.J., Elliott, I. (eds.), Cambridge University Press, 346.

Großmann, V., Bässgen, G., Evans, D.W., Grenon, M., Grewing, M., Halbwachs, J.L., Høg, E., Mauder, H., Snijders, M.A.J., Wagner, K., Wicenec, A., 1995. *Results on Tycho photometry.* A&A, 304, 110.

Groten, E., 1982. *Geodetic applications of Hipparcos results.* Proc. Strasbourg Coll. 'Scientific Aspects of the Hipparcos Space Astrometry Mission', 22–23 February 1982, Perryman, M.A.C., Guyenne, T.D. (eds), ESA SP-177, 71.

Guibert, J., Egret, D., 1982. *Interstellar reddening and distribution of B stars in the solar neighbourhood: impact of the Hipparcos/Tycho Mission*. Proc. Strasbourg Coll. 'Scientific Aspects of the Hipparcos Space Astrometry Mission', 22–23 February 1982, Perryman, M.A.C., Guyenne, T.D. (eds), ESA SP-177, 195.

Guyenne, T.D., Battrick, B. (eds.), 1975. Proc. Frascati Symp. 'Space Astrometry', 22–23 October 1974.

Ha, J.C. van der, 1987. *Initial attitude determination for the Hipparcos satellite*. Acta Astronautica, 15, 421.

Ha, J.C. van der, 1987. *The ground segment's vital role in the Hipparcos scientific mission*. ESA Bulletin, 51, 27.

Ha, J.C. van der, 1988. *Implementation and validation of Hipparcos payload support*. Proc. Sitges Coll. 'Scientific Aspects of the Input Catalogue Preparation', 25–29 January 1988, Torra, J., Turon, C. (eds.), 121.

Ha, J.C. van der, Caldwell, S.P., 1986. *Hipparcos precise attitude determination: a balance between on-board and on-ground capabilities.* Proc. Sec. Int. Symp. on Spacecraft Flight Dynamics, Darmstadt, ESA SP–255, 385.

Halbwachs, J.L., 1988. *Tycho et les binaires à éclipses.* CR de la X^e journée de Strasbourg, 21 avril 1988, 'Détection et classification des étoiles variables', 53.

Halbwachs, J.L., 1988. *Tycho et les étoiles doubles.* l'Astronomie, décembre 1988, 503.

Halbwachs, J.L., 1992. *First double star observations in the Tycho project of the Hipparcos satellite*. IAU Coll. 135, 'Complementary approaches to double and multiple star research', ASP Conference Series, Vol. 32, 429.

Halbwachs, J.L., 1992. *Tycho, millionnaire en étoiles.* l'Astronomie, octobre 1992, 11.

Halbwachs, J.L., 1992. *Le traitement des données Tycho.* Hipparcos, une nouvelle donne pour l'astronomie', Benest, D., Frœschlé, C. (eds.), Editions Société Française des Spécialistes d'Astronomie, 137.

Halbwachs, J.L., 1993. *La mission Tycho.* J. des Astr. Français, 45, 26.

Halbwachs, J.L., Bässgen, G., Bastian, U., Egret, D., Høg, E., van Leeuwen, F., Petersen, C., Schwekendiek, P., Wicenec, A., 1994. *A preliminary list of stars from Tycho observations.* A&A, 281, L25.

Halbwachs, J.L., Egret, D., 1995. *Tycho: état actuel et perspectives.* Atelier du GDR 051, 'De l'utilisation des données Hipparcos', Frœschlé, M., Mignard, F. (eds.), 75.

Halbwachs, J.L., Høg, E., Bastian, U., Hansen, P.C., Schwekendiek, P., 1992. *Tycho star recognition*. A&A, 258, 193.

Halbwachs, J.L., Høg, E., Makarov, V.V., Wagner, K., Wicenec, A., 1996. *The treatment of double stars in the Hipparcos Tycho programme*. Workshop 'Visual double stars: foundation, dynamics and evolutionary tracks', Santiago de Compostela, Spain, 1996, Astrophysics and Space Space Science Library Series, Kluwer Academic Publishers

Hassan, H., Perryman, M.A.C., Clausen, K., van der Ha, J., Heger, D., 1990. *Hipparcos - on the road to recovery.* ESA Bulletin 64, 59.

Hemenway, P.D., 1985. *Using space telescope to tie the Hipparcos and extragalactic reference frames together.* Proc. Aussois Coll. 'Scientific Aspects of the Input Catalogue Preparation', 3–7 June 1985, Turon, C., Perryman, M.A.C. (orgs), ESA SP-234, 261.

Hemenway, P.D., 1986. *The use of Space Telescope to tie the Hipparcos reference frame to an extragalactic reference frame*. In Eichhorn, H.K., Leacock, R.J. (eds), Astrometric Techniques, 613.

Hemenway, P.D., Benedict, G.F., Jefferys, W.H., Shelus, P.J., Duncombe, R.L., 1988. *The extragalactic link. Operational preparations for the Hubble Space Telescope observations.* Proc. Sitges Coll. 'Scientific Aspects of the Input Catalogue Preparation', 25–29 January 1988, Torra, J., Turon, C. (eds.), 461.

Hemenway, P.D. Jefferys, W.H., Shelus, P.J., Duncombe, R.L., 1982. *Fiducial reference for the Hipparcos reference system*. Proc. Strasbourg Coll. 'Scientific Aspects of the Hipparcos Space Astrometry Mission', 22–23 February 1982, Perryman, M.A.C., Guyenne, T.D. (eds), ESA SP-177, 61.

Henseberge, H., Jongenelen, A., Le Poole, R.S., 1988. *Wide binaries in a Hipparcos sample centred around* $b = 0^\circ, l = 300^\circ$. Astrophys. Space Sci., 142, 259.

Hering, R., Röser, S., 1983. *On the spatial, brightness and colour distribution of IRS stars.* Proc. Asiago Coll. 'Processing of Scientific Data from Hipparcos', The FAST Thinkshop, 24–27 May 1983, Bernacca, P.L. (ed.), 131.

Hering, R., Walter, H.G., 1986. *The current state of astrometric parameter determination*. Proc. Bari Coll. 'Processing of Scientific Data from Hipparcos', Third FAST Thinkshop, 3–6 November 1986, Bernacca, P.L., Kovalevsky, J. (eds), 121.

Hestroffer, D., Morando, B., Mignard, F., Bec-Borsenberger, A., 1995. *Astrometry of minor planets with Hipparcos.* A&A, 304, 168.

Heuvel, F.A. van den, 1986. *Astrometric Satellite Hipparcos: grid-step inconsistency correction during reduction on circles.* Thesis, Delft University of Technology.

Heuvel, F.A. van den, van Daalen, D.T., 1985. *Grid-step inconsistency correction during reduction on circles.* Proc. Marseille Coll. 'Processing of Scientific Data from Hipparcos', Second FAST Thinkshop, 21–25 January 1985, Kovalevsky, J. (ed.), 221.

Høg, E., 1978. *The ESA astrometry satellite*. IAU Coll. 48, 'Modern Astrometry', Vienna, 12–14 September 1978, Prochazka, F.V., Tucker, R.H. (eds.), 557.

Høg, E., 1979. *A new start for astrometry.* Proc. Padova Coll. on European Satellite Astrometry, Barbieri, C., Bernacca, P.L. (eds.), 7.

Høg, E., 1980. *Space astrometry as NASA and ESA projects.* Mitteil. der Astron. Ges., 48, 127.

Høg, E., 1980. *The European astrometry satellite Hipparcos.* Highlights of Astronomy, 5, 783.

Høg, E., 1985. *Exchange of information between FAST and NDAC.* Proc. Marseille Coll. 'Processing of Scientific Data from Hipparcos', Second FAST Thinkshop, 21–25 January 1985, Kovalevsky, J. (ed.), 365.

Høg, E., 1985. *Meridian Observation of the faint stars proposed for Hipparcos.* Proc. Aussois Coll. 'Scientific Aspects of the Input Catalogue Preparation', 3–7 June 1985, Turon, C., Perryman, M.A.C. (orgs), ESA SP-234, 201.

Høg, E., 1985. *Overview of the Tycho data analysis.* Proc. Aussois Coll. 'Scientific Aspects of the Input Catalogue Preparation', 3–7 June 1985, Turon, C., Perryman, M.A.C. (orgs), ESA SP-234, 225.

Høg, E., 1985. *Tycho astrometry and photometry.* IAU Symp. 109, 'Astrometric Techniques', Gainsville, 9–12 January 1984, Eichhorn, H.K., Leacock, R.J. (eds).

Høg, E., 1986. *Tycho astrometry and photometry.* In Astrometric Techniques, Eichhorn, H.K., Leacock, R.J. (eds), 625.

Høg, E., 1990. *The Tycho project on-board the Hipparcos satellite*. IAU Proc. 'Inertial coordinate system on the sky', Lieske, J.H., Abalakin, V.K. (eds.), 307.

Høg, E., 1994. *Astrometri fra rummet: nu og i fremtiden*. KVANT, Fysisk Tidsskrift, 25.

Høg, E., 1995. *Tycho astrometry from 30 months of the mission*. IAU Symposium No. 166, The Hague, August 1994, 'Astronomical and Astrophysical Objectives of Sub-milliarcsecond Optical Astrometry', Høg, E., Seidelmann, P.K. (eds.) 61.

Høg, E., 1995. *Mælkevejens historie: Astrometri med Hipparcos-Tycho-Roemer-Gaia*. ESA Følgeforskning 1994, Forskningsministeriet, Internationalt forskningskontor 1995, XI–XIV.

Høg, E., 1995. *Tycho properties from 30 months of satellite mission*. IAU Proc. 'Astronomical and Astrophysical objectives of sub-milliarcsecond optical astrometry', Høg, E., Seidelmann, P.K. (eds.), 61.

Høg, E. 1995. *A new era of global astrometry and photometry from space and from ground.* Proc. 'G. Colombo' Memorial Conference, Padova, 1994, 'Ideas for Space Research after the year 2000', University of Padova, Angrilli, F., Bernacca, P.L., Bianchini, G. (eds.), 247.

Høg, E., Bässgen, G., Bastian, U., Egret, D., Halbwachs, J.L., 1988. *An early Tycho astrometric catalogue*. Proc. Sitges Coll. 'Scientific Aspects of the Input Catalogue Preparation', 25–29 January 1988, Torra, J., Turon, C. (eds.), 423.

Høg, E., Bässgen, G., Bastian, U., Egret, D., Halbwachs, J.L., 1991. *An early Tycho astrometric catalogue*. IAU Coll. 100, 'Fundamentals of Astrometry', Astrophys. Space Sci., 177, 109.

Høg, E., Bastian, U., Egret, D., Grewing, M., Halbwachs, J.L., Wicenec, A., Bässgen, G., Bernacca, P.L., Donati, F., Kovalevsky, J., van Leeuwen, F., Lindegren, L., Pedersen, H., Perryman, M.A.C., Petersen, C., Scales, D., Snijders, M.A.J., Wesselius, P.R., 1992. *Tycho data analysis. Overview of the adopted reduction software and first results.* A&A, 258, 177.

Høg, E., Bastian, U., Halbwachs, J.L., van Leeuwen, F., Lindegren, L., Makarov, V.V., Pedersen, H., Petersen, C.S., Schwekendiek, P., Wagner, K., Wicenec, A., 1995. *Tycho astrometry from half of the mission.* A&A, 304, 150.

Høg, E., Bastian, U., Hansen, P.C., van Leeuwen, F., Lindegren, L., Pedersen, H., Saust, A.B., Schwekendiek, P., Wagner, K., 1992. *Tycho astrometry calibration.* A&A, 258, 201.

Høg, E., Fogh Olsen, H.J., 1977. *Future astrometry from space and from ground.* Highlights of Astronomy, 4, Part I.

Høg, E., Jaschek, C., Lindegren, L., 1982. *Tycho: a planned astrometric and photometric survey from space*. Proc. Strasbourg Coll. 'Scientific Aspects of the Hipparcos Space Astrometry Mission', 22–23 February 1982, Perryman, M.A.C., Guyenne, T.D. (eds), ESA SP-177, 21.

Høg, E., Lindegren, L., 1985. *Precision and method for Hipparcos photometry.* Proc. Marseille Coll. 'Processing of Scientific Data from Hipparcos', Second FAST Thinkshop, 21–25 January 1985, Kovalevsky, J. (ed.), 133.

Høg, E., Makarov, V.V., Pedersen, H., 1994. *Tycho astrometry of one million stars.* Galactic and Solar System Optical Astrometry, Morrison, L.V., Gilmore, G. (eds.), Cambridge University Press, 71.

Høg, E., Wicenec, A., 1991. *Tycho assessment.* Advances in Space Research, 11-2, 35.

Høyer, P., Poder, K., Lindegren, L., Høg, E., 1981. *Derivation of positions and parallaxes from simulated observations with a scanning astrometry satellite*. A&A, 101, 228.

Huc, C., 1985. *The general structure of the data reduction and its consequences on the exploitation phase*. Proc. Marseille Coll. 'Processing of Scientific Data from Hipparcos', Second FAST Thinkshop, 21–25 January 1985, Kovalevsky, J. (ed.), 387.

Huc, C., Villenave, M., Pieplu, J.L., Guerry, A., 1991. *Hipparcos project main reduction operations within the FAST consortium*. Advances in Space Research, 11-2, 45.

Husson, J.C., 1974. *Faisabilité d'un satellite astrométrique: résultat d'une étude CNES*. Proc. Frascati Symp. 'Space Astrometry', 22–23 October 1974, Nguyen, T.D., Battrick, B.T. (eds), ESA SP-108, 43.

Jahreiß, H., 1985. *Astrometric data for nearby stars.* Proc. Aussois Coll. 'Scientific Aspects of the Input Catalogue Preparation', 3–7 June 1985, Turon, C., Perryman, M.A.C. (orgs), ESA SP-234, 189.

Jahreiß, H., 1988. *The compilation of astrometric data for the Hipparcos input catalogue*. Proc. Sitges Coll. 'Scientific Aspects of the Input Catalogue Preparation', 25–29 January 1988, Torra, J., Turon, C. (eds.), 289.

Jahreiß, H., Réquième, Y., Argue, A.N., Dommanget, J., Rousseau, M., Lederle, T., Le Poole, R.S., Mazurier, J.M., Morrison, L.V., Nys, O., Penston, M.J., Périé, J.P., Prévot, L., Tucholke, H.J., de Vegt, C., 1992. *The Hipparcos Input Catalogue. II. Astrometric data*. A&A, 258, 82.

Jahreiß, H., Réquième, Y., Crifo, F., Schwan, H., Röser, S., Bastian, U., Frœschlé, M., Lindegren, L., 1995. *Comparison of ground-based proper motions from meridian observations and Astrographic Catalogue plates with Hipparcos proper motions.* A&A, 304, 127.

Jaschek, C., 1982. *Photometric aspects of Tycho.* Proc. Strasbourg Coll. 'Scientific Aspects of the Hipparcos Space Astrometry Mission', 22–23 February 1982, Perryman, M.A.C., Guyenne, T.D. (eds), ESA SP-177, 133.

Jaschek, C., 1985. *The CDS and Hipparcos: afterthoughts.* Proc. Aussois Coll. 'Scientific Aspects of the Input Catalogue Preparation', 3–7 June 1985, Turon, C., Perryman, M.A.C. (orgs), ESA SP-234, 47.

Jaschek, C., 1988. *Some reflections on calibration and stellar kinematics.* Proc. Sitges Coll. 'Scientific Aspects of the Input Catalogue Preparation', 25–29 January 1988, Torra, J., Turon, C. (eds.), 97.

Johnston, K.J., Florkowski, D., Vegt de, C., 1988. *Precise VLA astrometry of Hipparcos radio link stars.* Proc. Sitges Coll. 'Scientific Aspects of the Input Catalogue Preparation', 25–29 January 1988, Torra, J., Turon, C. (eds.), 447.

Jonge, P.J. de, 1987. *On the ordering of unknowns during the Hipparcos reduction on circles.* Thesis, Delft University of Technology.

Kok, J.J., 1985. *Some notes on numerical methods and techniques for the least squares adjustments.* Surveying Science in Finland, 2, 1.

Kovalevsky, J., 1974. *Contributions possibles de l'astrométrie spatiale à la définition d'un système de référence absolu*. Proc. Frascati Symp. 'Space Astrometry', 22–23 October 1974, Nguyen, T.D., Battrick, B.T. (eds), ESA SP-108, 67.

Kovalevsky, J., 1979. *The expected accuracy of the astrometric satellite and its consequences for possible programmes.* Bull. Inf. CDS, 16, 24.

Kovalevsky, J., 1980. *Global astrometry by space techniques.* Celestial Mechanics, 22, 153.

Kovalevsky, J., 1984. *Prospects for space stellar astrometry.* Space Science Reviews, 39, 1.

Kovalevsky, J., 1985. *Systèmes de référence terrestres et célestes.* Bulletin Astronomique, Observatoire Royal de Belgique, Vol. X, 2, 87.

Kovalevsky, J. (ed.), 1985. Proc. Marseille Coll. 'Processing of Scientific Data from Hipparcos', Second FAST Thinkshop, 21–25 January 1985.

Kovalevsky, J., 1986. *Astronomical support to double and multiple star reduction*. Proc. Bari Coll. 'Processing of Scientific Data from Hipparcos', Third FAST Thinkshop, 3–6 November 1986, Bernacca, P.L., Kovalevsky, J. (eds), 235.

Kovalevsky, J., 1986. *Hipparcos and celestial reference frames.* IAU Highlights of Astronomy Vol. 7, Swings, J.P. (ed.), 85.

Kovalevsky, J., 1986. *The Hipparcos satellite and the organisation of the project*. In Astrometric Techniques, Eichhorn, H.K., Leacock, R.J. (eds), 581.

Kovalevsky, J., 1986. *The Hipparcos satellite and the organisation of the project*. IAU Symp. 109, 'Astrometric Techniques', Gainsville, 9–12 January 1984, Eichhorn, H.K., Leacock, R.J. (eds), 581.

Kovalevsky, J., 1986. *The project Hipparcos.* Manuscripta Geodaetica, 11, 89.

Kovalevsky, J., 1988. *Double and multiple star reduction procedures in FAST.* Proc. Sitges Coll. 'Scientific Aspects of the Input Catalogue Preparation', 25–29 January 1988, Torra, J., Turon, C. (eds.), 245.

Kovalevsky, J., 1990. *Astrometry from earth and space*. Sky and Telescope, May 1990, 493.

Kovalevsky, J., 1992. *Bilan d'Hipparcos.* Journal des Astronomes Français, 43, 17.

Kovalevsky, J., 1992. *Hipparcos: Astrometry enters space age*. Science International, Sept.-Dec., 39.

Kovalevsky, J., 1993. *The Hipparcos mission*. Memorie Soc. Astron. Ital., 64, 23.

Kovalevsky, J., 1993. *The mission Hipparcos.* 'Galactic High Energy, High Accuracy timing and Positional Astronomy', van Paradijs, J., Maitzen, H.M. (eds.), Springer Verlag, 255.

Kovalevsky, J., 1995. *The Hipparcos extragalactic link*. IAU Proc. 'Astronomical and Astrophysical objectives of sub-milliarcsecond optical astrometry', Høg, E., Seidelmann, P.K. (eds.), 127.

Kovalevsky, J., 1996. *Bilan d'Hipparcos.* 'Interférométrie visible et IR dans l'espace', Vakili, F., Loiseau, S. (eds.), Observatoire de Paris, 21.

Kovalevsky, J., Bois, E., 1986. *Attitude determination of the Hipparcos satellite*. Space Dynamics and Celestial Mechanics, Bhatnagan, K.B. (ed.), 345.

Kovalevsky, J., Dumoulin, M.T., 1983. *Observing and dwell time strategies.* Proc. Asiago Coll. 'Processing of Scientific Data from Hipparcos', The FAST Thinkshop, 24–27 May 1983, Bernacca, P.L. (ed.), 271.

Kovalevsky, J., Falin, J.L., 1985. *Reception and preparation task*. Proc. Marseille Coll. 'Processing of Scientific Data from Hipparcos', Second FAST Thinkshop, 21–25 January 1985, Kovalevsky, J. (ed.), 309.

Kovalevsky, J., Falin, J.L., Frœschlé, M., Mignard, F., 1985. *The nominal scanning law and the interruptions by the moon*. Proc. Marseille Coll. 'Processing of Scientific Data from Hipparcos', Second FAST Thinkshop, 21–25 January 1985, Kovalevsky, J. (ed.), 59.

Kovalevsky, J., Falin, J.L., Pieplu, J.L., Bernacca, P.L., Donati, F., Frœschlé, M., Galligani, I., Mignard, F., Morando, B., Perryman, M.A.C., Schrijver, H., van Daalen, D.T., van der Marel, H., Villenave, M., Walter, H.G., Badiali, M., Borriello, L., Brouw, W.N., Canuto, E., Guerry, A., Hering, R., Huc, C., Iorio-Fili, D., Lacroute, P., Lattanzi, M.G., Le Poole, R.S., Murgolo, F.P., Preston, R.A., Röser, S., Sansò, F., Wielen, R., Belforte, P., Bernstein, H.H., Bucciarelli, B., Cardini, D., Emanuele, A., Fassino, B., Lenhart, H., Lestrade, J.F., Prezioso, G., Tommasini Montanari, T., 1992. *The FAST Hipparcos Data Reduction Consortium: overview of the reduction software*. A&A, 258, 7.

Kovalevsky, J., Frœschlé, M., 1993, *Hipparcos, three years after launch*. IAU Proc. 'Developments in Astronomy and their impact on Astrophysics and Geodynamics', Mueller, I.I., Kolaczek, B. (eds.), 1.

Kovalevsky, J., Frœschlé, M., Falin, J.L., Mignard, F., 1985. *Weighting of phases and grid coordinates.* Proc. Marseille Coll. 'Processing of Scientific Data from Hipparcos', Second FAST Thinkshop, 21–25 January 1985, Kovalevsky, J. (ed.), 119.

Kovalevsky, J., Frœschlé, M., Mignard, F., Falin, J.L., Donati, F., Hering, H., Schrijver, H., van der Marel, H., Walter, H.G., 1994. *Premiers résultats de la réduction de 30 mois de données du satellite Hipparcos.* Comptes rendus de l'Académie des Sciences, Paris, 318, serie II, 1203.

Kovalevsky, J., Lindegren, L., Frœschlé, M., van Leeuwen, F., Perryman, M.A.C., Falin, J.L., Mignard, F., Penston, M.J., Petersen, C.S., Bernacca, P.L., Bucciarelli, B., Donati, F., Hering, R., Høg, E., Lattanzi, M.G., van der Marel, H., Schrijver, H., Walter, H.G., 1995. *Construction of the intermediate Hipparcos astrometric catalogue*. A&A, 304, 34.

Kovalevsky, J., Lindegren, L., Perryman, M.A.C., Hemenway, P.D., Johnston, K.J., Kislyuk, V.S., Lestrade, J.-F., Morrison, L.V., Platais, I., Röser, S., Schilbach, E., Tucholke, H.-J., de Vegt, C., Vondrák, J., Arias, F., Gontier, A.M., Arenou, F., Brosche, P., Florkowski, D.R., Garrington, S.T., Hirte, S., Kozhurina-Platais,

V., Preston, R.A., Ron, C., Rybka, S.P., Zacharias, N., 1996. *The Hipparcos Catalogue as a realisation of the extragalactic reference system*. A&A.

Kovalevsky, J., Mignard, F., Frœschlé, M., 1986. *Space Astrometry prospects and limitations.* IAU Proc. 'Relativity in Celestial Mechanics and Astrometry', Kovalevsky, J., Brumberg, V.A. (eds), 369.

Kovalevsky, J., Pacault, R., 1981. *Hipparcos: le satellite astrométrique de l'Agence Spatiale Européenne*. L'Aéronautique et l'Astronautique, 89, 22.

Kovalevsky, J., Petersen, C., van der Marel, H., Donati, F., 1992. *Performances of the Hipparcos data reduction on the great circle*. Highlights of Astronomy, 9, 409.

Kovalevsky, J., Schrijver, H., 1986. *Objectives and principles of the FAST calibration task*. Proc. Bari Coll. 'Processing of Scientific Data from Hipparcos', Third FAST Thinkshop, 3–6 November 1986, Bernacca, P.L., Kovalevsky, J. (eds), 359.

Lacroute, P., 1974. *Space astrometry projects.* Proc. Frascati Symp. 'Space Astrometry', 22–23 October 1974, Nguyen, T.D., Battrick, B.T. (eds), ESA SP-108, 5.

Lacroute, P., 1976. *Perspectives spatiales pour l'astrométrie*. l'Astronomie, 90, 223.

Lacroute, P., 1982. *Histoire du projet d'astrométrie spatiale: évolutions et perspectives.* Proc. Strasbourg Coll. 'Scientific Aspects of the Hipparcos Space Astrometry Mission', 22–23 February 1982, Perryman, M.A.C., Guyenne, T.D. (eds), ESA SP-177, 3.

Lacroute, P., 1983. *Le lissage d'attitude dans le projet Hipparcos.* Proc. Asiago Coll. 'Processing of Scientific Data from Hipparcos', The FAST Thinkshop, 24–27 May 1983, Bernacca, P.L. (ed.), 141.

Leeuwen, F. van, Evans, D.W., Lindegren, L., Penston, M.J., Ramamani, N., 1992. *Early improvements to the Hipparcos Input Catalogue through the accumulation of data from the satellite (including the NDAC attitude reconstruction description)*. A&A, 258, 119.

Leeuwen, F. van, Penston, M.J., Perryman, M.A.C., Evans, D.W., Ramamani, N., 1992. *Modelling the torques affecting the Hipparcos satellite*. A&A, 258, 53.

Leeuwen, F. van, Snijders, M.A.J. (eds.), 1986. *Hipparcos Data Simulations.* In RGO Workshop Proceedings, 22–23 September.

Lestrade, J.F., Jones, D.L., Preston, R.A., Phillips, R.B., Titus, M.A., Kovalevsky, J., Lindegren, L., Hering, R., Frœschlé, M., Falin, J.L., Mignard, F., Jacobs, C.S., Sovers, O.J., Eubanks, M., Gabuzda, D., 1995. *Preliminary link of the Hipparcos and VLBI reference frames.* A&A, 304, 182.

Lestrade, J.F., Phillips, R.B., Preston, R.A., Gabuzda, D.C., 1992. *High-precision VLBI astrometry of the radio-emitting star σ CrB – a step in linking the Hipparcos and extragalactic reference frames.* A&A, 258, 112.

Lestrade, J.F., Preston, R.A., Gabudza, D.C., Phillips, R.B., 1991. *VLBI astrometry and the Hipparcos link to extragalactic reference frame*. Advances in Space Research, 11-2, 129.

Lestrade, J.F., Preston, R.A., Mutel, R.L., Niell, A.E., Phillips, R.B., 1985. *Linking the Hipparcos catalogue to the VLBI inertial reference system, high angular resolution structures and VLBI positions of 10 radio stars.* Proc. Marseille Coll. 'Processing of Scientific Data from Hipparcos', Second FAST Thinkshop, 21–25 January 1985, Kovalevsky, J. (ed.), 87.

Lestrade, J.F., Preston, R.A., Niell, A.E., 1986. *Astrometric precision in very long baseline interferometry observations of radio stars.* Proc. Bari Coll. 'Processing of Scientific Data from Hipparcos', Third FAST Thinkshop, 3–6 November 1986, Bernacca, P.L., Kovalevsky, J. (eds), 383.

Lestrade, J.F., Preston, R.A., Niell, A.E., Mutel, R.L., Phillips, R.B., 1986. *VLBI observations of radio stars and the link between the Hipparcos and extragalactic reference frames.* IAU Symp. 109, 'Astrometric Techniques', Gainsville, 9–12 January 1984, Eichhorn, H.K., Leacock, R.J. (eds), 779.

Lestrade, J.F., Preston, R.A., Réquième, Y., Rapaport, M., Mutel, R.L., 1985. *Milli-arcsecond structures, VLBI and optical positions of 8 Hipparcos radio stars.* Proc. Aussois Coll. 'Scientific Aspects of the Input Catalogue Preparation', 3–7 June 1985, Turon, C., Perryman, M.A.C. (orgs), ESA SP-234, 251.

Lestrade, J.F., White, G.L., Jauncey, D.L., Preston, R.A., 1988. *VLBI astrometry in the southern hemisphere sky for the link of the Hipparcos and extragalactic frames.* Proc. Sitges Coll. 'Scientific Aspects of the Input Catalogue Preparation', 25–29 January 1988, Torra, J., Turon, C. (eds.), 481.

Lindegren, L., 1985. *Data reduction for Hipparcos.* IAU Symp. 109, 'Astrometric Techniques', Gainsville, 9–12 January 1984, Eichhorn, H.K., Leacock, R.J. (eds).

Lindegren, L., 1985. *Hipparcos data reductions: principles and limitations.* Proc. Aussois Coll. 'Scientific Aspects of the Input Catalogue Preparation', 3–7 June 1985, Turon, C., Perryman, M.A.C. (orgs), ESA SP-234, 31.

Lindegren, L., 1986. *Hipparcos data reductions.* In Astrometric Techniques, Eichhorn, H.K., Leacock, R.J. (eds), 593.

Lindegren, L., 1986. *Hipparcos observations of minor planets and natural satellites.* Proc. Bari Coll. 'Processing of Scientific Data from Hipparcos', Third FAST Thinkshop, 3–6 November 1986, Bernacca, P.L., Kovalevsky, J. (eds), 285.

Lindegren, L., 1986. *Treatment of double stars in the overall NDAC data processing.* Proc. Bari Coll. 'Processing of Scientific Data from Hipparcos', Third FAST Thinkshop, 3–6 November 1986, Bernacca, P.L., Kovalevsky, J. (eds), 169.

Lindegren, L., 1988. *A correlation study of simulated Hipparcos astrometry.* Proc. Sitges Coll. 'Scientific Aspects of the Input Catalogue Preparation', 25–29 January 1988, Torra, J., Turon, C. (eds.), 179.

Lindegren, L., 1991. *Hipparcos data reduction overview.* Advances in Space Research 11, (2)25,

Lindegren, L., 1992. *Status and early results of the Hipparcos astrometry project.* Proc. Conf. 'Space Sciences with particular emphasis on High-Energy Astrophysics', Munich, 30 March–4 April 1992, ESA ISY-3, 3.

Lindegren, L., 1995. *Properties of the Hipparcos Catalogue: what confidence can we have in the final data?* IAU Proc. 'Astronomical and Astrophysical objectives of sub-milliarcsecond optical astrometry', Høg, E., Seidelmann, P.K. (eds.), 55.

Lindegren, L., 1995. *Estimating the external accuracy of Hipparcos parallaxes by deconvolution.* A&A, 304, 61.

Lindegren, L., Høg, E., van Leeuwen, F., Murray, C.A., Evans, D.W., Penston, M.J., Perryman, M.A.C., Petersen, C., Ramamani, N., Snijders, M.A.J., Söderhjelm, S., Andreasen, G.K., Cruise, A.M., Elton, N., Lund, N., Poder, K., 1992. *The NDAC Hipparcos data analysis consortium. Overview of the reduction methods.* A&A, 258, 18.

Lindegren, L., Kovalevsky, J., 1986. *Hipparcos: activities of the data reduction consortia.* IAU Highlights of Astronomy Vol. 7, Swings, J.P. (ed.), 699.

Lindegren, L., Kovalevsky, J., 1992. *Accuracy predictions and final prospects for the Hipparcos mission.* Highlights of Astronomy, 9, 425.

Lindegren, L., Kovalevsky, J., 1995. *Linking the Hipparcos Catalogue to the extragalactic reference system.* A&A, 304, 189.

Lindegren, L., Kovalevsky, J., Høg, E., Turon, C., Perryman, M.A.C., 1994. *Some insights into the Hipparcos results.* ESA Bulletin No. 77, 42.

Lindegren, L., Leeuwen, F. van, 1985. *Attitude reconstitution by the Northern Data Analysis Consortium.* Proc. Marseille Coll. 'Processing of Scientific Data from Hipparcos', Second FAST Thinkshop, 21–25 January 1985, Kovalevsky, J. (ed.), 103.

Lindegren, L., Leeuwen, F. van, Petersen, C., Perryman, M.A.C., Söderhjelm, S., 1992. *Positions and parallaxes from the Hipparcos satellite. A first attempt at a global astrometric solution.* A&A, 258, 134.

Lindegren, L., Petersen, C., 1985. *Great circle reduction by the Northern Data Analysis Consortium.* Proc. Marseille Coll. 'Processing of Scientific Data from Hipparcos', Second FAST Thinkshop, 21–25 January 1985, Kovalevsky, J. (ed.), 183.

Lindegren, L., Le Poole, R.S., Perryman, M.A.C., Petersen, C., 1992. *Geometrical stability and evolution of the Hipparcos telescope.* A&A, 258, 35.

Lindegren, L., Röser, S., Schrijver, H., Lattanzi, M.G., van Leeuwen, F., Perryman, M.A.C., Bernacca, P.L., Falin, J.L., Frœschlé, M., Kovalevsky, J., Lenhardt, H., Mignard, F., 1995. *A comparison of ground-based stellar positions and proper motions with provisional Hipparcos results.* A&A, 304, 44.

Lindegren, L., Söderhjelm, S., 1985. *Sphere reconstitution by the Northern Data Analysis Consortium*. Proc. Marseille Coll. 'Processing of Scientific Data from Hipparcos', Second FAST Thinkshop, 21–25 January 1985, Kovalevsky, J. (ed.), 237.

Makarov, V.V., Bastian, U., Høg, E., Großmann, V., Wicenec, A., 1994. *35 new bright medium- and high-amplitude variables discovered by the Tycho instrument of the Hipparcos satellite*. Inf. Bull. Variable Stars, No. 4118, 1.

Makarov, V.V., Høg, E., 1995. *Random errors of Tycho astrometry.* IAU Symposium No. 166, 'Astronomical and Astrophysical Objectives of Sub-milliarcsecond Optical Astrometry', Høg, E., Seidelmann, P.K. (eds.), Kluwer Academic Publishers, Holland, 376.

Manuscripta Geodaetica, 1986. *Special Issue on Hipparcos.* Springer International, 11, No. 2.

Marel, H. van der, 1983. *Numerical smoothing of attitude data*. Proc. Asiago Coll. 'Processing of Scientific Data from Hipparcos', The FAST Thinkshop, 24–27 May 1983, Bernacca, P.L. (ed.), 263.

Marel, H. van der, 1985. *Large-scale calibration during reduction on circles.* Proc. Marseille Coll. 'Processing of Scientific Data from Hipparcos', Second FAST Thinkshop, 21–25 January 1985, Kovalevsky, J. (ed.), 209.

Marel, H. van der, 1985. *Star abscissae improvement by smoothing of attitude data*. Proc. Marseille Coll. 'Processing of Scientific Data from Hipparcos', Second FAST Thinkshop, 21–25 January 1985, Kovalevsky, J. (ed.), 197.

Marel, H. van der, 1988. *On the Great-Circle Reduction in the data analysis for the astrometry satellite Hipparcos.* PhD Thesis, Delft University of Technology. Neth. Geodetic Comm., Publ. on Geodesy, 8, No. 2.

Marel, H. van der, van Daalen, D.T., 1986. *On the geodetic aspects of the astrometry satellite Hipparcos.* Proc. CSTG Symp., Toulouse.

Marel, H. van der, van Daalen, D.T., 1986. *Recent results in reduction on circles.* Proc. Bari Coll. 'Processing of Scientific Data from Hipparcos', Third FAST Thinkshop, 3–6 November 1986, Bernacca, P.L., Kovalevsky, J. (eds), 65.

Marel, H. van der, Petersen, C., 1992. *Hipparcos great-circle reduction. Theory, results and intercomparisons.* A&A, 258, 60.

Mattei, J.A., 1988. *The AAVSO and its variable star data bank*. Proc. Sitges Coll. 'Scientific Aspects of the Input Catalogue Preparation', 25–29 January 1988, Torra, J., Turon, C. (eds.), 379.

Mauder, H., Høg, E., 1987. *Expected number of new variable stars by Tycho photometry with Hipparcos.* A&A, 185, 349.

Mayor, M., 1982. *Radial velocity measurements complementary to Hipparcos.* Proc. Strasbourg Coll. 'Scientific Aspects of the Hipparcos Space Astrometry Mission', 22–23 February 1982, Perryman, M.A.C., Guyenne, T.D. (eds), ESA SP-177, 217.

Mayor, M., 1985. *Radial velocity measurements of late spectral-type stars.* Proc. Aussois Coll. 'Scientific Aspects of the Input Catalogue Preparation', 3–7 June 1985, Turon, C., Perryman, M.A.C. (orgs), ESA SP-234, 217.

Mennessier, M.O., 1985. *Specific problems related to the variability.* Proc. Aussois Coll. 'Scientific Aspects of the Input Catalogue Preparation', 3–7 June 1985, Turon, C., Perryman, M.A.C. (orgs), ESA SP-234, 127.

Mennessier, M.O., 1988. *How accurate will be the absolute magnitudes deduced from Hipparcos parallaxes?.* Proc. Sitges Coll. 'Scientific Aspects of the Input Catalogue Preparation', 25–29 January 1988, Torra, J., Turon, C. (eds.), 113.

Mennessier, M.O., Baglin, A., 1988. *The variable stars in the Hipparcos mission*. Proc. Sitges Coll. 'Scientific Aspects of the Input Catalogue Preparation', 25–29 January 1988, Torra, J., Turon, C. (eds.), 361.

Mennessier, M.O., Barthés, D., Boughaleb, H., Figueras, F., Mattei, J.A., 1992. *Computation of ephemerides for long-period variable stars for the Hipparcos mission*. A&A, 258, 99.

Mennessier, M.O., Guibert, J., Nguyen Quang Rieu, 1982. *Mira-type variable stars and the impact of the Hipparcos mission*. Proc. Strasbourg Coll. 'Scientific Aspects of the Hipparcos Space Astrometry Mission', 22–23 February 1982, Perryman, M.A.C., Guyenne, T.D. (eds), ESA SP-177, 137.

Mermilliod, J.C., 1985. *Selection of stars in open clusters for the Hipparcos mission*. Proc. Aussois Coll. 'Scientific Aspects of the Input Catalogue Preparation', 3–7 June 1985, Turon, C., Perryman, M.A.C. (orgs), ESA SP-234, 141.

Mermilliod, J.C., Mermilliod, M., 1985. *Photometric data related to the formation of the Input Catalogue*. Proc. Aussois Coll. 'Scientific Aspects of the Input Catalogue Preparation', 3–7 June 1985, Turon, C., Perryman, M.A.C. (orgs), ESA SP-234, 111.

Mermilliod, J.C., Turon, C., 1988. *The choice of stars in galactic clusters for Hipparcos observation*. Proc. Sitges Coll. 'Scientific Aspects of the Input Catalogue Preparation', 25–29 January 1988, Torra, J., Turon, C. (eds.), 91.

Mignard, F., 1988. *FAST catalogues from IC1*. Proc. Sitges Coll. 'Scientific Aspects of the Input Catalogue Preparation', 25–29 January 1988, Torra, J., Turon, C. (eds.), 171.

Mignard, F., 1989. *Où sont les étoiles?* La Recherche, 206, 34.

Mignard, F., 1990. *Hipparcos and reference systems.* IAU Proc. 'Inertial coordinate system on the sky', Lieske, J.H., Abalakin, V.K. (eds.), 311.

Mignard, F., 1992. *La réduction des données Hipparcos.* 'Hipparcos, une nouvelle donne pour l'astronomie', Benest, D., Frœschlé, C. (eds.), Editions Société Française des Spécialistes d'Astronomie, 37.

Mignard, M., 1995. *Double star astrometry with the Hipparcos data*. IAU Proc. 'Astronomical and Astrophysical objectives of sub-milliarcsecond optical astrometry', Høg, E., Seidelmann, P.K. (eds.), 69.

Mignard, F., Falin, J.L., Frœschlé, M., Granès, P., 1985. *About the accuracy in magnitude determination*. Proc. Marseille Coll. 'Processing of Scientific Data from Hipparcos', Second FAST Thinkshop, 21–25 January 1985, Kovalevsky, J. (ed.), 143.

Mignard, F., Frœschlé, M., Badiali, M., Cardini, D., Emanuele, A., Falin, J.L., Kovalevsky, J., 1992. *Hipparcos double star recognition and processing within the FAST consortium*. A&A, 258, 165.

Mignard, F., Frœschlé, M., Falin, J.L., 1986. *Photometry with the IDT: I. single stars.* Proc. Bari Coll. 'Processing of Scientific Data from Hipparcos', Third FAST Thinkshop, 3–6 November 1986, Bernacca, P.L., Kovalevsky, J. (eds), 247.

Mignard, F., Frœschlé, M., Falin, J.L., 1986. *Photometry with the IDT: II. double stars.* Proc. Bari Coll. 'Processing of Scientific Data from Hipparcos', Third FAST Thinkshop, 3–6 November 1986, Bernacca, P.L., Kovalevsky, J. (eds), 263.

Mignard, M., Frœschlé, M., Falin, J.L., 1992. *Hipparcos main mission photometric processing.* Highlights of Astronomy, 9, 418.

Mignard, F., Frœschlé, M., Falin, J.L., 1992. *Hipparcos photometry: FAST main mission reduction*. A&A, 258, 142.

Mignard, M., Grenon, M., Falin, J.L., Frœschlé, M., 1991. *Hipparcos: First results of the photometric processing.* Advances in Space Research, 11-2, 63.

Mignard, F., Söderhjelm, S., Bernstein, H.H., Pannunzio, R., Kovalevsky, J., Frœschlé, M., Falin, J.L., Lindegren, L., Martin, C., Badiali, M., Cardini, D., Emanuele, A., Spagna, A., Bernacca, P.L., Borriello, L., Prezioso, G., 1995. *Astrometry of double stars with Hipparcos.* A&A, 304, 94.

Moine, M. le, Ranzoli, P., Clausen, K., 1985. *The Hipparcos mission: from system design to spacecraft hardware*. Proc. 36th Congress International Astronautical Federation, Pergammon.

Monet, D.G., 1988. *Recent advances in optical astrometry.* Ann. Rev. Astron. Astrophys., 26, 413.

Morando, B., 1985. *The modulation curve of a minor planet*. Proc. Marseille Coll. 'Processing of Scientific Data from Hipparcos', Second FAST Thinkshop, 21–25 January 1985, Kovalevsky, J. (ed.), 125.

Morando, B., 1986. *A more elaborate model for the modulation curve of a minor planet*. Proc. Bari Coll. 'Processing of Scientific Data from Hipparcos', Third FAST Thinkshop, 3–6 November 1986, Bernacca, P.L., Kovalevsky, J. (eds), 277.

Morando, B., Bec-Borsenberger, A., 1990. *The reference frame determined from the observations of minor planets by Hipparcos.* IAU Proc. 'Inertial coordinate system on the sky', Lieske, J.H., Abalakin, V.K. (eds.), 329.

Morel, P., 1988. *Improvement of the mass ratio determination in binaries from Hipparcos data*. Proc. Sitges Coll. 'Scientific Aspects of the Input Catalogue Preparation', 25–29 January 1988, Torra, J., Turon, C. (eds.), 235.

Morin, D., Arenou, F., 1985. *The INCA data base: sub-base from Simbad.* Proc. Aussois Coll. 'Scientific Aspects of the Input Catalogue Preparation', 3–7 June 1985, Turon, C., Perryman, M.A.C. (orgs), ESA SP-234, 63.

Morrison, L.V., Gibbs, P., 1985. *Carlsberg automatic transit circle observations for INCA*. Proc. Aussois Coll. 'Scientific Aspects of the Input Catalogue Preparation', 3–7 June 1985, Turon, C., Perryman, M.A.C. (orgs), ESA SP-234, 197.

Muiños, J.L., Quijano, L., Morrison, L.V., Gibbs, P., Helmer, L., Fabricius, C., 1988. *Carlsberg automatic meridian circle observations for INCA II*. Proc. Sitges Coll. 'Scientific Aspects of the Input Catalogue Preparation', 25–29 January 1988, Torra, J., Turon, C. (eds.), 273.

Murgolo, F.P., Schirone, M.G., 1986. *Sphere reconstitution: numerical experiments and operative software implementation*. Proc. Bari Coll. 'Processing of Scientific Data from Hipparcos', Third FAST Thinkshop, 3–6 November 1986, Bernacca, P.L., Kovalevsky, J. (eds), 111.

Murray, C.A., 1981. *Relativistic astrometry.* Mon. Not. R. Astr. Soc., 195, 639.

Murray, C.A., 1982. *Catch a hundred thousand stars.* New Scientist, 95 (1321), 31.

Murray, C.A., 1985. *Trigonometric parallaxes from the ground and from Hipparcos.* Proc. Strasbourg Coll. 'Scientific Aspects of the Hipparcos Space Astrometry Mission', 22–23 February 1982, Perryman, M.A.C., Guyenne, T.D. (eds), ESA SP-177, 115.

Murray, C.A., 1987. *Optical astronomy in the UK*. Quart. J. R. Astr. Soc., 28, 347.

Nicolet, B., Crézé, M., 1985. *Simulations: the role played by static pressures.* Proc. Aussois Coll. 'Scientific Aspects of the Input Catalogue Preparation', 3–7 June 1985, Turon, C., Perryman, M.A.C. (orgs), ESA SP-234, 75.

Nicolet, B., Crézé, M., 1988. *Static pressures: effects of some refinements on the selection*. Proc. Sitges Coll. 'Scientific Aspects of the Input Catalogue Preparation', 25–29 January 1988, Torra, J., Turon, C. (eds.), 55.

Nuñez, J., Hernández, M., Moreno, M., Codina, J.M., Torras, N., 1988. *Complementary astrometric activities in Barcelona*. Proc. Sitges Coll. 'Scientific Aspects of the Input Catalogue Preparation', 25–29 January 1988, Torra, J., Turon, C. (eds.), 335.

Nuñez, J., Jordi, C., Calaf, J., Codina, J.M., 1985. *Complementary astrometric observations of minor planets at Barcelona*. Proc. Aussois Coll. 'Scientific Aspects of the Input Catalogue Preparation', 3–7 June 1985, Turon, C., Perryman, M.A.C. (orgs), ESA SP-234, 179.

Nys, O., 1985. *New wide double stars in the Hipparcos input catalogue*. Proc. Aussois Coll. 'Scientific Aspects of the Input Catalogue Preparation', 3–7 June 1985, Turon, C., Perryman, M.A.C. (orgs), ESA SP-234, 161.

Oblak, E., Mermilliod, M., 1988. *Photométrie des étoiles doubles du catalogue d'entrée Hipparcos.* Proc. Sitges Coll. 'Scientific Aspects of the Input Catalogue Preparation', 25–29 January 1988, Torra, J., Turon, C. (eds.), 207.

Pannunzio, R., 1991. *The anomalous cases in the double star reductions of the Hipparcos missions.* Advances in Space Research, 11-2, 75.

Pannunzio, R., Scaltriti, F., 1983. *Statistical model of double stars: approach to the Hipparcos mission*. Proc. Asiago Coll. 'Processing of Scientific Data from Hipparcos', The FAST Thinkshop, 24–27 May 1983, Bernacca, P.L. (ed.), 119.

Pannunzio, R., Spagna, A., Lattanzi, M.G., Morbidelli, R., Sarasso, M., 1992. *The treatment of Hipparcos observations of some peculiar double stars: anomalous cases.* A&A, 258, 173.

Paredes, J.M., Estalella, R., Rius, A., 1987. *Flux density and polarisation observations of Hipparcos radio stars.* A&A, 186, 177.

Paredes, J.M., Estalella, R., Rius, A., 1987. *Recent radiometric observations of radio stars from the Hipparcos Input Catalogue*. Proc. 5th Working Meeting on European VLBI for Geodesy and Astrometry, Campbell, J., Schuh, H. (eds), Bonn.

Paredes, J.M., Estalella, R., Rius, A., 1988. *Monitoring of the radio emission of Hipparcos stars.* Proc. Sitges Coll. 'Scientific Aspects of the Input Catalogue Preparation', 25–29 January 1988, Torra, J., Turon, C. (eds.), 453.

Peraldi, A., 1982. *The Hipparcos Payload Optics.* American Institute of Aeronautics, 82–1852.

Perrin, M.-N., 1982. *Hipparcos and the determination of the helium content of some low-mass, non-evolved halo and disk stars of the solar neighbourhood, inferred from the fine structure of the H-R diagram*. Proc. Strasbourg Coll.

'Scientific Aspects of the Hipparcos Space Astrometry Mission', 22–23 February 1982, Perryman, M.A.C., Guyenne, T.D. (eds), ESA SP-177, 125.

Perryman, M.A.C., 1981. *The Hipparcos space astrometry mission: a report on the project (I)*. Bull. Inf. CDS, 21, 40.

Perryman, M.A.C., 1982. *The Hipparcos space astrometry mission: a report on the project (II)*. Bull. Inf. CDS, 22, 87.

Perryman, M.A.C., 1982. *Scientific organisation of the Hipparcos project*. Proc. Strasbourg Coll. 'Scientific Aspects of the Hipparcos Space Astrometry Mission', 22–23 February 1982, Perryman, M.A.C., Guyenne, T.D. (eds), ESA SP-177, 31.

Perryman, M.A.C., 1983. *The Hipparcos space astrometry mission: a report on the project (III)*. Bull. Inf. CDS, 24, 57.

Perryman, M.A.C., 1983. *The Hipparcos Mission: astrometry from space*. *Surveys of the Southern Galaxy.* Burton, W.B., Israel, F.P. (eds.), Reidel Pub. Co., 281.

Perryman, M.A.C., 1983. *The Hipparcos space astrometry mission*. COSPAR Symposium, Ottawa, Adv. Space Research, 1983, Vol. 2, No. 4, 51.

Perryman, M.A.C., 1985. *Ad Astra - Hipparcos: The European Space Agency's Astrometry Mission*. ESA BR-24.

Perryman, M.A.C., 1986. *Hipparcos - the ESA space astrometry mission: overview and status*. In IAU (1986) Highlights of Astronomy, ed. J.P. Swings, 673.

Perryman, M.A.C., 1986. *Measuring the stars.* in Space Education (British Interplanetary Society Publication), 1, No. 12, 557.

Perryman, M.A.C., 1986. *The ESA Space Astrometry Mission: Overview and Status.* IAU Highlights of Astronomy Vol. 7, Swings, J.P. (ed.), 673.

Perryman, M.A.C., 1986. *The Hipparcos space astrometry mission and its scientific goals.* The Observatory, 106, 137.

Perryman, M.A.C., 1987. *Hipparcos - high precision astrometric data from space*. Proc. 10th IAU Regional Meeting, Prague, Vol. 3, Sidlichovsky, M. (ed.), 11.

Perryman, M.A.C., 1989. *Hipparcos: astrometry from space.* Nature, 340, 111.

Perryman, M.A.C., 1990. *In-orbit status of the Hipparcos astrometry mission*. IAU Symposium 141: The Inertial Reference Frame, Leningrad, 297.

Perryman, M.A.C., 1990. *The Hipparcos mission - will it be a scientific success?*. IAU Colloquium 123: Observatories in Earth Orbit and Beyond, GSFC, 1990, Y. Kondo (ed.), 27.

Perryman, M.A.C., 1991. *Hipparcos revised mission overview.* Proceedings of XXVIII COSPAR (The Hague, 1990), 1991, Adv. Space Research Vol. 11, 15.

Perryman, M.A.C., 1992. *The Hipparcos astrometry satellite: two years after launch*. Highlights of Astronomy, 9, 383.

Perryman, M.A.C., 1994. *Some insights into the Hipparcos results.* ESA Bulletin 77, 42.

Perryman, M.A.C., 1994. *Astrometric and astrophysical insight into the Hipparcos data quality.* IAU General Assembly, The Hague. In 'Astronomical and Astrophysical Objectives of Sub-Milliarcsecond Optical Astrometry', Høg, E., Seidelmann, P.K. (eds), 83.

Perryman, M.A.C., 1995. *Astrometric and astrophysical insights into the Hipparcos data quality.* IAU Proc. 'Astronomical and Astrophysical objectives of sub-milliarcsecond optical astrometry', Høg, E., Seidelmann, P.K. (eds.), 83.

Perryman, M.A.C. and the Hipparcos Science Team, 1992. *Early scientific results from Hipparcos and future expectations.* ESA Bulletin 69, 51.

Perryman, M.A.C. and the Hipparcos Science Team, 1994. *The contribution of Hipparcos to fundamental astronomy.* 27th ESLAB Symp., Frontiers of Space and Ground-Based Astronomy, Wamsteker W. *et al.* (eds), Kluwer, 95.

Perryman, M.A.C., Hassan, H., 1989. *Hipparcos.* ESA Bulletin, 58, 77.

Perryman, M.A.C., Hassan, H. *et al.*, 1989 *The Hipparcos Mission, Pre-Launch Status, Volume I: The Hipparcos Satellite*. ESA SP-1111.

Perryman, M.A.C., Heger, D., 1993. *Hipparcos - four years after launch*. ESA Bulletin 75.

Perryman, M.A.C., Høg, E., Kovalevsky, J., Lindegren, L., Turon, C., Bernacca, P.L., Crézé, M., Donati, F., Grenon, M., Grewing, M., van Leeuwen, F., van der Marel, H., Murray, C.A., Le Poole, R.S., Schrijver, H., 1992. *In-orbit performance of the Hipparcos astrometry satellite*. A&A, 258, 1.

Perryman, M.A.C., Lindegren, L., Arenou, F., Bastian, U., Bernstein, H.H., Leeuwen van, F., Schrijver, H., Bernacca, P.L., Evans, D.W., Falin, J.L., Frœschlé, M., Grenon, M., Hering, R., Høg, E., Kovalevsky, J., Mignard, F., Murray, C.A., Penston, M.J., Petersen, C.S., Le Poole, R.S., Söderhjelm, S., Turon, C., 1996. *Hipparcos distances and mass limits for the planetary system candidates: 47 UMa, 70 Vir, and 51 Peg*. A&A, 310, L21.

Perryman, M.A.C., Lindegren, L., Casertano, S.C., Lattanzi, M.G., 1996. *Searches for planets beyond our Solar System: how astrometry helps.* ESA Bulletin, 87, 65.

Perryman, M.A.C., Lindegren, L., Kovalevsky, J., Turon, C., Høg, E., Grenon, M., Schrijver, H., Bernacca, P.L., Crézé, M., Donati, F., Evans, D.W., Falin, J.L., Frœschlé, M., Gómez, A., Grewing, M., van Leeuwen, F., van der Marel, H., Mignard, F., Murray, C.A., Penston, M.J., Petersen, C.S., Le Poole, R.S., Walter, H., 1995. *Parallaxes and the Hertzsprung-Russell diagram from the preliminary Hipparcos solution H30.* A&A, 304, 69.

Perryman, M.A.C., Lindegren, L., Murray, C.A., Høg, E., Kovalevsky, J. *et al.*, 1989 *The Hipparcos Mission, Pre-Launch Status, Volume III: The Data Reductions.* ESA SP-1111.

Perryman, M.A.C., Schuyer, M., 1985. *The present status of the Hipparcos project*. Proc. Aussois Coll. 'Scientific Aspects of the Input Catalogue Preparation', 3–7 June 1985, Turon, C., Perryman, M.A.C. (orgs), ESA SP-234, 13.

Perryman, M.A.C., Turon, C., 1988. *Publication of the INCA and Hipparcos data*. Proc. Sitges Coll. 'Scientific Aspects of the Input Catalogue Preparation', 25–29 January 1988, Torra, J., Turon, C. (eds.), 409.

Perryman, M.A.C., Turon, C. *et al.*, 1989 *The Hipparcos Mission, Pre-Launch Status, Volume II: The Input Catalogue*. ESA SP-1111.

Pieplu, J.L., 1983. *Review of the data processing task*. Proc. Asiago Coll. 'Processing of Scientific Data from Hipparcos', The FAST Thinkshop, 24–27 May 1983, Bernacca, P.L. (ed.), 333.

Pieplu, J.L., 1985. *Review of the data processing task*. Proc. Marseille Coll. 'Processing of Scientific Data from Hipparcos', Second FAST Thinkshop, 21–25 January 1985, Kovalevsky, J. (ed.), 379.

Pieplu, J.L., 1986. *Hipparcos balaiera 120 000 étoiles.* Journal de liaison du CNES, 44, 2.

Pieplu, J.L., 1986. *Progress status of the data processing task*. Proc. Bari Coll. 'Processing of Scientific Data from Hipparcos', Third FAST Thinkshop, 3–6 November 1986, Bernacca, P.L., Kovalevsky, J. (eds), 135.

Pieplu, J.L., 1988. *FAST main reduction system structure*. Proc. Sitges Coll. 'Scientific Aspects of the Input Catalogue Preparation', 25–29 January 1988, Torra, J., Turon, C. (eds.), 145.

Pinard, M., Stellmacher, I., van der Marel, H., Kovalevsky, J., Saint-Crit, L., 1983. *Hipparcos attitude simulation*. Proc. Asiago Coll. 'Processing of Scientific Data from Hipparcos', The FAST Thinkshop, 24–27 May 1983, Bernacca, P.L. (ed.), 91.

Platais, I., Girard, T.M., van Altena, W.F., Ma, W.Z., Lindegren, L., Crifo, F., Jahreiß, H., 1995. *A study of systematic positional errors in the SPM plates.* A&A, 304, 141.

Poole le, R.S., Hensberge, H., Jongeneelen, A., 1988. *Plate measurements at Leiden Observatory.* Proc. Sitges Coll. 'Scientific Aspects of the Input Catalogue Preparation', 25–29 January 1988, Torra, J., Turon, C. (eds.), 279.

Preston, R.A., Lestrade, J.F., Mutel, R.L., 1983. *Linking Hipparcos observations to an extragalactic VLBI frame by use of optically bright radio stars.* Proc. Asiago Coll. 'Processing of Scientific Data from Hipparcos', The FAST Thinkshop, 24–27 May 1983, Bernacca, P.L. (ed.), 395.

Prévot, L., 1985. *Stars in the direction of the Magellanic Clouds.* Proc. Aussois Coll. 'Scientific Aspects of the Input Catalogue Preparation', 3–7 June 1985, Turon, C., Perryman, M.A.C. (orgs), ESA SP-234, 137.

Prévot, L., 1988. *Choice of stars in and around the Magellanic Clouds.* Proc. Sitges Coll. 'Scientific Aspects of the Input Catalogue Preparation', 25–29 January 1988, Torra, J., Turon, C. (eds.), 89.

Quijano, L., Muiños, J.L., Cano, F., 1988. *Photographic observations of minor planets at San Fernando.* Proc. Sitges Coll. 'Scientific Aspects of the Input Catalogue Preparation', 25–29 January 1988, Torra, J., Turon, C. (eds.), 331.

Rapaport, M., Ducourant, C., 1988. *The observations of the 62 minor planets of Hipparcos programme at Bordeaux Observatory. Comparison with ephemerides.* Proc. Sitges Coll. 'Scientific Aspects of the Input Catalogue Preparation', 25–29 January 1988, Torra, J., Turon, C. (eds.), 333.

Ratier, G., 1985. *Performances of Hipparcos optical telescope*. Proc. Aussois Coll. 'Scientific Aspects of the Input Catalogue Preparation', 3–7 June 1985, Turon, C., Perryman, M.A.C. (orgs), ESA SP-234, 23.

Ratier, G., Arnoux, J.J., Fruit, M., 1985. *Some optical test methods used in performance evaluation of the Hipparcos telescope*. Proc. SPIE/ANRT Conf., Cannes.

Ratier, G., van Katwijk, K., Fade, G., Perryman, M.A.C., 1992. *The Hipparcos payload's in-orbit performance*. ESA Bulletin 69, 27.

Réquième, Y., 1986. *Hipparcos: preparation of the mission: earth-based astrometry.* IAU Highlights of Astronomy Vol. 7, Swings, J.P. (ed.), 695.

Réquième, Y., 1988. *Ground-based astrometry for Hipparcos: the end of the task?* Proc. Sitges Coll. 'Scientific Aspects of the Input Catalogue Preparation', 25–29 January 1988, Torra, J., Turon, C. (eds.), 267.

Réquième, Y., Morrison, L.V., Helmer, L., Fabricius, C., Lindegren, L., Frœschlé, M., van Leeuwen, F., Mignard, F., Perryman, M.A.C., Turon, C., 1995. *Meridian circle reductions using preliminary Hipparcos positions.* A&A, 304, 121.

Réquième, Y., Turon, C., 1991. *The Hipparcos Input Catalogue: a progress report from an astrometric point of view.* Astrophys. Space Sci., 177, 115.

Reynolds, J.E., Jauncey, D.L., Staveley-Smith, L., Tzioumis, A.K., de Vegt, C., Zacharias, N., Perryman, M.A.C., van Leeuwen, F., King, E.A., McCulloch, P.M., Russell, J.L., Johnston, K.J., Hindsley, R., Malin, D.F., Argue, A.N., Manchester, R.N., Kesteven, M.J., White, G.L., Jones, P.A., 1995. *Accurate registration of radio and optical images of SN1987A*. A&A, 304, 116.

Robichon, N., Turon, C., Makarov, V.V., Perryman, M.A.C., Høg, E., Frœschlé, M., Evans, D.W., Guibert, J., Le Poole, R.S., van Leeuwen, F., Bastian, U., Halbwachs, J.L., 1995. *Schmidt plate astrometric reductions using preliminary Hipparcos and Tycho data.* A&A, 304, 132.

Röser, S., 1983. *Link of the Hipparcos system with the FK5.* Proc. Asiago Coll. 'Processing of Scientific Data from Hipparcos', The FAST Thinkshop, 24–27 May 1983, Bernacca, P.L. (ed.), 391.

Röser, S., 1986. *Connection between the Hipparcos catalogue and the FK5.* In Astrometric Techniques, Eichhorn, H.K., Leacock, R.J. (eds), 773.

Röser, S., Høg, E., 1993. *Tycho Reference Catalogue: a catalogue of positions and proper motions of one million stars.* Workshop 'Databases for galactic structure', Davis Philip, A.G., Hauck, B., Upgren, A.R. (eds.), L. Davis Press.

Röser, S., Walter, H.G., 1986. *Astrometry satellite Hipparcos: star selection and data reduction.* Bull. Inf. CDS, 20, 55.

Roulet, M.E., Oppliger, Y., Stauffer, L., Luginbuhl, H., Fontijn, L.A., van der Kraan, M.R., 1986. *Diffraction grid fabricated by advanced microelectronics techniques for Hipparcos.* Proc. SPIE Symp., Santa Clara, 632.

Rousseau, J.M., Périé, J.P., Gachard, M.T., 1996. *Hémisphère Sud, Catalogue de Bordeaux, Volumes 1-5.* Observatoire de Bordeaux.

Rousseau, J.M., Périé, J.P., Gachard, M.T., 1996. *Stars of the southern hemisphere proposed for the Hipparcos mission*. A&A SS, 116, 301.

Russell, J.L., Egret, D., 1986. *Hipparcos: the Tycho Input Catalogue*. IAU Highlights of Astronomy Vol. 7, Swings, J.P. (ed.), 713.

Scales, D.R., Snijders, M.A.J., Andreasen, G.K., Grenon, M., Grewing, M., Høg, E., van Leeuwen, F., Lindegren, L., Mauder, H., 1992. *Tycho photometry calibration and first results.* A&A, 258, 211.

Schober, H.J., 1982. *Search for binary asteroids with the ESA space astrometry satellite Hipparcos.* Proc. Strasbourg Coll. 'Scientific Aspects of the Hipparcos Space Astrometry Mission', 22–23 February 1982, Perryman, M.A.C., Guyenne, T.D. (eds), ESA SP-177, 169.

Schrijver, J., 1983. *Aspects of the FAST quick-look processing.* Proc. Asiago Coll. 'Processing of Scientific Data from Hipparcos', The FAST Thinkshop, 24–27 May 1983, Bernacca, P.L. (ed.), 339.

Schrijver, J., 1985. *First look processing.* Proc. Marseille Coll. 'Processing of Scientific Data from Hipparcos', Second FAST Thinkshop, 21–25 January 1985, Kovalevsky, J. (ed.), 375.

Schrijver, J., 1986. *Hipparcos: the instrument.* Manuscripta Geodaetica, 11, 97.

Schrijver, J., 1986. *The advancement of the first-look task.* Proc. Bari Coll. 'Processing of Scientific Data from Hipparcos', Third FAST Thinkshop, 3–6 November 1986, Bernacca, P.L., Kovalevsky, J. (eds), 345.

Schrijver, H., 1991. *Hipparcos calibration.* Advances in Space Research, 11-2, 51.

Schrijver, H., 1992. *Calibration and characteristics of the Hipparcos payload.* Highlights of Astronomy, 9, 401.

Schrijver, H., 1992. *Comparison of Hipparcos results obtained on different dates on the same great circle.* A&A, 258, 70.

Schrijver, H., van der Marel, H., 1992. *Geometrical calibration and assessment of the stability of the Hipparcos payload.* A&A, 258, 31.

Schutz, B.F., 1982. *Relativistic effects in Hipparcos data.* Proc. Strasbourg Coll. 'Scientific Aspects of the Hipparcos Space Astrometry Mission', 22–23 February 1982, Perryman, M.A.C., Guyenne, T.D. (eds), ESA SP-177, 181.

Schuyer, M., 1985. *Hipparcos: a European astrometry satellite. Mission objectives, technical issues and approaches.* IAF-22-206.

Schuyer, M., 1985. *The Hipparcos satellite mission: the objectives and their implementation.* ESA Bulletin, 42, 22.

Schuyer, M., 1987. *Hipparcos: a breakthrough in fundamental astronomy; an achievement in inertial guidance.* Advances in the Astronautical Sciences, 55.

Söderhjelm, S., 1985. *Statistical models for Hipparcos binaries.* Astrophys. Sp. Sci. 110, 77.

Söderhjelm, S., 1986. *NDAC simulations of double and multiple stars: detectability and astrometric accuracy.* Proc. Bari Coll. 'Processing of Scientific Data from Hipparcos', Third FAST Thinkshop, 3–6 November 1986, Bernacca, P.L., Kovalevsky, J. (eds), 155.

Söderhjelm, S., 1988. *Double star processing by NDAC.* Proc. Sitges Coll. 'Scientific Aspects of the Input Catalogue Preparation', 25–29 January 1988, Torra, J., Turon, C. (eds.), 257.

Söderhjelm, S., 1991. *Double star observations with Hipparcos.* Proc. 'Nordic-Baltic Astronomy Meeting', 18–21 June 1990, Lagerkvist, C.-I., Kiselman, D., Lindgren, M. (eds), 329.

Söderhjelm, S., Evans, D.W., van Leeuwen, F., Lindegren, L., 1992. *Detection and measurement of double stars with the Hipparcos satellite: NDAC reductions.* A&A, 258, 157.

Söderhjelm, S., Lindegren, L., 1982. *Inertial frame determination using minor planets: a proposal for Hipparcos observations.* Proc. Strasbourg Coll. 'Scientific Aspects of the Hipparcos Space Astrometry Mission', 22–23 February 1982, Perryman, M.A.C., Guyenne, T.D. (eds), ESA SP-177, 191.

Söderhjelm, S., Lindegren, L., 1982. *Inertial frame determination using minor planets: a simulation of Hipparcos observations.* A&A, 110, 156.

Söderhjelm, S., Lindegren, L., 1986. *Accuracy estimates for the determination of the solar space-time metric by Hipparcos.* IAU Proc. 'Relativity in Celestial Mechanics and Astrometry', Kovalevsky, J., Brumberg, V.A. (eds), 393.

Söderhjelm, S., Lindegren, L., van Leeuwen, F., Evans, D.W., 1992. *Detection and measurement of double stars with Hipparcos: Provisional results from NDAC.* Proc. IAU Coll. 135, Astronomical Society of the Pacific Conference Series, Vol. 32, McAlister, H.A., Hartkopf, W.I. (eds), 412.

Strim, B., Cugno, W., 1986. *Assembly, integration and testing of the Hipparcos satellite in Aeritalia.* Proc. Bari Coll. 'Processing of Scientific Data from Hipparcos', Third FAST Thinkshop, 3–6 November 1986, Bernacca, P.L., Kovalevsky, J. (eds), 7.

Strim, B., Cugno, W., Morsillo, G., 1987. *The Hipparcos satellite: Aeritalia involvement and system test activities and results.* IAF-87-453.

Swings, J.-P. (ed.), 1986. *The ESA Space Astrometry Mission Hipparcos.* IAU Highlights of Astronomy Vol. 7.

Tammann, G., 1979. *Implications of astrometric programmes for the extragalactic distance scale*. Proc. Padova Coll. on European Satellite Astrometry, Barbieri, C., Bernacca, P.L. (eds.), 271.

Teunissen, P.J.G., 1985. *The geometry of geodetic inverse linear mapping and non-linear adjustment*. Neth. Geodetic Commission, Publ. on Geodesy. Vol. 8, 1.

Tommasini Montanari, T., Bucciarelli, B., Lattanzi, M.G., 1985. *Continuous experiments on the great circle reduction*. Proc. Marseille Coll. 'Processing of Scientific Data from Hipparcos', Second FAST Thinkshop, 21–25 January 1985, Kovalevsky, J. (ed.), 229.

Tommasini Montanari, T., Bucciarelli, B., Tramontin, C., 1985. *Two different methods for the solution of the large least squares problem in the sphere reconstitution*. Proc. Marseille Coll. 'Processing of Scientific Data from Hipparcos', Second FAST Thinkshop, 21–25 January 1985, Kovalevsky, J. (ed.), 243.

Torra, J., Figueras, F., Jordi, C., Paredes, J.M., Rosselló, G., 1988. *A contribution to the photometric observations for Hipparcos.* Proc. Sitges Coll. 'Scientific Aspects of the Input Catalogue Preparation', 25–29 January 1988, Torra, J., Turon, C. (eds.), 355.

Torra, J., Figueras, F., Paredes, J.M., Rosselló, Sala, F., 1985. *Complementary photometric observations for Hipparcos.* Proc. Aussois Coll. 'Scientific Aspects of the Input Catalogue Preparation', 3–7 June 1985, Turon, C., Perryman, M.A.C. (orgs), ESA SP-234, 219.

Tucholke, H.J., 1988. *Astrometry of southern open cluster stars for the preparation of the Hipparcos Input Catalogue*. Proc. Sitges Coll. 'Scientific Aspects of the Input Catalogue Preparation', 25–29 January 1988, Torra, J., Turon, C. (eds.), 285.

Tuohey, W.G., Campbell, J.G., O'Mongain, E., Gardelle, J.P., Wills, R.D., 1987. *In-Orbit scientific calibration of Hipparcos.* ESA Journal, 87/1, 1.

Turon, C., 1975. *Some astrophysical consequences of an improvement in parallaxes.* Proc. Frascati Symp. 'Space Astrometry', 22–23 October 1974, Nguyen, T.D., Battrick, B.T. (eds), ESA SP-108, 115.

Turon, C., 1979. *Some consequences of Space Astrometry on Galactic Astrophysics.* European Satellite Astrometry, Barbieri, C., Bernacca, P.L. (eds), 231.

Turon, C., 1980. *Hipparcos, une nouvelle base pour l'astronomie*. La Recherche, 11, No. 12, 709.

Turon, C., 1981. *Hipparcos et les étoiles proches.* Bull. Inf. CDS, 20, 49.

Turon, C., 1984. *Compilation of the Hipparcos Input Catalogue: an extensive use of Schmidt Sky Surveys.* IAU Coll. 78.

Turon, C., 1985. *Progress report of the Input Catalogue preparation*. Proc. Marseille Coll. 'Processing of Scientific Data from Hipparcos', Second FAST Thinkshop, 21–25 January 1985, Kovalevsky, J. (ed.), 77.

Turon, C., 1986. *A first possible Input Catalogue*. Proc. Bari Coll. 'Processing of Scientific Data from Hipparcos', Third FAST Thinkshop, 3–6 November 1986, Bernacca, P.L., Kovalevsky, J. (eds), 17.

Turon, C., 1988. *A very special catalogue: the Hipparcos Input Catalogue*. IAU Symp. 133, 'Mapping the Sky', Paris, 1–5 June 1987, Débarbat, S., Eddy, J.A., Eichhorn, H.K., Upgren, A.R. (eds)

Turon, C., 1988. *Content and publication of INCA catalogues.* Proc. Sitges Coll. 'Scientific Aspects of the Input Catalogue Preparation', 25–29 January 1988, Torra, J., Turon, C. (eds.), 397.

Turon, C., 1988. *Double star and veiling glare processing in INCA simulations.* Proc. Sitges Coll. 'Scientific Aspects of the Input Catalogue Preparation', 25–29 January 1988, Torra, J., Turon, C. (eds.), 215.

Turon, C., 1988. *Fulfilment of astrometric proposals. INCA tuning.* Proc. Sitges Coll. 'Scientific Aspects of the Input Catalogue Preparation', 25–29 January 1988, Torra, J., Turon, C. (eds.), 71.

Turon, C., 1996. *Hipparcos, a new start for many astronomical and astrophysical topics.* Rev. Mod. Astron., 9, 69.

Turon, C., Arenou, F., Baylac, M.-O., Boumghar, D., Crifo, F., Gómez, A., Marouard, M., Mekkas, M., Morin, D., Sellier, A., 1991. *The Hipparcos INCA Database*. Databases and On-line Data in Astronomy, Albrecht, M.A., Egret, D. (eds), 67.

Turon, C., Arenou, F., Crifo, F., Gómez, A., Morin, D., 1992. *The Hipparcos observing programme: performances of the Input Catalogue*. Highlights of Astronomy, Vol. 9, 388.

Turon, C., Arenou, F., Crifo, F., Gómez, A., Morin, D., Sellier, A., 1992. *The Hipparcos Input Catalogue: contents of the printed version*. Highlights of Astronomy, Vol. 9, 397.

Turon, C., Arenou, F., Evans, D.W., van Leeuwen, F., 1992. *Comparison of the first results from the Hipparcos star mappers with the Hipparcos Input Catalogue*. A&A, 258, 125.

Turon, C., Arenou, F., Frœschlé, M., Van Leeuwen, F., Lindegren, L., Mignard, F., Morin, D., Perryman, M.A.C., 1992. *The performance of the Hipparcos Input Catalogue as compared with the first results of the Hipparcos mission*. Astronomy from Large Databases II, Heck, A., Murtagh, F. (eds), 135.

Turon, C., Crifo, F., 1986. *Hipparcos: Activities of the Input Catalogue Consortium*. IAU Highlights of Astronomy Vol. 7, Swings, J.P. (ed.), 683.

Turon, C., Crifo, F., 1986. *Le satellite Hipparcos: préparation du catalogue d'entrée ou un dialogue nouveau entre astrophysiciens et astrométristes.* Journal des Astronomes Français, 26, 4.

Turon, F., Crifo, F., Morin, D., 1994. *Hipparcos and the red dwarf populations.* Astrophys. Space Sci., 217, 77.

Turon, C., Gómez, A., Crifo, F., 1988. *Scientific uses of the INCA data base*. Astronomy from large databases: scientific objectives and methodological approaches, Garching, Murtagh, F., Heck, A. (eds), 73.

Turon, C., Gómez, A., Crifo, F., Crézé, M., Perryman, M.A.C., Morin, D., Arenou, F., Nicolet, B., Chareton, M., Egret, D., 1992. *The Hipparcos Input Catalogue*. *I. Star selection*. A&A, 258, 74.

Turon, C., Gómez, A., Morin, 1994. *Scientific content of the Hipparcos Input Catalogue*. IAU Symp. 166., Høg, E., Seidelmann P.K. (eds), 77.

Turon, C., van Leeuwen, F., 1995. *Hipparcos data on pulsating stars.* IAU Coll. 155, Astronomical Society of the Pacific Conferences Series, Vol. 83, Stobie, R.S., Whitelock, P.A. (eds), 241.

Turon, C., Nicolet, B., Crézé, M., 1985. *Expected fulfilments of observation proposals versus ESA priority.* Proc. Aussois Coll. 'Scientific Aspects of the Input Catalogue Preparation', 3–7 June 1985, Turon, C., Perryman, M.A.C. (orgs), ESA SP-234, 83.

Turon, C., Perryman, M.A.C. (eds.), 1985. Proc. Aussois Coll. 'Scientific Aspects of the Input Catalogue Preparation', 3–7 June 1985, ESA SP-234.

Turon, C., Réquième, Y., 1986. *Preparation of the Hipparcos Input Catalogue: preliminary astrometric observations.* IAU Symp. 109, 'Astrometric Techniques', Gainsville, 9–12 January 1984, Eichhorn, H.K., Leacock, R.J. (eds), 605.

Turon, C., Réquième, Y., Grenon, M., Gómez, A., Morin, D., Crifo, F., Arenou, F., Frœschlé, M., Mignard, F., Perryman, M.A.C., Argue, A.N., Crézé, M., Dommanget, J., Egret, D., Jahreiß, H., Mennessier, M.O., Pham, A., Evans, D.W., van Leeuwen, F., Lindegren, L., 1995. *Properties of the Hipparcos Input Catalogue*. A&A, 304, 82.

Turon, C. *et al.*, 1992. *The Hipparcos Input Catalogue, Volumes 1–7.* ESA SP-1136.

Turon, C. *et al.*, 1992. *The Hipparcos Input Catalogue*. Tape version, Bull. Inf. CDS, 41, 9.

Turon, C. *et al.*, 1993. *Version 2 of The Hipparcos Input Catalogue*. Tape version, Bull. Inf. CDS, 43, 5.

Turon, C. *et al.*, 1994. *The Hipparcos Input Catalogue and HICIS*. CD-ROM Version.

Vaghi, S., 1985. *The star observation strategy for Hipparcos.* Data Analysis in Astronomy, (Di Gesu, V. *et al.*, eds.), Plenum Publishing Co.

Vaghi, S., 1988. *Development, testing and on-ground calibration of the Hipparcos payload.* Proc. Sitges Coll. 'Scientific Aspects of the Input Catalogue Preparation', 25–29 January 1988, Torra, J., Turon, C. (eds.), 13.

Vargas, A., 1985. *Present estimate of the computer workload.* Proc. Marseille Coll. 'Processing of Scientific Data from Hipparcos', Second FAST Thinkshop, 21–25 January 1985, Kovalevsky, J. (ed.), 397.

Vegt, C. de, 1982. *On the importance of the Hipparcos stellar net for photographic catalogue work*. Proc. Strasbourg Coll. 'Scientific Aspects of the Hipparcos Space Astrometry Mission', 22–23 February 1982, Perryman, M.A.C., Guyenne, T.D. (eds), ESA SP-177, 49.

Vegt, C. de, Johnston, K.J., Florkowski, D.R., 1985. *Relating the Hipparcos reference frame to the radio reference frame*. Proc. Aussois Coll. 'Scientific Aspects of the Input Catalogue Preparation', 3–7 June 1985, Turon, C., Perryman, M.A.C. (orgs), ESA SP-234, 247.

Vegt, C. de, Johnston, K.J., Russell, J., Hughes, J.A., Jauncey, D., Nicholson, G., 1988. *Towards the establishment of a radio-optical reference frame*. Proc. Sitges Coll. 'Scientific Aspects of the Input Catalogue Preparation', 25–29 January 1988, Torra, J., Turon, C. (eds.), 469.

Vegt, C. de, Zacharias, N., Johnson, K.J., 1991. *Ground-based and radio astrometry of Hipparcos extragalactic link objects.* Advances in Space Research, 11-2, 133.

Vilain, D.P., Harris, R.S., 1984. *Attitude Determination and Control of the Hipparcos Satellite*. Annual Rocky Mountain Guidance and Control Conference, American Astronautical Society.

Vilain, D.P., Pauvert, C.M., 1985. *On-ground attitude reconstitution for the Hipparcos satellite*. IFAC Automatic Control in Space, 59.

Wagner, K., Halbwachs, J.L., 1996. *Double-star detection in the Tycho photon counts.* Workshop 'Visual double stars: foundation, dynamics and evolutionary tracks', Santiago de Compostela, Spain, 1996, Astrophysics and Space Space Science Library Series, Kluwer Academic Publishers

Walter, H.G., 1982. *Radio stars as connecting link of the Hipparcos and VLBI reference frames.* Proc. Strasbourg Coll. 'Scientific Aspects of the Hipparcos Space Astrometry Mission', 22–23 February 1982, Perryman, M.A.C., Guyenne, T.D. (eds), ESA SP-177, 65.

Walter, H.G., 1983. *Astrometric parameters determination.* Proc. Asiago Coll. 'Processing of Scientific Data from Hipparcos', The FAST Thinkshop, 24–27 May 1983, Bernacca, P.L. (ed.), 325.

Walter, H.G., 1983. *Recognition of grid step ambiguities.* Proc. Asiago Coll. 'Processing of Scientific Data from Hipparcos', The FAST Thinkshop, 24–27 May 1983, Bernacca, P.L. (ed.), 275.

Walter, H.G., 1985. *Generation of geometric and apparent star positions.* Proc. Marseille Coll. 'Processing of Scientific Data from Hipparcos', Second FAST Thinkshop, 21–25 January 1985, Kovalevsky, J. (ed.), 323.

Walter, H.G., 1986. *Astrometric treatment of double star abscissae*. Proc. Bari Coll. 'Processing of Scientific Data from Hipparcos', Third FAST Thinkshop, 3–6 November 1986, Bernacca, P.L., Kovalevsky, J. (eds), 223.

Walter, H.G., Frœschlé, M., Falin, J.L., Hering, H., Kovalevsky, J., Lenhardt, H., 1993 *Analysis of Hipparcos measurements: positions, proper motions and parallaxes.* IAU Proc. 'Developments in Astronomy and their impact on Astrophysics and Geodynamics', Mueller, I.I., Kolaczek, B. (eds.), 11.

Walter, H.G., Hering, R., 1988. *Revised positions and proper motions of radio stars.* Proc. Sitges Coll. 'Scientific Aspects of the Input Catalogue Preparation', 25–29 January 1988, Torra, J., Turon, C. (eds.), 487.

Walter, H.G., Hering, R., Bastian, U., Bernstein, H.H., 1985. *Astrometric parameter determination, methods, algorithms and program implementation*. Proc. Marseille Coll. 'Processing of Scientific Data from Hipparcos', Second FAST Thinkshop, 21–25 January 1985, Kovalevsky, J. (ed.), 281.

Walter, H.G., Mignard, F., Hering, R., Frœschlé, M., Falin, J.L., 1986. *Apparent and geometric star positions for the Hipparcos mission*. Manuscripta Geodaetica, 11, 103.

Walter, H.G., de Vegt, C., Kleine, T., 1985. *A critical examination of radio star data*. Proc. Aussois Coll. 'Scientific Aspects of the Input Catalogue Preparation', 3–7 June 1985, Turon, C., Perryman, M.A.C. (orgs), ESA SP-234, 241.

Westerhout, G., Hughes. J.A., 1982. *US Naval Observatory parallaxes and the fundamental reference frame: their interaction with Hipparcos.* Proc. Strasbourg Coll. 'Scientific Aspects of the Hipparcos Space Astrometry Mission', 22–23 February 1982, Perryman, M.A.C., Guyenne, T.D. (eds), ESA SP-177, 69.

White, G.L., Jauncey, D.L., Preston, R.A., 1985. *A radio-optical frame tie programme in the southern hemisphere*. Proc. Aussois Coll. 'Scientific Aspects of the Input Catalogue Preparation', 3–7 June 1985, Turon, C., Perryman, M.A.C. (orgs), ESA SP-234, 259.

Wicenec, A., 1991. *Tycho/Hipparcos: A successful mission. First results and further improvements.* Rev. Mod. Ast. 4, 188.

Wicenec, A., Bässgen, G., 1992. *Tycho background determination and monitoring.* A&A, 258, 206.

Wicenec, A.J., Bässgen, G., Großmann, V., Snijders, M.A.J., Wagner, K., Bastian, U., Schwekendiek, P., Egret, D., Halbwachs, J.L., Høg, E., Makarov, V.V., 1993. *Data analysis and expected results of the Tycho mission*.

Astronomical Data Analysis Software and Systems III (ADASS), Crabtree D.R., Hanisch R.J., Barnes J. (eds.), A.S.P. Conference Series, Vol. 61, 147.

Wicenec, A., van Leeuwen, F., 1995. *The Tycho star mapper background analysis.* A&A, 304, 160.

Wielen, R., 1982. *Hipparcos proper motions.* Proc. Strasbourg Coll. 'Scientific Aspects of the Hipparcos Space Astrometry Mission', 22–23 February 1982, Perryman, M.A.C., Guyenne, T.D. (eds), ESA SP-177, 77.

Wielen, R., 1988. *Precise proper motions and positions of stars from a combination of fundamental catalogues with the Hipparcos Catalogue*. IAU Symp. 133, 'Mapping the Sky', Paris, 1–5 June 1987, Débarbat, S., Eddy, J.A., Eichhorn, H.K., Upgren, A.R. (eds)

Wielen, R., Dettbarn, C., 1985. *Hipparcos proper motions for open star clusters.* Proc. Aussois Coll. 'Scientific Aspects of the Input Catalogue Preparation', 3–7 June 1985, Turon, C., Perryman, M.A.C. (orgs), ESA SP-234, 145.

Wills, R.D., Tuohey, W.G., O'Mongain, E., Gardelle, J.P., 1986. *In-Orbit calibration of the Hipparcos Payload.* Proc. Bari Coll. 'Processing of Scientific Data from Hipparcos', Third FAST Thinkshop, 3–6 November 1986, Bernacca, P.L., Kovalevsky, J. (eds), 349.

Yoshizawa, M., Andreasen, G.K., Høg, E., 1985. *Astrometric and photometric estimators for Tycho photon counts.* A&A, 147, 227.

Zeis, E., Camus, J.P., Wills, R.D., van Katwijk, K., 1985. *The Hipparcos mission: overall approach for scientific performance assessment*. Proc. 36th Congress International Astronautical Federation, Pergammon.

APPENDIX E

THE HIPPARCOS MISSION COSTS

Project Costs

The following table summarises the costs of the Hipparcos mission to the European Space Agency, since the time of the project's acceptance within the Agency's mandatory scientific programme in 1980. These costs cover industrial development and management, satellite manufacture and testing, manpower, 'overhead charges', computer, travel, test facilities (ESTEC and external), launch, satellite operations, and all post-operation costs.

Item	Cost mixed (kAU) (1)	Cost 82 EC (MAU) (2)	Updated Cost 90 EC (MAU) (3)	Updated Cost 95 EC (MAU) (4)
A. Satellite development	225 221	177.6	259.6	337.0
B. ESA internal costs	49 506	39.0	57.0	74.1
C. Launch	41 391	32.6	47.7	62.0
D. Satellite operations	70 590	55.7	81.3	105.7
E. Science operations	817	0.6	0.9	1.2
Total	387 525	305.5	446.5	580.0

Economic Conditions

In the table, 'cost' refers to the 'cost at completion' in ESA terminology, with figures calculated in 'accounting units' (or AU; in 1990 and 1995, 1 AU = 1 ECU) according to specific economic conditions (EC). The columns having the following meanings:

(1) cost to completion in 'mixed economic conditions'. Basically the cumulative costs reflect the actual prices in the year for which the costs were incurred, up to 1995. These costs, therefore, ignore the effects of inflation. Since these costs were directly accountable, they are presented at the level of kAU.

(2) the formally backdated cost at '1982 economic conditions', using a backdating index of 0.7882. Backdated costs must be taken as indicative, since the actual costs were not tracked on this basis (columns 2–4 are therefore presented only at the level of MAU).

(3) the backdated cost at 1982 economic conditions (column 2) updated to 1990 economic conditions, using the Wiesbaden indices for the total ESA scientific programme. These combine the weighted price variation and the weighted conversion rate variation of the AU, together resulting in an updating index of 1.4616. Costs in 1990 economic conditions can be transformed to national currencies using the relevant exchange rates (for example, average 1990 conversion rates were 6.926 FF, 2.059 DM, 0.715 GBP, or 1.223 $ per AU).
(4) as column 3, but updated to 1995 economic conditions, resulting in an updating index of 1.8989. Costs in 1995 economic conditions can be transformed to national currencies using the relevant exchange rates (for example, average 1995 conversion rates were 6.545 FF, 1.865 DM, 0.835 GBP, or 1.331 $ per AU).

Columns (1–4) include the additional contributions to the operations costs incurred as a result of the non-nominal orbit. These costs, which were met from outside of the scientific programme (4700 kAU in 1990, 7227 kAU in 1991, and 6941 kAU in 1992) amounted to 18 868 kAU (mixed economic conditions) or 12 162 kAU (backdated to 1982 economic conditions). Without these additional costs, the cost at completion in 1982 economic conditions was 293 302 kAU, to be compared with a target envelope cost of 243 750 kAU at the time of the project's acceptance, again in 1982 economic conditions, a cost over-run of 20 per cent over the 15 year project duration. Part of these cost over-runs were attributed to the launch delay of almost one year resulting from Ariane launch delays. A small part, approximately 2 MAU, was attributed to the inclusion of the Tycho experiment in 1981. The target envelope cost updated to 1990 or 1995 economic conditions would be 356.3 MAU or 462.9 MAU respectively.

Breakdown of Project Costs

The figures in the table cover the following items:
(A) Satellite development: these costs include the industrial costs during the project definition phase (Phase B) (9%); and the industrial cost for the development of the satellite (including spacecraft, payload, and all sub-systems), i.e. Phase C/D, as well as the industrial support for launch preparations (91%). [Phase A studies were funded outside the scientific programme.]
(B) ESA internal costs: these costs include the cost for ESA project management (67%), technical support within ESTEC (9%), and the utilisation of test facilities (24%). [These are further broken down as follows. The principal contributions to the costs for ESA project management comprised the salary of permanent ESA staff associated with the project (37%); missions (travel) of ESA staff during the project lifetime (8%); and ESA internal overheads (50%). The remaining costs (5%) were incurred for local and part-time staff, young graduates, packing and freight, public relations and international affairs, rental of internal ESTEC facilities, technical consumables and spare parts, 'experts and consultants' including the Hipparcos Science Team, software development, costs of the ESA team at the launch range, and mission specific launch services. The costs for technical support covered ESTEC manpower (50%) and ESA internal overheads (50%). The cost for test facilities comprises the cost for utilising ESTEC and coordinated test facilities (95%), and ESA internal overheads (5%).]
(C) Launch: this was the cost to ESA of the shared Ariane 4 launch of the Hipparcos satellite (dual launch with TV-SAT2).

(D) Satellite operations: this covered the total cost for the satellite operations, broken down into the cost for development of the Mission Operations Centre at ESOC (15%), operational costs at ESOC (60%), and ESA internal overheads (25%). The spacecraft operations costs covered permanent staff and contractual manpower at ESOC, computers and associated equipment, and the operation of all four ground stations, including industrial manpower, dedicated equipment, data communications, and tracking, telemetry and ranging. The cost figure includes the additional costs incurred by the non-nominal orbit (see above) which were funded by a Council contribution outside the 'science level' of the ESA scientific programme.

(E) Science operations: the total cost to ESA of the three-year post operational phase, including external contracts, and 'experts and consultants' including the Hipparcos Science Team costs, covering the costs of coordinating and supervising the catalogue completion, publication, and archival on ASCII CD-ROM. The printed catalogue publication costs do not appear under this heading, since they are intended to be fully covered by catalogue sales.

These figures are finally supplemented by the cost of the ESA Project Scientist (one ESA staff member for 16 years), and approximately one man-year of contractual support related to the preparation of the final mission products financed from within the ESA Space Science Department.

Costs of the European Scientific Participation in the Mission

Detailed estimates of the additional costs of the mission incurred through the participation of the scientific consortia, as funded directly by participating nations, are less easy to quantify than the ESA project costs, due to the different accounting procedures, charging policies, and incompleteness of detailed records. The total involvement of nearly 200 scientists within the four scientific consortia, would probably correspond to some 60 man-years per year averaged over the 16 year lifetime of the project (INCA 25; NDAC 7; TDAC 8, FAST 20), supplemented by the appropriate computer, infrastructure, and travel costs. An indicative cost of around 80 MAU (1990 economic conditions) would probably be a realistic estimate, but this figure must be viewed as somewhat dependent on the charges for overheads, computer resources, etc.

APPENDIX F

THE HIPPARCOS SATELLITE DURING DEVELOPMENT

Figure F1. *(top): the beam combiner at REOSC during verification. The clearly defined inner reflective part of each mirror half was a flat surface for alignment purposes. The support structure minimised loads during on-ground activities.*

Figure F2. *(bottom): preparation of the spherical mirror wavefront error test, Zeiss, Germany (1987).*

ESA 86.09.026-025

ESA 86.09.026-118

Figure F3. *(top): integration of the spherical mirror into the flight model telescope structure, Matra, Toulouse (1987).*

Figure F4. *(bottom): alignment of the flight model telescope at Matra (1987); the baffle entrance aperture is visible at the front.*

Figure F5. *The payload, in its 'clean tent', in preparation for thermal vacuum testing, Liège, October 1986 (courtesy D. Morin).*

ESA: picture report 88077.1

Figure F6. *Integration of the satellite flight model. The payload is at the top, enclosed in its thermally protective multi-layer insulation. The satellite subsystems are the black boxes lying between the two lower horizontal plates. The apogee boost motor is at the bottom.*

Figure F7. *The Hipparcos spacecraft qualification model in preparation for vibration tests at Intespace, Toulouse.*

Figure F8. *The satellite flight model in ESTEC's Large Solar Simulator undergoing thermal vacuum testing, at a spin rate of 5 rpm.*

Figure F9. *Testing of the Hipparcos satellite thermal model using the solar simulation facilities at IABG, München (1987).*

ESA: 88.04.022.002

Figure F10. *Satellite testing (including electrical checkout tests) at ESTEC (1988).*

ESA: picture report 88075.2

Figure F11. *The Hipparcos satellite in the Large Solar Simulator, ESTEC, February 1988. In these tests of the satellite's thermal equilibrium under simulated solar illumination, the solar panels are in their stowed (launch) configuration.*

ESA: picture report 88096.2

Figure F12. *The Hipparcos satellite in the Large Solar Simulator, ESTEC, February 1988, with solar panels deployed.*

Figure F13. *The Main Control Room at ESOC.*

Figure F14. *The Hipparcos satellite before launch, at CSG, Kourou (Photo CSG Kourou).*

INDEX